HAKONE XIII

International Symposium on High Pressure Low Temperature Plasma Chemistry

25th Anniversary

Book of Contributed Papers



Kazimierz Dolny, Poland
September 9-14, 2012

HAKONE XIII

International Symposium on High Pressure
Low Temperature Plasma Chemistry

25th Anniversary

Book of Contributed Papers







Kazimierz Dolny, Poland
September 9-14, 2012

Book of Contributed Papers of 13th International Symposium on High Pressure Low Temperature Plasma Chemistry.

Symposium organized by

Institute of Electrical Engineering and Electrotechnologies
Lublin University of Technology

Commission of Low-Temperature Plasma Chemistry
Polish Academy Of Sciences
Branch in Lublin

Editors: Local Organizing Committee

© Copyright by Politechnika Lubelska
ISBN: 978-83-62596-99-7

Publisher: Lublin University of Technology
Realization: Lublin University of Technology Library
Ośrodek ds. Wydawnictw i Biblioteki Cyfrowej
www.biblioteka.pollub.pl
Print: TOP Agencja Reklamowa Agnieszka Łuczak
www.agencjatop.pl

PREFACE

25 years already passed from 1987 informal meeting of few ISPC'8 Participants in Japan that has given origination for HAKONE meetings – HIGH PRESSURE LOW TEMPERATURE PLASMA CHEMISTRY SYMPOSIUMS.

Professor Iwo Pollo was one of the HAKONE Initiators and the LOC Chairman of the HAKONE II in Kazimierz Dolny in 1989. Then, Polish Group has regularly participated in successive meetings in France (1991 and 2008), Slovakia (1992 and 2011), Czech Republic (1996), Ireland (1998), Germany (2000), Estonia (2002), Italy (2004) and Japan (1987, 2006). Prof. Iwo Pollo was co-chairing the International Scientific Committee of HAKONEs up to 2005, being ever and forever the Good Spirit of HAKONE symposiums. His attitude to the scientific work and contribution to the HAKONE symposiums' story is for us unforgettable guidepost.

HAKONE Symposium traditionally gathers scientists and engineers working on atmospheric pressure low temperature plasma chemistry, physics and engineering. The scope of the conference is devoted to theoretical mechanisms of dielectric barrier and corona discharges for ozone synthesis, basic oxidants generation and applications in water treatment and environment protection. Every next Hakone, the area of interest has being extended to new emergent and innovative fields of research and development, like biomedical plasma application, surface modification, micro-plasmas, alternative materials, fuels and other interdisciplinary plasma topics.

This year, for the second time, Poland and Kazimierz Dolny have a pleasure to welcome 85 HAKONE XIII Participants from 16 countries from Europe, Asia and North America. Meeting contains 6 invited lectures, 20 oral presentations and more than 50 poster presentations in the 9 scientific topics.

The proceedings of HAKONE XIII enclose about 80 contributed papers. The Authors submitted their papers as a camera ready electronic files. No correction of the papers were made and Authors are responsible for the scientific and technical contents of their contributions. 26 papers chosen by the Reading Committee of HAKONE XIII will be recommended after extension and peer review for publication in European Journal of Applied Physics, the next 20, dedicated to applied electrical engineering, will be suggested for publication in the Polish Electrotechnical Review.

LOC wishes all Participants of HAKONE XIII fruitful exchange of new results and ideas as well as enjoyable stay in Kazimierz Dolny. We believe that symposium will be creative and contribute to the further development in the area of high pressure low temperature plasma chemistry, physics and engineering.

In the name of LOC
Henryka Danuta Stryczewska

Poland, Lublin, Kazimierz Dolny, September 2012



Professor Iwo POLLO

MEMOIRS

Professor Iwo Pollo from Lublin Technical University, was a great Contributor, Chairman and Organizer of previous HAKONE meetings, who to our deepest grief passed away in 2005.
He was born in 1927 in Delatyń. After completing chemical studies in 1954 he started work in Chemical Compounds Factory and afterwards he became a scientific worker in Silesian University. Main scope of his research was synthesis of nitrogen oxides in glow discharges in the cooperation with the famous school of electrochemistry of Moscow University. In 1975 he became a professor of Lublin Technical University, where he set up the Department of Chemical Technology, which he chaired for 20 years.
Prof. Pollo was a leader and spiritual guide of a large group of his co-workers: scientists, academic teachers and students. He developed studies on various plasma processes for environmental and industrial purposes, which gained international acknowledgment. He was also vice-President (1984-1990) and President (1993-1996) of Lublin Technical University and also important member of many scientific boards and organizations (PAS, IUPAC, IOA, etc.). He was an erudite, polyglot and poet having extremely broad knowledge and teaching talent. Despite of his high academic position he was also a very understanding, modest person. This natural kindness, which unfortunately becomes more and more rare in present times, made him the way to all his students and co-workers' hearts fully opened. After Professor Pollo's first visit in Japan he developed deep interest in culture and language of this country, gaining there many friends, starting international cooperation and one of His many collections: of Japanese pottery, books, and paintings.
Also at present, after 7 years of his absence forever, Professor Iwo Pollo is beloved and missed by many of us.

Local Organizing Committee

Lublin, Kazimierz Dolny, September 2012

International Scientific & Organizing Committee

Miroslav Cernak	(Czech Republic)
Nicolas Gherardi	(France)
Tony Herbert	(Ireland)
Haruo Itoh	(Japan)
Ulrich Kogelschatz	(Switzerland)
Masuhiro Kogoma	(Japan)
Kirill Vadimovich Kozlov	(Russia)
Matti Laan	(Estonia)
Stefan Matejcik	(Slovakia)
Jerzy Mizeraczyk	(Poland)
Cristina Paradisi	(Italy)
Henryka-Danuta Stryczewska	(Poland)
Hans-Erich Wagner	(Germany)
Chobei Yamabe	(Japan)

Local Organizing Committee
(Lublin University of Technology)

Prof. Tadeusz Janowski - honorary chairman
Prof. Henryka D. Stryczewska - chairman
Prof. Justyna Jaroszyńska-Wolińska
Prof. Janusz Ozonek
Dr Grzegorz Komarzyniec
Dr Joanna Pawłat
Dr Jarosław Diatczyk
M. Sc Renata Jaroszyńska - secretary

Reading Committee

Prof. Jerzy Mizeraczyk
Prof. Zbigniew Kołaciński
Prof. Janusz Ozonek,
Prof. Justyna Jaroszyńska-Wolińska
Prof. Henryka Danuta Stryczewska
Dr Joanna Pawłat

Organizers

Institute of Electrical Engineering and Electrotechnologies
Lublin University of Technology

Commission of Low-Temperature Plasma Chemistry
Polish Academy Of Sciences
Branch in Lublin

ACKNOWLEDGMENT

HAKONE XIII gratefully acknowledges the sponsorship and financial support of The Polish Academy of Science PAN.

POLSKA AKADEMIA NAUK
ODDZIAŁ W LUBLINIE

THE LUBLIN BRANCH OF THE POLISH ACADEMY OF SCIENCES

ODDZIAŁ POLSKIEJ AKADEMII NAUK W LUBLINIE

Pałac Czartoryskich, Plac Litewski 2,
20-080 Lublin
phone/fax: 48 (81) 441 30 00
e-mail: lublin@pan..pl
www.pan-ol.lublin.pl

Presidium:
President: Professor **Tomasz Trojanowski**, Corresponding Member of the Academy
Vice-President: Professor **Jan Gliński**, Full Member of the Academy
Vice-President: Professor **Marian Truszczyński**, Full Member of the Academy



The Czartoryski Palace – the seat of the Lublin Branch of the Polish Academy of Sciences

The Lublin Branch was established on May 23, 1997. It presently includes 12 members of the Academy. In accordance with its statutes, the Branch helps to integrate the academic life of the region in cooperation with all its universities and research institutes, especially in the two main scientific centers of the region – Lublin and Puławy – which include about 7,000 scientists and 100,000 students. It maintains a close relationship with the only institute of the Polish Academy of Sciences in this region of Poland: the Institute of Agrophysics in Lublin. The Branch also supports and carries out research of considerable importance for the national economy and culture, with special consideration given to the Lublin region. The Branch also helps local authorities with their strategic innovation programs for the Lublin voivodship. The Branch plays an integrative role, both among local scientific institutions and between them and public administration.

The Branch operates in the Lublin and Podlasie Voivodships and it is the only Polish Academy of Sciences branch situated on the right bank of the Vistula river. That is why it considers cooperation with scientific centers in neighboring countries – Ukraine, Belarus, Russia, and Lithuania – to be especially important. The Branch has gained wide acceptance in the region, as has been confirmed by local scientific and administrative authorities.

There are 18 scientific commissions operating within the Branch (together with about 600 members), covering various disciplines represented by the universities and institutes of the region: humanities, technological sciences, agriculture, environment protection, medicine, economics, legal studies, architecture, and theology. The results of the commissions' work are published in the *TEKA, MOTROL and ECONTECHMOD* journals (presenting the files of commissions) and monographs published by the Lublin Branch. Every year are organized about 10 national and international conferences in cooperation with Polish and foreign partners. As an example of some important international conferences from last years: Theary of administrative sciences – devoted to works of Professor J. Stephan Langrod (Paris Scientific station PAN), V International conferences ENERGY (Lviv International University of Agriculture in Dublany),. V Conference on Problems of diagnosis, treatment and prophylaxis of a disabled child (Lublin). Together with the Lublin Society of Science there are organized once a month popular lectures WSZECHNICA.

Once a year the Branch issues an *Information Booklet* about the 42 teaching and research institutions in the Lublin region, a *Bulletin* presenting the Branch's activities, scientific research, and events, and biographies of distinguished scholars associated with the region. A quarterly journal *Maintenance and Reliability* is also published under the auspices of the Branch. Additionally, a bilingual website is being continuously updated and developed.

The Branch has established a Foundation of the Polish Academy of Sciences entitled "Science and the Development of the Lublin Region." Its main goal is to support the scientific, social, and economic activities associated with the development of junior scientific staff, the transfer of scientific achievements towards business and use of European funds in educational programs.

TABLE OF CONTENTS

INVITED LECTURES

PLASMA FOR SAVING ENERGY, HEALTH AND ENVIRONMENT
Zbigniew Kolacinski 1

PROTON TRANSFER REACTION-MASS SPECTROMETRY: FUNDAMENTALS, RECENT ADVANCES AND APPLICATIONS
T.D.Märk, B.Agarwal, K.Becker, A.Edtbauer, S.Feil, S.Haidacher, G.Hanel, E.Hartungen, S.Jaksch, A.Jordan, S.Jürschik, C.A.Mayhew, L.Märk, F.Petersson, H.Seehauser, R.Schottkovsky, P.Sulzer 6

PHOTO AND BACKGROUND IONIZATION/STREAMER PROPAGATION
S. Nijdam, E.M. van Veldhuizen, U. Ebert 10

DECOMPOSITION OF PERFLUORO COMPOUNDS IN WATER USING DISCHARGE PLASMA
Koichi Yasuoka 15

ORAL PRESENTATIONS

STUDY OF HIGH-SPEED CAMERA MEASUREMENT OF 6 ELECTRODES TYPE GLIDING ARC SYSTEM AND A NEW PRE-IGNITION SYSTEM
Shin-ichi Aoqui, Fumiaki Mitsugi, Tamiko Ohshima, Hiroharu Kawasaki, Toshiyuki Kawasaki 23

EXCITED ATOMS IN CAVITIES OF LIQUID HE I: LONG-RANGE INTER-ATOMIC REPULSION AND BROADENING OF ATOMIC LINE
V.M. Atrazhev J. Eloranta N. Bonifaci, Hai van Nguyen, F Aitken, K von Haeften, G Vermeulen 28

OPERATION MODES IN BARRIER DISCHARGES: DISCHARGE DEVELOPMENT AND SURFACE CHARGE ACCUMULATION
Marc Bogaczyk and Hans- Erich Wagner 33

TEMPORALLY AND SPATIALLY RESOLVED INVESTIGATION OF PULSED DRIVEN BARRIER MICRODISCHARGES IN REACTIVE GASES
Ronny Brandenburg, Tomáš Hoder, Hans Höft, Manfred Kettlitz, Klaus-Dieter Weltmann 38

HYDROGEN PRODUCTION FROM BIOMETHANE USING DBD
Mirosław Dors, Tomasz Izdebski, Jerzy Mizeraczyk, Marek Kocik 43

DECOLORATION OF WATER CONTAMINATED BY DYES USING NON-THERMAL PLASMA
Tomasz Izdebski, Mirosław Dors, Jerzy Mizeraczek 48

TEMPERATURE EFFECTS UNDER OZONE SYNTHESIS PROCESS CONDITIONS
Sławomir Jodzis 53

OXIDATION OF NITROGEN OXIDE IN HYBRID PLASMA-CATALYTIC REACTORS BASED ON DBD AND Fe_2O_3
Indrek Jõgi, Kalev Erme, Ants Haljaste, Matti Laan.....58

AFFECT OF WATER AND OXYGEN ON THE CONVERSION OF METHANE AND CARBON DIOXIDE IN A PLUG FLOW REACTOR SUPPORTED BY A DBD
Torsten Kolb, Jan H. Voigt, Karl-Heinz Gericke.....63

METHANE CONVERSION WITH OXYGEN IN PLASMA-CATALYTIC SYSTEM
Krzysztof Krawczyk, Michał Młotek, Bogdan Ulejczyk, Krzysztof Pryciak, Krzysztof Schmidt-Szałowski.....68

BACTERICIDAL EFFECTS AND FORMATION OF ROS/RNS IN WATER SPRAYED THROUGH COLD AIR PLASMA
Z. Machala, B. Tarabová, P. Lukeš, E. Špetlíková, L. Šikurová, K. Hensel.....73

ATMOSPHERIC PRESSURE LOW-POWER MICROWAVE MICROPLASMA SOURCE FOR DECONTAMINATION OF MICROORGANISMS
Jerzy Mizeraczyk, Dariusz Czylkowski, Bartosz Hrycak, Mirosław Dors, Mariusz Jasiński.....79

DECOMPOSITION OF VOCS BY GLIDING DISCHARGE PLASMA
Michał Młotek, Ewelina Pawelska, Bogdan Ulejczyk, Krzysztof Krawczyk, Krzysztof Schmidt – Szałowski.....84

A METHOD OF GAS INTRODUCTION INTO THE PLASMA REACTOR EMPLOYING THE GLIDING DISCHARGE PRINCIPLES
Teresa Opalińska, Małgorzata Majdak, Janusz Piechna, Witold Selerowicz, Bartłomiej Wnęk.....89

GENERATION OF HIGH PRESSURE HOMOGENEOUS DIELECTRIC BARRIER DISCHARGE IN AIR
Naoki Osawa, Ami Takashi, Yoshio Yoshioka, Ryoichi Hanaoka.....94

LIGHTNING AS A NATURAL TOOL FOR AIR CLEANING FROM AN ENVIRONMENTALLY HARMFUL IMPURITIES BY LOW-TEMPERATURE PLASMA
A.Z Ponizovsky., S.G. Gosteyev.....99

SPENT OIL DEGRADATION BY GLIDING ARC DISCHARGE
Maria Prantsidou, J. Christopher Whitehead.....104

THE ROLE OF BARRIER SURFACE PROPERTIES IN BARRIER SURFACE DISCHARGE BEHAVIOUR
M.V. Sokolova, K.V. Kozlov, A.N. Mitin, P.A. Tatarenko.....111

SIMULTANEOUS REMOVAL OF ACETALDEHYDE AND ACETYLENE BY AN ATMOSPHERIC PULSED DISCHARGE
Touchard S., Klett C., Jia Z.,Vega-Gonzalez A., Hassouni K., Duten X.....116

OPTIMIZATION OF SONICATION TREATMENT PROCESS TO SATURATED FREE FATTY ACIDS DEGRADATION AS AN APPLICATION IN GREASE TRAP PURIFICATION
Michał Piotr Kwiatkowski, Saburoh Satoh, Chobei Yamabe, Satoshi Ihara, Masanori Nieda.....121

POSTER PRESENTATIONS

INFLUENCE OF THE APPLIED VOLTAGE SHAPE ON THE BARRIER DISCHARGE OPERATION MODES IN HELIUM
Marc Bogaczyk, Goran B. Sretenović , Hans-Erich Wagner 129

APPROACH OF THE SIMPLEST EQUIVALENT CIRCUIT FOR DETERMINATION OF CHARGE TRANSFERRED THROUGH THE GAS GAP IN PULSED DIELECTRIC BARRIER DISCHARGE
Andrei V. Pipa, Tomáš Hoder, Jeff Koskulics, Ronny Brandenburg.....134

TREATMENT OF WATER AND SUSPENDED *E.COLI* WITH OZONE AND DBD EXHAUST GAS IN COMPARISON WITH DIRECT DBD TREATMENT: LIQUID CHEMISTRY AND ANTIMICROBIAL EFFECTS
Katrin Oehmigen, Ronny Brandenburg, Klaus-Dieter Weltmann, Thomas von Woedtke 139

OZONE-MIST SPRAY STERILIZATION FOR PEST CONTROL IN AGRICULTURAL MANAGEMENT
Kenji Ebihara, Fumiaki Mitsugi, Tomoaki Ikegami, Norihito Nakamura,
Yukio Hashimoto, Yoshitaka Yamashita,Seiji Baba, Henryka D.Stryczewska,
Joanna Pawlat, Shinriki Teii, Ta-Lun Sung 144

NANOPARTICLES CONTAINING COATINGS DEPOSITION ASSISTED BY ATMOSPHERIC PRESSURE PLASMA JET
Marina Fantin, Paolo Scopece, Stefano Costacurta, Alessandro Patelli, Marino Colasuonno,
Arianna Gambirasi, Monica Favaro 149

RESONANT INVERTER WITH RESONANCE FREQUENCY TRACKING FOR DBD PLASMA REACTOR SUPPLY
Tomasz Jakubowski, Marcin Hołub, Stanisław Kalisiak 155

THE APPLICATION OF DC ATMOSPHERIC PRESSURE GLOW DISCHARGES GENERATED IN CONTACT WITH FLOWING LIQUID CATHODE IN THE DISCHARGE TREATMENT WATER PROCESSES
Piotr Jamróz, Krzysztof Gręda, Paweł Pohl and Wiesław Żyrnicki.....160

OZONIZERS OF UNCONVENTIONAL GAS FLOW ORGANIZATION
Sławomir Jodzis 165

VISUALISATION OF UNDERWATER PULSED DISCHARGE
S. Kanazawa, T. Sato, M. Kocik, J. Mizeraczek 170

DEGRADATION OF UNDECANE AND TOLUENE IN AIR BY WATER FALLING FILM DBD REACTOR
Vesna V. Kovačević, Ronny Brandenburg, Bratislav M. Obradović, Goran B. Sretenović,
Milorad M. Kuraica.....175

ANTIMICROBIAL ACTIVITY OF SODIUM CHLORIDE SOLUTION TREATED IN WATER FALLING FILM DBD REACTOR
Vesna V. Kovačević, Mareike Hänsch, Ronny Brandenburg, Thomas von Woedtke,
Bratislav M. Obradović, Goran B. Sretenović, Milorad M. Kuraica.....180

STABILIZATION OF A LEAN METHANE–AIR FLAME USING TRANSIENT SPARK DISCHARGE
M. Janda, Z. Machala, D. A. Lacoste, G. D. Stancu, C. O. Laux.....185

BIOFILM INACTIVATION ON TEETH AND PLASTIC SURFACES WITH DC CORONA DISCHARGES
Zuzana Šipoldová, Zdenko Machala 190

PULSED CORONA DISCHARGE FOR THE DEGRADATION OF METHYLENE BLUE IN WATER
Monica Magureanu, Corina Bradu, Daniela Piroi, Nicolae Bogdan Mandache, Vasile Parvulescu 195

DEPOSITION OF THIN LAYERS CONTAINING TITANIUM AND BARIUM WITH THE USE OF DIELECTRIC BARRIER DISCHARGE PROPERTIES
Małgorzata Majdak, Teresa Opalińska, Bartłomiej Wnęk 200

OBSERVATION OF DYNAMIC BEHAVIOR OF GLIDING ARC DISCHARGE
Fumiaki Mitsugi, Jin Furukawa, Tamiko Ohshima, Hiroharu Kawasaki, Toshiyuki Kawasaki, Shin-ichi Aoqui, Henryka D. Stryczewska 205

A TOMOGRAPHIC VISUALIZATION OF ELECTRIC DISCHARGE SOUND FIELDS IN ATMOSPHERIC PRESSURE PLASMA USING LASER DIFFRACTION
T. Nakamiya, Y. Iwasaki, F. Mitsugi, T. Ikegami, R. Tsuda, and Y. Sonoda 210

SPATIO-TEMPORALLY RESOLVED DENSITY OF NITROGEN METASTABLES IN BARRIER DISCHARGES
Sebastian Nemschokmichal, Jürgen Meichsner 215

FORMATIONS OF NEGATIVE ION IN SF_6/N_2 MIXTURES
Yui Okuyama, Martin Sabo, Haruo Itoh, Štefan Matejčík 220

FLUORESCENCE OF METHANE INDUCED BY ELECTRON IMPACT
Juraj Országh, Marián Danko, Štefan Matejčík, Anita Ribar 225

PLASMA PARAMETERS AFFECTING DEPOSIT GROWTH DURING ARC CARBON NANOTUBES SYNTHESIS
Grzegorz Raniszewski 228

PLASMA ARC FOR CARBON NANOTUBES SYNTHESIS DEDICATED FOR MEDICAL APPLICATIONS
Grzegorz Raniszewski 233

TEMPORAL AND SPECTRAL CHARACTERISTICS OF ATMOSPHERIC PRESSURE PLASMA JET
Jüri Raud, Indrek Jõgi, Matti Laan 238

ANTIMICROBIAL PROPERTIES OF SULFUR CONTAINING COATINGS
Zenobia Rżanek-Boroch, Paulina Dziadczyk, Danuta Czajkowska, Krzysztof Krawczyk, Wojciech Fabianowski 243

ETHANOL CONVERSION IN THE DC ATMOSPHERIC PRESSURE AIR GLOW DISCHARGE
V.I. Arkhipenko, A.A. Kirillov, L.V. Simonchik, S.M. Zgirouski 248

SPECTROSCOPIC STUDY OF HELIUM DBD PLASMA JET
Goran B. Sretenović, Ivan B. Krstić, Vesna V. Kovačević, Bratislav M. Obradović, Milorad M. Kuraica 253

MECHANISM OF 4-CHLOROTOLUENE DECOMPOSITION IN AIR MIXTURE IN AN ELECTRON BEAM GENERATED NON-THERMAL PLASMA REACTOR
Yongxia Sun, A.G.Chmielewski 258

SECONDARY IONIZATION COEFFICIENT OF DIELECTRIC ELECTRODE MATERIALS
Susumu Suzuki, Yasuhide Kashiwagi, Haruo Itoh 263

MAGNETIC FIELD CONTROLLED CNTS SYNTHESIS IN AN ELECTRICAL ARC
Lukasz Szymanski, Grzegorz Raniszewski, Zbigniew Kołaciński 268

COMPACT PLASMA SYSTEM FOR ORGANIC COMPOUNDS DECOMPOSITION
Lukasz Szymanski 274

CARBON NANOTUBES DEPOSITION USING ATMOSPHERIC PRESSURE GLOW BARRIER DISCHARGE IN ARGON WITH ACETYLENE ADMIXTURE
Marek Elias, Petr Kloc, Ondrej Jasek, Vera Mazankova, David Trunec, Lenka Zajickova 279

DECOMPOSITION OF CHLORINATED ORGANIC COMPOUNDS USING NON-EQUILIBRIUM PLASMA REACTOR
Bogdan Ulejczyk, Krzysztof Krawczyk, Magdalena Hajduk, Marta Musiał, Bartłomiej Wnęk, Michał Młotek, Krzysztof Schmidt-Szałowski 284

COMPARATIVE STUDY OF DECOMPOSITION OF TETRACHLOROMETHANE USING DIELECTRIC BARRIER DISCHARGE POWERED BY DIFFERENT POWER SUPPLIES
Bogdan Ulejczyk, Krzysztof Krawczyk, Alicja Kosik, Michał Młotek, Krzysztof Schmidt-Szałowski, Łukasz Nogal, Bolesław Kuca 289

BREAKDOWN OF ORDER IN A SELF-ORGANISED BARRIER DISCHARGE
Robert Wild, Lars Stollenwerk 294

VUV IRRADIATION OF BIOLOGICAL OBJECTS
Galina Zvereva 299

POWER CONTROL OF GLIDING ARC DISCHARGE BY CHANGING THE TRANSFORMERS LEAKAGE REACTANCE
Grzegorz Komarzyniec 303

RF-POWERED ATMOSPHERIC PRESSURE PLASMA JET FOR SURFACE TREATMENT
Joanna Pawłat, Radosław Samoń, Tomasz Giżewski, Jarosław Diatczyk, Włodzimierz Janowski, Henryka D. Stryczewska 308

ANALYSIS OF OXIDATION NO AND NO2 WITH THE APPLIED LOW TEMPERATURE PLASMA PRODUCTS
Justyna Jaroszyńska-Wolińska 313

INVESTIGATION OF A HOMOGENEOUS DISCHARGE GENERATED IN A BARRIER DISCHARGE DEVICE USING ALUMINA
Yoshio Yoshioka, Naoki Osawa 318

MECHANISTIC STUDIES OF ADVANCED OXIDATION OF BINARY MIXTURES OF ORGANIC POLLUTANTS IN AIR NON-THERMAL PLASMA
Ester Marotta, Milko Schiorlin, Elisa Ceriani, Volodymyr Shapoval, Cristina Paradisi 323

DIELECTRIC BARRIER TOWNSEND DISCHARGE IN AIR AT ATMOSPHERIC PRESSURE
Haiyun Luo, Junxia Ran, Xinxin Wang 324

AUTHOR INDEX 327

INVITED LECTURES

PLASMA FOR SAVING ENERGY, HEALTH AND ENVIRONMENT

Zbigniew Kolacinski

Technical University of Lodz, Institute of Mechatronics and Information Systems, 18/22 Stefanowskiego Street, 90-924 Lodz, Poland
E-mail: zbigniew.kolacinski@p.lodz.pl

Plasma aided manufacturing is the use of charged particles for producing new materials with unusual and superior properties. The near LTE plasma is a nice tool for material engineering which in consequence upgrades performance of most of the consumer goods. The paper presents few samples of the own research results related to toxic or hazardous materials destruction with their conversion into valuable products and synthesis of nanomaterials showing their application for supercapacitors for energy store and application as carriers for biological cell destruction.

1. Introduction

Thermal plasma in the state of LTE (Local Thermodynamic Equilibrium) or near LTE (in a reduced pressure) can be an efficient medium for breaking bonds of unwanted molecular chains and/or the synthesis of wanted chains to generate new materials or their composites. Some examples of plasma application for materials engineering are here presented. They are focused on synthesis of nanomaterials represented by carbon nanotubes (CNTs) and on gas or fluid waste destruction and especially on solid waste conversion into valuable materials or products. Applications of nanotubes cover numerous disciplines including construction, manufacturing, medicine, electronics, nanotechnology, and so on.

The arc and microwave plasma reactors will be applied for CNTs synthesis. In the field of gas and fluid waste treatment three plasma reactors with cylindrical and divergent channels have been used in the laboratory testing. The arc was magnetically driven between electrodes, which resulted in fast arc expansion and a thermal tail formation called the near LTE dispersed plasma. These plasma reactors have been successfully used in thermal destruction of chlorinated wastes. A furnace with the arc-plasma immersed in the feed charge has been elaborated for solid waste treatment purposes. The theory of utilization of materials by electric arc has been verified by experimental tests in the laboratory furnace presenting some end-products.

2. Plasma assisted energy saving

The properties of plasma synthesised CNTs are certainly amazing; but even more remarkable are the countless applications that may be possible when these newly discovered materials are integrated into mainstream products. This will be demonstrated on the development of supercapacitors only. The supercapacitors can be vastly used in Kinetic Energy Recovery Systems (KERS) for mobile vehicles, for frequently starting/stopping machines to storage of harvested energy etc. Electrochemical double layer capacitors have in comparison to dielectric capacitors a significantly higher energy density. Their high capacity is based on the large electrode surface and the dissociation of ions in a liquid electrolyte, which forms a dielectric of a few atomic layers; therefore define distances in the range of a nanometer. In contrast, the electrode gaps in ordinary dielectric capacitors lie in micrometer range. Supercapacitors consist of two electrodes, which are surrounded by a electrolyte. When voltage is applied, that has to be smaller as the decomposition voltage of the electrolyte. Ions of opposite polarity form a few molecular layers. The electrodes form over the electrically conductive electrolyte, two capacitors connected in series, which store energy electrostatically. The electrostatic form of energy storage allows a fast retrieve of the accumulated charge carriers and high peak loads. Besides the the distance between the electrodes the capacity of a capacitor depends on the size of the electrode surface. Because of its large surface activated carbon is frequently used as electrode material. A further enlargement of the surface can be obtained by the use of carbon nanotubes. They have a very

fine “nano-porosity” for the absorption of electrolytes, which acts as a nanoscale dielectric. In Fig.2 a layer of 150 micrometer forest of multiwall carbon nanotubes (MWNTs) received in our experimental setup (Fig.1) is shown. The MWNTs forest gives enormous increase of the electrode working surface. The layer of forest is oryginally uniform in structure however the scratch seen in Fig.2 has been specially done to measure the thickness of the MWNTs layer. With such electrodes very high capacities can be achieved, which enables a high charge storage at relatively low voltages. As recent studies have shown, SWNTs have an electrical capacity of up to one electron per 32 carbon atoms [1] but MWNTs should be even more efficient.
Several years ago, the intensive research of CNTs based supercapacitors started. The results show a large variability of the achieved capacity as a function of the physical properties of the particular nanotubes (diameter, length, chirality, SWNT, MWNT, etc.) Furthermore the method of production is important. The following table list some reached capacity values of CNT based electrodes [1].

Tab.1 Capacity values of CNT based electrodes [1].

Source	CNT Type	Capacity (F/g)
[Niu, 1997]	MWNT (Arc discharge)	49-102
[An, 2001]	MWNT (Arc discharge)	71
[Ma, 1999]	MWNT (CVD)	15-25
[Ren, 2002]	MWNT (CVD)	115
[Frackowiak, 2001]	SWNT	18-40
[Frackowiak, 2001]	MWNT (CVD)	36-172
[Shiraishi, 2002]	SWNT (Arc discharge)	45
[Emmenegger, 2002]	MWNT (CVD)	10

In our laboratory we are using the arc discharge and microwave plasma methods for CNTs synthesis. The photo of microwave plasma reactor is shown in Fig. 1 and a received forest of MWNTs carbon nanotubes in Fig. 2. The table below presents some values, that are needed by listed vehicles only to start moving in 6 seconds (or to take off) of different vehicles assuming voltage on capacitors equal to 200 V and comparing of traditional capacitors and supercapacitors with nanotubes [1]

Tab. 2. Comparison nanotechnology vs traditional capacitors for vehicles start.

		Nanotechnology		Traditional capacitors	
Type of vehicle	Power needed	Weight/kg	Size/m^3	Weight/kg	Size/m^3
Usual car (1300kg)	75 kW	2,4	0,002	20,2	1,2
Usual bus	180 kW	6,0	0,01	50,0	2,5
Little airplane	70 kW	2,2	0,002	18,9	1,1

Most of the personal cars has the power of 75kW. To store such energy in traditional capacitors the volume required is about $1m^3$.. The weight of capacitors will be equal to 20kg. In the case of nanotechnology use, dimensions of such a device will be much smaller. Supercapacitors storing amount of energy to release 75kW of power weight only 2.4 kg. This is the only one energy saving example in many other applications.

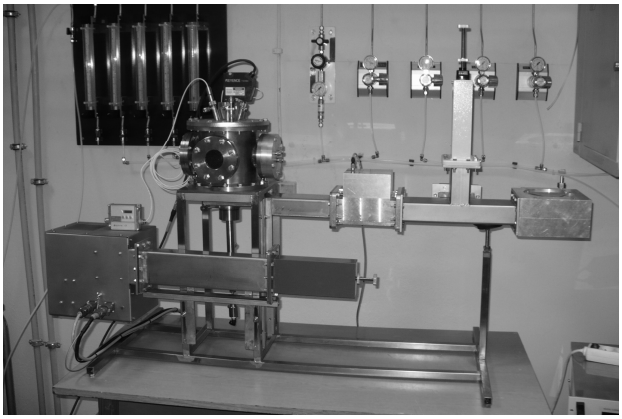


Fig. 1 Microwave plasma set up

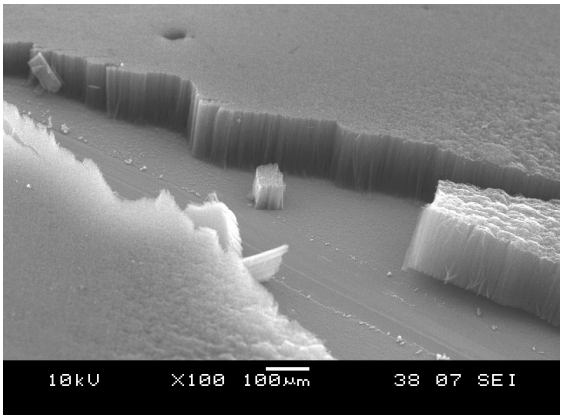


Fig. 2 SEM photo of MWNTs forest

3. Plasma made nanomaterials for cancer treatment

Nanotechnology has become a new opportunistic and dynamically developing brand of today's industry and it has been found to have various prospective applications in medicine as well. Some of these applications exist still only as futuristic approaches while others are at the experimental stages or have already been introduced to the market. Nanomedicine ranges from the medical applications of nanomaterials to nanoelectric biosensors and applications of molecular nanotechnology. Nanotechnology innovations are implicated in several medical fields as: diagnostic and imaging techniques, therapy techniques, drug delivery, anti-microbial techniques and cell repair.

The classification made regarding to specific areas of medicine includes: drug delivery/ drug targeting/drug release, molecular imaging/ biophotonics/ medical imaging, biochips/ high throughput, screening/ lab-on-chip devices, biomolecular sensors.

Another approach to treat cancer involves destroying cancer cells via hyperthermia. One of currently used method is RF ablation. Although, it is today used in clinical practice, this therapy suffers from serious drawbacks. RF currently is an invasive treatment that requires the insertion of needle electrodes directly into the tumour to be treated. According to the report prepared by the University of Texas, incomplete tumour destruction occurs in from 5% to 40% of the treated lesions. Moreover, the treatment is nonspecific and induces thermal necrosis in both malignant and normal tissues surrounding the needle electrode and complications related to thermal injury to normal tissues arise in up to 10% of patients. Finally, invasive RF is limited to the treatment of tumours in only a few organ sites (liver, kidney, breast, lung, bone) [3]. On the other hand, it is known that the tissue penetration by RF energy fields is excellent. Thus, non-invasive RF treatment of malignant tumours at any site in the body should be possible if agents that convert RF energy into heat can be delivered to the malignant cells.

The latest idea to solve this problem is Kanzius RF Therapy [2] that aims to insert metallic nanoparticles in or around cancerous cells and then exciting these particles using radio waves The energy from the radio waves creates heat which burns the cancerous cells. This technique is in developmental and experimental stages in our laboratory. Our plasma reactors are able to make ferromagnetic CNTs which can be the activators of cancer cell destruction.

4. Plasma for waste treatment

Effective destruction of gaseous organic compounds requires optimization of three process parameters: temperature, time and turbulence, which is known as "3-t principle". One way of an effective treatment of gaseous wastes is to allow them to pass through the dispersed plasma bulk to be treated by the highest temperature produced in the plasma generator. The dispersed thermal plasma is in here a high-pressure arc discharge, which moves fast enough to produce effective linear plasma dispersion. This kind of plasma can be produced in plasma reactors for effective treatment of gaseous or liquid (atomised) wastes allowing them to pass through the plasma wall. Generation of such plasma bulk can be done by fast rotation of the DC arc between electrodes. In our laboratory we have designed the

ROTARC and SPIRARC reactors to be used for decomposition of chloroorganic gaseous wastes. The raectors principle is presented in Fig. 3 and Fig.4.
In this two systems the electric arc is ignited in a co-axial setup of two electrodes and it is driven by an external magnetic field produced by axial magnetic coil. These results in creation of not uniform plasma bulk in a shape of an open ring. The rotating arc temperature behavior is similar to the comet view with a hot head and a cooler tail The more power is dissipated in the arc column and the faster is the arc rotation the shorter is the non-thermal plasma gap in the open ring. On the other hand the arc rotation is necessary to avoid excessive vaporization of the electrodes. If gaseous organic waste is forced to cross the plasma bulk the chemical bonds are broken and the waste can be decomposed. Some results of chlorinated gaseous destruction with the ROTARC plasma generator were already presented [4]. The destruction efficiency better than 99.999% has been achieved.

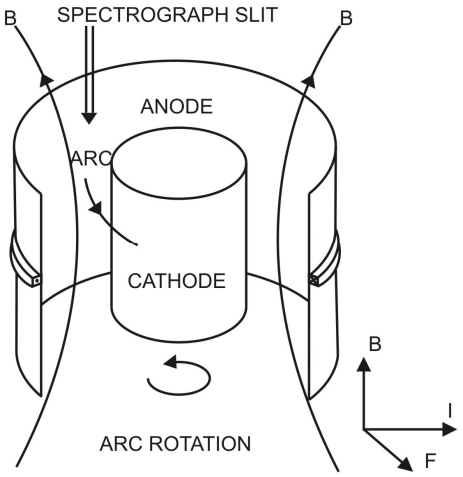


Fig.3 ROTARC plasma reactor principle

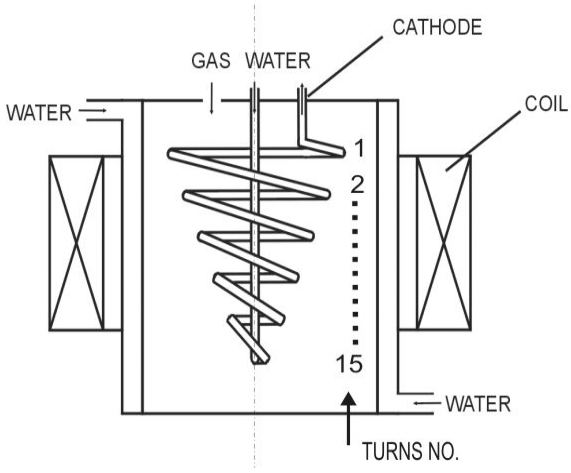


Fig. 4. The SPIRARC plasma reactor cross section

In the laboratory of the Technical University of Lodz a DC plasma furnace has been designed as an Immersed Arc Furnace (IAF) and applied to treat the inorganic wastes. The furnace is water-cooled and the transferred arc-plasma system has a maximum output power of 250 kW.

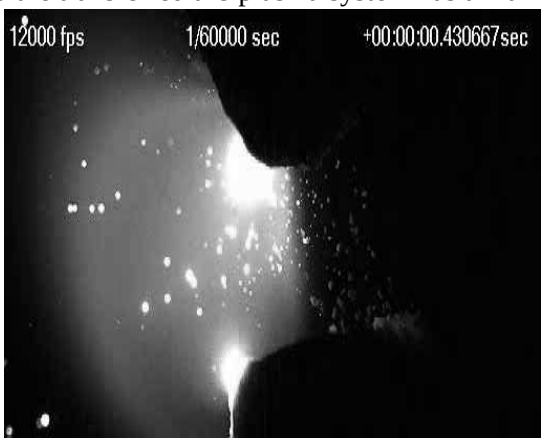


Fig. 5 The immersed arc in IAF

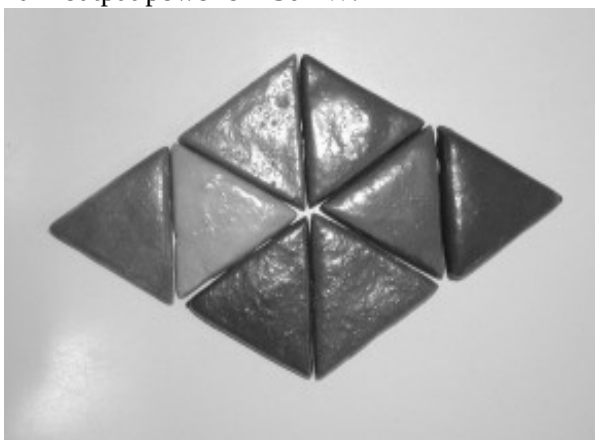


Fig. 6 Samples of colored ceramic tiles

In axially - symmetrical configuration of an anode - the crucible and a cathode – the rod graphite electrode (or plasma torch) the mineral feed charge files a space between them. Initially (in solid state) the feed does not conduct an electric current. Anode has got in its bottom a hole enabling flowing out of excess of gas as well as tapping of the melt (bath). A DC arc, burning in the environment formed by gaseous mineral substance was named here the gas-mineral-arc (GMA). In Fig. 5 the high speed camera frame shows the immersed arc in the mineral waste.

The Plasma Technologies & Environmental Protection Group of the Lodz Technical University together with 9 partner's institutions from Poland, United Kingdom, Spain and Hungary in 2001-2004 were being involved in EU project [5]. The target of that project was to involve end-users in research to develop and to demonstrate technology directed towards modernization of existing and newly build waste incinerator plants to convert them into "zero emission" factories. The aim of the project was to treat with plasma a composite waste consisting of hazardous waste ash and of toxic chemicals, to produce near-to-net shape building materials. Successful laboratory tests were done. Technology demonstration unit has been designed and built [6]. In Fig. 6 one can see a sample of the product being the output of this newly demonstrated technology. In Poland as well as in many Eastern European Countries a number of used capacitors and transformers containing mineral oil with polychlorinated biphenyls (PCB's) are stored. Some experiments were done also for ashes mixed with PCB's. The destruction rate of efficiency was always better than 99.99**%.** The main advantages of thermal plasma waste treatment are: complete pyrolysis of organic and hazardous wastes – no need of oxygen, vitrification of inorganic toxic leftovers – high temperature, high calorific value of gas fuel generated, smaller size of installation - high energy density, minimum total gas throughput - no excess gas for combustion required, rapid start-up and shutdown - easy automatic control. It has been shown and demonstrated elsewhere [5] that plasma destruction of wastes towards zero residues and sustainable energy use is possible and it can be an attractive tool for the nearest future.

5. Conclusions

Mentioned here plasma application examples of saving energy, health and environment are only a droplet in the sea of possible use of this nice tool in emerging field of materials processing. It can not be discussed in a brief 5 pages paper. More datails will be presented during the lecture of HAKONE XIII Conference.

6. References:

[1] P. Czurak, M. Dolata, I. Korczyńska, S. Morales Diaz: How to extract maximum energy from KERS? PBL Project TU of Łódź 2012, Supervisor: Zbigniew Kołaciński,

[2] Christopher J. Gannon, MD; Paul Cherukuri, PhD; Boris I. Yakobson, PhD; Laurent Cognet, PhD; John S. Kanzius; Carter Kittrell, PhD; R. Bruce Weisman, PhD; MatteoPasquali, PhD; Howard K. Schmidt, PhD; Richard E. Smalley, PhD; Steven A. Curley, MD "Carbon Nanotube-enhanced Thermal Destruction of Cancer Cells in a Noninvasive Radiofrequency Field", University of Texas M. D. Anderson Cancer Center, 2010,

[3] A. Olejnik, M. Sobieraj, E. Ewertowska, J. Walczak, M. Kostrzewski, Nanotechnology for Medical Diagnostics and Therapy, PBL Project, TU of Lodz, 2011, Supervisors: Zbigniew Kołaciński, Grzegorz Raniszewski,

[4] Z. Kolacinski, W. Sroczynski, Z. Muszczynko, P. Krystofiak, H. Duński, Ł. Szymański: Plasma treatment of spent chemical reagents, Problemy Eksploatacji 4/2006 pp.239-246,

[5] EU project WASTILE No G1RD-CT-2001-000468 on "A Generic Plasma-Arc Process for Toxic Waste Destruction with Co-Generation of High Value Construction Materials" – see CORDIS Database Int. Co-ordinator Zbigniew Kołaciński,

[6] L. Szymański, Z. Kolacinski, G. Raniszewski: Thermal decomposition of mineral oxides treated by an immersed arc-plasma, Czechoslovak Journal of Physics, Vol. 56 (2006), Suppl. B1231-B1236.

PROTON TRANSFER REACTION-MASS SPECTROMETRY: FUNDAMENTALS, RECENT ADVANCES AND APPLICATIONS

T.D.Märk[1,2], B.Agarwal[1,2], K.Becker[3], A.Edtbauer[2], S.Feil[2], S.Haidacher[2], G.Hanel[2], E.Hartungen[2], S.Jaksch[2], A.Jordan[2], S.Jürschik[1,2], C.A.Mayhew[4], L.Märk[2], F.Petersson[2], H.Seehauser[2], R.Schottkovsky[2], P.Sulzer[2]

[1]*Institut für Ionenphysik und Angewandte Physik, Universität Innsbruck, Technikerstr.25, A-6020 Innsbruck*

[2]*Ionicon Analytik GmbH, Eduard Bodem Gasse 3, A-6020 Innsbruck, Austria*

[3]*Polytechnic Institute of New York University, NY 11201, USA*

[4]*School of Physics and Astronomy, University of Birmingham, B15 2TT, UK*

E-mail: Tilmann.Maerk@uibk.ac.at

Proton Transfer Reaction-Mass Spectrometry (PTR-MS) offers many advantages for trace gas analysis, including no sample preparation, real-time analysis, high selectivity and sensitivity, ultra-low detection limits, and very short response times. These characteristic features have made it an ideal tool for many applications in science, technology and society. Here we will discuss recent developments, in particular advances concerning sensitivity, selectivity and general applicability.

1. Introduction

Trace gas analysis is not only of importance in environmental studies and in atmospheric chemistry, where detection of biogenic and/or anthropogenic volatile organic compounds is of utmost relevance, but also in other fields of science, technology and society including for instance food and flavour science and technology, biological and biotechnical research, process monitoring and control, hazardous material detection, all the way to medical applications.

Gas chromatography and/or mass spectrometry have been reference methods for many years, but need to overcome some of the inherent drawbacks, for instance time consumption in case of QC, have led to the development of alternative methods of analysis. Proton Transfer Reaction-Mass Spectrometry (PTR-MS) first developed in the labs of the Institut für Ionenphysik at the University of Innsbruck in the early nineties (see [1]) offers many advantages for trace gas analysis, including no sample preparation, real-time analysis, high selectivity and high sensitivity, ultra-low detection limits, and very short response times.

Despite being a well established method by now in many fields of applications [2,3,4], only recently a number of decisive instrumental developments took place and will be summarized in this review. They include *inter alia*:

1. the increase of mass resolution and mass accuracy,
2. the improvement of sensitivity and detection limit,
3. the extension from gas phase samples to liquid samples,
4. and the use of ionization methods beyond proton transfer reactions including electron transfer and other ion molecule reactions.

2. Fundamentals of PTR-MS

In a standard PTR-MS instrument water vapor coming from a distilled water reservoir is converted into hydronium ions H_3O^+ in a customized hollow cathode ion source. This source is designed in such a way as to achieve a high intensity and purity of the primary H_3O^+ ion beam from the ion source reaching purity values of 99% and more, thus making a signal-diminishing mass filter (e.g. quadrupole as used in instruments based on technologies similar to PTR-MS but different in the ion production

and selection, e.g. SIFT-MS) for purifying the primary ion beam obsolete. After production and extraction the H_3O^+ ions enter into a drift tube reactor where the sample air is admitted usually without any pretreatment. Whenever a chemical compound C present in the air has a proton affinity (PA) that is larger than the PA of water, proton transfer will take place resulting in neutral H_2O and the protonated substance molecule C^+, i.e.,

$$H_3O^+ + C \rightarrow C^+ + H_2O$$

Accidentally all PAs of all common air constituents (N_2, O_2, Ar, CO_2, etc.) are much lower than that of water, so that air itself can act as a buffer gas in the drift tube reactor and only the trace gas compounds will become ionized. At the end of the drift tube reactor ions enter a mass spectrometer and the secondary ions produced are analyzed.

As a result of this experimental set-up and its known parameters (such as reaction time, primary ion current, reaction rate coefficients, transmission coefficients) one gets highly accurate concentration readings in real-time (about 100 ms reaction time) without the need of sample preparation down to a typical detection limit in the single digit pptv region.

3. Advances and Applications

3.1. Increase of mass resolution and mass accuracy.

The first PTR-MS instruments were constructed with a quadrupole mass spectrometer [5]. While utilizing a quadrupole mass filter allows to achieve good sensitivities and has its advantages in monitoring the concentration of a single distinct substance, the mass resolution (unity mass resolving power) makes the clear identification of unknown substances somehow difficult. Moreover, the recording of full mass spectra is rather slow (as one has to scan with the mass filter the whole mass range) and separation of isobaric substances is impossible.

Therefore we recently coupled the well established PTR hollow cathode ion source with a high resolution ($m/\Delta m$ up to 8000) time-of-flight (TOF) mass analyzer. This led to the so-called PTR-TOF 8000 [6] which is due to its high mass resolution capable of separating isobars (e.g. ketene and propene). Moreover, ultra high mass accuracy in the ppm range allows to identify unknown mass species in a complex food matrix [7]. Full spectra can be acquired in split-seconds, while still achieving a detection limit of below 10 pptv.

For areas of application where this impressive mass resolving power is of less importance, but where more sensitivity is needed, we incorporated a different type of TOF analyzer. This PTR-TOF 2000 [8] has a sensitivity which is about a factor of five better than compared to that of the PTR-TOF 8000, however, at the cost of a somewhat lower mass resolution of about $m/\Delta m = 2000$.

3.2.Improvement of sensitivity and detection limit

In the course of recent instrumental developments we were able to further improve sensitivities and detection limits. Using gas standards to illustrate these advances, we were able to reach for the PTR-TOF 8000 for 1s integration time 170 cps/ppbv for mass 79 m/z (protonated benzene) all the way up to 276 cps/ppbv for 147 m/z (protonated dichlorobenzene). For the PTR-TOF 2000 we could even reach a record number of 750 cps/ppbv for 121 m/z. The limits of detection (LoD) determined using the 3σ method with 1 min integration time range for the PTR-TOF 8000 from 3 pptv for mass 79 m/z down to 1 pptv for 147 m/z. The LoD for the PTR-MS 2000 could be pushed down to several hundred parts-per-quadrillion (ppqv), such a value below 1 pptv could previously only be reached with the high sensitivity quadrupole based instruments, i.e. 890 ppqv for trichlorobenzene at an integration time of 180 s [9].

3.3. Extension from gas phase samples to liquid samples

One inherent limitation to chemical analysis by the standard PTR-MS technique is the fact that PTR-MS requires for proper analysis gas phase samples to be introduced via the gas phase inlet. This means that liquids can only be analyzed indirectly via the headspace above the liquids' surface. In particular

compounds having a high Henry constant therefore need to be present at very high concentrations in the liquid in order that they can be detected in the headspace. To overcome this limitation we developed recently a "direct aqueous injection" (DAI) system, where the liquid can be introduced directly for PTR-MS analysis. In short, in such a DAI system the liquid to be measured is introduced into a syringe and then injected with this syringe via a computer controlled syringe pump into a purified, dried and heated stream of air, which is subsequently introduced into the drift tube of the PTR-MS instrument. In [10] we present proof-of-principle investigations of this DAI system achieving response times around 20 s and a detection limit of about 100 pptw and in [11] we discuss applications about the detection of solid high explosives in air and water.

3.4. From conventional PTR-MS to a universal trace gas analyser. The use of ionization methods beyond proton transfer reactions including electron transfer and other ion molecule reactions.

Another "limitation" of PTR-MS so far, was the fact that only H_3O^+ ions could be produced in the hollow cathode ion source with high purity and intensity and thus used effectively as primary ions. This was amended by us in 2009 [9] by the development of the so-called "switchable reagent ion" (SRI) source. It is now possible to choose between H_3O^+, NO^+ and O_2^+ as reagent primary ions with a switching time of below 10 s. While all advantages of PTR ionization are preserved with H_3O^+, charge transfer from O_2^+ extends the number of substances that can be analyzed, e.g. the very important molecules ethylene and acetylene having lower PAs than water can now be accessed. Moreover, NO^+ which can be produced in high purity from normal air without the need of a NO gas cylinder as a primary ion leads to an additional benefit. According to Spanel et al. [12] NO^+ interactions with aldehydes follow the reaction:

$$NO^+ + XH \rightarrow X^+ + NOH$$

whereas ketones follow:

$$NO^+ + XH \rightarrow XH^+ + NO \text{ (and clustering).}$$

This means that we can even detect and distinguish isomeric compounds on different nominal masses and can identify them unambiguously.

Nevertheless, even the SRI technique, where O_2^+ (and NO^+) can be used to ionize trace gas molecules via charge transfer, are limited to compounds having ionization energies below 12.1 eV (the ionization energy of the neutral O_2). This still excludes the detection of important substances like CO, CO_2, SO_2, CH_4, etc.

Very recently, we therefore extended the conventional SRI technique using a novel concept [13] avoiding these limitations while preserving all advantages of conventional PTR-MS (fast response times, high sensitivity, no sample treatment, etc.). In this case (patent pending (PCT/EP2011/064170)) we use instead of the SRI ions the rare gas ions Kr^+ and Xe^+ as additional reagent ions (SRI+). The principal instrumental setup stays the same. This means that even in the modified version no mass filter is necessary between the ion source and the drift tube reactor still reaching very high reagent ion yields, e.g. about 9 x 10^6 cps for Kr+. Pure Kr or Xe gas from an external gas cylinder is introduced into the hollow cathode ion source where Kr^+ or Xe^+ is formed, respectively. These reagent ions are subsequently introduced into the adjacent drift tube where they can interact with air containing traces of the sample and very importantly an inert dilution gas.

The ionization energy (IE) of Xe is similar to the IE of O_2 (12.13 and 12.07 eV respectively) and therefore Xe^+ can be used as a substitute in environments where oxygen gas cylinders are prohibited (because of fire protection or ex-proof laws). The ionization energy of Kr with 14.00 eV is much higher than that of most neutrals. Because of this in case of Kr^+ primary ions also some of the main compounds of air get ionized, therefore a buffer gas having a higher IE than Kr has to be added to the sample gas for proper dilution, i.e., for instance He (IE 24.59 eV) and/or N_2 (IE 15.58 eV), respectively, using a simple mixing set-up. This novel SRI+ feature now allows to ionize via charge transfer reactions important molecules like CO, CO_2, NO_x, N_2O, SO_2, CH_4, etc.

Fig.1 shows as an example the detection of two molecules (CO^+ and $C_2H_4^+$) that could not be detected and quantified earlier with PTR-MS. Fig.1 represents an analysis performed on cigarette smoke. Although in this cigarette smoke sample there are three isobaric compounds present at nominal mass 28 m/z, we can clearly distinguish the true signals CO^+ at 27.99 m/z and $C_2H_4^+$ at 28.03 m/z from N_2^+ at 28.01 m/z (impurity from the ion source).

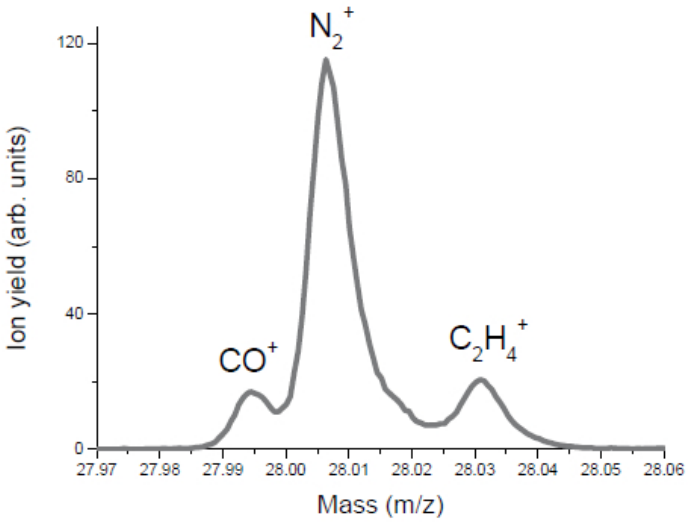


Fig. 1: Analysis of cigarette smoke with a PTR-TOF 8000 instrument equipped with SRI+ after [13].

4. Conclusions

As a consequence of its many analytical advantages, PTR-MS technology (in particular in its TOF and SRI+ variants) represents one of the few devices that can provide a broad-based analytical technique, corresponding applications will be discussed in detail in the lecture. Quite importantly, we have demonstrated that through a series of new developments discussed above we have considerably enhanced the technology's capabilities, thus enabling its use not only for fundamental questions in chemical analysis in physics, chemistry, medicine, biology, food science, environmental sciences and technology, but also for completely new fields of application, e.g. the unambiguous detection of illicit substances in gas and liquid phase.

5. References

[1] Lindinger W 1998 *Int.J.Mass Spectrom. Ion Proc.* **173** 191
[2] de Gouw J and Warneke C 2007 *Mass Spectrom.Rev.* **26** 223
[3] Blake R S, Monks P S and Ellis A M 2009 *Chem.Rev.* **109** 861
[4] Biasioli F, Yeretzian C, Gasperi F and Märk T D 2011 *TRAC* **30** (7)
[5] Hansel A, Jordan A, Warneke C, Holzinger R and Lindinger W 1998 *Rapid Commun.Mass Spectrom.* **12** 871
[6] Jordan A, Haidacher S, Hanel G, Hartungen E, Märk L, Seehauser R, Schottkowsky R, Sulzer P and Märk T D 2009 *Int.J.Mass Spectr.* **286** 122
[7] Cappellin L, Biasioli F, Fabris A, Schuhfried E, Soukoulis C, Märk T D and Gasperi F 2010 *Int.J.Mass Spectrom.* **290** 60
[8] Mayhew C A, Sulzer P, Petersson F, Haidacher S, Jordan A, Märk L, Watts P and Märk T D 2009 *Int. J.Mass Spectrom.* **289** 58
[9] Jordan A, Haidacher S,Hanel G, Hartungen E, Herbig J, Märk L, Schottkowsky R, Seehauser H, Sulzer P and Märk T D 2009 *Int.J.Mass Spectrom.* **286** 32
[10] Jürschik S, Tani A, Sulzer P, Haidacher S, Jordan A, Schottkovsky R, Hartungen E, Hanel G, Seehauser H, Märk L and Märk T D, 2010 *Int.J.Mass Spectrom.* **289** 173
[11] Jürschik S, Sulzer P, Petersson F, Mayhew C A, Jordan A, Agarwal B, Haidacher S, Seehauser H, Becker K and Märk T D 2010 *Anal.Bioanal.Chem.* **398** 2813
[12] Spanel P, Ji Y, and Smith D 1997 *Int.J.Mass Spectrom.Ion Proc.* **165/166** 25
[13] Jordan A, Edtbauer A, Hartungen E, Jürschik S, Sulzer P, Märk L and Märk T D 2012 *ASMS Conference* USA

PHOTO AND BACKGROUND IONIZATION/ STREAMER PROPAGATION

S. Nijdam[1], E.M. van Veldhuizen[1], U. Ebert[1,2]
[1] *Eindhoven University of Technology, Dept. Applied Physics, Eindhoven, NL*
[2] *Centrum Wiskunde & Informatica, Amsterdam, The Netherlands*
E-mail: s.nijdam@tue.nl

Positive streamers in air and other oxygen-nitrogen mixtures are generally believed to propagate against the electron drift direction due to photo-ionization. Photo-ionization is the non-local ionization of O_2-molecules by UV radiation from excited N_2-molecules. This facilitates the streamer propagation by creating free electrons ahead of it. The relative importance of photo-ionization depends on the O_2/N_2 ratio. Another possible source of free electrons in front of the positive streamer is background ionization. This can be ionization left by previous discharges or by other processes such as cosmic rays or (natural) radio-activity. We study the effects of both photo- and background-ionization on propagation and morphology of positive streamers by changing gas composition and repetition frequency. One particular gas composition is pure nitrogen with a small amount of radio-active ^{85}Kr added to increase background ionization.

1. Introduction

Positive streamers need a continued source of free electrons in front of them in order to propagate. Because of the electronegativity of molecular oxygen, free electrons in air quickly attach to oxygen if the electric field is below about 30 kV/cm. If this is the case, a high field is needed to detach the electrons so that they can be accelerated. According to Pancheshnyi [1] and Wormeester et al. [2], a good value for the instant detachment field under standard conditions in air is 38 kV/cm.
The detached free electrons can form avalanches that feed the front of the streamer head and enable it to propagate. The density of the electrons influences the morphology of the streamers as was demonstrated in [3].

In most streamer models the medium is air and the major source of electrons in front of the streamer head is taken as photo-ionization. In air, photo-ionization occurs when a UV photon in the 98 to 102.5 nm range, emitted by an excited nitrogen molecule, ionizes an oxygen molecule, thereby producing a free electron:

$$N_2^* \rightarrow N_2 + \gamma_{98*102.5\,nm} \qquad (0.1)$$

$$O_2 + \gamma_{98*102.5\,nm} \rightarrow O_2^+ + e. \qquad (0.2)$$

1.2 Photo-ionization

As the emitted photon can ionize an oxygen molecule some distance away from its origin, this is a non-local effect and therefore excited nitrogen molecules in the streamer head can create free electrons in front of the streamer head (as well as at other places around the streamer head). The average distance that a UV photon can travel depends on the density of the absorbing species, oxygen in this case. In atmospheric pressure air under standard conditions, this distance will be about 1.3 mm [4].

A straightforward method to test the effects of photo-ionization is by varying the oxygen concentration in nitrogen-oxygen mixtures and studying the effect of this on streamer properties. We performed such experiments with oxygen concentrations ranging from less than 0.1 ppm (parts per million) to 20% (artificial air).

1.2 Background ionization

Besides photo-ionization, there is another source that can provide free electrons in front of a positive streamer head: background ionization. Background ionization is ionization that is already present in the gas before the streamer starts, or at least it is not produced by the streamer. It can have different sources. In ambient air, radioactive compounds (e.g. radon) from building materials and cosmic rays are the most important sources of background ionization. They lead to a natural background ionization level of 10^9 -10^{10} m^{-3} at ground level (Pancheshnyi [1] and references therein).

Another source of background ionization can be leftover ionization from previous discharges. This is especially important in repetitive discharges types like DC corona discharges or repetitive pulsed discharges. Already at a slow repetition rate of about 1 Hz, leftover charges can lead to background ionization densities of order 10^{13} m^{-3} [2]. Background ionization can also be created by external UV-radiation sources, x-ray sources, addition of radioactive compounds to the gas or surfaces, electron or ion beam injection and more.

Independently of the source of background ionization, in air the created electrons will always quickly attach to oxygen. This means that they will have to be detached by the high field of the streamer before they can be accelerated and form avalanches.

We have used both methods to test for the effects of background ionization on positive streamers: we have added traces of radioactive ^{85}Kr to pure nitrogen to increase background ionization levels and we have varied the pulse repetition frequency of discharges in pure nitrogen. (Purity is defined below in Table 1.)

2. Experimental methods

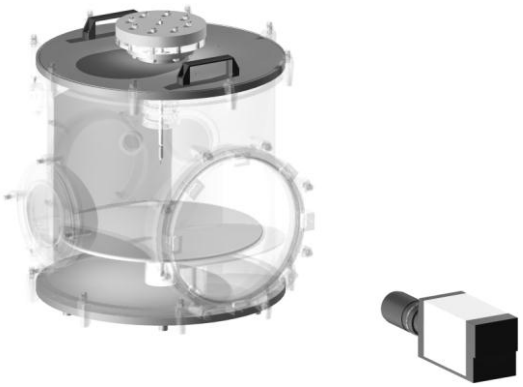


Figure 1. Overview of the vacuum vessel with the ICCD camera. The wall of the vessel has been rendered transparent in the figure to make the anode tip and cathode plane clearly visible.

We have built a set-up that is specifically designed to ensure the purity of the enclosed gasses. For this reason, the set-up can be baked to reduce outgassing, it contains no plastic parts, except for the o-ring seals and it stays closed all the time. We have used this set-up with three different gas mixtures. They are specified in table 1.

Table 1. Gas composition and impurity levels of relevant gasses as provided by the gas supplier. Impurity levels are in parts per million (ppm). They are given as upper limits, except for ^{85}Kr, which is dosed on purpose in the nitrogen/krypton mixture.

Gas	N_2	O_2	^{85}Kr	H_2O	Other
Artificial Air	80%	20%	n/a	0.5	0.5
Pure Nitrogen	100%	0.03	n/a	0.05	0.1
Nitrogen/ Krypton	100%	0.5	0.0099	0.5	8

The vacuum vessel contains a sharp tungsten tip, placed 16 cm above a grounded plane. The vacuum vessel with the camera is sketched in figure 1.

We have employed two pulsed power sources to provide the high voltage pulses required for streamer initiation. These two power supplies are a so-called C-supply and a Blumlein pulser. The C-supply consists of a capacitor that is discharged by means of a sparkgap and thereby creates a voltage pulse with exponential rise and decay. In our measurements with the C-supply rise times are typically of the order 100 ns and decay times are of order 5 μs. More details about the C-supply can be found in [5]. The Blumlein pulser consists of two ten meter long coaxial cables that are charged and then discharged by means of a multiple sparkgap. This creates a more or less rectangular voltage pulse

with a duration of about 130 ns and a risetime of about 10 ns. This circuit is treated in more detail in [3].

The streamer discharge is imaged by a Stanford Computer Optics 4QuickE ICCD camera. In the images presented here, the original brightness is indicated by the multiplication factor Mf, similar to what Ono and Oda introduced in [6] and as described by us in [3]. We have normalized the Mf value in such a way that the brightest image presented in [3] has an Mf value of 1.

More information about the circuit, discharge vessel and imaging system can be found in [3, 7, 8].

3. Results

3.1 General overview

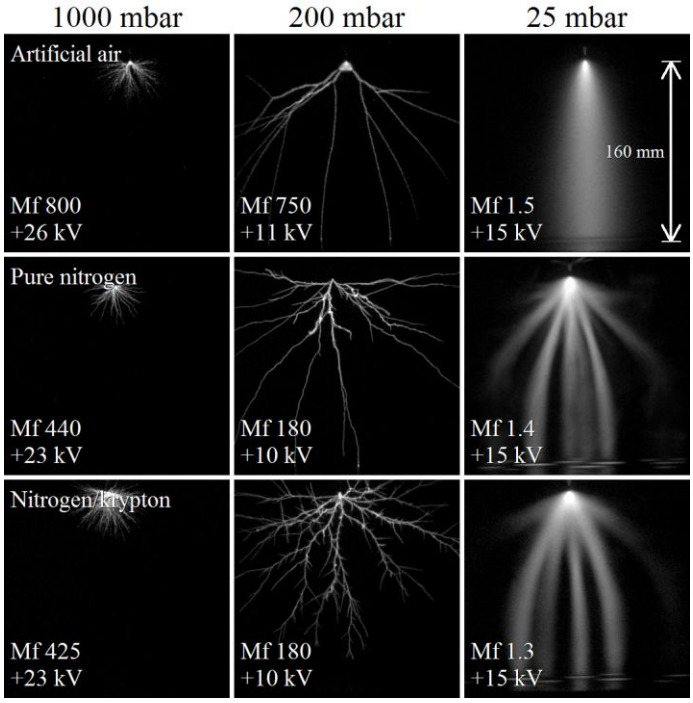


Figure 2. Overview of streamer discharges produced with the C-supply for our three gas mixtures (rows), at pressures of 1000, 200 and 25 mbar (columns) and 1 Hz repetition frequency. All measurements have a long exposure time and therefore show one complete discharge event, including transition to glow for 25 mbar. The multiplication factor (Mf) gives an indication of the real intensity of the discharge. The length scale is indicated with the arrow at the top right. Measurements in artificial air and nitrogen were previously published in [**3**].

Overview images of streamer discharges in the three different gasses are shown in figure 2. It shows that there are some differences in appearance between the gasses, but they are limited. When comparing artificial air and pure nitrogen we can see that even with a change of more than six orders of magnitude in oxygen content, streamer length and appearance remain more or less the same, as was already shown in [3]. At 25 mbar there seems to be a clear distinction between artificial air and pure nitrogen. However, with a few kilovolts higher pulse, both gasses will show the same morphology (one single streamer). When zooming in, or when using pulses from the Blumlein pulser, more differences between pure nitrogen and artificial air become apparent. Most notable is the fact that in pure nitrogen the streamers get a feather-like appearance. We attribute this to the lower density of electrons or negative ions produced by photo-ionization in front of the streamer head. This leads to a more stochastic distribution of these electrons and therefore to single (visible) avalanches and/or more easy breakup of the streamer head and thus to more branching. This is shown and discussed in more detail in [3, 9].

When adding a small amount of radioactive krypton to pure nitrogen (note that its purity is somewhat less than of the pure nitrogen above), the background ionization is increased by secondary ionization from the emitted beta particles of ^{85}Kr decay (half-life 10.756 years, decay by a 251 keV average energy β-particle). The 9 parts per billion of ^{85}Kr in our mixture lead roughly to an additional background ionization level of $2 \cdot 10^{12}$, $4 \cdot 10^{11}$ and $1 \cdot 10^{10}$ m^{-3} at 1000, 200 and 25 mbar respectively.

At 25 and 1000 mbar the discharges in the nitrogen/krypton mixture are quite similar to the pure nitrogen discharges. At 200 mbar some differences are visible: the streamers in the nitrogen/krypton mixture branch more and do not reach the other side.

3.2 Effects of pulse repetition frequency

A second way of influencing the background ionization levels is to vary the pulse repetition frequency. Even though the frequencies we used (0.01-10 Hz) are very slow compared to plasma reactions like recombination, some leftover ionization can remain because the ionization levels within a streamer are about 10 orders of magnitude higher than background ionization levels in virgin air.

The effect of repetition frequency on streamer morphology in pure nitrogen is shown in the top row of figure 3, where there is a distinct difference between streamers in pure nitrogen made with the same pulse shape but at 10, 1 and 0.1 Hz pulse repetition frequency. At higher frequencies, the streamers are smoother and fewer or no feather-like structures are visible. Streamers in the nitrogen/krypton mixture show a somewhat similar trend, although in this mixture the streamers remain much smoother at 0.1 and 1 Hz than the ones in pure nitrogen. The smoothness of the streamer channels has been quantified by counting the number of irregularities per unit length of streamer channel. All visible irregularities have been counted including feathers, branching events and sudden turns. Results of this counting are shown in figure 4.

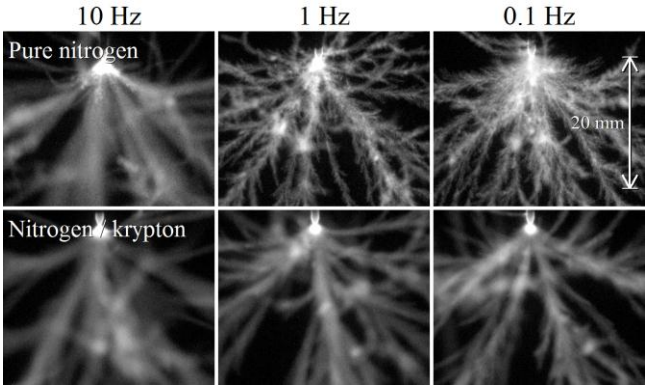


Figure 3. Zoomed images around the cathode tip of repetitive streamer discharges created with the Blumlein pulser (pulse length 130 ns) at 25 kV at three different pulse repetition frequencies in pure nitrogen and the nitrogen/krypton mixture.

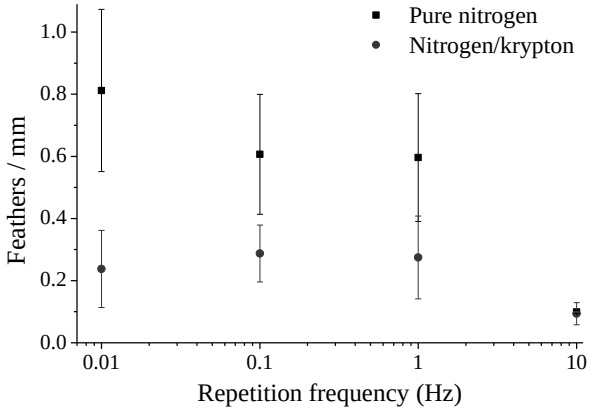


Figure 4. Feather density as function of repetition frequency in pure nitrogen and in the nitrogen/krypton mixture. Measurements are performed on discharges under the same conditions as shown in figure 3, but on channels extending further from the tip, outside the visible areas of figure 3 (to ensure a clean view of the channel). The measured values are the number of visible bumps, feathers, branches and all other irregularities per mm of streamer length and are not corrected for projection effects. The error bars give the standard deviation of the measurements.

The quantitative results confirm the observations from the images that streamers become smoother at higher repetition frequencies and that at repetition frequencies below 10 Hz, the streamers in the nitrogen/krypton mixture are smoother than the ones in pure nitrogen.

4. Discussion and conclusions

The background ionization levels left by previous discharges at 200 mbar and 1 Hz in pure nitrogen are estimated as about 10^{12} m^{-3} in [2]. In this calculation, an effective recombination rate of $5 \cdot 10^{-7}$ cm^3 s^{-1} was used. This calculation will be an overestimate as it assumes a homogeneous distribution of leftover ionization of 10^{20} m^{-3} while in fact such levels are only obtained within a streamer channel and the channels fill only a small percentage of our vessel. Therefore, a more realistic estimate is about one order of magnitude lower. This brings the value just below the estimate of the background ionization from radioactive decay in the nitrogen/krypton mixture ($4 \cdot 10^{11}$ at 200 mbar).

The estimated ionization levels due to repetition or radioactivity agree around 1 Hz; this fits well with the observed behaviour that shows differences in streamer morphology between pure nitrogen and nitrogen/krypton at 1 Hz and lower repetition frequencies, but no differences at 10 Hz. At the lower frequencies the (fixed) radioactive ionization source dominates over the ionization from previous discharges, while at 10 Hz the leftover ionization is dominant.

Note that the nature of the ionization can vary between the two ionization mechanisms. In leftover ionization, only ions exist, as all free electrons will have attached to oxygen impurities (even at low oxygen concentrations). However, with radioactive ionization, there is a constant source of free electrons. Some of them will have attached to oxygen, but the ones produced shortly before the voltage pulse will still be free. Such free electrons can more easily produce an avalanche as they don't need to be detached from negative ions by a high field.

In general we do not observe large differences in streamer properties between air, pure nitrogen and the nitrogen/krypton mixture or between different repetition frequencies. Minimal streamer diameters and propagation velocities are very similar even though photo- and background ionization vary many orders of magnitude. This confirms that streamers are very insensitive for the exact value of photo- and background ionization levels as was already discussed in [2, 3]. The observations also confirm the explanation of feather-like structures in streamers given in these papers. Again, it is found that higher ionization levels (photo or background) lead to smoother streamers and less feathers. This supports the theory that the feathers are caused by the stochastic nature of the ionization distribution that occurs at low ionization levels and that the feathers may be visible remnants of single avalanches.

5. References

[1] S. Pancheshnyi, M. Nudnova and A. Starikovskii. *Development of a cathode-directed streamer discharge in air at different pressures: Experiment and comparison with direct numerical simulation.* Phys. Rev. E **71**, 016407 (2005).

[2] G. Wormeester, S. Pancheshnyi, A. Luque, S. Nijdam and U. Ebert. *Probing photo-ionization: Simulations of positive streamers in varying N$_2$:O$_2$-mixtures.* J. Phys. D: Appl. Phys. **43**, 505201 (2010).

[3] S. Nijdam, F. M. J. H. van de Wetering, R. Blanc, E. M. van Veldhuizen and U. Ebert. *Probing photo-ionization: Experiments on positive streamers in pure gases and mixtures.* J. Phys. D: Appl. Phys. **43**, 145204 (2010).

[4] A. Luque, U. Ebert and W. Hundsdorfer. *Interaction of Streamer Discharges in Air and Other Oxygen-Nitrogen Mixtures.* Phys. Rev. Lett. **101**, 075005 (2008).

[5] T. M. P. Briels, J. Kos, E. M. van Veldhuizen and U. Ebert. *Circuit dependence of the diameter of pulsed positive streamers in air.* J. Phys. D: Appl. Phys. **39**, 5201 (2006).

[6] R. Ono and T. Oda. *Formation and structure of primary and secondary streamers in positive pulsed corona discharge--effect of oxygen concentration and applied voltage.* J. Phys. D: Appl. Phys. **36**, 1952-1958 (2003).

[7] T. M. P. Briels, J. Kos, G. J. J. Winands, E. M. van Veldhuizen and U. Ebert. *Positive and negative streamers in ambient air: measuring diameter, velocity and dissipated energy.* J. Phys. D: Appl. Phys. **41**, 234004 (2008).

[8] S. Nijdam, C. G. C. Geurts, E. M. van Veldhuizen and U. Ebert. *Reconnection and merging of positive streamers in air.* J. Phys. D: Appl. Phys. **42**, 045201 (2009).

[9] G. Wormeester, S. Nijdam and U. Ebert. *Feather-like Structures in Positive Streamers.* Revised for: Jpn. J. Appl. Phys. (2011).

DECOMPOSITION OF PERFLUORO COMPOUNDS IN WATER USING DISCHARGE PLASMA

Koichi Yasuoka

Tokyo Institute of Technology
E-mail: yasuoka@ee.titech.ac.jp

Discharge plasmas generated in gas bubbles can efficiently decompose the restricted-use compound perfluorooctane sulfonic acid (PFOS). During PFOS decomposition, perfluorocarboxylic acids (PFCAs: $C_nF_{2n+1}COOH$) with shorter carbon chains (n = 1–7) were generated and decomposed by the plasma. The decomposition reaction constants of the PFCAs were measured individually and used in a numerical simulation of PFOS decomposition. The results clarified that the plasma at a gas–liquid interface decomposed PFOS into PFCAs simultaneously, not sequentially.

1. Introduction

Discharge plasmas generated in the liquid phase or at the gas–liquid boundary have been studied extensively [1] for the decomposition of harmful substances. However, no plasma application has been reported for the decomposition of perfluoro compounds (PFCs), which are widely used because of their chemical and physical stabilities. PFCs, particularly long-chain PFCs, exhibit biopersistence and unexpected toxicity. Therefore, their effluents are strictly regulated, and the efficient decomposition of perfluorooctane sulfonic acid (PFOS; $C_8F_{17}SO_3H$) or perfluorooctanoic acid (PFOA; $C_7F_{15}COOH$) is urgently needed. Several methods of degrading PFOA have been reported, and a limited number of reports discuss PFOS degradation using zero-valent iron in subcritical water [2], photodegradation in a 2-propanol solution [3], or by sonochemical methods [4].

We recently found that the plasma generated at a gas–liquid interface can easily decompose PFOS and PFOA with decomposition energy efficiency significantly higher than that of other methods [5]. PFOS and perfluorocarboxylic acids (PFCAs; $C_nF_{2n+1}COOH$) with longer carbon chains show surfactant adsorption on the bubble–water interface; thus, the plasma in bubbles can effectively decompose the PFCs [6]. After complete decomposition of PFOA and PFCAs (n = 1–6), electrodialytic treatment enabled 96% recovery of fluorine ions from the solution [7].

The decomposition rates probably differ depending on the surfactant behavior of PFCAs. In this study, we individually measured the decomposition rate constants of trifluoroacetic acid (TFA; CF_3COOH, n = 1), perfluoropropionic acid (PFPrA; C_2F_5COOH, n = 2), perfluorobutanoic acid (PFBA; C_3F_7COOH, n = 3), perfluoro-n-pentanoic acid (PFPeA; C_4F_9COOH, n = 4), perfluorohexanoic acid (PFHxA; $C_5F_{11}COOH$, n = 5), perfluoroheptanoic acid (PFHpA) ($C_6F_{13}COOH$, n = 6), and PFOA under the same PFOS decomposition conditions. To examine the PFOS degradation processes, those constants were used in a numerical simulation analysis, which revealed a new decomposition scheme and explained why the plasma method is suitable for PFOA/PFOS decomposition.

2. Experimental setup

A schematic diagram of the plasma reactor is shown in Fig. 1. A high-density polyethylene container was filled with 20 mL of a 50 mg/L PFOS or PFCA (n = 1–7) solution. These compounds exist in solution in their ionic states and are not presumed to vaporize in air. The electrode system consisted of a high-voltage electrode and a grounded ring electrode immersed in the solution. A 0.3-mm-thick dielectric alumina spacer having a 0.3-mm-diameter central hole separated the high-voltage electrode from the solution and contributed to initiating the discharge within the tiny central hole. Oxygen gas was fed into the solution through the central hole at a flow rate of 100 sccm. Small gas bubbles formed in the hole, expanded into the solution, and detached from the spacer surface. The high-voltage electrode was connected to a dc power supply that was operated at a constant current of 10 mA.

The PFCA concentrations were measured by liquid chromatography–mass spectrometry (Shimadzu, LCMS-2020). The concentrations of F^- and SO_4^{2-} anions in the solution were measured

with a pH/ion meter (Mettler-Toledo, SevenMulti S47) and an ion chromatograph (Metrohm 861). Water was circulated through a stainless-steel pipe immersed in the solution to maintain the solution at 20°C. The conductivity of the 50 mg/L PFOA solutions was 29 μScm^{-1}.

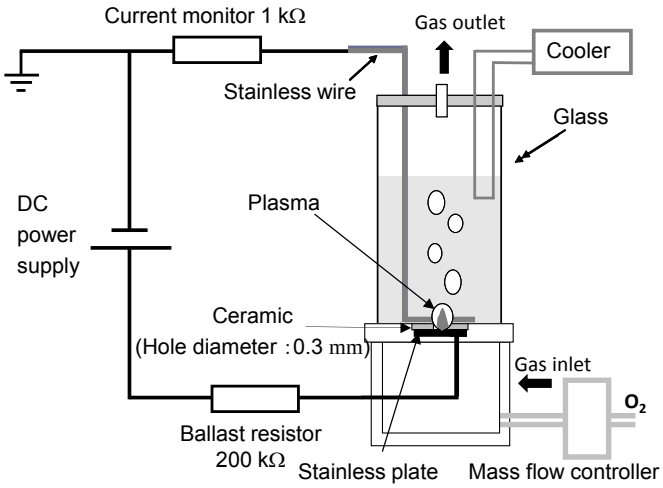


Fig. 1 Schematic diagram of plasma reactor.

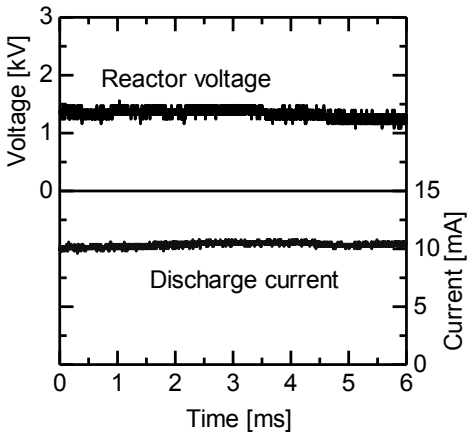


Fig. 2 Voltage and current waveforms.

3. Experimental results and discussion

Fig. 2 shows typical voltage and current waveforms with an oxygen flow of 100 sccm after 60 min of operation. Although the reactor voltage included the voltage drops between the bubble surface and the grounded electrode in the solution, the voltage drop in the liquid was almost negligible. Although the DC power source was operated with a constant current, the plasma current fluctuated because of the limited ability to regulate the power source, particularly in the early stage of operation. The amplitude of the current fluctuation decreased with time owing to an increase in the solution's conductivity.

Images of the bubble shapes and the plasmas generated inside the bubbles were taken by a high-speed camera (Redlake HS-4) with an exposure time of 330 μs. Fig. 3 shows pictures of a spindle-shaped bubble approximately 4 mm in width and 5–10 mm in height. The bubbles initially formed at the surface of the spacer and expanded upward until they finally detached from the surface within 11 ms. The plasma was initiated at the metal electrode just under the central hole in the ceramic plate and terminated at the bubble surface.

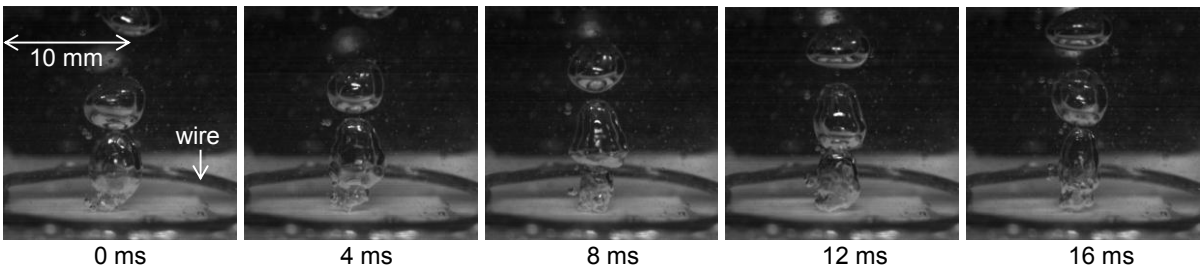


Fig. 3 Time-varying oxygen bubbles at a flow rate of 100 sccm into a 50 mg/L PFOS.

The PFOS decomposition was evaluated by measuring the concentrations of PFOS and F^- and SO_4^{2-} ions generated in the solution. Fig. 4 shows the time variation of the PFOS and F^- concentrations. After 240 min of operation, 99% of the PFOS was decomposed. The F^- concentration at 240 min was 27.6 mg/L, and the defluorination efficiency was 12.6 mg/kWh, which is significantly higher than those of other decomposition methods. [2–4]

The decomposition reactions of PFOS and PFCAs are almost first-order reactions, the reaction rate constant (k) of which is expressed as

$$k = \frac{1}{t}\ln\left(\frac{C_0}{C}\right), \tag{1}$$

where C_0 is the initial concentration, and C is the concentration after treatment. The decomposition reaction constant of PFOS is $k_{PFOS} = 4.35 \times 10^{-4}$ s^{-1} from 0 to 150 min. The reaction constant was constant during the first 150 min of operation but then decreased. It seems that the reduction in the reaction rate was caused by the increasing concentrations of SO_4^{2-} in the solution.

The residual ratios of PFCAs are shown in Fig. 5 as a function of operation time. As mentioned in section 2, the initial concentration and amount of each PFCA (n = 1–7) solution were 50 mg/L and 20 mL, respectively. The discharge input power was the same for all the plots. The decrease in PFOA (n = 7) was similar to that in PFOS; after 150 min of operation, 99% of PFOA was decomposed. The reduction rates of shorter-chain PFCAs were smaller than those of longer-chain PFCAs. TFA (n = 1) exhibited a minimum value; at 150 min, 36% of the TFA remained in solution. The shorter-chain PFCAs showed a larger residual ratio upon decomposition due to the decrease in the surfactant adsorption on the bubble–water interface. The decomposition reaction constants of the PFCAs were calculated using equation (1) assuming first-order reactions, as shown in Tab. 1.

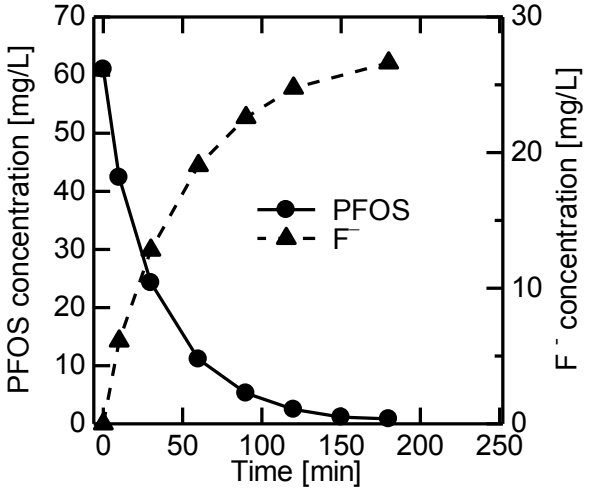


Fig. 4 Time variations in PFOS and F^- concentrations during oxygen plasma treatment.

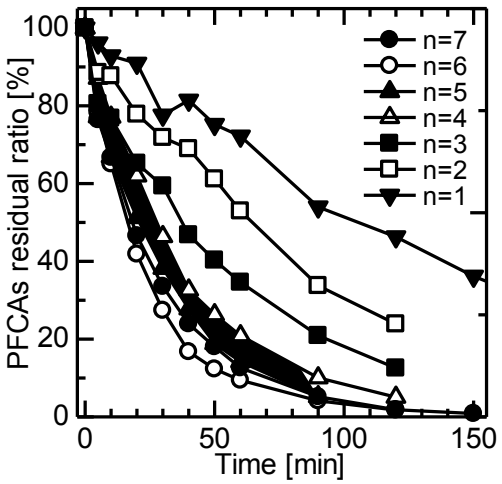


Fig. 5 Time variations in concentrations of PFCAs (n = 1–7).

Tab. 1. Decomposition reaction constants [s^{-1}] of PFOS and PFCAs (n = 1–7) .

$k_{PFOS} = 4.35 \times 10^{-4}$	$k_{PFOA(n=7)} = 5.27 \times 10^{-4}$	$k_{PFHpA(n=6)} = 5.63 \times 10^{-4}$	$k_{PFHxA(n=5)} = 5.35 \times 10^{-4}$
$k_{PFPeA(n=4)} = 4.18 \times 10^{-4}$	$k_{PFBA(n=3)} = 2.78 \times 10^{-4}$	$k_{PFPrA(n=2)} = 1.93 \times 10^{-4}$	$k_{TFA(n=1)} = 1.15 \times 10^{-4}$

Fig. 6 shows the time-varying concentrations of PFOS and PFCAs ($C_nF_{2n+1}COOH$, n = 1–7) generated in the solution as byproducts. The PFCA amounts were small; thus, expanded plots of the PFCA concentrations are shown in Fig. 7. The positive species M^+ should react with the PFOS at the bubble–water interface because the interface has negative polarity. A possible reaction between the plasma and PFOS is shown in equation (2). The shorter-chain perfluoroalkyl sulfonates ($C_6F_{13}SO_3H$ and $C_4F_9SO_3H$) were not detected, but PFOA was generated in the solution.

$$C_8F_{17}SO_3^- + M^+ + 3H_2O \rightarrow C_7F_{15}COO^- + 2F^- + SO_4^{2-} + 5H^+ + H + M\,. \tag{2}$$

Plasma decomposed the generated PFOA into shorter-chain PFCAs. Previously [5], we assumed that the shorter-chain PFCAs might be generated in sequence, for example, $C_7F_5COOH \rightarrow C_6F_{13}COOH \rightarrow C_5F_{11}COOH \rightarrow C_4F_9COOH$ and so on, as shown in equation (3) and Fig. 8(A).

$$C_nF_{2n+1}COO^- + M^+ + 2H_2O \rightarrow C_{n-1}F_{2n-1}COO^- + 2F^- + 3H^+ + H + CO_2 + M\,. \quad (3)$$

Using the decomposition reaction constants, the PFOS decomposition processes were numerically simulated assuming sequential decomposition. The results showed that sizable amounts of byproducts were generated. The calculated concentrations differed from the data obtained experimentally; therefore, the assumption of the simulation should be changed.

The revised assumption is shown in Fig. 8(B). Here the decomposition processes are assumed to be simultaneous, not sequential; therefore, more than one PFCA product is generated in one reaction. The calculated result agreed well with the experimental results, as indicated by the solid lines in Fig. 7.

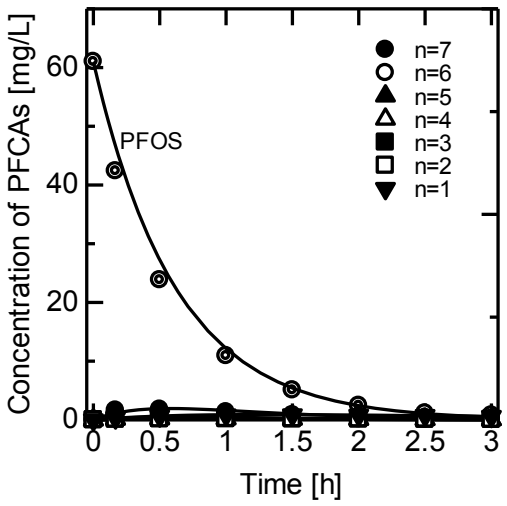


Fig. 6 Time variation in PFOS and PFCA concentrations and calculated PFOS concentrations (solid lines).

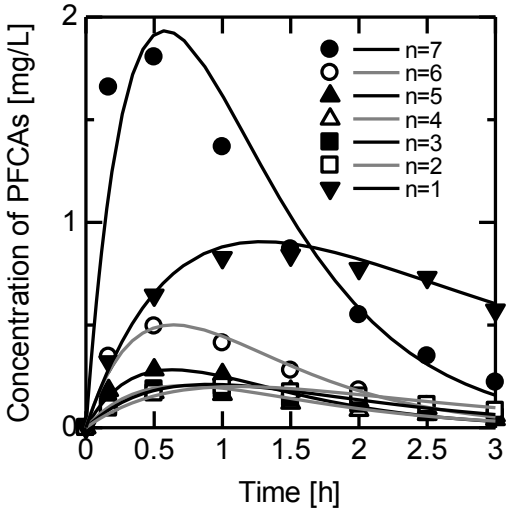


Fig. 7 Measured and calculated concentrations of PFCAs as a function of operating time.

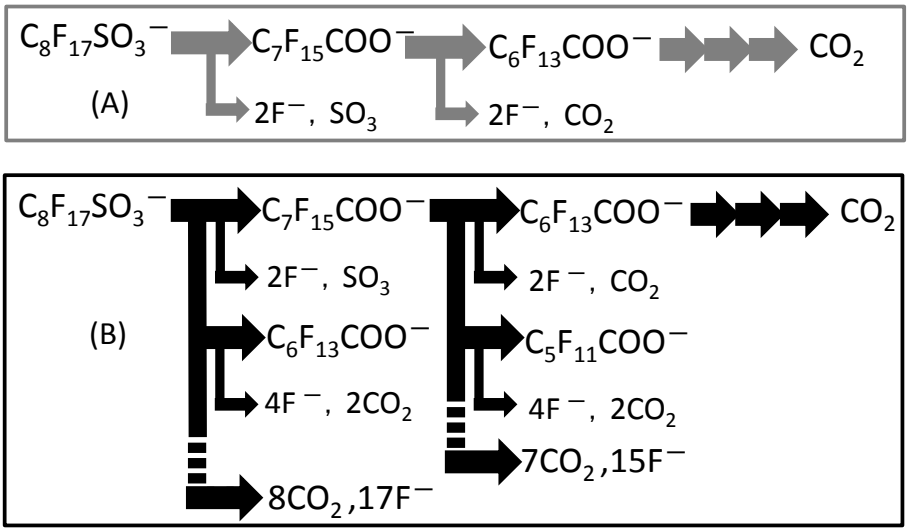


Fig. 8 Decomposition processes of PFOA: sequential decomposition (A) and simultaneous decomposition (B).

4. Conclusion

The application of dc discharge plasmas generated in gas bubbles in a solution for achieving efficient PFOS decomposition was studied. Complete decomposition of PFOS in 20 mL of a 50 mg/L PFOS solution was achieved using the plasma. To validate the PFOS decomposition processes, the decomposition reaction constants of individual PFCAs were measured. The constant was small for shorter-chain PFCAs because there was less surfactant activity. A numerical simulation was conducted using the decomposition reaction constants assuming sequential decomposition of PFOS and PFCA generation. The results differed from the experimental results, suggesting that a new decomposition scheme should be introduced to adjust the calculated values to those obtained by experiments. In conclusion, PFOA is decomposed into many shorter-chain PFCAs simultaneously at the plasma–solution interface.

Acknowledgment

This work was supported by the Environment Research and Technology Development Fund of the Ministry of the Environment, Japan K2324.

5. References

[1] Locke B R, Sato M, Sunka P, Hoffmann M R and Chang J S 2006 *Indust. Eng. Chem. Res*. 45 882.
[2] Hori H, Nagaoka Y, Yamamoto A, Sano T, Yamashita N, Yaniyasu S, and Kutsuna S, 2006 *Environ. Sci. Technol*. **40** 1049.
[3] Yamamoto T, Noma Y, Sakai S, Shibata Y 2007 *Environ. Sci. Technol*. **41** 5660.
[4] Vecitis C D, Wang Y, Cheng H, Park H, Hoffmann M R 2010 *Environ. Sci. Technol*. **44**, 432.
[5] Yasuoka K, Sasaki K, Hayashi R, 2011 *Plasma Sources Sci. Technol*. **20** 034009.
[6] Takeuchi N, Oishi R, Kitagawa Y, Yasuoka K 2011 *IEEE Trans. Plasma Sci*. **39** 3358.
[7] Takeuchi N, Saito Y, Kosugi A, Obo H, Yasuoka K 2012 *IEEE Trans. Plasma Sci*. (in press).

ORAL PRESENTATIONS

STUDY OF HIGH-SPEED CAMERA MEASUREMENT OF 6 ELECTRODES TYPE GLIDING ARC SYSTEM AND A NEW PRE-IGNITION SYSTEM

Shin-ichi Aoqui[1], Fumiaki Mitsugi[2], Tamiko Ohshima[3], Hiroharu Kawasaki[3], Toshiyuki Kawasaki[4]

[1]*Department of Computer and Information Sciences, Sojo University*
[2]*Graduate school of science and technology, Kumamoto University*

[3]*Department of Electrical & Electronics Engineering, Sasebo National College of Technology*
[4]*Department of Mechanical and Electrical Engineering, Nippon Bunri University*

E-mail: aoqui@cis.sojo-u.ac.jp

A gliding arc discharge was nonequilibrium, a kind of the non-steady discharge, and a large number of applied research has been performed to a technique of the exhaust gas decomposition. And in recent years a gliding arc attracts attention in the field of biochemical such as sanitization, the sterilization. Many studies relate to decomposed chemical species, and there are a few papers about the discharge mechanism. We carried out the observation using a high-speed camera (Max flame rate of 1300000 fps) about the discharge mechanism of the gliding arc discharge without any kind of pre-ignition system. It was confirmed by using the high-speed camera where paths of discharge between electrodes existed temporally. This measurement had been performed in the gliding arc discharge system of 2, 3 and 6 electrodes type. However, discharge voltage rose when a pre-ignition did not exist in comparison with the system which equipped pre-ignition system. In this study, it was proposed a new pre-ignite process which was not based on an electric discharge, and the discharge mechanism with 6 electrodes type was confirmed by high-speed camera and I-V characteristics.

5. Introduction

The development of the sanitization and sterilization technology in a medical, agriculture, biotech field using atmospheric pressure plasma is remarkable now [1-8].
However it is not so easy to generate plasma under the atmospheric pressure environment. As a typical method, there is Inductively Coupled Plasma (ICP) discharge, but it requires a large electrical power for starting and maintenance of a discharge. It is certain that ICP is important, as field of application of plasma, but electric power is too large for sanitization, sterilization. On the other hand, in recent years micro-plasma which development is advanced rapidly has an element similar to ICP, but its power consumption is not large. When we consider the large-scale utilization, for example sanitization of farm products which were harvested, a micro-plasma may have a too small electric power. Also dielectric barrier discharge (DBD) is a superior discharge type that status is established in fields such as ozone generators and so on, but it is not a discharge type to use large electric power.
A gliding arc (GA) discharge has a word to express "arc" in a part of the name but it is a discharge type that is considerably different from so-called DC arc and AC arc. Furthermore it is hard to say that the discharge mechanism of GAD is understood well. As for a GA plasma production is possible with the power consumption that is smaller than an arc discharge that is generally used under atmospheric pressure environment. With electric power lower than an arc, generation of atmospheric pressure plasma is possible for a GA.

We continue researching a discharge mechanism explication of a GA using an ultra high-speed camera and IV characteristic and discharge sound measurement [9,10].
It is the big target in our research to reduce power consumption. An electric power lower enough than ICP is already accomplished. We want to generate plasma in stability with electric power of around 100 W to equipment of diameter of around 300 ~ 500 mm as a discharge tube. In a case of ICP, 10 kW or more power is necessary in this discharge tube diameter.
In this study we introduced a new approach into a discharge starting method of the GA.
The concept of now idea is shown in the following.

A design including the capacity value of the electric power supply is important to a discharge device of GA [11,12]. In other words a discharge voltage (V) depends on gas pressure and a distance between electrodes shown by the Paschen's law,

$$V = f(pd) \quad (1)$$

Where p is gas-pressure [Torr] and d is distance [m] between electrodes

However, an electrode shape used by a gliding arc has a remarkable, different shape with uniform electric field. Therefore a non-uniform electric field coming from an electrode shape occurs, and strong electric field concentration occurs partially. Therefore, we should recognize that the Paschen's law is out of the applicability sufficiently. In addition, although an electrode has a shape to spread from a gas introduction towards a down stream, a shape of the electrode and a gaseous rate of flow and/or a velocity associate with a discharge phenomenon. When we consider a GA discharge circuit one system, it should become important what percentage of all provided electric power is spent on a discharge phenomenon by an electric power supply. Fig.1 (a) and (b) shows typical discharge circuit of GA. With research papers of general GA discharge, a protection resistor of several ohm - around 100 ohm is often inserted in primary power source of a commercial power supply from the viewpoint of protection of the power supply circuit (Fig.1 (a)). Because a distance between electrode is in a condition almost a short-circuit simultaneously with a discharge breakdown, this is arrangement to be taken to prevent a winding damage by the secondary side short circuit of a high voltage transformer. However, this resistor has many problems. In other words heavy current is passed to primary side when in a condition almost a secondary side short-circuit of a high voltage transformer. When the current exceeds a rating of a transformer, the transformer breaks, but the transformer is protected to reduce voltage which the resistor of the primary side deals with primary current, and is supplied for a transformer. Because the resistor of the primary side reduces voltage supplied for a transformer then the transformer is protected. However, the resistor will use much electric power. When the electric circuit which took out only a discharge part is investigated that a having resistor is put in high value of resistance (~ 10 k ohm, Fig.2(b)) in secondary side is considered to protect a high voltage transformer in the state that is almost this secondary side short-circuit, but characteristic of GA discharge is different greatly. In other words a voltage is generated with an almost all secondary side resistor and will amount to a most of the power consumption. Power consumption with this protection resistor is a big problem about a plasma generation.

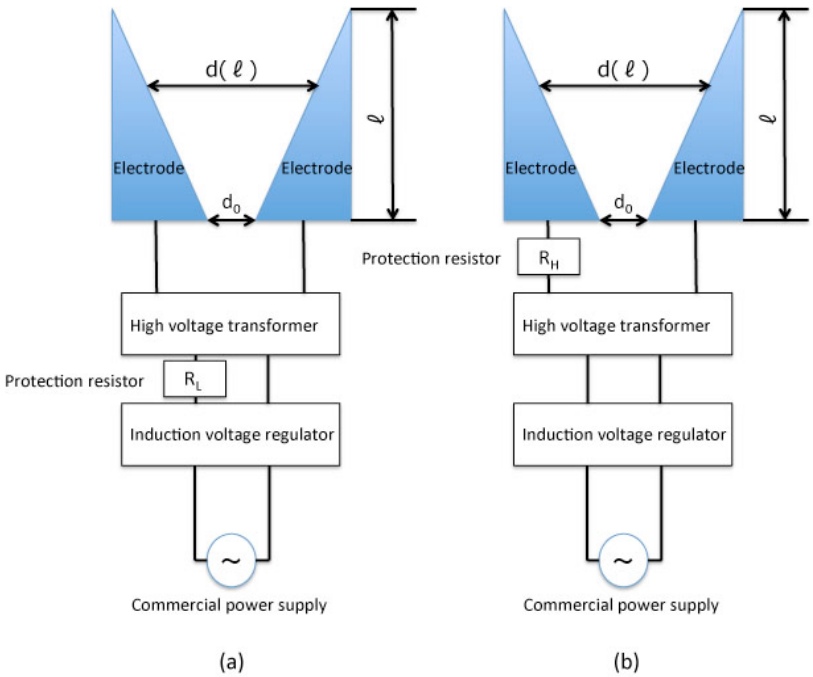


Fig.1. Gliding arc discharge system

To avoid this problem following three points become the important problem.

1. Reduce the breakdown voltage
2. Enlarge the capacity of the power supply
3. Realize a discharge that can maintain an impedance of paths of discharge highly

Damage of a electric source disappears a problem if we apply an infinitely great electric power supply (e.g., more than 100kVA in it) about 2., electric power supplied in plasma grows big and electrode temperature finally rises from the viewpoint of thermal load and reaches melting failure at a stage beyond melting point. A most effective thing is reduction of a starting voltage of a discharge. However, the breakdown voltage increases when distance between electrodes expands because the Paschen's law that a starting voltage of a discharge is expressed in the pd product controls it.
It is not possible for a rise of an impedance by taking a paths of discharge long to be easily wide at a discharge electrode distance from a limit by the pd product of the Paschen's law. In other words when we are going to reduce a breakdown voltage, the distance between electrodes shortens, and a length of paths of discharge shortens.
This situation is not the demand that we find. Then how can we satisfy 1 and 3?

Pre-ionization equipment is equipped with to prepare into an electron and/or ion becoming the seed by a lot of gliding arcs. It generates charge in a space between electrodes by putting pre-ionization equipment between main discharge electrodes. This is a good idea; it is not necessary to follow the Paschen's law and can expect an effect to suppress breakdown voltage lower. However, a part of the main discharge current cannot avoid flowing into a pre-discharge circuit even if this pre-ionization system designs circuit impedance highly. Therefore, when we consider it to be as an electric circuit, two kinds of discharge circuitry exist and will have a definite influence on mutual current paths. Because main discharge current flows, it is necessary to consider a damage of a pre-ionization electrode. As a method to reduce breakdown voltage not a technique of an electric circuit, ultraviolet irradiation to electrode is proposed in this study.
When ultraviolet (UV) rays is irradiated with in metal electrode(s), photoemission occurs by a formula of the photoelectric effect of Einstein,

$$E = h\nu - W \quad (2)$$

Where, h is Planck's constant, ν is frequency and W is work function of material

Photoemission occurs from electrode(s) if photon energy is larger than a work function of the electrode material. This electron emission must lower breakdown voltage. When UV ray with less than 317 nm of wavelength is irradiated iron electrode with because work function of pure iron is 3.91 eV, photoelectron emission occurs. The breakdown voltage can decrease by irradiating electrode with the UV ray that is lower than this wavelength by an appropriate method. The possibility that can increase distance between electrodes is found.

5. Experimental

In this study, we used 6 phases alternating current as a power supply system to supply 6 electrodes. Fig.2 shows 6 electrodes type GA discharge equipment including power supply. Pure iron was used for the electrode material. The distance between countered electrodes was adjusted at 3-10 mm. Argon gas was introduced from the electrode lower part. Ar gas flow rate was adjusted 10-50 litter/min. The voltage was regulated 0-6600 V. The electrode was surrounded with optics glass tube (diameter of 248 mm, IWAKI, TE-32 Glass), and the upper part edge was thrown open by the atmosphere. As ultraviolet light source, UV-LED (Nicha, NC4U134A) and low-pressure mercury lamp (HAMAMATSU, L937-02) were used. Because wavelength is 365nm on UV-LED (photon energy: 3.40 eV), therefore it is smaller than iron work function value of 3.91 eV. On the other hand, dominant wavelength is 254 nm (photon energy: 4.88 eV), and, as for the low-pressure mercury lamp, component of 254 nm amounts to overall 92%. The photon energy of this wavelength exceeds a work

function of iron. UV-LED and low pressure mercury lamp set it up for six pieces of electrode at the position of 120 degrees respectively, and those were irradiated electrode by 3 directions shown by Fig.3.
The discharge was photographed with two type ultra-high-speed cameras (Photron, FASTCAM SA5 and Ditect, HAS-D3). Table.1 shows discharge condition of GA discharge system.

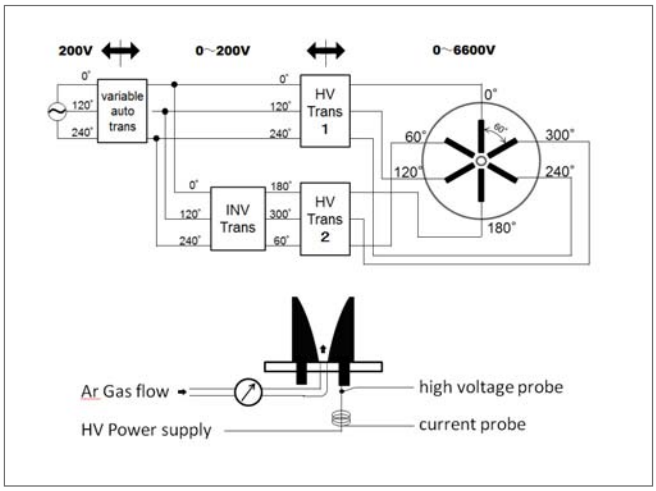


Fig.2. Experimental setup

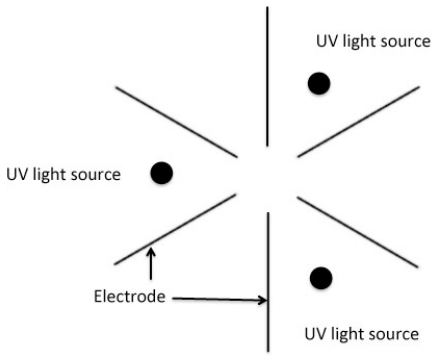


Fig. 3. Top view of electrodes and UV light source

Table.1 discharge condition

Applied voltage	1.5-6.6kV
Electrode material	Fe (99.5%)
Distance between electrodes	3~10 mm
Gas	Ar
Gas flow rate	0 L/min – 100 L/min
Pressure	760Torr (Atmospheric pressure)

3. Results and discussions

3.1 In case UV-LED used

UV - LED of 365 nm cannot have an effect when we considered it from the viewpoint of photon energy. The breakdown voltage of distance between electrodes of 4mm required 6 kV in case there was not pre-ionization equipment. However, it decreased 4. 8 kV by irradiation of UV - LED. As a result, we were able to widen distance between electrodes to 7 mm in applied voltage of 6 kV. Because there was a deviation of a strong electric field by the GA discharge, the Paschen's law was not effective at all, and ultraviolet radiation affected the electric field convergence part, and it enabled the voltage reduction of approximately 20% for the reason. This result was very important, but a decreasing rate of the discharge starting voltage was insufficient.

3.2 In case low-pressure mercury lamp used

A photon energy of low-pressure mercury lamp was large enough even in the case of distance between electrodes to 8mm, the breakdown voltage was able to be reduced to 2 kV. Distance between electrodes doubled and the breakdown voltage became one-third in comparison with the case of without pre-ionization equipment. In addition, as a result the volume of discharge current path increased therefore most of electric power was spent to plasma.
Fig.4 shows the images of ultra high-speed camera (5000 fps) of discharge photographed from the top view of GA system. It was confirmed that the paths of discharge were far beyond the upper end of the electrode and it blew up to 2.5 times of the electrode length.

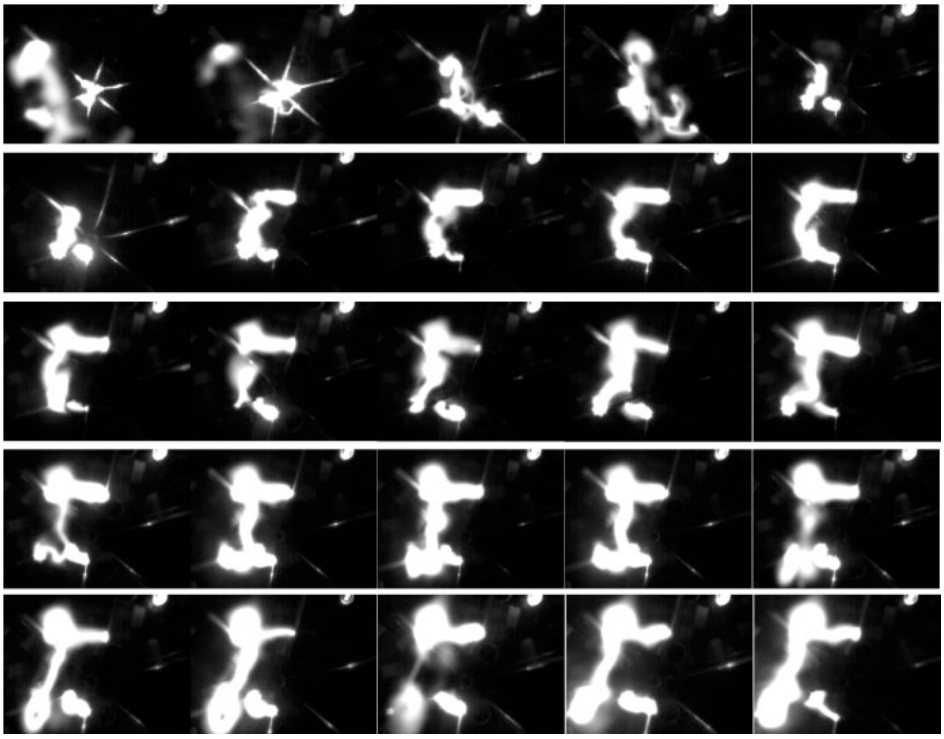


Fig. 4. Discharge images of high-speed camera (Top view) Flame rate: 5000 fps

4. Conclusions

We proposed an ultraviolet light starting method of GA discharge. Using this method, reduction of the breakdown voltage was realized. In case low-pressure mercury lamp was used, condition that expanded an electrode distance to 2.1 times the voltage was able to be reduced from one-third. As a result, the protection resistor of the supply circuit became unnecessary and was able to spend almost all power consumption in discharge plasma. This method suggests that a capacity of a power transformer is lowered and may downsize gliding arc discharge equipment.

5. References

[1] A. Fridman, S. Nester, L. A. Kennedy, A. Saveliev and O. Mutaf-Yardimci, Progress in Energy and Combustion Science 25, 211 (1999)

[2] M. Mlotek, J. Sentek, K. Krawczyk and K. Schmidt-Szalowski, Applied Catalysis A: General 366, 232 (2009)

[3] K. Krawczyk, B. Ulejczyk, H. K. Song, A. Lamenta, B. Paluch and K. Schmidt-Szalowski, Plasma Chemistry and Plasma Processing 29, 27 (2009)

[4] Z. Bo, J. Yan, X. LI, Y. Chi, K. Cen, Journal of Hazardous Materials 166, 1210 (2009)

[5] L. Yu, X. Li, X. Tu, Y. Wang, S. Lu and J. Yan, Journal of Physical Chemistry A 114, 360 (2010)

[6] R. Burlica, R. G. Grim, K. –Y. Shih, D. Balkwill, B. R. Locke, Plasma Processes and Polymers 7, 640 (2010)

[7] R. Burlica, K. –Y. Shih, B. R. Locke, Industrial and Engineering Chemistry Research 49 (14), 6342 (2010)

[8] C. M. Du, Y. W. Sun, X. F. Zhuang, Plasma Chemistry and Plasma Processing 28 (4), 523 (2008)

[9] T. Baba, Y. Takeuchi, H.D. Stryczewska and S. Aoqui, PRZEGLĄD ELEKTROTECHNICZNY, ISSN 0033-2097, R. 88 NR 6 (2012)

[10] F. Mitsugi, T. Ikegami, S. Aoqui, Y. Tashima, H. Kawasaki, T. Nakamiya, Y. Sonoda and H.D. Stryczewska, PRZEGLĄD ELEKTROTECHNICZNY, ISSN 0033-2097, R. 88 NR 6(2012)

[11] G. Komarzyniec, J. Diatczyk and H. D. Stryczewska, Journal of Advanced Oxidation Technologies 9(2), 178 (2006)

[12] G. Komarzyniec, H. D. Stryczewska and J. Diatczyk, Przeglad Elektrotechniczny 84(7), 60 (2008)

EXCITED ATOMS IN CAVITIES OF LIQUID HE I: LONG-RANGE INTER-ATOMIC REPULSION AND BROADENING OF ATOMIC LINE

V.M. Atrazhev[1] J. Eloranta[2] N. Bonifaci[3], Hai van Nguyen[3], F Aitken[3], K von Haeften[4], G Vermeulen[5]

[1] *Joint Institute for High Temperatures, RAS, Moscow, 125412*
[2] *Department of Chemistry and Biochemistry, California State University at Northridge, Northridge, California 91330, USA*
[3] *Laboratoire G2Elab CNRS & Joseph Fourier University. 25 rue des Martyrs, 38042 Grenoble, France*
[4] *University of Leicester, Department of Physics and Astronomy, Leicester, UK.*
[5] *Laboratoire IN CNRS & Joseph Fourier University. 25 rue des Martyrs, 38042 Grenoble, France*
E-mail: atrazhev@yandex.ru

Abstract. A theoretical description of the properties of excited atoms in normal liquid He and the luminescence of liquid Helium excited by a corona discharge are presented. The long-range interaction between excited He* atoms and He atoms in the ground state was studied in bulk liquid helium by a combination of fluorescence measurements. The 'hump' like repulsive part of the inter-atomic potential at intermediate internuclear separations around 5 Å was modelled using a power-function of the inter-atomic distance and calculated by using the full configuration interaction (CI) method as implemented in the MOLPRO code. The repulsion at intermediate internuclear distances gives rise to the establishment of cavities around excited atoms in liquid helium and here the radius and profiles of the cavity boundaries were calculated for this potential and different pressures. The potential was used to simulate the atomic line fluorescence profile as a function of external pressure between 0.1 and 3.5 MPa. The fluorescence shows characteristic line shifts and widths as a function of pressure. By comparison with the theoretical predictions, we found evidence that for corona discharge-excited liquid helium the He* atoms reside in a cavity and hence emit from within the liquid phase.

1. Introduction

Spectroscopic studies of internal excitations in liquid helium have a long history [1–6]. Experimental techniques, such as α-particle bombardment [1], high energy electron bombardment [2-4], strong field ionization by femtosecond laser pulses [7,8], synchrotron radiation [9–11], and corona discharge [5,6,12–14], have been employed. The latter technique has been applied to study intrinsic excitations in a bulk of liquid helium. Common to all these techniques is the first step, which involves direct ionization of helium atoms creating the corresponding positive ions and electrons in the liquid. This can directly lead to the formation of positive He_2^+ and subsequently through electron-ion recombination He_2*, or through electron impact ionization/excitation in the liquid electronically excited helium atoms He* may also form. These species are formed both in their singlet and triplet electronic manifolds and they relax towards lower energy states by emitting photons in the visible and infrared regions. The light is observed and analysed in experiments.

Pressure broadening of spectral lines depends on the surrounding matter (ionized gas in the case of discharge in the gas) density. The “impact” interaction of radiator with surrounding atoms determines the Lorentzian profile of spectral lines emitted by a discharge in low pressure gases [15-16]. In this case the width $\Delta\lambda$ (Full Width Half Maximum) of a line and the line shift S relative its non-perturbed location is proportional to gas density [17,18]. The analysis of the line broadening and shift has been made in [19] for the Lennard-Jones potential of an interaction between excited atom and surrounded atoms in the ground state. The shift sign (“red shift” for the shift toward longer wavelengths and “blue shift” for the shift toward shorter wavelengths) depends on character of radiator-perturbator interaction. The blue shift corresponds to significant repulsion. The “impact” interaction shifts the centre of line

weaker than the broadening of the line. The ratio Shift/Width does not exceed 0.2 for "impact" distortion of the line shape. The low shift of line compare with its broadening is a feature of the "impact" broadening by pressure in a gas. Growth of the density of a gas is accompanied by distortion of the "impact" Lorentz profile of a line. It has been shown [20] that the van der Waals attraction between a radiator and perturbators results in increasing of the intensity of a "red wing" of a line as compared with its "blue wing". The asymmetry of a spectral line shape was described using "quasi-static" approach where perturbators are assumed immobile. The asymmetric shape of spectral lines has been observed in He gas at 300K and under high pressures [21]. The lines studded had more intensive their "blue wing" that was a result of repulsion between excited atom and surrounding atoms. The experiments in negative corona have been carried out at temperature 570 K and pressure 3.2 MPa. The number density of a gas did not exceed $4.4*10^{20}$ cm^{-3}. The line width reached 3 nm in these conditions. The number density of the liquid He is $2*10^{22}$ cm^{-3}, which is 45 times larger than the highest gas density in the experiments at 570 K. If one extrapolates the width of the line in a gas to width at the liquid He, the non-realistic width of the line will be obtained. Though, good recognized atomic lines have been observed in the LHe excited by corona discharge [22]. The line had a symmetric profile with large width and blue shift. The lines observed in experiments at 570 K and at 4.2 K are shown for comparison in Fig.1.

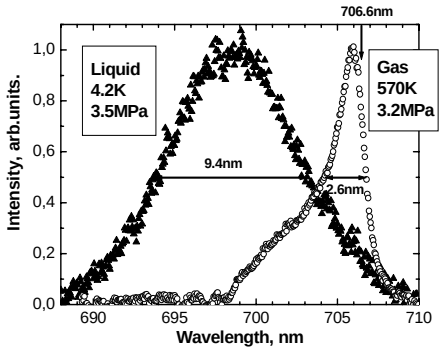


Fig. 1. Experimental spectra obtained for 706 nm line in negative corona under the same pressure and at different temperatures. Gas density at 570K is $4.4*10^{20}$ cm^{-3}. Liquid density at 4.2 K is $2*10^{22}$ cm^{-3}.

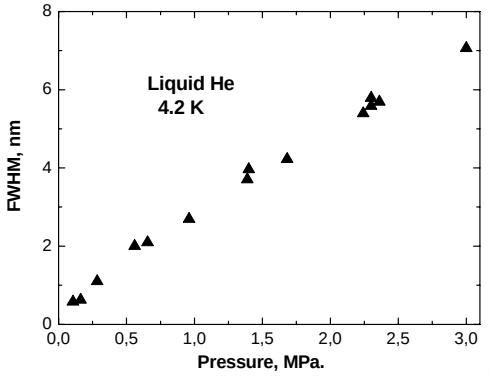


Fig. 2. Width (Full Width Half Maximum) of 706 nm HeI atomic line measured in liquid Helium at 4.2 K under different pressures.

So, the line observed in liquid He is strongly different than the line observed in gaseous He. Moreover, the shape of the line has strong pressure dependence in the LHe. The pressure dependence of the line width is a gas is a result of the linear relations between the gas density and the pressure. In the liquid variation of density with the pressure increasing is less than that in a gas. The pressure dependence of line width in a liquid has another reason.

The "blue" shift observed in spectroscopic experiments with gaseous and liquid He is an indicator of inter-atomic repulsion. The interaction between excited He* and ground state helium atoms provides example where a long-range barrier in the intermediate distance regime occurs. Both He* and He_2* species have been established to reside inside voids ranging from (7 – 15) Å ("bubble states"), which are slightly smaller than for free electron in the liquid (18.5 Å) [23-27]. Such structures are the result of the repulsive Pauli exchange interaction between the Rydberg electron and the surrounding closed shell helium atoms. Since the bubble radius depends strongly on the electronic state in question, both absorption and fluorescence spectra exhibit strong shifting and broadening due to the coupling between the Rydberg electron and the surrounding liquid ("bath"). In general, absorption lines experience stronger coupling to the surrounding bath [12,13]. The fluorescence lines are located near their vacuum values. This behavior is expected based on the fact that the higher Rydberg states have larger electron extent and thus in an absorption process the lower state is strongly coupled to the liquid whereas in fluorescence such coupling of the upper state is usually less. However for electronic states with repulsive long-range interaction, fluorescence spectroscopy, as demonstrated in the work, can provide detailed information about the upper state itself if the spectra are recorded systematically as a

function of external pressure. Since the helium density is much higher in the liquid phase as compared to helium gas, the liquid phase experiments provide much higher sensitivity to this interaction.
In this work, we have compared spectroscopic experiments and first principles theoretical calculations to characterize the long-range repulsive potential between $3s^3S$ He(3s) and the ground state helium atom. It is demonstrated that the current experimental approach offers a great advantage over the gas phase measurements providing more efficient sampling of the pair potential and thus giving a greater sensitivity for its energetic and curvature.

2. Bubble characteristics

Theoretical modeling of the bubble states in liquid helium have been mostly based on the application of the well-known model where the liquid part is described by the surface tension energy penalty for creating a void in the liquid ($4\pi\sigma R_b^2$; σ is the liquid surface tension and R_b is the bubble radius) with the external pressure contribution on the bubble interface included through the classical pressure-volume work term ($4\pi R_b^3/3 \cdot P$; P is the external pressure) [28–30]. An accurate description of the liquid density in the boundary region is very important for calculating the spectral line shapes While the bubble model itself does not consider the liquid – excited atom interaction directly, this interaction must be present to balance the surface tension and the external pressure. This is often included in the calculation through a combined one electron - effective core potential (ECP) treatment [27,30]. It is difficult to judge the accuracy of such ECP models, especially when they are used in conjunction with the semi-empirical bubble model. There is a need for a first principles theory model that can reproduce the spectral line shapes without empirical adjustment of any model parameters.
The $3s^3S$ He*(3s) - $1s^1S$ He(1s) and $2p^3P$ He*(2p) - $1s^1S$ He(1s) pair interactions were obtained by using the full configuration interaction (CI) method as implemented in the Molpro code [31,32]. The full CI method is a size consistent approach, which allows to correct for the basis set superposition error (BSSE). Provided that the basis set convergence is sufficient, this approach has been shown to provide highly accurate results for rare gas containing systems even with a limited treatment of electron correlation (typical accuracy 1 cm^{-1}) [33,34]
The pair potentials for $3s^3S$ He*(3s) - $1s^1S$ He(1s) and $2p^3P$ He*(2p) - $1s^1S$ He(1s) have been calculated. The repulsive hump around 5 Å distance corresponds to the Rydberg transition region going from the atomic He* to the molecular He_2*. The hump is more appreciable for the upper state $3s^3S$ He*(3s). The state $2p^3P$ He*(2p) appears to be essentially flat for distance near to 5 Å. The He*-He potentials have been used for calculation of structure of an environment of the excited atom. The repulsion leads to creation of the cavity around the atom. Bosonic Density Functional Theory (DFT) has been shown to be a computationally tractable approach capable of accurately describing solvation of impurities in liquid helium [35]. The liquid helium surrounding He* was modeled by bosonic DFT where the He* - He pair potential obtained above acted as an external potential for the liquid. An extension of the DFT model of Stringari et al. (the Orsay-Trento functional) was used to model the liquid when T > 0 K [36,37] The external pressure was accounted for by adjusting the bulk liquid density according to the known equation of state for liquid helium at 4.2 K. In addition to the bosonic DFT description for the liquid degrees of freedom, zero-point motion for He* was included in the model by minimizing its energy simultaneously with the liquid DFT equation. As the bubbles have a fairly large radius the liquid profiles are very smooth with only weak density oscillations from the liquid correlations visible especially at higher external pressures. The effect of pressure on the liquid density surrounding the He* is remarkable, allowing experiments to probe the long-range region of the repulsive hump at several different distances. The experimentally observed line shifts and broadening are very sensitive to the pair potential although indirectly as it is convoluted with the liquid density.

3. Line characteristics

Difference between energies of upper and lower terms is determine shift and broadening of the spectral line [38]. The difference $\Delta U(R)$ is presented in Fig. 3 and is fitted by Gaussian function limited by R > 5.3 Å:

$$\Delta U(R) = 103(cm^{-1}) * \exp\left(-\left(\frac{R-5.3\text{A}}{3.1\text{A}}\right)^2\right), \qquad \text{R} > 5.3 \text{ Å} \tag{1}$$

Here the potential is in cm^{-1} and the inter-atomic distance is in Å. The model potential is assumed not zero for $R > 5.3$ Å only. Real hump-like potential is not determined for distances less 5 Å, Fig.3.

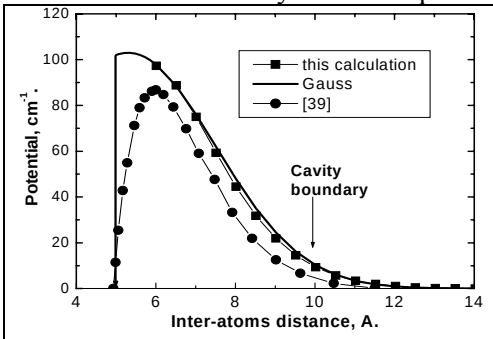


Fig. 3. Difference $\Delta U(R)$ between potentials $3s^3S$ He* and $2p^3P$ He*(2p) calculated:
Squares – this calculation. Circles – [39].
Line – fitting by Gauss curve Eq.(1).

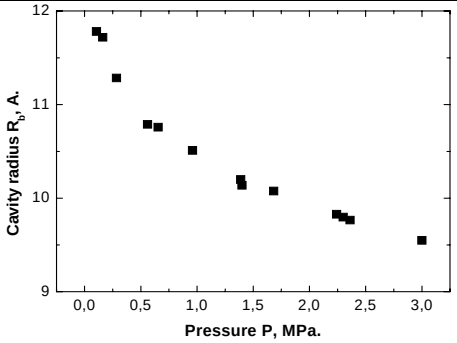


Fig. 4. Radius of cavities for different pressures recalculated from the experimental data for the line width (Fig. 2).

Because the temperature 4.2 K is less than the potential at $R_b \approx 10$ cm^{-1} ≈ 14.5 K the "static" approximation [20] was used for calculation of line profile $I(\omega)$

$$I(\omega) \propto \int_{-\infty}^{\infty} \exp\left[i\omega\tau - V(\tau)\right] d\tau$$
$$V(\tau) = 4\pi N \int_{R_b}^{\infty} \left[1 - \exp\left(-i\tau \frac{\Delta U(R)}{\hbar}\right)\right] R^2 dR = \text{Re}V(\tau) + i\,\text{Im}V(\tau) \tag{2}$$

Here ω is the frequency detunning (ω=0 is a center of the line), $N = 2.2*10^{22}$ cm^{-3} is the number density of the liquid He and it weak depends on the applied pressure. The transformations of the Eq.(2) [20] give

$$I(\omega) = \int_{0}^{\infty} \exp\left[-\text{Re}V(\tau)\right] \cdot \cos\left[\omega\tau - \text{Im}V(\tau)\right] d\tau \tag{3}$$

The expression Eq.(4) is an integral form of the Gauss-function if $ImV(\tau) \sim \tau$ and $ReV(\tau) \sim \tau^2$

$$I(\omega) = \exp\left(-\frac{\left(\omega - \text{Im}V(\tau)/\tau\right)^2}{4\,\text{Re}V(\tau)/\tau^2}\right) \tag{4}$$

The imaginer part $\text{Im}V(\tau)/\tau$ determines the shift of the line center relative to its location in vacuum. The real part $\text{Re}V(\tau)/\tau^2$ determines width of the line in frequency scale. The width is a result of an interaction of the emitting atom with surrounding atoms of the liquid Helium.

The required properties of $ImV(\tau)$ and $ReV(\tau)$ is realized if $\tau \frac{\Delta U(R)}{\hbar} << 1$ and the exponent in Eq.(2) can be expanded into Taylor series. It gives for the line width (in wavelength scale)

$$FWHM(P) = 4\sqrt{\ln 2} \cdot U_{\max} \cdot {\lambda_0}^2 \cdot \left(4\pi N \int_{R_b(P)}^{\infty} \frac{R^2}{2} \left(\frac{\Delta U(R)}{\hbar}\right)^2 dR\right)^{0.5} \tag{5}$$

Here the $FWHM$ is in nm as the wavelength $\lambda_0 = 706.6$ nm, $U_{max} = 103$ cm^{-1} is maximal value of perturbation potential, Eq.(1). In this model the cavity radius $R_b(P)$ is a function of applied pressure P that leads to the pressure dependence of the line width $FWHM(P)$ measured in experiments, Fig. 2. So, the cavity radii can be recalculated using the experimental data on the line broadening as a function of the applied pressure. The result of the calculations is presented in Fig.4.

Russian participant of the work (V. M. A.) thanks the Russian Foundation for Basic Researches, grant 12-08-91052, for support.

4. References

[1] C. M. Surko and F. Reif, 1968 *Phys. Rev*. **175**, 229.
[2] W. S. Dennis, J. E. Durbin, W. A. Fitzsimmons, O. Heybey, and G. K. Walters 1969 *Phys. Rev. Lett.* **23**, 1083.
[3] F. J. Soley and W. A. Fitzsimmons 1974 *Phys. Rev. Lett*. **32**, 988.
[4] J. W. Keto, F. J. Soley, M. Stockton, and W. A. Fitzsimmons 1974 *Phys. Rev*. *A* **10**, 872.
[5] P. H. Zimmermann, J. F. Reichert, and A. J. Dahm 1977 *Phys. Rev. B* **15**, 2630.
[6] V. A. Goncharov and V. I. Levitov 1975 *Izvestiya Academii Nauk, Energetica i Transport* **12**, 134.
[7] A. V. Benderskii, R. Zadoyan, N. Schwentner, and V. A. Apkarian 1999 *J. Chem. Phys*. **110**, 1542.
[8] A. V. Benderskii, J. Eloranta, R. Zadoyan, and V. A. Apkarian 2002 *J. Chem. Phys.* **117**, 1201.
[9] K. von Haeften, A. R. B. de Castro, M. Joppien, L. Moussavizdeh, R. von Pietrowski, and T. Moller 1997 *Phys. Rev. Lett.* **78**, 4371.
[10] K. von Haeften, T. Laarmann, H. Wabnitz, and T. Moller 2002 *Phys. Rev. Lett.* **88**, 233401.
[11] K. von Haeften, T. Laarmann, H. Wabnitz, and T. Moller 2005 *J. Phys. B* **38**, S373.
[12] S. G. Kafanov, A. Y. Parshin, and I. A. Todoshenko 2000 *JETP* 91, 991.
[13] A. Y. Parshin, I. A. Todoshenko, and S. G. Kafanov 2000 *Physica B* **91**, 284.
[14] Z.-L. Li, N. Bonifaci, F. Aitken, A. Denat, K. von Haeften, V. M. Atrazhev, and V. A. Shakhatov 2009 *Eur. Phys. J. Appl. Phys.* **47**, 22821.
[15] Traving G. 1968 *Interpretation of line broadening and line shift in Plasma Diagnostic* (Chap. 2), edited by W. Lochte-Holtgreven, North-Holland Publishing Company, Amsterdam.
[16] Allard N. and Kielkopf J. 1982 *Rev. Mod. Phys.* **54** 1103.
[17] Lindholm E. 1945 *Ark. Fis. A* **32** 1.
[18] Foley H. M. 1946 *Phys. Rev.* **6**9 616.
[19] Hindmarsh W. R., Petford A. D. and Smith G. 1967 *Proc. of the Royal Soc. Series A* **297** 296.
[20] Margenau H. 1935 *Phys. Rev.* **48** 755.
[21] N. Bonifaci, Z.-L. Li, A. Denat, K. V. M. Atrazhev, and V. A. Shakhatov 2011 *Eur. Phys. J. Appl. Phys*. **55**, 13809.
[22] Z.-L. Li, N. Bonifaci, A. Denat, V. M. Atrazhev, and V. A. Shakhatov, K. von Haeften, 2011 *J. Low Temp.Phys.* **37**, 484.
[23] J. Eloranta and V. A. Apkarian 2002 *J. Chem. Phys.* **117**, 10139.
[24] J. Eloranta, N. Schwentner, and V. A. Apkarian 2002 *J. Chem. Phys.* **116**, 4039.
[25] D. Mateo, D. Jin, M. Barranco, and M. Pi, 2011 *J. Chem. Phys.* **134**, 044507.
[26] H. J. Maris, *J. Low Temp. Phys.* 2000 **120**, 173.
[27] A. P. Hickman, W. Steets, and N. F. Lane 1975 *Phys. Rev.* B **12**, 3705.
[28] J. Jortner, W. R. Kestner, S. A. Rice, and M. H. Cohen 1965 *J. Chem. Phys*. **43**, 2614.
[29] K. Hirioke, N. R. Kestner, S. A. Rice, and J. Jortner 1965 *J. Chem. Phys.* **43**, 2625.
[30] A. P. Hickman and N. F. Lane 1971 *Phys. Rev. Lett.* **26**, 1216.
[31] H.-J.Werner, P. J. Knowles, G. Knizia, F. R. Manby, M. Sch¨utz, P. Celani, T. Korona, R. Lindh, A. Mitrushenkov, G. Rauhut, et al. 2010 Molpro, version 2010.1, a package of ab initio programs, see http://www.molpro.net.
[32] P. J. Knowles and N. C. Handy 1989 *Comp. Phys. Comm*. **54**, 75, URL http://dx.doi.org/10.1016/0010-4655(89)90033-7.
[33] T. Kiljunen, J. Eloranta, and H. Kunttu 1999 *J. Chem. Phys.* **110**, 11814.
[34] J. Ahokas, T. Kiljunen, J. Eloranta, and H. Kunttu 2000 *J. Chem. Phys.* **112**, 2420.
[35] J. Eloranta, H. Y. Seferyan, and V. A. Apkarian 2004 *Chem. Phys. Lett.* 396, 155.
[36] F. Dalfovo, A. Lastri, L. Pricaupenko, S. Stringari, and J. Treiner 1995 Phys. Rev. B 52, 1193.
[37] F. Ancilotto, F. Faccin, and F. Toigo 2000 Phys. Rev. B 62, 17035.
[38] Anderson P. W. 1952 *Phys. Rev.* **86** 809.
[39] N. F. Allard, N. Bonifaci, and A. Denat 2011 *Eur. Phys. J.* D **61** 365.

OPERATION MODES IN BARRIER DISCHARGES: DISCHARGE DEVELOPMENT AND SURFACE CHARGE ACCUMULATION

Marc Bogaczyk and Hans- Erich Wagner

Institute of Physics, University of Greifswald, Germany
E-mail: bogaczyk@uni-greifswald.de

A discharge cell configuration was developed to combine the spatio-temporally and spectrally resolved spectroscopic measurements (cross-correlation spectroscopy) and the phase resolved detection of surface charges via the electro-optic Pockels effect. The Townsend-like discharge mode was studied in nitrogen and surprisingly even in helium. Usually, in this gas the barrier discharges (BDs) operate in the glow-like mode. Small admixtures of nitrogen to helium change the operation into the filamentary mode. In the latter, the so-called memory effect was verified showing clearly the important role for the re-ignition of microdischarges in the following half periods of the applied voltage. The positive and negative surface charge density profiles show significantly different lateral extents. Both are Gaussian distributed. The measured surface charges are excellent agreement with the transferred charge by current pulse.

1. Introduction

Barrier discharges (BDs) at atmospheric pressure are effective sources of radicals and excited species. They have found many applications, e.g. for the ozone synthesis, surface treatment, and in the environmental chemistry [1]. They have still a high technological potential. It is well-known that BDs can operate in different discharge modes, namely the diffuse and filamentary one. The diffuse operation mode can appear in the so-called atmospheric pressure Townsend-like discharge (APTD) and the atmospheric pressure glow-like discharge (APGD) [2, 3]. The occurrence of both is affected by the feeding gas mixture and flow rate, gas pressure, operation frequency and shape of the feeding voltage, dielectric material and the reactor geometry. The investigation of the elementary processes in the discharge volume in combination with the interaction with dielectric surfaces enables detailed contributions to the mechanisms (ignition, discharge mode, stability, etc.). The plasma-surface interaction is connected with the accumulation of surface charges and secondary emission of electrons by ions and metastables [4]. The discharge operation mode is connected by the ratio of processes at the electrodes by e.g. exoemission of electrons to the ionization in the discharge volume (Townsend and Penning ionization). Furthermore, negative surface charges play an important role because of the low energy to release electrons from the dielectric surface. The necessary energy can be provided by metastables. In the filamentary mode the surface charge distribution influences the position of the re-ignition of the next microdischarge, the so-called memory effect. Results about the discharge modes in helium and nitrogen are presented. Also, results for the surface charge accumulation in the diffuse and filamentary operation mode are shown.

2. Experimental set-up

The experimental set-up of the discharge cell configuration is shown in fig. 1. It consists of two parallel dielectric electrodes. Important properties of the dielectrics are given in table 1. On top of the grounded and polished aluminum mirror an electro-optic BSO ($Bi_{12}SiO_{20}$) crystal is mounted to enable the surface charge measurement due to its birefringent properties. The upper dielectric electrode is a glass plate (epsilon = 7.6) covered on its topside with a optically transparent and electrically conductive ITO (Indium tin oxide) layer allowing the surface charge measurement from top via a

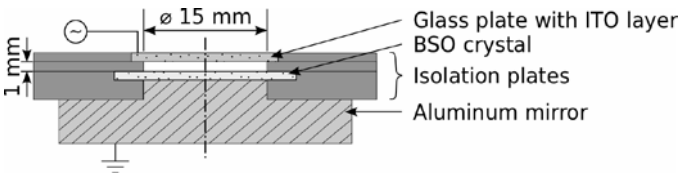


Fig. 1. Side-view of the discharge cell configuration.

Tab. 1. Properties of the dielectric materials.

	BSO ($Bi_{12}SiO_{20}$)	glass plate
diameter [mm]	22.5	22.5
thickness [mm]	0.7	0.7
dielectric const [ε_r]	56	7.6

CCD camera and the electrical contacting of the external voltage. The gap distance of both dielectric materials is 1mm provided by insulated gap spacer. The application of the cross-correlation spectroscopy (CCS) and the gas flow are realized by four sidewise orientated orifices. The working gases are pure helium (< 10 ppm nitrogen impurities) and pure nitrogen and mixture of both at a pressure of 500 mbar. The sinusoidal external feeding voltage has been used at frequencies of 0.5 kHz and 2 kHz. The applied voltage amplitude was varied from about 0.35 kV to 3.7 kV depending on the working gas.

The complete experimental set-up for the investigation of surface charges and the optical discharge evolution is illustrated in fig. 2. Surface charges have been detected on the BSO surface under utilization of the electro-optic Pockels effect [5]. The details are given in fig. 2A. A combined arrangement of a cooled LED ($\lambda = 634\,\mathrm{nm}$) and a Koehler illumination (two lenses and apertures) illuminates the BSO crystal homogeneously. The latter controls the beam diameter, its brightness and focusing. Between the lenses of the Kohler illumination a linear polarization filter is placed. The initially linearly polarized light is reflected onto the BSO crystal by a beam splitter. In the following, a telescopic system enlarges the beam diameter by the factor of five up to 30 mm. A λ/8 wave plate (placed close to the upper lens of the telescopic system) changes the linearly polarized light to elliptically polarized light. The ellipticity is influenced also by the applied external voltage and the voltage drop of deposited surface charges because the BSO becomes birefringent under presence of an electrical field. On the Al-mirror the light is reflected. Hence, the ellipticity changes again after passing the BSO crystal and the λ/8 wave plate. After that, the light runs through the beam splitter before a high speed camera detects the light. In front of the camera a polarizing filter is installed which transmits only linearly polarized light. The coloured filter (transparent from 620 to 640 nm) fades out the light emission of the BD. In this way, the camera detects only the intensity changes of the reflected light. At first, the surface charge measurement requires a reference image without any residual charges. After that, the charges can be calculated from the relative ratio of the intensity with surface charges I and the intensity without surface charges I_r. The surface charge density σ(x,y) can be calculated with the following formula [6]

$$\sigma(x,y) = \frac{\varepsilon_0 \varepsilon_{BSO}}{a_{BSO}} \left(\frac{I(U_{app} + U_\sigma)}{I_r(U_{app})} - 1 \right) \left(U_{app} + \frac{1}{2k} \right) \qquad \text{with} \qquad k = \frac{2\pi}{\lambda} n_0^3 r_{41}, \tag{1}$$

where λ is the wavelength, n_0 is the refraction index, r_{41} is the optoelectronic coefficient, U_{app} and U_σ are the voltage drops over the BSO crystal caused by the external applied voltage and surface charges, respectively, ε_0 is the vacuum dielectric constant and ε_{BSO} is the dielectric constant of BSO. Fig. 2B shows the configuration of the cross-correlation spectroscopy (CCS) allowing the investigation of the optical emission evolution spectrally, spatio-temporally and phase resolved. Because the BD operates under the conditions studied in the diffuse mode, the CCS is triggered electrically by a PC pattern generator (PPG), details in [2]. The mean idea of the CCS technique is the time-correlated single photon counting from about 10^6 consecutive discharges. The emission signal is focused onto a vertically moveable slit via a 1:-1 imaging. Afterwards, the image is focused with a second lens onto an optical fibre connected with a monochromator. The spatial and spectral resolution is 0.05 mm and 0.1 nm, respectively. A single photon counting photomultiplier (PM) detects the spectrally resolved signal and converts it into an electrical signal and analyzed by a constant fraction discriminator (CFD). If a predefined voltage amplitude is reached, a second voltage signal is increased linearly by a time-to-amplitude converter (TAC). An analogue-to-digital converter (ADC) enables the corresponding correlation of the voltage in a time-depending channel memory device (MEM). The result is a temporally and phase resolved intensity distribution of the discharge emission development.

3. Results and discussion

The BD in pure helium and nitrogen usually operates in the diffuse discharge mode. Small admixtures of nitrogen in the percent range to helium result in the filamentary mode [3]. The BD operating in pure helium (<10 ppm nitrogen impurities) is dominated by the 0-0 transition of the second positive system (SPS, $\lambda = 337\,\mathrm{nm}$) and the first negative system (FNS, $\lambda = 391\mathrm{nm}$) of nitrogen. The so-called

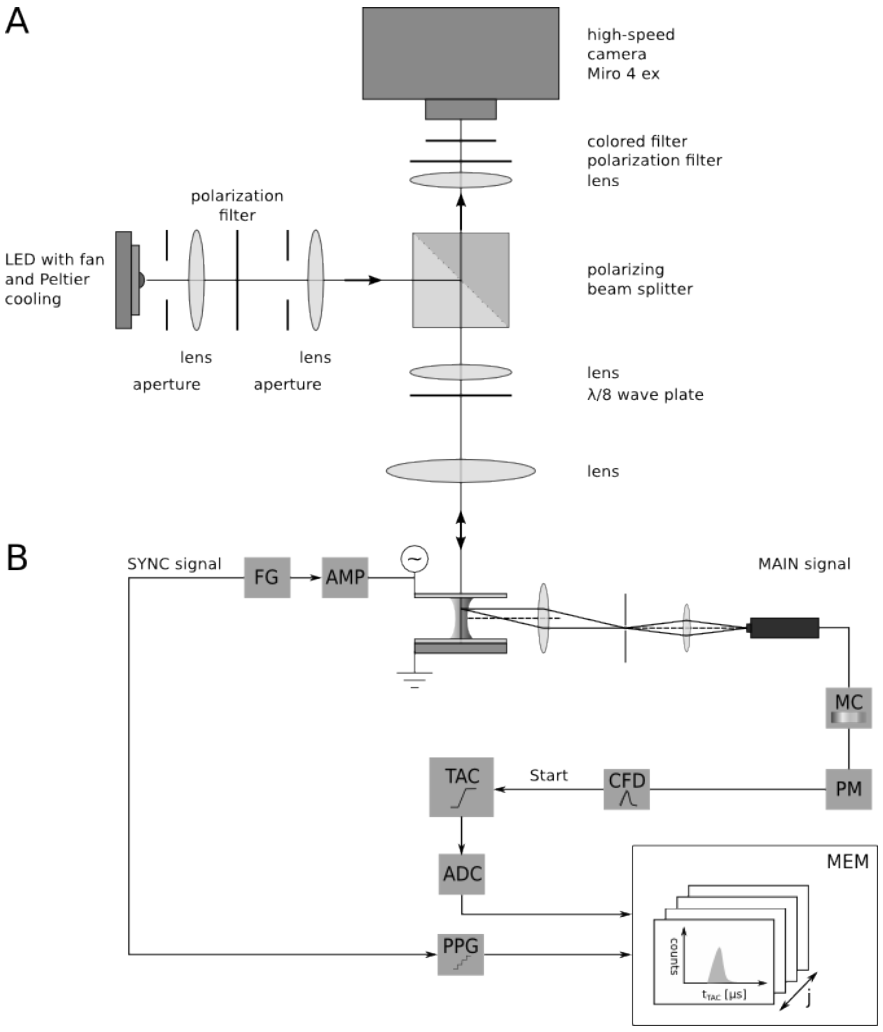


Fig. 2. Experimental set-up for surface charge measurements (A) and spatio-temporally resolved spectroscopic measurements in the volume (B). CCS set-up with PC pattern generator (PPG) triggering: PM - photomultiplier, MC – monochromator, CFD - constant fraction discriminator, TAC - time to amplitude converter, ADC - analogue-digital converter, PPG - pattern generator, MEM - memory.

Penning ionization, inelastic collisions between electrons and nitrogen in the ground state, causes the FNS emission of the exited $N_2^+(B^2\Sigma_u^+)$ ions. The emission of the SPS results from inelastic collisions of electrons with nitrogen in the ground state to the excited $N_2(C^3\Pi_u)$ state. It is followed by the de-excitation to $N_2(B^3\Pi_g)$. Fig. 3 shows the spatio-temporally and spectrally resolved emission evolution of the SPS ($\lambda = 337\,\text{nm}$) and FNS ($\lambda = 391\,\text{nm}$) of the BD operating in pure helium and pure nitrogen. For nitrogen this is well-known that the discharge operates in the APTD [2, 3]. The emission maximum is located near the anode (Fig. 3c) and 3d)). It is characterized by a relatively long duration of the current pulse (several tens of microseconds).The corresponding current density amplitude is in the order of 0.1mA/cm^2. The BD in pure helium operates usually in the APGD (emission maximum near the cathode) at gap distances in the range of $2...5\,\text{mm}$ [3]. But surprisingly, under our experimental conditions (gap distance 1 mm and sinusoidal feeding voltage) appeared the APTD mode, too. Fig. 3a) and 3b) show for helium clearly a similar behaviour like for nitrogen. A reason for the APTD in pure helium is the too small gap distance for the development of the cathode fall region. The APTD in helium is also characterized by a small current density and a current pulse duration of $30\mu\text{s}$, as shown

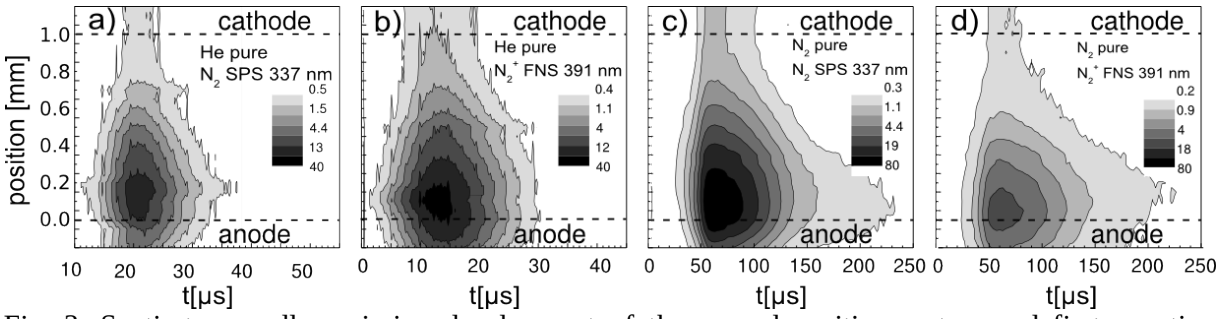


Fig. 3. Spatio-temporally emission development of the second positive system and first negative system in the diffuse helium and nitrogen BD.

in fig. 4. Here, an example for the surface charge development (circles) and the discharge net current (solid line) is presented in the diffuse pure helium discharge Surface charges remain constantly until the current pulse occurs. During the current pulse, it changes its sign according to the current polarity and remains again constantly on the BSO surface until the next current pulse in the next half period. The deposited charge density amounts in both polarities $|\sigma| = 0.5\,\mathrm{nC/cm^2}$. For a quantitative comparison the net current is temporally integrated (dashed line). Besides, the corresponding Lissajous figure is also plotted in fig. 4. It shows directly the transported charge $\Delta Q = 1.75\,\mathrm{nC}$ within one current pulse. For the filamentary mode (conditions: $p = 500\,\mathrm{mbar}$, $\upsilon = 2\,\mathrm{kHz}$, $U = 0.91\,\mathrm{kV}$), in fig. 5a) and 5b) the spatial resolved surface charge distributions for both half periods and the accordant averaged radial profiles of positive and negative surface charges are shown for a of $9{:}1\,\mathrm{He/N_2}$ gas mixture, respectively. The deposited surface charges mark the positions of previous microdischarges. Negative charges deposited on the BSO surface are electrons. The most probable mechanism for positive surface charges is the recombination of ions with electrons from the bulk material. Negative surface

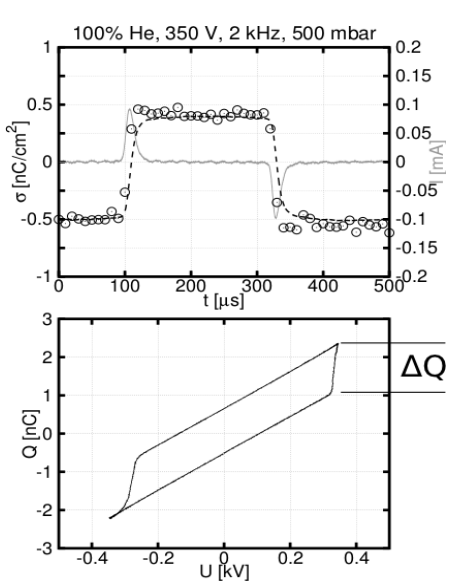


Fig. 4. Phase resolved surface charge from the electro-optic measurement (circles) with the corresponding net current (solid line) and the temporally integration of the net current (dashed line).

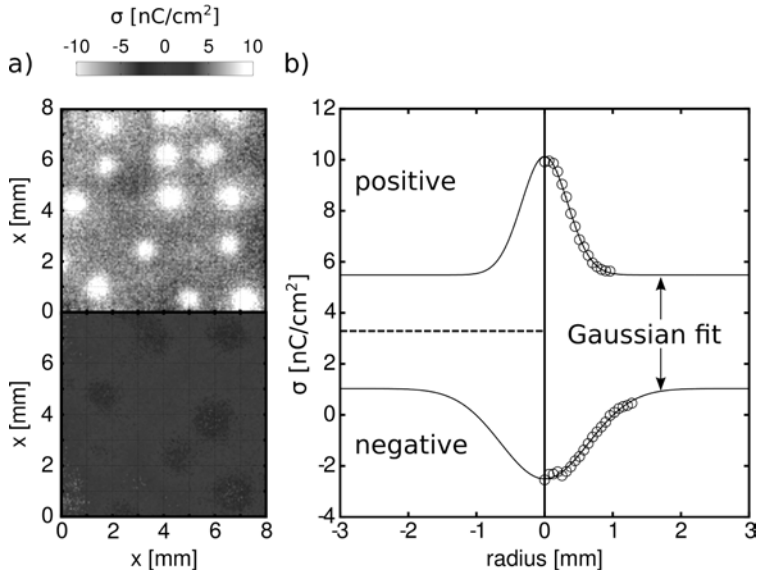


Fig. 5. Charge distribution in the filamentary mode ($90\,vol.\%\,\mathrm{He}$ and $10\,vol.\%\,\mathrm{N_2}$ mixture) of positive (bright spots) and negative surface (dark spots) charges in the positive and negative half-period, respectively. b) Radial profile of positive and negative surface charges, FWHM: $\sigma_+ = 0.9\,\mathrm{mm}$ and $\sigma_- = 1.6\,\mathrm{mm}$, respectively. $p = 500\,\mathrm{mbar}$, $\upsilon = 2\,\mathrm{kHz}$, $U = 0.91\,\mathrm{kV}$.

charges are more extended than the positive ones. The full width at half maximum (FWHM) is 1.6mm to 0.9mm, respectively. The reason is the higher electron mobility in the volume in front of the electrodes in comparison to the ions.
This can be clearly seen in fig. 6. Here, the surface charge measurement of four consecutive half periods is presented. In the subsequent half periods the microdischarges prefer to re-ignite again on positions of deposited surface charges. This is known as the memory effect.

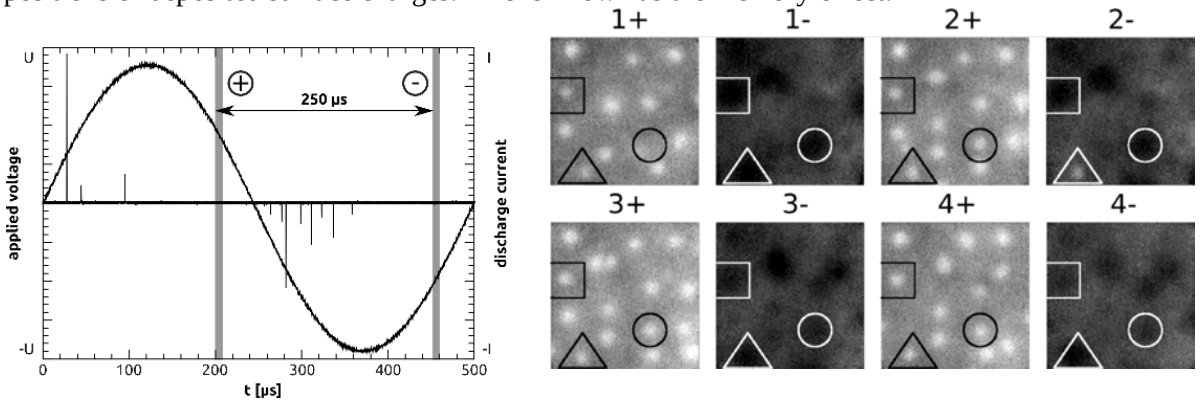


Fig. 6. Left: Timing of the surface charge measurement. At the end of each half period, when no discharge occurs, a record is made. The sign "+" or "-"given in the right image depicts the polarity of the voltage as indicated above. Right: Four consecutive periods. Surface charge measurement at fixed phase positions in the positive (200 µs) and negative 450 µs half period. Positive surface charges: bright spots, negative ones: dark spots. □: long-living filament, Δ: filament misses one or a few driving periods, and O: generating a filament in discharge free area.

Conclusions

For the first time a discharge cell configuration was developed allowing the joint investigation of volume and surface processes of different BD operation modes. In nitrogen the APTD mode was studied. Surprisingly, the unusual APTD mode in helium was found and investigated by the CCS. The measurement of deposited surface charges shows an excellent agreement with the transported charges during a breakdown. In the filamentary discharge mode the memory effect has been clearly confirmed.

Acknowledgement. This work was supported by "Deutsche Forschungsgemeinschaft, SFB/TRR 24,'Complex plasmas' ".

4. References

[1] U. Kogelschatz. *Plasma Chem. Plasma Process.*, 23:1–46, 2003.
[2] K. V. Kozlov, R. Brandenburg, H.-E. Wagner, A. M. Morozov, and P. Michel. *J. Phys. D: Appl. Phys.*, 38:518, 2005.
[3] R. Brandenburg, Z. Navrátil, J. Jánsky, P. Stáhel, D. Trunec, and H.-E. Wagner. J. Phys. D: Appl. Phys., 42:085208, 2009.
[4] S. Nemschokmichal, J. Meichsner, Spatio-temporally resolved density of nitrogen metastables in barrier discharges this issure
[5] A. Yariv. *Quantum electronics*. WILEY New York, 1989.
[6] M. Bogaczyk, S. Nemschokmichal, A. Zagoskin, G. B. Sretenović, J. Meichsner, and H.-E. Wagner. *J. Adv. Oxid. Technol.*, 15:310–320, 2012.

TEMPORALLY AND SPATIALLY RESOLVED INVESTIGATION OF PULSED DRIVEN BARRIER MICRODISCHARGES IN REACTIVE GASES

Ronny Brandenburg, Tomáš Hoder, Hans Höft,
Manfred Kettlitz, Klaus-Dieter Weltmann
Leibniz Institute for Plasma Science and Technology (INP Greifswald),
Felix-Hausdorff-Str. 2, 17489 Greifswald, Germany
E-mail: brandenburg@inp-greifswald.de

Pulsed driven Dielectric Barrier Micro-Discharges (MDs) are investigated by means of fast electrical and optical methods, namely ICCD and streak cameras. The gas mixture (O_2 admixture to N_2) and the parameters of the pulsed power supply (amplitude, duty cycle) are systematically varied in order to investigate their effects on the breakdown processes. In case of asymmetric pulses significant changes in the spatio-temporal development of MDs have been observed. The zone of lower intensity in front of the cathode is larger during the rising than the falling slopes and the velocity of the cathode directed ionizing front changes, too. In case of high voltage pulses below 10 µs even the starting point of MD development changes within the falling slope. Positive and negative streamers are caused by electric field rearrangement in the gap due to the different positive ion densities in relation with their gap transit times.

1. Introduction

There is an increasing interest in atmospheric pressure discharges for technological applications. Due to their low gas temperature, high electron energy and the presence of active species these discharges have a high potential for plasma chemistry e.g. for ozone production as well as gas and water purification [1]. Dielectric barrier discharges (DBDs) are often used in these fields of application. Here, sinusoidal driven ones are basically used in practice [2], but DBDs show a higher efficiency in the production of active species when driven with pulses instead of sinusoidal high voltage [3,4].
The aim of this work is to extend the understanding of the basic processes of filamentary pulsed driven DBDs with precise measurements on single, repetitive micro-discharges (MDs), since the overall effect of filamentary DBDs is determined by the concurrent action of short lived MDs. Fast electrical and optical methods (ICCD and streak cameras) are used for the systematic study of DBD-MDs in dependence on the gas mixture and the parameters of the pulsed power supply.

2. Experiment

A symmetric DBD arrangement (see fig. 1) is used to investigate single MDs. It consists of a gas cell made of plexiglas, including alumina covered half sphere metal electrodes and quartz glass windows to allow the observation of the MDs. The dielectric barrier thickness is about 0.5 mm and the gap of the electrodes is 1 mm. The N_2/O_2 gas mixture (0.1 vol% O_2 in N_2) at 1 atm with a total flow of 100 sccm is flushed through the cell. For pulsed operation of the DBD a pulse generator is used. It is supplied by a high voltage power supply (pulse generator DEI, PVX-4110). In this case, the DBD is driven by unipolar square wave pulses (10 kV amplitude, repetition rate10 kHz). The duty cycle D is varied from 50 % (symmetrical pulse) down to 0.2 %. This corresponds to pulse widths t_{pulse} of 50 µs to 200 ns. The rise time of the high voltage pulse slopes is about 150 V/ns. Thus, the voltage rise time for pulsed mode is three orders of magnitude higher than for sinusoidal operation in the kHz-range. Electrical measurements are performed with fast probes and recorded with a 5 GS/s digital sampling oscilloscope to estimate the electrical power of the discharge. The MDs are observed simultaneously by a fast iCCD camera and a streak camera system connected to a far-field microscope (figure 1). With the iCCD (Andor, iStar) it is possible to get high resolution pictures of single MDs and their propagation on the electrode surfaces ($\Delta t \geq 2$ ns, $\Delta x \approx 10$ µm). The streak camera system (Hamamatsu, C5680) delivers the spatio-temporal MD development along the discharge axis during rising and falling slopes of the electrical pulse with high temporal ($\Delta t \geq 50$ ps) and spatial resolution ($\Delta x \approx 10$ µm). The camera is sensitive in the visible and UV spectral range.

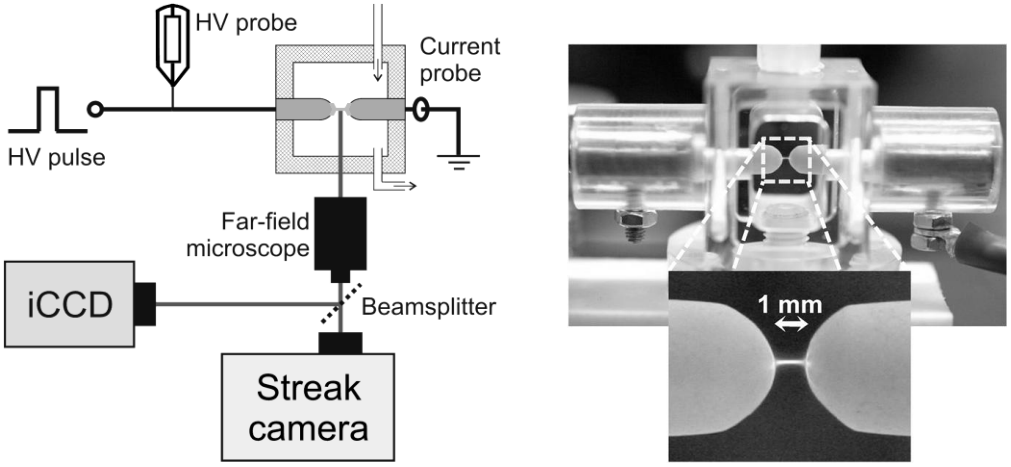


Fig. 1. Experimental set-up with diagnostic (left) and photos of the discharge cell with MD (right).

3. Results

All the results presented here have been taken for a gas mixture of 0.1 vol% O_2 in N_2 and a positive unipolar pulse. The electrical characteristic is presented exemplarily for D = 10 % in fig. 2. The pulsed operation leads to one single MD at the rising and one at the falling slope, respectively. The MD current maximum depends on D. In case of D = 10% it has nearly twice the value the rising slope as in the falling slope. For D = 50% it is the same and reverses for D = 90%.

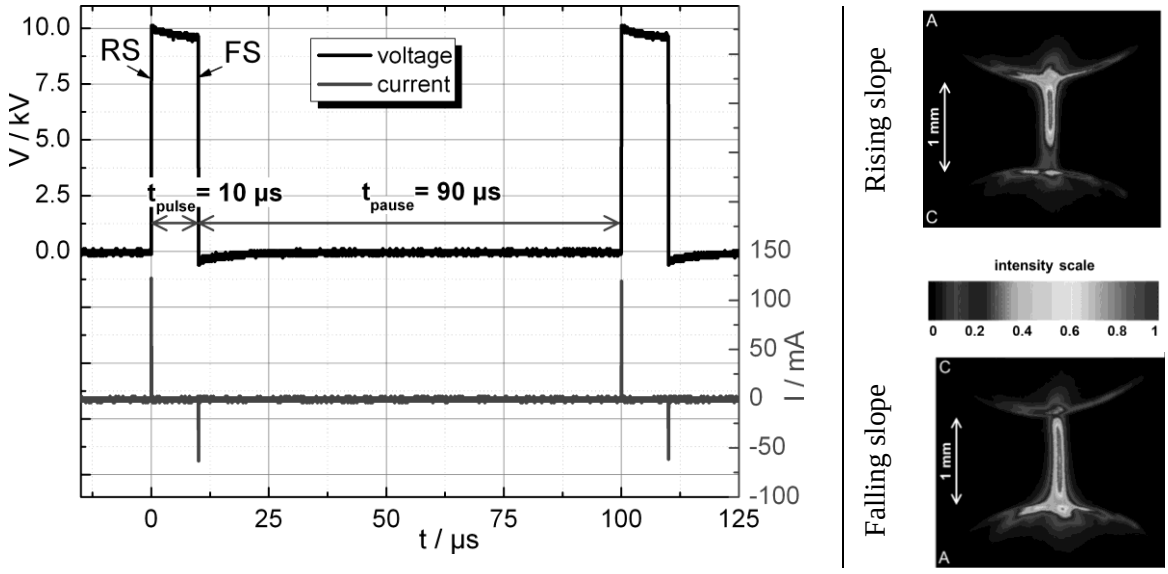


Fig. 2. Electrical characteristics of a pulsed DBD (left) and iCCD-photos (right; accumulation of 1,000 MDs; A= anode, C= cathode) at V_{pulse} = 10 kV with D = 10% at 0.1 vol% O_2 in N_2.

Fig. 2 (right) shows iCCD images of MDs generated in rising and falling slopes of high voltage pulses for D = 10%. All pictures are in pseudo colour. The MD consists of a constricted channel in the volume and branching surface discharges which described in literature [1, 5, 6]. The MD branches are more pronounced at the anode but there are surface discharge channels observed at both electrodes. The diameter of the MD channel in the middle of the gap can be estimated from single iCCD pictures and is about 100 µm which is in good agreement with results for streamer discharges in air [7]. There is a zone of reduced emission of the MD channels in front of the cathode.

The streak camera images of MDs at both slopes under the same conditions as in fig. 2 are displayed in fig. 3. They are taken in the centre along the axis of the discharge channel and visualize its spatio-temporal development. This leads to a one dimensional space diagram over time. The position of the electrode tips is marked by white lines.

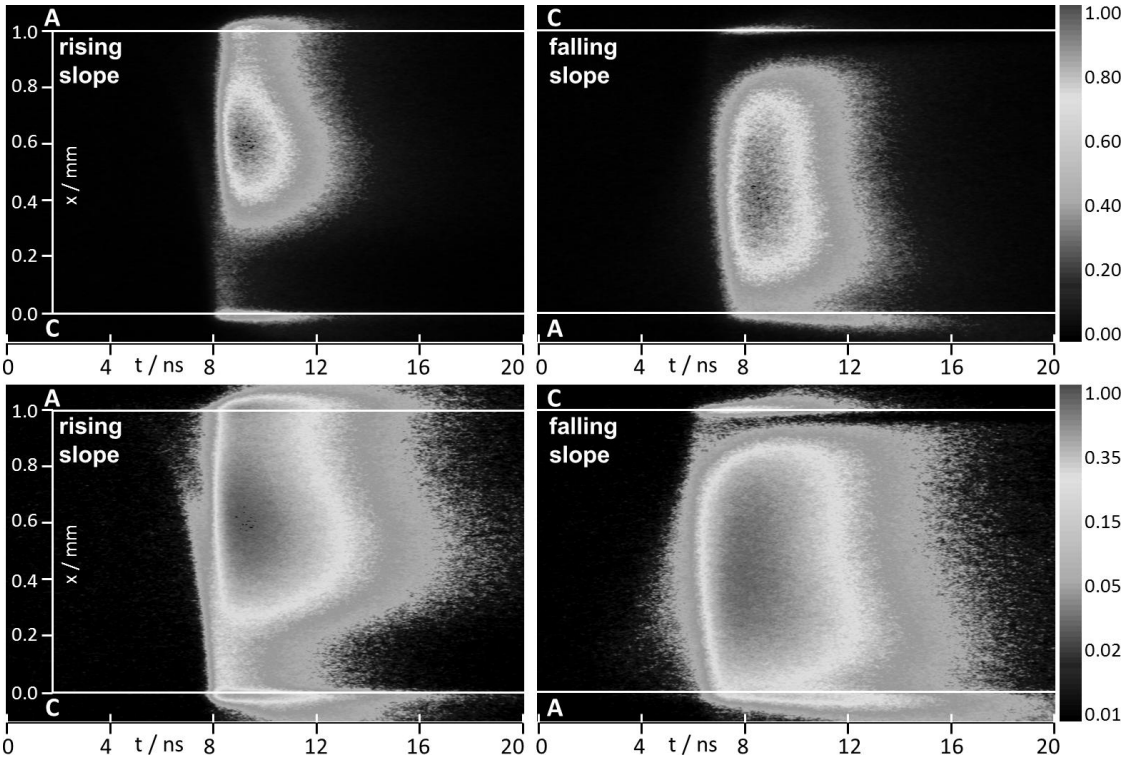


Fig. 3: Spatio-temporal development of MDs along the axis during rising and falling slopes (same conditions as in figure 2), accumulation of 1,000 MDs in linear (top row) and logarithmic intensity scale (bottom row).

The propagation of a cathode directed ionization front or streamer followed by a glow behind the streamer passage is clearly seen and in agreement with results from ac-sinusoidal driven DBDs [8]. The pre-breakdown phase cannot be estimated properly from these measurements because of the low emission and limited sensitivity of the streak camera detector. Its duration is at least 3 ns [9]. The surface discharges in their temporal development can also be seen on the electrodes. For $D \neq 50$ % there are distinct differences in the MD development and structure for the two different slopes [10]. For D = 10 % the MD at the rising slope has a shorter duration than at the falling slope. The zone of lower emission after the passage of the streamer in front of the cathode is much shorter in case of the rising slope. Consequently the glow phase is concentrated at the anode for the rising slope and more located in the volume in case of falling slope. In the same manner the phase of cathode directed streamer is affected.

Figure 4 shows the comparison of the spatio-temporal MD development for the duty cycle variation at the example of the rising slope. The streamer propagation velocity clearly depends on the time delay to the preceding MD. The MD lasts longer during the falling slope and the cathode directed streamer propagates faster in the rising slope for D = 10%. The differences between the discharge current maxima are consistent with the streamer velocity behaviour. When the streamer propagates faster it generates more charge carriers at this certain time and so the discharge current maximum rises, too. However, the total transferred charge is equal for both slopes due to the short discharge duration. For symmetric pulses (D = 50%) there are no significant differences between the MDs at rising and falling slopes and if the time between them is reversed then all effects are reversed, too [10]. Thus, the time between the MDs has a significant effect on the discharge physics. Obviously residuals from the preceding MD influence the breakdown and plasma formation. Both volume as well as surface processes taking place on a 10 µs time scale must be considered to explain the dependence of MD

development on duty cycle. At the conditions being considered nitrogen metastables $N_2(A)$ have an effective lifetime in the same order of magnitude than t_{pulse} and may influence the MD generation. Ionization of metastables requires less energy than from the ground state, which demands for less direct ionization and has a significant influence on the positive streamer characteristics as shown for high operation frequencies [11, 12]. Furthermore, metastables are considered to lead to secondary emission of electrons from charge dielectric surfaces (so-called exo-emission) [13]. The general discharge development as described above remains in principle the same at both slopes as long as t_{pulse} is larger than the ion drift time for the 1 mm gap (about 1µs) [9]. This result is shown in fig. 5.

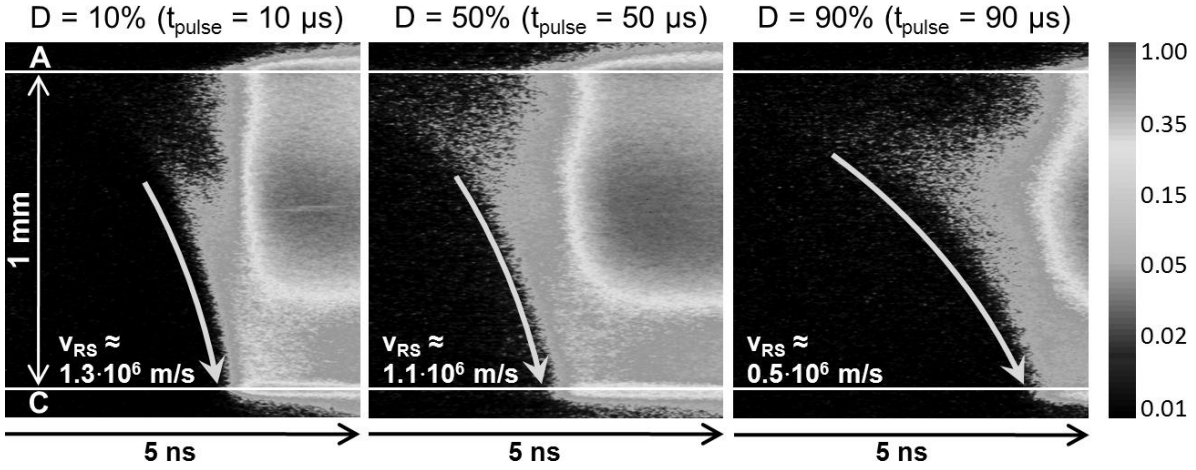


Fig. 4. Comparison of the change of the velocity of the cathode directed streamer at rising slope by changing the duty cycle D = 10%; 50%; 90% (logarithmic intensity scale).

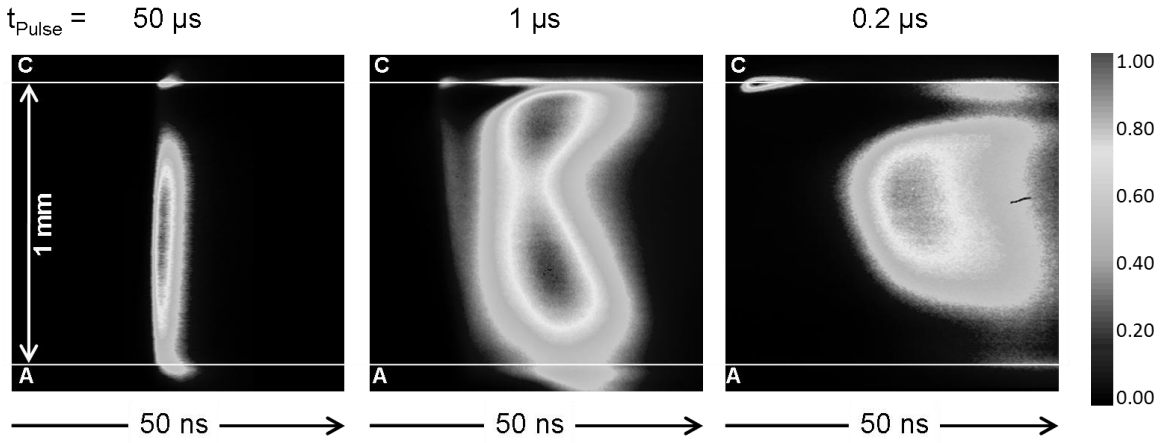


Fig. 5. MD development at falling slope by changing D respc. t_{Pulse} (accumulation of 1,000 MDs, linear intensity scale).

For the pulse width of 1 µs (fig. 5, middle), the MD development starts with a very short emission close to the cathode. There, the cathode directed streamer is ignited followed by an anode directed streamer. Both streamers are hardly seen in fig. 5 due to the linear intensity scale. They reach velocities in the order of 10^5 m/s [9]. After the positive and negative streamers impact onto the electrodes, a structure similar to glow discharge (cathode spot and positive column at the side of the anode) is created. In this phase two overall maxima of emission with slow propagation towards the neighbouring electrodes are observed. Simultaneously the filament diameter increases from the middle of the gap towards the electrodes where they impact and create surface discharges. The development of the MD for t_{pulse} = 200 ns also shows the emission close to the cathode at the beginning and the two local maxima. The explanation of this effect is supposed to be the variation of the positive nitrogen ion density in the gap originating within the preceding MD in the rising slope, since the time of flight for

positive ions of nitrogen and oxygen through the whole gap correlates with the duration of the applied voltage pulse widths. These ions will not reach the cathode before the next breakdown in the falling slope and therefore will be present in the gap. During the falling slope ions rearrange the electric field changing the starting conditions for the next breakdown changes. This affects the electrical parameters and MD. The role of an accumulated positive ion cloud in front of metallic cathode has already been discussed for the phenomenon of Trichel pulse ignition [14, 15] and is of fundamental importance in breakdown theory.

4. Summary and outlook

Simultaneous streak and iCCD recording of MDs in a 1 mm gap pulsed-driven DBD are presented. For the conditions being considered (gas mixture 0.1 vol% O_2 in N_2, pulse rising of 150 V/ns) the same principle phases of discharge development as known from sinusoidal and pulsed-driven DBDs are observed, namely pre-breakdown, cathode directed streamer, anode glow and surface discharges. Novelty of the results is that in case of asymmetric high voltage pulses significant differences in the formation of MDs in the rising and in the falling slopes have been investigated. As shorter the time between two MDs, as lower is the current peak maximum in the second MD. This behaviour is along with a slight increase of MD duration, a slower streamer, a shorter zone of lower intensity in front of the cathode and the expansion of the anode glow into the volume. For symmetric pulses there are no significant differences between the MDs at rising and falling slopes. Volume as well as surface processes must be considered to explain this behaviour. Elevated densities of nitrogen metastables may enhance background ionization in the volume as well as from the dielectric (charged) surface leading to changes in the dynamics of streamer propagation and thus MD structure and properties. At small duty cycles ($D \leq 1$ %) accumulated positive ions rearrange the local electric field and change the starting conditions for the next breakdown which leads to significant different MD development.

The results show that pulse width variation gives the possibility to control MD properties down to the level of fundamental plasma parameters [9, 10]. In contrast to sinusoidal driven DBDs the transferred charge and power of single repetitive MDs can be controlled, which offers new possibilities for the optimization and control of plasma chemistry, e.g. for exhaust gas treatment, life-science applications or synthesis.

5. References

[1] Kogelschatz U 2003 *Plasma Chemistry and Plasma Processing* **23**, 1.

[2] Penetrante B M, Schultheiss S E (Eds.) 1993 *Non-thermal Plasma Techniques for Pollution Control*, Springer-Verlag Berlin Heidelberg.

[3] Ono R, Nakagawa Y, Oda T 2011 *J. Phys. D: Appl. Phys.* **44** 485201.

[4] Namihira T, Tsukamoto S, Wang D Y, Katsuki S, Hackam R, Akiyama H, Uchida Y. Koike M, 2000 *IEEE Trans. Plasma Sci.* **28** 434–42.

[5] Brandenburg R, Wagner H-E, Morozov A M, Kozlov K V 2005 *J. Phys. D: Appl. Phys.* **38** 1649.

[6] Kumada A, Okabe S and Hidaka K 2009 *J. Phys. D: Appl. Phys.* **42** 095209.

[7] Nijdam S, Wormeester G, van Veldhuizen E M, Ebert U 2011 *J. Phys. D: Appl. Phys.* **44** 455201.

[8] Kozlov K V, Brandenburg R, Morozov A M Wagner H-E, Michel P 2005 *J. Phys. D: Appl. Phys.* **38** 518.

[9] Hoder T, Höft H, Kettlitz M, Weltmann K-D and Brandenburg R 2012 *Physics of Plasmas* **19**, *in press.*

[10] Kettlitz M, Höft H, Hoder T, Reuter S, Weltmann K-D and Brandenburg R 2012 *J. Phys. D: Appl. Phys.* **45** 245201.

[11] Nijdam S, Wormeester G, van Veldhuizen E M and Ebert U 2011 *J. Phys. D: Appl. Phys.* **44** 455201.

[12] Bourdon A, Bonaventura Z, Celestin S 2010 *Plasma Sources Sci. Technol.* **19** 034012.

[13] Marbach J, Bronold FX, Fehske H 2012 *Europ. Phys. Jour D* **66**, 4, 106.

[14] Cernak M, Hosokawa T 1991 *Phys. Rev. A* **43** 1107.

[15] Bessieres D, Paillol J, Soulem N 2004 *J. Appl. Phys.* **95** 3943.

HYDROGEN PRODUCTION FROM BIOMETHANE USING DBD

Mirosław Dors[1], Tomasz Izdebski[1], Jerzy Mizeraczyk[1,2], Marek Kocik[1]

[1] *Centre for Plasma and Laser Engineering, The Szewalski Institute of Fluid Flow Machinery, Gdańsk, Poland*

[2] *Department of Marine Electronics, Gdynia Maritime University, Gdynia, Poland*

E-mail: mdors@imp.gda.pl

Production of hydrogen from CH_4:CO_2 (70%:30%) mixture simulating dry biogas in a DBD reactor supplied with AC of 1.0-2.0 kHz or nanosecond negative pulses is presented. We have found that hydrogen production and methane conversion degree increase linearly with discharge power in the range of up to 50 W. Nanosecond voltage pulses are much more efficient in hydrogen production than sine AC voltage.

1. Intorduction

So far most plasma methods of hydrogen production use such substrates as natural gas, gasoline, heavy oils, and kerosene. Many of them uses combination of plasma with catalysts either as single-stage or two-stage system. The single-stage type is constructed by packing catalyst pellets within the plasma zone or coating catalyst on the surface of electrode(s). As for the two-stage type, the plasma zone is located either upstream or downstream the catalyst bed, which is termed as plasma preprocessing and plasma postprocessing, respectively.

Unfortunately, plasma-catalytic systems are not useful when biogas containing sulphides (mainly H_2S) are going to be processed due to catalyst poisoning. There are several publications claiming to describe production of hydrogen from biogas using plasma-catalyst systems [1-4]. However, the authors has used a mixture of methane with carbon dioxide simulating a biogas but without any additives which are present in real biogas such as water vapour, H_2S and NH_3. Such a simple simulation of biogas is not appropriate when the outlet gas is going to be used with fuel cells, which are very sensitive to H_2S traces. There are only 2 papers on using real biogas and they were published by one research group in 2008 and 2010. Sekine et al [5, 6] studied application of pulsed corona discharge (PCD) reactor and dielectric barrier discharge (DBD) reactor without any catalyst and they found that PCD could convert biomethane into syngas and H_2S into solid sulfur simultaneously. This is due to the high electron energy of PCD and the electron has enough energy to dissociate C–C bond and C–S bond. On the other hand, DBD could convert H_2S into solid sulfur too, but methane and CO_2 in the biogas were not reacted at lower input power. The investigation by Sekine et al. showed that proper choice of electrical discharge can brings elective reaction for dry reforming of biomethane and desulfurization, and this is due to the correlation between the bond dissociation energy of each molecule and electron energy level of each discharge. Our proposal is to verify this conclusion by parametrical studies of biomethane reforming using DBD and real biogas or a mixture simulating biogas with its trace components (influence of voltage pulses shape, duration and frequency, influence of reactor geometry).

In this work a first stage of our studies concerning hydrogen production from simple biogas-like mixture of methane and carbon dioxide is presented.

2. Experimental set-up

A. DBD Reactor

In this paper results obtained in one specific DBD reactor are presented. The scheme of the reactor is shown in Fig. 1. It is made of a quartz glass tube of inner diameter 15 mm in which a high voltage RVC (Reticulated Vitreous Carbon) electrode is placed. The glass tube is covered with aluminum foil remaining a 4 mm wide slit along the reactor. RVC electrode is formed in a tube of outer diameter 8 mm, inner diameter 3 mm and length 150 mm. Through that RVC tube a mixture of methane and

carbon dioxide (70%:30%, respectively) simulating dry biogas was introduced into the reactor. Due to relatively low porosity of the RVC tube, which is 80 ppi (pores per inch), it does not obstruct the gas flow which was kept at 200 cm^3/min.

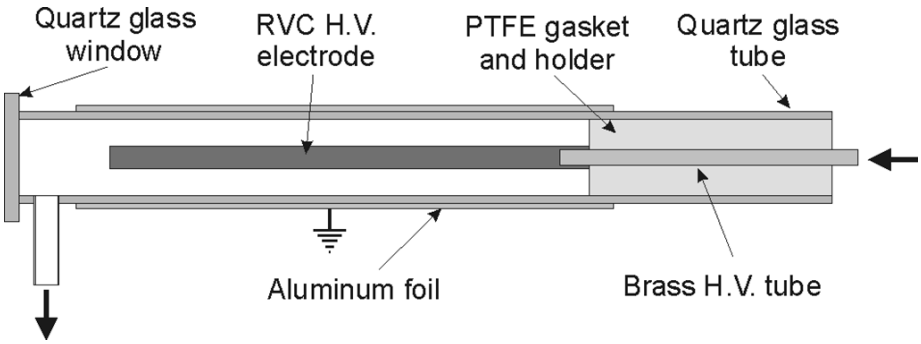


Fig. 1. DBD reactor with RVC electrode.

B. High Voltage Power Supply

Two different type of supply for DBD reactor have been used. The first one is composed of function generator Tektronix AFG3101 and amplifier TREK 40/15. It allows to modify voltage pulses shape and frequency up to 2 kHz. In this work results for AC sine voltage of up to 35 kV_{p-p} and repetition rate of 1 kHz, 1.5 kHz and 2 kHz are presented. Discharge power was determined from Lissajous curves (Fig. 2).

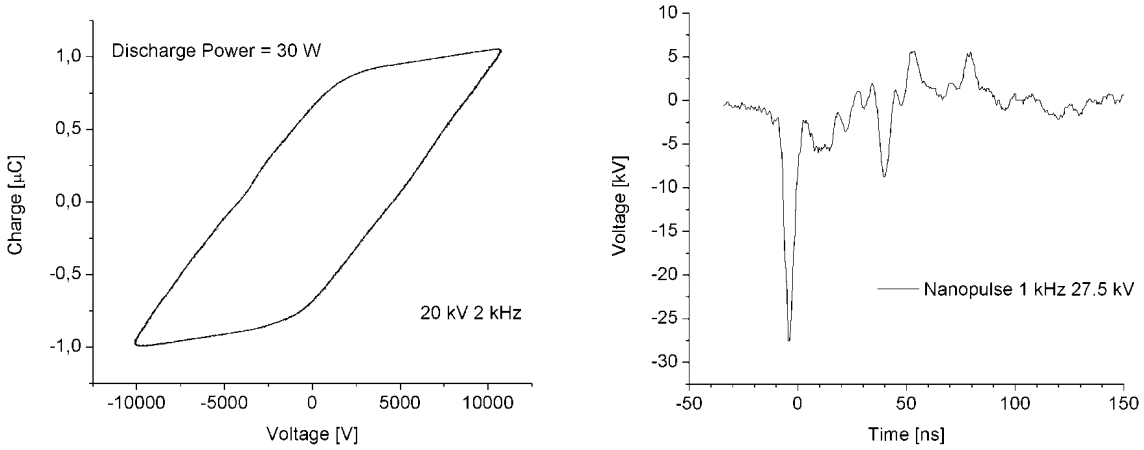


Fig. 2. a) Typical Lissajous curve obtained during DBD. Presented curve concerns sine voltage of 20 kV and 2 kHz. Determined discharge power was 30 W; b) Typical voltage and current pulses generated by nanosecond pulse generator NPG-15/2000 in our DBD reactor. Pulse energy 5 mJ.

The second power supply for DBD reactor was a nanosecond pulse generator NPG-15/2000 by Megaimpulse Ltd. Typical negative voltage pulse shape obtained from that power supply is shown in Fig. 3a. In this work we used voltage pulses of 29 kV and repetition rate in the range 50 Hz – 2.5 kHz. Voltage pulses were measured using high voltage probe Tektronix P6015A whereas current pulses (Fig. 3b) were measured using Pearson 2878 coil.

C. Diagnostics

Gas composition before and after the processing in the DBD reactor was analyzed using FTIR spectrophotometer and gas chromatograph. For measurements of CO as well as for detection of other heterogenic molecules the FTIR Nicolet 380 spectrophotometer with gas cell of 10 cm optical path length and $CaCl_2$ windows was used. Diagnostics of H_2 and CH_4 was carried out using SRI 8610C gas chromatograph with TCD and molecular sieve column and argon as a carrier gas.

Temperature of the processed gas at inlet and outlet of the DBD reactor was measured with thermocouples. Initial gas temperature was kept at 19°C all the time during the experiment.

3. Results

A. AC sine supply

Processing the mixture simulating dry biogas in the DBD reactor with RVC high voltage electrode results in formation of hydrogen, carbon monoxide and acetylene as the only gaseous products. Production of hydrogen in the DBD reactor supplied with sine high voltage shows typical dependence on discharge power and frequency. As it is seen in Fig. 5a, hydrogen concentration in the outlet gas grows linearly when increasing discharge power. The highest concentration of hydrogen of 4.4% was recorded at 1.5 kHz sine voltage of 30 kVp-p which corresponds to discharge power of 46.5 W which is the maximum discharge power used in the experiment. Resulted efficiency of hydrogen production is 0.94 g/kWh.

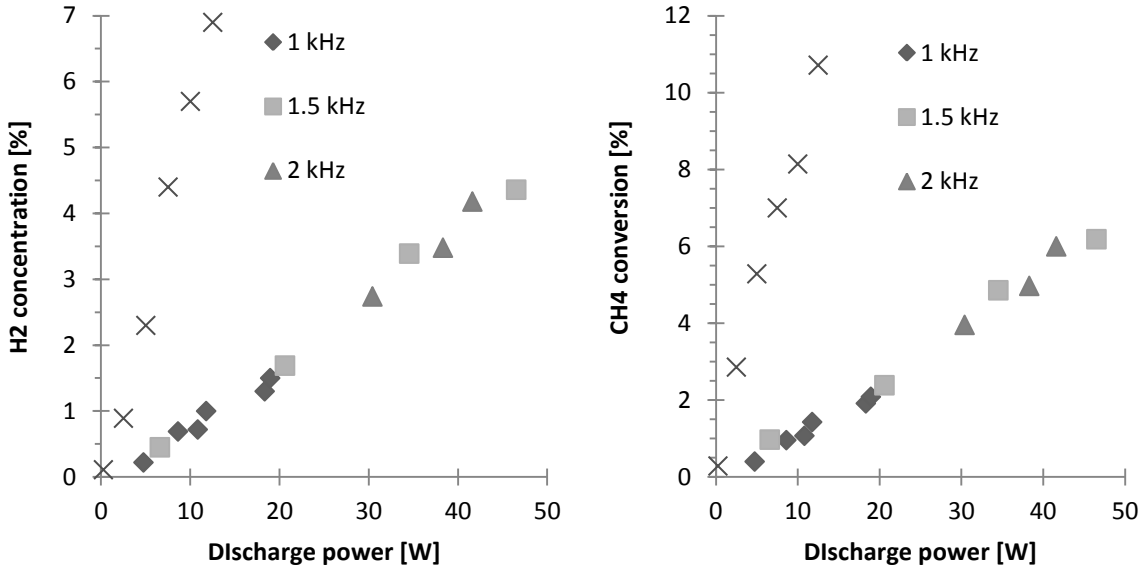


Fig. 5. Hydrogen concentration and methane conversion in CH_4:CO_2 (70%:30%) gas mixture as a function of discharge power for different AC sine frequency and for nanosecond negative pulses.

As methane is the only source of hydrogen, the production of hydrogen corresponds to consumption of methane. Relation of methane conversion degree on the discharge power and frequency is shown in Fig. 5b. The conversion degree is low but it must be noted that the experiment was conducted using gas of room temperature and without water vapor normally present in the real biogas. Similar methane conversion degree was observed in CH_4:CO_2 mixture processed in DBD reactor by Sekine et al. [6].

When methane conversion proceeds in the thermodynamic equilibrium then concentrations of products are governed by the summary reaction:

$$CH_4 + CO_2 = 2\ CO + 2\ H_2, \qquad (1)$$

and can be calculated for a wide range of temperature (Fig. 6). It is clear that ratio CO:H_2 should be as 1:1. In such a case, basing on experimentally obtained concentration of H_2, one can conclude that temperature of gas in the DBD plasma, i.e. in filaments, is close to 700 K.

However, experimentally measured concentration of CO is much lower than hydrogen concentration. Concentration of carbon monoxide formed from CO_2 in the DBD is shown in Fig. 7a. From non-linear increase of CO concentration as well as from the ration of CO:H_2, which is much higher than 1:1, it is seen that CO is not produced in a dry reforming reaction (1) but in a dissociation reaction typical for non-thermal plasma. The same ratio CO:H_2 was observed by Nagazoe et al. [7] in their experiment with CH_4:CO_2 processed by microwave plasma.
Concentrations of acetylene produced from methane in the DBD reactor with RVC high voltage electrode do not exceed 300 ppm (Fig. 7b) and again increase linearly with discharge power.

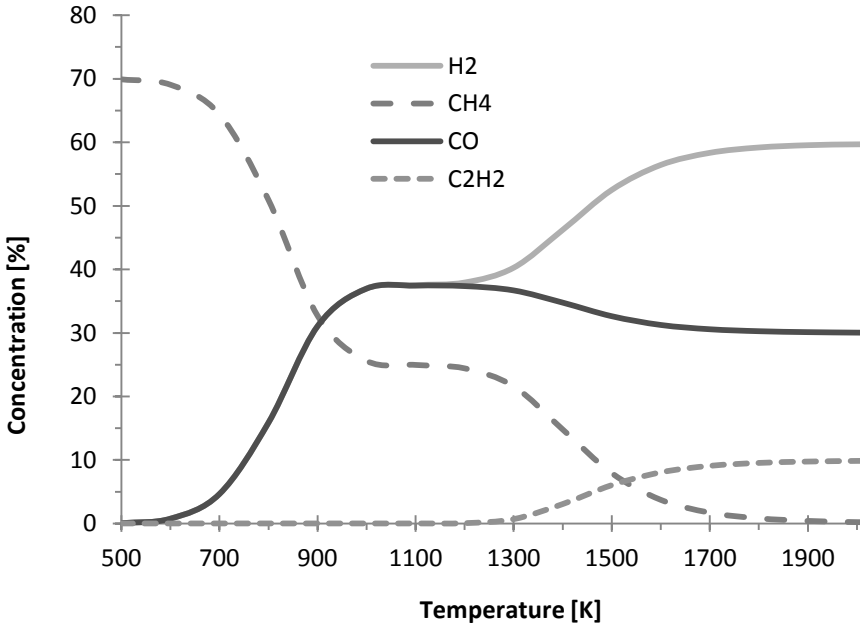


Fig. 6. Concentrations of CH_4 and its conversion products calculated for thermodynamic equilibrium.

B. Supply by nanosecond high voltage pulses

When the DBD is generated using nanosecond high voltage pulses production of hydrogen and corresponding methane conversion increases linearly with pulse repetition rate (Fig. 5). Obtained concentration of H_2 and conversion of CH_4 are slightly higher comparing to those for the DBD generated by sine AC voltage. Maximum hydrogen concetration is 6.9% at 2.5 kHz repetiton rate. However, resulted efficiency of hydrogen production is 5.47 g/kWh which is 5,8 times higher than that obtained when applying sine AC voltage.

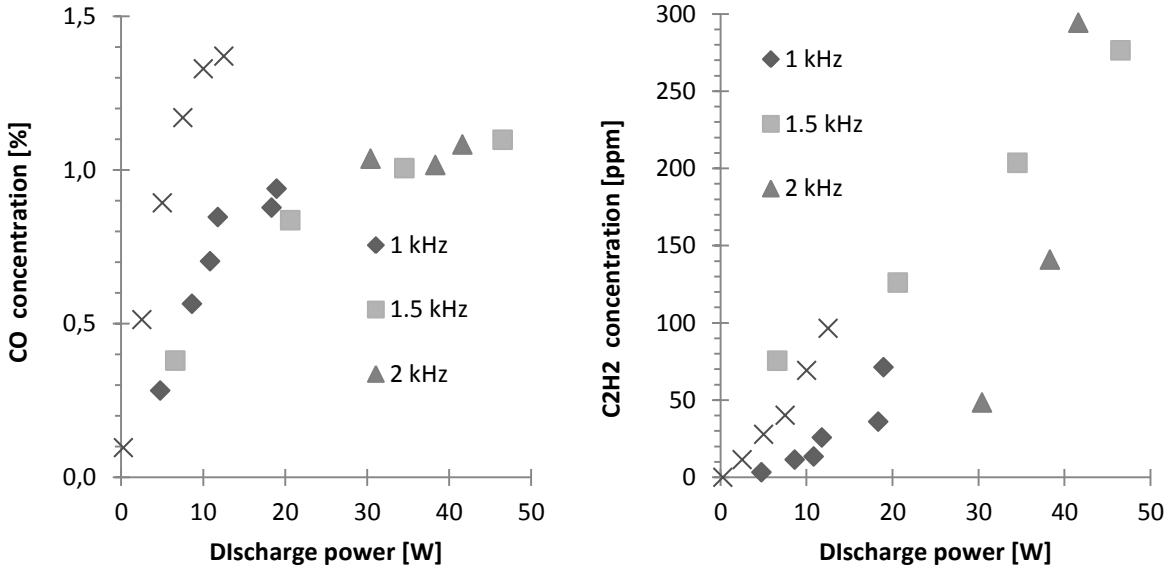


Fig. 8. Carbon monoxide concentration produced in CH_4:CO_2 (70%:30%) gas mixture as a function of discharge power for different AC sine frequency and for nanosecond negative pulses.

Concentration of CO formed from CO_2 in the DBD supplied with nanosecond pulses is shown in Fig.8a. Both non-linear CO concentration increase and ratio CO:H_2 is similar to that observed when applying AC voltage. Concentrations of acetylene do not exceed 100 ppm (Fig. 8b) and again increase linearly with discharge power. In contrast to AC voltage supplied DBD nanosecond pulses results in 3 times lower acetylene concentration.

4. Conclusions

Processing of CH_4:CO_2 (70%:30%) gas mixture simulating dry biogas using dielectric barrier discharge reactor with reticulated vitreous carbon high voltage electrode showed that:

- Hydrogen production and methane conversion degree increase linearly with discharge power in the range of up to 50 W;
- Nanosecond voltage pulses are much more efficient in hydrogen production than sine AC voltage;
- DBD supplied with nanosecond voltage pulses produces much lower acetylene than in the case of sine AC voltage supply;
- Conversion of methane in DBD exhibits different chemistry than that typical for thermodynamic equilibrium.

This work was carried out using gas of room temperature and without water vapor normally present in the real biogas. Thus, in real biogas we may expect much higher hydrogen production efficiency and methane conversion degree as observed by other researchers conducting plasma assisted steam reforming of methane.

ACKNOWLEDGEMENT

This work was supported by the National Science Centre under the project No. 2011/01/B/ST8/04131.

5. References

[1] T. Nozaki, H. Tsukijihara, W. Fukui, K. Okazaki, "Kinetic Analysis of the Catalyst and Nonthermal Plasma Hybrid Reaction for Methane Steam Reforming", *Energy & Fuels*, vol. 21, pp. 2525-2530, 2007.

[2] V. Goujard, J.M. Tatibouet, C. Batiot-Dupeyrat, "Use of a non-thermal plasma for the production of synthesis gas from biogas", *Appl. Catal. A: General, vol.* 353, pp. 228–235, 2009.

[3] Y.C. Yang, B.J. Lee, Y.N. Chun, "Characteristics of methane reforming using gliding arc reactor", *Energy*, vol. 34, pp. 172–177, 2009.

[4] Y.N. Chun, Y.C. Yang, K. Yoshikawa, "Hydrogen generation from biogas reforming using a gliding arc plasma-catalyst reformer", *Catalysis Today*, vol. 148, pp. 283–289., 2009.

[5] Y. Sekine, J. Yamadera, M. Matsukata, E. Kikuchi, "High-efficiency dry reforming of biomethane directly using pulsed electric discharge at ambient condition", *Energy & Fuels*, vol. 22, pp. 693–694, 2008.

[6] Y. Sekine, J. Yamadera, M. Matsukata, E. Kikuchi, "Simultaneous dry reforming and desulfurization of biomethane with non-equilibrium electric discharge at ambient temperature", *Chemical Engineering Science*, vol. 65, pp. 487-491, 2010.

[7] H. Nagazoe, H. Naito, M. Kobayashi, T. Yamaguchi, H. Kimuro, K. Onoe, „CH_4 reforming with CO_2 using microwave plasma technique", in *Proc. 16th Int. Symp. on Plasma Chemistry*, 2003, Taormina, Italy, pp. 321-326

DECOLORATION OF WATER CONTAMINATED BY DYES USING NON-THERMAL PLASMA

Tomasz Izdebski[1], Mirosław Dors[1], Jerzy Mizeraczyk[1,2]

[1] *Centre for Plasma and Laser Engineering, The Szewalski Institute of Fluid Flow Machinery, Gdańsk, Poland*

[2] *Department of Marine Electronics, Gdynia Maritime University, Gdynia, Poland*

E-mail: tizdebski@imp.gda.pl

In this paper an AC corona discharge is proposed for methylene blue decoloration which because of its stable molecular structure, is the most commonly used organic contaminant that imitates bacteria. Two configuration of reactors were investigated. Results showed that AC corona discharge with a wire-to-plate type configuration of electrodes is highly efficient in the decoloration process. Different mechanisms of methylene blue decoloration were observed as different reaction rate constants (k0, k1) were obtained. In the first reactor the zero order constant was dominating, in the second reactor type the first order reactions were the dominant.

1. Introduction

The most frequent reason of epidemic formation is the pollution of the surface and drinking water by wastewater bacteria. The largest part of this pathogenic microorganisms are fecal bacteria, for example *Escherichia coli* (*E. coli*). The wastewater treatment plants reduce the amount of the fecal bacteria by 1-3 orders of magnitude, depending on the initial number of bacteria, which can be 104-106 colony forming units (cfu) in 1 ml. To enhance efficiency of bacteria inactivation in the wastewater and drinking water various methods are tested, like electrochemical and photocatalytic disinfections, Fenton reaction, UV irradiation, and electrohydraulic discharges, i.e. electrical discharges in water, such as pulsed arc between needle electrodes, pulsed corona between wire and plate, pulsed corona with addition of gas as bubbles and without added gas. Electrical discharges in water or at the water gas interface have been investigated as well for the degradation of various organic compounds, including organic dyes [1-4].

There is much research in applying plasma discharges to water purification and inactivation of microorganisms present in water. Recently the use of AC corona discharge above water is being investigated [5,6].

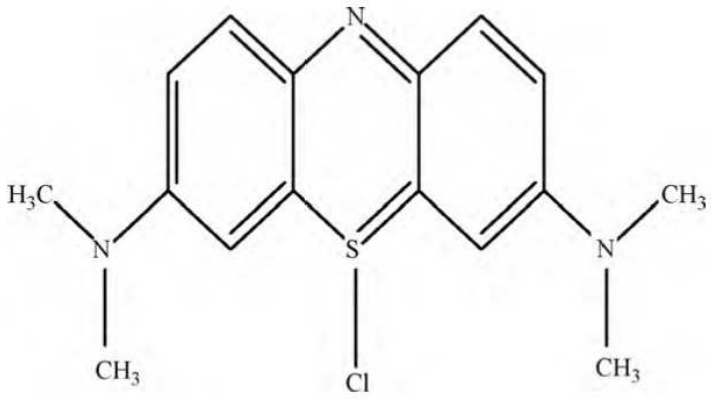


Fig. 1. Chemical structure of methylene blue molecule.

Because of its stable molecular structure Fig. 1, the most commonly used organic contaminant that imitates bacteria is methylene blue [7,8]. This study focuses on exploring the reaction mechanism of AC corona plasma action and methylene blue molecules by analyzing the degradation process of methylene blue solution.

The typical degradation mechanism of methylene blue molecule involves a strong oxidant like O_3 [9]. It can directly oxidize the molecule:

$$O_3 + M \rightarrow M^+ + O_3 \quad (1)$$

O_3 triggers decomposition reactions and generates hydroxyl radicals. These radicals have grater oxidation potentials and are formed through reactions (2) and (3). Due to high oxidative potential of 2.72 V, the organic molecules could even be directly mineralized by hydroxyl radicals.

$$OH^- + O_3 \rightarrow \bullet O_2 + HO_2\bullet \quad (2)$$

$$O_3 + 3HO_2\bullet \rightarrow 3\bullet OH + 3O_2 \quad (3)$$

The zero-order reactions were also observed in gliding discharge reactors as first kinetic step for concentrated solutions [10,11]. In these reactors, the electrodes are positioned in the gas phase above the liquid surface. The plasma discharge is producing active species and they are carried by the flux gas and bombard the target molecules at the gas-liquid interface so that the organic molecule concentration is a linear function of the exposure time to the discharge. When the target solution becomes more diluted a first order reaction is observed and the process is governed by the diffusion phenomena.

2. Experimental setup

Methylene blue decoloration was performed in a cylindrical reactor of the inner diameter of 50 mm and 45 mm height (Fig. 2). The water level was at 10 mm from the grounded electrode and the gap between the electrodes was 25 mm. Volume of treated water was 20 ml. Two configuration of electrodes were used. The first one was with the plexiglass barrier between the water and grounded steel plate electrode (Fig. 2a). The second configuration is a wire-to-mesh type configuration (Fig. 2b). Two types of wire electrode were used: Kanthal D steel wire and a platinum wire.

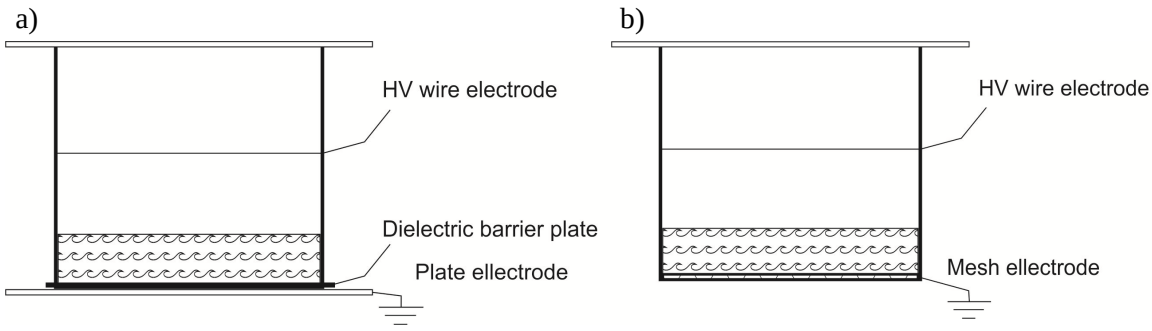


Fig. 2. Reactor schematics - a) reactor 1 – wire-to-plate configuration, b) reactor 2 – wire-to-mesh configuration.

The reactor is powered by a an AC power supply set to 28 kV, but due to the heating of power supply, the voltage dropped about 1 kV per 5 min to a 22 kV minimum. The frequency was established for optimal power and was stable at 6 kHz.
Discharge power was estimated using Lissajous curves measured with a Tektronix oscilloscope [12]. The voltage waveforms were registered with a high voltage probe Tektronix P6015. Typical Lissajous figure is presented in Fig. 3.

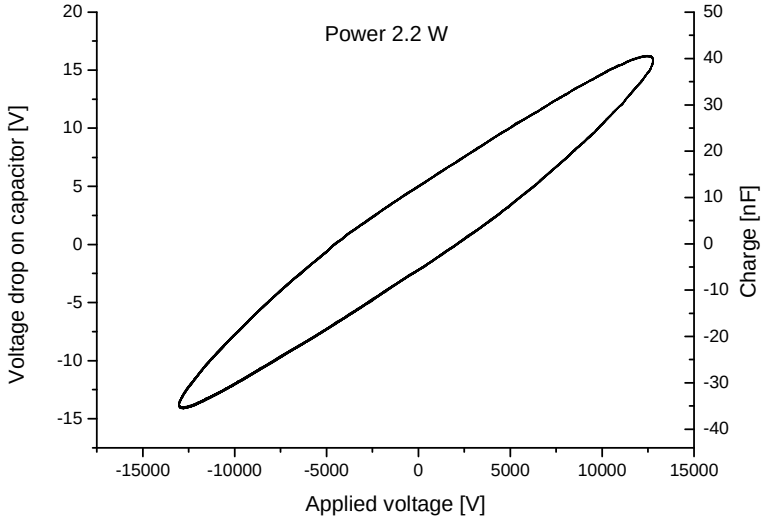


Fig. 3. Standard Lissajous curve for discharge power measurement.

The concentration of methylene blue in target solution was measured with Metertech SP8001 spectrometer at the strongest absorption peak λ=665 nm. Initial concentration of methylene blue was 4 ppm. Temperature and pH of the target solution were 22^0C and 7 respectively.

3. Results

Results of decoloration in two types of reactors are shown in Fig. 4. It is seen that the wire-to-meshe reactor is more efficient than the wire-to-plate reactor.

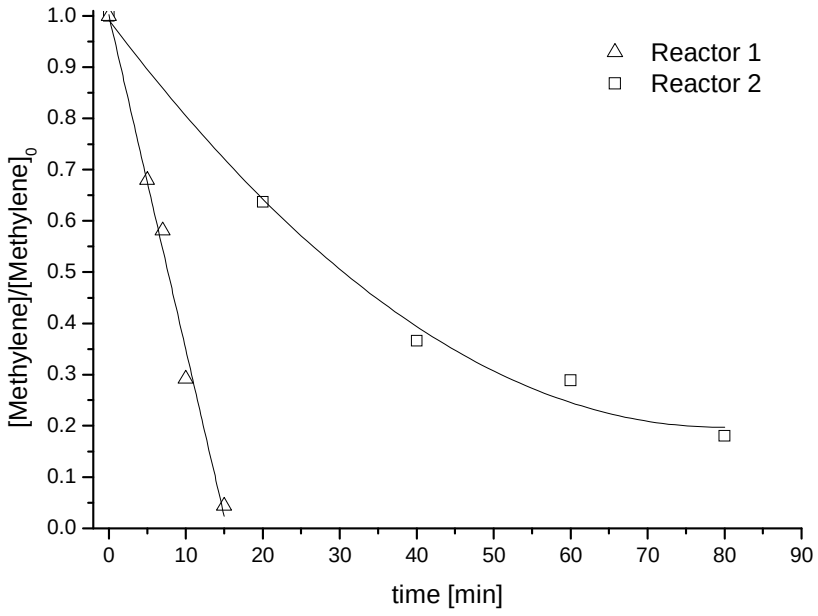


Fig. 4. Methylene blue decoloration efficiency in each reactor type. Reactor 1 – wire-to-mesh. Reactor 2 – wire-to-plate configuration.

We can observe zero order reaction in the first reactor and first order reaction in the second reactor. Rate constants k_0 and k_1 for the first and second reactor, respectively, obtained from interpolation of the data presented in Fig. 4 using equations (4) and (5) are shown in Table 1.

$$\frac{[Methylene]}{[Methylene]_0} = e^{-k_1 t} \quad (4)$$

$$\frac{[Methylene]}{[Methylene]_0} = k_0 t \quad (5)$$

Tab. 1. Decoloration constant for each reactor

Reactor type	*k(min^{-1})*	*Comments*
Reactor 1	k_0=0,065	R=0,987
Reactor 2	k_1=0,021	R=0,984
Underwater discharge with air bubbles [5]	k_1= 0,0226	R=0,992

Similarity in results obtained by us with those obtained by Benetoli et al. [5] suggests that the methylene blue decoloration in the first order reaction is driven by oxidative agents formed from air. The rate of the decolloration, i.e. oxidation, depends on the gas composition and water conductivity [5] but not on the reactor configuration, power delivered to the discharge and the way of gas supplying.

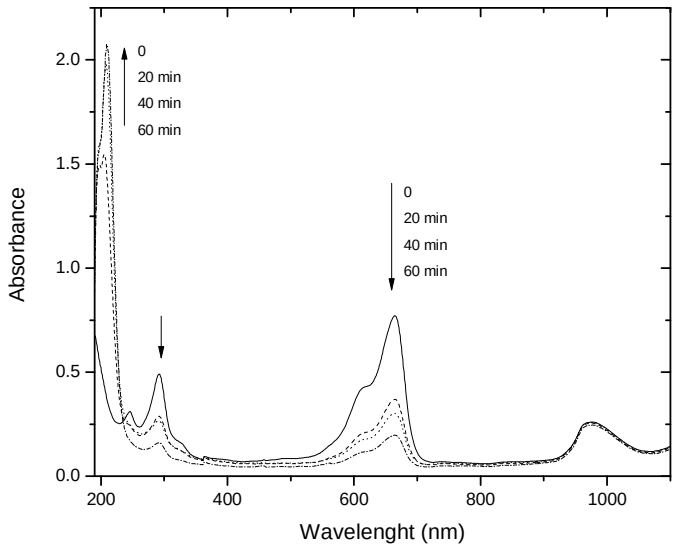


Fig. 5. Absorbance spectra of methylene blue solution after treatment in AC corona reactor. Reactor 1.

In Fig. 5. absorbance peak of methylene blue at 665 nm decreased from initial 0.75 to 0.2 after 60 min. On the other hand absorbance at 205 nm increased exponentially from 0.45 to 2.05 abs at 60 min. which is an evidence of formation of colourless methylene blue processing by-products.

4. Conclusions

The decoloration process of methylene blue solution in a AC corona discharge reactor was studied. Reaction rate constants were interpolated and were similar to the study [5]. Two systems were observed wire-to-mesh and wire-to-plate. The wire-to-mesh system was more efficient. It is seen that

decoloration of methylene blue in such system zero order reactions occur, whereas in the wire-to-plate the methylene blue decoloration proceeds through different mechanism.

5. References

[1] Malik MA, Rehman U, Ghaffar A, Ahmed K, *Plasma Sources Sci Technol* **11,** 3, pp 236–240, 2002

[2] Malik, MA *Plasma Sources Sci Technol*, **12,** 4, pp 26–32 2003

[3] Magureanu M, Mandache NB, Parvulescu VI, *Plasma Chem Plasma Process* **27,** 5, pp 589–598, 2007

[4] Grabowski LR, van Veldhuizen EM, Pemen AJM, Rutgers WR, *Plasma Sources Sci Technol*, **16,** 2 pp 226–232, 2007

[5] L.O.B. Benetoli, B.M. Cadorin, V.D. Tralli, N.A. Debacher, J.S. Chang, The Role of Non-Thermal Plasma Discharge Applied at the Gas-Liquid Interface on the Methylene Blue Decolorization, 8th International Symposium on Non-Thermal/Thermal Plasma Pollution Control Technology & Sustainable Energy ISNTP-8, Camaret, France, 2012

[6] E. Marotta, E. Ceriani, V. Shapoval, M. Schiorlin, C. Ceretta, M. Rea and C. Paradisi, Characterization of plasma-induced phenol advanced oxidation process in a DBD reactor, *The European Physical Journal App. Physics*, **55** , 2011

[7] M. Magureanu, D. Piroi, F. Gherendi, N. B. Mandache, V. Parvulescu, Decomposition of Methylene Blue in Water by Corona Discharges, *Plasma Chem. Plasma Proc*., **28**, 6, pp 677-688, 2008

[8] F.Huang, L. Chen, H. Wang, Z. Yan, Analysis of the degradation mechanism of methylene blue by atmospheric pressure dielectric barrier discharge plasma, *Chem. Eng. Journal*, **162,** pp 250–256, 2010

[9] Y.S. Mok, J.O. Jo, C. Whitehead, Degradation of an azo dye orange II using a gas phase dielectric barrier discharge reactor submerged in water, *Chem. Eng. Journal*, **142,** pp 56–64, 2008

[10] Brisset, J-. L.; Moussa, D.; Doubla, A.; Hnatiuc, E.; Hnatiuc, B.; Youbi, G. K.; Herry, J-. M.; Naïtali, M.; Bellon-Fontaine, M-. N., Chemical Reactivity of Discharges and Temporal Post-Discharges in Plasma Treatment of Aqueous Media: Examples of Gliding Discharge Treated Solutions, *Ind. Eng. Chem. Res*., **47**, pp 5761, 2008

[11] L. O. de B. Benetoli, B. M. Cadorin, C. da S. Postiglione, I. G. de Souza, N. A. Debacher, Effect of Temperature on Methylene Blue Decolorization in Aqueous Medium in Electrical Discharge Plasma Reactor, *J. Braz. Chem. Soc.*, **22**, 9, pp 1669-1678, 2011

[12] H.-E. Wagner, R. Brandenburg, K.V. Kozlov, The barrier discharge: basic properties and applications to surface treatment, *Vacuum,* **71,** pp 417–436, 2003

TEMPERATURE EFFECTS UNDER OZONE SYNTHESIS PROCESS CONDITIONS

Sławomir Jodzis

Warsaw University of Technology, Faculty of Chemistry, Noakowskiego 3, 00-664 Warszawa
e-mail: jodzis@ch.pw.edu.pl

It is commonly believed that the "temperature" causes the ozone decomposition. Such a statement is not quite true. Neither the gas temperature nor the temperature of the cooling liquid is an essential reason of ozone decomposition in typical conditions of the process. In the actual ozonizer in which the gas stays for tens of seconds, ozone decomposition doesn't occur at high temperature of a cooling liquid (50°C) until the microdischarges does not occur. A method of determining the boundary concentrations of ozone was presented.

1. Introduction

In studies on the kinetics of ozone synthesis process, the occurrence of reactions inside the discharge gap under stable gas temperature conditions is assumed. The acceptance of such an assumption simplifies the calculations but omits the effect of diversified process conditions in the ozonizer gap. This is not in agreement with the commonly accepted mechanism of the process [1,2], according to which, the temperature in various parts of the reaction space is diversified.

The effects obtained (ozone concentration, yield, energy efficiency) are correlated with easy to permanently control parameters of the process (gas flow rate, energy consumed, a cooling liquid temperature). Sometimes this causes simplified interpretation of the phenomena occurring in the discharge gap. An example of such simplification is the opinion that the "temperature" influences the ozone concentration, the ozone yield, etc. Such an opinion results from the direct observation of the process, i.e. lower and lower ozone concentrations are obtained, when the temperature of the cooling liquid increases. The ozone concentration decreases also at high specific energy values, when the gas temperature inside the gap increases. These observations correctly illustrate the practical aspect of the ozone synthesis process, however, the ambiguous understanding of the „temperature" term could raise doubts. The aim of this studies is to explain the actual reasons of the low ozone concentration obtained at higher temperature using the process rate measurement with the differential method.

Ozone synthesis with the use of barrier-type discharges is a specific chemical process, which is initiated by electrons with a high energy, which flow through the microdischarge channels of the discharge gap. These channels are a special part of the inter-electrode space. In the channels the fast reactions with the electrons and the subsequent reactions, in which the atomic oxygen is involved, occur. The temperature T_{ch} in the channels is much higher than that of the gas around them. The basis of the occurring phenomena is explained by a simplified process mechanism [2]:

$$O_2 + e \rightarrow O + O + e \quad \text{(R1)}$$

$$O_3 + e \rightarrow O_2 + O + e \quad \text{(R2)}$$

$$O + O_2 + M \rightarrow O_3^* + M \rightarrow O_3 + M \quad \text{(R3)}$$

$$O_3 + O \rightarrow O_2 + O_2 \quad \text{(R4)}$$

$$O + O + M \rightarrow O_2 + M \qquad (M = O, O_2 \text{ or } O_3) \quad \text{(R5)}$$

Despite the fact that energy is consumed only in the microdischarge channels, its effect is noted in the entire discharge zone. It can be stated that the energy is used in two essential ways, namely in ozone formation and in the heating of the reaction space. The change of the electric energy into heat is an undesired effect in ozone synthesis, however, this is difficult to avoid. The temperature (in the channels) influences not only the values of the reaction rates, but also the local concentration of the reagents in the reaction space. Therefore, the kinetic models of the process should take into

consideration the dynamics of the temperature changes in the microdischarge channels and its influence on the reagent concentration.

Since the process mechanism is very complex, some simplifications in the macroscopic description of the phenomenon need to be made. The following chemical equation is the basis of the analysis:

$$3O_2 \underset{r_d}{\overset{r_f}{\rightleftharpoons}} 2O_3 \qquad \text{(R6)}$$

where two competitive processes occur with the rates $\mathbf{r_f}$ and $\mathbf{r_d}$.

The convention assumed allows the analysis of the process using the macroscopic: formation $\mathbf{k_f}$ and decomposition $\mathbf{k_d}$ rate constants. Also, the basic process parameters such as the energy uptake, the gas flow rate and the temperature of the cooling medium, are used. The "specific energy" (the ratio of active power and gas flow rate, P/V) is commonly used. The relationship between ozone content **a** and $\mathbf{E_v}$ (the equivalent of P/V ratio) is described by the useful modification of Vasilev-Kobosev-Eromin equation is the relation [3-5]:

$$a = a_e\left[1-\exp\left(\frac{-k^+c}{a_e}E_v\right)\right] \qquad (1)$$

Another way of correlating the effects of the process with its parameters, could be an experimental determination of the technical rate of the process. This procedure is not directly connected with the macrokinetics Equation 1, but it can be used for the analysis of the process macrokinetics when the ozone boundary contents $\mathbf{a_e}$ are experimentally determined.

The reaction rate **r** of a process is a parameter expressed number of moles of ozone produced in a reaction space in a unit of time. In order to calculate the dependence of the process rate **r** and the conversion **x**, it was assumed that the process occurs under constant pressure (p=const) in pure oxygen with flow rate V_0.

Figure 2 depicts the method used for determining the process rate as a function of the process extent, i.e. the conversion degree **x**. In ozonizer Oz-1 ozone of mole fraction a_1 is generated. In ozonizer Oz-2 the mole fraction of ozone changes from a_1 to a_2, i.e. the conversion degree from x_1 to x_2. For minute changes of conversion in ozonizer Oz-2 it can be assumed that the reaction rate of the process is constant, and the average reaction rate $\bar{r}$ equals [6]:

$$\bar{r} = \frac{V_0(1-a_1)}{120960 \cdot V_R}(x_2 - x_1) \qquad (2)$$

The reaction rate correlates with the temperature of the thermostating liquid.

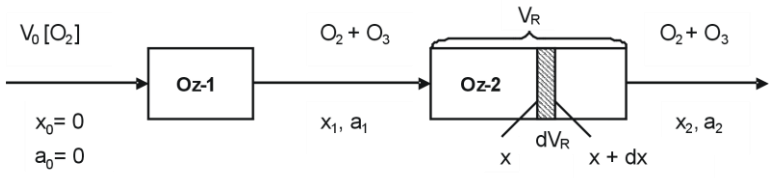


Fig 1. Idea of determining the differential reaction rate of ozone synthesis.

2. Experimental

The kinetic measurements were carried out in a set-up consisting of two DBD-type ozonizers connected in series. The first ozonizer (Oz-1) generated the oxygen-ozone mixture, which feeds the measuring ozonizer Oz-2. At the oxygen flow-rate of V_0= 4 Ndm^3/h, it allows to obtain the mixture containing 0, 1.9, 3.2, 4.3 and 5.4 % of ozone. The second ozonizer [7] was double-side thermostated. The length of the thermostated part of an ozonizer was ca. 25 cm, and the length of the discharge gap was 10 cm. The gas residence time in the both discharge and thermostated zone was ca. 12 s and 30 s, respectively. The measurements were carried out at the temperature of cooling liquid 0, 25 and 50°C.

3. Results and discussion

Figure 2a depicts an experimental data, which were used for determining the rate of the ozone synthesis process: ozone content a_2 in the post-reaction gas as a function of the discharge active power, initial ozone content a_1 and the cooling liquid temperature T_c. As can be seen, independently of the initial ozone content, the energy is consumed at first for the increase in ozone content. The concentrations attain certain maximal values, then decrease systematically. The diversification of the maximal concentration levels depending on the cooling liquid temperature is evident.

It is worth to notice the characteristics obtained at 50°C. At the highest initial ozone content a_1=5.4 % and the power of 0 W, the ozone concentration in the post-reaction gas is equal to that initial one (a_2=a_1). Therefore, relatively high temperature of the gas in the discharge gap, which was produced by the thermostating system, does not cause the ozone destruction. However, the systematic ozone decomposition starts at very low discharge power. Because in such conditions the increase in gas temperature is equal zero ($\Delta T \approx 0$, see: Fig. 3), it indicates that the decrease in ozone concentration must result from the reactions occurring in the microdischarge channels.

Figure 2b depicts the process rates as a function of conversion degree, obtained at the cooling liquid temperature 25ºC in the mixtures containing 0, 1.9, 3.2, 4.3 i 5.4 mole % of ozone. The process rates decrease when both the conversion degree and the initial ozone content increases. The lines connecting the experimental points obtained at the constant (low) power determines the maximum conversion degree (x_2=0.105), theoretically possible to obtain in such conditions. That x value corresponds to the ozone content in the gas at the level of 7.25 %. It is the boundary ozone content (a_e) at 25ºC. The boundary ozone contents at 0 and 50ºC equal ca. 9.1 and 4.8 %, respectively. In practice, those values are not obtained, because suitably high energy should be delivered, which could result in unavoidable heating of the reaction space.

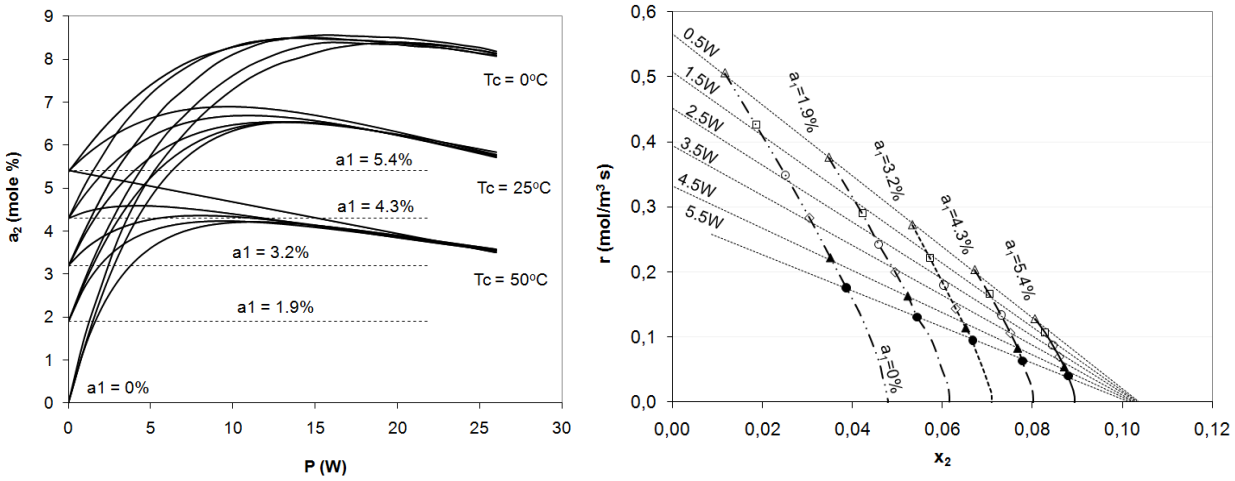
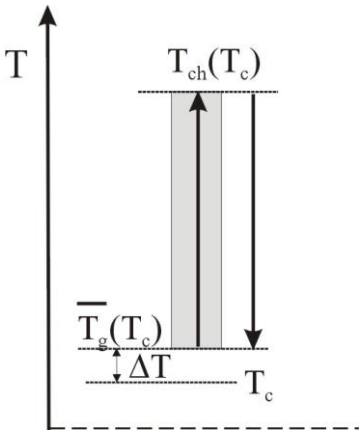


Fig. 2. Outlet ozone content a_2 vs. initial ozone content a_1 and active power; temperature of cooling liquid T_c = 0, 25 and 50°C (left); Ozone synthesis process rate vs. conversion degree and low powers (right); temperature of cooling liquid T_c = 25°C; initial ozone content a_1 = 0, 1.9, 3.2, 4.3 and 5.4 %.

Ozone losses in the real process

Figure 4 depicts the experimentally determined relations between ozone content and the energy factor E_v as well the analogous dependences calculated on the basis of the determined boundary ozone contents a_e were taken into account. The calculations were carried out using the (E_v,a) values, obtained for the low power of the discharge when the effect of energy on the gas temperature is negligible. The difference between the actual and calculated ozone contents deepens above the specific energy of ca. 1 Wh/Ndm^3, which corresponds to the power of 4W.



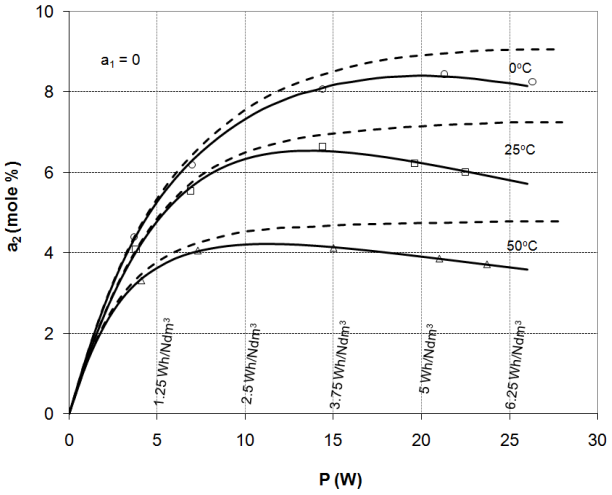


Fig. 3 (left). Schematic diagram of the temperatures in the microdischarge channel under stationary state conditions in the discharge gap (T_c, P, V_0 = const). The increase of temperature in the microdischarge channel has no influence on the average temperature of the gas T_g.

Fig. 4 (right). Ozone content a_2 vs. power; temperature of cooling liquid T_c = 0, 25 and 50°C; initial ozone content a_1 = 0%. Experimental (solid lines) and calculated (dashed lines) data based on Eq. 1.

The experimental data (E_v,a) and the determined boundary ozone contents a_e in the gas leaving the ozonizer were used for the calculation of ozone formation k^+ and decomposition k^- rate constants. The calculations were made using the Eq. 1 and the dependence describing the relation between the rate constants and the ozone boundary contents a_e in the gas [3-5]:

$$k^- = k^+(\frac{1}{a_e} - 1) \qquad (3)$$

It was found that in the range of the cooling liquid temperature of 0-50ºC the ozone formation rate constant is independent of temperature, whereas the value of ozone decomposition rate constant increases (Tab. 1). It explains the reason of ozone concentration decrease. The ozone is decomposed as a result of the reactions, which at the higher temperature (in the microdischarge channels) occurs faster. Obviously, the temperature of the cooling liquid used, is only an easy to control equivalent parameter. The chemical reaction occurs in the gap at temperatures suitably higher (see: Fig. 3). The change of the cooling liquid temperature corresponds, however, to the change of both the gas and microdischarge channels temperature levels. At the steady-state conditions the gas temperature T_g is by ΔT higher than that of the cooling liquid T_c (ΔT ≈ 0, i.e. $T_g \approx T_c$ when the energy delivered is low). Independently of the cooling liquid temperature, the temperature T_{ch} in the channel during its life-time is high, and after the channel decay decreases to the T_g level.

Tab. 1. Macroscopic rate constants vs. the temperatures of the cooling liquid T_c = 0, 25 and 50°C.

Cooling liquid temperature	0ºC	25ºC	50ºC
Formation rate constant k^+, Nm^3/J	$5.78 \cdot 10^{-4}$	$5.67 \cdot 10^{-4}$	$5.27 \cdot 10^{-4}$
Decomposition rate constant k^-, Nm^3/J	$5.80 \cdot 10^{-3}$	$7{,}37 \cdot 10^{-3}$	$1.05 \cdot 10^{-2}$

Ozone decomposition

As was shown in Fig. 2 (a_1 = 5.4 % O_3, T_c = 50°C, P = 0 W), at high temperature of the cooling liquid the ozone outlet concentration is equal to the inlet one. The concentrated ozone is not decomposed despite the long residence time of the gas inside the heated reactor (ca. 30 s). Its decomposition starts when the discharges occur. Therefore, in the range of temperatures occurring in the actual ozonizers, even when the ozone concentration is high (here ca. 120 g/Nm^3), its decomposition is a result of the

discharges not the gas temperature. It cannot, however, be excluded that if the ozone concentration were considerably higher, its decomposition at 50°C could be noticeably (without the discharges participation).
Figure 5 depicts the temperatures in discharge channel.

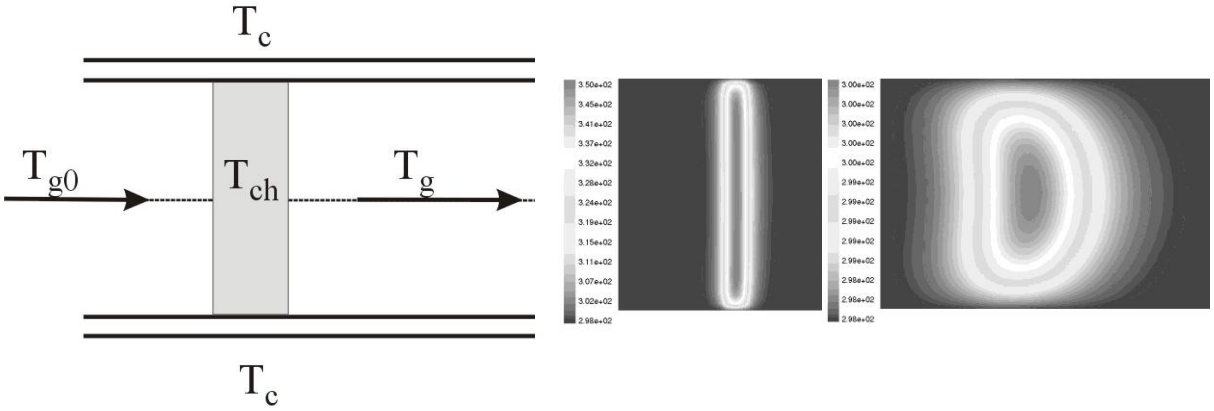


Fig. 5. Temperatures in the discharge gap according the model [1] (a) and calculated gas temperature fields after microdischarge decay: 0.1 ms (b) and 2 ms (c) [8,9]. The temperature scale is various. T_{g0} – inlet gas temperature, T_{ch} – temperature in discharge channel, T_g – temperature of a gas after microdischarge occurrence, T_c – cooling liquid temperature.

4. Sumary

It was measured the ozone synthesis process rate in the gas rich in ozone. It was found that the opinion stating that the ozone destruction is caused by temperature is not sufficiently correct. Even at the high temperature (50°C) the ozone does not decompose until it is hazarded to the both atomic oxygen and electrons action. The results presented and discussed above allows to conclude that:

1. The rate of the ozone synthesis process decreases when the ozone concentration increases. It is not important whether the high ozone concentration is generated in the process occurring in the main ozonizer or the ozone is introduced from another source.
2. The ozone formation rate is temperature-independent.
3. The ozone decomposition occurs in the microdischarge channels. It competes with the ozone forming reaction. If the ozone concentration in the discharge space is high, its decomposition is possible also outside the discharge channels, however, the gas residence time in the inter-electrode space should be suitably long, and its temperature should be especially high. In practice, the ozone is destructed, however, under the significantly higher temperature, which prevails in the low volume of the microdischarge channels. Although the duration of such conditions is short, the effect of those actions cannot be unnoticeable.

5. References

[1] Eliasson B, Hirth M, and Kogelschatz U 1987 *J. Phys. D: Appl. Phys.* 20 1421.
[2] Kogelschatz U, Eliasson B, and Hirth M 1988 *Ozone: Sci. Eng.* **10** 367.
[3] Schmidt-Szałowski K, and Jodzis S 1993 *Acta Physica Univ. Comenianae* **34** 19.
[4] Schmidt-Szałowski, K.; Jodzis, S. 1994 *Acta Physica Univ. Comenianae* **35** (1) 75.
[5] Schmidt-Szałowski K, Jodzis S, Krawczyk K, Młotek M, and Górska A 2006 *Curr. Top. Catal.* **5** 39.
[6] Jodzis S 2011 *Ind. Eng. Chem. Res*. **50** 6053.
[7] Jodzis S 2003 *Ozone Sci. & Eng.* **25** 63.
[8] Jodzis S, and Petryk J 2011 *IEEE Trans. Plasma Sci.* **39**(11) 2120.
[9] Jodzis S, and Petryk J 2011 *IEEE Trans. Plasma Sci.* **39**(11) 2126.

OXIDATION OF NITROGEN OXIDE IN HYBRID PLASMA-CATALYTIC REACTORS BASED ON DBD AND Fe_2O_3

Indrek Jõgi, Kalev Erme, Ants Haljaste, Matti Laan

University of Tartu, Institute of Physics, Tähe 5, 51010 Tartu, Estonia
E-mail: indrek.jogi@ut.ee

In the present study, Fe_2O_3 was used as catalyst for the removal of NO in a hybrid plasma reactor. The catalyst was located either directly inside the hybrid plasma-catalytic reactor or in a separate catalytic reactor, which followed ozone producing and injecting plasma reactor. Ozone production in such a reactor was depending on the state of the electrode surface. In the case of pure O_2, comparison of fresh and used catalysts showed that the fresh catalyst ensured an order of magnitude smaller ozone concentration in the outlet of the hybrid reactor and a total absence of ozone in ozone injection reactor. After a short treatment of the plasma-catalytic reactor with NO_2, its ability to destroy ozone diminished but was regained after heating of the reactor up to 100°C. Similarly to earlier results obtained with TiO_2, the removal of NO in the hybrid reactor with Fe_2O_3 was enhanced compared to that in an ordinary plasma reactor. The enhanced removal of NO occurred due to both adsorption and catalytic oxidation on the catalyst surface. In ozone injection reactor without catalyst, oxidation of NO to NO_2 took place with considerably higher efficiency compared to the hybrid reactor. The use of catalyst in the ozonation stage further improved the oxidation of NO_2 to N_2O_5. The time-dependence of NO removal during plasma and ozone oxidation was explained by reactions between NO_2 adsorbed on surface, with surface bound NO_3 and gas phase NO as reaction product. This reaction was reversed after switching-off the reactor.

1. Introduction

Hybrid plasma-catalytic reactors have become under intensive investigations because they are regarded as efficient devices for removal of pollutants by oxidation [1, 2]. The catalyst may be incorporated either directly into the plasma reactor (single-stage device) or a separate catalytic reactor will be connected in the gas line after the plasma reactor (two-stage device). In the first configuration, various types of short-living active plasma species and UV radiation may activate the catalyst. In the second configuration, only long-living plasma products, e.g. ozone, can reach the catalyst. In some two-stage devices, oxygen plasma is used for production of reactive oxygen species (O radical, ozone) in the first stage [3]. Then these species are injected into the catalytic reactor in parallel with the contaminated gas flow.

In an ordinary dielectric barrier discharge (DBD) reactor, NO is oxidised to NO_2 and N_2O_5 by oxygen radicals and ozone produced in plasma. However, the oxidation efficiency is limited by undesired reactions in which O radical converts NO_2 back to NO [4]. If NO is oxidized only by ozone, these back-reactions are not efficient [3].

We have found that the TiO_2 catalyst inside the hybrid plasma-catalytic reactor improved the efficiency of NO oxidation [5, 6]. Our speculation was that O radicals oxidized some NO on TiO_2 surface where the back-reaction was not efficient. To check this supposition, we first replaced TiO_2 with Fe_2O_3 to see whether different type of catalyst could change the oxidation of NO in the single-stage configuration. Secondly, to reduce the effect of back-reactions, we produced ozone in a separate reactor (ozone generator) and directed its flow into the second catalytic stage of the reactor i.e. into the catalytic reactor.

2. Experimental

Coaxial type DBD reactor was used for the production of plasma. The inner electrode was a stainless steel tube with outer diameter of 14 mm. The quartz tube with inner diameter of 16.3 mm was used as a dielectric barrier. A perforated metal foil around the quartz tube formed the second electrode. In the single-stage hybrid device, the catalyst powder was pressed on the inner electrode of the DBD reactor. In the absence of the catalyst, the reactor represented a simple ozone generator with coaxial electrodes. Similar reactor without the outer coaxial electrode was used as the catalytic reactor in ozone injection device (Fig 1).

The inlet mixture with 360 ppm NO and 10% O_2 in N_2 was processed in the hybrid plasma-catalytic device at the flow rate of 1000 sccm. In the ozone injection reactor the ozone was produced from pure O_2 and injected into a mixture of 450 ppm NO in N_2. The flow rates were 1000 sccm.

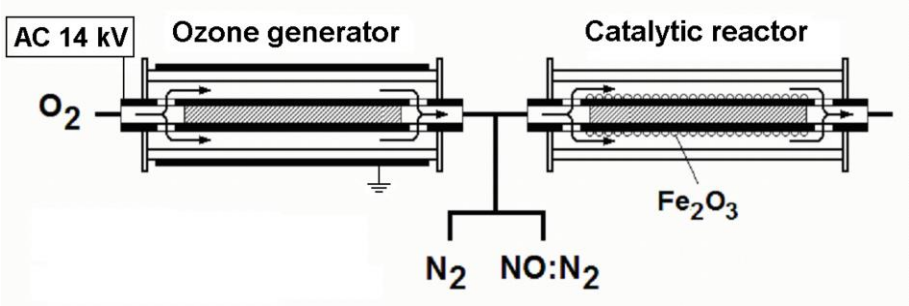


Fig. 1. Sketch of the ozone injection reactor.

The powder of γ-Fe_2O_3 (Sigma-Aldrich) consisted from particles of 50 nm in diameter. The total specific surface area of the catalyst was larger than 50 m^2/g. The mass of the catalyst in the catalytic reactor was approximately 0.4 g, which gives the upper boundary of total surface area of about 20 m^2. The estimated number of active surface sites was $2 \cdot 10^{20}$ when the surface site density was assumed to be equal to 10^{15} cm^{-2} as in the case of TiO_2 [7],
The plasma was produced applying sinusoidal AC voltage to the inner electrode. The peak-to-peak value of the voltage was 14 kV. The input power was finely adjustable by varying AC frequency from 100 to 5000 Hz. The power was measured by the Lissajous' method [8]. The values of specific input energy (*SIE*) were calculated by dividing the power with the flow rate. In the present study, *SIE* values were varied from 10 to 500 J/L. The outlet concentrations of gas species was determined by optical absorption spectroscopy in the UV range.

3. Results and discussion

Fe_2O_3 is known to destroy ozone [9]. In our experiments, in pure O_2 the presence of Fe_2O_3 catalyst in the hybrid reactor decreased the ozone production by an order of magnitude (Fig. 2a). When 20% O_2/N_2 mixture was used for ozone production in the same hybrid reactor, the outlet ozone concentration was time-dependent (Fig. 2b). The concentration increased during the first 20 minutes of reactors operation until it reached the value characteristic to the ordinary DBD reactor (Fig. 2b). The destruction of ozone by Fe_2O_3 remained suppressed after the experiment with 20% O_2/N_2 mixture even when ozone was produced from pure oxygen; the outlet ozone concentration increased close to the level which was obtained without the catalyst. The destruction ability remained low even after one week and it was regained only after heating the catalyst above 100°C. Thus, the presence of N_2 changed considerably the ozone destruction ability.

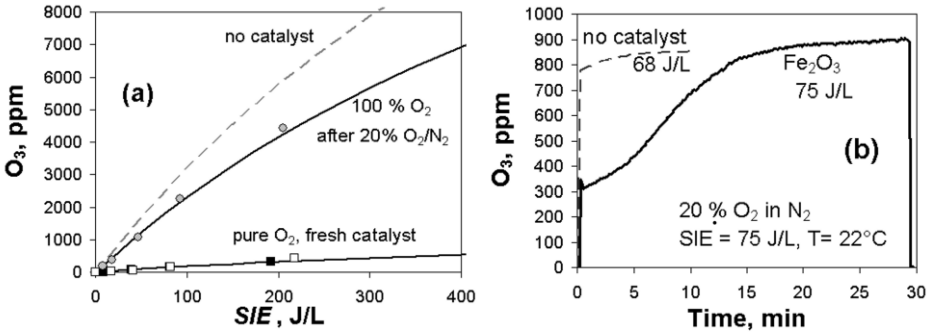


Fig. 2. Ozone concentration in the outlet of the hybrid plasma-catalytic reactor. (a) Stabilized values when ozone was produced from pure O_2 either in the presence of the fresh catalyst (Fe_2O_3) or in the presence of catalyst, which was previously exposed to discharge in the mixture of 20% O_2/N_2. (b) Time dependence of the ozone concentration produced from 20% O_2/N_2 mixture without the presence of catalyst (dashed line) and in the presence of Fe_2O_3 catalyst (solid line).

The effect of various nitrogen and nitrogen containing species (N_2, NO, NO_2 etc.) on ozone destruction ability of Fe_2O_3 was studied further using ozone generator and the catalytic reactor (Fig. 1). When ozone was produced from pure oxygen, Fe_2O_3 totally decomposed ozone even when the inlet ozone concentration reached 10000 ppm. Ozone was still destroyed when N_2 was injected into the catalytic reactor. This experiment demonstrated that N_2 did not affect the Fe_2O_3 ability to destroy ozone. The treatment of the catalyst by the flow of 450 ppm NO/N_2 mixture also did not change the ozone destruction ability of Fe_2O_3. However, when NO and ozone were directed into the catalytic reactor simultaneously, the ozone destruction ability of Fe_2O_3 was lost. As ozone converts NO to NO_2 and N_2O_5 [4], the loss of ozone destruction ability is caused by oxidized NO_x species.
In the case of the hybrid plasma-catalytic reactor with Fe_2O_3 catalyst, the removal of NO was practically the same as with TiO_2 [5, 6] in spite of the fact that Fe_2O_3 efficiently destroys ozone. In comparison with the DBD reactor without catalyst, in the hybrid plasma-catalytic reactor the NO removal increased by about 40-50 ppm at higher *SIE* values (Fig. 3). The unexpected similarity with the results obtained by TiO_2 is explainable keeping in mind that NO_x produced in plasma decreased the ability of Fe_2O_3 to destruct ozone.

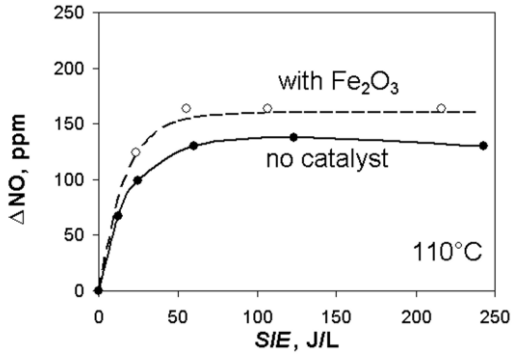


Fig. 3. The difference between inlet and outlet NO concentrations (ΔNO) in hybrid plasma-catalytic reactor as a function of *SIE* at 110°C if the concentration of NO at the inlet was 450 ppm.

The oxidation results of NO in ozone injection reactor are shown in figure 4. The full oxidation of NO to NO_2 was achieved already at *SIE* values of 10-12 J/L and was not affected by the catalyst. The oxidation by injected ozone was considerably more effective compared to oxidation in the hybrid reactor. At higher *SIE* values (i.e. ozone concentrations), further oxidation to N_2O_5 took place (Fig. 4). Rate coefficient of NO_2 oxidation by ozone is considerably lower than that of NO and the total NO_2 removal was achieved only at *SIE* > 60 J/L (Fig. 4a). The presence of Fe_2O_3 in the catalytic reactor led to a further improvement of the oxidation of NO_2 to N_2O_5 (Fig. 4b). It should be pointed out that at *SIE* > 60 J/L, the outlet concentration of O_3 decreased from 1000 ppm to 100 ppm if Fe_2O_3 was used.

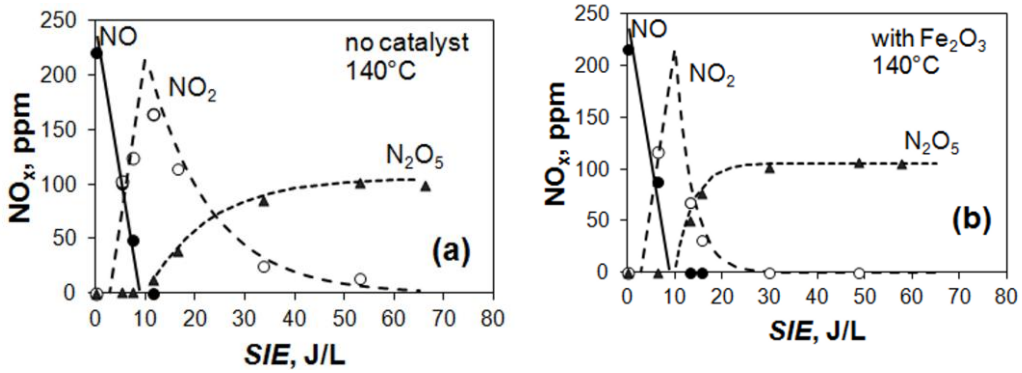


Fig. 4. The oxidation of NO to NO_2 and N_2O_5 in ozone injection reactor at 140°C (a) without catalyst and (b) with Fe_2O_3. Circles and triangles mark experimental points.

Similarly to TiO_2 catalyst, the NO removal was time-dependent in the presence of Fe_2O_3. When the hybrid plasma-catalytic reactor was switched on, only NO and NO_2 were detectable in the outlet but the sum of these NO_x species was smaller than the inlet concentration of NO (Fig. 5). The deficiency of NO_x decreased gradually in the outlet and after several minutes, the outlet concentration of NO_x stabilized. We attributed the NO_x deficit to the adsorption of NO_x species on the Fe_2O_3 surface. The total amount of adsorbed NO_x was obtained by integrating the difference below the final stabilized value (shown as grey area in figure 5a) over the time. At *SIE* values above 100 J/L, the total amount of adsorbed NO_x molecules saturated at the level of $3.5 \cdot 10^{18}$, which is approximately 2% of the total amount of surface sites. After the switch-off of the reactor, the NO_2 value decreased and NO value increased gradually (Fig. 5a). The concentration of outlet NO_x was now larger than the inlet concentration. This finding confirmed the assumption that the adsorption of NO_x species was the reason for the deficiency of outlet NO_x observed at the onset of reactor's operation.

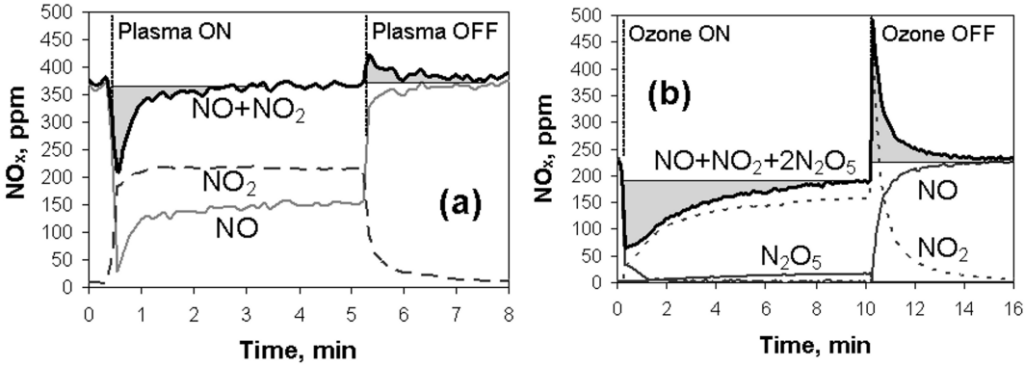


Fig. 5. Time-dependence of NO, NO_2, N_2O_5 and NO_x concentration in (a) hybrid reactor and (b) ozone injection reactor with Fe_2O_3 catalyst at room temperature.

Similar time-dependences were observed in the device with ozone injection (Fig. 5b). In this case N_2O_5 was also detectable but the sum of NO_x species was still remarkably lower than the inlet NO concentration. Under the steady NO flow and after the switch-off of the ozone generator the outlet NO_2 concentration reached much larger values compared to the inlet NO concentration and then decreased slowly. When the flow of NO and the production of ozone were interrupted simultaneously, NO_2 turned undetectable in the outlet. This fact indicates that the occurrence of NO_2 in the outlet after the end of oxidation was not due to simple desorption of NO_2 from the catalyst.

In ozone injection reactor, the changes in the outlet concentration of NO_2, ΔNO_2, were always related to the changes in concentration of NO, ΔNO. A decrease in one of them led to an increase in the other one and the amount of ΔNO_2 was always two times larger than that of ΔNO (Fig. 6), i.e. on the catalyst surface there appeared or disappeared two NO_2 molecules for every NO molecule. Similar trend was observed for hybrid plasma-catalytic reactor after switching off the reactor.

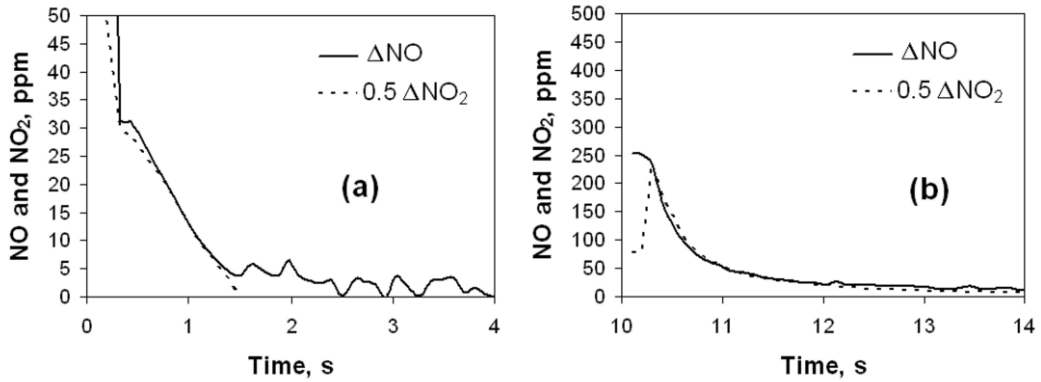


Fig. 6. Time-dependences of outlet values of ΔNO and ΔNO_2 (a) at the switch-on and (b) after the switch-off of the ozone generator.

The two-fold difference of ΔNO and $|\Delta NO_2|$ values could be explained as follows. NO is not adsorbed on the catalyst surface but the amount of NO_2 adsorbed on the surface is determined by the adsorption-desorption equilibrium [10, 11]. Adsorbed molecules of NO_2 are partly transformed into NO_3 in reactions

$$NO_2(s) + O(s) \rightarrow NO_3(s) \quad (1)$$
$$2NO_2(s) \leftrightarrow NO_3(s) + NO(g) \quad (2)$$

where (s) denotes surface species and (g) gas phase species. It should be pointed out that the formed NO_3 is not desorbing from the surface [10,11].
Reaction (2) explains the trends in figure 6. At the switch-on of the ozone generator, there is no NO_3 on the surface of the catalyst and reaction (2) proceeds towards equilibrium. At the switch-off of the ozone generator, there are high concentrations of NO and NO_3 and the reverse reaction prevail. The formed NO_2 desorbs from the surface and can be detected in gas phase. This reaction proceeds until adsorbed NO_3 is removed from the surface.

4. Conclusions

Following conclusions can be drawn from the present study:

- Fe_2O_3 as catalyst is a good for ozone destruction; under our conditions it removed up to 10 000 ppm of ozone. NO_x species originating from inlet gas or from discharge plasma can contaminate the surface of Fe_2O_3 catalyst but the surface could be regenerated by heating.
- Hybrid plasma-catalytic reactor with Fe_2O_3 catalyst enhanced NO oxidation similarly to TiO_2; this effect was not suppressed by the ability of Fe_2O_3 to destroy ozone.
- The oxidation of NO by ozone injection reactor was considerably improved compared to hybrid reactor. The presence of Fe_2O_3 catalyst led to further increase in N_2O_5 formation.
- Time-dependent outlet concentrations observed during NO oxidation on Fe_2O_3 are explainable by surface reactions between adsorbed NO_2 and gas-phase NO molecules which produced surface bound NO_3. The proposed reaction mechanism also explains the effects occurring after the switch-off of the reactor.

5. Acknowledgements

This study was partially financed by the European Union (European Regional Development Fund) Interreg IVb Baltic Sea Region program (project PlasTEP) and Estonian Science Foundation (grant no. 9310).

6. References

[1] Kim H H 2004 *Plasma Process Polym* **1** 91.
[2] Durme J, Dewulf J, Leys C and Langenhove H 2008 *Appl Catal B Environm* **78** 324.
[3] Barman S and Philip L 2006 *Environ Sci Technol* **40** 1035.
[4] Penetrante B M, Brusasco R M, Merritt B T and Vogtlin GE 1999 *Pure Appl Chem* **71** 1829.
[5] Jõgi I, Bichevin V, Sabre V, Haljaste A, Laan M and Käämbre H, in Hakone XII, 2010, Trencianske Teplice, Slovakia, Bratislava: Library and Publishing Centre CU, p. 338.
[6] Jõgi I, Haljaste A and Laan M, submitted to *Surf Coat Technol.*
[7] Wu Q and Krol R 2012 *J. Am. Chem. Soc.* **134** 9369.
[8] Falkenstein Z and Coogan J J 1997 *J. Phys. D: Appl. Phys.* **30** 817.
[9] Chen H, Stanier C O, Young M A and Grassian V H 2011 *J Phys Chem A* **115** 11979.
[10] Olsson L, Sjövall H and Blint R J 2009 *Appl Catal B Environm* **87** 200.
[11] Hixon B C, Jordan J W, Wagner E L and Bevsek H M 2011 *J Phys Chem A* **115** 13364.

AFFECT OF WATER AND OXYGEN ON THE CONVERSION OF METHANE AND CARBON DIOXIDE IN A PLUG FLOW REACTOR SUPPORTED BY A DBD

Torsten Kolb[1], Jan H. Voigt[1], Karl-Heinz Gericke[1]

[1]Institut für Physikalische und Theoretische Chemie, Technische Universität Braunschweig, Hans-Sommer-Str. 10, D-38106 Braunschweig
E-mail: k.gericke@tu-bs.de

A plug flow reactor with a dielectric barrier discharge was used to study the conversion of methane and carbon dioxide as a function of added water or oxygen. A 13.56 MHz power supply generated the atmospheric plasma discharge. A mixture of methane (80%) and carbon dioxide (20%) was diluted to 2.5% either with pure helium, with helium partly bubbling through a water tank or with helium and oxygen at a flow rate of 200 sccm. The amount of additives was hereby fixed at 0.25%. The product stream was monitored online at a total pressure of 100 mbar by a FTIR spectrometer supported by a White-cell and a quadrupole mass spectrometer. In general, this paper unfolds that additives decrease the conversion of methane and carbon dioxide. The produced amount of hydrogen and the ration (H_2:CO) increases if water is added. In addition, the carbon monoxide yield increases with increasing oxygen. The methanol and formaldehyde yields have the highest values at low electric discharge power and oxygen as an additive. At higher power additional water supports the generation of formaldehyde.

1. Introduction

Intense research is performed to develop new ways for the production of basic organic chemicals as synthesis gas, C2 hydrocarbons, or oxygenates. Nowadays, these compounds are industrially manufactured from crude oil which will expand in the near future. The conversion of methane and carbon dioxide is a possible solution for this problem. Both compounds are highly unreactive. Non-thermal plasma as a gliding arc, a DBD (dielectric barrier discharge) or a corona discharge are used to increase the reactivity. This paper deals with a DBD reactor, a plasma source that prevents the formation of sparks or arcs and uses the entire electrode area effectively for generating the discharge.[1] Various research groups[2], [3], [4] concentrate their work on the conversion of CH_4 and CO_2 in a DBD reactor. Here, the main products are hydrogen, carbon monoxide, hydrocarbons and oxygenates.
This paper analyzes the impact of additives on the conversion of the starting material and on the product distribution. The results of the water and oxygen measurements are compared with the measurements without an additive. During the research, the power in the DBD reactor is varied on contrary to the concentration of the inlet flow that is fixed.

2. Experimental Setup

The experimental setup has been discussed in detail in a previous paper[5], this justifies a brief description of the setup that will be given here.
Four mass flow controller are used to adjust the inlet flow (flow rate: 200 sccm) consisting of 1.5% methane, 1% carbon dioxide, 97.25% helium and 0.25% of the additives (water, oxygen or helium for the measurement without an additive). The water vapor is generated by helium bubbling through a water tank. A 13.56 MHz plasma generator is used to convert this gas mixture in a cylindrical plug flow reactor at atmospheric pressure. The plasma power in the DBD reactor is then adjusted between 30 and 70 W. The product stream and the inlet flow are analyzed at a pressure of 100 mbar in FTIR spectrometer supported by a White cell with an optical path length of 6 m. IR inactive compounds and substances without a characteristic IR peak are analyzed at a pressure of $9.9 \cdot 10^{-6}$ mbar in a quadrupole mass spectrometer.

3. Results and Discussions

The generated products are discussed qualitatively in previous papers.[3],[5] Our DBD reactor generates synthesis gas (methane and carbon monoxide), C2 hydrocarbons, formaldehyde and methanol. To

improve the ignition of the plasma, helium is used as a buffered gas. The buffered gas is neglected in the following discussion.

3.1. Conversion of the starting material

The following formula is used to calculate the conversion of the starting material:

$$C_x = \frac{n_{x,conv.}}{n_{x,0}}, \text{ were x represents } CO_2, CH_4 \qquad n_{x,conv} = n_{x,0} - n_{x,end} \qquad (1)$$

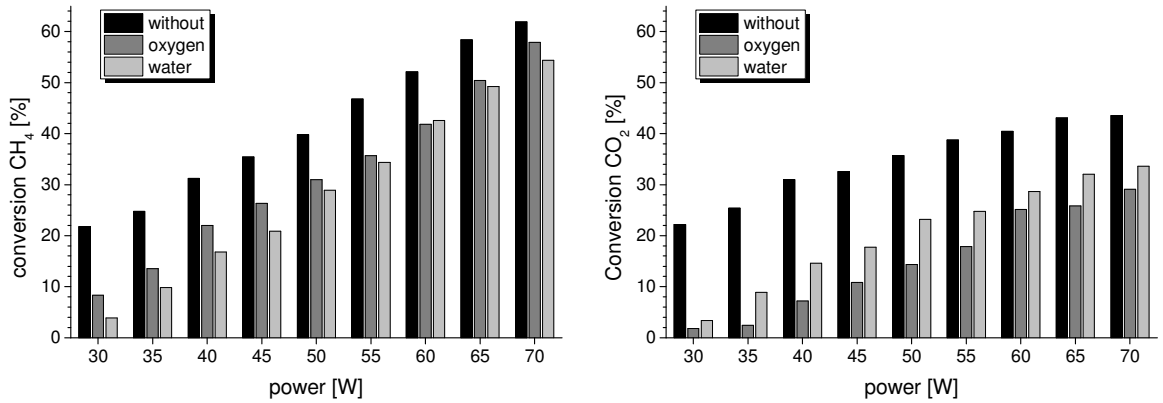


Fig. 1. Conversion of methane (left) and carbon dioxide (right) as a function of power and different additives.

The conversion of methane and carbon dioxide rises when the power of the plasma generator was increased from 30 to 70 W. These results are shown in figure 1. The following reactions are occurring while methane and carbon dioxide are flowing through the DBD reactor:

$$CH_4 \xrightarrow{e^-} CH_3 + H \qquad (2)$$

$$CO_2 \xrightarrow{e^-} CO + O \qquad (3)$$

Reaction (2) and (3) are ignited by energy rich electrons, being accelerated in the DBD rector by the electric field. The electric field in the reactor increased after the plasma power was changed to higher values. In that case, the electrons need a shorter path to carry the required dissociation energy. The result is a higher number of converted molecules.

For all power values, the conversion of methane is always higher than that for carbon dioxide because reaction (3) requires more energy (5.72 eV [6]) than reaction (2) (4.60 eV [6]).

Moreover, additional water and oxygen decreases the conversion of both methane and carbon dioxide. Oxygen as well as water catch the electrons in the DBD reactor, resulting in a decrease of the number of collision of a molecule with a free plasma electron. The additives can also dissociate via the following reactions:

$$O_2 \xrightarrow{e^-} O + O \qquad (4)$$

$$H_2O \xrightarrow{e^-} OH + H \qquad (5)$$

These reactions require electrons at energies of at least 5.2 eV.[6] This energy gets lost to convert the main substances. Reaction (2) to (5) can occur in the DBD reactor because this plasma source generates electrons of an energy up to 10 eV.[1]

The conversion of oxygen is rather high and oxygen is completely converted when the power is increased to 35 W. The amount of water remains constant during these measurements. The formed OH radical (reaction (5)) will react with a methane molecule to water and a methyl radical.

3.2. Product distribution

The synthesis gas components (hydrogen and carbon monoxide) are the main products for this process. Their yield and its ratio (H_2:CO) as a function of the plasma power are illustrated in figure 2. The concentration of H_2 and CO rises after increasing the power. Reaction (3) and (6) are the main reactions to generate these compounds.

$$CH_4 + H \rightarrow CH_3 + H_2 \quad (6)$$

The required hydrogen radical to form molecular hydrogen are generated in a primary plasma reaction of methane with a plasma electron (reaction (2)). The concentration of this radical as well as the concentration of CO increases by higher power.

The research shows that additional oxygen does not affect the hydrogen yield in comparison to water. Water is an extra source for the generation of hydrogen. The highest concentration of hydrogen (46%) is produced with additional water at a power of 70 W. Both additives affect the formation of carbon monoxide slightly at higher powers. The yield of CO increases for measurements with oxygen if the power in the DBD reactor is higher than 45 W. In that case, the energy of the oxygen radicals is high enough to react with methane to carbon monoxide and hydrogen. The amount of CO increases to about 22% at a power of 70 W by adding oxygen. There are no reactions with water or the formed OH radical to generate CO.

The ratio of this two products (H_2:CO) is important for industrial applications as the Fischer Tropsch Synthesis to unsaturated hydrocarbons or methanol (H_2:CO=2) or Hydroformylations (H_2:CO=1). This ratio increases after changing the power to higher values for the measurements with additional oxygen and without an additive. The higher the power is, the higher becomes the concentration of available H radicals forming molecular hydrogen and consequently the higher is the ratio. This ratio is nearly independent of the power after adding water.

The highest ratios (H_2:CO≈1.35) are obtained for measurements with extra water in comparison to the other two types of measurement (oxygen, and no additive). Water is another source for molecular hydrogen which increases the concentration of H_2 and thereby the ratio of the synthesis gas components (H_2:CO). The lowest ratio is observed after adding oxygen. This additive can react with methane to carbon monoxide (Reaction (7))

$$CH_4 + \frac{3}{2}O_2 \rightarrow CO + 2H_2O \quad (7)$$

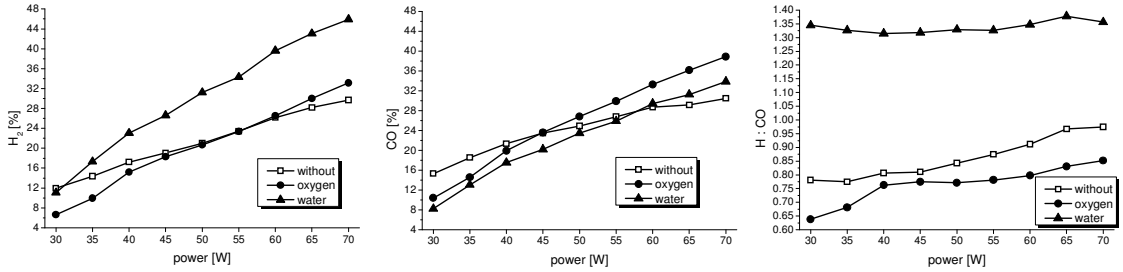


Fig. 2. Hydrogen (left) and carbon monoxide (middle) yield and its ratio (right) as a function of the power and different additives.

Formaldehyde and methanol are exactly identified oxygenates being generated in the used DBD reactor. Figure 3 shows the influence of the additives and the power on the yield of these two products. The mechanism to generate methanol and formaldehyde is given by the following formulas:[7]

$$CH_3 + O \rightarrow H_2CO + H \quad (8)$$

$$CH_3 + OH \rightarrow H_3COH \quad (9)$$

The methyl radicals are generated in this apparatus via reaction (2) and the O or the OH origin from carbon dioxide (reaction (3)), oxygen (reaction (4)) or from water (reaction (5)). An important secondary reaction is given by reaction (10) that increases the concentration of the starting material for reaction (8) and (9).

$$CH_4 + O \rightarrow CH_3 + OH \quad (10)$$

The highest concentration of methanol (≈4500 ppm) is observed at low power and oxygen as an additive. Under these conditions, the concentration of hydroxyl- and methyl radicals reaches an optimum value. The measurement without an additive generates the lowest concentration of methanol because the source for OH is reduced to carbon dioxide. The concentration of methanol decreases after increasing the power higher than 35 W. This product has a high reactivity after a collision with the formed radicals like O, OH, or H. The concentration of methanol reaches nearly the same values at a power of 50 W or higher if water or oxygen were added.

In contrast to methanol, the concentration of formaldehyde increases for the measurement with water or without an additive after changing the power to a higher level. The concentration of the O radical rises after increasing the plasma power. The amount of formaldehyde is for low power values (till 50 W) independent of water because there are no possibilities to create the O radical which is required for reaction (8). At high power levels it is possible to create formaldehyde via the following reaction:

$$CH_2 + OH \rightarrow H_2CO + H \qquad (11)$$

The power of the plasma has to be high enough to create the CH_2 through a second collision of methyl radicals with plasma electrons.

The formaldehyde yield reaches at low and high plasma power the highest values (approximately 6000 ppm) after adding oxygen. Enough O radicals are generated at a low power. The concentration of all radicals increases after changing the power to a higher level. These radicals destroy the formed formaldehyde molecules and the concentration of formaldehyde decreases up to a power of 50 W. A higher power increases the formaldehyde concentration because more molecular oxygen or carbon dioxide is able to dissociate in the reactor and collide with a methyl radical to get formaldehyde.

The amount of methanol and formaldehyde are fairly low compared to the formation of these products because a collision of two radicals is required. The plasma in a DBD reactor is weakly ionized[1] and, thus, the radical concentrations are also low.

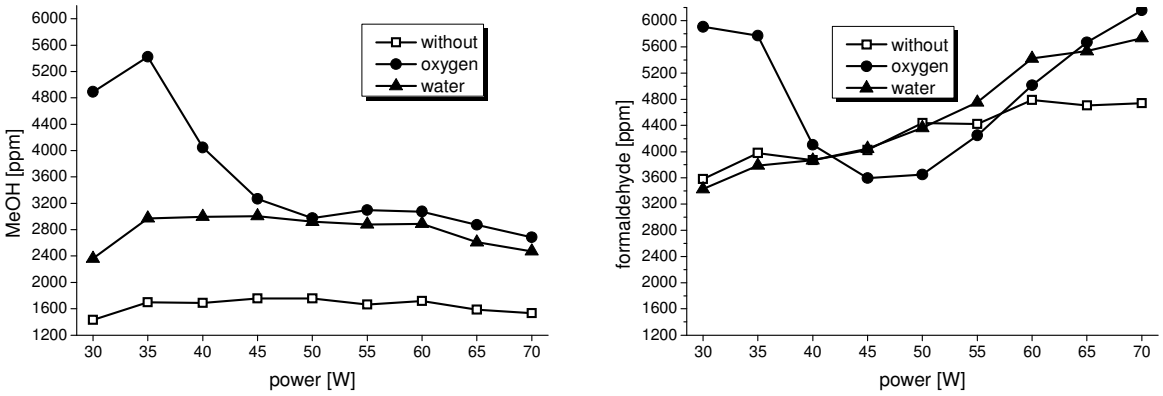


Fig. 3. Concentration of methanol (left) and formaldehyde (right) as a function of the power and different additives.

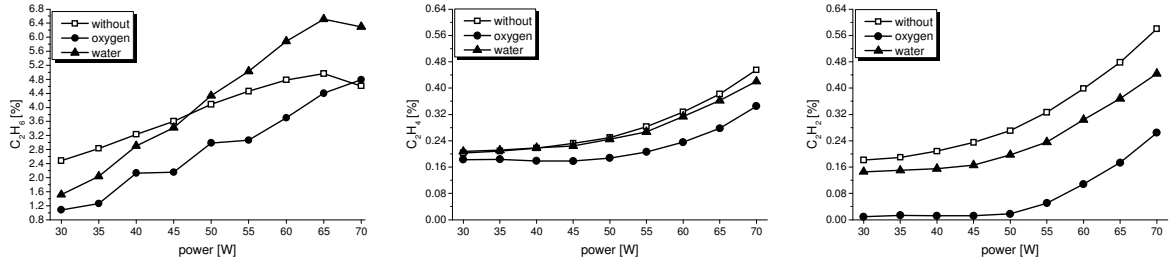


Fig. 4. Amount of the C2 hydrocarbons as a function of the power and different additives (ethane (left), ethene (middle), and ethine (right).

C2 hydrocarbons are also generated in the DBD reactor. The C2 concentrations for different plasma power and additives are shown in figure 4. Ethane is beside the synthesis gas components the third main product. Ethene and ethine are generated at lower concentrations. The yield of these three

components rises with increasing the power. The mechanisms for this process are discussed in detail in a previous paper.[2] A collision of a CH_3, CH_2, or CH radical with methane are required to form the C2 hydrocarbons. A higher power increases the concentration of these radicals.
The effect of water and oxygen on the yield of ethane and ethene is low because from these additives are no radicals required. For all three C2 hydrocarbons water has a slightly negative effect. Only at higher power a positive effect on the ethane yields is observed. The H or OH radicals react with methane to form methyl radicals.

4. Conclusion

Furthermore we found out, that additional water and oxygen have different influence on the conversion of methane and carbon dioxide and on the product distribution. Both additives reduce the conversion of the starting material. Water enhances the yield of hydrogen and methanol, the ratio of the synthesis gas components (H_2:CO), and at higher power the yield of ethane and formaldehyde. The concentration of ethene and ethine diminishes with water.
Oxygen does not influence the yield of hydrogen, but increases the amount of carbon monoxide and also the concentration of methanol and formaldehyde at low power. The yield of the C2 hydrocarbons and ratio (H_2:CO) is lowered after adding oxygen.
Both additives influence the plasma assisted conversion of methane and carbon dioxide. Adding water or oxygen can change the product distribution depending on the desired products.
More plasma power leads to an increase of nearly all product concentrations and also the conversion of methane and carbon dioxide is enhanced. Only the methanol yield decreases. The concentration of formaldehyde reaches a minimum at 50 W with additional oxygen.

5. References

[1] Kogelschatz U 2003 *Plasma Chemistry Plasma Processing* **23** 1-46.
[2] Kroker T, Kolb T, Schenk A, Krawczyk K, Młotek M and Gericke K-H 2012 *Plasma Chemistry Plasma Processing* **32** 565–582.
[3] Istadi N and Amin A S 2006 *Fuel* **85** 577–592.
[4] Eliasson B, Liu C-J and Kogelschatz U 2000 *Industrial & Engineering Chemistry Research* **39** 1221-1227
[5] Kolb T, Kroker T and Gericke K-H 2012 *Vacuum* doi:10.1016/j.vacuum.2012.01.013.
[6] deB. Darwent B 1970 *NBSDS-NBS* **31**.
[7] Tsang W and Hampson RF 1986 *Journal of Physical and Chemical Reference Data*, **15** 1087-1279.

Methane conversion with oxygen in plasma-catalytic system

Krzysztof Krawczyk, Michał Młotek, Bogdan Ulejczyk, Krzysztof Pryciak, Krzysztof Schmidt-Szałowski

Warsaw University of Technology, Faculty of Chemistry, Noakowskiego 3, 00-664 Warszawa, Poland

e mail address of the corresponding author: kraw@ch.pw.edu.pl

The hybrid plasma-catalytic system (HPCS) was used for the oxidative coupling of methane (OCM) with oxygen at the pressure of 1.2 bar. A dielectric barrier discharge (DBD) reactor was powered at the frequency of about 6 kHz. Molar ratio $[CH_4]:[O_2]$ in the inlet gas mixtures (CH_4+O_2+Ar) was 3:1. Two kinds of packing were tested: Fe/Al_2O_3 and Al_2O_3.

The effects of temperature (110, 150 and 340 ^{O}C) on the conversion of methane and oxygen were studied. Hydrogen, carbon oxides, hydrocarbons, and alcohols (mainly methanol) were identified in the outlet gas. The highest amount of methanol was obtained in the system without packing. In the homogeneous system the increase of the temperature decreases the conversion of methane to methanol. The maximum conversion of methane to methanol was obtained at 110 ^{O}C without packing. The presence of Fe/Al_2O_3 increased the methane conversion to C_2H_2/C_2H_4 and decreased the amount of other hydrocarbons.

Keywords
methane, dielectric barrier discharge, plasma - catalytic system

1. Introduction

Activation of methane in relatively mild conditions is extremely difficult. The reason is the high binding energy of hydrogen-carbon in methane, which is very high. Nowadays, the methane conversion for chemical production is based on multistage operations, where the generation and purification of synthesis gas is the fundamental stage, characterized by high energy demand. New methods of methane processing, which will activate the methane at low temperatures and low pressure are being looking for.

The non-oxidative, oxidative coupling of methane into aliphatic or aromatic hydrocarbon and direct oxidation into oxygenates such as methanol are the new processes for methane conversion [1]. Methanol is one of the most desired products of oxidation of methane because it easily undergoes further conversion to carbon oxides and water vapor.

The oxidative coupling of methane (OCM) is based on an active catalyst for example: zeolites, metal oxides or metals deposited on metals oxides (CaO, Al_2O_3, MgO) and occurs at high temperature [1-4].

Over the last decade the hybrid system of non-thermal plasma and catalysts has been used as an alternative to catalytic conversion of methane. The chemical reactions may be initiated in non-equilibrium plasma, involving free radicals and excited molecules. The selectivity and efficiency of plasma processes may be improved when a suitable selective catalyst is used. Nowadays the hybrid plasma-catalytic systems (HPCS), based on non-equilibrium plasma of gliding, DBD and corona discharges are the object of numerous studies [5-12]. Among a variety of plasma techniques there is dielectric barrier discharge (DBD)[6,13-16]. Non-thermal plasma of dielectric barrier discharge combined with a catalyst is regarded as a new way for a production of valuable chemicals, such as unsaturated hydrocarbons, aromatics, alcohols and formaldehyde.

The aim of this work was the study of methane conversion under oxidative coupling conditions (with oxygen) in homogeneous and plasma – catalytic systems. The solid particles - iron on alumina ceramics were the object of our study of methane conversion in HPCS with DBD.

2. Experimental Section

Two kinds of packing were tested: commercial Al_2O_3 and Fe/Al_2O_3.

To obtain Fe/Al_2O_3 alumina-ceramic carrier 1.0 – 2.0 mm in size were impregnated with aqueous solutions of ferric nitrate, dried, calcined at 100^{O}C and reduced with hydrogen at 400°C. Fe/Al_2O_3 containing about 3 wt.% of metal.

A quartz-glass reactor with an internal diameter of 26 mm was used. The reactor was made of a quartz-glass tube (2) of inner diameter 40 mm and length 250 mm. The inner high-voltage electrode was made of aluminum (Fig. 1). A length of active part of aluminum high voltage electrode was 160 mm. The discharge gap between the electrode and the quartz tube, (the dielectric barrier), was about 3 mm. The grounded electrode was made of silver deposited on the external side of the quartz tube. The temperature was controlled by the outer electrical heater and measured with a thermocouple placed at the external reactor wall (Fig. 1). The reactor was powered at the frequency of about 6 kHz and was operated at the pressure of 1.2 bar. Electric parameters (voltage and current) were measured with Tektronix TDS 3032 (Fig. 2). The value of the discharge power was determined as an average of 3 measurements, calculated from the voltage and current intensity courses in time.
Methane 99.5, argon 99.999% and oxygen 99,999 were the components of the feeding gas mixtures. The gas flow rates were controlled by mass controllers. The components of inlet and outlet gases were determined by chromatographic method (GC Agilent 6890N). The share of other products, i.e. higher than C4 and that of non-volatile products, mainly soot, were calculated from the carbon balance.

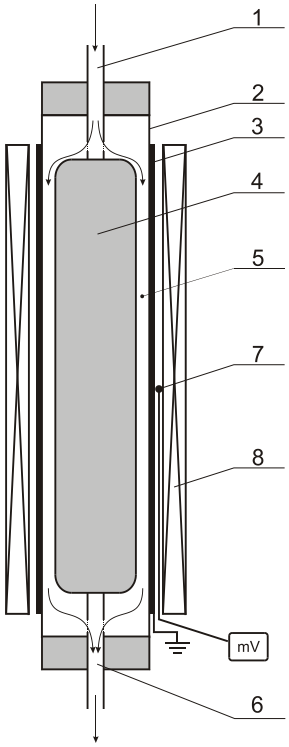


Fig. 1. Reactor for methane conversion.1 – gas inlet, 2 – quartz tube, 3 – grounded electrode, 4 – high voltage electrode, 5 – discharge gap, 6 – gas outlet 7 - thermocouple, 8 – heater.

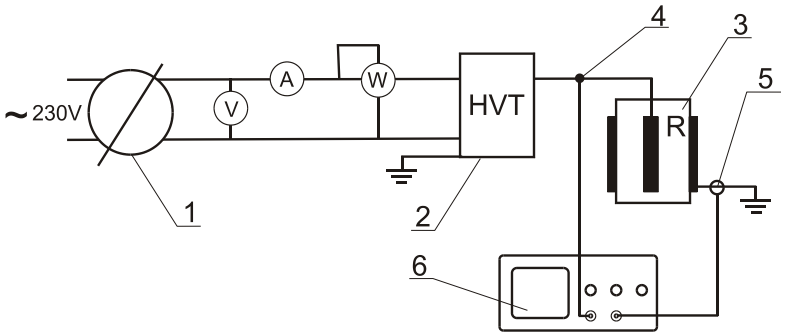


Fig. 2. Electric circuit for the dielectric barrier discharge reactor. 1 – autotransformer, 2 – high voltage transformer, 3 – reactor, 4 – high voltage probe, 5 – current probe, 6 – oscilloscope, A – ammeter, V – voltmeter, W – wattmeter

Parameters and definitions

$W_0[CH_4]$, $W_0[O_2]$; [mmol/h] – methane and oxygen flow rates at the inlet

$W[CH_4]$, $W[O_2]$, $W[CO]$, $W[CO_2]$, $W[H_2]$, $W[H_2O]$, $W[C_mH_n]$ $W[C_mH_{2m+1}OH]$; [mmol/h] – methane, oxygen, carbon dioxide, carbon dioxide, hydrogen, water, C_mH_n hydrocarbons and alcohols flow rates, respectively at the outlet

C_N – unidentified volatile (higher than C4) and non-volatile products. The amount of unidentified volatile (higher than C4) and non-volatile products, mainly soot, was calculated from the carbon balance.

1. Overall methane conversion:

$$X[CH_4] = \frac{W_0[CH_4] - W[CH_4]}{W_0[CH_4]}$$

2. Overall oxygen conversion: $$X[O_2] = \frac{W_0[O_2] - W[O_2]}{W_0[O_2]}$$

3. Methane conversion to higher than C_4 and non-volatile products: $$X_C = \frac{W[C_N]}{W_0[CH_4]}$$

4. Methane conversion to C_mH_n: $$X[CH_4 \rightarrow C_mH_n] = \frac{mW[C_mH_n]}{W_0[CH_4]}$$

5. Methane conversion to CO: $$X[CH_4 \rightarrow CO] = \frac{W[CO]}{W_0[CH_4]}$$

6. Methane conversion to alcohols $$X[CH_4 \rightarrow C_mH_{2m+1}OH] = \frac{mW[C_mH_{2m+1}OH]}{W_0[CH_4]}$$

7. Methane conversion to CO_2: $$X[CH_4 \rightarrow CO_2] = \frac{W[CO_2]}{W_0[CH_4]}$$

8. Methane conversion to H_2 : $$X[CH_4 \rightarrow H_2] = \frac{W[H_2]}{2W_0[CH_4]}$$

9. Methane conversion to H_2O : $$X[CH_4 \rightarrow H_2O] = \frac{W[H_2O]}{2W_0[CH_4]}$$

3. Results

The conversion of methane in homogeneous system was studied in gases containing 50% or 25% of argon. In all experiments molar ratio of methane to oxygen was 3:1 and gas flow rate was 2 or 1 Nl/h. The effect of the presence of a catalysts in discharge gap on the electrical parameters was not observed. The effect of temperature (power 19 W) on overall methane conversion and its conversion to hydrocarbons was observed. The overall conversion and conversion of methane to hydrocarbons generally increased with the increase of temperature (Figs. 3 and 4). The obtained results have shown that the CH_4 conversions to methanol strongly decreased with the increase of temperature from 150 to 340^{O}C (Fig. 4).

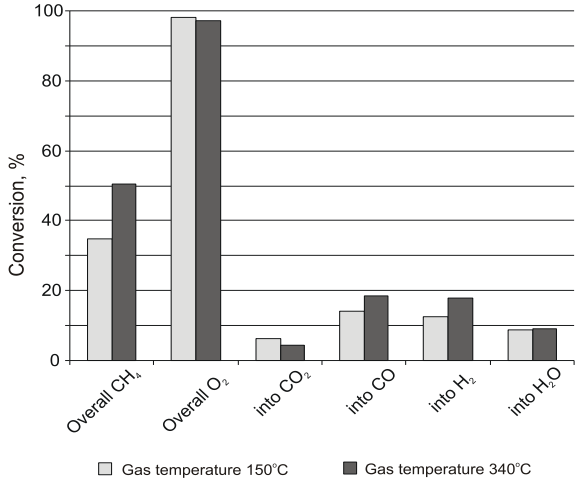


Fig. 3. Effect of temperature on overall conversion of methane and oxygen and conversion of methane to H_2, CO, CO_2, and H_2O. Power – 19 W, initial argon concentration 50%. Gas flow rate 2 Nl/h.

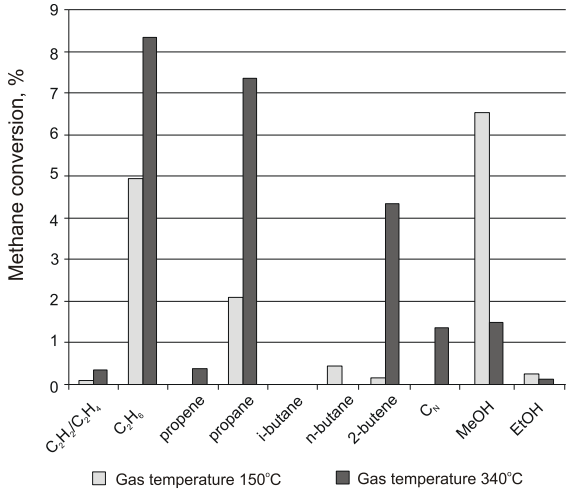


Fig. 4. Effect of temperature on methane conversion to hydrocarbons and alcohols. Power – 19 W, initial argon concentration 50%. Gas flow rate 2 Nl/h.

The effect of gas flow rate on overall methane conversion and its conversion to hydrocarbons was observed (Figs. 5, 6). The conversion of methane to all hydrocarbons increased with the decrease of the gas flow rate. Conversion of methane to methanol decreased when gas flow rate decreased (Fig. 6).

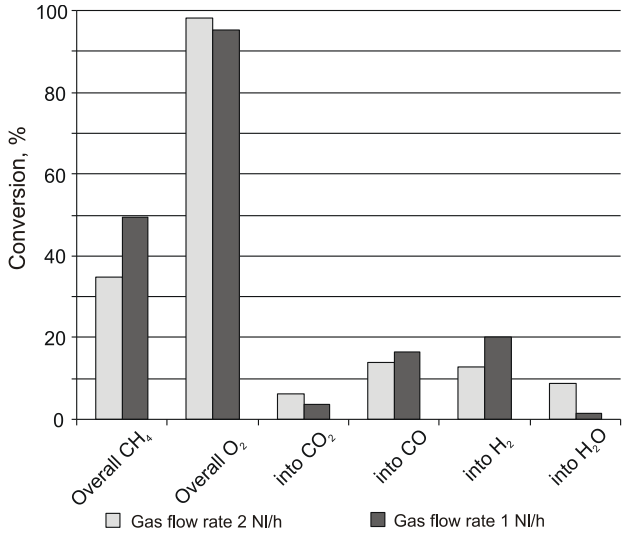


Fig. 5. Effect of the gas flow rate on overall conversion of methane and oxygen and conversion of methane to H_2, CO, CO_2, and H_2O. Power – 19 W, argon conc. 50%.

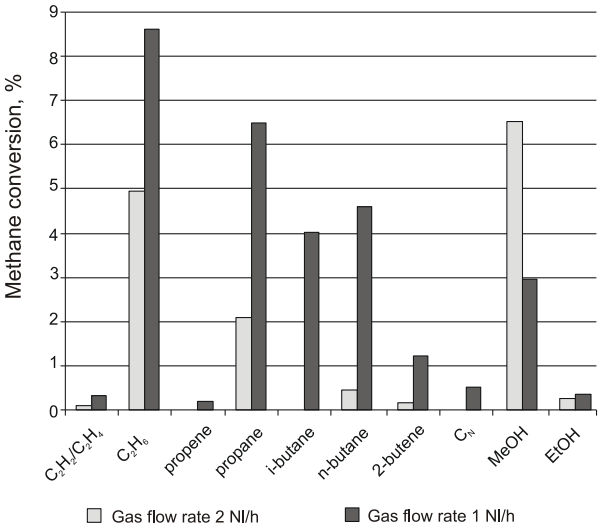


Fig. 6. Effect of the gas flow rate on conversion of methane to hydrocarbons and alcohols. Molar ratio $[CH_4]$: $[O_2]$=3:1, Power – 19 W, argon conc. 50%.

Similar effect of temperature on conversion of methane, oxygen and conversion of methane to hydrocarbons and alcohols for power of 15 W and argon initial concentration of 25% ($[CH_4]$:$[O_2]$=3) was observed (Figs. 7, 8). The conversion of methane to other hydrocarbons is not presented on Fig. 8. The amount of methanol strongly decreased with the increase of temperature from 110 to 340^{O}C.

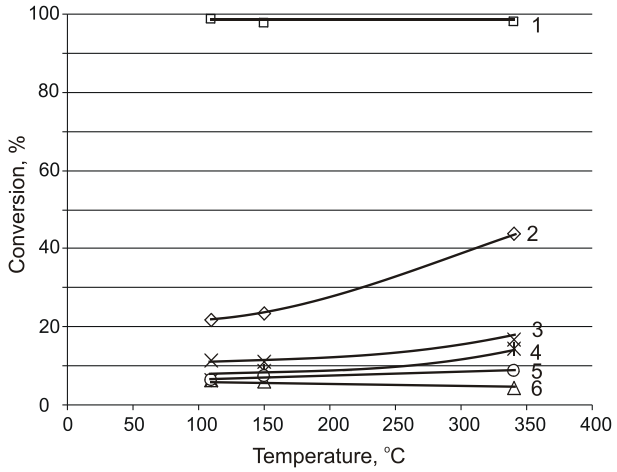


Fig. 7. Effect of temperature on overall conversion of methane (2) and oxygen (1) and conversion of methane to CO (3), H_2 (4), H_2O (5) and CO_2 (6). Molar ratio $[CH_4]$: $[O_2]$=3, Power – 15 W, argon conc. 25%. Gas flow rate 2 Nl/h.

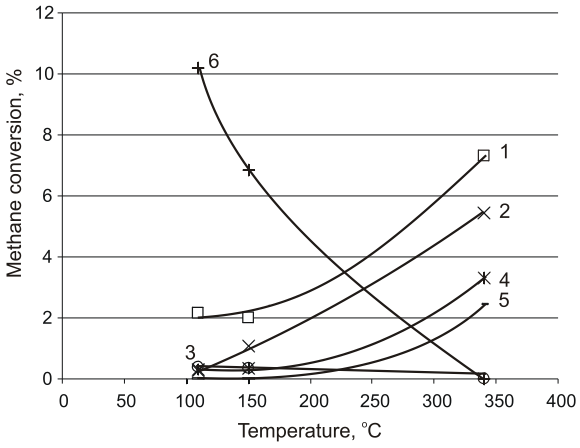


Fig. 8. Effect of temperature on methane conversion to hydrocarbons (1- C_2H_6, 2- propane, 3 – n-butane, 4 – i-butane, 5 – 2-butene) and methanol (6). Molar ratio $[CH_4]$: $[O_2]$=3:1, Power – 15 W, argon conc. 25%. Gas flow rate 2 Nl/h.

The gaseous products obtained at 110^{0}C in homogeneous system and in HPCS with Al_2O_3 and Fe/Al_2O_3 was different in studied systems (Figs. 9, 10). With Al_2O_3 and Fe/Al_2O_3 the conversion of methane to methanol was lower than that obtained in homogeneous system. In HPCS with Fe/Al_2O_3 the conversion of oxygen was below 50% and in outlet gas mixture CO was not observed.
Generally with Fe/Al_2O_3 the conversion of methane occurs to C_2H_2/C_2H_4 and the conversion of methane to other hydrocarbons do not exceed 0.5% (Fig. 10)

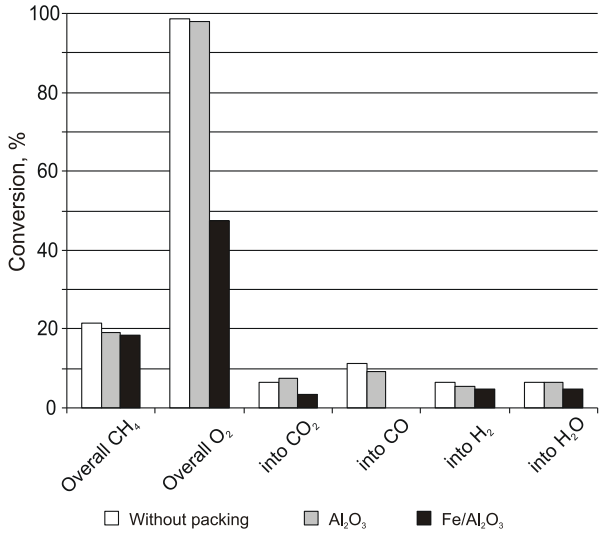


Fig. 9. Effect of the packing of discharge gap on overall conversion of methane and oxygen and conversion of methane to H_2, CO, CO_2, and H_2O. Power – 15 W. Argon conc. 25%. Gas flow rate 2 Nl/h.

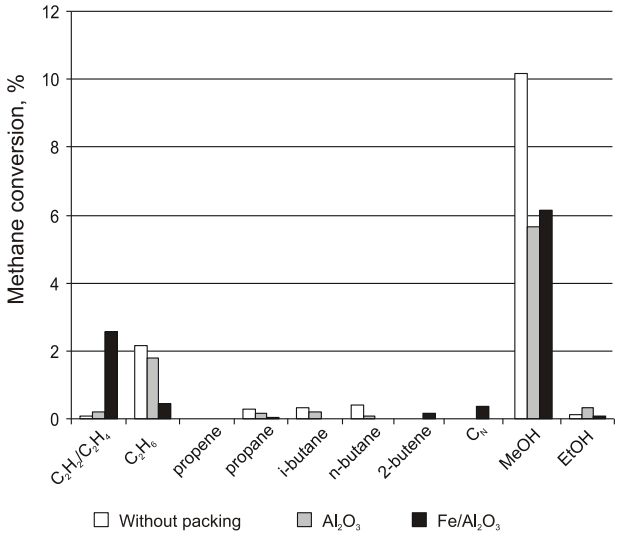


Fig. 10. Effect of the packing of discharge gap on methane conversion to hydrocarbons and methanol and ethanol. Molar ratio $[CH_4]$: $[O_2]$=3:1, Power – 15 W. Argon conc. 25%. Gas flow rate 2 Nl/h.

4. Conclusions

The highest amount of methanol was obtained in the system without packing at 110^{O}C. In the homogeneous system the increase of the temperature decreases the conversion of methane to methanol. The presence of Fe/Al_2O_3 increased the methane conversion to C_2H_2/C_2H_4 and decreased the amount of the others hydrocarbons. The highest conversion of methane to C_2H_2/C_2H_4 reached 2.6%.

5. Acknowledgment

This work was financially supported by Warsaw University of Technology.

6. Referencess

1. Holmen A., 2009, *Catal. Today* **142**, 2.
2. Skutil K., Taniewski M., 2007, *Fuel Process. Technol*. **88**, 877.
3. Papa F., Gingasu D., Patron L., Miyazaki A., Balist I., 2010 *Appl. Catal. A: Gen*. **375** 172.
4. Havran V., Duduković M. P., Lo C. S., 2011 *Ind. Eng. Chem. Res*. **50** 7089.
5. Górska A., Krawczyk K., Jodzis S., Schmidt- Szałowski K., 2011 *Fuel* **90** 1946.
6. Sentek J., Krawczyk K., Młotek M., Kalczewska M., Kroker T., Kolb T., Schenk A., Gericke K-H., Schmidt-Szałowski K., 2010 *Appl. Catal. B: Environ*. **94** 19.
7. Młotek M., Sentek J., Krawczyk K., Schmidt-Szałowski K., 2009 *Appl. Catal. A: Gen*. **366** 232.
8. Wang W., Ji S., Pan D., Li C., 2011 *Fuel Process. Technol*. **92** 541.
9. Nozaki T., Fukus W., Ozaki K., 2008 *Energy Fuels*; **22** 3600.
10. Kraus M., Eliasson B., Kogelschatz U., Wokaun A., 2001 *Phys. Chem. Chem. Phys*. **3** 294.
11. Zhang K., Li Y., Wang Y., Liu C.-J., Eliasson B., 2003 *Fuel Process. Technol.* **83** 101.
12. Eliasson B., Liu C.-J., Kogelschatz U., 2000 *Ind. Eng. Chem. Res*. **39** 1221.
13. Indarto A., Yang D. R., Palgunadi J., Choi J.W., Lee H., Song H. K., 2008 *Chem. Eng. and Proc*. **47** 780.
14. Wang B., Zhang X., Liu Y., Xu G., 2009 *J. of Natural Gas Chem.*, **18** 94.
15. Lu J., Li Z., 2010 *J. of Natural Gas Chem.*, **19** 375.
16. Chen L., Zhang X.W., Huang L., Lei L.C., 2009 *Chem. Eng. and Proc.* **48** 1333.

BACTERICIDAL EFFECTS AND FORMATION OF ROS/RNS IN WATER SPRAYED THROUGH COLD AIR PLASMA

Z. Machala[1], B. Tarabová[1], P. Lukeš[2], E. Špetlíková[2,3], L. Šikurová[1], K. Hensel[1]

[1]*Faculty of Mathematics, Physics and Informatics, Comenius University, Mlynská dolina, 84248 Bratislava, Slovakia*

[2]*Institute of Plasma Physics AS CR, Za Slovankou 3, 182 00 Prague, Czech Republic*

[3]*Institute of Chemical Technology, Technicka 5, 166 28 Prague, Czech Republic*

E-mail: machala@fmph.uniba.sk

Bio-decontamination and chemical effects induced by plasma in water upon electro-spraying through cold atmospheric pressure plasma of DC-driven positive transient spark discharge in air were investigated. Inactivation of *Escherichia coli* in plasma treated water was determined in dependence on the solution pH (controlled by buffers) and correlated with chemical changes induced in water. Productions of H_2O_2, nitrites, nitrates, peroxynitrites and pH changes were determined. The degree of inactivation and oxidative damage of bacteria increased with increasing acidity of the solution. Acidified nitrites interacting with H_2O_2 were determined as the most important bactericidal ROS/RNS agents in water treated by air plasma.

1. Introduction

Nowadays it is evident that cold atmospheric pressure plasmas can efficiently kill various microbes, even highly resistant forms such as bacterial spores and biofilms, and foster interesting phenomena in the cells of higher organisms leading to various therapeutic effects. The mechanisms of plasma-cell interaction are not fully understood yet, although a great research effort has been dedicated to elucidate the respective roles of various plasma agents in the interaction with live cells, such as charged particles, neutral reactive species, UV radiation, electric field and heat [1]. The most studies agree on that the bactericidal effects of atmospheric pressure cold plasmas are dominantly due to reactive neutral species (mostly radicals) and perhaps some ions, such as superoxide anion O_2^-.

Plasmas generated in air in contact with water are of the great interest because they produce large quantities of reactive oxygen species (ROS) and reactive nitrogen species (RNS) and seem to be the most efficient in bio-decontamination [2-8]. Even He or Ar plasma jets perform the strongest bactericidal efficacy with O_2 or air admixtures or when the rare gas plasma entrains air components [2]. Air plasma treatment of water and aqueous solutions typically leads to acidification [2-3, 9-15] which can normally be explained by dissolution of NO_x species formed in the air plasma in water [2, 9-13]. Some authors report acidification by other mechanisms, even in pure O_2 plasma by the action of O_2^- anions [14]. Acid environment itself, despite being crucial in bactericidal effect of plasma treated water, did not prove to be the main antibacterial agent. Several authors reported that addition of various acids resulting in the same pH as in the plasma treated solutions (usually 2.5-4.8) does not lead to the same bactericidal efficacy. It is acid environment in synergy with plasma agents leads to the bacterial inactivation [2, 9-10]. However, it is not clear enough yet, which plasma agents and which ROS/RNS have dominant roles in water decontamination and what is the associated plasma-induced water chemistry. Hydrogen peroxide, nitrate and nitrite anions, as well as other species such as peroxynitrites, have been identified in plasma-activated water [2-3, 7-10, 16].

In this work we investigated the chemical effects induced in water electro-sprayed through DC-driven positive transient spark discharge. We measured formations of hydrogen peroxide (H_2O_2), nitrites (NO_2^-) and nitrates (NO_3^-) and peroxynitrites ($ONOO^-$) in plasma treated water. Production of these chemical species was correlated with the pH changes and with bactericidal effects observed on *Escherichia coli,* suspended in plasma treated solutions. This work follows our previous studies of bio-decontamination of electro-sprayed water in the transient spark [17-18].

2. Methodology

The experimental setup for DC-driven transient spark in point-to-plane geometry, with a high voltage (HV) hypodermic hollow needle electrode enabling water flowing through the discharge zone and a mesh electrode is depicted in Fig. 1. The inter-electrode spacing was usually kept at 10 mm. A positive DC high voltage was applied through the ballast resistor *R* (5-10 MΩ). The discharge voltage was measured by a high voltage probe Tektronix P6015A. The discharge current was measured: on a 1 Ω resistor or by a current monitor Pearson 2877. The current and voltage signals were processed by a digitizing 200 MHz oscilloscope Tektronix TDS 2024. The contaminated water flowed directly through the high voltage hollow needle electrode. The effect of electrostatic spraying occurred when the high voltage was applied on the needle electrode [17-19]. The typical discharge visual appearance is shown in the photograph in Fig. 2.

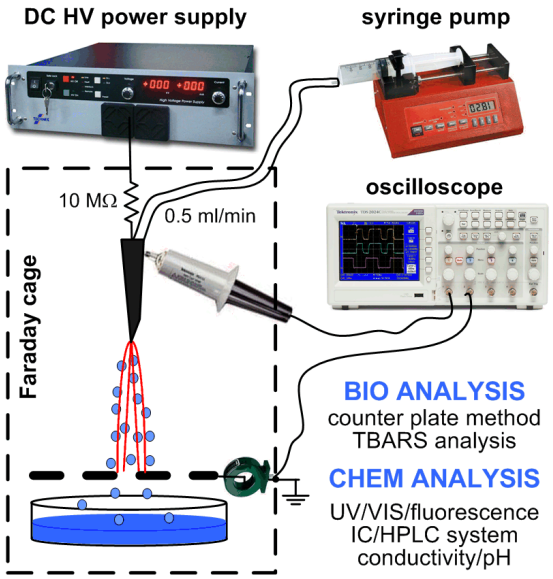


Fig. 1. The experimental setup

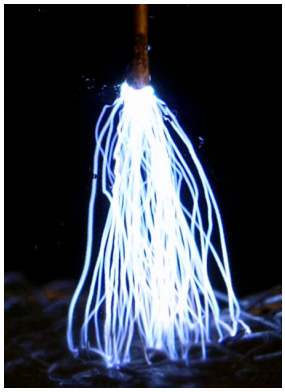


Fig. 2. Photograph of the transient spark with electro-spray of water in 1 cm needle-mesh gap, water flow rate 0.5 mL/min, 14 kV.

Measurements of hydrogen peroxide and peroxynitrite formed in plasma treated water were performed by colorimetric methods using UV/VIS spectrophotometer Unicam Helios Gamma and UV/VIS/ Fluorescence microplate reader Thermo VarioScan Flash, respectively. The concentration of hydrogen peroxide was determined by the reaction of H_2O_2 with titanyl ions with the absorbance measurements at 407 nm. The concentration of peroxynitrite was determined by the reaction with 2,7-dichlorodihydrofluorescein diacetate (DCF-DA) with absorbance measurements at 500 nm and with fluorescence measurements using excitation and emission wavelengths of 502 and 523 nm, respectively (PerkinElmer LS 45, 50 Hz) [20, 21]. The concentrations of nitrites and nitrates were measured by ion chromatography using a HPLC system Shimadzu LC-10A*vp* with UV (210 nm) and suppressed conductivity detection. Analyses were made by means of a 7-µm Allsep A1 anion exchange column (10 cm × 4.6 mm) with 0.85 mmol L^{-1} $NaHCO_3$/0.9 mmol L^{-1} Na_2CO_3 as the eluent (flow rate of 1.2 mL min^{-1}). Changes of pH and electrolytic conductivity in plasma treated water were measured by pH and conductivity probes (WTW, Adwa).

Aqueous solutions of various initial pH and conductivities σ used for plasma treatment experiments were prepared by addition of different salts to deionized water (σ= 1 µS/cm, pH=5.5):

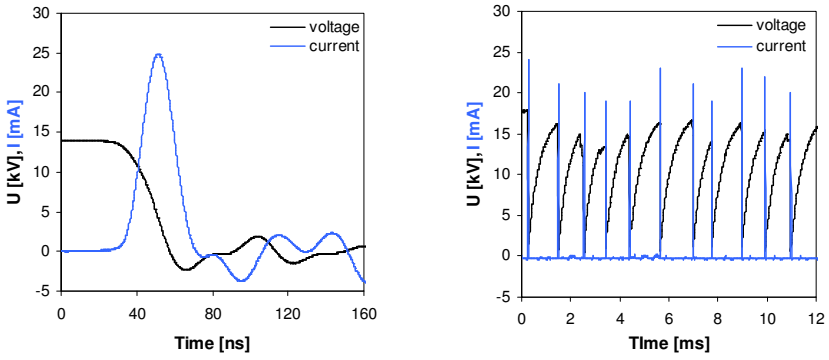
- NaH_2PO_4 solutions (σ=0.6 mS/cm, pH=5.5) mimic the natural conductivity of tap water (~0.6 mS/cm). NaH_2PO_4 salt has similar chemical composition with the phosphate buffer described below but no buffering activity. In this work we designated these non-buffered solutions as **'water'**.
- Na_2HPO_4/KH_2PO_4 phosphate buffered (PB) solutions (σ=0.6 mS/cm, pH=6.9), designated as **'PB'**.
- physiological NaCl (saline) solutions (NaCl concentration 0.85% vol., σ= 6.35 mS/cm, pH=6.7), non-buffered, designated as **'saline'**. Saline solution is a natural cell environment.
- physiological NaCl (saline) solutions (concentration 0.85% vol., σ= 6.0 mS/cm, pH=6.9) with Na_2HPO_4/KH_2PO_4 phosphate buffer, designated **'PBS'**.

Bio-decontamination effects were tested on Gram-negative *Escherichia coli* (CCM3954) in water with initial populations from 10^6 to 10^8 colony forming units per mL (CFU/mL). Cultivated bacteria in the liquid nutrient were centrifuged several times and diluted in water/saline solution to obtain desired concentrations. Alternatively, bacteria pre-cultivated on gel discs were directly dissolved in the desired solution under study. The plasma experiments with bacteria suspensions were performed with positive transient spark and repeated 10-15 times. The number of bacteria cells in the solution was assayed by counting colony forming units cultivated on agar plates (MFC, HiMedia, Mumbai, India; Biolab).

3. Results and discussion

3.1. Transient spark discharge (TS)

Electrical parameters and emission spectra of transient spark discharge (TS) operating in atmospheric air with water spray were documented in detail in our previous works [22-23]. The typical voltage and current waveforms of positive TS discharges in 10 mm gap (with electro-spray of water) are shown in Fig. 3. The TS plasma cannot reach equilibrium conditions and remains relatively cold. With water electro-spray through TS, a great care was taken to keep the constant electrical parameters throughout each experiment since the water spray substantially perturbs the discharge regularity (especially jitters the pulse frequency). In order to keep the constant power dissipated into the discharge, the pulse frequency was controlled at ~1 kHz. The typical applied power used in this work was 1-2 W, with energy 1-2 mJ per pulse. The water was sprayed through the high voltage hollow needle electrode under a constant flow rate of 0.5 mL/min.

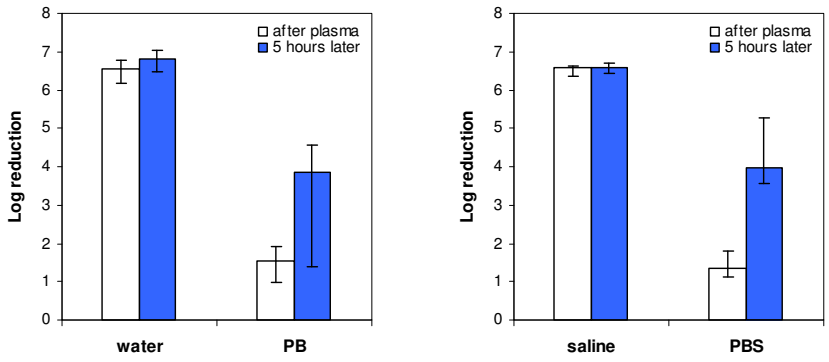


(a) (b)

Fig. 3. Typical voltage and current waveforms of TS discharge with electro-spray of water in (a) ns time scale – one pulse, and (b) ms time scale – several pulses, 10 mm gap.

3.2. Bactericidal effects of plasma treated water

Bacterial suspensions of *E. coli* in aqueous solutions were electro-sprayed through the discharge. The bactericidal efficiency expressed as log reduction reached up to 7 logs for both non-buffered water and saline, directly after plasma treatment. A slight enhancement of the bactericidal effect was observed when bacteria were left in the plasma treated water or saline for 4-5 h longer. This indicates ongoing biochemical processes in the plasma activated water post treatment, also reported in [3-4, 10, 14, 15].
The bactericidal effect of plasma treated water and saline was always accompanied with the decrease of pH (down to pH ~3) and the increase in the solution conductivity (water 0.6 → ~1.04 mS/cm, saline solution ~6.35 → ~6.85 mS/cm). However, additional tests (not shown) performed to evaluate whether low pH is the main bactericidal agent showed that the nitric or hydrochloric acid solution of the same pH did not lead to the same biocidal effects. In agreement with [2, 9, 10, 15], we confirm that rather acid environment in synergy with plasma agents leads to the bacterial inactivation.
To elucidate the role of pH in the plasma induced bactericidal effects, we performed experiments with phosphate buffered solutions (PB and PBS) of sufficient buffer capacity (pH=6.9 remained fairly constant upon treatment or decreased very little). As a consequence, the bactericidal effect was strongly reduced in PB and PBS with respect to non-buffered solutions, but not completely stopped (about 1-log). Fig. 4 compares the bactericidal effect of water vs. PB, and saline vs. PBS obtained immediately after plasma treatment and 5 h later. Interestingly, the decontamination in plasma treated PB and PBS increased substantially after 5 h, without further pH change.

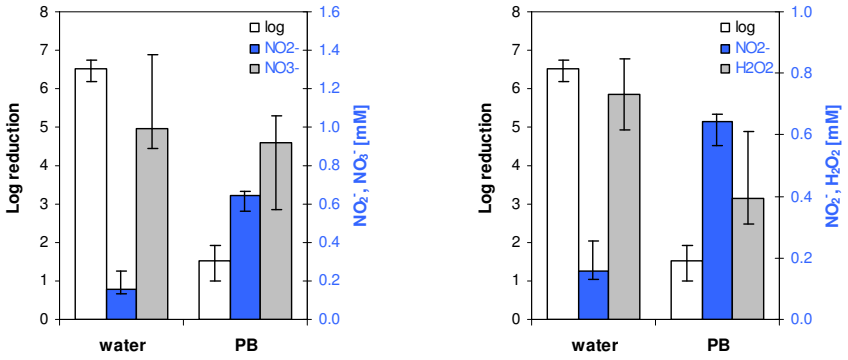


(a) (b)

Fig. 4. *E. coli* inactivation of log reduction after plasma treatment and 5 h later obtained in: (a) water (pH~3.3 after plasma and ~3.4 5h later, respectively) and PB solutions (pH~6.2 and ~5.8, respectively); (b) saline solution (pH~2.8 after plasma and ~2.9 5h later, respectively) and PBS (pH~5.6). Medians with error bars showing 25 and 75 percentiles.

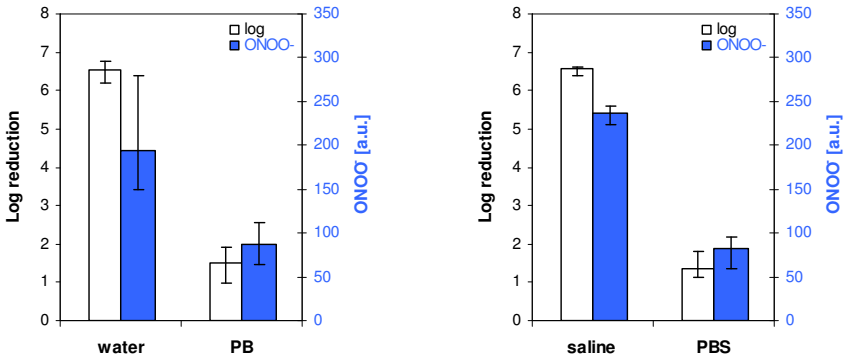
3.3. Chemical effects induced in water by plasma

In order to evaluate the mechanisms participating in bacterial inactivation, the chemical effects induced in water sprayed through the transient spark discharge were studied in more detail. Since the discharge operates in atmospheric humid air, we focused mainly on the formation of ROS and RNS: hydrogen peroxide (H_2O_2), nitrites (NO_2^-) and nitrates (NO_3^-) and peroxynitrites ($ONOO^-$).



(a) (b)

Fig. 6. Bactericidal effect (log reduction) of water and PB solutions related to (a) NO_2^- and NO_3^- and (b) NO_2^- and H_2O_2 concentrations. Medians with error bars showing 25 and 75 percentiles.



(a) (b)

Fig. 7. Bactericidal effect (log reduction) of (a) water and PB solutions, and (b) saline and PBS, after plasma treatment correlated with the relative $ONOO^-$ concentrations (fluorescence emission at 523 nm with reference subtracted). Medians with error bars showing 25 and 75 percentiles.

Fig. 5 shows the concentrations of nitrites, nitrates and hydrogen peroxide obtained in water and PB solutions after spraying through the discharge. Fig. 5 shows that non-acidic environment of PB buffers resulted in much higher concentrations of nitrites (~0.6 mmol/L) and slightly lower concentrations of

H_2O_2 (~0.4 mmol/L) and nitrates (~0.9 mmol/L) compared to that for non-buffered solutions, in which the concentrations of H_2O_2 were ~ 0.7 mmol/L, nitrites ~ 0.2 mmol/L and nitrates ~ 1 mmol/L.
Such a significant pH effect on the concentrations of nitrites is result of disproportionation of nitrites into nitrates occurring under acidic conditions:

$$3\ NO_2^- + 3H^+ \rightarrow 2\ NO + NO_3^- + H_3O^+ \qquad \text{(Eq. 1)}$$

This route is greatly accelerated at pH below ~ 3.5 which correlates with acid-base properties of nitrites (pK_a = 3.3). Since the only difference between buffered and non-buffered solutions was pH, it is reasonable to assume that the initial production rates of nitrites and nitrates by the discharge were the same under both conditions. The mechanism of their formation in water is the result of dissolution of NO_x formed in air plasma by gas-phase reactions of dissociated N_2 and O_2. Along with formation of NO_2^- and NO_3^- in the plasma treated water, dissolution of NO_x in water leads to the decrease of pH:

$$NO_2 + NO_2 + H_2O \rightarrow NO_2^- + NO_3^- + 2\ H^+ \qquad \text{(Eq. 2)}$$
$$NO + NO_2 + H_2O \rightarrow 2\ NO_2^- + 2\ H^+ \qquad \text{(Eq. 3)}$$

The difference in the concentrations of NO_2^- and NO_3^- measured in both solutions is then a result of subsequent post-discharge reactions leading to disproportionation of nitrites into nitrates (Eq. 1).
The formation of nitrates may also proceed via the liquid-phase reaction of NO_2 with OH radical to form peroxinitrous acid (ONOOH) or its conjugate base peroxynitrite ($O{=}NOO^-$), which subsequently decay into NO_3^-. Or in the presence of hydrogen peroxide, peroxynitrite can be also formed by the reaction of nitrite anion with H_2O_2.

$$NO_2^- + H_2O_2 \rightarrow O{=}NOO^- + H_2O \qquad \text{(Eq. 4)}$$

This route occurs under acidic conditions and might be responsible for lower concentrations of hydrogen peroxide determined in non-buffered water. Peroxynitrites are relatively strong oxidants with a large bactericidal effect and they may significantly contribute to inactivation process induced by air plasma in water. Under acidic conditions their bactericidal effect is determined mainly by OH radicals formed by the decomposition reaction of peroxynitrous acid [8]. It is likely that with the decreasing pH, the contribution of $ONOO^-$ to bactericidal effects of plasma increased. The attempt was made to correlate the concentrations of nitrites and H_2O_2 with the concentrations of $ONOO^-$ formed in plasma treated water. Since $ONOO^-$ are highly reactive under acidic conditions, their lifetime is very short and their detection in plasma treated water was possible only qualitative with concentrations estimated in the order of tens of μmol/L. Nevertheless, Fig. 7 shows that the relative amounts of $ONOO^-$ measured by fluorescence spectroscopy correlate directly with the bactericidal effect. These qualitative measurements indicate an important role of $ONOO^-$ in bio-decontamination.
At the same time, the antimicrobial properties of nitrites under acidic conditions have to be considered. These so-called “acidified nitrites” are capable of great effect on bacteria [3, 16]. In fact, it seems more reasonable to assume that acidified nitrites are more important route of bactericidal effects then through their reaction with H_2O_2 upon formation of peroxynitrites (Eq. 4).

4. Conclusions

We investigated the treatment of water or saline non-buffered and buffered solutions contaminated with *E. coli* bacteria electro-sprayed through the cold air plasma of transient spark. The treatment lead to acidification and the production of nitrites, nitrates, peroxides and peroxynitrites. At lowered pH, nitrites are quickly oxidized to nitrates with H_2O_2 and this is associated with the strong bactericidal effect. At neutral pH in buffered solutions, nitrites are less oxidized and the biocidal effect is weaker. The bactericidal effect correlates with the relative amount of the formed peroxynitrites. The estimated concentrations of peroxynitrites are, however, too low compared to the measured nitrites and H_2O_2 to consider the reaction (Eq. 4) as the main mechanism of their formation and consider peroxynitrites as the key bactericidal agent. It rather seems that synergistic effects of nitrites and peroxides in acidic conditions are the most responsible for bactericidal properties of water sprayed through air plasma.

5. Acknowledgements

This work was supported by Slovak Grant Agency VEGA 1/0668/11, Slovak Research and Development Agency APVV SK-CZ-0179-09, the Grant Agency of AS CR (project No. IAAX00430802) and the project Ministry of Education, Youth and Sports of the Czech Republic (No. MEB0810116).

6. References

[1] M. Laroussi, *IEEE Trans. Plasma Sci.* **2002**, 30 (4), 1409.
[2] S. Ikawa, K. Kitano, and S. Hamaguchi, *Plasma Process. Polym.* **2010**, 7 (1), 33.
[3] M. J. Traylor, M. J. Pavlovich, S. Karim, P. Hait, Y. Sakiyama, D. S. Clark, and D. B. Graves, *J. Phys. D: Appl. Phys.* **2011**, 44 (47), 472001.
[4] M. Naitali, G. Kamgang-Youbi, J. M. Herry, M. N. Bellon-Fontaine, and J. L. Brisset, *Appl. Environ. Microbiol.* **2010**, 76 (22), 7662.
[5] D. Dobrynin, G. Friedman, A. Fridman, and A. Starikovskiy, *New J. Phys.* **2011**, 13 103033.
[6] Y. Akishev, N. Trushkin, M. Grushin, A. Petryakov, V. Karal'nik, E. Kobzev, V. Kholodenko, V. Chugunov, G. Kireev, Y. Rakitsky, I. Irkhina, "Inactivation of Microorganisms in Model Biofilms by an Atmospheric Pressure Pulsed Non-thermal Plasma," in *Plasma for Bio-Decontamination, Medicine and Food Security*, NATO Science for Peace and Security Series A: Chemistry and Biology (Eds.: Z. Machala, K. Hensel, Y. Akishev), Springer, Dordrecht, **2012**, p. 149.
[7] P. Lukes, B. R. Locke, J. L. Brisset, "Aqueous-Phase Chemistry of Electrical Discharge Plasma in Water and in Gas-Liquid Environments," in *Plasma Chemistry and Catalysis in Gases and Liquids*, (Eds.: V. I. Parvulescu, M. Magureanu, P. Lukes), Wiley-VCH, Weinheim, **2012**, Ch. 7, p. 241.
[8] P. Lukes, J. L. Brisset, B. R. Locke, "Biological Effects of Electrical Discharge Plasma in Water and in Gas-Liquid Environments," in *Plasma Chemistry and Catalysis in Gases and Liquids*, (Eds.: V. I. Parvulescu, M. Magureanu, P. Lukes), Wiley-VCH, Weinheim, **2012**, Ch. 8, p. 309.
[9] K. Oehmigen, M. Hahnel, R. Brandenburg, C. Wilke, K. D. Weltmann, and T. von Woedtke, *Plasma Process. Polym.* **2010**, 7 (3-4), 250.
[10] K. Oehmigen, J. Winter, M. Hahnel, C. Wilke, R. Brandenburg, K. D. Weltmann, and T. von Woedtke, *Plasma Process. Polym.* **2011**, 8 (10), 904.
[11] Y. Z. Tang, X. P. Lu, M. Laroussi, and F. C. Dobbs, *Plasma Process. Polym.* **2008**, 5 (6), 552.
[12] J. L. Brisset, B. Benstaali, D. Moussa, J. Fanmoe, and E. Njoyim-Tamungang, *Plasma Sources Sci. Technol.* **2011**, 20 (3), 034021.
[13] J. L. Brisset, D. Moussa, A. Doubla, E. Hnatiuc, B. Hnatiuc, G. K. Youbi, J. M. Herry, M. Naitali, and M. N. Bellon-Fontaine, *Ind. Eng. Chem. Res.* **2008**, 47 (16), 5761.
[14] N. Shainsky, D. Dobrynin, E. Ercan, Joshi S. G., H. Ji, A. Brooks, G. Fridman, Y. Cho, A. Fridman, and G. Friedman, *Plasma Process. Polym.* **2012**, doi: 10.1002/ppap.201100084.
[15] J. Julák, V. Scholtz, S. Kotúčová, and O. Janoušková, *Physica Medica*, **2012**, 28 (3), 230239.
[16] D. B. Graves, *J. Phys. D: Appl. Phys.* **2012**, 45 (26), 263001.
[17] Z. Machala, I. Jedlovsky, L. Chladekova, B. Pongrac, D. Giertl, M. Janda, L. Sikurova, and P. Polcic, *Eur. Phys. J. D* **2009**, 54 (2), 195.
[18] Z. Machala, L. Chladekova, and M. Pelach, *J. Phys. D: Appl. Phys.* **2010**, 43 (22), 222001.
[19] B. Pongrac and Z. Machala, *IEEE Trans. Plasma Sci.* **2011**, 39 (11), 2664.
[20] H. Possel, H. Noack, W. Augustin, G. Keilhoff, and G. Wolf, *Febs Lett.* **1997**, 416 (2), 175.
[21] J. P. Crow, *Nitric Oxide: Biol. Chem.* **1997**, 1 (2), 145.
[22] M. Janda, V. Martisovits, and Z. Machala, *Plasma Sources Sci. Technol.*, **2011**, 20 (3), 035015.
[23] Z. Machala, M. Janda, K. Hensel, I. Jedlovsky, L. Lestinska, V. Foltin, V. Martisovits, M. Morvova, *J. Mol. Spectrosc.* **2007**, *243*, 194.

ATMOSPHERIC PRESSURE LOW-POWER MICROWAVE MICROPLASMA SOURCE FOR DECONTAMINATION OF MICROORGANISMS

Jerzy Mizeraczyk[1,2], Dariusz Czylkowski[1], Bartosz Hrycak[1], Mirosław Dors[1], Mariusz Jasiński[1]

[1] *Centre for Plasma and Laser Engineering, The Szewalski Institute of Fluid Flow Machinery, Gdańsk, Poland*

[2] *Department of Marine Electronics, Gdynia Maritime University, Gdynia, Poland*

E-mail: mdors@imp.gda.pl

Atmospheric pressure low-temperature microwave microplasma source (MmPS) was used in experimental investigations for decontamination of different types of microorganisms like bacteria (Escherichia coli, Bacillus subtilis) and fungus (Aspergillus niger). The influence of the microorganism type, oxygen concentration, absorbed microwave power, microplasma treatment time and MmPS distance from the treated sample on the microorganism decontamination efficiency was investigated.

1. Introduction

Recently, there is a growing interest in the low-temperature microplasmas used in the biomedical applications such as sterilization of medical instruments, high-precision surgery, cells treatment and deactivation of bacteria and viruses [1-4]. Sterilization is a physical or chemical process that impairs or eliminates, especially microorganisms like bacteria. In a plasma the sterilization is achieved due to the reactive species in the plasma (electrons, ions, radicals, reactive molecules), UV light, etc. [5, 6].
Due to many plasma sterilization systems like low pressure [7] or atmospheric pressure [8], DBD [9], RF [10], we designed, built and tested experimentally a small atmospheric pressure low-temperature microwave microplasma source (MmPS). It has structure of a coaxial line, formed by an inner conductor, made of a brass rod with a tungsten rod top, and outer conductor in the form of a brass cylinder. The MmPS is operated at standard microwave frequency of 2.45 GHz. The generated by MmPS plasma has the form of a microflame forming at the tip of the inner conductor. The main advantages of our MmPs are atmospheric pressure operation, low microplasma temperature, simplicity and low cost. Using it we performed experimental investigations concerning microorganisms deactivation by atmospheric pressure low-temperature microplasma. The investigations involved Ar and Ar/O_2 microwave microplasma treatment of two types of bacteria (*Escherichia coli*, *Bacillus subtilis*) and one fungus (*Aspergillus niger*) samples.

2. Microwave microplasma source (MmPS) and experimental set-up

A number of various designs of the microplasma sources have been developed. Supply through a waveguide [11, 12], consisting of coaxial line [13, 14] or stripline structures [15, 16] are known. Waveguide based structures, in contrast to coaxial line and stripline structures, have much bigger size and allow to operate with higher microwave powers. The sketch and photo of our MmPS is presented in Fig. 1. It is based, as it was previously described in [17-20], on a coaxial line, formed by the inner conductor, made of a brass rod with a tungsten rod top, and outer conductor in the form of a brass cylinder. The inner conductor is fixed inside the outer conductor tightly with a PTFE centering disc.

The MmPS is supplied from the microwave generator at standard frequency of 2.45 GHz through a 50 Ω coaxial line using an N-type connector. The operating gas is introduced through a duct between the inner and outer conductors. The microplasma was generated by the MmPS in the form of a tiny candle-like flame (in Ar, Ar/O_2 at low absorbed powers) or a plasma jet (in Ar/O_2 at high absorbed powers) above the inner conductor top. The length and diameter ranged from 5 - 25 mm and 0.5 - 2 mm, respectively for Ar microplasma and from 2 - 30 mm and 2 - 16 mm, respectively for Ar/O_2, depending on the operating parameters. Optionally, the MMS could be operated with MACOR® ceramic tip. This tip played three functions: it formed a kind of nozzle that increased the

velocity of argon in plasma forming zone, it prevented breakdowns between the inner and outer conductors, specially in case operating in the Ar, and it covered the hotter part of the microplasma column, thus exposing only the lowest temperature microplasma (i.e. its tip). Fig. 2 shows photos of the microwave microplasma for various operating conditions. The operation of MMS is described in detail in [20].

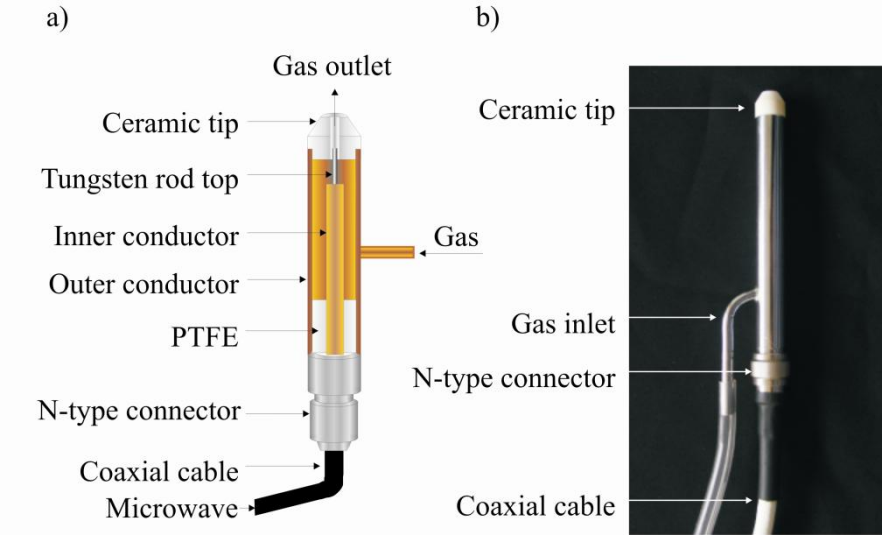


Fig. 1. Sketch (a) and photo (b) of the coaxial-line based MmPS.

3. Results

The experimental investigations concerning microorganisms deactivation by our MmPS took place in the microbiological laboratory of Innovation Enterprise "IMPULS" which carries out the researches defining microbiological purity, an active concentrations of antiseptic and fungicidal preparations. We performed quality as well as quantity tests. The influence of the microorganism type, O_2 concentration, microwave power level, treatment time and microplasma distance from the treated sample on the microorganisms deactivation efficiency were investigated. The following type of microorganisms were treated by the microplasma: bacteria (*Escherichia coli*, *Bacillus subtilis*), fungus (*Aspergillus niger*). The test was performed for Ar microplasma and Ar/O_2 microplasma with up to 2% of O_2. Absorbed microwave power P_A was up to 50 W. The Ar flow rate was up to 10 l/min. The sample treatment time was up to 240 s.

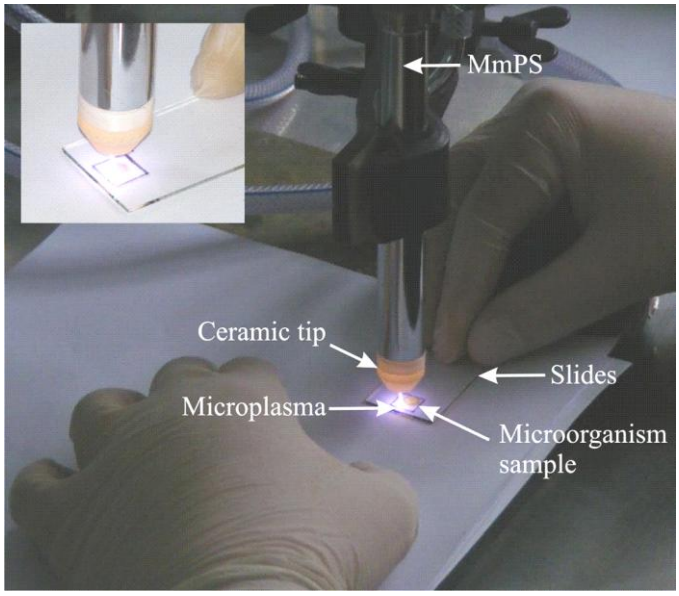


Fig. 2. Microwave microplasma sample treatment

In Fig. 2 a photo of the microwave microplasma processing of the microorganism sample is shown. The MmPS placed perpendicularly to the treated sample can be seen. The microorganism sample in the form of droplet was placed on the rectangular sterile laboratory slides. The sample droplet volume and the initial sample number of colony forming units were choose individually for each kind of test. The distance between the MmPS and the sample during the treatment microplasma was fixed. The slides was manually moved below the microplasma to scan the sample full area. Depending on the treatment time the different sample treatment speed was was applied.

The tests of the influence of the additive O_2 concentration on the biocidal microplasma effect were performed with *Escherichia coli* for Ar, and Ar/O_2 microplasma. The sample treatment time was 45 s, the incident microwave power 72 W, the reflected microwave power 42 W. The Ar flow rate was 10 l/min. Fig. 3a presents results of tests under above described conditions. Fig. 3b relates two sets of tests. First one concerns the case with the initial number of colony forming units was 2.87×10^7 per sample droplet volume of 20 µl. The incident microwave power 68 W, the reflected microwave power 41 W. In the second case the initial number of colony forming units was 4.41×10^7 per sample droplet volume of 50 µl. The incident microwave power was equal 72 W and the reflected microwave power was 42 W. As it can be seen, the result indicated reduction of bacteria population for all treated samples. The reduction seemed to be grater for Ar/O_2(0.5%) than for Ar/O_2(1%), Ar/O_2(2%), and pure Ar microplasma.

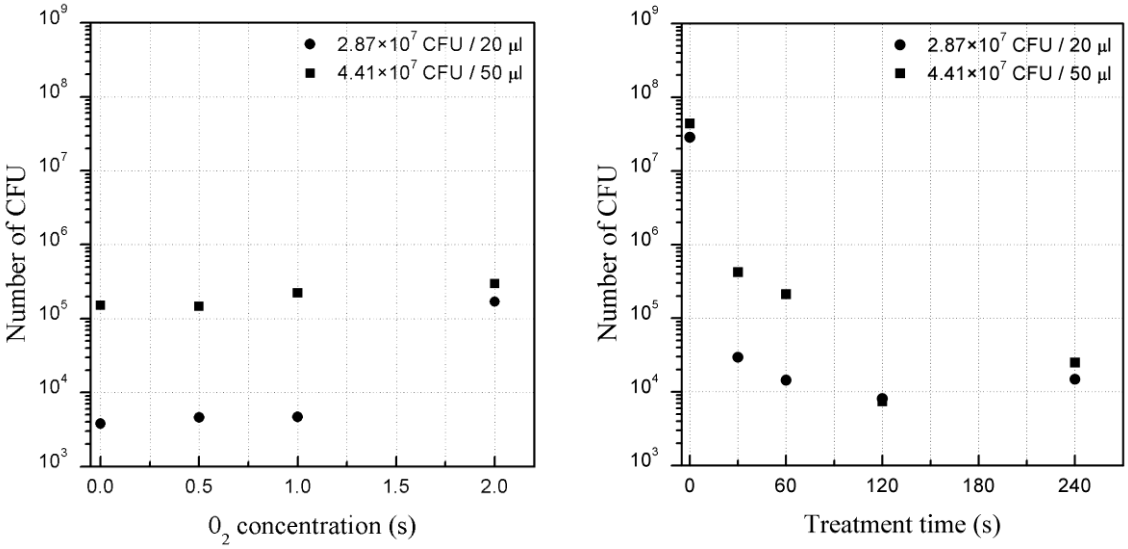
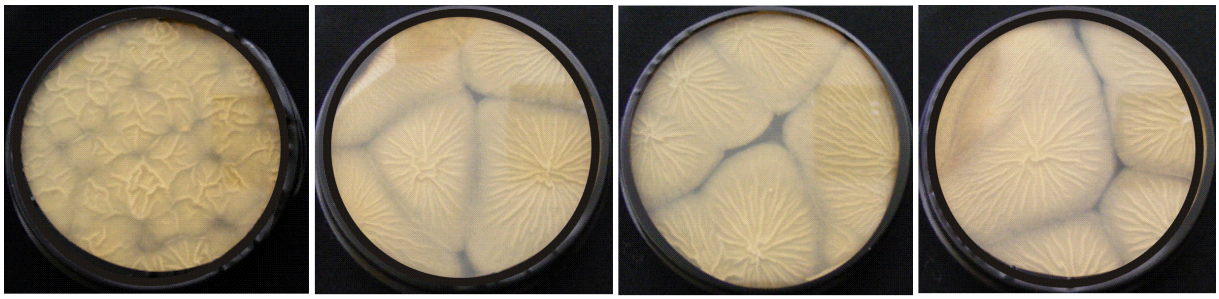


Fig. 3. The influence of the O_2 admixture (a) and treatment time (b) on the *Escherichia coli* deactivation. Ar flow rate of 10 l/min. In (b) the admixture of O_2 0.5 %. (●) The initial number of colony forming units was 2.87×10^7 per sample droplet volume of 20 µl. The incident microwave power 68 W, the reflected microwave power 41 W. (■) The initial number of colony forming units was 4.41×10^7 per sample droplet volume of 50 µl. The incident microwave power 72 W, the reflected microwave power 42 W.

The results of the influence of the treatment time on the *Escherichia coli* deactivation are presented in Fig. 3b. As in the case of Fig. 3a, Fig. 3b relates two sets of tests. First one concerns the case with the initial number of colony forming units was 2.87×10^7 per sample droplet volume of 20 µl. The incident microwave power 68 W, the reflected microwave power 41 W. In the second case the initial number of colony forming units was 4.41×10^7 per sample droplet volume of 50 µl. The incident microwave power was equal 72 W and the reflected microwave power was 42 W. For both tests the Ar flow rate was 10 l/min and the admixture of O_2 was 0.5 %. Generally, the results show that the increasing of the microplasma treatment time resulted in the higher deactivation efficiency. For microplasma treatment time higher then 120 s the deactivation efficiency was reduced by more then three order of magnitude.

The visualization of the influence of the microwave microplasma treatment time on the fungus deactivation can be seen in Fig. 4. Fig. 4a shows the *Aspergillus niger* fungal on the sample not treated by microplasma. In that case almost 150 fungal centers can be seen. The fungus on the sample treated by microplasma over 15 s are shown in Fig. 4b. Fig. 4c shows the fungus on the sample treated by microplasma over 45 s. Fig. 4d shows the results of microplasma treating sample over 60 s. In the case of 15 s and 60 s treating time, the are 6 and 5 fungal centers, respectively. The photos were taken seven days after microplasma sample treatment. The microplasma operating conditions were as follows: Ar flow rate of 10 l/min, the admixture of O_2 0.5 %, the incident microwave power 58 W, the reflected microwave power 33 W.



a) b) c) d)

Fig. 4. The photos of the fungal reflecting the influence of the treatment time on the *Aspergillus niger* deactivation: a) sample not treated by microplasma, b) sample treated time 15 s, c) sample treated time 45 s, d) sample treated time 60 s. Ar flow rate of 10 l/min, the admixture of O_2 0.5 %. The incident microwave power 58 W, the reflected microwave power 33 W.

4. Summary and conclusions

Using the low-temperature Ar and Ar/O_2 microplasma generated by coaxial microwave microplasma source (MmPS) the deactivation of the microorganisms (*Escherichia coli*, *Bacillus subtilis*, *Aspergillus nigeri*) was studied experimentally. The unquestioned merits of such a microplasma are small size (from μm to several mm), portability of the source, easy to use, low investment and operation costs.

The influence of the O_2 concentration, absorbed microwave power, microplasma treatment time and microplasma distance from the treated microorganism sample on the deactivation efficiency were investigated. Our experiments showed the possibility of microorganism colony reduction by even a few order of magnitude of the initial number of colony forming units. The reduction effect seemed to be grater for Ar microplasma with the 0.5 % admixture of O_2 than for Ar/O_2(1%), Ar/O_2(2%) and pure Ar microplasma. The increasing of the treatment time resulted in the higher deactivation efficiency.

The presented in this paper experimental results allows to conclude that our MmPS is a promising device for the biomedical applications thus further test are under preparation.

ACKNOWLEDGEMENT

This research was supported by The Szewalski Institute of Fluid-Flow Machinery, Polish Academy of Sciences under the program IMP PAN O3Z1T1 and by Innovation Enterprise "IMPULS", ul. Jelenia 2, 80-336 Gdańsk.

5. References

[1] J. Ehlbeck, U. Schnabel, M. Polak, J. Winter, Th. von Woedtke, R. Brandenburg, T. von dem Hagen and K. D. Weltmann, "*Low temperature atmospheric pressure plasma sources for microbial decontamination*", J. Phys. D: Appl. Phys., vol. 44, no.1, 013002 (18pp), 2011.

[2] H.W. Lee, G.Y. Park., Y.S. Seo, Y.H. Im, S.B. Shim, H.J. Lee, *"Modelling of atmospheric pressure plasmas for biomedical applications*", J. Phys. D: Appl. Phys., vol. 44, no. 5, 053001 (27pp), 2011.

[3] K. Becker, A. Koutsospyros, S-M. Yin, C. Christodoulatos, N. Abramzon, J. C. Joaquin and G. Brelles-Mariño, "*Environmental and biological applications of microplasmas*", Plasma Phys. Control. Fusion, vol. 47, no. 12B, B513-B523, 2005.

[4] F. Iza, G. J. Kim, S. M. Lee, J. K. Lee, J. L. Walsh, Y. T. Zhang and M. G. Kong, "*Microplasmas: sources, particle kinetics, and biomedical applications*", Plasma Processes and Polymers, vol. 5, no. 4, pp. 322–344, 2008.

[5] M. Moisan, J. Barbeau, S. Moreau, J. Pelletier, M. Tabrizian, L.H. Yahia, "*Low-temperature sterilization using gas plasmas: a review of the experiments and an analysis of the inactivation mechanisms"*, Int. J. Pharm., 226, 1-2, pp. 1-21, 2001.

[6] M. Moisan, J. Barbeau, M.-Ch. Crevier, J. Pelletier, N. Philip, B. Saoudi, *"Plasma sterilization. Methods and mechanisms*", 74, 3, pp. 349-358, 2002.

[7] A. von Keudell, P. Awakowicz, J. Benedikt, V. Raballand, A.Yanguas-Gil, J. Opretzka, C. Flotgen, R. Reuter, L. Byelykh, H. Halfmann, K. Stapelmann, B. Denis, J. Wunderlich, P. Muranyi, F. Rossi, O. Kylian, N. Hasiwa, A. Ruiz, H. Rauscher, L. Sirghi, E. Comoy, C. Dehen, L. Challier, J.P. Deslys*, "Inactivation of bacteria and biomolecules low-pressure plasma discharges",* Plasma Process Polym., 7, 3-4, pp. 327–352, 2011.

[8] K.-Y. Lee, B.J. Park, D.H. Lee, I.-S. Lee, S.O. Hyun, K.-H Chung, J.-C. Park, *"Sterilization of Escherichia coli and MRSA using microwave-induced argon plasma at atmospheric pressure",* Surf. & Coat. Technol., 193, 1-3, pp. 35-38, 2005.

[9] M. Laroussi, F. Leipold, *"Evaluation of the roles of reactive species, heat, and UV radiation in the inactivation of bacterial cells by air plasmas at atmospheric pressure",* Int. J. Mass Spectrom., 233, 1-3, pp. 81-86, 2004.

[10] L. Yang, J. Chen, J. Gao, Y. Guo, *(2009) "Plasma sterilization using the RF glow discharge",* Appl. Surf. Sci., 255, 22, pp. 8960–8964, 2009.

[11] J. Gregório, O. Leroy, P. Leprince, L. L. Alves and C. Boisse-Laporte, „*Design of a microwave microplasma source at atmospheric pressure"*, IEEE Transactions on Plasma Science, vol. 37, no. 6, pp. 797-808, 2009.

[12] S. Kanazawa, R. Daidai, S. Akamine and T. Ohkubo, "*Generation of microplasma jet at atmospheric pressure using a modified waveguide-based plasma torch"*, Surface and Coatings Technology, vol. 202, pp. 5275–5279, 2008.

[13] J. Benedikt; S. Hofmann; N. Knake; H. Böttner, R. Reuter; A. von Keudell and V. Schulz-von der Gathen, **„***Phase resolved optical emission spectroscopy of coaxial microplasma jet operated with He and Ar***",** The European Physical Journal D, vol. 60, no. 3, pp.539-546, 2010.

[14] J. Choi, F. Iza, H. J. Do, J. K. Lee, M. H. Cho, "*Microwave-excited atmospheric-pressure microplasmas based on a coaxial transmission line resonator"*, Plasma Sources Sci. Technol., vol. 18, 025029, 2009.

[15] J. Kim and K. Terashima, "*2.45 GHz microwave-excited atmospheric pressure air microplasmas based on microstrip technology*", Applied Physics Letters, vol. 86, 191504, 2005.

[16] A. M. Bilgic, U. Engel, A. M. Voges, M. Kuckelheim and J. A. C. Broekaer, "*A new low-power microwave plasma source using microstrip technology for atomic emission spectrometry"*, Plasma Sources Sci. Technol., vol. 9, no. 1, pp. 1-4, 2000.

[17] M. Goch, M. Jasiński, J. Mizeraczyk, Z. Zakrzewski, *„Microwave microdischarge generator based on coaxial line",* Electr Rev 84:80-82. ISSN 0033-2097, 2008.

[18] M. Jasiński, Ł. Kroplewski, Z. Zakrzewski, J. Mizeraczyk, *„Atmospheric Pressure Microwave Microplasma Sources"*, Chemicke Listy 102:S1322-S1326, 2008.

[19] B. Hrycak, M. Jasiński, J. Mizeraczyk, "*Spectroscopic investigations of microwave microplasmas in various gases at atmospheric pressure"*, Eur. Phys. J. *D*, vol. 60, no. 3, pp. 609-619, 2010.

[20] J. Mizeraczyk, B. Hrycak, M. Jasiński, M. Dors, *"Low-temperature microwave microplasma for bio-decontamination"*, Electr. Rev. [in print].

Decomposition of VOCs by gliding discharge plasma

Michał Młotek, Ewelina Pawelska, Bogdan Ulejczyk,
Krzysztof Krawczyk, Krzysztof Schmidt - Szałowski

Warsaw University of Technology, facoulty of Chemistry,
Noakowskiego 3, 00-664 Warszawa, Polska

e-mail: michalm74pw@gmail.com

Decomposition of volatile pollutants emission is a very important problem, especially for the industrial profile countries. The aim of the investigations was to develop a plasma-catalytic system for removal of volatile chlorinated hydrocarbons from waste industrial gases and exhaust gases from incineration plants. Plasma - catalyst with stationary bed systems were investigated. Measurements were performed for characterizing the catalysts, and to determine the optimal process conditions for removal of the model pollutant – CCl_4. The highest obtained overall CCl_4 conversion was 0.79 in homogeneous system, and 0.97 in plasma catalytic system

1. Introduction

Nowadays, the task of hazardous VOC gas abatement is performed in different ways. High temperature or catalytic processes is being the most commonly used. In recent years an attempts have been made for decomposition of volatile organic compounds by the use of non-equilibrium plasma [1]. In non-equilibrium plasmas most of the energy supplied is not consumed for the heating of the gas mixture, but for initiating of chemical reactions. The non-equilibrium plasma of gliding discharge (GD) has been used for the initiation of chemical reactions at atmospheric pressure. Usually the bulk gas temperature in this type of discharge does not exceed 1000 K.

A number of experiments was performed with different types of GD reactors applied for processing of miscellaneous gases and other materials. These processes were found to be efficient for destroying chemically stable pollutants occurring in the industrial waste gases, e.g. volatile organic substances, nitrogen oxides, hydrogen sulphide [1-3]. The GD techniques were also used for other processes, assistant to the environment protection, e.g. decomposition of chlorofluorocarbons and a number of other chlorine organic compounds [4-7]. In non-equilibrium plasmas, through the action of energized electrons, a number of chemical reactions may be initiated. The formation of active species (excited molecules and radicals) is a starting stage which usually opens a chain of consecutive reactions. It seems, however, possible to increase the yield (and/or selectivity) of plasma processes using a catalyst. Therefore, a number of solid materials, expected catalysts, have been tested in coupled plasma-catalytic processes [8].

2. Experimental

The homogeneous system (GD) and the reactor with stationary bed (GDS) (Fig 1) of vanadium oxide catalysts were used for decomposition of CCl_4. Reactor was provided with a conic reaction chamber with ceramic lining and two vertical diverging stainless steel electrodes. The reactor was powered by a 50 Hz system with the supplied active power measured for the low voltage (primary) circuit by means of the energy meters Pafal MOD A5. The discharge power was 150 – 460 W. The temperature was measured by a thermocouple at the vessel axis over the upper ends of electrodes. The gas temperatures was 250 - 500 °C. The gas mixture composition was

oxygen and air (1:2) and the gas flow rate was 200 or 300 Nl/h controlled by mass flow controllers. The initial concentration of CCl_4 in the gas was 0.1 or 0.5 vol.%. The CCl_4 concentration was controlled by CEM system by Bronkhorst (Fig. 2).

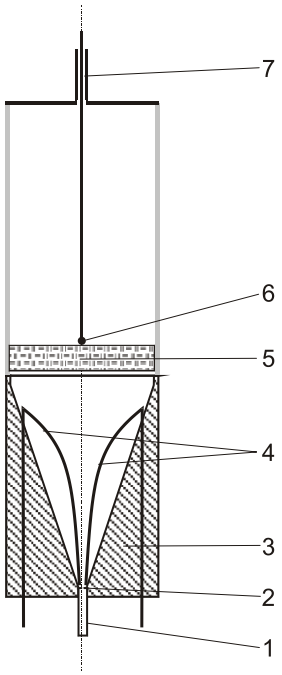


Fig. 1. Gliding discharge reactor for CCl_4 decomposition with stationary bed. 1 – gas inlet, 2 – nozzle, 3 – ceramic body, 4 – electrodes, 5 – catalyst bed, 6 – thermocouple, 7 – gas outlet.

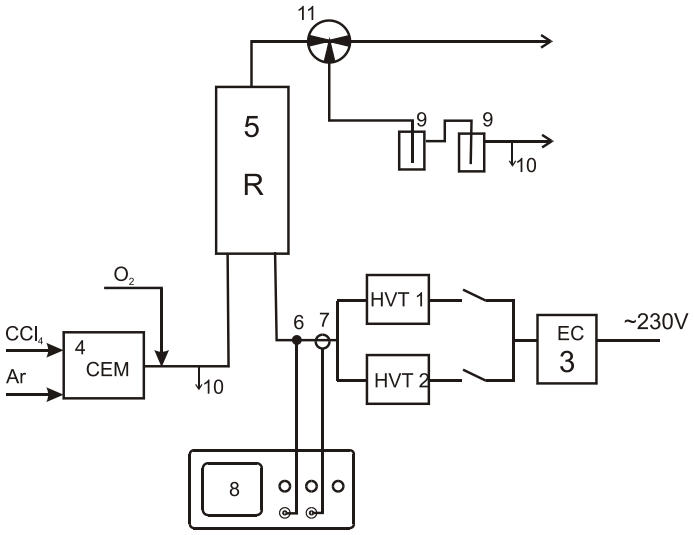


Fig. 2. Setup for CCl_4 decomposition. 1, 2 - high voltage transformers, 3 – energy meter, 4 – CEM system for CCl_4 supply, 5 – gliding discharge reactor, 6 – voltage probe, 7 – current probe, 8 – oscilloscope, 9 - scrubber with KI, 10 – point for gas sample for chromatography, 11 – valve.

The vanadium oxide catalysts containing about 7 wt.% of V_2O_5 was supported on ceramic carrier. The catalysts, were obtained by impregnation of ceramic carrier with aqueous solutions of $VOSO_4$ and K_2SO_4, dried and calcined in ambient air at 600^{o}C for 4 h. Two kinds of catalysts were prepared. First V_2O_5 + K_2O supported on diatomite, second V_2O_5 + K_2O supported on honeycomb structure cordierite. Catalysts were packed into the reactor without additional pretreatment. The BET absorption isotherm was used for carrier and catalysts surface determination. Measurements were performed using Micromeritics 2020 apparatus by absorption of N_2 at liquid nitrogen temperature, with the p/p_o ratio in the range 0.05-0.3 (Table 1).

Tab. 1. Surface of catalysts for CCl_4 decomposition.

Packing	S_{BET} m^2/g
cordierite	0.28
V_2O_5+K_2O/cordierite	0.15
V_2O_5+K_2O/diatomite	7.52

The catalyst particles or honeycomb was placed to the reactor in a single batch of 10 ml. Products of the plasma decomposition of CCl_4 were analyzed using gas chromatography (Agilent 6890) with an FID detector and packed column with 5% Fluorocol on 60/80 Carbopack B. Cl_2 and $COCl_2$ were determinated by the titrate method. Outlet gases were periodically passed by two bubblers with KI solution. In this solution Cl_2 react with KI to I_2 and KCl. $COCl_2$ react with H_2O to HCl and CO_2.

The solution was titrated first with a 0.05 M $Na_2S_2O_3$ solution to determine the amount of I_2 and second with 0.1 M NaOH to determine the HCl. The overall CCl_4 conversion (X) was calculated according to formula:

$$X = \frac{W_0[CCl_4] - W[CCl_4]}{W_0[CCl_4]}$$

$W_0[CCl_4]$ - CCl_4 flow rate at the inlet gas, mol/h
$W[CCl_4]$ - CCl_4 flow rate at the outlet gas, mol/h

3. Results and Discussion

The main product of CCl_4 decomposition was chlorine. However chlorine present in the outlet gas caused corrosion of the electrodes and elements of the reactor made of brass. That might be the reason of loses in chlorine balance. In homogeneous system when 0.1 initial CCl_4 concentration was used traces of fosgen were observed. In outlet gas any other chlorohydrocarbons than nonreacted CCl_4 had not been detected (Table 2.).

Tab. 2. Effect of catalysts on CCl_4 conversion. Gas flow rate 300 Nl/h.

CCl_4 concentration Gas flow rate, Nl/h		0.1% 300							
Catalyst		homogeneous		$VOSO_4+K_2SO_4$/ diatomite		$VOSO_4+K_2SO_4$/ cordierite		cordierite	
Power, W		163	253	214	401	267	457	227	421
CCl_4 conv.	overall	0.44	0.51	0.67	0.89	0.72	0.82	0.69	0.95
	into Cl_2	0.23	0.23	0.54	0.35	0.40	0.45	0.46	0.63
	loss in Cl_2 balance	0.16	0.19	0.13	0.54	0.32	0.37	0.23	0.32
	into $COCl_2$	0.05	0.09	0	0	0	0	0	0
CCl_4 concentration Gas flow rate, Nl/h		0.5% 300							
Catalyst		homogeneous		$VOSO_4+K_2SO_4$/ diatomite		$VOSO_4+K_2SO_4$/ cordierite		cordierite	
Power, W		199	330	218	369	267	446	268	424
CCl_4 conv	overall	0.58	0.71	0.63	0.83	0.85	0.93	0.63	0.94
	into Cl_2	0.36	0.47	0.47	0.51	0.42	0.64	0.63	0.65
	loss in Cl_2 balance	0.22	0.24	0.16	0.32	0.43	0.29	0	0.29
	into $COCl_2$	0	0	0	0	0	0	0	0

In a homogeneous and plasma catalytic system the rise of the discharge power increases in the overall CCl_4 conversion. Higher conversions were obtained at 200 Nl/h than at 300 Nl/h when both CCl_4 concentrations were used. The rise of the CCl_4 concentration increased overall CCl_4 conversion at a flow rate of 300 Nl/h. When 200 Nl/h gas flow rate was used this effect was negligible. Higher conversion of CCl_4 was obtained for the concentration of 0.5 %. The highest overall CCl_4 conversion was obtained for 200 Nl/h and 0.5 % concentration. In plasma catalytic system initial gas concentration did not affect on overall CCl_4 conversion. The highest obtained overall CCl_4 conversion was 0.79 in homogeneous system, and 0.97 in plasma catalytic system (Fig. 3 A, B).

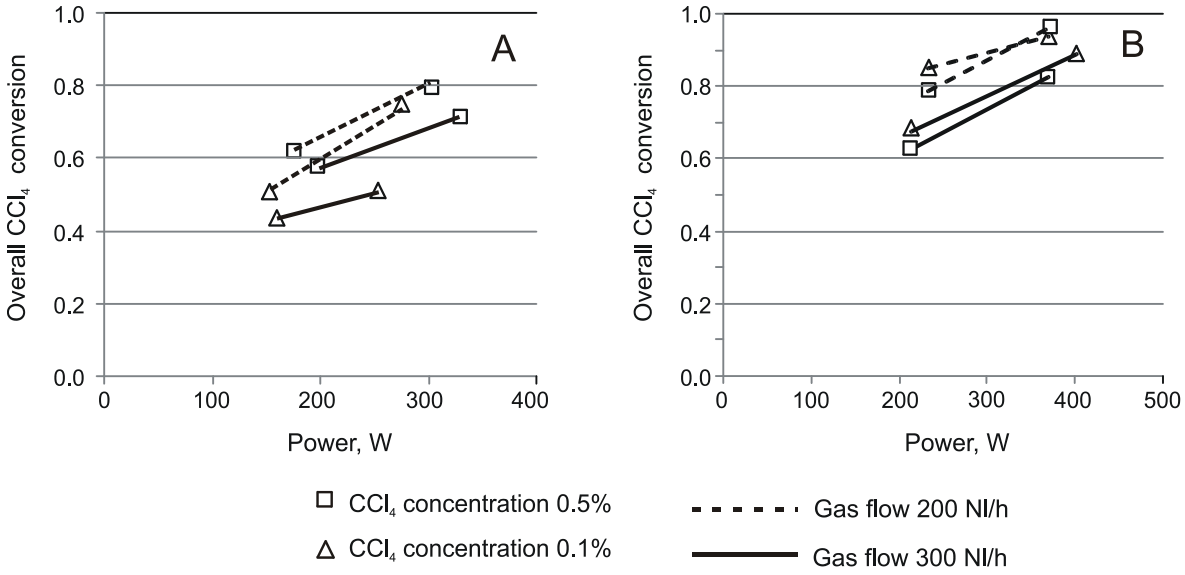


Fig. 3. Effect of gas flow and CCl_4 concentration on overall CCl_4 conversion. A – homogeneous system, B - plasma catalytic system with V_2O_5+K_2O/diatomite.

Increase of discharge power in homogeneous system had increased the conversion of CCl_4 to Cl_2 for majority of experiments. When gas flow rate was 300 Nl/h and CCl_4 concentration was 0.1% the conversion of CCl_4 to Cl_2 was stable (0.25) and did not rise with discharge power (Fig. 4A). When plasma - catalytic system was used conversion of CCl_4 to Cl_2 decreased with the rise of discharge power. The effect was more distinct when 200 Nl/h gas flow rate and 0.5 % CCl_4 concentration was used (Fig. 4B). However, the disadvantage of the gas flow 200 Nl/h was instability of the gliding discharge, especially for the 0.5 initial CCl_4 concentration.

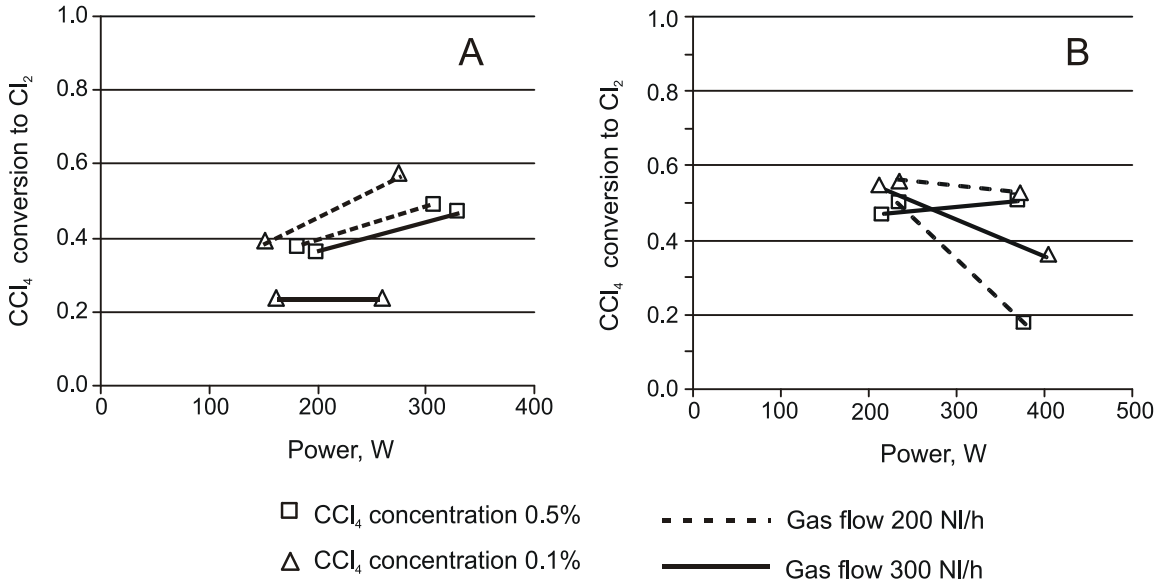


Fig. 4. Effect of gas flow rate and CCl_4 concentration on conversion of CCl_4 into Cl_2. A – homogeneous system, B - plasma catalytic system with V_2O_5 /diatomite.

Both catalysts containing V_2O_5 were active in plasma catalytic CCl_4 decomposition. Overall CCl_4 conversion was higher when catalyst were used for both initial CCl_4 concentration (0.1 and 0.5 %). For initial CCl_4 concentration of 0.1% overall CCl_4 conversion was similar to that plasma catalytic system and did not exceed 0.80. CCl_4 conversion to Cl_2 was higher in plasma catalytic system than in homogeneous one. Applying cordierite in discharge zone of GD plasma CCl_4 conversion to Cl_2

reached more than 0.50. When 0.5% initial CCl_4 concentration was used overall CCl_4 conversion reached 0.85 with $V_2O_5 + K_2O$/ cordierite (Fig. 5).

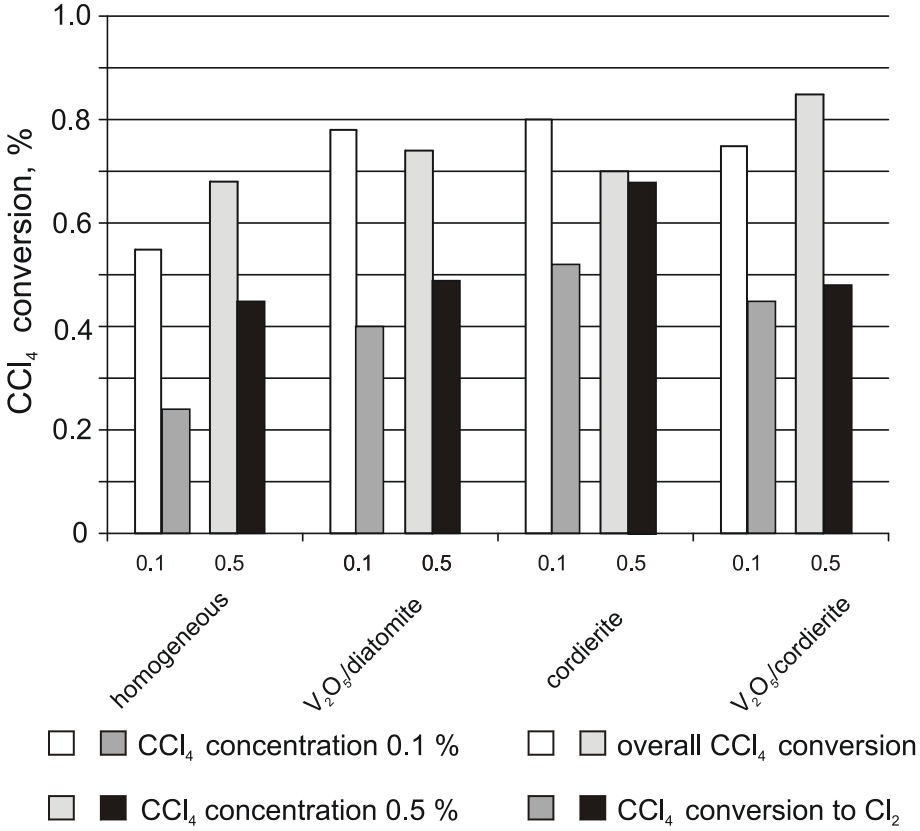


Fig. 5. Effect of catalysts on CCl_4 decomposition. Gas flow 300 Nl/h, discharge power 300W.

4. Conclusions

CCl_4 can be effectively decomposed in gliding discharge reactor. The highest overall CCl_4 conversion (0.97) was achieved when 200Nl/h gas flow was used in plasma catalytic system. The chlorinated hydrocarbons compounds were not produced by gliding discharge from CCl_4 in gas mixtures with argon and oxygen. In plasma catalytic system fosgen was not observed.

5. Acknowledgment

This work was financially supported by the Polish Ministry of Science and Higher Education from Research Program UMO – 2011/01/B/ST8/0757.

6. References:

[1] Krawczyk K., Ulejczyk B., 2003, *Plasma Chem. Plasma Proc*., ***23, 2****, 265*
[2] Caramel A., Czernichowski A., Gorius A., 1998, *US Patent 5 711 85.*
[3] Krawczyk K., Młotek M., 2001, *Appl. Catal. B: Environmental*, ***30****, 233*.
[4] Vanderbroucke A. M., Morent R., De Geyter N., Leys Ch., 2011, *J. Hazard. Mater.* ***195****, 30.*
[5] Krawczyk K., Ulejczyk B., 2004, *Plasma Chem. Plasma Proc*, ***24, 2****, 155*.
[6] Czernichowski A., Czech T., 1991, *Proc. 3rd ISPC, Strasbourg,* 147.
[7] Opalińska T., Opalska A., Schmidt-Szałowski K., 2005, *Plasma Processes and Polymers (red. R. d'Agostino i in.), 415.*
[8] Schmidt – Szałowski K., Krzysztof Krawczyk K., Sentek J., Ulejczyk B., Górska A., Młotek M., 2011, *Chemical Engineering Research and Design* ***89(12)****, 2643.*

A METHOD OF GAS INTRODUCTION INTO THE PLASMA REACTOR EMPLOYING THE GLIDING DISCHARGE PRINCIPLES

Teresa Opalińska[1], Małgorzata Majdak[1], Janusz Piechna[2], Witold Selerowicz[2],

Bartłomiej Wnęk[1]

[1]*Tele & Radio Research Institute*
[2] *Warsaw University of Technology*
E-mail: teresa.opalinska@itr.org.pl

The modular device for the waste utilization, using the pyrolitic-plasma method consists of, among others, the plasma reactor operating on the gliding discharge principles. The reactor is applied to oxidize hydrocarbons that are produced in the process of the waste pyrolysis. Thus, the plasma reactor operation influences significantly the qualitative and quantitative composition of the output gases. Finding the most advantageous construction of the plasma reactor and the process parameters ensures full and complete oxidation of hydrocarbons. The aim of the study was to determine the most useful method of gas introduction into the plasma reactor with the use of the numerical calculations and the experimental verification of the calculations results.

1. Introduction

A nonequlibrium plasma is generated at the atmospheric pressure in the gliding discharge supplied from a DC or AC source. The plasma is characterized by the electron energy about 1eV and a neutral gas temperature of 1500-2000 K, depending on the power applied [1,2]. The properties of the generated plasma and a relatively easy way of the discharge generation cause that a practical application for this discharge is investigated [3,4]. The gliding discharge is applied, among the others, in a plasma reactor, which may be a part of the waste utilisation device. The utilization process in this device consists of: 1- the pyrolysis of waste without the air access; 2 -the oxidation of the pyrolysis products in gliding discharge and 3- the purification of the process gases.

The oxidation process has a cardinal influence on the quality of gases leaving the device. For this the plasma reactor should enable the efficient oxidation of hydrocarbons, which are the main products of the waste pyrolysis. An important structural element of the reactor is the system of feeding the reactants to the plasma rector. The system consists of two individually designed coaxial nozzles. One of them is used for transporting the pyrolysis gases by means of the argon agent into the plasma reactor. The second nozzle is used to add up oxygen. It is very important that both streams are exactly mixed before they enter into the zone of electric discharge.

The resultant stream of mixed gases should have a shape enabling the generation of discharge in the whole stream volume. The proper design of nozzles having the correct shape required several theoretical studies and their practical verification. The aim of this project was to determine the methods of gases introduction into the plasma reactor for the designed nozzle system. Two methods have been verified. The first consisted in introducing hydrocarbons and argon through the central nozzle and oxygen through the outer one. The second method consisted in introducing oxygen through the central nozzle and mixture of argon and hydrocarbons through the outer one. Methane was used as a test gas for the research.

2. Theoretical calculations

Assumptions

The plasma reactor is a part of apparatus for waste utilisation. Its principle of operation can be described as follows. The waste is pyrolysed in the atmosphere of argon. The hydrocarbons generated in the process are introduced into the plasma reactor in the stream of argon. Oxygen is introduced into the reactor separately. The process of hydrocarbons oxidation takes place in the plasma reactor.

The hypothetical reactor consisted of a reaction chamber in a form of a cylinder of 200 mm diameter and a length of 500 mm, which was equipped with a set of two coaxial nozzles at one end and was open at the other. The shape of nozzles facilitated the process of mixing of both gas streams (Fig. 1.)

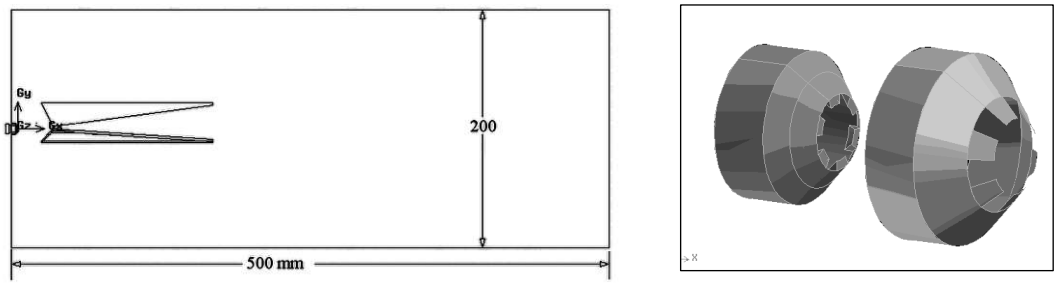


Fig. 1 The plasma reactor and the system of nozzles applying in calculations.

It was assumed that the 1.5 kg of waste that contained 90% of elemental carbon was fully decomposed to methane during 1 hour the process of pyrolysis. Methane was mixed with argon and fed into the plasma reactor through one of the two nozzles. Oxygen was introduced through the second nozzle. Calculations were performed for the following mass flow rates: methane - $4.9 \cdot 10^{-4}$ kg/s, argon - $9.8 \cdot 10^{-4}$ kg/s; oxygen - $1.9 \cdot 10^{-3}$ kg/s. The flow rate of oxygen was calculated including the stoichiometry of the reaction of methane oxidation into carbon dioxide. The mixture temperature of methane with argon was 1100 K and the temperature of oxygen was 273 K. The gases were mixed in the plasma reactor. The stream of the mixed gases should reach the stoichiometric composition before the zone of discharge. The shape of the mixed gases stream should facilitate the generation of discharge in the whole volume of the stream.

Calculations

Calculations were performed for two cases. In the first case the composition of gases in the stream was calculated ignoring the reaction of methane oxidation. Only the process of gas streams mixing was taken into account. In the second case, apart from the streams mixing, the reaction of methane oxidation was considered. For each case two methods of gas introducing into the reactor were taken into account. The first method consisted in introducing into the reactor the mixture of argon and methane through the central nozzle and oxygen through the outer one. In the second method oxygen was introduced through the central nozzle and the mixture of argon and methane through the outer one.

A computer simulation of gas streams supplying the plasma reactor was performed using a computational fluid dynamics commercial program (CFC) FLUENT.

In the domain representing the chamber the following boundary conditions were used: 1- zero gas velocity at the wall, 2 - condition representing the outflow to an area of constant pressure, 3-axis condition in axially-symmetric system. Navier-Stokes equations for steady flow of compressible, viscous, multi-component fluid have been solved using a coupled solver (density -based formulation). We used two models of turbulence: the model of Spalart-Allmaras and k-epsilon model. The robust S-A model was used at the initial steps of investigation and was later replaced by the k-epsilon model required in some simulations of methane oxidation process. The Arrhenius' equation was used for calculation of methane oxidation reaction. The heat transferred by radiation was calculated using the Rosseland's model of radiation.

Results of calculations

The runs of streamlines in the reactor chamber (Fig. 2) showed that the gas flow calculated without the oxidation process was stable and regular. For the methane oxidation in the plasma reactor the distribution of the weight ratio of methane to oxygen along the reactor axis plays an important role. The ratio should be 0.26, because then the composition of gas stream corresponds to the stoichiometric composition of methane and oxygen in the reaction of complete methane oxidation. The distribution of mass ratio of methane to oxygen along the axis of reactor was calculated at a distance of 2 and 4 mm from the axis. The distance of 2 mm was selected because it is the smallest distance between the reactor electrodes. The distance of 4 mm was chosen for calculations because the distance between electrodes increases with the length of electrodes. The calculations showed that the stoichiometric composition of methane and oxygen in the stream of gases was achieved when the mixture of argon

and methane was introduced into the reactor through the central nozzle and oxygen through the outer one, irrespectively of the distance from the reactor axis (Fig. 3). For both distances the stoichiometric composition of the stream was achieved at a distance of 60 mm from the face of the nozzles.
In the further calculations the methane oxidation process was taken into account. The distribution of shear stress was more uniform when the methane entered the reactor through the central nozzle (Fig. 4). In such a case the values of shear stress were larger than those for the gases introduced into the reactor using the second method. It means that the mixing of gases was more intensive when the first method was used.

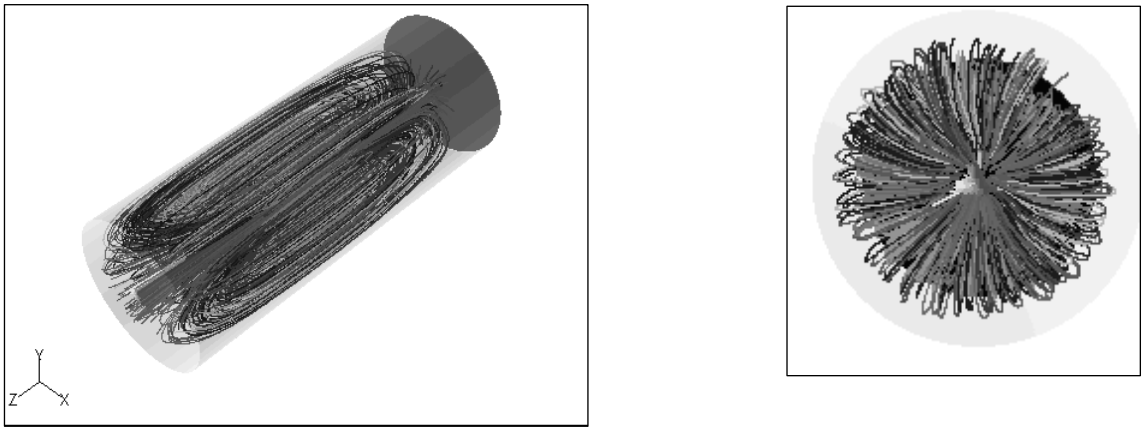


Fig. 2 Runs of stream lines in the rector. Methane oxidation was not considered.

a) b)

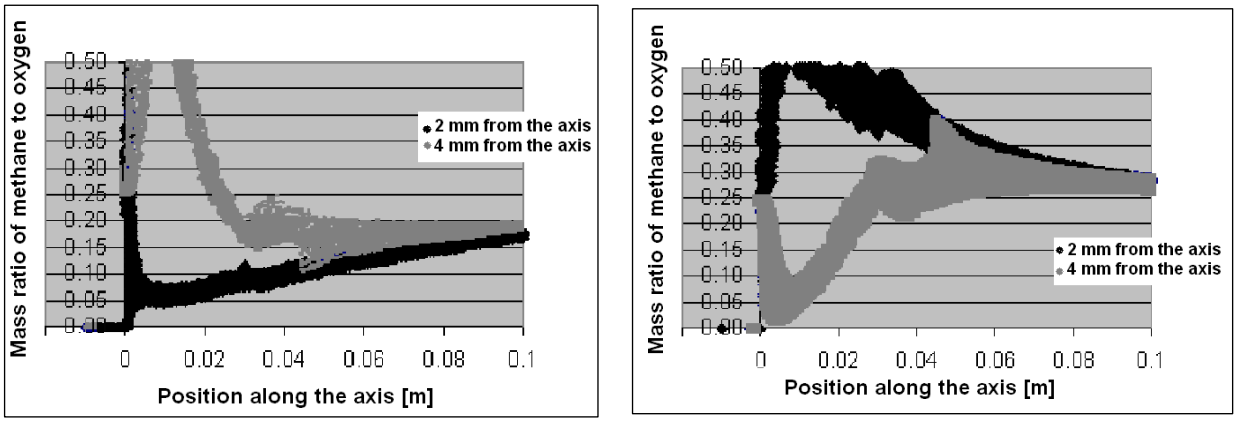


Fig.3 The variation of mass ratio of methane to oxygen along the axis of the reactor calculated numerically in the distance from the axis of reactor of 2 mm and 4 mm. The methane was introduced into the reactor applying: a- the second method, b – the first method (methane oxidation was not considered).

The results of oxidation can be best assessed by the concentration of methane at the chamber outlet that has not reacted in the process. The largest methane mass fraction was 0.005 when methane was introduced into the reactor by the first method but when the second method was used the mass fraction was 0.008 (Fig. 5).
The results of calculation showed that the first method of feeding methane into the reactor is better than the second one, regardless of whether the methane oxidation is taken into account or not.

3. Experimental part

Experimntal set-up

The verification the correctness of the conclusions drawn from the calculations required designing and building a plasma reactor of dimensions corresponding to the one used for the calculation. The reactor was equipped with a set of two coaxial nozzles, which was a slightly modified in comparison with that

shown in Fig. 1. The central nozzle was simultaneously a mixing nozzle. It had six slots breaking the gas stream into six smaller jets that facilitated the process of mixing. The outer nozzle was plain. The reactor had three knife-shaped electrodes of the size and shape selected on the basis of numerical calculations and was supplied with a high voltage 50 Hz AC source. The reactor supply power was calculated on the basis of electric energy measured on the transformer primary winding supplying the reactor.

The reactor was surrounded with the systems of argon, methane and oxygen feeding. The gas input flow was measured with the BRONKHORST mass flow meters, and the post-reaction gas flow was measured with a gas meter. A heat cooler was placed behind the reactor to cool down the post reaction gases. The samples of gases were collected from behind the cooler.

Process parameters:

- The total conversion of methane (X):

$$X = (V_{0CH_4} - V_{kCH_4}) / V_{0CH_4} \quad (1)$$

where: V_{0CH_4} - methane flow at the reactor inlet [Nm^3/h]; V_{kCH_4} - methane flow at the outlet of the heat exchanger [Nm^3/h].

- The conversion of methane into carbon dioxide (XCO_2):

$$XCO_2 = V_{kCO_2} / V_{0CH_4} \quad (2)$$

where: V_{kCO_2} - flow of carbon dioxide at the outlet of the heat exchanger [Nm^3/h]

- The conversion of methane into carbon oxide (XCO):

$$XCO = V_{kCO} / V_{0CH_4} \quad (3)$$

- The specific energy (E_w):

$$E_w = P \cdot 60 \cdot \frac{22.4}{V_{wej}} \quad \text{[kJ/mol]} \quad (4)$$

where: P- power [kW], V_{wej} –the total inlet flow rate (the sum of flow rates of argon, methane and oxygen at the the reactor inlet [Nm^3/h]); 22.4 [Ndm^3/mol] the volume of one mol of ideal gas in normal conditions.

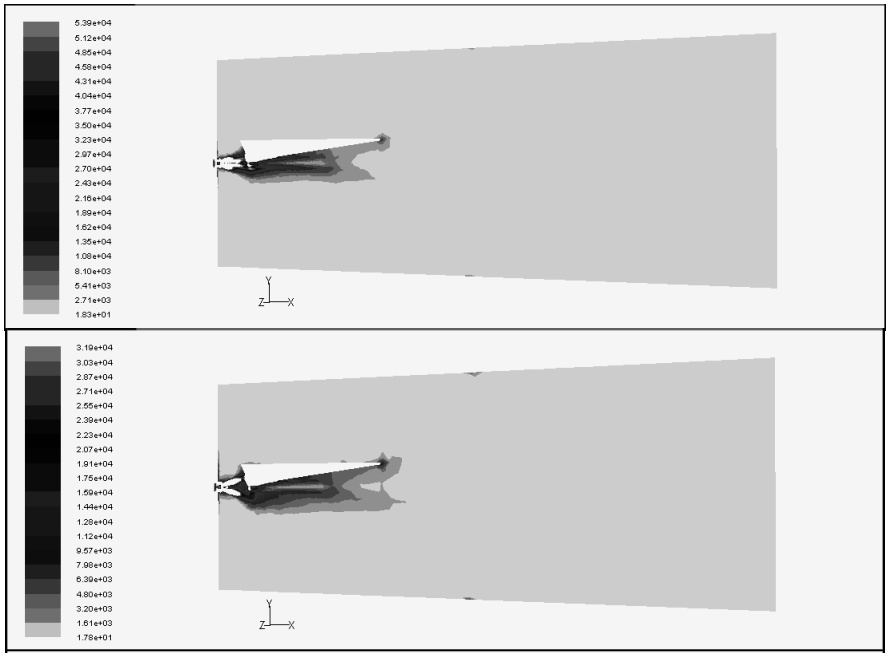


Fig.4 The distribution of shear stresses in the stream of gases in the plane of symmetry. The mixture of methane and argon was introduced into the reactor using: a - the first method, b – the second method (methane oxidation was considered).

Results

Experiments were made for three total inlet flow rates of gases 3.45; 5.38 and 7.50 Nm^3/h for each of the two methods of the gas introduction into the reactor. The supplied power changed in the range of

1.7÷2.4 kW. Methane concentration in the total inlet flow was 3.15 ± 0.09 vol%. The ratio of oxygen to methane molar flow rates was 3.46±0.06. Results of experiments are presented in Fig. 6.
Results of experiments confirmed the conclusion drawn on the basis of calculations. The first method of gas introduction into the reactor was better than the second one. When gases were introduced by the first method X and XCO_2 were higher and XCO was lower than the respective parameters for the gases introduced by the second method.

a) b)

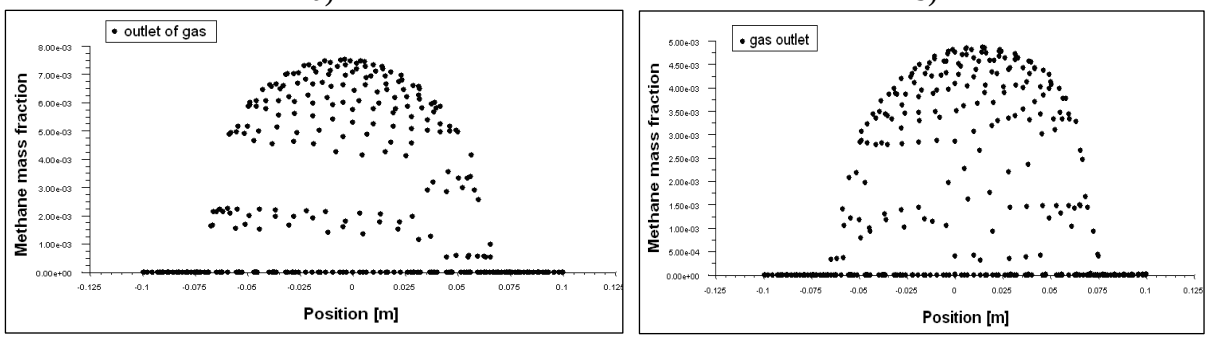


Fig.5 The distribution of methane mass fraction at the outlet of reactor calculated numerically including the methane oxidation: a) – methane was introduced through the outer nozzle; b) – methane was introduced through the central mixing nozzle.

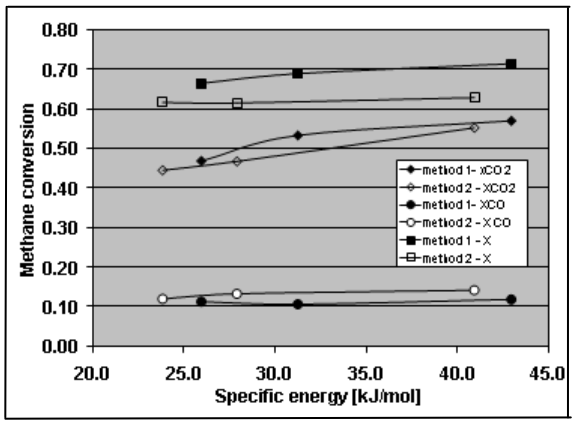


Fig 6. Methane conversion vs. specific energy of the total flow of all gases introduced into the reactor for two methods of the mixture of methane and argon introduction into the reactor: 1- through the mixing nozzle; 2- through the outer nozzle. The experiments conditions were as follows: 1- an initial concentration of methane in the mixture of input gases was 3.15 ± 0.09 vol.% and 2- the total flow of input gases was 3.45 ÷ 7.50 Nm^3/h.

4. Summary

The application of plasma reactor to the oxidation of hydrocarbons in the device for the waste disposal required the theoretical work-out and the experimental verification of the methods of gas feeding by means of two nozzles. The calculations made with the CFC Fluent program led to the conclusion that the most effective oxidation of hydrocarbons in the plasma reactor takes place when the stream of argon and hydrocarbons is introduced into the reactor through the central nozzle and oxygen through the outer one. Methane was used as a test hydrocarbon. The results of experiments confirmed the correctness of conclusion drawn from the calculations.

Acknowledgments
Scientific work financed by The National Centre for Research Development and carried out within the frame of project N R14 0023 06/2009

5. References

[1] Kalra Ch S, Gustol A F and Fridman A A 2005 *IEEE Transactions on Plasma Science* **33** 32
[2] Fridman A, Chapelle J, Czernichowski A, Lesueur L, Petrusev A, Potapkin B and Stevefelt J 1993 *11th ISPC Loughborough England Symposium Proceedings* p. 275
[3] Krawczyk K and Ulejczyk B 2003 *Plasma Chemistry and Plasma Processing* **23** 265
[4] www.glidarc-tech.com

GENERATION OF HIGH PRESSURE HOMOGENEOUS DIELECTRIC BARRIER DISCHARGE IN AIR

Naoki Osawa[1], Ami Takashi[2], Yoshio Yoshioka[3], Ryoichi Hanaoka[1]

[1]*Center for Electric, Optic and Energy Applications, Dept. of Electrical and Electronic Engineering, Kanazawa Institute of Technology, Japan*
[2]*Dept. of Electrical and Electronic Engineering, Kanazawa Institute of Technology, Japan*
[3]*Office of Industry-University Collaboration, Kanazawa Institute of Technology, Japan*
E-mail: n.osawa@neptune.kanazawa-it.ac.jp

We succeed in generating an Atmospheric Pressure Townsend Discharge (APTD) in air by using a simple DBD device consists of alumna barriers and plane electrodes. So far, we applied the APTD to an ozonizer and found that the ozone generation efficiency was higher by the APTD mode than by the conventional DBD mode in larger specific input energy region. It is well known that an operation under an optimized high gas pressure is advantageous for efficient ozone generation from air. In this paper, we investigated whether the Townsend Discharge (TD) in dry air in the pressure range of 0.1 and 0.17 MPa can be generated or not. From the observation results of current waveforms and discharge photographs, we found that (1) the current flows continuously and has only one peak in a half cycle in all gas pressure tested and (2) filamentary discharges are not recognized between barriers in all gas pressure tested. These features completely agree with the features of the APTD we reported. Therefore, we concluded that our TD can be generated even in dry air in the pressure range of 0.1 and 0.17 MPa.

1. Introduction

The Dielectric Barrier Discharge (DBD) is composed of many Filamentary Discharges (FDs), and it can be applied to ozone generation [1], gaseous pollution control [2], surface treatment [3] and so on. Regarding ozone generation and gaseous pollution control, various methods have been studied to improve the energy efficiency. In our laboratory, we investigated efficient cleaning methods of diesel exhaust gas by DBD [2]. One of the investigations was a numerical simulation of chemical reactions. The conclusion was that the efficiency was governed by the diffusion process of radicals, which were generated in the very thin micro-discharge column [4]. Therefore, a homogeneous DBD was expected to improve the efficiency of pollution control and also that of ozone generation. Up to now, we succeed in generating an Atmospheric Pressure Townsend Discharge (APTD) in air by using a simple DBD device consists of alumna barriers (purity of Al_2O_3 : 92%) and plane electrodes [5]. This discharge is homogeneous between barriers. So far, we set up two ozonizers with different discharge modes of FD and APTD, and compared the ozone generation efficiency [6]. The experimental results showed that the efficiency was higher by the FD mode than by the APTD mode in smaller specific input energy region. However in the region that the specific input energy is larger than 420 J/L, the APTD mode showed higher efficiency than FD mode. In the literature [7], an operation under short discharge gap and optimized high gas pressure is advantageous for efficient ozone generation from air. Therefore, we considered if a High Pressure Townsend Discharge (HPTD) is available, ozone generation performance by the Townsend Discharge (TD) may increase further. In this paper, we investigated whether the TD in dry air in the pressure range of 0.1 MPa and 0.17 MPa can be generated or not.

2. Experimental setup

Fig. 1 shows experimental setup for APTD generation. In this system, dry air was supplied to a discharge chamber. This system consists of a HV power source, a measurement system of electrical characteristics, a DBD device and a digital camera. AC high voltage was applied to the DBD device by a step-up transformer. The maximum applied voltage was 27.2 kVp. The applied voltage (V) and the current were measured by an oscilloscope (Tektronix 2024B, 200 MHz, 2.0 GS/s) using a HV probe (Pulse Electronic Engineering, EP-50K, 1/2000) and a differential probe (Yokogawa Electric Corporation, 700924, 100MHz) respectively. An integral of the current (charge q) was measured from

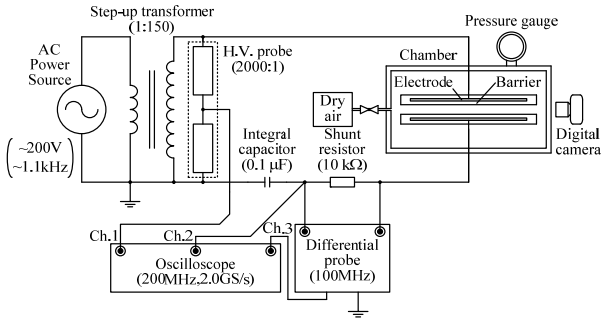


Fig. 1. Experimental setup.

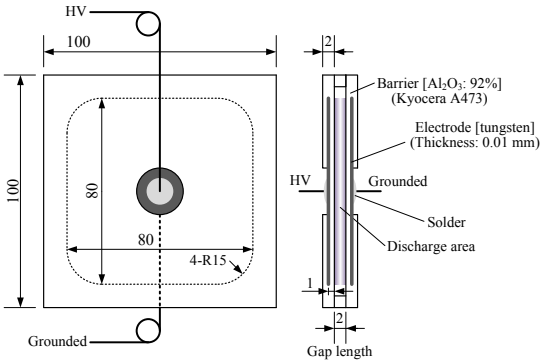


Fig. 2. DBD device.

the voltage drop across a integral capacitor. Besides, the discharge power was calculated by multiplying the area of V - q lissajous figure by power frequency. Discharge photographs were taken by the digital camera. The exposure time and the apparature of the lens were 10 s and F5.6 respectively. Gas pressure in the chamber were changed from 0.1 to 0.17 MPa.

Fig. 2 shows the DBD device. The gap length was fixed to 2 mm. The barrier material is alumina (purity of Al_2O_3: 92%, Kyocera Corp., Type: A473), and its size and thickness are 100 cm^2 and 2 mm respectively. The electrode material is tungsten, and its size and thickness are 62 cm^2 and 0.01 mm, respectively. The electrode was implanted into alumina barrier in order to avoid a generation of abnormal discharge and increase a stable working domain of APTD [8]. Therefore, the barrier thickness from tungsten film electrode surface and discharge area is 1 mm.

3. Results

Fig. 3 (a) shows waveforms of the applied voltage, gap voltage and current at 0.1 MPa. The discharge started at around 2 and 12 ms, and the current flowed continuously and had no pulse in a half cycle. This current waveform was completely different from the high pulse current observed in typical DBD. Once a discharge generates in the gap, the gap voltage was maintained to almost a constant value of 8.5 kV. These waveforms are very much like the waveforms of current and gap voltage of our APTD in air [5]. Next, a gas pressure was increased from 0.13 to 0.17 by 0.01 MPa step. Fig. 3. (b) - (f) show the waveforms of the applied voltage, gap voltage and current. Despite high gas pressure, the current flowed continuously and had no pulse in a half cycle in all gas pressure tested. Under the 12.3 kVp applied voltage experiments, we found that peak current value decreased with the increase of gas pressure and it attained to 0.2 mA at 0.17 MPa. On the other hand, the maximum gap voltage increased with the increase of gas pressure and it attained to 10.6 kV at 0.17 MPa.

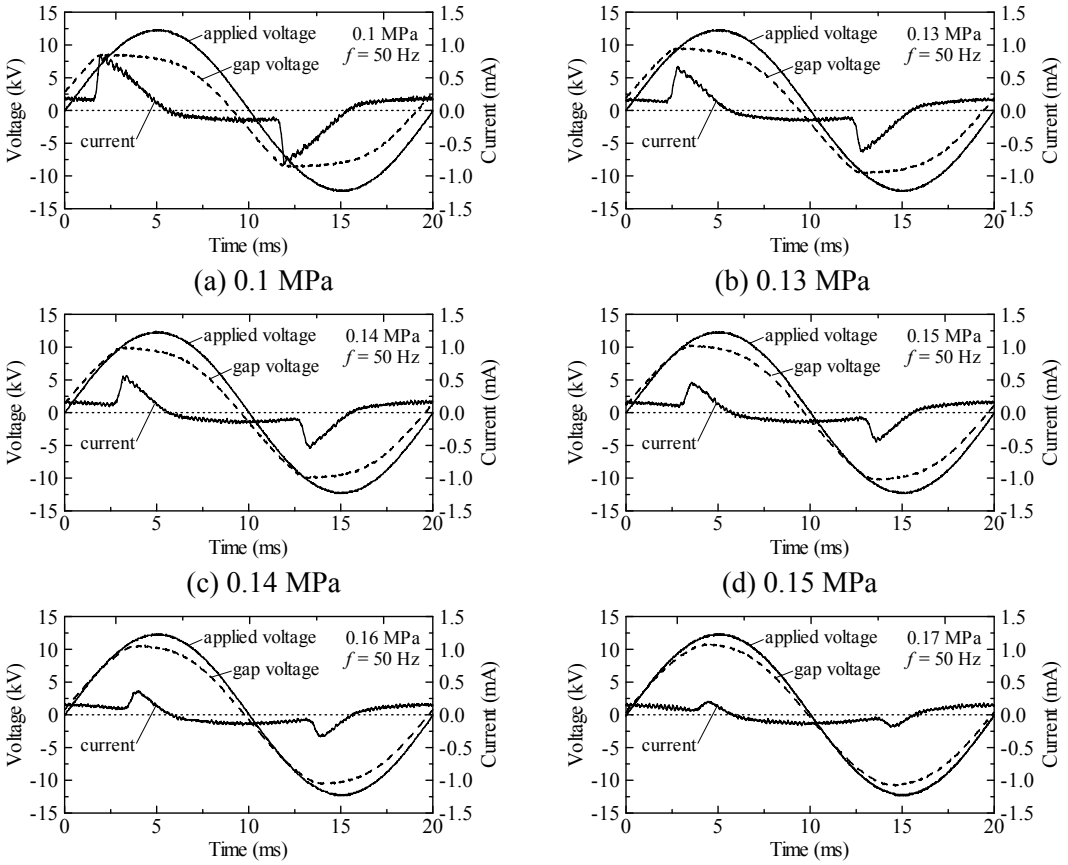
Fig. 4 (a) shows a discharge photograph of a discharge at 0.1 MPa. FDs are not recognized between barriers and the discharge is homogeneous. Next, a gas pressure was increased from 0.13 to 0.17 by 0.01 MPa step. Fig. 4 (b) - (f) show the discharge photographs. As it is seen, FDs are not recognized between barriers as well. From the observation results of current waveforms and discharge photographs, we concluded that High Pressure Townsend Discharges (HPTDs) were generated even in dry air in the pressure range of 0.1 and 0.17 MPa.

Fig. 5 shows V - q lissajous figures at different gas pressures. All of the figures show a parallelogram shape. However, the amount of the charge during discharge (Δq) decreased with the increase of gas pressure, because the discharge current decreased with the increase of gas pressure. Fig. 6 shows the relation between the power dissipated in the DBD device and the gas pressure. The power decreased with the increase of gas pressure and it attained to 0.26 W at 0.17 MPa.

Fig. 7 shows the reduced electric field and the average electron density at a constant applied voltage. The reduced electric field E/n (Td) was calculated from the following equation:

$$E/n = \frac{V_g}{d \cdot n} \cdot \frac{1}{10^{-17}} = \frac{V_g \cdot kT}{d \cdot P} \cdot \frac{1}{10^{-17}} \quad (1)$$

where V_g is the discharge sustaining voltage (V), which was measured by V - q lissajous figure, d is the gap length (cm), n is the number density of gas (cm^{-3}), k is the Boltzmann constant (1.3806×10^{-23} J/K), T is the gas temperature (300 K) and P is the gas pressure (Pa).

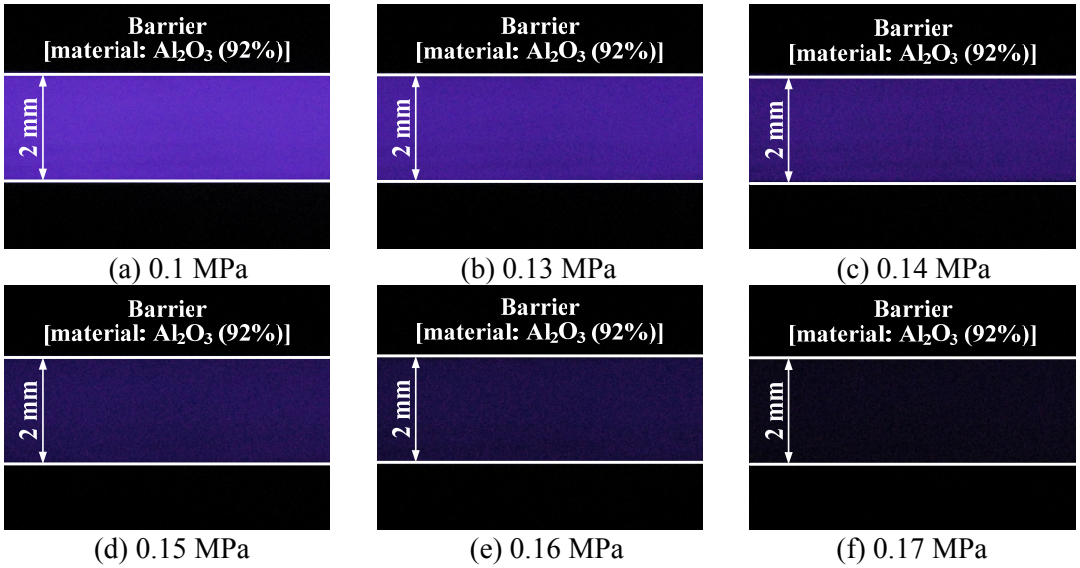


(a) 0.1 MPa (b) 0.13 MPa

(c) 0.14 MPa (d) 0.15 MPa

(e) 0.16 MPa (f) 0.17 MPa

Fig. 3. Applied voltage, gap voltage and current waveforms.



(a) 0.1 MPa (b) 0.13 MPa (c) 0.14 MPa

(d) 0.15 MPa (e) 0.16 MPa (f) 0.17 MPa

Fig. 4. Discharge photographs.

The average electron density n_e in the HPTD can be calculated using the formula [9]

$$n_e = \frac{j}{e \cdot v_d} \tag{2}$$

where j and e is the current density (A/cm^2) and electron charge (1.6×10^{-19} C). v_d is the drift velocity, which can be calculated as a function of E/n [10]. The current density in the APTD is calculated by dividing the peak current value by the cross section of the APTD, which is assumed to be 62 cm^2. Under the same applied voltage and frequency experiments, the reduced electric field decreased with

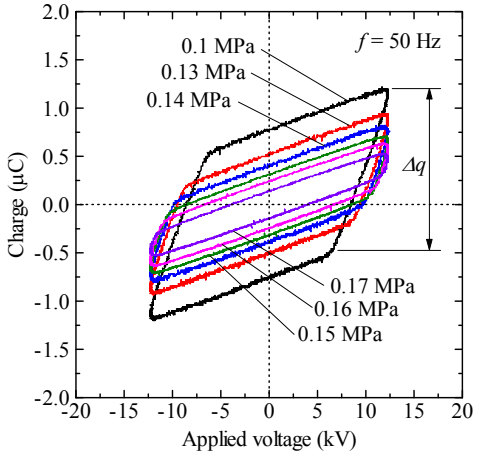


Fig. 5. Lissajous figures.

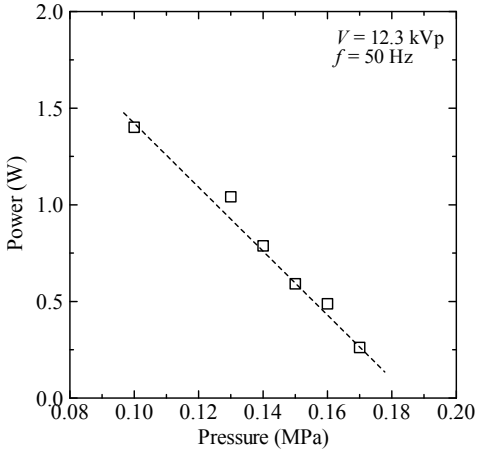


Fig. 6. Power dissipated in DBD device.

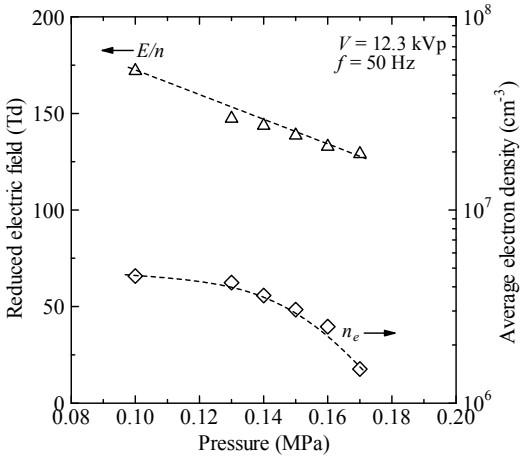


Fig. 7. E/n vs. n_e (effect of gas pressure).

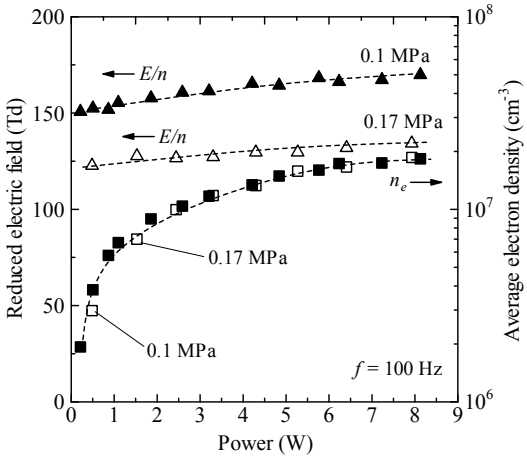


Fig. 8. E/n vs. n_e (effect of power).

the increase of gas pressure and it attained to 129 Td. On the other hand, average electron density also decreased with the increase of gas pressure and it attained to 1.5×10^6 cm^{-3}.

Fig. 8 shows reduced electric field and average electron density. In this experiment, gas pressures were fixed to 0.1 and 0.17 MPa respectively. The power was changed by increasing the applied voltage. As for reduced electric field, in case of 0.1 MPa, it increased with the increase of power, and it attained to 170 Td. On the other hand, in case of 0.17 MPa, it increased slightly with the increase of power, and it attained to 134 Td. As for average electron density, in the both cases, it increased with the increase of power, and it attained to 1.8×10^7 cm^{-3} at 8.1 W. Therefore, we can say that the reduced electric field decreases with the increase of gas pressure, and the average electron density does not change by changing gas pressure.

4. Discussions

Here, we discuss why HPTDs in dry air were generated even in the pressure range of 0.1 and 0.17 MPa. In the leterture [11], it is reported that nitrogen metastabeles play an important role for suplying seed electrons, however, O atoms quench nitrogen metastables. On the other hand, in the literture [12], it is reported that low gas pressure enhances the radial diffusion of electron avalache. However in our experiment, since HPTD was generated even in pressurized dry air. Therefore, the existence of nitrogen metastables and radial diffusion process of electron avalanche are not a cause of the generation of HPTD.

Next, we consider a model of HPTD in dry air, which neglects the contribution of nitrogen metastable and radial diffusion process of electron avalanche. After the generation of HPTD, many electrons are absorbed on the barrierr surface on the anode. Under this condition, when the polarity of applied voltage is reversed, homogeneous electron desorption from the barrier surface over the cathode occurs and the uniform electric field is formed in the gap. This uniform elecrtric field ensures

a homogeneous slow breakdown in the gap and it enables homogeneous ion bombardments to the barrier surface on the cathode. If a distribution of the secondary emission of electrons over our alumina barrier plate is homogeneous and high, the secondary electrons can generate HPTD. Therefore, we are now thinking that an electron desorption and secondary emission from barrier is very important for the generation of HPTD. Further study on the desorption of electrons and secondary emission from barrier material is necessary.

5. Conclusions

The effect of gas pressure on the stable generation of Townsend discharge in dry air was investigated. The conclusions are as follows;

(1) The current flows continuously and has only one peak in a half cycle, and FDs are not recognized between barriers in all gas pressure tested. These features completely agree with the features of the APTD we reported.

(2) As for 0.1 MPa, the reduced electric field increased with the increase of power, and it attained to 170 Td. On the other hand, average electron density increased with the increase of power, and it attained to 1.8×10^7 cm^{-3} at 8.1 W.

(3) As for 0.17 MPa, the reduced electric field increased slightly with the increase of power, and it attained to 134 Td. On the other hand, average electron density increased with the increase of power, and it attained to 1.8×10^7 cm^{-3} at 8.1 W.

(4) In summary, our HPTD can be generated in dry air in the pressure range of 0.1 and 0.17 MPa, and it was found that the reduced electric field decreased with the increase of gas pressure, and the average electron density does not change by changing gas pressure.

6. Acknowledgements

This work was supported by a MEXT (Ministry of Education, Culture, Sports, Science and Technology) - Supported Program for the Strategic Research Foundation at Private Universities, 2011-2016 and a Grant-in-Aid for Young Scientists (B), (23760270).

The authors thank Kyocera Corporation for providing A473 alumina barrier plate and thank Professor K. Takaki of Iwate University for valuable comments of a calculation method about the average electron density.

7. References

[1] Eliasson B and Kogelschatz U, 1991, *IEEE Trans. on Plasma Sci.*, Vol. 19, No. 6, 1063-1077.
[2] Yoshioka Y, 2007, *Int. J. Plasma Environmental Sci. and Technol.*, Vol. 1, No. 2, 110-122.
[3] Caquineau H, Enache I, Gherardi N, Naudé N and Massines F, 2009 *J. Phys. D: Appl. Phys*., 42, 125201
[4] Yoshioka Y and Shoyama T, 2004, *Proc. of the 9th Int. Symp. on High Pressure and Low Temperature Chemistry (HAKONE 9)*.
[5] Osawa N and Yoshioka Y, 2012, *IEEE Trans on Plasma Sci.*, Vol. 40, No. 1, 2-8.
[6] Osawa N, Kaga H, Fukuda Y, Harada S, Yoshioka Y and Hanaoka R, 2011, *Eur. Phys. J. Appl. Phys.*, 55, 13802.
[7] Kitayama J and Kuzumoto M, 1999, *J. Phys. D: Appl. Phys*, 32, 3032-3040.
[8] Nakai Y, Kabeya T, Ninoyuu K, Osawa N, Yoshioka Y and Hanaoka R, 2011, *Annual Conf. Recored of Fundamentals and Materials Society IEE Japan*, P-14.
[9] Takaki K, Kirihara H, Noda C, Mukaigawa S and Fujiwara T, 2006, *Plasma Process. Polym.*, 3, 734-742.
[10] Urquijo J D, Yousfi M, Juárez A M, Bekstein A, Basurto E, Benhenni M, Henrández-Ávila J L, Eichwald O, Merbahi N, 2009, *Proc. of the 29th Int. Conf. on Phenomena in Ionized Gases*.
[11] Massines F, Gherardi N, Naudé N and Ségur P, 2009, *Eur. Phys. J. Appl. Phys*, 47, 22805.
[12] Kogoma M, 2006, Science and Technology Co, Ltd., first press, Tokyo, pp. 23-24.

Lightning as a natural tool for air cleaning from an environmentally harmful impurities by low-temperature plasma

A.Z Ponizovsky., S.G. Gosteyev
FMKB "Horizon" Russia horizontl56@rambler.ru

Lightning is a natural generator of low-temperature non-equilibrium plasma during both the leader and return-stroke stages. It efficiently clears air of both ~~the~~ fine particles and gaseous impurities. As a long spark is an analog for lightning, the possibility of using a long spark as a tool for ~~the~~ cleaning air of harmful admixtures in large population centers is discussed.

Everyone knows that the air feels much cleaner after a lightning storm than after a similarly-intense rain storm. This is due to the fact that lightning is a natural generator of low-temperature, non-equilibrium plasma (LTP). LTP is an effective form of air treatment to remove gaseous polluting substances and fine aerosols [1-3].

In our LTP units, [1] nanosecond pulsed streamers in corona discharges are used as a substitute source of lightning. The movement of streamers represents a so-called wave of ionization. According to existing representations [4], ~~before~~ the front of a wave is preceded by an avalanche of ionized molecules of gas. Electrons, moving toward a positive electrode, i.e. against the wave movement, leave the area occupied with positive ions that permits avalanches to be formed again. As a result, this process occurs with a positive charge quasi -movement with velocities of the order of 10^8 cm/s. The ionization front is followed by a low-temperature quasi equilibrium positive and negative ions plasma.

Gaseous admixtures are successfully treated when flue gas passes through a zone of LTP, producing highly active intermediate particles that react with the contaminating molecules. As a result the harmful gaseous admixtures are transformed into harmless gaseous substances or aerosols. For example, sulfur dioxide or nitrogen oxide convert to sulfuric or nitric acid respectively. Gaseous organic admixtures as a rule convert into primary substances such as CO_2 or H_2O and in some cases, aerosols of lower organic acids.

On an industrial scale, this process is implemented in a coaxial reactor chamber (RC), with a central multicusp electrode fed from a HF HV Fitch pulse generator [1]. The removal of converted products and original dust ~~is dusting off~~ on the external RC wall due to a constantly applied HVDC electrostatic field. Simultaneously, the inner wall of the RC is continuously washed by circulating water. As a result the installation works both as a LTP generator and a wet precipitator.

In nature, the above processes take place during the development of lightning. In the industrial case, a channel of ~~a~~ lightning operates as the HV electrode and rain drops as the contamination collector.

In this paper we consider only continuous positive lightning, reaching the ground from a positive charge cloud. Despite the fact that the overwhelming

number of lightning strikes are negative, the process of cleaning ~~the~~ air by negative lightning does not differ substantially from positive lightning.

As is well known the development of lightning is due to the so-called leader process [4]. The essence of this process involves the inter-action of a thin high-temperature equilibrium plasma channel between the cloud and the ground. The development of the channel is due to the current generated by streamers, starting from the starting point of the channel, called the head of the leader. The ensemble of streamers is called the streamer zone. It has been shown, both theoretically and experimentally, that a space charge is located on the front of the streamer zone. For this reason the leader channel is covered by a so-called sheath. The second, visible part of ~~the~~ lightning is called the return-stroke. It is a transient phenomenon. In it, a discharge takes place through a sheath covering the leader channel on the ground.

Since the voltage drop along the channel leader is small, then the estimates the size of the streamer zone and the channel cover can be assumed that the potential leader channel, as well as the potential lightning heads U_l, is approximately equal to potential of the cloud and ≈ 50 MW [4] The average field strengths in streamer zone (E_{st}) is 5kV/cm. The length of a average lightning is $L_l \approx$ 4000m. [4]. The radius of the streamer zone (R_{sz}) can be calculated from the equation # 1 but the radius of sheath (R_c) – on equation # 2(Table 1).

Fig. 1 shows the calculated dependences Rc and R_{sz} from the potential of head of leader. Top value of 50MV refers to the lightning, bottom - 5MV to the long spark generated by modern GIN.

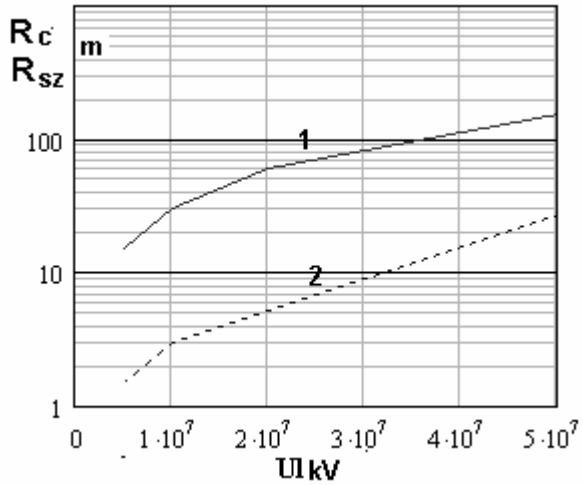


Fig.1 The calculated dependences R_{sz} (1) and Rc (2) from the potential of head.

During of the leader stage air treatment occurs at the wave of front the streamer zone. On the U_l= 50 MV R_{sz} equal 300 m (fig.1) and L_l=4000 m. It means that the one lightning stroke would be treated about 10^6 m^3 of air. In fact, due to the amount of branching of the lightning leader the processed gas by approximately ten time larger. As speed of lightning leader is ≈ 4 10^5 m/s [5] time of leader stages is 0.01c. If the average leader current is 100 – 200 A, U_l = 50 MV that energy injected into the gas is $W_l \approx 10^8$ J, introduced volume charge - Q ≈ 1-2 Cl [5]. On the time return-stroke LTP is generated by the corona sheath. If

duration of the return-stroke ≈ 10^{-4}s and average current is 50 kA that energy introduced into the air is ≈ $2.5 \cdot 10^8$ J. For multi component lightning W_{rs} may be estimate ≈ 10^9J. Then the specific energy expended has an order of $W_{sp} \approx 10^2$ J/m^3.

If the area of middle storms is ≈10 km^2 that volume of air is ≈10^{10} m^3. The number of lightning is assessed as 20 for a storm duration of one hour [5]. It means that lightings will be processed by the volume of air about 10^9 m^3. Thus only directly for the LTP lightning storm can treat about 10% the total volume of air. Indirectly, these estimates are confirmed by available after the storm ozone. It is known that the person feels ozone (O_3) with a concentration of 0.015 mg/m^3. This means that for the appearance of the smell of O_3 during storm must be executed ≈$0.15 \cdot 10^6$ g. Experimental studies show that in pulsed power ozone generators energy consumption for the formation of O_3 in the order of 10^4 J/g. In this manner during a lightning storm in the air must implement the order of 10^{10}J, that is consistent with the estimates given above.

Naturally, in the zone of LTP is intense charge as airborne dust particles and water drops. The drops are uncharged dust collectors, as well as charged dust settles on the uncharged drops. The equations allow calculating the efficiency of air cleaning of uncharged dust drops of rain, dust from the uncharged charged uncharged droplets and droplet charged dust are shown in Table 1.

Table. 1 The equations for calculation dimension streamer zone and sheath of lightning and efficiency of air cleaning of uncharged dust drops of rain, dust from the uncharged charged uncharged droplets and droplet charged dust

#	The title	The formula	The designation	Ref.
1	The radius of the streamer zone Rsz,	$Rsz=3 \cdot Ul/2 \cdot Est$		[4]
2	Dimensions of sheath Rc,m	$Est \cdot Rc \cdot (1+\ln(2 \cdot H/Rsc)) = U_l$	H-Distance to earth	[5]
3	Limit charge of water drop Q_{lim} and dust q_{lim}	$Q_{lim} = 10^7 \cdot \pi \cdot \varepsilon_0 \cdot D^2$ $q_{lim} = 10^7 \cdot \pi \cdot \varepsilon_0 \cdot d^2$	D- Ó of water drop d - Ó of dust	[6]
4	Stoks's criterion St	$St=v \cdot d^2 \cdot \rho \cdot /18 \cdot \mu \cdot D$	μ- dynamic viscosity	[6]
5	The efficiency of air cleaning of uncharged dust drops of rain	$\eta_N = St^2/(0.125+St)^2$		[6]
6	The efficiency of air cleaning charged dust and uncharged droplets	$\eta_{CD}=(q_{lim}^2/2 \cdot \varepsilon_0 \cdot \pi \cdot \mu \cdot d \cdot v)^{0.4} + \eta_N$	v-velocity of water drop	[6]
7	The efficiency of air cleaning charged droplets and uncharged dust	$\eta_{CH}=(K \cdot Q_{lim} \cdot d/^2 2 \cdot \varepsilon_0 \cdot \pi \cdot \mu \cdot D \cdot v)^{0.4}$ $K=\varepsilon-1/\ \varepsilon+2$	ε- permittivity of dust	[6]

Figure 2 shows the calculated from equations (3-7) of degree of air cleaning at different combinations of charged droplets and dust. That a charging is considerably increase efficiency of purification of air, especially for a fine dust.

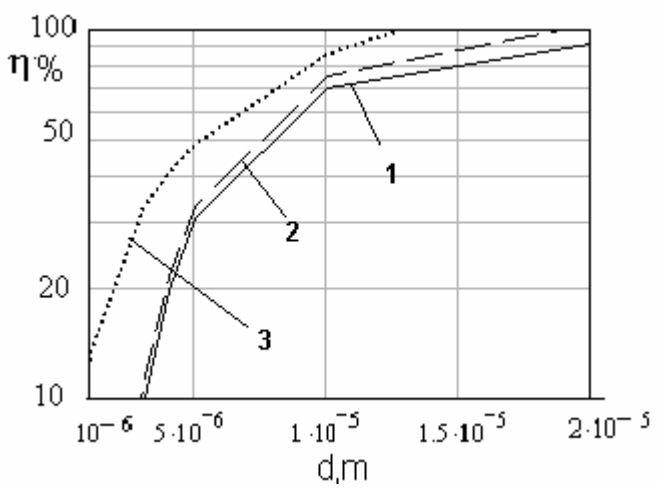


Figure 2 Dependence of air cleaning degree from dust (η) at the size of dust (d) for different charged combinations of the water drops (D = 5mm) and dust

1 - uncharged dust and drops (rain)

2 – charged dust and uncharged drops (storm)

3 -charged drops and uncharged dust (storm)

On the other hand, a high field strength near the front of ionization of leader stage and a sheath corona of the return-stroke should make conversion of impurity as it takes place in LTP installations. The experimental results received on purification of atmospheric air and flue gases from gaseous and fine aerosol pollution by means of LTP [1-3] show that energy consumption on the is average 300 J/m^3·mg for gas pollution and 8 J/m^3·mg for dust pollution.

In such a manner that W_{sp} ≈100 J/m3 in time of storm air could be purified ≈ 0.3 mg/m^3 of gas pollution and ≈ 10 mg of a dust.

In table 2 are submitted data on concentration of pollution (mg/m^3) from the environmental survey station located on a building of the Moscow State University to, during time and after a storm.

Table 2 Data on concentration of pollution from the environmental survey station

The period of time	CO	SO2	O_3	NO2	NO	PM10
to storm	0,7	0,0048	0,038	0,072	0,04	0,025
Storm	0,35	0,0047	0,061	0,052	0.001	0,006
After storm	0,45	0,0037	0,015	0,056	0,012	0,016

Table 2 generally confirms made above the assumption of a lightning, as devices for purification of air of ecologically harmful substances especially nitrogen oxides and dust and O_3.genarated.

All aforesaid gives an approach to a creation problem without the electrode clearing LTP installations using as sources of LTP long sparks, and as a collector – the sprayed water. In the present HV pulses generators of available generate pulses with amplitude 5·10^6 and duration ≈ 5 ms which is created electrical discharges more than 200 meters with current ≈ 3A [4]. According to fig. 1 R_{sz} is ≈15 m. It means one long spark can be processed air volume 6*10^3 м^3 with W_{sp}≈20J/m^3. At

pulses frequency 1 Hz the volume $2*10^7$ m^3 could be treat for an hour. Now installations for generation of long sparks of hundreds meters successfully function for the research purposes. As an example on fig. 3 the photo of the dischar in length of 200 m received on installation VNITZ VEI (Istra) is presented



Fig. 3 The photo of the discharges in length of 200 m received on installation VNITZ VEI (Istra) (Photo from site of VNITZ VEI (Istra)).

Of course such installations can not used for cleaning flue gases of industrial processes but can be potentially possible for cleaning air in mega polis.

In this case will be realized idea of Nicola Tesla [7]. "Many municipal improvements based on the use of electricity are soon to be introduced. There will be smoke annihilators, dust absorbers, ozonizers, sterilizers of water, air, food, and clothing, and accident preventers on streets, elevated roads, and in subways. It will become next to impossible to contract diseases from germs or get hurt in the city. Country folk will go to town to rest and get well."

References

[1] A.Z. Ponizovsky. Flue gas cleaning by means of pulse and DC corona discharges. "Ecology systems and devices." #11 2007 p.9-14 (In Russian).
[2] A..Ponizovsky, A.Shvedchicov, L.Ponizovsky, and all. Hakone YI Ireland 1998 pp.68-71
[3] A.Z.Ponizovsky, L.Z.Ponizovsky, S.P.Kryutchkov, and all.. Hakone YII Germany. 2000 pp.345-349.
[4] E.M.Bazelian, J.P.Raizer. Physic of lightning and protection against lightning 2000 Bristol:IOP 325 p.
[5] E.M.Bazelian, B.N.Gorin, V.I.Levitov. Physical and engineering foundations of protection against lightning M.-Gidrometeoizdat 1978 p. 223.
[6] W.Strauss. Industrial Gas Cleaning. Pergamon Press 2th Edition `
[7] N. Tesla. WONDERS OF THE FUTURE. Collier's Weekly, December 2, 1916

SPENT OIL DEGRADATION BY GLIDING ARC DISCHARGE

Maria Prantsidou, J. Christopher Whitehead

School of Chemistry, The University of Manchester, Manchester, M13 9PL, UK

E-mail: maria.prantsidou@postgrad.manchester.ac.uk

Abstract—Waste oils can be found in all power generating plants since they use a wide range of petroleum based products in their systems. The management and treatment of this waste is complicated and expensive. Low temperature plasma technology can be an alternative solution to this problem. In this work, gliding arc discharge has been used as a source of low temperature atmospheric plasma to investigate the treatment of n-dodecane ($C_{12}H_{26}$) as an example of common spent hydrocarbon oil. Dodecane gliding arc plasma degradation mechanism is studied separately in the gas and liquid phase under different carrier gases, using FTIR and OES spectroscopy for quantitative and qualitative analysis .

1. Introduction

Petroleum-based products, ranging from fuel oil and hydraulic fluid to lubricating greases and oils, can be found in all power generating plants. Specifically in nuclear plants, hydrocarbon oils are also used in spent fuel reprocessing plants leading to a large amount of waste oils, normally with low level radioactivity (LLW). This type of waste is more challenging compared to the aqueous waste since it cannot be easily treated and disposed to the environment, resulting in complicating management and expensive treatment methods [1]. Non-thermal plasma technology could be a promising method for the treatment of this waste as it can essentially provide the same outcome as incineration but at low temperatures, thus providing advantages such as lower process cost and construction simplification. In addition, plasma systems could be produced in almost any scale for waste treatment, giving the potential of portable plasma devices for on-site or spillages treatment.

Gliding-arc discharge (GAD) is considered as non-thermal plasma but it can also be described as preserving the dual character of thermal and non-thermal plasma which makes its interactions with matter the same as those of quenched plasma [2]. Its characteristics make it an attractive tool for both scientists and industry [3] and it was initially developed for gas treatment applications, but it has also recently been developed for liquid treatment [4].

In this work, a gliding arc discharge has been used as a source of low temperature atmospheric plasma for the investigation of waste oil treatment. The plasma-liquid clean-up process in its different forms initially involves reaction at an interface between the gaseous plasma (which contains the reactive species) and the target liquid. Reaction takes place either as a gas-surface process or by diffusion of the reactive species into the bulk of the liquid. Thus, it was considered important as a first step to study the gliding arc discharge degradation of the oil in the gas phase, as a key for the second step, the study of the degradation mechanism in the liquid phase.

2. Methodology

Low temperature atmospheric plasma was generated using an AC gliding arc discharge reactor as illustrated in Figure 1.The plasma degradation of n-dodecane ($C_{12}H_{26}$) as simulant target oil has been investigated under different gas compositions such as dry or humid Ar, N_2 and air. The decomposition efficiency and distribution of end-products is investigated quantitatively and qualitatively by FTIR spectroscopy. Optical Emission Spectroscopy (OES) was used to identify reactive species in the plasma under the different conditions.

The GAD reactor mainly consists of two stainless steel diverging electrodes, with a minimum gap of 3mm, located under a feeding gas nozzle of i.d. 1.5 mm. Reactions are performed in a double walled jacketed Pyrex glass vessel of 1 L capacity with water cooling at 25 °C . An AC neon sign power supply provided a high voltage up to 20 kV_{p-p} at a frequency of 50 Hz. For the experiments in the gas phase, the carrier gases used were N_2, synthetic air (80% N_2, 20% O_2) and Ar (99.998% purity) in dry

or humid conditions. For the humid conditions, the inlet gas relative humidity was RH=65%±2%, t=24 °C, measured with a HTD-625 thermo-hygrometer. The total flow was 5 L min^{-1} passing through a bubbler filled with dodecane to create a vapour of initial concentration 90 ppm. For the experiments in liquid phase 5 ml of dodecane were placed underneath the gliding arc plasma plume as a plasma-liquid surface treatment. On-line FTIR spectroscopy (Shimadzu 8300) with a long path IR cell (5 m) at resolution 1 cm^{-1} was used for the identification and concentration determination of the gaseous products. Optical emission spectroscopy measurements occurred in the integration of the whole plasma plume using a multi-mode quartz optical fiber connected to a CCD Princeton Instrument 320PI spectrograph with a 2400, 1200 or 600 g/mm grating (0.03–0.13 nm resolution) and in the range 200-800 nm.

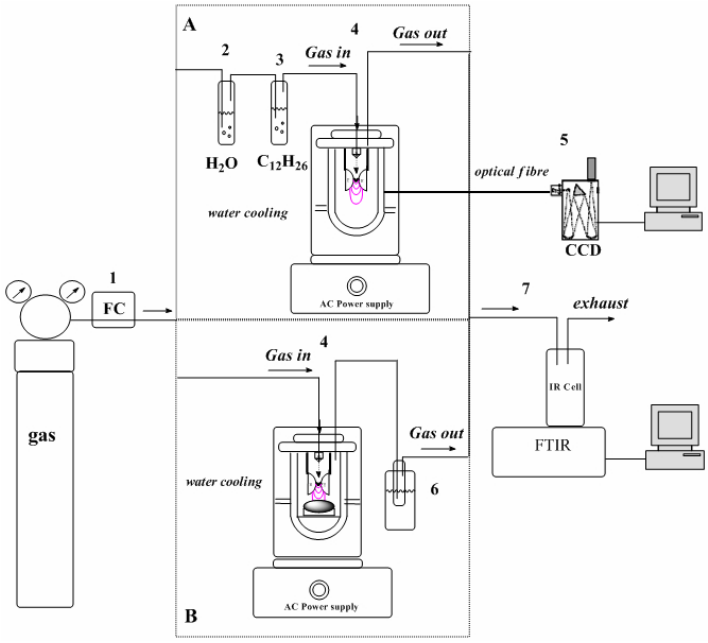


Fig 1. Schematic diagram of experimental configuration for experiments A) in the gas phase and B) in the liquid phase: 1) mass flow controller, 2) bubbler with water, 3)bubbler with dodecane, 4)AC GAD reactor, 5)Optical emission spectrograph,6) liquid N_2 cold trap, 7) gas FTIR sample inlet

The results obtained for the dodecane ($C_{12}H_{26}$) conversion were expressed as follows:

$$\%\ C_{12}H_{26}\ Conversion = (C_i - C_o)/C_i \times 100 \quad (1)$$

where C_i and C_o are the input and output dodecane concentrations, respectively.

$$\%\ Product\ Selectivity = (C_{product} \times 100)/(12 \times C_{Dod\ converted}) \quad (2)$$

$$\%\ IC\ Selectivity = (C_{HCN} + C_{CO} + C_{CO2}) \times 100/(12 \times C_{Dod\ converted}) \quad (3)$$

$$\%\ OC\ Selectivity = (C_{CH4} + C_{C2H4} + C_{C2H2}) \times 100/(12 \times C_{Dod\ converted}) \quad (4)$$

where *IC Selectivity* is the selectivity of dodecane conversion to inorganic carbon products such as HCN, CO, or CO_2 and *OC* is the selectivity towards the major organic products measured, such as methane (CH_4) and the unsaturated hydrocarbons ethylene (C_2H_4) and acetylene (C_2H_2). Existence of ethane (C_2H_6) is possible but could not be confirmed by FTIR, as ethane absorption frequencies overlap with those of dodecane.

For the experiments in the liquid phase, the same reactor was used but this time 5 ml of dodecane was placed underneath the GAD plasma plume for the plasma-liquid treatment. A cold trap of liquid N_2 was used at the outlet of the reactor to trap excess vapour.

3. Comparison between the intermediate species and end-products formation in dry and humid GAD gas compositions

The GAD degradation of dodecane in the gas phase was studied using Ar, N_2 and air in dry or humid (RH=65%, 24 °C) conditions in order to investigate the effect of the different carrier gas composition on the conversion efficiency and end-products distribution.

Changing the carrier gas causes observable changes in the plasma plume characteristics such as length, colour and carbon deposition. These changes are an indication of the different plasma chemistry occurring under the different carrier gases. Table 1 summarises the reactive intermediate species that were identified by optical emission spectroscopy measurements together with the decomposition gaseous end-products observed by FTIR spectroscopy between the different gas composed plasmas.

Table 1 Summary of the intermediate species observed by OES and the end-products observed by FTIR. The input power of the reactor is maximum achievable in each case. The dodecane concentration is 90 ppm.

GAD Plasma	OES Intermediate species	Region (nm)	FTIR end-products
N_2 200w	N_2 $C^3\Pi u$-$B^3\Pi g$	315.9,337.1,353.6,357.7	-
	N_2^+ $B^2\Sigma^+u$-$X^2\Sigma^+g$	391.4	
N_2/C_{12} 185W	N_2 $C^3\Pi u$-$B^3\Pi g$	315.9,337.1,353.6,357.7	HCN, CH_4
	C_2 $d^3\Pi g$-$a^3\Pi u$	516.4	C_2H_4, C_2H_2
	CN $B^2\Sigma$ -$X^2\Sigma$	386.1,387.1,388.3	(CO)
			NH_3
$N_2/C_{12}/H_2O$ 190W	N_2 $C^3\Pi u$-$B^3\Pi g$	315.9,337.1,353.6,357.7	CO, CO_2,
	N_2^+ $B^2\Sigma^+u$-$X^2\Sigma^+g$	391.4	HCN,CH_4,
	C_2 $d^3\Pi g$-$a^3\Pi u$	516.4	C_2H_4, C_2H_2
	CN $B^2\Sigma$ -$X^2\Sigma$	386.1,387.1,388.3	NO
	OH $A^2\Sigma u$-$X^2\Pi g$	309	
Ar 105W	Ar	numerous	-
Ar/C_{12} 105W	Ar	numerous	CH_4
	C_2 $d^3\Pi g$-$a^3\Pi u$	516.4	C_2H_4, C_2H_2
	CH $A^2\Delta$-$X^2\Pi$	431.1	(CO)
$Ar/C_{12}/H_2O$ 120W	Ar	numerous	
	C_2 $d^3\Pi g$-$a^3\Pi u$	516.4	CO,CO_2
	OH $A^2\Sigma u$-$X^2\Pi g$	309	C_2H_4, C_2H_2
	CH $A^2\Delta$-$X^2\Pi$	431.1	*oxygenated products
	Hα *(n=3-2)*	656.3	
	O (5p-5s)	777	
Air 200W	N_2 $C^3\Pi u$-$B^3\Pi g$	315.9,337.1,353.6,357.7	NO,
	N_2^+ $B^2\Sigma^+u$-$X^2\Sigma^+g$	391.4	NO_2
	O (5p-5s)	777	N_2O_4
			*oxygenated products
Air/C_{12} 200W	N_2 $C^3\Pi u$-$B^3\Pi g$	315.9,337.1,353.6,357.7	CO,CO_2, HCN
	N_2^+ $B^2\Sigma^+u$-$X^2\Sigma^+g$	391.4	C_2H_4, C_2H_2
	O (5p-5s)	777	NO, NO_2
	OH $A^2\Sigma u$-$X^2\Pi g$	309.01	HNO_2, N_2O_4
			*oxygenated products
$Air/C_{12}/H_2O$ 200W	N_2 $C^3\Pi u$-$B^3\Pi g$	315.9,337.1,353.6,357.7	CO,CO_2, HCN
	N_2^+ $B^2\Sigma^+u$-$X^2\Sigma^+g$	391.4	C_2H_4, C_2H_2
	O (5p-5s)	777	NO, NO_2
	OH $A^2\Sigma u$-$X^2\Pi g$	309	HNO_2 N_2O_4
			*oxygenated products

*Other oxygenated products are observed, such as aldehydes or ketones (RCHO, RCO) but cannot be specified.

It can be seen that different gas mixtures lead to different electronically-excited reactive species which can be related to particular end-products. In case of argon GAD, strong emission of the C_2 Swan and CH band agrees with the strong selectivity towards the C_2 hydrocarbons C_2H_4 (~949 cm^{-1}), C_2H_2 (~ 3341,730 cm^{-1}) and CH_4 (~3016, 1303 cm^{-1}), but also some CO is observed resulting from oxygen impurities in the carrier gas and some solid carbon was deposited on the electrodes. In N_2 GAD, the N_2* metastable seems to play an important role to the dodecane degradation, since the second positive nitrogen emission is weaker and first negative is not detectable. Among major end-products is HCN (~712 cm^{-1}) which is correlated with the strong CN emission, but there is also a high concentration of CH_4 and C_2H_2 and a smaller amount of C_2H_4, and some solid carbon deposited on the electrodes. A small concentration of NH_3 (~966 cm^{-1}) and CO is also observed. In air GAD the oxygen and nitrogen reactive species have many reactions pathways in dodecane to produce a wider range of products. The

major mineralisation products observed are CO, CO_2 (~2370 cm^{-1}) and HCN, while the organics identified were only lower concentrations of C_2H_4 and C_2H_2 and no CH_4. Nevertheless, indication of other organic oxygenated products exists at the regions of 1715-1680 cm^{-1} and 1550-1500 cm^{-1} being the characteristic carbonyl group stretching of saturated aldehydes or ketones (RCHO, RCO) and the asymmetrical stretching of NO in nitroso compounds (RNO) respectively. Other inorganic products formed include NO (~1900 cm^{-1}), NO_2 (~1629 cm^{-1}), N_2O_4 (~1740 cm^{-1}) and HNO_2 (~1263 cm^{-1}), which are common in air discharges due to the rapid recombination of N and O radicals, but no N_2O and HNO_3 were observed. The introduction of water to argon and nitrogen plasma produces O and OH intermediate reactive species from the dissociation of water , while C_2 and CN signals weakens. That agrees with the additional formation of CO, CO_2 and oxygenated products, while hydrocarbons are produced in lower concentrations and there is no soot formation. The humidity does not create a big impact to the air GAD, where N_2*, N_2^+ and O emission is dominant and OH is observed in both dry and humid air /dodecane plasma processing.

4. Gas effect on the GAD oil vapour conversion and products selectivity

Dodecane degradation in vapour phase was studied using dry and humid Ar, N_2 and air gliding arc discharge with the maximum achievable input voltage for each gas. Figure 2 illustrates the conversion efficiencies in each case.

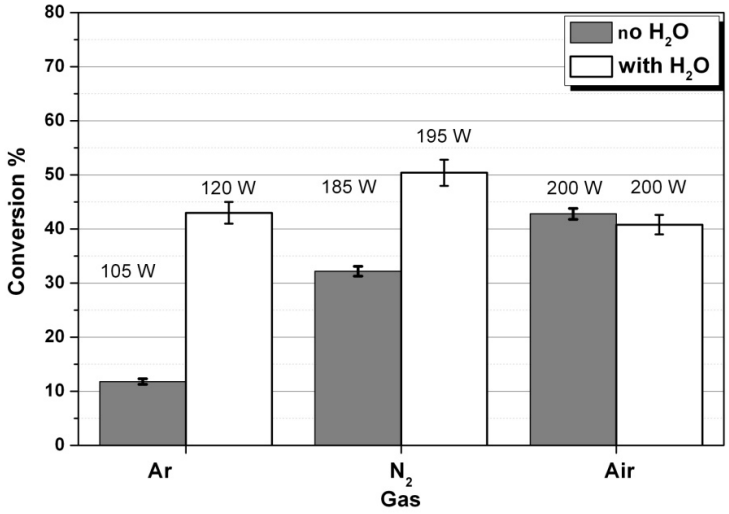
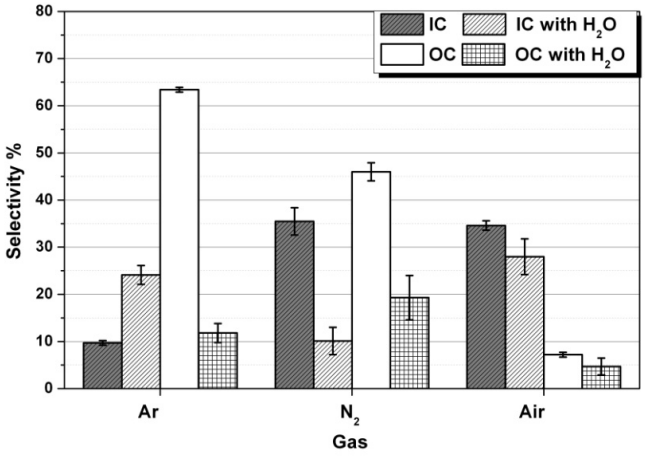


Fig 2. Dodecane conversion in dry and humid (RH=65%) argon, nitrogen and air gliding arc discharge

In dry conditions, the maximum conversion is observed in air plasma at 43% for an input power of 200W. N_2 plasma was less efficient at 32% in 185W. The maximum input power achieved in Ar gliding arc plasma was only 105 W and resulted in lower conversion of 12%. The injection of humidity to the non-oxidative environment of argon and nitrogen plasma produces OH and O reactive radicals which enhance the dodecane conversion significantly to 42% and 51%, respectively. In case of the oxidative air plasma, the water causes no effect to the power and the conversion.

Figure 3 illustrates the gas effect to dodecane conversion end-products selectivity expressed as inorganic carbon (*IC*) such as CO, CO_2 and HCN in case and organic carbon products (*OC*), such as CH_4, C_2H_4, and C_2H_2. The selectivity towards the inorganic and organic products observed, differs in any case.



Gas	Product selectivity (%)					
	CH_4	C_2H_4	C_2H_2	HCN	CO	CO_2
Dry Ar	19.1	13.2	31	-	9	-
Dry N_2	10.2	13.7	22.8	29.8	5.7	-
Dry air	-	4.3	3	5.5	19.8	9.3
Humid Ar	10.5	0.6	0.6	-	20	4
Humid N_2	14	2.7	2.5	3.8	5.1	1.3
Humid air	-	4.1	0.6	2.8	16.5	8.7

Fig 3. Dry and humid gas effect to the selectivity of inorganic (IC) and organic carbon (OC) end-products

In the non-oxidative dry argon gliding arc plasma, dodecane degradation leads to methane, ethylene and acetylene with a selectivity C_2H_2> CH_4>C_2H_4, while there is also low selectivity to CO due to the oxygen impurities. Similarly in dry nitrogen plasma dodecane degradation has a higher selectivity towards the organic hydrocarbons rather the inorganic products of HCN and the overall sequence in selectivity is HCN>C_2H_2>C_2H_4>CH_4. In the case of air, a low selectivity occurs towards the specified organic hydrocarbon products, since the reactive O radical oxidises them to CO and CO_2. The addition of water in argon and nitrogen plasma is seen in Figure 2 that enhances significantly the dodecane degradation. Nevertheless, Figure 3 shows the selectivity towards the organic products is very much decreased, as the O and OH leads to CO, CO_2 and other oxygenated products such as aldehydes or ketones (RCHO, RCO). Humidity in air plasma causes no effect to the dodecane degradation and products selectivity, probably because the reactive O and OH species are already sufficient enough in the dry plasma.

5. Gliding arc plasma degradation of liquid dodecane

Gliding arc discharge has been used for the treatment of liquid dodecane with the experimental configuration as given previously, in Figure 1B. In this work, gliding arc discharge was generated with 5 l min^{-1} nitrogen in 200 W input power to treat 5 ml of dodecane. Because of the excess vaporisation and gaseous products during the treatment, a liquid nitrogen cold trap was used to avoid the signal loss in the IR cell. After 4 min of treatment only 1 ml of dodecane was left in the reaction cell and was collected for future liquid analysis.

Figure 4 shows the degradation products of the gliding arc treatment of liquid dodecane compared to those in the vapour phase as measured by FTIR. Overall, the major end-products that were observed in the nitrogen plasma treatment of dodecane vapour, such as HCN, C_2H_2, C_2H_4, CH_4 and some CO, were the same as in the case of nitrogen plasma-liquid treatment, but in higher concentration levels. Nevertheless, there are some new peaks observed in the case of the plasma-liquid treatment that could be an evidence of potential organic intermediates. The peak at the region of 1240-1230 cm^{-1} could be correlated with the C-O ether stretching (R-O-R$^{'}$) as a possible intermediate due to the oxygen impurities in the nitrogen gas. The peak at ~ 627cm^{-1} could be the C-H deformation vibrations of other potential gaseous organic intermediates formed during the plasma-liquid treatment of the oil.

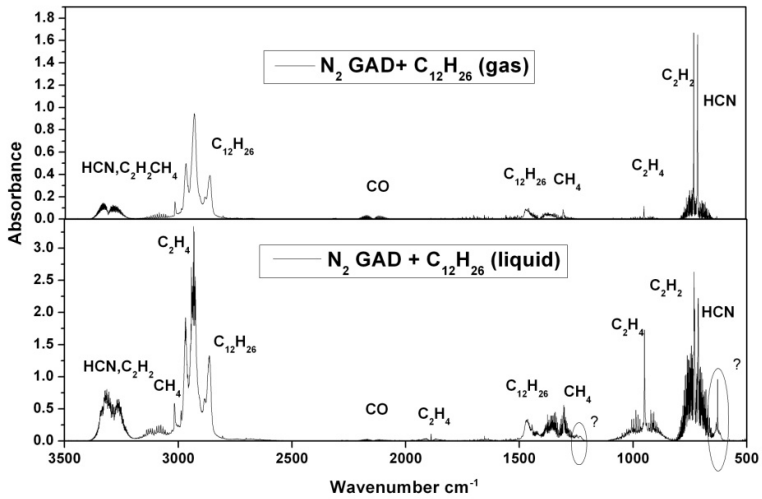


Fig 4.Comparison between the FTIR absorption spectra of the gaseous products after nitrogen gliding arc plasma treatment of dodecane in vapour and liquid phase in maximum achievable input power, P=185W and P=200W respectively. The spectra resolution is 1 cm^{-1}.

During nitrogen gliding arc plasma-liquid treatment of dodecane some conversion of the liquid dodecane into gaseous end-products is expected and Figure 5 shows how the concentration of the gaseous products changes during the 4 min of treatment. All product concentrations are increasing with time, apart from CO which seems to remain quite stable. Although the gaseous products observed are the same as in case of the dodecane vapour treatment, it is interesting that the selectivity differs. In the liquid case, there is greater selectivity to C_2 unsaturated hydrocarbons (C_2H_2 and C_2H_4), rather than HCN as observed in the vapour phase (Figure 3). Furthermore, HCN and CH_4 formation have slower increases compared to the C_2 hydrocarbons.

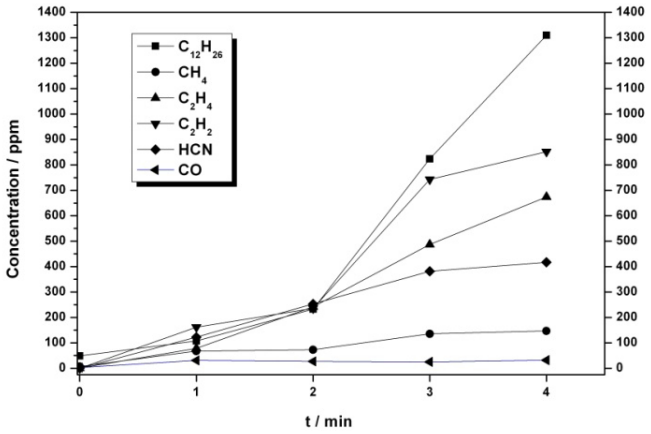


Fig 5. Gaseous products distribution during nitrogen gliding arc plasma-liquid treatment of dodecane

6. Conclusions

The gas effect to plasma degradation of vapour dodecane has been investigated as an essential step before the plasma-liquid treatment using OES and FTIR spectroscopy for the plasma intermediate and end-products investigation.

Changing the carrier gas between argon, nitrogen and air causes changes in the colour of the plasma plume, degradation conversion and end-products. In dry conditions, the maximum dodecane conversion achieved was 43% with air plasma, then 32% in nitrogen plasma and only 12% in case of argon. Dodecane processing in argon plasma is controlled by the primary steps of electron impact dissociation and electron-induced excitation creating metastable Ar^* which lead to high selectivity of

CH_4, C_2H_4, C_2H_2 organic products which is correlated with the excited C2* and CH* observed by OES. Similarly in nitrogen, plasma metastable N_2^* seem to play an important role to dodecane degradation leading to hydrocarbons, but also N radicals lead to a high selectivity of HCN which is correlated with the strong signal of CN* seen in OES. In air plasma, formation of atomic oxygen initiates the dodecane destruction, and can create OH radical by hydrogen abstraction leading finally to oxygenated products, but also forms NOx.
In humid conditions, dodecane conversion is enhanced in the argon and nitrogen plasmas by the OH radicals whose presence is confirmed by OES. In these cases, the reactive O, OH radicals lead to a domination of CO/CO_2 and other oxygenated products such as aldehydes or ketones (RCHO, RCO), but low selectivity towards the hydrocarbons. In case of air plasma, humidity has no effect to the destruction efficiency or products selectivity.
In the plasma-liquid treatment using nitrogen gliding arc discharge a high degree of vaporisation and gaseous products is observed. The same gaseous products as in vapour phase treatment are identified such as HCN, C_2H_2, C_2H_4, CH_4 and some CO, although with a higher selectivity towards C2 unsaturated hydrocarbons in this case. Also, in difference to the vapour phase treatment, the FTIR analysis indicates ethers (ROR') could be possible organic end-products.
On going future work includes use of dry /humid argon and air to treat dodecane as well as the post-plasma treatment liquid analysis in order to correlate the degradation mechanism in the vapour and liquid phase.

7. References

[1] International Atomic Energy Agency, IAEA, "Handling and Processing of Radioactive Waste from Nuclear Applications", in *technical reports Series No. 402*, IAEA, Editor. 2001: Vienna.

[2] Fridman, Alexander, et al., "Gliding arc gas discharge" in *Progress in Energy and Combustion Science,* 1998. p. 211.

[3] Czernichowski, A., "Gliding arc: Applications to engineering and environment control", in *Pure Appl. Chem.*, 1994. **66**(6): p. 1301.

[4] Brisset, J. L., et al., "Chemical reactivity of discharges and temporal post-discharges in plasma treatment of aqueous media: Examples of gliding discharge treated solutions", in *Industrial & Engineering Chemistry Research,* 2008. **47**(16): p. 5761.

THE ROLE OF BARRIER SURFACE PROPERTIES IN BARRIER SURFACE DISCHARGE BEHAVIOUR

M.V. Sokolova[1], K.V. Kozlov[2], A.N. Mitin[1], P.A. Tatarenko[2]

[1]*National Research University "Moscow Power Engineering Institute"*
[2] *Moscow State University*
E-mail: mvsokolova@mail.ru

Measured profiles of barrier surface structures by means of a laser scanning microscope are used to calculate the electric field distribution in air in the vicinity of the barrier surface. The local electric field near the surface is shown to have strong dependence on the surface profile elements (highness of juts, curvature radii of their peaks and the distance between neighbour juts). It is shown that the values of local fields are sufficient for ionization processes in air and it is supposed that such additional ionization is one of the main factors to change the discharge behaviour. Possible effect of the films of different chemical composition on the charge accumulation on the surface is analysed.

1. Introduction

Recent experiments [1] have shown that there is distinct dependence of the surface microdischarge structure and electric characteristics of the discharge on the structure of the dielectric barrier surface and its material. In a range of works [2, 3] a marked influence of the roughness of the dielectric barrier surface on the secondary electron emission from dielectric coated electrodes has been shown. But it is difficult to explain only by secondary electron emission the change in the microdischarge structure and intensity when an additional dielectric layer is deposited on the barrier. The aim of the present work was to analyse a possibility of additional ionization processes in gas near the dielectric barrier surface due to electric field created by protrusions (or juts) on the surface of the barrier and to connect the change in the surface discharge characteristics with a change in the barrier surface structure.

2. Experimental results used in the analysis

Barriers used in [1] were in a form of Alumina or Pyroceramics (glass ceramic composite - polycrystal silicium oxide) plates 1.1 mm of thickness with different surface roughness and covered by films of SiO_2, TiO_2, Barium-Strontium Titanate (BST) or Al_2O_3. The films were deposited on the barrier surface by a radio-frequency ion-plasma sputtering method. The thickness of the films was about (70-100) nm. High voltage up to 3 kV, its frequency 14 kHz, was used to initiate surface discharge from the edges of the surface grounded electrode, while the HV electrode was at the reverse side of the plate. Photos of the surface discharge made with a Panasonic LUMIX DMC-FS3 camera are given in Fig.1 and show distinct change in the structure of microdischarges and in their intensity for different films.
To explain the results presented in [1] careful measurements of all barrier surface structures by means of a laser scanning microscope LEXT OLS3100 were carried out. An example of the surface profile for Alumina barrier is given in fig. 2 where all main parameters of the profile used in the analysis are indicated. Values of H_i were measured relative a middle line of the profile *m*. Each value in table 1 is a mean one for at least 5 different profiles measured for a given surface. Besides, two significant characteristics of the profile that are connected with the roughness of the surface were estimated using the measured profiles: the mean value H_{mean} of the height of the juts relative the middle line of the profile and the mean radius of the curvature of the jut tip *r*. It must be noted that there was registered a big variety of profiles for each surface. So each value in table 1 is a mean one that correspond to a unit region of the surface equal to 250 x 250 μm. The parameters of the measured profiles show strong dependence on the roughness of the barrier surface and on the type of the film that is additionally deposited on the surface.

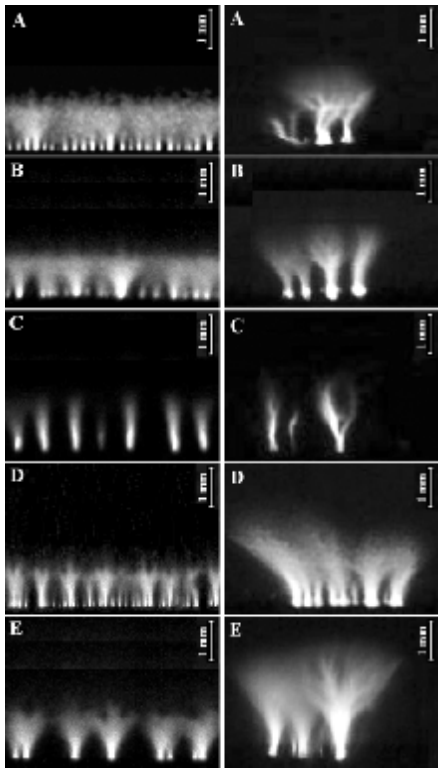


Fig. 1. Images of discharge across barriers with films of Alumina (left) and rough Pyroceramics (right). A - without a film, B – BST film, C – TiO_2 film, D – Al_2O_3 film, E – SiO_2 film.

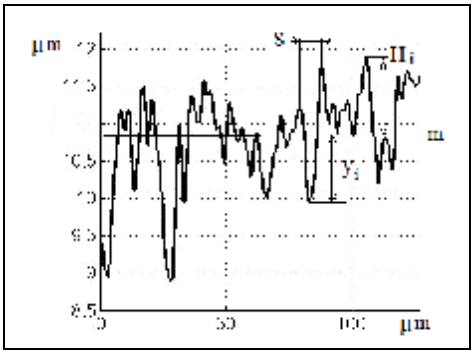


Fig. 2. An example of measured Alumina barrier surface profile and its main parameters.

Tab. 1. Characteristics of surface structure of barriers.

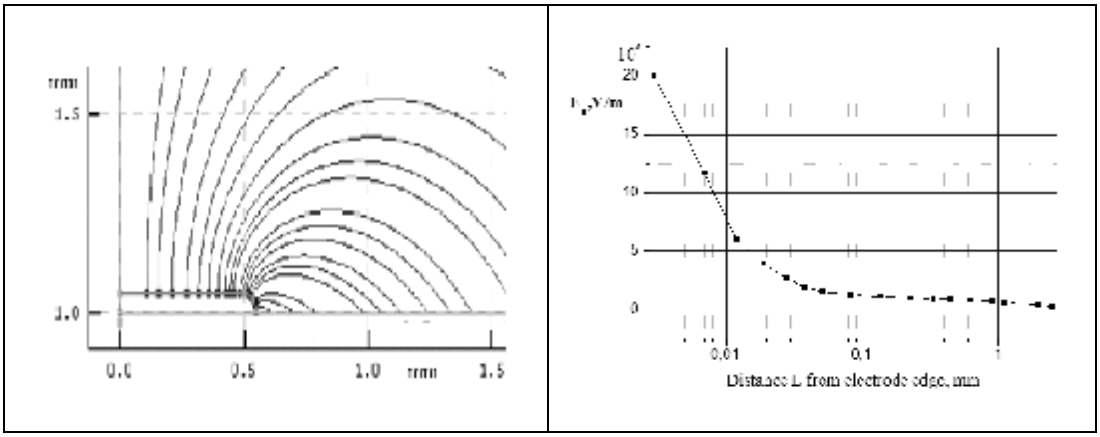
Material of the barrier surface	H_{mean} , μm	r, μm	S_m
Alumina without a film	0.8	1.8	13.5
Al_2O_3 on Alumina	1.0	0.25	8.0
BST on Alumina	0.8	2.1	11.0
TiO_2 on Alumina	1.4	1.5	11.5
SiO_2 on Alumina	1.0	1.2	12.0
Pyroceramics without a film	1.5	6.3	32
Al_2O_3 on Pyroceramics	1.5	5.1	34
SiO_2 on Pyroceramics	1.4	8.8	36

3. Discussion

Elucidation of the role of surface structure in the discharge behaviour is based on an assumption that there is an additional ionization in air in the vicinity of the barrier due to the barrier surface roughness. The possibility of such process requires an analysis of electric field distribution in the air gap above

the barrier surface for the electrode arrangement used in present work. The procedure used to evaluate the field strength values (E) near barrier surface included two steps. The first step was to calculate the electric field distribution created by the electrode in the gas above the barrier and to evaluate its normal component. The second step was to analyse the local fields near tips of single juts. The superposition of these two fields permits to evaluate the field near the surface protrusions. A detailed description of the 2D model and the procedure used to calculate the electrostatic field distribution near the electrode edge and the model to calculate the field near the jut tips are given in [4, 5]. We produce here only the main results of the calculations based on the above models and done for measured profiles of the used barrier surfaces.

The main force lines of the electric field formed by the electrode edge near an Alumina barrier for applied voltage U=2.5 kV are given in fig. 3a, whereas in fig. 3b the normal component of E at the barrier surface for different force lines is presented. The surface roughness is not taken into account.



a) b)

Fig. 3. Distribution of the applied electric field force lines (a) and normal component values E_n at the barrier surface. The electrode thickness is 10 μm.

Pictures of the calculated electrostatic field distribution near juts on the rough surface of Pyroceramics and Alumina barriers without a film are presented in fig. 4 as an example. The light regions in fig. 4 are for higher values of the field and show that only relatively high juts on the surface ("significant" juts) create high field near their peaks whereas small juts and the juts in the hollows are screened by high juts. In the following analysis only significant juts were taken into consideration to compare the situation near the surface of different barriers. So the values H_{mean} in table 1 correspond to mean values of all "significant" jut heights H_i above the middle line of the profile. As a "significant" height $H_i > 0.5\ H_{max}$ was taken where H_{max} is the maximal height value for juts in a given profile. The values in table 1 of radii of curvature of the jut peaks r and the mean distance between them S_m are also for "significan" juts.

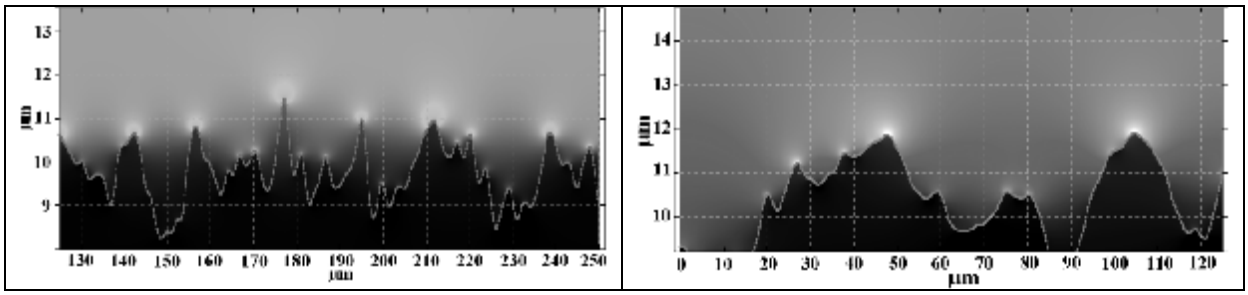


Fig. 4. An example of calculated electrostatic field distribution near surface of Alumina (left) and rough surface of Pyroceramics (right) without a film.

The calculated field distribution near barrier surface was used to analyse the field near single juts as a function of distance t from the jut peak away into the gap along a line perpendicular to the barrier (fig.5). The parameters of each jut are as in table 1.

The values of the electrostatic field $E^*=E/E_{gas}$ are normalized to the field value E_{gas} that corresponds to the field in the air gap away from the barrier surface where the field is not influenced by the barrier structure. E_{gas} corresponds to data shown in fig. 3. The E^*_{max} values near the peaks of the juts can be up to 4.6 times higher than the mean value of the field E_{gas} and fall down practically exponentially with t (fig. 5). Calculations show that $E^*=f(t)$ curves depend on three factors: the whole surface profile of the analysed barrier, the height of the jut in view (fig. 6), on the radius of its peak and, to some extent, on the distance between neighbour juts.

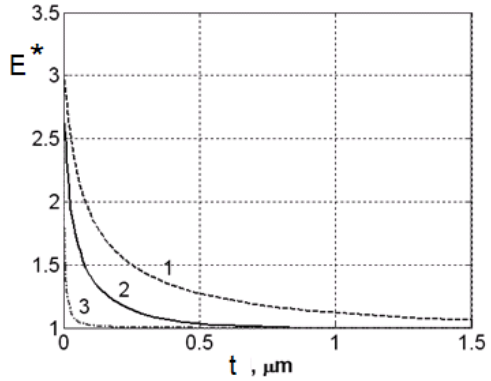


Fig.5. Field distribution neat a single jut as a function of the distance from the jut tip.
1- rough Pyroceramics, 2 – Alumina, 3 – smooth Pyroceramics

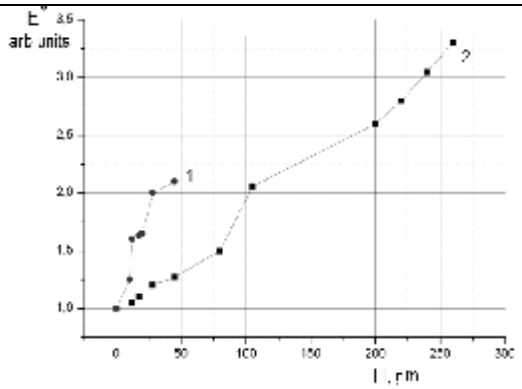


Fig.6. Maximum values of E^* as a function of the jut height for smooth (1) and rough (2) Piroceramics barriers

When a film is placed on the barrier surface the surface structure is changed and it leads to a change in E*(t) curves but this change is seen only near the jut tip (fig. 7).

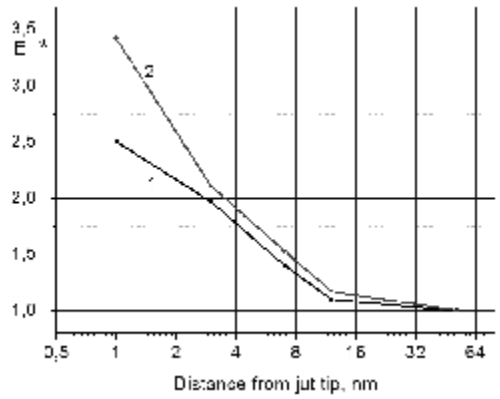


Fig.7. Influence of a Al_2O_3 layer on the field distribution near the gut tip. 1- Alumina without a cover, 2 - with a layer of Al_2O_3

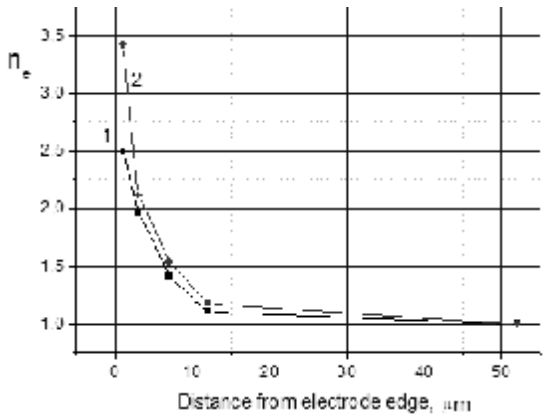


Fig.8. Number of electrons created near one jut at different distances from electrode edge.
1-Alumina without cover, 2-with a layer of Al_2O_3

Calculations show that there is a certain influence of the dielectric constant ε of the film on the field distribution near the jut tip. The E^*_{max} values and E^* values at a distance 0.1 μm from the jut tip are given in table 2 for different layers on the Pyroceramics barrier.

Table 2. Influence of layer characteristics on the field neat a jut tip.

ε of the layer material	ε = 500	ε=80	ε=4	without layer (ε=9)
E^*_{max}	4	3.8	2.95	2.35
E^* at 0.1 μm from jut tip	1.45	1.4	1.2	1.3

In a whole the electric field that governs the microdischarge appearance near the electrode edge and the microdischarge development across the barrier surface is a superposition of three fields: the applied field at the electrode edge, the field of charges left on the barrier during the previous half-cycles of the applied voltage and the field created by juts on the barrier surface. It is possible to compare the field along a certain force line calculated in the present work (without the surface charges taken into account) and the one given in [5] for the charges on the surface being taken into account. The comparison shows that the difference is not more than 30% and corresponds to the regions on the barrier surface where the charge density on the surface is maximal.

If all components of the summary field near the jut tips are summarized using values from fig.3b and fig.5 than the values of the reduced field *E/N* where *N* is the number of the molecules in the gas for normal conditions p = 760 mm Hg and t = 293K, permit to evaluate the values of ionization coefficient α/N using well known dependence of $\alpha/N = f(E/N)$. The next step is to evaluate the number of ion pairs created by ionization according to the equation

$$n = \exp\left(\int_{t_1}^{t_2} a\left(E\right) \cdot dt \right),$$

where t_1 corresponds to the jut tip and t_2 corresponds to a point where the value of the field $E^* = 1.01\ E^*_{max}$. The results of such calculations for juts at different distances from the electrode edge along the barrier surface are given in fig. 8 and are for one single jut. It is seen that at least one new electron can be created in the field near the jut. As the development of the microdischarge channel goes over a surface with many juts the number of charges created by ionization depends on the number of juts on a surface which in its turn is defined by the distance *S* between neighbour juts. A very rough estimation shows that summary values of charges that can be created in gas above barrier surface area with dimensions 1 mm x 30 μm (along the electrode edge) are in the range 280 for Alumina barrier and 712 for the same barrier with an Al_2O_3 film on its surface. As the additional charges in the gas where the microdischarge channel develops can influence the discharge [6], the intensity of this influence depends on the characteristics of the barrier surface.

4. Conclusion

The role of the surface structure of the barrier and its chemical composition in the microdischarge behaviour is proposed to be connected with the production of additional charges in ionization processes that go on in high electric field near juts on the barrier surface, the values of this summary field being dependent on the parameters of the surface layer. The other factor to change the discharge behaviour is the chemical composition of the barrier surface layer. As the memory effect of the surface charge left on the barrier surface defines the position of microdischarge channels relative the barrier surface it can concluded that films of different chemical composition create different conditions for the charge accumulation on the surface which leads to a change in the electric field near surface juts. Calculations show a possibility of such influence.

5. References

[1] M.V. Sokolova, K.V. Kozlov, S.A. Krivov, L.A. Maslova, A.N. Mitin, P.A. Tatarenko, V.G. Samoilovich. 2010 *Proc.of the 12th Int.Symp.on High Pressure Low Temperature Plasma Chemistry* . Slovakia **1** 84-88

[2] J.M. Elizondo, K. Meridit, N. Lapetina. 2002 *IEEE Trans. on plasma sci.* **30** No 5 1955

[3] R. Josepson, M. Laan, J. Aarik, A. Kasikov. 2008 *J.Phys. D: Appl. Phys.* **41** 135209

[4] S.A. Krivov, V.S. Larin, M.V. Sokolova, L.L. Chernensky, and M.A. Egorova. 2010 *Technical Physics Letters*, **36,** No. 2 126–129.

[5] A.N. Mitin, M.V. Sokolova. 2012 *Technical Physics Letters.* **38**, No. 5 474–477.

[6] N.L. Allen, A.A.R. Hashem. 2002 *J.Phys. D: Appl. Phys.* **35** 2551-2557

Acknowledgements

The work has been done with a financial support of Russian Fund of Basic Researches, grant No 11-08-00156.

SIMULTANEOUS REMOVAL OF ACETALDEHYDE AND ACETYLENE BY AN ATMOSPHERIC PULSED DISCHARGE

Touchard S., Klett C., Jia Z.,Vega-Gonzalez A., Hassouni K., Duten X.

Laboratoire des Sciences des Procédés et des Matériaux, CNRS UPR 3407 – Université Paris 13, 93430 Villetaneuse, France

E-mail: touchard@lspm.cnrs.fr

The present work proposes to study the efficiency of a corona discharge working in a pulsed regime to eliminate 1000 ppmC of an equimolar mixture of acetylene (C_2H_2) and acetaldehyde (CH_3CHO) present in a N_2 gas stream containing 5% of oxygen. In these experimental conditions, a specific input energy around 200 J/L has been sufficient to remove 99% of the initial acetaldehyde and 66% of the initial acetylene. The simulations performed by using a quasi-homogenous model have showed that acetaldehyde is mainly removed by short lived excited species generated during the pulse time, while acetylene is mainly destroyed by oxygenated species (O, OH) during the post-discharge time.

1. Motivation

Among the air and industrial exhaust gas possible treatments, atmospheric plasma processes have been the subject of many studies for the last two decades and have demonstrated their good efficiency for the removal pollutant molecules diluted alone in N_2/O_2 gas flows [1]. Concerning the removal of a mixture of pollutants by atmospheric discharges, even if some studies have been proposed since a decade [2-5], few of them have concerned processes at ambient temperature and atmospheric conditions [6-7]. In this context, this work have been focused on the efficiency of an atmospheric pulsed discharge to remove 1000 ppmC of acetaldehyde and acetylene, two representative molecules of volatile organic compounds emitted in the exhaust gas [8-9].

2. Experimental part

The experimental setup is described briefly here. For more details see [10-12].

The reactor used in the present work consists in a 100 µm diameter tungsten wire anode placed in a 20 mm diameter cylindrical steel cell (Figure 1). The pulsed atmospheric discharge is generated by a Marx generator delivering 20-30 kV voltage on the cathode. The typical current rise time is around 5 ns. The mean pulse duration is around 200 ns. The discharge repetition rate can be varied between 1 and 20 pulses per second. Mean electrical energy provided in the discharge at each pulse vary between 15 mJ and 20 mJ.

The gas inlet is mainly composed by a 1000 ppmC of acetylene and/or acetaldehyde mixture diluted in a N_2 flow containing 5% of O_2.

In the outlet flow, residual pollutants and other oxidation end products are identified via a Shimadzu GC-2110 Gas chromatography device. The continuous monitoring of CO and CO_2 concentrations is done by a multi-gas analyser provided by Environnement S.A.

Process efficiency is evaluated by measuring the pollutants residual concentrations and the $CO+CO_2$ global selectivity as a function of the specific input energy which corresponds to the energy deposited per unit volume of gas flow treated in the discharge cell. It is obtained from the discharge pulse frequency in Hertz, the energy deposited per pulse in J and the gas flow rate in L per second using the following expression:

$$SIE\ (J.L^{-1}) = \frac{Pulse\ energy\ (J) \times Frequency\ (Hz)}{Flow\ rate\ (L.s^{-1})}$$

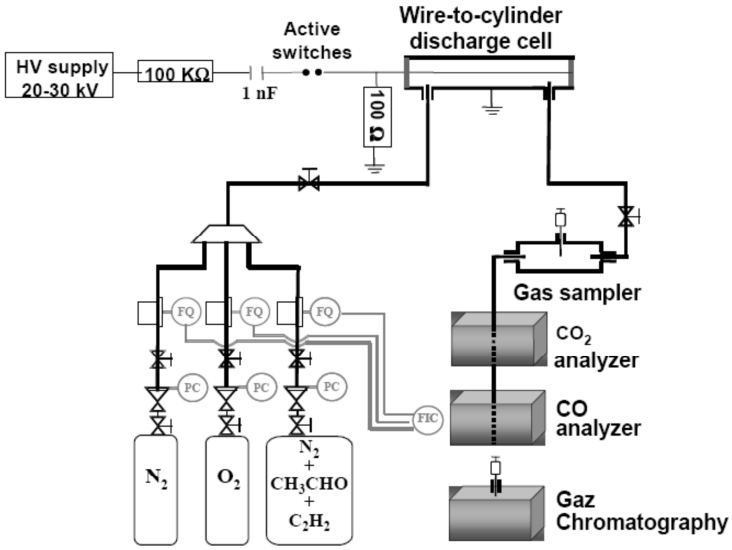


Fig. 1. Experimental set-up for investigation of mixture oxidation in WTC corona discharge.

3. Experimental results

One of the main objectives of this work was to evaluate the efficiency of the discharge to remove simultaneously equivalent amount of two different pollutants. First experimental results obtained in our plasma configuration are reported on figure 2 which represents the residual amounts of both pollutants when 500 ppmc of acetaldehyde and 500 ppmC of acetylene are initially alone and in mixture in the gas flow inlet. According to this figure, when pollutants are both diluted in the initial N_2/O_2 gas flow, the discharge is globally more efficient to remove acetaldehyde than acetylene. Thus, at a specific energy of 150 J/L, 96% of initial acetaldehyde is removed, whereas for a specific energy of 200 J/L only 65% of the initial acetylene present in the flow has been removed.

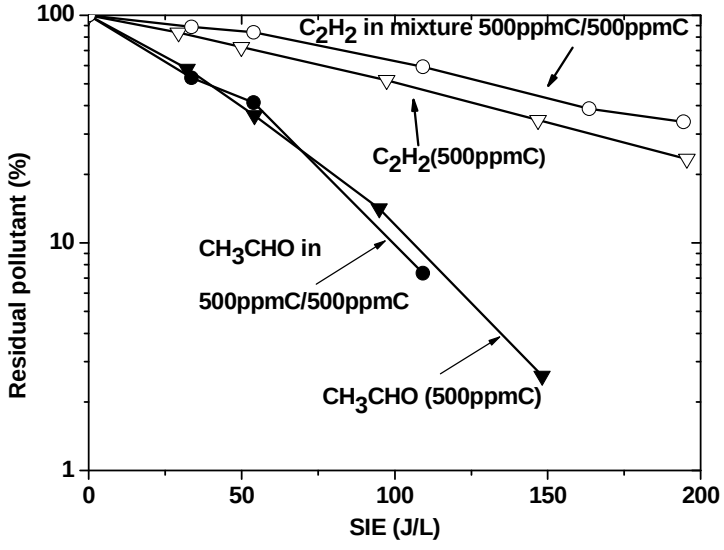


Fig. 2. Comparison of degradation of 500 ppmC of acetaldehyde and 500 ppmC of acetylene alone and in mixture in a 94.5% N_2/5%O_2 gas flow.

The figure 3 represents the influence of the initial concentration of each pollutant, injected as a single molecule. We observe that, whatever the studied pollutant, doubling the initial amount of carbon to convert leads to a depletion of plasma efficiency. This means that, at constant energy deposited in the discharge, concentration of active species are not high enough to oxidise with the same efficiency 500 ppmC and 1000 ppmC of pollutant.

Nevertheless one exception must be noticed, since, according to figure 2, the plasma allows removing 500 ppmC of acetaldehyde with the same efficiency whether alone or mixed with acetylene into the initial gas flow.

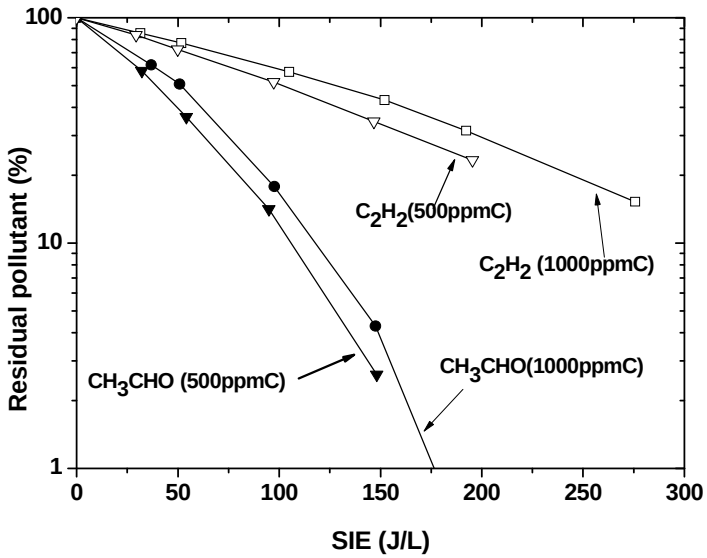


Fig. 3. Comparison of the degradation of both pollutants when individually dilute in a 94.5% N_2/5%O_2 gas flow for two different initial concentrations (500 and 1000 ppmC).

To understand this difference of reactivity, a modelling study of the process has been achieved.

4. Modelling part

To improve our knowledge of the chemical phenomena occurring in the discharge, a modelling study has been achieved with a quasi-homogeneous 0D chemical model [10-12] taking into account 90 species involved in 460 reactions.

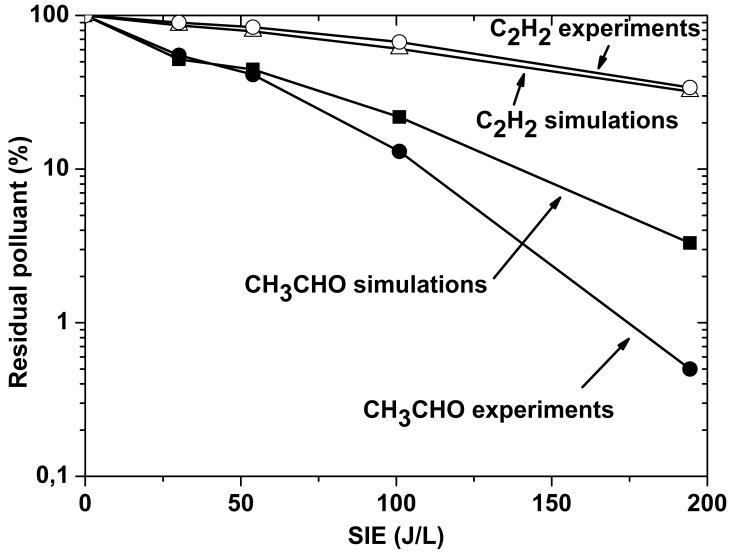


Fig. 4. Comparison between simulations and experiments for a mixture containing 500 ppmC of CH_3CHO and 500 ppmC of C_2H_2.

This model has been validated by the good accuracy observed between simulations and experiments for the pollutants removal results (see figure 4).
The reliability of this model has allowed us to use it to compute the consumption flow of the two pollutants in a streamer area (figure 5 and 6) during one period between two successive pulses generation.

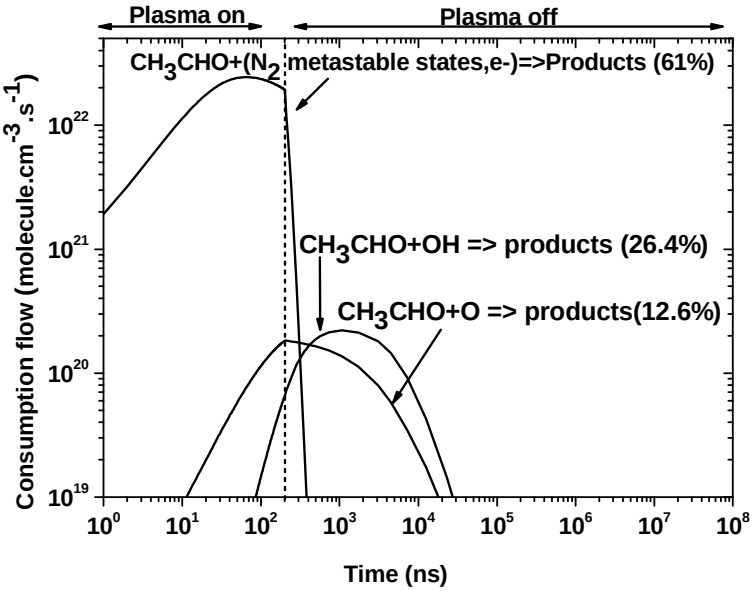


Fig. 5. Computed consumption flow of acetaldehyde for an initial mixture containing 500 ppmC of acetaldehyde and 500 ppmC of acetylene in a 94.5% N_2/5%O_2 gas flow

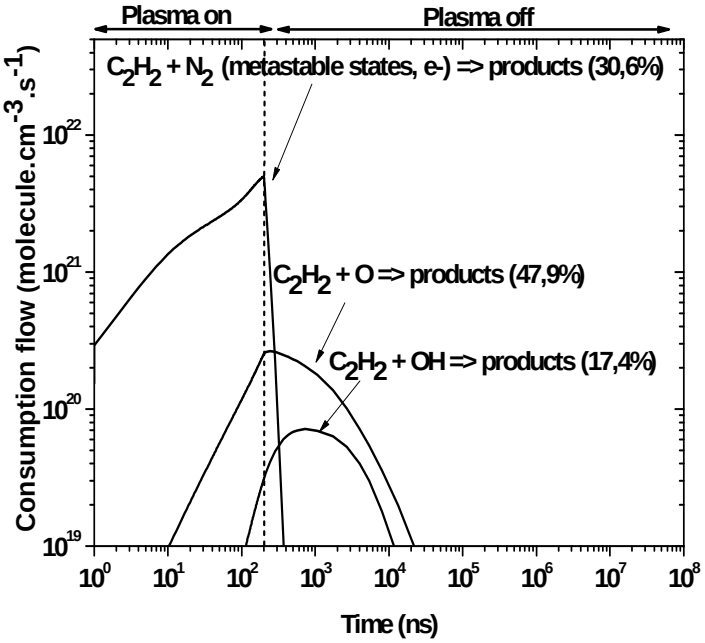


Fig. 6. Computed consumption flow of acetylene for an initial mixture containing 500 ppmC of acetaldehyde and 500 ppmC of acetylene in a 94.5% N_2/5%O_2 gas flow

The analysis of the computed consumption profiles represented figure 5 and figure 6 indicates that both pollutants are consumed during the discharge and the post-discharge time. But around 60% of acetaldehyde initially present in the streamer area is consumed during the discharge phase by reactions with short live active species (mainly electron and N_2 metastable state), whereas only 30% of initial acetylene is consumed during this period with a consumption flow one order of magnitude lower than

for acetaldehyde. Consequently acetylene is mainly consumed during the post discharge time by reaction with O and OH, but theses processes are directly in competition with acetaldehyde consumption reactions with the same radicals. In addition, according to kinetic parameters (see table 1) for these processes, reactions with acetaldehyde are respectively 100 and 3 times more rapid than the one with acetylene. Consequently for each pulse acetaldehyde is three times more consumed than acetylene.

Tab. 1. Kinetics data for main pathways of pollutants decomposition.

Reaction	k_{300} (cm^3.molecule.s^{-1})	Reference
C_2H_2 + O => products	$1.45x10^{-13}$	[13]
CH_3CHO + O → products	$4.5x10^{-13}$	[13]
C_2H_2 + OH => products	$1.07x10^{-13}$	[14]
CH_3CHO + OH → products	$1.62x10^{-11}$	[15]

5. Conclusion

This study shows the possibility of eliminating simultaneously two representative molecules of pollutants by an oxygenated pulsed corona discharge. As for individual removal of each pollutant, in mixture conditions, acetaldehyde is more efficiently removed than acetylene by the discharge. Concerning individual chemical behaviour of each pollutant, mixing has better benefit for acetaldehyde which is decomposed more rapidly than acetylene, consuming the radicals which could react with acetylene. This behaviour has been observed by Wang and al. [6] for mixtures of BTX where xylene decomposition kinetics is slowed down by the presence of benzene and toluene. The analyses from our kinetic model suggest that differences observed between pollutant decomposition kinetic is due to the fact that acetaldehyde is decomposed rapidly during the pulse period and reacts with O and OH two times more rapidly than acetylene during the post discharge period. The competition between the two pollutants for reacting with these radical being in favour of acetaldehyde, this could explain why acetylene is less converting in a mixture.

6. References

[1] Vandenbroucke A M, Morent R, De Geyter N and Leys C 2011 *J. Hazard. Mat.*, **195** 30-54
[2] Sano N, Nagamoto T, Tamon H, Suzuki T and Okazaki M 1997 *Ind Eng Chem Res* **36** 3783-3791
[3] Hoard J, Wallington T J, Bretz R L, Malkin A, Dorai R and Kushner M J 2003 *J. of Intern. Chem. Kin.* **35** 231-238
[4] Ogata A, Ito D, Mizuno K and Kushiyama S 2002 *Applied Catalysis A: General* **236** 9-15.
[5] Sobacchi M G, Saveliev A V, Fridman A A, Gutsol A F and Kennedy L A 2003 *Plasma Chemistry and Plasma Processing* **23** 347-370.
[6] Wang H, Li D, Wu Y, Li J and Li G 2009 *Journal of Electrostatics* **67** 547-553.
[7] Chen J, Yang J, Pan H, Su Q, Liu Y and Shi Y 2010 *J. Hazard. Mat.*, **177** 908-913
[8] Graham L A, Belisle S L and Baas C L 2009 *Atmospheric Environment* **42** 4498-4516
[9] Schmitz T, Hassel D and Weber F J 2000 *Atmospheric Environment* **34** 4639- 4647
[10] Redolfi M, Aggadi N, Duten X, Touchard S, Pasquiers S and Hassouni K 2009 *Plasma Chemistry and Plasma Processing* **29** 173-195
[11] Klett C, Touchard S, Vega A, Redolfi M, Duten X and Hassouni K 2011 *Acta Technica* **56** 43-55
[12] Klett C, Touchard S , Vega-Gonzalez A , Redolfi M , Bonnin X , Hassouni K and Duten X 2012 *Plasma Sources Sci. Technol.* **21** 045001
[13] DeMore W B, Sander S P, Golden D M, Hampson R F, Kurylo M J, Howard C J, Ravishankara A R, Kolb C E and Molina M J 1997 JPL Publication **97-4** 1-266
[14] Bohn B, Siese M and Zetzsch C 1996 *J. Chem. Soc. Faraday Trans*. 1459 – 1466
[15] Baulch, D L, Cobos C J, Cox R A, Esser C, Frank P, Just T, Kerr J A, Pilling M J, Troe J, Walker R W and Warnatz J 1992 *J. Phys. Chem. Ref. Data* 411 – 429

OPTIMIZATION OF SONICATION TREATMENT PROCESS TO SATURATED FREE FATTY ACIDS DEGRADATION AS AN APPLICATION IN GREASE TRAP PURIFICATION

Michał Piotr Kwiatkowski[1], Saburoh Satoh[2], Chobei Yamabe[1,3], Satoshi Ihara[1], Masanori Nieda[3]

[1] *Graduate School of Science and Engineering, Saga University, 1 Honjo-machi, Saga 840-8502, Japan*
[2] *Agency of Liaison and Innovation in Saga, Saga University, 1Honjo-machi, Saga 840-8502, Japan*
[3] *Ohnit Co. Ltd, 3-3-765 Sakuragaoka-Higashi, Akaiwa-shi, Okayama 709-0721, Japan*
E-mail: yamabec@cc.saga-u.ac.jp

The optimization of sonication process was studied for saturated fatty acids degradation. The saturated fatty acids are the most hard-degradable compounds of the fats, oils and greases (FOG) from the grease trap device. The influence of the various parameters, especially immersion level of the ultrasound probe into the liquid and simultaneous bubbling of various gases (Ar, O_2, air, O_3) on the sonochemical and energy efficiency of the sonication process were investigated. Finally, the best parameters were selected to decompose hydrophobic compounds such as saturated free fatty acids. Treatment results of fatty acids were analyzed by GC/MS. The most effective degradation treatment method for saturated free fatty acids, as it turned out, was a sonication simultaneously with low flow rate of argon bubbles and with ultrasound probe deep immersion level into the liquid under controlled temperature process.

Keywords: sonication, grease trap, free fatty acids degradation, hydrophobic compounds, argon, ozonation

1. Introduction

The presence of hardened and insoluble fats, oils and greases (FOG) that deposit in sewerage is a main cause of pipes blockages. To resolve this problem, grease trap devices based on various treatment methods, e.g. physical gravity separation or application of microbial cultures and enzymes is used.

Recent studies discovered that saponification reaction between free fatty acids and metal ions was response of FOG deposit formation [1]. To prevent this phenomenon, the free fatty acids, which are the major and the most hard-degradable components of FOG, must be removed or degraded. The conventional type of grease trap based on physical gravity separation is inefficient in removing oil droplets less than 10 μm diameter in fine oil-in-water colloidal suspension and less than 20 μm diameter in the wastewater containing surfactants. The biological treatment (biodegradation rate with microbes) is satisfactory but it is time dependent, and is the best degradation method only if a large space is available and the investment timeframe is sufficiently long as well. Therefore, the common methods such as physical gravity separation and biological treatment grease trap do not give a perfect solution for FOG removal/degradation. An alternative such as carried out in this paper needs to be invented to tackle this unsolved problem.

Various studies and patents have addressed the sonication removal methods of oil-in-water colloidal suspension of wastewater, based on separation of FOG phase from water phase due to hydrophobic character of FOG [2-3]. The best removal method is sonoelectrocoagulation, based on sonication simultaneous with electrolysis, which give 100 % removing of FOG from grease trap [4]. However, while a large number of studies have been referred to sonication removal methods, very few work has been done on the evaluation of sonication grease trap treatment method based on FOG degradation and lack of data. Previous research [5] was proven that hybrid AOP sonication/ozonation was a suitable treatment degradation method using only electric power for the effective degradation of free fatty acids in the water medium. However, low mass degradation efficiency of saturated free fatty acids was contributed to the development of grease trap purification by sonication such as carried out in the present work.

2. Experimental setup and methods

2.1 Ultrasonic device and reaction system

The ultrasonic power supply converts 50/60 *Hz* voltage to high frequency electrical energy at constant value of 20 *kHz* and controls the ultrasound amplitude ζ at the probe. Electrical power delivered to the transducer P_{DT} was measured by the Ultrasonic Processor and data were collected by Graphtec midi Logger GL200A.

Reaction system shown in Fig.1 was made up of glass tubular reactor (22 *cm* length, Ø 3.3 *cm*). In the central, from the top of the reactor, the ultrasonic probe connected with the reactor by silicon tube was placed. In the bottom of the reactor in the blank silicon plug, the temperature probe (K type thermocouple connected with Graphtec midi Logger GL200A) and stainless cylindrical gas filter (Flowell, Japan, Ø 1.2 *cm* with 2 μm pore size) was installed. In the experiments with simultaneous bubbling, small gas bubbles (air, oxygen, argon and

ozone) were generated by 2 μm pore in the stainless filter under constant flow rate 0.1 *l/min*. The gas outlet was introduced from the top of silicon tube through the condenser. Water in the condenser was kept at 5 °*C*, which removed vapor from the gas phase and turned back to the reactor. The reactor was located in the tubular cooling water bath (25 *cm* length, *Ø* 12 *cm*) with cooling water at 20 °*C*.

2.2 Materials

A 0.1 *M* potassium iodide aqueous solution was purchased from Kanto Chemical (Japan). Two saturated fatty acids (palmitic acid C16:0, stearic acid C18:0) were used in this study and were purchased from Wako Pure Chemical Industries (Japan). Derivatization agent hydrogen chloride – methanol (1.4 *N*, HCl: 5~10 %) was purchased from Tokyo Chemical Industry (Japan). Analytical standards F.A.M.E. mix RM-6 (Supelco), nonadecanoic acid, hexan, luminol (3-aminophthalhydrazide) and sodium carbonate monohydrate were purchased from Sigma Aldrich (USA). Purified water (class A2, conductivity ≤ 0.1 *mS/m*) purchased from Takasugi-Seiyaku (Japan) was used for all experiments.

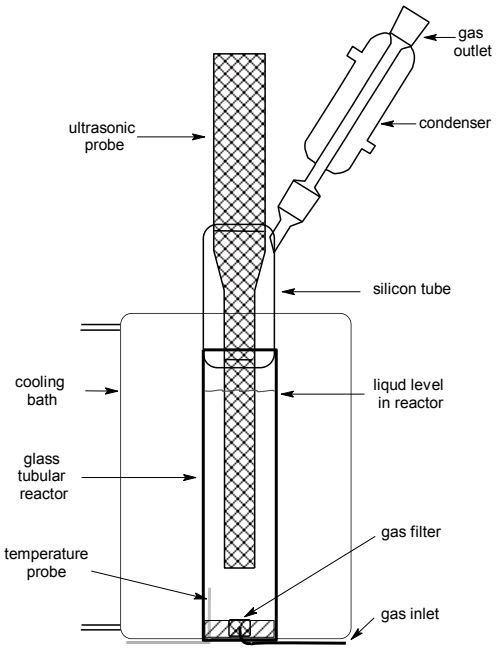


Figure 1: Reaction system setup (with high immersion level of the ultrasound probe into the liquid).

In the experiment with ozonation process, ozone was generated by dielectric-barrier discharge ozone generator Sensui AS-500SS (Ohnit, Japan) from mixture gas (N_2:O_2 4:1 *w/w*) with 2.5 *l/min* flow rate (controlled by digital mass flow controller, Yamatake CMQ, Japan) under atmospheric pressure. The ozone gas concentration was measured by ozone UV monitors (Ebara Jitsugyo, model-600, G6SHE-T, Japan connected with Graphtec Midi Logger GL200A for collecting data) on the inlet and the outlet of reaction system. Residual ozone was decomposed by the ozone destructor.

2.3 Experimental parameters and Measurement methods

Optimization of sonication process was investigated under various procedures and parameters:

- ultrasound amplitude, ζ (70 % and 90 %, where $\zeta_{100\%} = 124\ \mu m$)
- with/without temperature process control (by cooling water bath at 20 °*C*)
- process time, *t* (10, 20, 30 minutes)
- procedure with simultaneous bubbling of argon, oxygen, air (N_2:O_2 4:1 *w/w*) and ozone
- immersion level of the ultrasound probe into the liquid (low 2.5 cm and high 10 *cm*)

2.4 Sonochemical and Energy efficiency

Standard methods (calorimetry and KI dosimetry [13]) are used to obtain sonochemical and energy efficiency of reaction system. The ultrasonic power dissipated into liquid P_{US} (*W*) is calculated by the following equation.

$$P_{US} = mC_p[dT/dt] \quad (1)$$

Where, *m* is the mass of water (*g*), C_p is the heat capacity of water (4.2 *J/g K*), *dT/dt* is the temperature slope of water per unit of sonication time (*K/s*). In this work, the sample volume is 0.1 *l*. The initial temperature is measured using a thermocouple (K type) and the average value is 20 ± 0.5 °*C*. Measurement is carried out at first minute of sonication process. To convert P_{US} and P_{DT} to power density *D (W/l)*, the power is divided by the sample volume *V* (*l*).

$$D_{US} = P_{US} / V \quad (2) \qquad D_{DT} = P_{DT} / V \quad (3)$$

The energy efficiency η_P is calculated from ultrasonic power density dissipated into liquid D_{US} and electrical power density delivered to the transducer D_{DT} at first minute of sonication process, it is shown by the following equation.

$$\eta_P = D_{US} / D_{DT} \quad (4)$$

The KI dosimetry method is one of the measurement methods of sonochemical efficiency of sonication process by calculation of triiodide ion concentration C_I. When ultrasound is irradiated into aqueous KI solution, I^- ions are oxidized to give I_2. When excess I^- ions are present in solution, I_2 reacts with the excess I^- ions to form I_3^- ion.

$$^{\bullet}OH + I^- \rightarrow OH^- + I \quad (5) \qquad I + I^- \rightarrow I_2^- \quad (6)$$

$2I_2^- \rightarrow I_2 + 2I^-$ (7) $I_2 + I^- \rightarrow I_3^-$ (8)

Hydroxyl radicals are considered to be the main oxidizing species generated during the sonolysis of aqueous solution. Nevertheless, when KI solution is under ultrasound irradiation and simultaneously with ozonation, the pathway of I_2 creation is determined by the following directly ozone reaction.

$O_3 + 2I^- + H_2O \rightarrow O_2 + OH^- + I_2$ (9)

The absorbance A of I_3^- ion is measured at 355 nm (ε = 26.303 *l/mol cm*) by using spectrophotometer (Hach, DR/4000U, USA) and concentration of triiodide ion C_I (*mol/l*) is calculated by the following equation.

$C_I = A / (\varepsilon\, b)$ (10)

Where A is the absorbance of I_3^-, ε is a molar absorption coefficient of I_3^- ion and b is path length of the spectrophotometer (measurement cell b = 1 *cm*).

The total efficiency of sonication process $\eta_{tot.}$ (*mol/J*) is described by the following equation.

$\eta_{tot} = C_I / (D_{DT}\, t)$ (11)

Where t is the sonication time.

After optimization of sonication process, the best conditions were chosen to run degradation treatment of saturated free fatty acids.

2.5.2 Sonochemiluminescence (SCL), Sample preparation and Sample analysis

The sonochemically active zone in the reactor was imaged by SCL method. The immersion level of the ultrasound probe into a liquid was at 10 *cm* and 2.5 *cm* under various processes such as sonication only, sonication simultaneously with argon bubbles, sonication simultaneously with ozone bubbles and ozone bubbling only. Experiment was run under constant amplitude $\zeta_{70\%}$ = 86.8 μm, constant gas flow rate 0.1 *l/min*, and ozone concentration 1.1 *g/ N* m^3. A luminol solution containing 0.1 g/l luminol and 0.5 g/l sodium carbonate in purified water was used.

Under ultrasound irradiation, luminol molecules react with *OH radicals generated from sonolysis of water molecules, transform to excited-state fluorescing 3-aminophthalate (3-APA), and then stabilize as 3-APA through emitting visible light called SCL. Because this reaction is related to OH radicals or other oxidizing radicals species generated by ultrasonic cavitation phenomena or ozone itself, the brighter regions indicate the active zones.

Samples were prepared in glass jar (1 *l*) with 1 *l* purified water and adding about 5 *g* of fatty acid, which is adequate concentration of the FOG in the wastewater from the restaurant cooking area. Palmitic and stearic acids have high melting points (62.9 °*C*, 69.6 °*C*, respectively) and under this temperature, fatty acids are in solid phase (granulated product). For saturated fatty acids, homogenization process started when temperature rose higher than 65 °*C*, as in the preview study was observed. To get fine oil-in-water colloidal suspension for saturated free fatty acids, it is necessary to run process above saturated fatty acids melting point. Hence, the glass jar with sample was heated in water-bath up to 75 °*C* and when temperature was stabled, homogenization process was run under "low" sonication conditions (3 minutes sonication time with 1 *cm* ultrasound probe immersion into the sample, P_{DT} = 65 *W*) to minimized degradation effect. Afterward, sample was cooled down under magnetic stirring. After cooling down to the room temperature (below to the saturated fatty acids melting point), emulsion (liquid-liquid colloidal suspension) was changed to sol (solid-liquid colloidal suspension). However, the colloidal suspension breaking was not achieved. Homogenization process was run without any homogenization agent and samples had to be kept under continuously magnetic stirring to prevent the samples from colloidal suspension breaking. Colloidal suspension stability was proven by viscosity measurement (Rheometer, Anton Paar MCR Physica 101, Austria). For the fine colloidal suspension, where water is continues phase (dispersion medium), the viscosity accepts the continuous phase viscosity. The viscosity of the saturated fatty acid sol at 20 °*C* was 1.273 ± 0.090 *cP* (viscosity of water at 20 °*C* is 1.002 *cP*) and stability of the colloidal suspension was proven.

Samples were prepared in the following way to eliminate energy spend on emulsification process during the treatment process. Each fatty acid was prepared separately and then was used to treatment process with samples volume of 100 *ml* each. After each treatment procedures, 0.5 *ml* samples were collected immediately in 4 *ml* vials and stored under -20 °*C* until GC/MS analysis. Zero samples were collected in the same way before each treatment processes. All samples were collected double. Every treatment procedure was repeated and analyzed for three times and average percent of fatty acids mass degradation rate was estimated by compared results to the zero samples.

3. Experimental results and discussion

3.1 Simultaneous bubbling of various gases

As was described in previews paper, under sonication process simultaneously with gas bubbles high flow rate 1.5 *l/min*, the high cavitation phenomena disruption was observed by reduction of one-third energy efficiency, and the higher energy was delivered to transducer instead of lower temperature process[5]. Generated relatively small bubbles by the stainless gas filter with flow rate at 0.1 *l/min* in the sonicated liquid (see Figure 1), was not influenced on the shock waves released while the acoustic impedance was reduced, and in consequence, the power delivered to transducer P_{DT} was slightly reduced, especially at 10 *cm* immersion level of the ultrasound probe. The energy efficiency η_P was not changed at 2.5 *cm* immersion level of the ultrasound probe but at 10 *cm* immersion level of the ultrasound probe was reduced from $\eta_P = 0.61$ to $\eta_P = 0.56$.

The presence of gas bubbles such as argon, oxygen or ozone, during sonication will promote a number of reactions within the bubbles (cavities). The thermolysis of water to form *OH radicals and *H radicals is one of the most prevalent reactions during sonication process. The *OH radicals is assumed to play the most significant role in sonochemical reactions, although other free radicals may be important oxidants.

Under oxygen saturation, low temperature pyrolysis would play a significant role because of oxygen's relatively low Cp/Cv ratio of 1.39. Sonolytic reactions of oxygen lead to *OH, *OOH and *O radicals that provide other reaction. The sonochemical efficiency is similar under oxygen as under air due to similar heat capacities of these gases. With delivered oxygen and air, production of *OH radicals were not slightly changed.

Based on the higher Cp/Cv ratio of Ar over O_2, a larger amount of hydroxyl radicals are expected to form in Ar saturation. However, it was found that a larger amount of H_2O_2 was formed from O_2 saturation rather than Ar saturation from the ultrasonic irradiation to pure water. Kima et al. found that the degradation of methyl tert-butyl ether (MTBE) in argon saturated solution shows similar rate compared to that in oxygen saturation but shows significantly different formations of products because of effective pyrolytic degradation under high temperatures and high pressures but restricted formations of peroxyl radicals [6]. Argon is less soluble in water than oxygen or ozone, and at 20 kHz the greatest intensity of sonoluminescence spectra has obtained in Ar. sonoluminescence is known to originate from the gas phase and not from the interface or bulk solution. Gases with low thermal conductivities (O_2 vs. Ar, 48.1 vs. 30.6 *mW/mK*) will lead to more intense conditions within a collapsing bubble because less heat is dissipated to the surrounding aqueous solution during the rapid explosion. Therefore, the bubble implosion in the presence of Ar favors a higher overall temperature. Hence, under argon saturation, high temperature pyrolysis would play a significant role.

The sonochemical efficiency was the greatest under argon bubbling, except results of ozone bubbling where sonochemical efficiency was disrupted by directly ozone reaction with I^- ions shown in Eq. (9). It is difficult to verify. However, the sonication under ozone bubbling can be also a high potential source of *OH radicals. Hence, all further experiments in this work were carried out with argon and ozone bubbles.

3.2 Saturated fatty acids degradation rate

The following sonication conditions were chosen: 20 kHz ultrasound frequency, $\zeta_{70\%} = 86.8$ *μm* ultrasound amplitude, procedure with temperature process control by cooling water bath at 20 *°C*, 10 *cm* immersion level of the ultrasound probe.

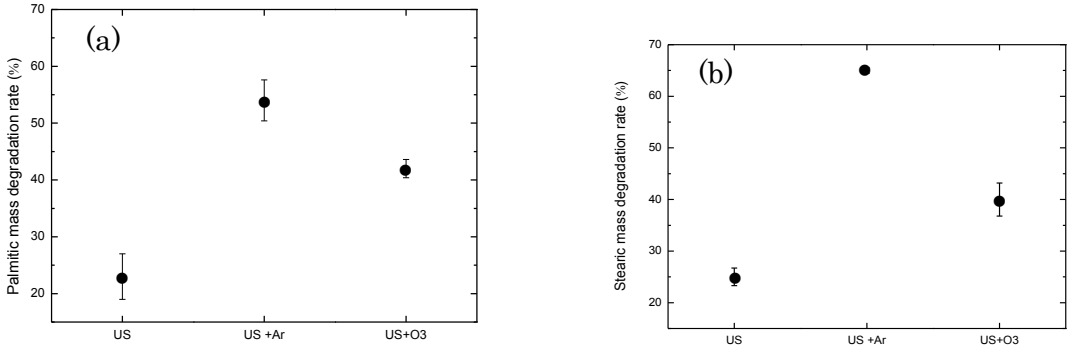


Figure 2: Percent of palmitic acid (a) and stearic acid (b) mass degradation rate under various treatment procedure: sonication only (US), sonication simultaneously with argon bubbles (US + Ar) and sonication simultaneously with ozone bubbles (US + O_3).

Treatment of saturated free fatty acids was run under three different procedures such as sonication only, sonication simultaneously with argon bubbles and sonication simultaneously with ozone bubbles. The percent of palmitic and stearic acid mass degradation rate is shown in Figure 2. The organic contaminants, under the ultrasound may be destroyed by the combined effects of pyrolytic decomposition and oxidative degradation. As demonstrated in Figure 2 the saturated free fatty acids mass degradation rate were achieved around 25 % for both fatty acids.

The treatment mechanism can be explained by similarity of pyrolytical degradation process to enzymes oxidation mechanism. The initial attack on FOG by microorganisms is the ester bonds by enzymes (lipases) which remove the fatty acids from glycerol molecules of the triglycerides. The main pathway for the oxidation of fatty acids involves repetition of a sequence of reactions, which results in the removal of two carbon atoms as acetylo-CoA with each repetition of the sequence: beta-oxidation, such as in the digestive system.
Sonication treatment was also achieved through the production of hydroxyl radicals, which are among the strongest oxidizing species. Due to absence of double carbon-carbon bonds at the carbon long chain of saturated fatty acids, only hydroxyl radicals can break down the single carbon-carbon bonds into carbon dioxide and water. This process is also familiar to enzymes oxidation mechanism.
At low ultrasound frequency (20 *kHz*), the hydrogen and hydroxyl radicals had more time to recombine to form water or other radicals inside the bubbles. However, with the concentration of organic substances the number of available hydroxyl radicals for the recombination is reduced. Due to hydrophobic saturated free fatty acids have a strong tendency to diffuse into the gaseous bubble interior, the hydroxyl radicals played the main role in the saturated fatty acids oxidative degradation.
In the sol (solid-liquid) colloidal suspension, disruption of the solid contaminants by the jetting phenomenon associated with the collapse of cavitation bubbles is taken place, especially at low frequency. Moreover, these nano-scale solid contaminants (RH) could be injected inside the bubbles by an asymmetrical collapse and react with *OH radicals or directly destroy by collisions with Ar.

$$RH + {}^*OH \rightarrow {}^*R + H_2O \quad (12)$$

$$RH + Ar \rightarrow {}^*R_1 + {}^*R_2 + \text{fragments} \quad (13)$$

This mechanism play crucial role in the sonication simultaneously with argon bubble treatment procedure and a high degradation rate was observed, as reported in Figure 2.
In the hybrid AOP method sonication/ozonation for a degradation of unsaturated fatty acids, the main roll was played by ozonation process, due to the direct reaction of ozone with carbon-carbon double bonds in long carbon chain of fatty acids, as was presented in previous paper [5]. Due to the absence of double bond in the chemical structure of saturated fatty acids, stearic and palmitic acids cannot react directly with ozone. To consider that fact, ozone can be only as a source of *OH radicals under saturated fatty acids degradation treatment procedure. As it shown in Figure 10, degradation rate is almost twice higher than sonication process alone, which suggest of a high efficiency of ozone transformation to hydroxyl radicals under ultrasound irradiation.

4. Conclusions

The results of optimization of sonication treatment process demonstrated about some important parameters for the hydrophobic contaminants degradation. However, many parameters depend on each type of sonication system and a few general conclusions are noticed as follows.

- The low ultrasound frequency is effective method for hydrophobic contaminants degradation.
- The deep level of the ultrasound probe immersion into the liquid is highly effective with sonication simultaneously with relatively small gas bubbles.
- In the treatment of saturated free fatty acids with three different procedures, the mass degradation rate obtained with the sonication simultaneously with argon bubbles was higher than that obtained with sonication only and sonication simultaneously with ozone bubbles.

Due to insoluble properties in water and hard degradable character of saturated free fatty acids, a high degradation rate by sonication simultaneously with argon bubbles was improved. These results can be used to pro ecological method in grease trap purification and be applied effectively as well as biological method and gravity separation method in grease trap devices. Moreover, the investigation about grease trap purification is easy to hold at the same time with laboratory scale and industrial scale such as being carried out in this study. The treatment contaminants concentration and the reactor size were carried on the industrial scale. In addition, cooling system is easy to apply by use the cold tap water. Hence, only investigation on the flow-reactor type must be done to the full-scale industrial application.

Reference:

[1] X.He, M.Iasmin, L.O.Dean, S.E.Lappi, J.J.Ducoste, F.L.de los Reyes, III; Evidence for Fat, Oil, and Grease (FOG) Deposit Formation Mechanisms in Sewer Lines, Environ. Sci. Technol.,*45*(10), 4385–4391 (2011).
[2] Ch.L.Yang; Electrochemical coagulation for oily water demulsification, Sep. Purif. Technol., 54, 388-395 (2007).
[3] T.Yoshino, D.Koyama, K.Nakamura, S.Ueha, K.Seino; Experimental Study on an Ultrasonic Purification Apparatus for Civil Engineering Use, Jpn. J. Appl. Phys., 47, 4296-4299 (2008).
[4] L.J.Satck, P.A.Carney, H.B.Malone, T.K.Wessels; Factors influencing the ultrasonic separation of oil-in-water emulsions, Ultrasonic Sonochemistry, 12, 153-160 (2005).
[5] M.P.Kwiatkowski, S.Satoh, Ch.Yamabe, S.Ihara, M.Nieda; Removing Fats, Oils and Greases from Grease Trap by Hybrid AOPs (Ozonation and Sonication), *IEEJ Trans. FM*, 132(6), (2012). (in press)
[6] D.K.Kima, K.E.O'Shea, W.J.Cooper; Mechanistic considerations for the degradation of methyl tert-butyl ether (MTBE) by sonolysis: Effect of argon vs. oxygen saturated solutions. Ultrasonic Sonochemistry 19, 959–968 (2012).

POSTER PRESENTATIONS

INFLUENCE OF THE APPLIED VOLTAGE SHAPE ON THE BARRIER DISCHARGE OPERATION MODES IN HELIUM

Marc Bogaczyk[1], Goran B. Sretenović [2], Hans-Erich Wagner[1]

[1] *Institute of Physics, University of Greifswald, Germany*
[2] *Faculty of Physics, University of Belgrade, Serbia*
E-mail: bogaczyk@uni-greifswald.de

Barrier discharges in helium were studied by temporally and phase resolved surface charge measurements, cross-correlation emission spectroscopy and electrical measurements. Depending on the discharge cell configuration, e.g. the gap distance, kind of dielectric surfaces and shape of the applied voltage, the diffuse discharge can operate either in the Townsend-like or in the glow-like mode. In small gaps (distance of 1 mm) with a sinusoidal feeding voltage, only the Townsend-like mode was investigated. But, for a rectangle voltage shape, the discharge operates in the glow-like mode, probably due to the fast rise and fall time of the applied voltage. Using a sawtooth voltage, both modes appear separately over one period. The presented results show clearly the correlation between the deposited surface charge and transported charge as well as the optical radiation with maxima near the anode or the cathode, respectively.

1. Introduction

The atmospheric pressure dielectric barrier discharges (BDs) have found many applications, e.g. polymer surface treatments, thin film coatings, sterilization and gas flow control [1, 2]. They have still a high technological potential. This study is focused on the homogeneous BD in helium. It can be distinguished between the so-called atmospheric pressure Townsend-like discharge (APTD) and atmospheric pressure glow-like discharge (APGD). The occurrence of both depends on the feeding gas mixture and flow rate, gas pressure, operation frequency and shape of the applied voltage, dielectric barrier material and the gap spacing. Furthermore, the diffuse mode as well as filamentary one depends on the ratio of secondary γ coefficients at the electrodes to ionization in the volume. The latter is connected with the Penning ionization and the α coefficient of the Townsend ionization. In helium the APGD is usually observed. This mode appears when the α coefficient in dependence on the reduced field strength E/n does not lead to a dramatic ion multiplication in the volume. In contrast to that, the probability for the APTD rises with a higher the ratio of γ coefficient to the ionization in the volume. The APTD is typical for BDs operating in pure nitrogen, whereas in helium the APGD usually occurs. Both diffuse discharge modes are quite different in their current densities (APTD: j~0.1 mA/cm^2, APGD: j~1 mA/cm^2). Their emission intensity maxima are located near the anode (APTD) and in front of the cathode (APGD), respectively. In this paper the spectroscopic investigations of the discharge development by the CCS commonly with the determination of the surface charge density are presented. The experiments were performed in pure helium. Experimental results of the discharge development and the surface charge density are discussed.

2. Experimental set-up

The set-up of the discharge cell is shown in fig. 1. Main component is the configuration of two parallel dielectric electrodes. An electro-optic BSO crystal is mounted on top of a grounded aluminium mirror allowing the surface charge measurement. The second dielectric electrode is a glass plate covered on its top side with a optically transparent and electrically conductive ITO layer. The gap distance between the dielectric materials is 1mm. Sidewise orientated orifices enable the direct gas flow in between the gap. Also, it allows the application of the cross-correlation spectroscopy (CCS) to measure the optical discharge development in the volume. The working gas is pure helium (< 10 ppm nitrogen impurities) at a pressure of 500 mbar. Three waveforms of feeding voltage have been used, namely sine wave, rectangle, and sawtooth at a frequency of 2 kHz. The applied voltage amplitude was varied from about 0.35 kV to 0.9 kV depending on the shape of the feeding voltage. The experimental set-up for the investigation of surface charges and the optical discharge evolution is illustrated in fig. 2. Surface charges have been measured on the BSO surface under utilization of the electro-optic Pockels effect [3]. The accordant detailed optical set-up is shown in fig. 2A. A Koehler

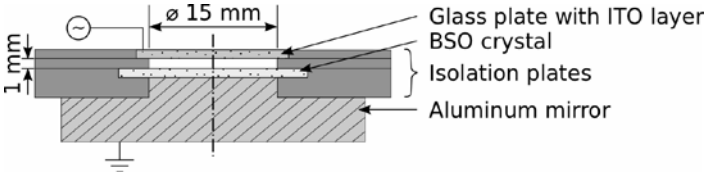


Fig. 1. Side-view of the discharge cell configuration.

illumination (two lenses and apertures) enables the homogeneous illumination of the BSO crystal via a red LED ($\lambda = 634\,\mathrm{nm}$). A linear polarization filter placed in the Koehler illumination provides linearly polarized light. The light is reflected onto the BSO crystal by a beam splitter. Afterwards it passes a telescopic system which enlarges the beam diameter by the factor of five. A λ/8 wave plate is placed in front of the upper lens of the telescopic system changing the linearly polarized light to elliptically polarized light. Depending on the electrical field across the BSO crystal caused by the applied voltage and deposited surface charges, the ellipticity is additionally modified. Because of the reflection on the aluminium mirror, the beam passes the BSO crystal and λ/8 wave plate twice. Hence, the ellipticity

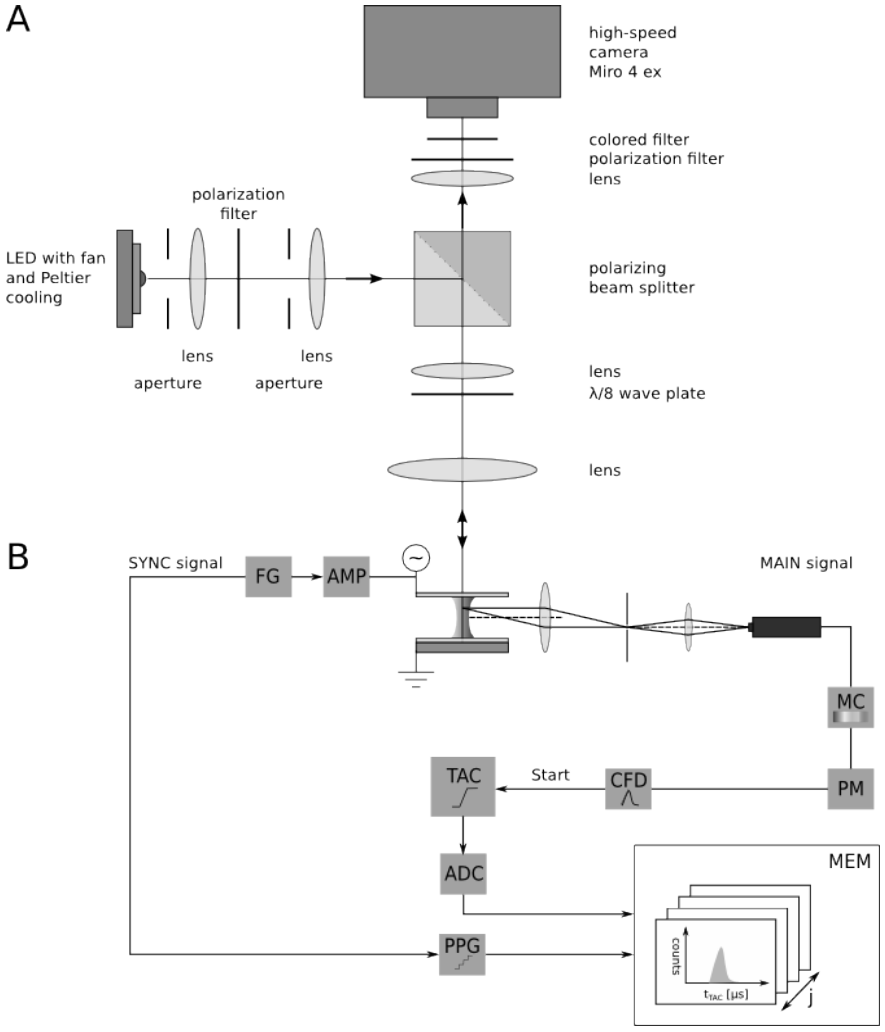


Fig. 2. Experimental set-up for surface charge measurements (A) and spatio-temporally resolved spectroscopic measurements in the volume (B). CCS set-up with PC pattern generator (PPG) triggering: PM - photomultiplier, MC - monochromator, CFD - constant fraction discriminator, TAC - time to amplitude converter, ADC - analogue-digital converter, PPG - pattern generator, MEM - memory.

changes again. After that, the light passes through a second linear polarization filter and a high speed camera (exposure time 10 µs) detects the light. A coloured filter (transparent from 620 to 640 nm) fades out the light emission of the BD. Hence, the camera detects only intensity changes of the reflected light. The latter allows the recalculation of surface charge density (sign and value) by the ratio of an image with surface charges to corresponding reference image taken without any surface charges.

The spectrally, spatio-temporally and phase resolved optical emission development has been recorded via the well-established cross-correlation spectroscopy (CCS). Details are shown in fig. 2B. Under the experimental condition studied, the BD operates in the diffuse mode. Hence the CCS is triggered electrically by a PC pattern generator (PPG) [4]. The CCS is based on the time-correlated single photon counting from about 10^6 consecutive discharges. The emission signal is focused onto a vertically moveable slit via a 1:-1 imaging. Afterwards, the image is focused with a second lens onto an optical fibre connected with a monochromator. The spatial and spectral resolution is 0.05 mm and 0.1 nm, respectively. A single photon counting photomultiplier (PM) detects the spectrally resolved signal and converts it into an electrical signal which is analyzed by a constant fraction discriminator (CFD). Reaching a pre-defined voltage amplitude, a second voltage signal increases linearly by a time-to-amplitude converter (TAC). An analogue-to-digital converter (ADC) enables the corresponding correlation of this voltage in a time-depending channel memory device (MEM) resulting in a temporally and phase resolved intensity distribution of the discharge emission development.

3. Results and discussion

BDs operating in pure helium (purity 99.999 %, <10 ppm nitrogen impurities) generally results in the diffuse mode. The accordant overview spectrum recorded with a sinusoidal applied voltage is shown in fig. 3. It is dominated by several bands of the second positive system (SPS) and first negative system (FNS). The FNS emission of the exited $N_2(B^2\Sigma_u^+)$ ions results from the Penning ionization between helium metastables and nitrogen in the ground state. The emission of the SPS is caused by inelastic collisions of electrons with nitrogen in the ground state to the excited state $N_2(C^3\Pi_u)$ followed by the de-excitation to $N_2(B^3\Pi_g)$.

The development of the SPS ($\lambda = 337$ nm) and FNS ($\lambda = 391$ nm) emission as well as the most intensive emission line of helium ($\lambda = 706$ nm) have been investigated by varying the feeding voltage shape, namely sine wave, rectangle and sawtooth. The latter will be presented in detail on the poster. Besides this, the corresponding electrical characteristic and the surface charges have been recorded phase resolved, respectively. Fig. 4 and 5 show the discharge characterization exemplarily for the sine wave and rectangle voltage shape. Contrary to our expectations in the case of the sinusoidal feeding voltage, the relatively weak emission intensity maximum was found near the anode and not near the cathode, shown exemplarily for He at $\lambda = 706$ nm in fig 4. (bottom). Also, the FNS and SPS emission are located in front of the anode, too. This indicates the appearance of an APTD. The phenomenon can be understood looking on the electrical measurements and the discharge cell geometry. The measurement of the applied voltage and the net current enables the recalculation of the voltage drop over the discharge gap, as illustrated in fig. 4 top image (gray solid line). It shows clearly that the gap

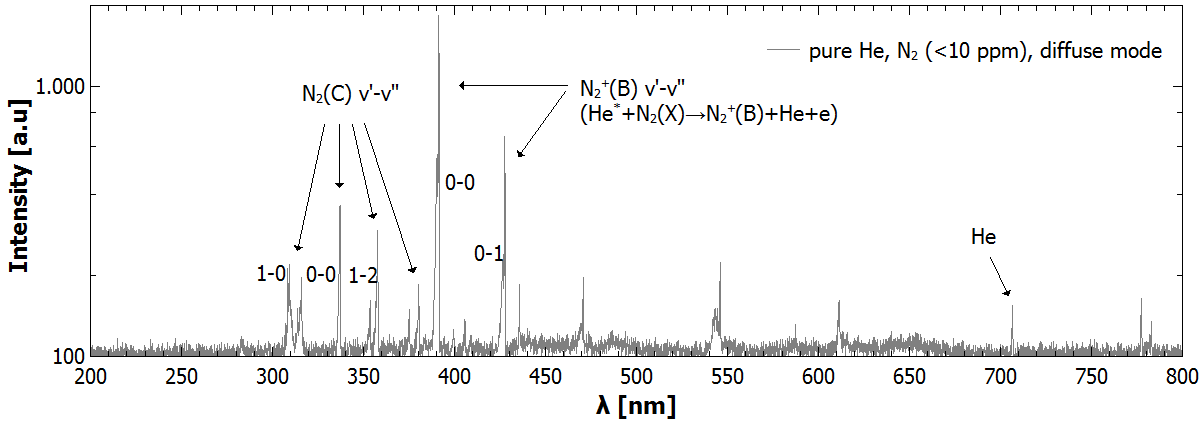


Fig. 3. Overview spectrum in pure helium, sinusoidal feeding voltage signal.

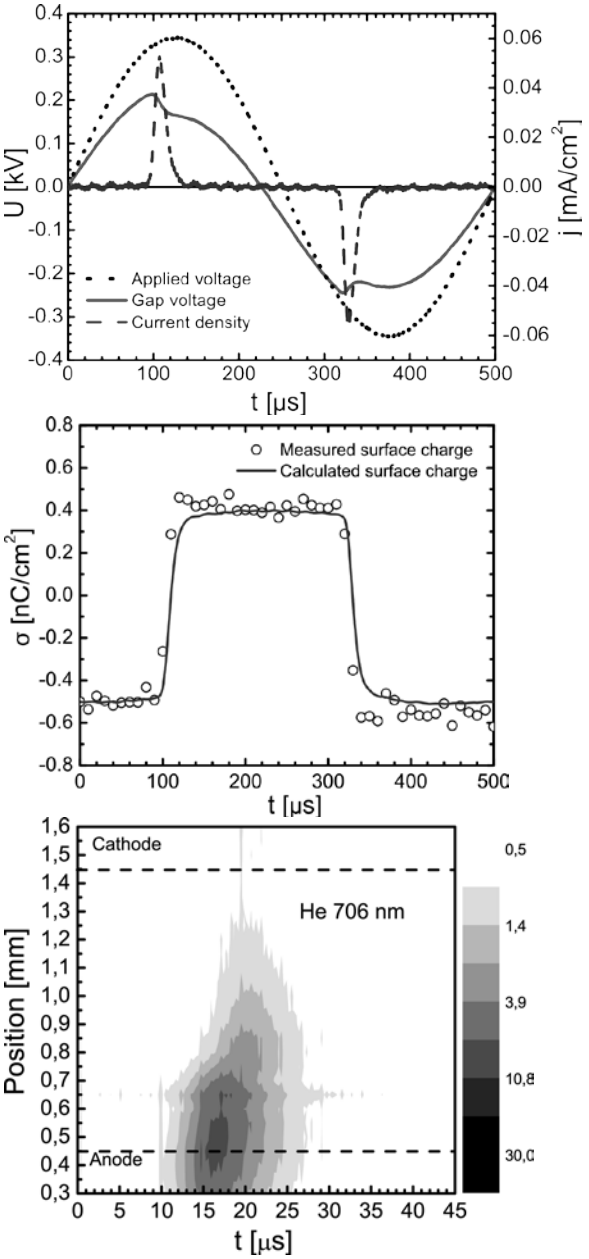


Fig. 4. **Sinusoidal feeding voltage shape** in a pure helium BD. Top: electrical characterization including applied voltage, gap voltage and net current. Centre: surface phase resolved charge measurement over one period. Bottom: emission development of helium at $\lambda = 706\,\mathrm{nm}$. Intensity maximum located in front of the anode.
Voltage amplitude: 0.35 kV, pressure: 500 hPa, frequency: 2 kHz.

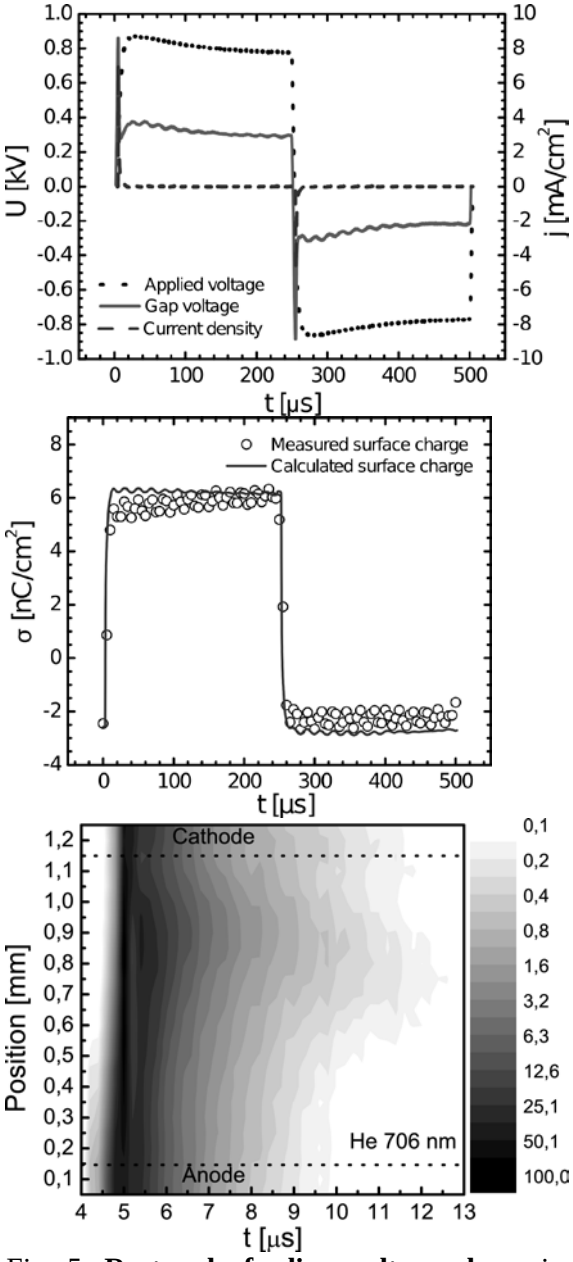


Fig. 5. **Rectangle feeding voltage shape** in a pure helium BD. Top: electrical characterization including applied voltage, gap voltage and net current. Centre: surface phase resolved charge measurement over one period. Bottom: emission development of helium at $\lambda = 706\,\mathrm{nm}$. Intensity maximum in front of the cathode.
Voltage amplitude: 0.9 kV. pressure: 500 hPa, frequency: 2 kHz.

voltage drop at the discharge breakdown is small because of a low space charge production in the volume [5]. Furthermore, the gap distance of 1 mm is too small to develop a cathode fall region. Additionally, the small current density is $j = 0.06\,\mathrm{mA/cm^2}$ with a duration time of several microseconds (30 µs) being in good agreement to the weak emission intensity and relatively long duration (fig. 4, top and bottom, respectively). The corresponding surface charge measurement is in excellent agreement with the net current integration. In every half period, the surface charges changes its sign and value. After a current pulse, it remains constantly on the BSO surface, details in [6]. The

results recorded for the sinusoidal feeding voltage indicate the rare APTD operation mode in helium. However, in pure helium the discharges usually operate in the glow-like mode with an emission maximum near the cathode [7]. But in contrast to our discharge cell configuration, the used gap distances of these investigations were in the range of 2 mm to 5 mm.
Nevertheless, the glow-like operation mode is possible by the application of a feeding voltage with a much steeper edge than in the case of the sinusoidal voltage, e.g. a rectangle voltage signal, as illustrated in fig. 5. The emission maximum is located in front of the cathode, shown in fig. 5 exemplarily for He at $\lambda = 706\,\mathrm{nm}$. FNS and SPS are also located near the cathode, in detail illustrated on the poster. The higher grow rate of d*V*/d*t* induces much stronger electrical field strengths in a short time which results in a faster ionization and space charge build-up. Beside this, the emission is obvious higher than in the case of the sinusoidal applied voltage. The electrical characteristic is in comparison to the sine wave quite different. The current pulse duration is ten times shorter ($\sim 1\,\mu\mathrm{s}$). The net current density ($j = 8\,\mathrm{mA/cm^2}$) is more than 10 times higher than for the APTD. A strong gap voltage drop in the moment of the current maximum implies the formation of a space charge sheath near the cathode and a cathode fall region. The existence of the cathode fall region with a length in order of $1\,\mathrm{mm}$ is predicted by models [5] and was confirmed by measurements [8]. The corresponding surface charge measurement shows a similar behaviour as for the sinusoidal voltage shape. But, the temporally net current integration results in a much higher transferred charge by current pulse, Hence, the deposited surface charges are also higher than in the APTD. However, it can be seen that the amount of deposited surface charges is not equal in both half periods. The reason is the asymmetric discharge cell configuration, namely the different dielectric materials. Nevertheless, the temporally integrated net current is in excellent agreement with the deposited charges.

4. Conclusion

A new discharge cell configuration was applied to enable the joint investigation of volume and surface processes in the diffuse helium BD. The spatio-temporally and spectrally resolved discharge development in the volume was studied by the cross-correlation spectroscopy. The temporally resolved measurement of surface charges on the dielectric BSO was succeeded by the application of the electro-optic Pockels effect in combination with a CCD camera. Surprisingly, in a discharge gap of 1 mm, the variation of the feeding voltage results in quite different discharge modes, namely the unusual APTD (sine wave) and the well-known APGD (rectangle). Hence, the derivation of d*V*/d*t* has a crucial influence on the ionization mechanism and discharge development. All diagnostics have shown an excellent correlation between the discharge development, electrical characteristic (net current and gap voltage) and surface charge measurements.

Acknowledgements. This work was supported by the “Deutsche Forschungsgemeinschaft, SFB/TRR 24,‘Complex plasmas‘ “.

5. References

[1] H.-E. Wagner, R. Brandenburg, K. V. Kozlov, A. Sonnenfeld, P. Michel, J. F. Behnke, 2003 *Vacuum* **71** 417–436
[2] F. Massines, N. Gherardi, N. Naudé and P. Ségur, 2009 *Eur. Phys. J. Appl. Phys.* **47**, 22805
[3] A. Yariv. *Quantum electronics*. WILEY New York, 1989.
[4] K. V. Kozlov, R. Brandenburg, H.-E. Wagner, A. M. Morozov, and P. Michel. *J. Phys. D: Appl. Phys.*, 38:518, 2005.
[5] Y. B. Golubovskii, V.A. Maiorov, J. Behnke and J. F. Behnke, 2003 *J. Phys. D: Appl. Phys.* **36** 39–49
[6] M. Bogaczyk and H.-E. Wagner, Operation modes in barrier discharges: discharge development and surface charge accumulation, this issue
[7] R. Brandenburg, Z. Navrátil, J. Jánsky, P. Stáhel, D. Trunec, and H.-E. Wagner. J. Phys.D: Appl. Phys., 42:085208, 2009.
[8] S. S. Ivković, B. M. Obradović, N. Cvetanović, M. M. Kuraica, J. Purić, *J. Phys. D: Appl. Phys.* **42** 25206

APPROACH OF THE SIMPLEST EQUIVALENT CIRCUIT FOR DETERMINATION OF CHARGE TRANSFERRED THROUGH THE GAS GAP IN PULSED DIELECTRIC BARRIER DISCHARGE

Andrei V. Pipa[1], Tomáš Hoder[1], Jeff Koskulics[2], Ronny Brandenburg[1]

[1] Leibniz Institute for Plasma Science and Technology (INP Greifswald), Felix-Hausdorff-Str. 2, D-17489 Greifswald, Germany

[2]Light and Life Laboratory, Department of Physics and Engineering Physics, Stevens Institute of Technology, Hoboken, NJ 07030, USA

E-mail: brandenburg@inp-greifswald.de, pipa@pisem.net

The method of determination of the charge transferred through the gas gap of dielectric barrier discharges (DBDs) is proposed. The method is based on the approach of a simple equivalent circuit, which was critically reviewed. In contrast to the state-of-art the presented consideration accurately accounts the displacement current, which allows significant reduction of experimental errors, the verification of the classical electrical theory of ozonizers and the development of a graphical determination of maximal charge from measured charge-voltage characteristics in the case of pulsed excitation. The method is experimentally examined by means of previously measured charge-voltage characteristics in pulsed driven DBD.

1. Introduction

Dielectric barrier discharges (DBDs) have been studied extensively due to numerous applications [1–3]. The electrical theory of DBDs was extendedly developed for large-scale sinusoidal-voltage driven industrial ozonizers [1-6]. In these reactors, measured charge-voltage characteristics (Q-V plots, also referred to as Lissajous-figures) appear as a parallelogram. The maximum charge transferred through the gas gap ($\mathbf{q_{max}}$) can be easily deduced from a Q-V plot as the variation of measured charge during the discharge period [5]. The form of Q-V plots for DBDs under short-pulse excitation is significantly different from the classical parallelogram and has not been used for $\mathbf{q_{max}}$ determination. The limited applicability of the classical theory for miniature laboratory DBDs driven by fast pulsed voltages was discussed in [7].

The simplest models of a DBD reactor by a lumped-element equivalent circuit have been found to be useful for the electrical characterization in numerous numbers of works, see for example [8–13]. This approach can be applied to pulsed-driven DBDs as well as for sinusoidal-voltage driven DBDs to determine such instantaneous discharge characteristics as the gas gap voltage, $\mathbf{U_g(t)}$, and the discharge current, $\mathbf{j_R(t)}$, from voltage, $\mathbf{V(t)}$, and current, $\mathbf{i(t)}$, waveforms measured at the external terminals of the reactor. The opportunity to deduce the charge transferred through the gas gap was analyzed in [10, 13] where it was concluded that the charge transfer through the gas gap is larger than the measured charge. This is in contradiction to [5].

The aim of the present work is to review the concept of the simplest equivalent circuit of a DBD to resolve the apparent contradiction with classical theory, and to suggest an approach for the determination of the gas gap charge transfer.

2. Equivalent circuit

All DBD reactors contain three main parts: metallic electrodes where the applied voltage, current and charge can be measured; isolating barriers which prevent spark or arc discharge formation; and the gas gap where the discharge takes place. The dielectric barriers are commonly treated as ideal capacitors. In case of symmetric DBD arrangements the effective capacitance of both dielectrics $\mathbf{C_d}$ is considered as a single lumped element equal to serial connection of two single layer capacitors. In [4] Manley concludes that: “To treat the air space as an Ohmic resistance led to no useful result”. It is clear that variable Ohmic resistance would not explain the change of the effective capacitance of the discharge reactor. Variable capacitance is also not suitable, because it will not describe non-zero gas gap voltage $\mathbf{U_g(t)}$ during the discharge ignition. The parallel connection of a variable resistor $\mathbf{R}$ and the gas gap

capacitor $\mathbf{C_g}$, see figure 1, is the simplest equivalent circuit that can be used for the analysis of the DBD electrical properties.

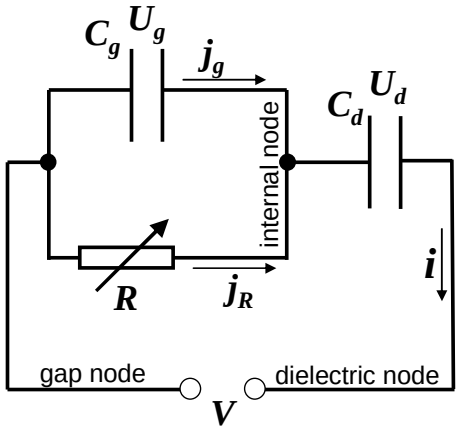


Figure 1. Simplest equivalent circuit of a DBD.

The presentation of the gas gap as the parallel connection of **R** and $\mathbf{C_g}$ was used also in [8, 11]. Zener diodes [2] can be considered as a specific case of variable resistor with denoted rules. They provide the simplest circuit model for a DBD reactor where the gas gap voltage is constant $\mathbf{U_g(t)=U_b}$ during the active part of the discharge. For pulsed-driven DBDs the resistor rules are more complex. Variable impedance [11] would be a most general consideration in particular for uniform DBDs, but the importance of including capacitive and inductive properties is unclear. The introduction of a current source [9, 10] conflicts with the fact, that a current source is an active element which deposit energy into the electrical circuit. Nevertheless, the change from the current source to a variable resistor would not make an influence on the considerations about uniform DBDs given in [9, 10]. Actually **R** in figure 1 can be considered as a "black box", whose properties are of interest.

3. Discharge current $j_R(t)$

The values: applied voltage **V(t)**, current **i(t)**, charge **Q(t)** on the reactor electrodes, total capacitance of the reactor cell $\mathbf{C_{cell}}$ and capacitance of the dielectric barriers $\mathbf{C_d}$ can be measured in experiment [7]. Following the ideas presented in [8-11] expression for discharge current $\mathbf{j_R(t)}$ can be obtained from the equivalent circuit in figure 1 in the form suggested in [8, 9]:.

$$j_R(t)=\left[1+\frac{C_g}{C_d}\right]i(t)-C_g\frac{dV(t)}{dt} \tag{1}$$

Lomaev [8] has assumed $C_g/C_d << 1$ and omitted the factor in brackets of equation (1). Massines et al. [11] also have suggested the equation for $\mathbf{j_R(t)}$ without this factor. Whereas Liu and Neiger [9] intently noted that this factor is important. Our point of view is that the simplification in [8] and [11] does not have general practical justification. In present work we suggest to write the equation (1) as:

$$j_R(t)=\frac{1}{1-\frac{C_{cell}}{C_d}}\left[i(t)-C_{cell}\frac{dV(t)}{dt}\right], \tag{2}$$

where C_{cell} is the total capacitance of the reactror cell: $C_{cell}=\dfrac{C_dC_g}{C_d+C_g}$ (3)

The equation (2) expresses the discharge current through the values that can be directly measured in an experiment, whereas equation (1) contained gas gap capacitance $\mathbf{C_g}$, which evaluation from $\mathbf{C_d}$ and $\mathbf{C_{cell}}$ values, see equation (3), would be associated with a significant increase of the experimental error.

Furthermore, equation (2) indicates that the difference of the measured current and scaled voltage derivative is proportional to the discharge current. The difference is easy to see when the measured current and scaled voltage derivative are plotted together as in [7]. The displacement current component $C_{cell}dV(t)/dt$ in equation (2) (in contrast to $C_g dV(t)/dt$ in equation (1)) can be measured without discharge ignition for the same form of the applied voltage V(t) [13, 14] or can be intuitively estimated especially in sinusoidal-voltage driven DBDs [15]. Nevertheless, it is necessary to account the factor $[1/(1 - C_{cell}/C_d)]$, which was omitted in [13-15]. In a certain discharge geometry, the disregard of the factor can bring a significant error. For example in [13] the ratio C_{cell}/C_d is about 0.5 and thus the discharge current $j_R(t)$ would be underestimated by a factor of 2. The works [14, 15] do not provide the capacitance values and therefore the error could not be estimated.

4. Charge transferred through the gas gap q(t)

Instantaneous charge transferred through the gas gap **q(t)** values can be obtained by the integration of equation (2):

$$q(t) = \frac{1}{1 - \frac{C_{cell}}{C_d}} \left[Q(t) - C_{cell} V(t) \right] + q_0 . \tag{4}$$

Equation (4) express **q(t)** through the measured values of charge on the reactor electrodes **Q(t)**, applied voltage **V(t)** and capacitances $\mathbf{C_{cell}}$ and $\mathbf{C_d}$. The integration constant $\mathbf{q_0}$ can be found if **q(t)** is known at zero time moment.

In [13, 15] the transferred charge **q(t)** was determined from the integral of the discharge current. The discharge current was accounting the displacement component but disregarding the factor $[1/(1 - C_{cell}/C_d)]$. The authors [13] include this factor to the charge determination in contrast to [15]. The authors of [12] came to the same relation between $\mathbf{j_R(t)}$ and measurement parameters as shown in equations (1) or (2) but neglect the term for the derivative of applied voltage. Thus they got to the conclusion that the ratio **q(t)**/**Q(t)** is only a function of DBD reactor capacitance. Only if V(t) and q_0 are set at zero in equation (4) the form suggested in [12] will be derived. Authors [10] come to the same confusing conclusion that internal charge transfer is larger then external charge transfer by a factor of $[1/(1 - C_{cell}/C_d)]$. However, they modified a part of measured charge and expressed $\mathbf{q_{max}}$ through the gas gap voltages in time moments of discharge ignition and extinction. How to determine this time moments experimentally was not mentioned.

The equation (4) has principle peculiarities: a) it is written for instantaneous charge **q(t)** rather then for $\mathbf{q_{max}}$; b) is expresses the **q(t)** though measured parameters in one step; c) it accounts accurately the displacement current and the DBD capacitance thus it does not requires any additional assumptions except the equivalent circuit given in fig. 1 itself.

5. $\mathbf{q_{max}}$ for ozonizer discharge

Equation (4) is used for the evaluation of the maximum charge transferred through the gas gap $\mathbf{q_{max}}$ in case of classical Q-V plot from electrical theory of ozonizers [1-6] reproduced in fig. 2 and verification of the conclusion given in [5]. Vertexes of the parallelogram A, B, C and D in fig. 2 define moments at which discharge ignites or extinguish. The difference of the instantaneous transferred charges **q(t)** in moments C and B can be expressed using equation (4):

$$q(C) - q(B) = \frac{1}{1 - \frac{C_{cell}}{C_d}} \left[Q(C) - Q(B) - C_{cell} \left(V(C) - V(B) \right) \right] \tag{5}$$

The value $\mathbf{C_{cell}}(\mathbf{V}(C)\text{-}\mathbf{V}(B))=\mathbf{a}$ is noted in fig. 2. The term [Q(C) – Q(B) – a] is denoted as $\mathbf{Q_0}$. in fig. 2. Thus the value in the square brackets in equation (5) is $\mathbf{Q_0}$. If equation (4) is written for the vertexes C and a one got:

$$q(C) - q(A) = \frac{1}{1 - \frac{C_{cell}}{C_d}} \left[Q(C) - Q(A) - C_{cell} \left(V(C) - V(A) \right) \right] \tag{6}$$

The term [$\mathbf{C_{cell}}$($\mathbf{V}$(C)-$\mathbf{V}$(A))] is noted a section **b** in fig. 2 and obvoius the term in the square brackets in equation (6) is again $\mathbf{Q_0}$. Thus the charge transfered through the gas gap between moments A and B or between moments A and C is the same, namely $\mathbf{q_{max}}$ which can be expressed as:

$$q_{max} = q(C) - q(B) = q(C) - q(A) = \frac{1}{1 - \frac{C_{cell}}{C_d}} Q_0 . \qquad (7)$$

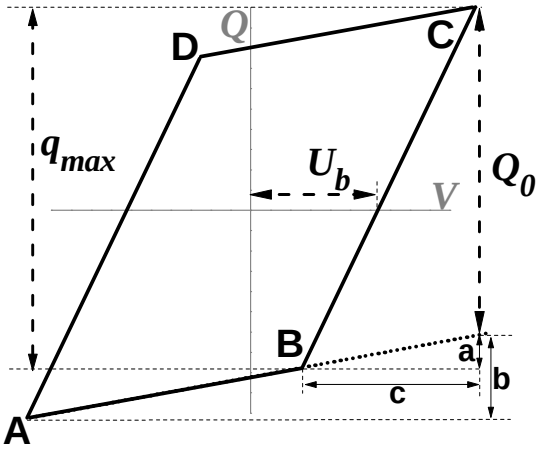


Figure 2. Schematic presentation of Q-V plot from classical electrical theory of ozonizers

Now the value q_{max} can be denoted in in fig. 2 using the geometrical relations:

$$\frac{q_{max}}{c} = C_d \qquad \text{and} \qquad \frac{q_{max} - Q_0}{c} = C_{cell} .$$

The result is in agreement with the statement of classical theory [5] that the variation of the measured charge **Q(t)** during the full discharge period is equal to the maximum charge transferred through the gas gap $\mathbf{q_{max}}$. It becomes obvious that the determination of $\mathbf{q_{max}}$ requires the quantitative knowledge about $\mathbf{C_d}$, see equation (4). The classical Q-V plot as shown in fig. 2 gives information about $\mathbf{C_d}$ and thus $\mathbf{q_{max}}$ can be easily denoted graphically. In case of Q-V plots measured under pulsed excitation the statement given in [5] fails. Equation (4) helps to clarify this question and to evaluate graphically the $\mathbf{q_{max}}$ for pulsed excited DBDs.

6. $\mathbf{q_{max}}$ for pulsed driven DBD.

The equation (4) can be used as well for analysis of Q-V plot measured in pulsed-driven DBD. Fig. 3 shows the Q-V plot measured in work [7] in a coaxial DBD reactor in argon at 100 mbar driven by square voltage pulses with a rise time of 20 ns. Taking into account that $\mathbf{Q}$(A)=0, $\mathbf{Q}$(C)=$\mathbf{Q_{max}}$, $\mathbf{V}$(A)=0 and $\mathbf{V}$(C)=$\mathbf{V_{max}}$ the charge transferred through the gas gap between time moments A and C can be written on the basis of equation (4):

$$q_{max} = q(C) - q(A) = \frac{1}{1 - \frac{C_{cell}}{C_d}} \left[Q_{max} - C_{cell} V_{max} \right]. \qquad (8)$$

Equation (8) expresses $\mathbf{q_{max}}$ through the measured parameters. For graphical presentation of $\mathbf{q_{max}}$ on Q-V plot two straight lines should be drawn: i) through the point A with the slope of $\mathbf{C_{cell}}$ and ii) through the point C with the slope of $\mathbf{C_d}$. The values $\mathbf{C_{cell}}$=(2.4±0.3)pF and $\mathbf{C_d}$=(15.7±0.4)pF were determined in [7] and the corresponding lines are plotted in fig. 3. The dotted lines denote the experimental error bar. The cross point between the $\mathbf{C_d}$- and $\mathbf{C_{cell}}$-lines, point B, defines $\mathbf{q_{max}}$. The value $\mathbf{C_{cell}V_{max}}$=**b** is marked in fig. 3 and the value corresponding to the square brackets of equation

(8) can be defined as $\mathbf{Q_0}$ by analogy with fig. 2 and equation (6). The variation of the applied voltage between moments C and B is **V**(C)-**V**(B)=**c**, a value which relates $\mathbf{Q_0}$ and $\mathbf{q_{max}}$ through the equations (6) and (7).

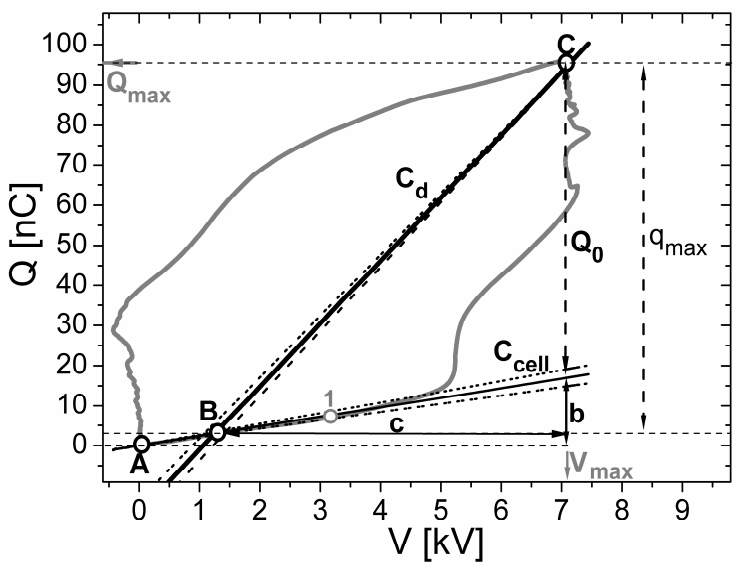


Figure 3. Q-V plot measured under pulsed excitation (data taken from in [7]).

7. Conclusions

The method of graphical determination of the charge transferred through the gas gap of DBDs from measured charge-voltage characteristics is proposed and examined by means of experimental data for a pulsed driven reactor. The method is based on the approach of a simple equivalent circuit and accurately accounts the role of the displacement current. It has been critically verified on the classical electrical theory of ozonizers. We believe that our method can lead to much accurate results regarding the electrical characterization of DBD reactors since it significantly reduces experimental errors.

Acknowledgments

The work was partly supported by Federal Ministry of Education and Research of Germany FKZ 03FO1072.

8. References

[1] Kogelschatz U 2003 Plasma Chemistry and Plasma Processing **23** 1-46.
[2] Kogelschatz U 2004 in Non-Equilibrium Air Plasmas at Atmospheric Pressure Institute of Physics, Editor(s): Becker K H, et al. ISBN: 9780750309622.
[3] Wagner H-E, Brandenburg R, Kozlov K V, Sonnenfeld A, Michel P and Behnke J F 2003 Vacuum 71 417-436.
[4] Manley T C 1943 Trans. Electrochem. Soc. **84** 83-96.
[5] Falkenstein Z and Coogan J J 1997 J.Phys.D:Appl.Phys. 30 817-825.
[6] Samoilovich V G, Gibalov I V, Kozlov K V 1997 Physical chemistry of the barrier discharge Dsseldorf, DVS-Verlag, ISBN 3-87155-744-7.
[7] Pipa A V, Hoder T, Koskulics J, Schmidt M and Brandenburg R, "Experimental determination of dielectric barrier discharge capacitances." Rev. Sci. Instrum. In press 2012.
[8] Lomaev M I 2001 Atmos.Oceanic Opt. **14** 1005-1008.
[9] Liu S and Neiger M 2001 J.Phys.D: Appl. Phys. **34** 1632-1638.
[10] Liu S and Neiger M 2003 J.Phys.D: Appl. Phys. **36** 3144-3150.
[11] Massines F, Gherardi N, Naude N and Segur P 2005 Plasma Phys. Control Fusion **47** B577-B588.
[12] Drimal J, Kozlov K V, Gibalov I V and Samoylovich V G 1988 Czech. J. Phys. B 38 159-165.
[13] Kettlitz M, Höft H, Hoder T, Reuter S, Weltmann K-D and Brandenburg R 2012 J. Phys. D: Appl. Phys. **45,** 245201.
[14] Bletzinger P and Ganguly B N 2003 J. Phys. D: Appl. Phys. **36**, 1550-1552 .
[15] Reichen P, Sonnenfeld A and Rudolf von Rohr Ph 2010 J. Phys. D: Appl. Phys. **43** 025207.

TREATMENT OF WATER AND SUSPENDED *E.COLI* WITH OZONE AND DBD EXHAUST GAS IN COMPARISON WITH DIRECT DBD TREATMENT: LIQUID CHEMISTRY AND ANTIMICROBIAL EFFECTS

Katrin Oehmigen, Ronny Brandenburg,
Klaus-Dieter Weltmann, Thomas von Woedtke

Leibniz Institute for Plasma Science and Technology (INP Greifswald),
Felix-Hausdorff-Str. 2,D-17489 Greifswald, Germany
E-mail: brandenburg@inp-greifswald.de

The treatment of water with a surface DBD under atmospheric pressure in air results in acidification and generation of NO_3^-, NO_2^- and H_2O_2. Suspended microorganisms were inactivated within a few minutes. Furthermore, O_3, N_2O, CO_2 and HNO_3/ONOOH were detected by FT-IR in the gas gap between the plasma and the liquid. To investigate the role of ozone a comparative study has been performed. Using an ozoniser and a FT-IR spectrometer, different ozone concentrations as reached during the direct plasma treatment were generated and the ozonized gas was blown over the liquid surface. In 5 ml ozone treated water a pH decrease to 4.7 was found after several minutes of plasma treatment. The concentration of H_2O_2 was much lower as compared to direct DBD treated water. To investigate the effect of stable DBD generated gas species, the experiments were performed with the exhaust gas of the DBD. In this situation nearly the same pH, NO_3^- and NO_2^- concentration, but no H_2O_2 are measured in the water. In both experiments weaker antimicrobial effects on suspended *E. coli* were found than in surface DBD treated water. Ozone gassing is not as antimicrobial effective as plasma treatment and the acidification is initiated by reactive nitrogen species mainly.

1. Introduction

The inactivation of bacteria in liquids by physical plasma is well known [1-3]. Many air plasmas produce ozone, which is known for its antimicrobial effects [4, 5] but other active species from the plasma are candidates for biological decontamination, too. The treatment of liquid with a surface dielectric barrier discharge (DBD) under atmospheric pressure in air results in pH decrease and the generation of nitrate (NO_3^-), nitrite (NO_2^-) and hydrogen peroxide (H_2O_2) in water. Even, after the plasma treatment antimicrobial effects on suspended microorganisms were investigated [1-3]. In order to resolve the role of ozone and other plasma generated stable reactive species in the gas phase above the liquid, comparing studies were performed. Therefore different gas compositions as reached during direct plasma treatment of liquids were generated by means of an ozoniser or in a separate discharge chamber (without liquid) and the ozonized/plasma-treated gas was blown over the liquid surface in a downstream petri dish. The pH and the NO_3^-, NO_2^-, and H_2O_2 concentrations were estimated in DBD exhaust gas and ozonised treated water, as well as, antimicrobial effects were investigated.

2. Materials and methods

Surface dielectric barrier discharge (DBD):
Plasma treatment of a 5 ml liquid volume was realized using a surface DBD arrangement based on an electrode array consisting of a 1.5-mm-thick epoxy-glass fiber bulk material (50 mm diameter; breakthrough voltage of 40 kV $\cdot$ cm^{-1}) coated with two 35-µm-thick copper electrodes (Fig. 1). On the one side, the high-voltage part of the DBD array had an etched line-like structure consisting of four concentric 0.75-mm-wide ring-shaped electrodes (diameter of the outer ring: 35 mm; distances between the ring-shaped electrodes: 3 mm). On the other side a 35-mm-diameter round non-structured flat copper surface served as counter electrode at ground potential. This electrode array was mounted into a special housing which was constructed in that way that it can be mounted on the lower shell of a 55-mm-petri dish forming a reaction chamber sealing off the outside. The distance between the high-voltage electrode surface and the surface of a liquid in the lower shell of the petri dish was adjusted at

5 mm. All experiments are performed at ambient air conditions (gas flow 0.5 slm) using a pulsed sinusoidal voltage of 10 kV_{peak} (20 kHz) with a 0.413/1.223 s plasma-on/plasma-off time. Energy of 2.4 mJ was dissipated into the plasma in each cycle of high voltage [2, 3].

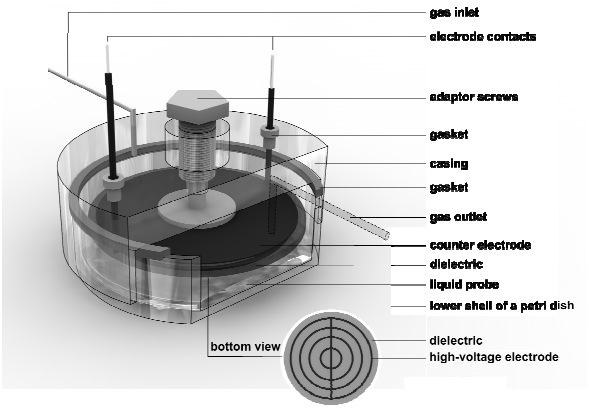


Fig. 1. Schematic drawing of the indirect surface DBD arrangement.

Ozone treatment:
For the ozone treatment the chamber of the DBD arrangement but without plasma in operation was used. First the arrangement was rinsed with argon to exclude air components. Then ozone was produced by an ozoniser from pure oxygen gas (Laborozonisator 300, Erwin Sander Elektroapparatebau GmbH). Different ozone concentrations were set at ~ 145 ppm (so-called condition A), ~ 380 ppm (B1), ~ 550 ppm (B2), 864 – 1020 ppm (C) up to 1695 – 1900 ppm (D). They were monitored by Fourier transform infrared spectrometer (FT-IR, see below) as shown in fig. 2, left. After that the treatment chamber was flushed with the adjusted ozone concentration and blown it over the liquid surface (0.5 slm, Fig. 2 right).

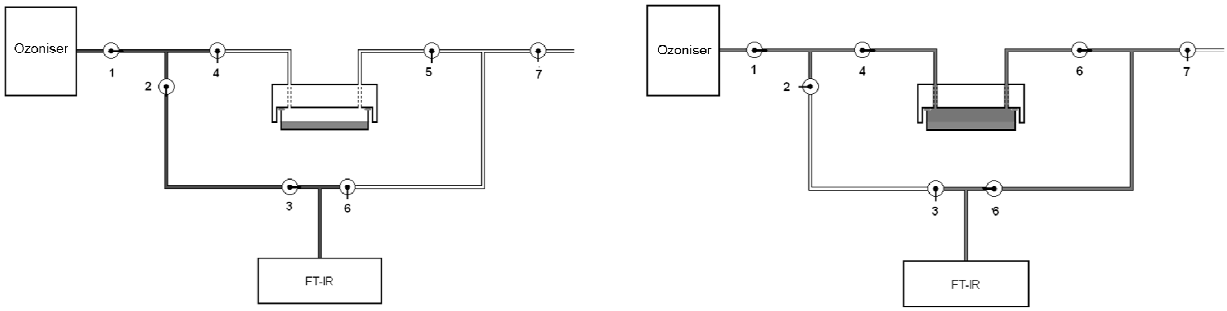


Fig. 2: Left: Adjustment of the ozoniser produced ozone, monitored by FT-IR (valves 1, 2, 3 open); Right: Gassing with adjusted O_3 concentration, monitored by FT-IR (valves 1, 4, 5 and 6 open).

DBD exhaust gas treatment:
For gassing the probe with DBD exhaust gas the DBD arrangement of Fig. 1 was used for plasma ignition (chamber 1). Now the liquid probe was in a second chamber with the same dimensions. Both chambers were connected with a 30 cm long tube through which the DBD exhaust gas was blown (air, 0.5 slm) in the chamber with the liquid sample (Fig. 3).

Physical methods:
FT-IR was performed with multicomponent gas analyser (Gasmet CR-2000, ANSYCO GmbH) with a resolution of 8 cm^{-1}. For data analyzing the software CALCMET was used.

Chemical methods [1, 2]***:***
For all photometric measurements a UV/VIS Spectrophotometer SPECORD® S 600 (Analytic Jena GmbH) was used. Nitrate as well as nitrite concentrations in plasma treated distilled water are measured by photometric analysis using commercially available test kits (Spectroquant®, Merck). Nitrate reaction with 2,6-dimethylphenol gives, after a reaction time of ten minutes 4-nitro-2,6-dimethylphenol, an orange colored product, whose absorption was measured at 340 nm. Nitrite reacts with sulfanilic acid and N-(1-naphthyl)-ethylen diamine hydrochloride via azo sulfanilic

acid to a magenta colored azo dye whose absorption at 525 nm was measured. The H_2O_2 detection based on the reaction of titanyl sulfate to yellow-colored peroxotitanyl sulfate, which was detected at 405 nm. For pH measurements, a semi-micro pH-electrode (SENTEK P13, Sentek Ltd.) was used.

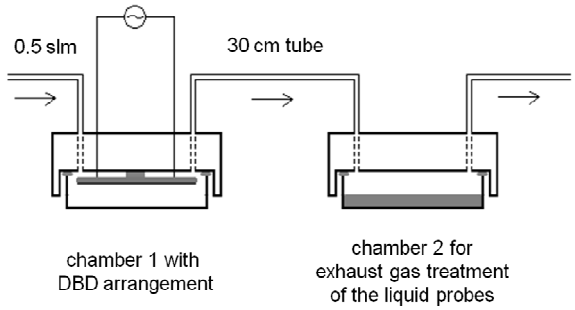


Fig. 3. Experimental setup of DBD exhaust gas treatment.

Biological methods [1, 2]***:***
As test microorganism overnight cultures of *Escherichia coli* NTCC 10538 (Institute of Hygiene and Environmental Medicine, University of Greifswald) were diluted using physiological saline (NaCl 0.85 %; 8.5 g NaCl per 1000 ml water), respectively, to get concentrations of 10^6-10^8 colony forming units per milliliter (cfu · ml^{-1}). The number of viable microorganisms was estimated by the surface spread plate count method using aliquots of serial dilutions of microorganism suspensions according to the European Pharmacopoeia. Detection limit of this procedure was 10 cfu · ml^{-1}. The inactivation kinetics of microorganisms is depicted in semi-logarithmic plots. If the number of microorganisms fell below the detection limit, i.e. no viable microorganisms have been found, for clearness these values in the graphs are set at 5 cfu · ml^{-1}.

3. Results and discussion

Chemical analytics of the DBD plasma/gas phase by FT-IR resulted in predominant generation of ozone O_3 (~ 150 ppm), dinitrogen oxide N_2O, carbon dioxide CO_2, and nitric acid/pernitrous acid HNO_3/HO-ONO. The chemical analysis of the liquid phase (5 ml water, 0.5 slm air) after DBD-treatment resulted in acidification (down to pH ~ 2.7) and detection of nitrate NO_3^- (up to 109 mg · l^{-1}), nitrite NO_2^- (up to 1.0 mg · l^{-1}), and hydrogen peroxide H_2O_2 (up to 4.9 mg · l^{-1}). In physiological saline suspended *E. coli* (5 ml) was completely inactivated after 7 min direct treatment by surface DBD.

Ozone treatment:
The ozone treatment of 5 ml water resulted in acidification (pH > 4.7) and the maximum H_2O_2 concentration was lower than 1 mg · l^{-1}. Neither nitrate nor nitrite were found. The pH decrease could be explained as given in equation (1) and H_2O_2 generation is a result of radical recombination as given by equation (2) and (3) [5, 6]:

$$HOO^{\bullet} \leftrightarrow H^+ + O_2^{\bullet -} \quad (pKa = 4.8) \qquad (1)$$

$$2\ HO^{\bullet} \leftrightarrow H_2O_2 \qquad (2)$$

$$2\ HOO^{\bullet} \leftrightarrow H_2O_2 + O_2 \qquad (3)$$

The produced O_3 concentrations of the ozoniser and the DBD is shown in Fig. 4 (left) and its related inactivation kinetics of *E. coli* are depicted in Fig. 4 (right). These results illustrate clearly that pure oxygen and similar ozone concentrations as produced by the DBD have not such strong inactivating effect on the microorganisms like the DBD treatment. Only about ten times higher O_3 concentration resulted in an inactivation within 7 min comparable to DBD treatment. Consequently, ozone gassing is NOT as effective as plasma treatment to inactivate *E. coli* suspended in liquid. Additionally, other presumably nitrogen-based reactive species may play a role in the effects of plasma-liquid interaction.

DBD exhaust gas treatment:
To investigate if other presumably nitrogen-based reactive species may play a role in the effects of plasma-liquid interaction liquids were fumigated with DBD exhaust gas and analyzed by chemical

methods, as well as, antimicrobial effects were investigated. The DBD exhaust gas treatment resulted in nearly the same acidification (down to pH ~ 2.7) compared to DBD treatment. The nitrate concentration after 30 min fumigation (up to 80 mg · l^{-1}) is slightly lower than after DBD treatment. The nitrite concentration is higher (up to 1.4 mg · l^{-1}) and the H_2O_2 concentration much lower (up to 0.4 mg · l^{-1}) than after DBD treatment of 5 ml water (Fig. 5). The higher nitrite concentration might be a result of lower H_2O_2 and NO_3^- concentrations since it may less oxidized by H_2O_2 to NO_3^-. Additionally, the oxidation from nitrite to nitrate by self catalysis via NO_3^- was reduced, both resulting in lower NO_3^- concentrations. These results suggest that the acidification is initiated by reactive nitrogen species (RNS) mainly. To confirm the results, experiments with argon as working gas instead of air were performed. By direct DBD treatment in argon pH decrease and H_2O_2, but no NO_3^- and nitrite NO_2^- were detected. The treatment with exhaust gas from DBD in argon resulted neither in acidification nor in formation of H_2O_2 (data not shown).

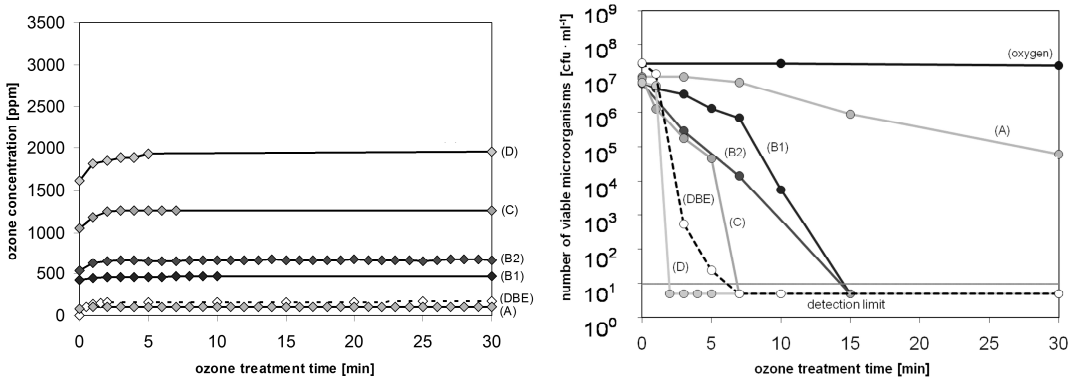


Fig. 4: left: O_3 concentrations in gas phase produced by ozoniser (A-D) and by surface DBD; right: Inactivation of *E. coli* suspensions by different O_3 concentrations compared to effect of DBD.

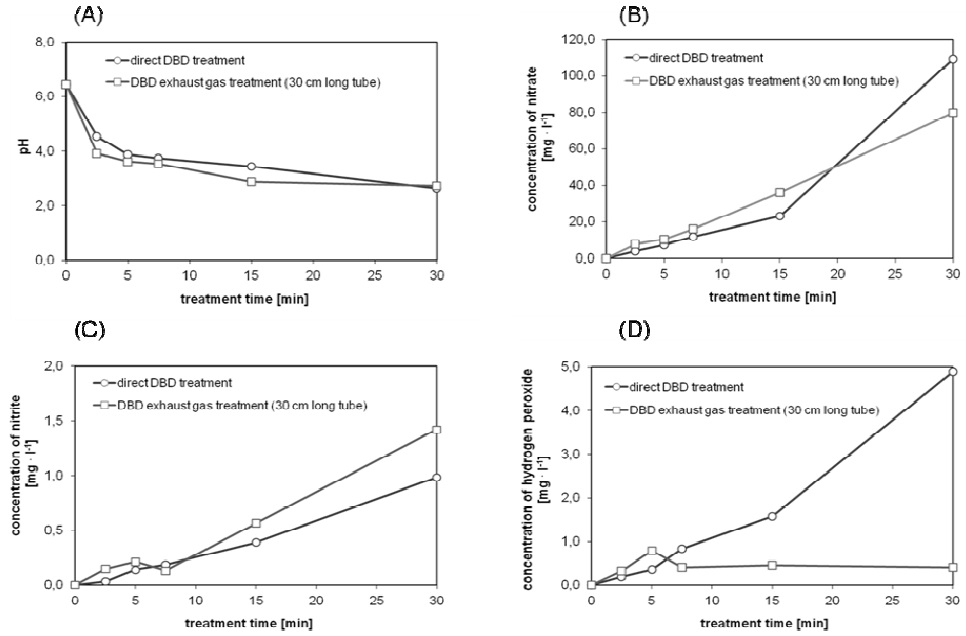


Fig. 5: Analytical results for pH (A), NO_3^- (B), NO_2^- (C) and H_2O_2 (D) in DBD treated water (-o-) or DBD exhaust gas treated water (-□-) in air.

Figure 6 shows that the DBD exhaust gas treatment resulted in a delayed complete inactivation within 17.5 min (number of viable microorganisms below detection limit) in comparison to DBD treatment of 5 ml suspended *E. coli* (7 min). Following, longer treatment times with DBD exhaust gas in comparison with direct DBD treatment were needed for complete bacteria inactivation. In argon

atmosphere, both, direct DBD treatment as well as treatment with exhaust gas from DBD resulted in no significant inactivation of *E. coli* within 30 min treatment times (data not shown).

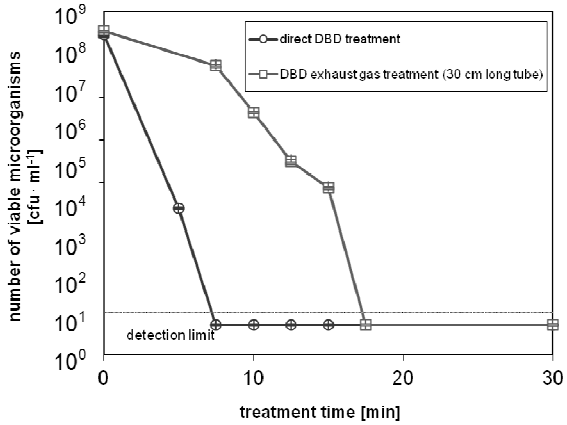


Fig. 6: Inactivation kinetics of *E. coli* by direct DBD treatment (-o-) and by DBD exhaust gas treatment (-□-) in air.

Following, H_2O_2 formation is a result of short lived plasma species and maybe radiation. Both short and long-lived reactive nitrogen and oxygen species are needed for fast and effective inactivation of microorganisms.

4. Conclusion

In the ozone gassing experiments a pH decrease to 4.7, but lower generation of H_2O_2 compared to direct DBD treated water was found. Inactivating effects on the microorganisms are weaker in case of O_3 gassing. Consequently, the observed effects of the DBD treatment were not dominated by O_3. The generation of acidic protons (H^+) and H_2O_2, as well as, the antimicrobial effects may result from reactions of ozone with water. Presumably, $HO^\bullet$ and $HOO^\bullet$ radicals were produced and may cause the inactivating effects of the microorganisms. Also the pH decrease could be explained. The H_2O_2 generation is a result of radical recombination. Additionally, other presumably nitrogen-based reactive species may play a role in the effects of plasma-liquid interaction.
In DBD exhaust gas treated water nearly the same pH, nitrate and nitrite concentration were found compared to direct DBD treatment of liquid but nearly no hydrogen peroxide. These results, and additional experiments using argon instead of air as working gas, suggest that the acidification is mainly initiated by reactive nitrogen species (RNS). The bactericidal effects on *E. coli* were reduced in case of all experiments with DBD exhaust gases. Therefore, H_2O_2 formation of liquids by means of direct plasma treatment in argon and air is a result of short lived plasma species and maybe radiation. In case of direct argon DBD treatment, acidification is not due to RNS but might be from short lived species like OH radicals. Therefore, more investigations have to be done to get further insight into mechanisms of plasma-liquid interaction and resulting biological effects.

Acknowledgements:
This study was realized within the joint research project “Campus PlasmaMed” supported by the German Federal ministry of Education and Research grant no. 13N9779 and 13N11188.

5. References

[1] Oehmigen K et al. 2010 *Plasma Processes and Polymers. Vol.* **7** *250-257.*
[2] Oehmigen K et al. 2011 *Plasma Processes and Polymers. Vol.* **8** *904-913.*
[3] von Woedtke Th et al. 2012 in: Machala Z et al. (eds.) *Plasma for Bio-Decontamination, Medicine and Food Security,* Springer, 67-78
[4] Burgassi S et al. 2009 *Journal of Applied Microbiology. Vol.* **106**, *1715-1721*.
[5] Restaino L et al.1995 *Applied and Environmental Microbiology. Vol.* **61**, *3471-3475*.
[6] Ikawa S et al. 2010 *Plasma Processes and Polymers. Vol.* **7**, *33-42*.
[7] Daiber A et al. 2002 *Chemie in unserer Zeit. Vol.* **6**, *366-375*.

OZONE-MIST SPRAY STERILIZATION FOR PEST CONTROL IN AGRICULTURAL MANAGEMENT

Kenji Ebihara[1,2], Fumiaki Mitsugi[2], Tomoaki Ikegami[2],
Norihito Nakamura[3], Yukio Hashimoto[3], Yoshitaka Yamashita[3],Seiji Baba[4],
Henryka D.Stryczewska[5], Joanna Pawlat[5], Shinriki Teii[6], Ta-Lun Sung[6]

[1]Environment and Energy Laboratory,[2] Kumamoto University,[3]Sanwa hi-tech Co.Ltd,
[4]Densoken Co.LTD,[5]Lublin University of Technology, [6]Lunghwa University of Science and Technology
E-mail:kankyo@mild.ocn.ne.jp

We have developed a portable ozone-mist sterilization system to exterminate pests (harmful insects) in agricultural field and the greenhouse. The system is composed of ozone generator, water spray ,and oxygen small container. The ozone generator can supply high dense ozone using the surface dielectric barrier discharge. Ozone-mist is produced using a developed nozzle. We studied the effects of ozone-mist spray sterilization on insects and agricultural plants. The sterilization conditions are estimated by monitoring the behavior of aphids and observing the damage of the plants. It was shown that aphids were exterminated in 30 sec without noticeable damages of the plant leaves.

1. Introduction

Ozone sterilization in agriculture is one of promising technologies to secure safety of food processing. Environmentally friendly alternatives to agricultural chemicals for plant fumigation have been required. The recent interest in organic products has been heightened by consumers' increased expectations regarding their food and the environment. Organic agricultural methods are internationally regulated and legally enforced by many nations. Biological pest control in organic farming includes herbicides, insecticides and fungicides.

Ozone (O_3) is the strongest commercially available disinfectant and also is very effective at destroying bacteria, viruses and odors. It has a very short half-life in air, water and soil, and decomposes in simple diatomic oxygen or forms oxide matters.

We have studied the application of gaseous ozone to soil sterilization and the biological effect of gas phase ozone on the DNA genome contained in bacteria and viruses [1-10]. We have developed the gaseous ozone sterilization system for agricultural soil which ensures a secure agricultural production. The reaction of the agricultural matter including air, water ,soil and plants with ozone causes complicated change in physical, chemical and biological properties.

Here, we proposed a portable ozone-mist sterilization system to exterminate pests (harmful insects) in agricultural field and the greenhouse. The system is composed of ozone generator ,water spray ,and oxygen small container. The ozone generator can supply high dense ozone of maximum concentration of 86 g/m^3 at a flow rate of 1 liter/min using the surface dielectric barrier discharge. Ozone-mist is produced using a developed nozzle. We studied the effects of ozone-mist spray sterilization on insects and agricultural plants. Most of pathogenic viruses like mosaic viruses are transmitted and spread by aphids and also by mechanical means.
The ozone-mist treatment conditions for aphid sterilization system were studied for practical use in agriculture.

2.Experimental

Figure 1 is the picture of the ozone-mist sterilization for agriculture. High dense ozone was generated by surface dielectric barrier discharge (1). The AC electric power to the high frequency generator was supplied from the AC-DC inverter (2) connected to Li-ion battery(3).

Figure 2 shows ozone concentration (g/m^3) as a function of oxygen gas flow rate. Maximum concentration of 86 g/m^3 was attained at a flow rate of 1 liter/min. Water mist was produced by supplying the water to the specific nozzle. The pump in the water container(4) to generate the mist was powered by Li-ion battery. High dense ozone was injected into the water mist through the gas nozzle. The ozone-mist generated near the nozzles was sprayed on the samples such as insects and plants.

The sterilization conditions was estimated by monitoring the dynamic behavior of aphids and observing the damage of agricultural plants (leaves of tomato and eggplant) when the ozone-mist was sprayed at various conditions of ozone concentration, mixture rate of ozone gas and water , their flow rates , spraying time and treatment location.

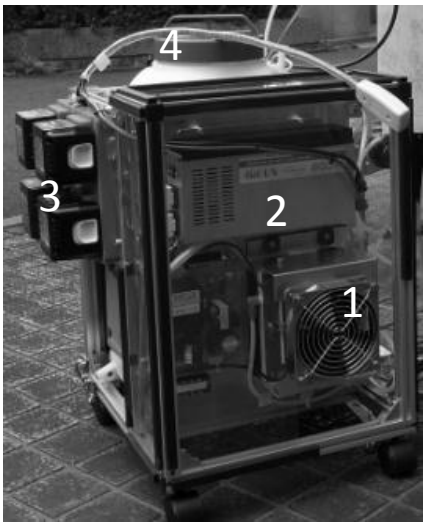


Fig.1 Ozone-mist sterilization system

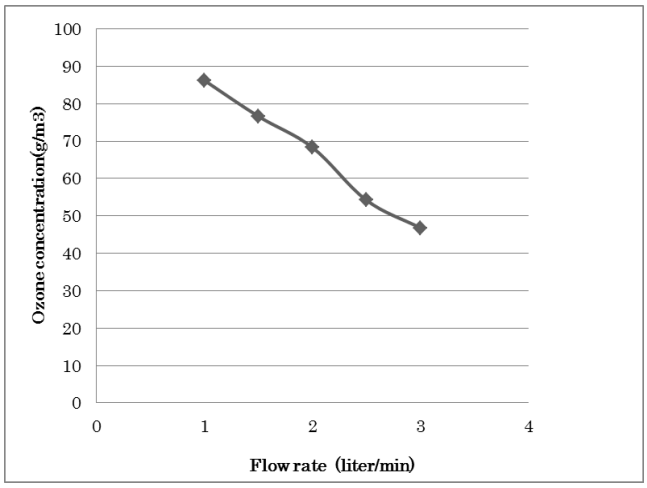


Fig.2 Ozone concentration characteristics of ozonizer.

We carried out the ozone-mist treatment for several insects, viruses and plants listed in Table 1.

Table 1. Insects, viruses and agricultural plants treated by ozone-mist spraying.

Insect	Virus	Plant
Aphid Red aphid(Uroleucon nigrotuberculatum) Cotton aphid (Gossypii glover) Crysanthermum aphid (Mocrosiphonella Sanbolnl) Rose aphid (Sitobion ibarae) Tobacco worm: Lasioderma serricorne (Fabricius) Green rice leaf hopper Caterpillar	Tobacco mosaic virus (TMV) Cucumber mosaic virus (CMV)	Tomato Eggplant Cucumber Tobacco

3. Results and Discussion

Figure 3 is a typical picture after ozone-mist treatment (30sec) for the red aphid (Uroleucon nigrotuberculatum). The conditions were ozone concentration of 68g/m^3 with a oxygen flow rate of 2 liter/min and water flow rate of 300ml/min. We found 98% of the aphids died. The treatment was performed at the distance (d) between the ozone ejection nozzle and the sample of 20mm. The survival rate(=survival account /total account) rapidly decreased with the distance(d).

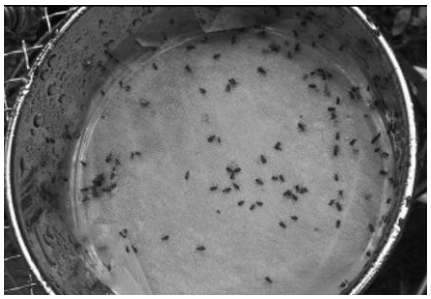


Fig.3 Photo of red aphids treated by ozone-mist spraying for 30 sec.

Figure 4 and 5 show the survival rate as a function of the treatment time at the distance of 50mm. The rate was about 8% at the short treatment time till 60 sec and then decreased rapidly with increasing time.

When ozone reacts with water-mist, highly unstable and rapid decomposition occurs.

The elementary reactions follow:

$OH^- + O_3 \rightarrow {}^*HO_2 + {}^*O_2^-$ (1)

${}^*HO_2 = H^+ + {}^*O_2^-$ (2)

${}^*O_2^- + O_3 \rightarrow O_2 + {}^*O_3^-$ (3)

${}^*O_3^- + H^+ \rightarrow HO_3$ (4)

$HO_3 \rightarrow O_2 + {}^*OH\cdot$ (5)

$O_3 + {}^*OH \rightarrow {}^*HO_2 + O_2$ (6)

Initial formation of the superoxide ion radical (${}^*O_2^-$) and the hydroperoxide radical (${}^*HO_2$) leads to the generation of the highly reactive hydroxl radical (*OH). The ozonide radical ion (${}^*O_3^-$) is formed as an intermediate reaction product [11]. The pH value defined by $pH= - \log_{10}[H^+]$ is dependent on hydrogen ion $[H^+]$ or hydroxide ion$[OH^-]$. A half-life time of ozone in aqueous solution was measured to be in the range from 2 min to 165 min depending on the conditions such as temperature, pH value and gas dynamics [11]. We observed increase of pH value of the mist water after the treatment. The ozone and its derivative radicals such as ${}^*O_2^-$,${}^*HO_2$, *OH, ${}^*O_3^-$ enter the respiratory system of the aphid and give fetal damage to kill aphids .

The biological effects of ozone on plants have been studied under the air pollutant ozone and plants have evolved a complex of defense response mechanisms to respond various environmental stresses triggered by ozone. We studied the ozone-mist effect on tomato and eggplant.

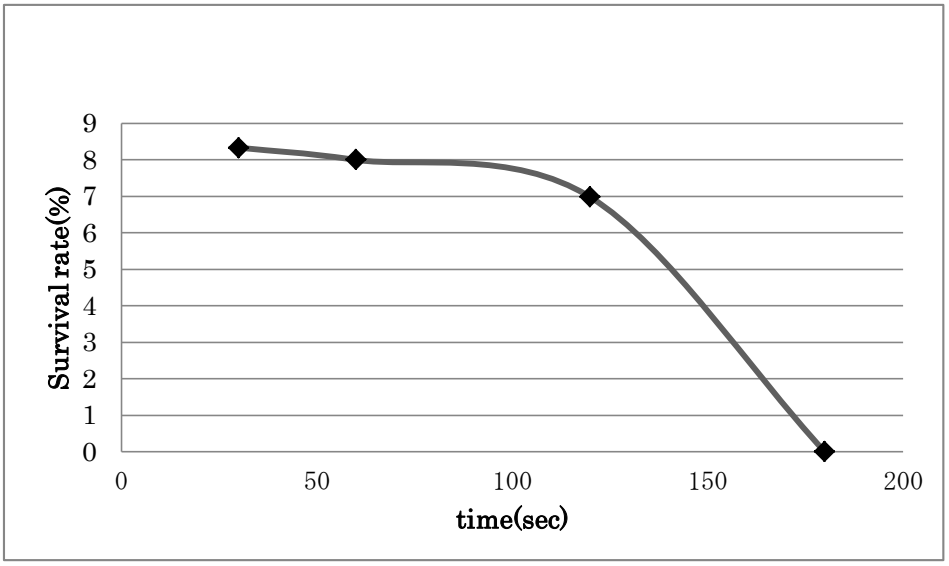


Fig.4 Survival rate of red aphid as a function of ozone-mist spraying time. Distance of ozone nozzle-sample is 50mm.

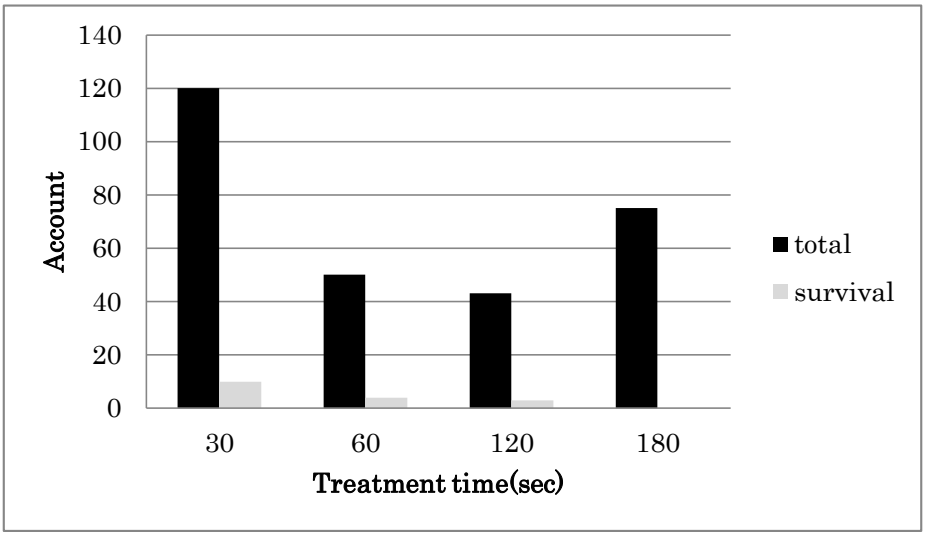


Fig.5 Survival number of aphids at various spraying times.

Figure 6 shows the picture of tomato young seedling. The left leaves and the right leaves were sprayed during 30 sec and 60 sec , respectively. We can notice remarkable damage on the leaves of young seeding. On the other hand, large eggplant sprayed by the similar conditions did not show noticeable damage. The stoma of plant is a pore in leaf and stem used for gaseous exchange. The microscopic measurement showed that the ozone-mist treatment gives serious damage on the stomata.

4. Conclusions

We have developed ozone-mist sterilization system to exterminate harmful insects in agricultural

management. Many kinds of aphids were tried for ozone-mist sterilization and biological effect on the sprayed pants were inspected. It was found that ozone derivative radicals in the ozone-mist play effective role on sterilization. Most of aphids were exterminated by 30 sec ozone-mist spraying.

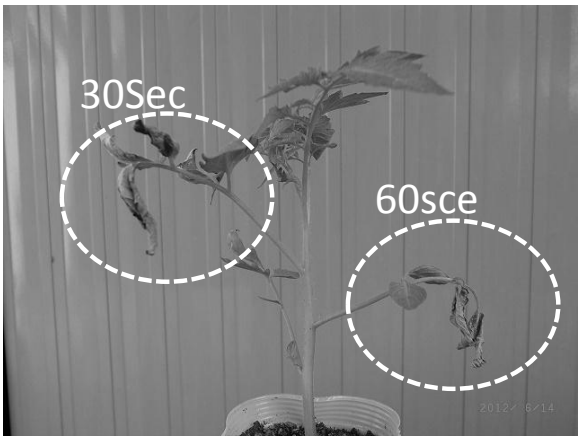


Fig.6 Photo of tomato leaves treated by ozone-mist during 30sec (left) and 60sec (right)

We would like to express sincere thanks to President Wang of Yunnan Science-Technology Trade Co. Ltd and Mr.Dai of Hongta Tobacco Group Co. Ltd. for their encouragement extended to our research and thoughtful support of tobacco farm experiment at Yunnan, China.

References

[1].Ebihara,K., Takayama,M.,Ikegami, T., Ogata,K. Stryczewska,H.D., Gyoutoku,Y., and Sakai,T ,J.Adv. Oxid. Technol. Vol.9,No.2,pp.170-173,2006.
[2]. Takayama, M., Ebihara,K., Stryczewska,H.D., Ikegami,T., Gyoutoku,Y., Kubo,K., Tachibana,M. , Thin Solid Films, 506-507, pp.396-399,2006.
[3].Ebihara,K., Takayama,M., Ikegami,T., Stryczewska,H.D., Gyoutoku,Y., Yokoyama,T., Gunjikake,N., Tachibana,M., Sakai,T , Proceedings of 17th International Symposium on Plasma Chemistry, Toronto, Canada,August 7th- 12th,CD(1201).,2005.
[4].Ebihara,K., Takayama,M., Strycewska,H.D., Ikegami,T., Gyoutoku,Y., Tachibana,M., IEEJ Transaction (in Japanese), 125, No.10, pp.963-969,2006.
[5]. Ebihara, Kenji., The Workshop on the Applications of Plasma to Green Environmental Technology ,Taoyuan, Taiwan, December 11-12,2006: Proceedings, pp.86-90,2006.
[6].Ebihara,K.,Sugimoto,S.,Ikegamo,T.,Mitsugi,F.,Stryczewska,H.D., 6th International Conference on Electromagnetic Devices and Processes in Environment Protection (ELMECO-6), Nateczow, Poland, June 24-28,2008.
[7].Ebihara,K.,Ikegami T.,Mitsugi, F.,Ikegami, T., Stryczewska,D.H.,Goutoku, Y., Proceedings of the applications of plasma to bio-medical Engineering, December 15-17, Lunghwa University of Science and Technology, Taoyuan,Taiwan,2008.
[8].Ebihara,K., Mitsugi,F.,Ikegami Tomoaki,Ikegami Takashi, D.H.Stryczewska, 6th Asia-Pacific International Symposium on Basic and Application of Plasma Technology, Dec.14-16,Hsinchu, Taiwan, X07,pp.7,2009.
[9].Ebihara,K.,Mitsugi,F.,Ikegami,Tomoaki , Sakai,T., Ikegami,Takashi, Stryczewska,H.D.,The 16th International Conference on Advanced Oxidation Technologies for Treatment of Water, Air and Soil, San Diego, California, Nov.15-18,2010,pp.104-105.
[10].Ebihara,K., Stryczewska,H., Ikegami,T., Mitsugi F., Pawlat,J. Electrical Review, R.87 NR7/2011, pp.148-152,2011.
[11]Khadre,M.A., Yousef, A.E.,Kim,J.-G., Journal of Food Science, Vol.66, No.9,pp.1242-1252,2001.

NANOPARTICLES CONTAINING COATINGS DEPOSITION ASSISTED BY ATMOSPHERIC PRESSURE PLASMA JET

Marina Fantin[2*], Paolo Scopece[1], Stefano Costacurta[1], Alessandro Patelli[2], Marino Colasuonno[2], Arianna Gambirasi[3], Monica Favaro[3]

[1]*Associazione CIVEN, via delle Industrie 5, Venezia, Italy*
[2]*Veneto Nanotech, via San Crispino 106, Padova, Italy*
[3]*Istituto di chimica inorganica e delle superfici CNR-ICIS, corso Stati Uniti 4, Padova, Italy*
E-mail: marina.fantin@venetonanotech.it

Nanostructured coatings are widely requested by industry in order to achieve innovative functionalities such as protective, antireflection, antibacterial and others. In this work we present a new method for the fabrication of nanostructured coatings with improved photocatalytic properties, in which titania dioxide nanoparticles are deposited and embedded in a ceramic film by mean of an atmospheric pressure plasma jet deposition. Results concerning two different strategies to obtain these coatings are here presented: a two-steps method in which titania nanoparticles are fixed after a sol-gel deposition, and a one step method in which titania nanoparticles are fluxed in a plasma jet together with a silica precursor.

1. Introduction

Nanostructured coatings are usually applied in industry thanks to their mechanical and functional properties, such as abrasion resistance, UV shielding, photocatalytic effect [1-3]. These coatings are defined by a nanoscale structure which cause a micro- and nanometer scale roughness and provide innovative mechanical or functional properties. Nanostructured surfaces are often obtained via sol-gel chemistry [4]: nanoparticles are dispersed in a liquid medium and deposited onto the surface by dip- or spin-coating techniques. An alternative method for the fabrication of transparent nanostructured antiscratch coatings was presented by our research group: a combined sol-gel/PECVD approach [5]. Sol-gel nanoparticles synthesises by a Stöber technique were deposited on a surface and fixed in a ceramic film by plasma-enhanced chemical vapour deposition. According to the nature of nanoparticles, it is possible to obtain coatings with different properties: alumina and silica nanoparticles are used to improve antiscratch properties [6], instead titania oxide nanoparticles can be used in sol-gel coatings to fabricate UV-cutting coatings and to fabricate self-cleaning coatings. In fact, the action of UV irradiation in TiO_2 leads to the generation of electron-hole pairs, which initiate the formation of active OH^* radicals capable of decomposing the majority of organic compounds [7, 8].
The latest challenge of our research group is to find a new route to embed nanoparticles on the surface. In this work we present two methods for the fabrication of nanostructured coatings with improved photocatalytic properties, in which titania dioxide nanoparticles are embedded in a ceramic film by atmospheric plasma deposition [4]. The first is a two-steps method (sol-gel and APPJ): nanoparticles are dispersed in a liquid medium and deposited onto surface by dip-coating techniques. After that, a silica matrix is grown via APPJ deposition to fully cover the nanoparticles and to create a complete bonding to the substrate. The second method (one-step) concerns only the deposition via atmospheric pressure plasma jet: a TiO_2 nanoparticles aerosol solution is fed into the discharge zone, and, at the same time the vapour silica precursor is fed in the same zone. The photocatalytic property of titanium dioxide nanoparticles has been measured as a function of UV irradiation time: FT-IR spectroscopy has been used to address the chemical changes in stearic acid films deposited on the photocatalytic surface [10,11]. Finally, UV-filtering capabilities of our film were studied through UV spectrometer.

2. Experimental

2.1 Sol-gel nanoparticles deposition

The substrates chosen for this work were silicon wafers and borosilicate glasses. They were cleaned with a solution of H_2O_2:NH_3 1:1 for 2 minutes and then with deionised water. Titania nanoparticles (VP Disp. W740X, Degussa) were dispersed in ethanol to obtain a 2% wt solution and sonicated for

10 minutes. The nanoparticles were deposited on the silicon wafers by dip-coating at controlled speed of 200 mm min^{-1} and relative humidity (RH<10%); on borosilicate glasses substrates samples are prepared at three different speeds (15, 80 and 200 mm min^{-1}).

2.2 APPJ silica deposition

The silica coating films were obtained on silicon substrates by atmospheric plasma deposition employing a jet system. The plasma is generated inside the nozzle by a discharge in the ionization gas flux, at atmospheric pressure, using kilohertz excitation and expelling the gas from the discharge zone through a circular orifice onto the substrate. Hexamethyldisiloxane (HMDSO, purity 98%, Fluka Analytical) and 3-methacryloxypropyltrimethoxysilane (MEMO, purity 98%, Sigma Aldrich) has been used as chemical precursors. HMDSO was vaporized at 125°C and introduced, at a rate of 15 g/hour, at the exit of the nozzle by mean of a carrier gas, while MEMO was introduced as aerosol at the exit of the nozzle (6 g/hour and nitrogen as carrier gas).

Tab. 1. Process condition to obtain HMDSO coatings.

Sample	Plasma Power (VA)	Ionization gas	Nozzle speed (m min^{-1})	Nozzle height (mm)	Treatments
HMDSO_10	710	N_2	80	12	4
HMDSO_11	1050	N_2	80	12	4
HMDSO_12	1210	N_2	80	12	4

Tab. 2. Process condition to obtain MEMO coatings.

Sample	Plasma Power (VA)	Ionization gas	Nozzle speed (m min^{-1})	Nozzle height (mm)	Treatments
MEMO_6	710	N_2	80	12	3
MEMO_7	1050	N_2	80	12	3
MEMO_8	1210	N_2	80	12	3

2.3 Two-steps composite preparation

Titania nanoparticles deposited onto the surface by dip-coating technique (as showed in §1.1) were encapsulated in a ceramic coating via APPJ deposition. Process conditions were the same described in Table 1 for HMDSO composite films and in Table 2 for MEMO composite films.
Borosilicate glasses substrates coated with nanoparticles were treated with different deposition conditions:

Tab. 3. Process conditions to obtain two-steps HMDSO composite coatings on borosilicate glasses.

Sample	Plasma Power (VA)	Ionization gas	Nozzle speed (m min^{-1})	Nozzle height (mm)	Treatments
NP15_2stepsG_HMDSO	710	N_2	10	10	3
NP80_2stepsG_HMDSO	710	N_2	10	10	3
NP200_2stepsG_HMDSO	710	N_2	10	10	3

2.4 One-step composite preparation

The second method concerns only the deposition via atmospheric pressure plasma jet: a TiO_2 nanoparticles aerosol solution (solution amount 6 g/hour and nitrogen as carrier gas) is fed into the discharge zone, where, at the same time, vapours of silica precursor are fed by a different carrier gas channel.

Tab. 4. Process conditions for one-step composite on Si wafers.

Sample	Plasma Power (VA)	Ionization gas	Nozzle speed (m min^{-1})	Nozzle height (mm)	Treatment numbers
NP_1step_HMDSO2	1050	N_2	80	12	3

2.5 Characterizations techniques

Coatings thickness measurements were performed by mean of a stylus profiler (Alpha Test IQ from KLA-Tencor) on the edge of the coatings obtained on silicon wafers.
Stearic acid degradation tests were carried out to characterize the photocatalytic activity. For this purpose, 50 µl of stearic acid dissolved in methanol was applied on each sample; the surface was rotated in a spin-coating apparatus for 30 seconds with a speed of 1500 rpm. All samples were irradiated with a UV light (365 nm). Stearic acid ($C_{18}H_{36}O_2$) degradation was monitored as a function of the UV irradiation time by measuring the absorbance of C-H bonds within the range of 2750-3050

cm^{-1} with a FTIR spectrometer (Perkin Elmer Spectrum One), performing 16 scans for each sample and with a spectra resolution of 4 cm^{-1}.
The absorption spectra of the films deposited on borosilicate glasses were measured with a Lambda UV-Vis spectrometer (Perkin-Elmer) within the range of 900-200 nm.

3. Results and discussion

3.1 SEM characterization

SEM images show that dip coated titania nanoparticles form a multilayer and homogeneous film, which appears poor in adhesion with its silicon substrate (Fig. 1a). By applying a silica coating on the dip-coated nanoparticles it is possible to notice a sort of nanoparticles embedding (Fig.1b). Finally, SEM observations show that by working with the one-step method it is possible to deposit a nanoparticles-silica composite, but the film is not homogenous and adherent to the silicon substrate. At this operative conditions the obtained nanoparticles density is too low (Fig. 1c).

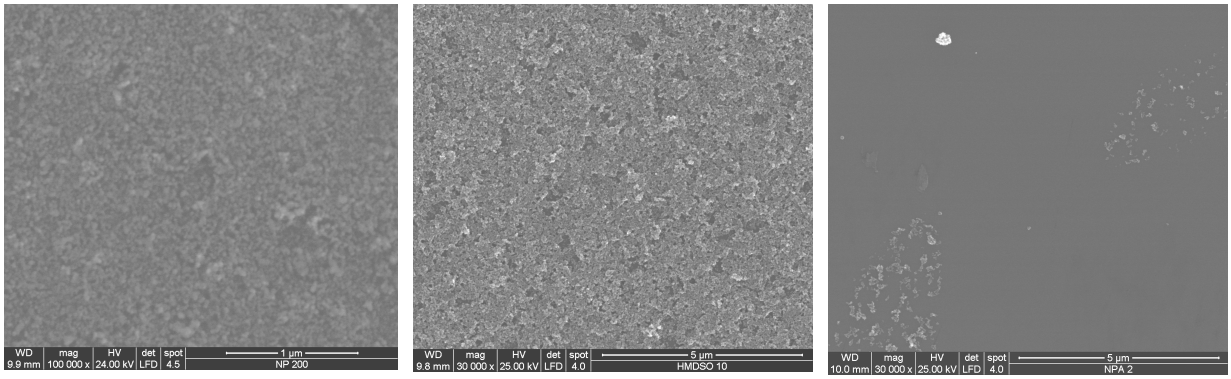


Fig. 1. SEM images of: (a) dip coated NP200 sample, (b) two-steps composite coating obtained with HMDSO, (c) NP_A sample: one-step composite coating.

3.2 Nanoparticles photocatalytic activity

The photocatalytic activity studies of NP200 show that there is a clear differences in the C–H bond absorbances of the FTIR spectra: titania nanoparticles are able to degrade stearic acid in only 30 minutes (Fig. 2a).
In order to understand if the plasma power can affect the nanoparticles photo-activity, the nanoparticles coatings were treated with three different plasma powers:

Tab. 5. Process conditions of plasma treatment on nanoparticles coatings.

Sample	Plasma Power (VA)	Ionization gas	Nozzle speed (m min^{-1})	Nozzle height (mm)	Treatment n
NP200_1	710	N_2	80	12	3
NP200_2	1050	N_2	80	12	3
NP200_3	1210	N_2	80	12	3

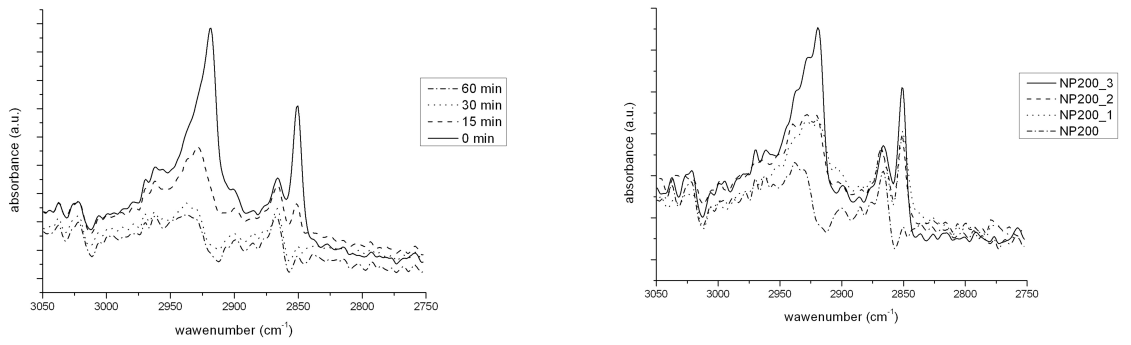


Fig. 2. FTIR spectra of C–H bonds in stearic acid of NP200 at three different exposure times (a), and the comparison of the photoactivity at 30 minutes of UV-light exposure, after three different plasma treatments (b).

The photocatalytic activity of titania nanoparticles coatings treated with lower power plasma (NP200_1 and NP200_2) is quite the same of NP200, so the low power doesn't affect the nanoparticles. Instead more powerful plasma (NP200_3) seems to inactivate the photocatalytic activity of nanoparticles film; this interesting fact needs to be further analyzed.

3.3 Silica film characterization

The silica coating films obtained on silicon substrates by atmospheric plasma deposition have three different thickness. HMDSO precursor allows to obtain thinner and more homogeneous films than MEMO precursor.

Tab. 6 and 7. Stylus profiler measurements of HMDSO coatings and MEMO coatings.

Sample	Thickness (nm±10%)
HMDSO_10	20
HMDSO_11	40
HMDSO_12	50

Sample	Thickness (nm±20%)
MEMO_6	70
MEMO_7	150
MEMO_8	200

By comparing the two FT-IR spectra it is clear that the MEMO coating contain its original acrylic functionalities.

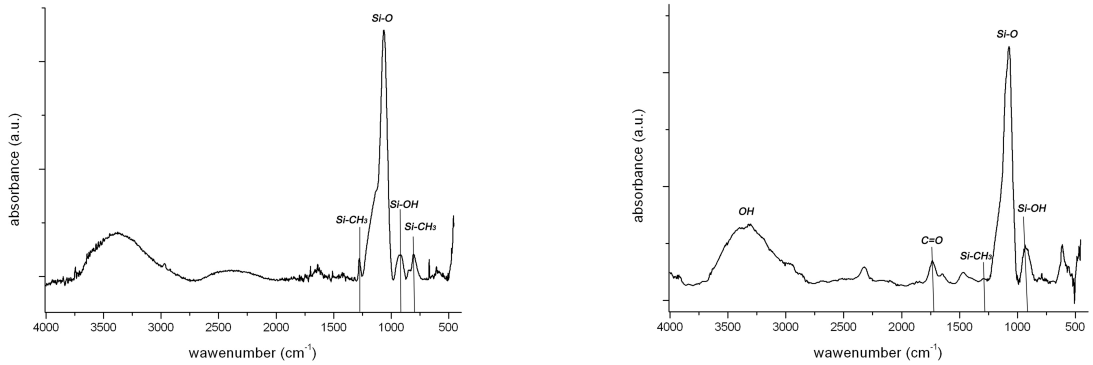


Fig. 3. Typical FT-IR spectra of HMDSO coating on the left (a) and MEMO coating on the right (b).

3.4 Composites characterization: photocatalytic activity and UV-filter properties

HMDSO composite coatings

The results of the stearic acid test show that NP200_2steps_HMDSO10 composite has a good fotocatalytic activity: after three hours all the stearic acid is degraded. Instead the degradation of stearic acid in samples NP200_2steps_HMDSO11 and NP200_2steps_HMDSO12 is much slower than untreated nanoparticles, maybe due to the higher thikness of the silica coating.

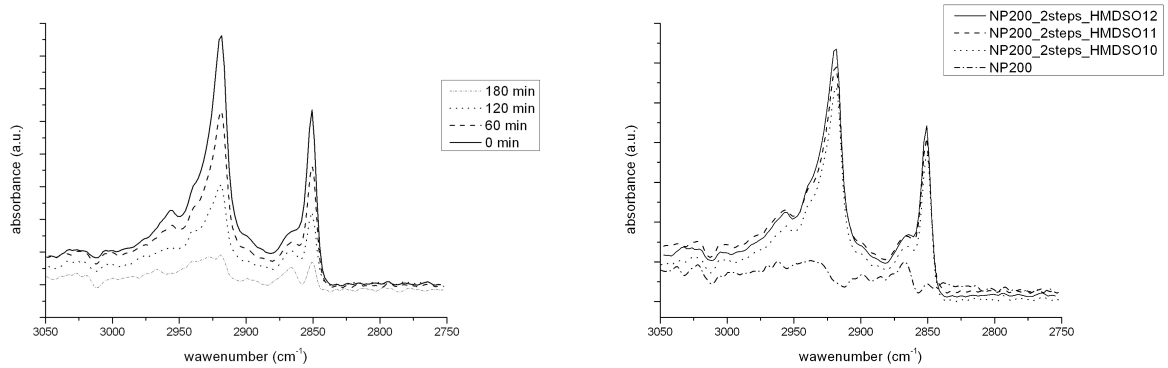
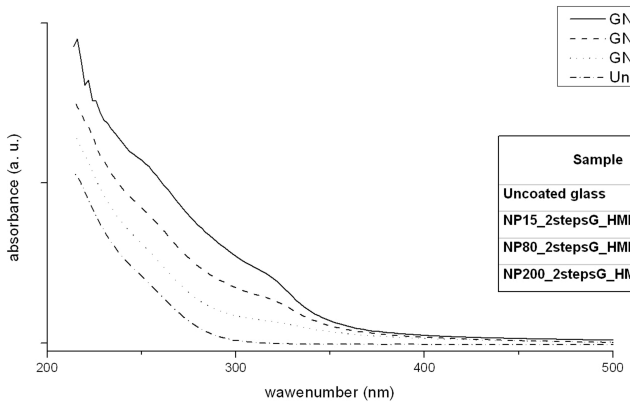


Fig. 4. FTIR spectra of C–H bonds in stearic acid: NP200_2steps_HMDSO10 on the left (a) and the comparison between the three composite films at 60 minutes of UV-light exposure on the right (b).

As Figure 5 shows, UV absorption spectra of the films deposited are different from the untreated glass one. At 300 nm wavelength the absorption rate of coated glasses is higher than borosilicate glass (see Fig. 5 inset), thanks to the presence of titania nanoparticles and their UV-absorbing properties [7].

Moreover the absorbance value is directly proportional to the quantity of nanoparticles on the surface: NP200 shows the higher value because the higher velocity deposition leads to a thicker nanoparticles film.



Sample	Absorbance at 300nm
Uncoated glass	0,09
NP15_2stepsG_HMDSO	0,4
NP80_2stepsG_HMDSO	0,77
NP200_2stepsG_HMDSO	1,14

Fig. 5. The absorption spectra of the composite films deposited on borosilicate glass.

MEMO composite coatings

Figure 6 shows the C–H bond absorption bands in the FTIR spectra of stearic acid before and during the UV light exposure of NP200_2steps_MEMO6. The clear difference between the absorbances suggests that nanoparticles is still able to degrade stearic acid even if there is the silica film. For the samples NP200_2steps_MEMO7 and NP200_2steps_MEMO8 big changes of the absorbances could not be seen (figure not shown): the degradation of stearic acid is much slower than untreated nanoparticles. This could suggest that the silica film thickness influences the photocatalytic activity, especially when it is higher than 100 nm. Moreover for the sample NP200_2steps_MEMO8 nanoparticles film could be also affected by plasma power, as seen in §3.2.
Comparing the photocatalytic activity of the samples NP200_2step_HMDSO10 and NP200_2step_MEMO6 made with the low power plasma (Fig. 6b), it is possible to see that the second sample presents a faster photocatalytic activity, despite the thickness is greater than the HMDSO composite coating. This fact can be explained by considering the higher carbon content of the MEMO coatings and its acrylic functionalities, which lead to a less compact silica coating. This precursor could be considered better for the deposition of siliceous matrix in this type of application because it does not affect so much the photocatalytic activity of the nanoparticles films.

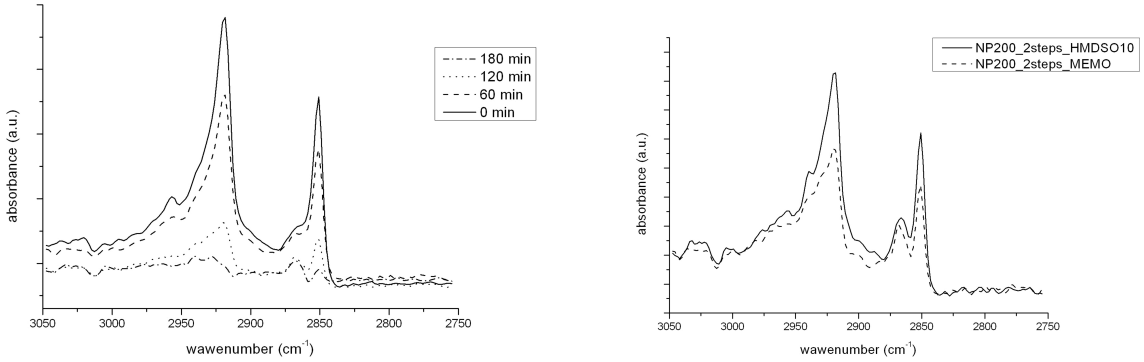


Fig.6. FTIR spectra of C–H bonds in stearic acid: NP200_2steps_MEMO6 on the left (a), and the comparison between NP200_2steps_HMDSO10 and NP200_2steps_MEMO6 at 120 minutes of UV-light (b).

One-step composite coatings:

For this composite the measurements of the photocatalytic activity do not show any positive effect at three hour of UV-light exposure, maybe due to the very low nanoparticles density (see Fig.1c). Also the limit of the aerosol used in this work could be the reason of the low amount of the deposited nanoparticles and we are working to find out the best process conditions.

4. Conclusions

Nanostructured coatings (titania nanoparticles in a silica matrix) were prepared by an innovative combined sol-gel/APPJ approach (two-steps method) and one step APPJ. In particular, by working with the two-steps method a composite film has been obtained with measurable photocatalytic activity. Silica matrix is obtained from HMDSO or MEMO precursors. They showed two different photocatalytic behaviours: MEMO precursor could be considered better for this type of application because it does not affect so much the photocatalytic activity of the nanoparticles films. The two-steps method allowed also to obtain UV-filters, working on borosilicate glasses.

The one-step method has shown its applicability, but the aerosol nanoparticles deposition needs to be operated with an higher throughput aerosol generator. In fact the limit of the aerosol used in this work was the low amount of conveyed nanoparticles solution (solution amount 6 g/hour). Finally, the fact that the titania nanoparticles treated under high plasma power conditions showed an inactivation of the phocatalytic effect will be further analysed and studied.

5. References

[1] Katangur P et al. 2006 *Polym. Degrad. Stab*. **91**:2437.
[2] Bautista Y et al. 2011 *Prog. Org. Coat.* **70**:178.
[3] Zhai L et al. 2004 *Appl. Surf. Sci.* **240**:318.
[4] Brinker C J, Scherrer C W 1990 *Sol-gel science. Academic Press*
[5] Costacurta S et al. 2011 *J. Sol-Gel Sci. Technogy.* **60**:340.
[6] Charitidis C et al. 2004 *Surf. Coat. Technology* **180**:357.
[7] Allen N S et al. 2005 *Photochem and Photobiology* **81**:279
[8] Wang D et al. 2011 *Mat. Letters* **65**:2526.
[9] Foest R et al. 2007 *Plasma Processes and Polymers* **4/0**:460
[10] Costacurta S et al. 2010 *Appl. Mater. Interfaces* **5**:1294.
[11] Piispanen M, Hupa L 2011 *Appl. Surface Sc.* **258**:1126

RESONANT INVERTER WITH RESONANCE FREQUENCY TRACKING FOR DBD PLASMA REACTOR SUPPLY

Tomasz Jakubowski[1], Marcin Hołub[1] and Stanisław Kalisiak[1]

[1] *West Pomeranian University of Technology, Szczecin, Electrical Engineering Department, ul. Sikorskiego 37, 70-313 Szczecin, Poland*

E-mail: tomasz.jakubowski@zut.edu.pl

This document gives an overview of a power supply construction suitable for DBD reactor excitation. The influence of temperature and voltage change on DBD reactor parameters is discussed. A power electronic supply system topology allowing for continuous resonant frequency tracking is proposed together with simulation and test stand results of operation. An additional feature of proposed topology is also discussed making the alternation of output peak – to –peak voltage possible only with the means of control pulse timing.

1. Introduction

Diesel engine exhaust treatment with low temperature plasma reactors [1-5] as well as other environmental plasma technologies such as odour abatement or VOC removal often implement dielectric barrier discharge (DBD) reactors as the main or additional source of oxidizing agents and radicals. Proposed paper deals with the problem of DBD supply under variable conditions including alternating reactor parameters. As a resonant topology is proposed, allowing for high supply system efficiency, with the change of plasma reactor parameters also the natural resonant frequency of the plasma source changes. Therefore a control system and/or power supply topology is beneficiary if it allows for continuous natural frequency tracking. A power electronic supply system is discussed due to the use of highly reliable and fully controllable solid state switches.

2. DBD reactor parameter change sensitivity

A laboratory DBD reactor was chosen for experiments. A modular, cylindrical type DBD reactor consisting of 58 single rods was constructed with the low voltage electrode on the outer side of each rod. Such reactors ore often implemented in ozone treatment facilities [6]. Electrodes were constructed from the stainless steel mesh. Reactor construction during operation is depicted in Fig. 1.

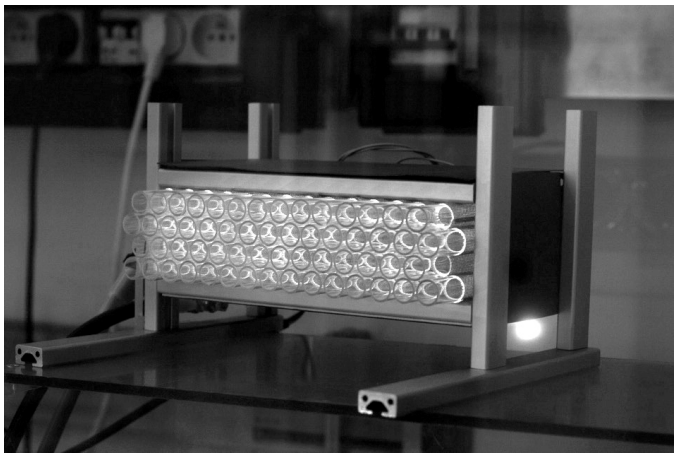


Fig. 1. The laboratory DBD reactor construction used for experiments.

Reactor parameters, due to the change of electrode peak – to – peak voltage, gas composition and humidity, temperature tend to change. Fig. 2 gives an overview of reactor's Lissajous curves for

different reactor power levels. As can be noticed the parallelograms are moved in the rotational axis around the point 0,0.

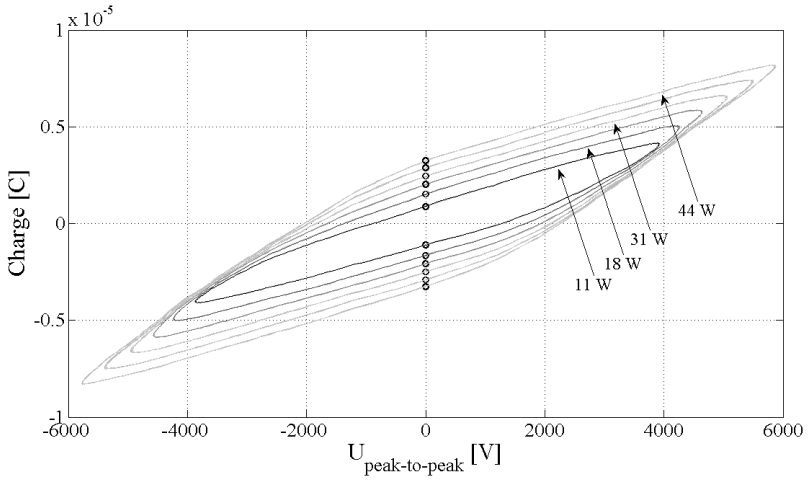


Fig. 2. Lissajous curves for alternating reactor power levels.

The reactor power was measured using the Lissajous curve method in order to establish main reactor parameters, to verify the temperature drift a cold (ambient temperature of 20 degrees Celsius) reactor parameters were obtained and after 5 minutes of continuous operation with the power of about 40W (5.79 kV peak, reactor temperature: 45 degrees Celsius), third measurement was done for lower operating voltage (3.88 kV peak). A WIMA 1mF FKP capacitor was used as an additional measurement element and is referred to as C_P. C_R represents the overall reactor capacity while C_D – dielectric capacity and C_G – gas gap capacity of the DBD reactor. Measured values are summarized in the Table 1, below. As can be noticed there are some temperature related drifts in reactor parameters, although the overall reactor capacitance does not change significantly. In contrast, reactor parameters for different operating voltage shows significantly different values in all cases.

Table 1. Measured reactor parameters as a function of reactor temperature and operating voltage

Measurement number	Measured average power [W]	C_R [nF]	C_D [nF]	C_G [nF]
1 – cold (20 degrees Celsius)	44.73	1.347	2.13	3.66
2 – after 5 minutes of operation (45 degrees Celsius)	42.3	1.356	2.08	3.9
3 – lower voltage	11.37	0.79	1.59	1.57

Variable reactor parameters increase the level of complexity of the power supply stage, most of all using resonance based supplies has to ensure proper power supply operation under variable load parameters.

3. Power electronic, resonant power supply topology

A series – parallel resonant inverter topology is proposed [7 ,8], where its operation is explained in detail. Fig. 3 gives an overview of basic source construction. L_Z – D_Z – connection represent an energy recovery snubber increasing systems overall efficiency.

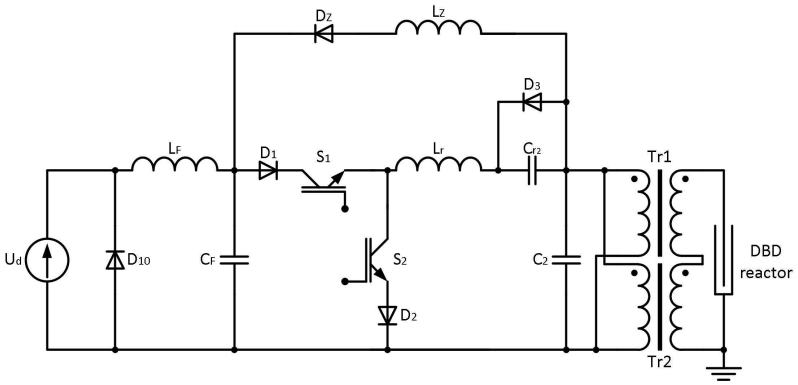


Fig. 3. The topology of power electronic, resonant supply suitable for continuous resonant frequency tracking.

Basic converter operation can be discussed as follows: energy delivery takes place between the serially connected resonant circuit L_r – C_{r2} in two stages. In order to simplify the analysis two theoretical waveform set examples are given in Fig. 4. Initially in time span $t_0 – t_1$ transistor S_1 starts conducting and resonantly recharges the capacitor C_{r2} while its voltage, due to parallel $C_2 – L_{Tr1}$ system resonance, is below the DC link charging voltage of U_d. The amount of energy transferred from voltage source U_d to the capacitor C_{r2} is a function of capacitors initial voltage and can therefore be controlled using variable S_1 and S_2 timing with respect to C_2 voltage zero point crossing (Fig. 4b). In the second recharge process ($t_2 – t_3$) the transistor S_2 is switched on, while the voltage across C_{r2} is decreasing. If the voltage across C_{r2} falls to zero D_3 diode starts conducting ($t_3 – t_4$).

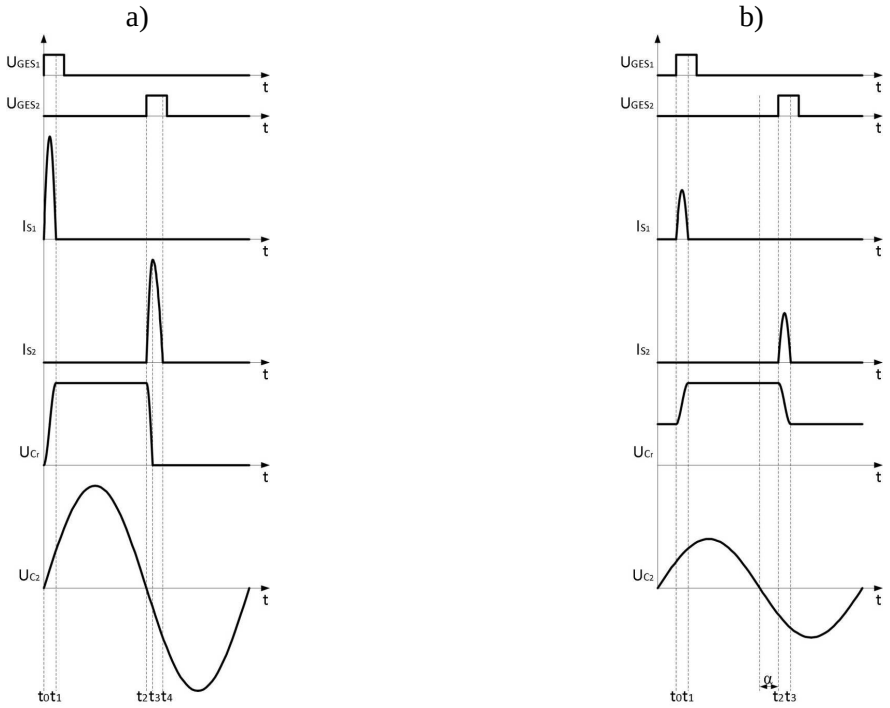


Fig. 4. Basic electrical waveforms during power supply system operation.

In consequence output voltage amplitude can be varied using transistor timing with respect to C_2 capacitor voltage and the system automatically adjusts to parallel circuit natural resonance frequency change. In addition the output voltage amplitude is controllable which is beneficiary for systems that require power controllability.

The tracking functionality was experimentally verified; results are depicted in Fig. 5. As can be noticed the system automatically adopted to a sudden resonant circuit parameter change.

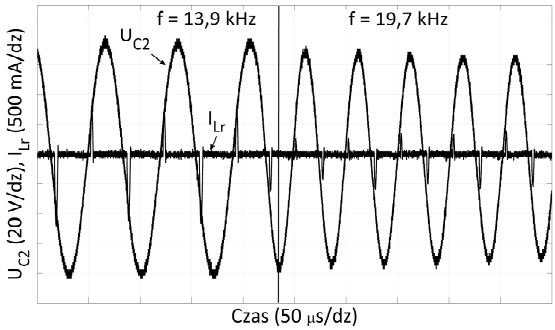


Fig. 5. The output voltage and current (primary high voltage transformer side) response to sudden resonant circuit parameter change.

Power transistor control signals are synchronized with the resonant capacitor C_2 voltage. Time delay between the natural resonance firing point (defined as delay electrical angle α) allows for output peak – to – peak voltage adjustment without the necessity of DC – link voltage control. Fig. 6 gives an overview of delay angle based controllability.

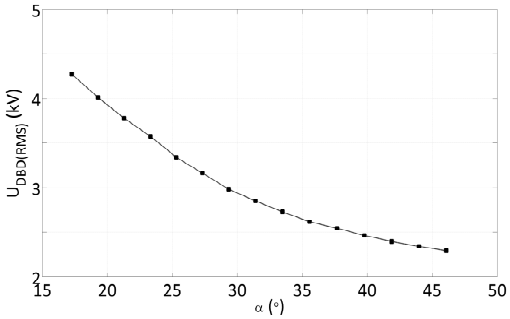


Fig. 6. The output voltage – control pulse phase delay (with respect to U_{C2} zero point crossing) dependency.

Output voltage controllability was experimentally examined. LeCroy Wave Runner 6100A digital oscilloscope was used for measurements together with high voltage, Tektronix probe P6015A and CPD31 current sensor. For efficiency measurements the input power was established using laboratory power supply EA-HV 9000-600-2000 readings and the overall efficiency was measured using Norma 6000 power analyser. Typical voltage and current waveforms are given if Fig. 7.

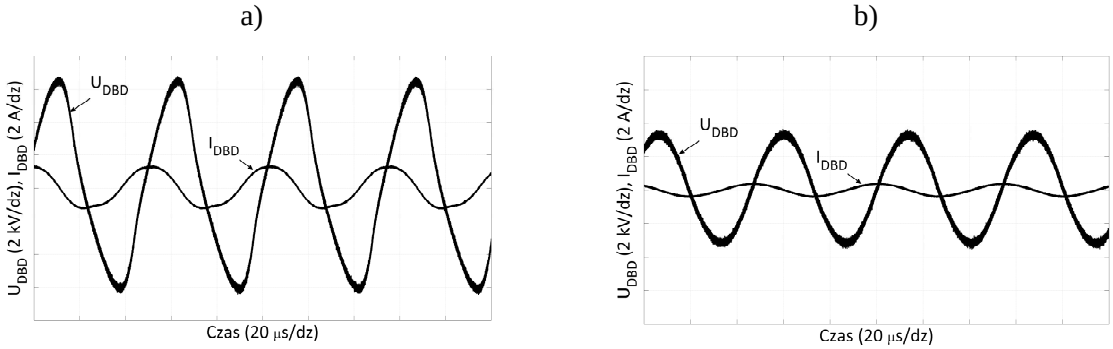


Fig. 8. DBD reactor voltage and current waveforms for two different delay angles: a) $\alpha = 17{,}2^{o}$; b) $\alpha = 46^{o}$.

Efficiency measurements were led in order to establish system's overall performance. Overall power supply unit efficiency (ηc), power electronic resonant converter (ηr) and high voltage transformer performance were evaluated (ηt). Measurement results are presented in Fig. 9.

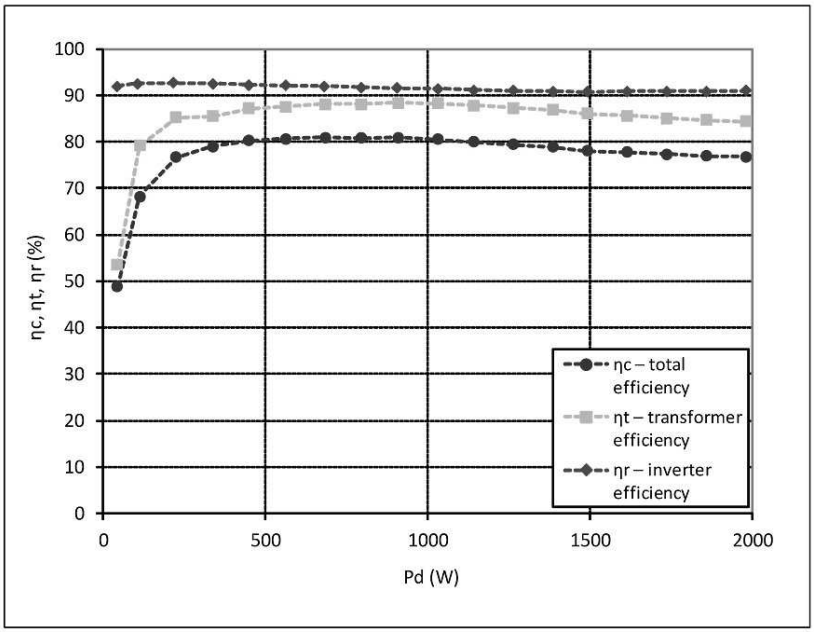


Fig. 9. Efficiency measurements of proposed power electronic supply construction and its main components.

4. Summary and conclusions

This document gives an overview of a power supply construction suitable for DBD reactor excitation. The influence of temperature and voltage change on DBD reactor parameters is discussed based on a series of experimental results. It can be noticed, that terminal voltage has a great impact on reactor electrical parameters. A power electronic, resonant power supply system topology is introduced allowing for continuous resonant frequency tracking and operation in reactor short – circuit state. An additional benefit is the property of synchronization with the capacitor voltage instead of the distorted reactor current waveforms. A high efficiency of 81% was obtained, most losses are generated in the high voltage transformer, the resonant power electronic converter itself obtained 91% efficiency.

5. References

[1] U. Kogelschatz: “Dielectric-barrier Discharges: Their History, Discharge Physics, and Industrial Applications”, *Plasma Chemistry and Plasma Processing*, Vol. 23, No. 1, March 2003.

[2] J.O. Chae: “Non-thermal plasma for diesel exhaust treatment”, *Journal of Electrostatics 57* (2003) 251–262.

[3] C.-L. Song, F. Bin, Z.-M. Tao, F.-C. Li, Q.-F. Huang: “Simultaneous removals of NOx, HC and PM from diesel exhaust emissions by dielectric barrier discharges”, *Journal of Hazardous Materials 2008, HAZMAT-9151*; No. of pages: 8.

[4] R. McAdams: “Prospects for non-thermal atmospheric plasmas for pollution abatement”, *J. Phys. D: Appl. Phys. 34* (2001) 2810–2821.

[5] T. Hammer: "Non-thermal plasma application to the abatement of noxious emissions in automotive exhaust gases”, *Plasma Sources Sci. Technol. 11* (2002) A196–A201.

[6] K. Ebihara, H. D. Stryczewska, F. Mitsugi, T. Ikegami, T. Sakai, J. Pawlat, S. Teii: „Recent development of ozone treatment for agricultural soil sterilization and biomedical prevention“, *Electrical Review*, R. 88, nr 6/2012, pp. 92 – 94.

[7] Jakubowski T., Kalisiak S., Holub M., Palka R., Borkowski T., Myskow J.: „New resonant inverter topology with active energy recovery in PDM mode for DBD plasma reactor supply“. *14th European Conference on Power Electronics and Applications*, pp. 1–8, 2011.

[8] Kalisiak S., Holub M., Jakubowski T.: Resonant inverter with output voltage pulse-phase-shift control for DBD plasma reactor supply. *13th European Conference on Power Electronics and Applications*, pp. 1–9, 2009.

THE APPLICATION OF DC ATMOSPHERIC PRESSURE GLOW DISCHARGES GENERATED IN CONTACT WITH FLOWING LIQUID CATHODE IN THE DISCHARGE TREATMENT WATER PROCESSES

Piotr Jamróz, Krzysztof Gręda, Paweł Pohl and Wiesław Żyrnicki

Wroclaw University of Technology, Faculty of Chemistry, Division of Analytical Chemistry, Wybrzeze Stanislawa Wyspianskiego 27, 50-370 Wroclaw, Poland
e-mail: piotr.jamroz@pwr.wroc.pl

Two kinds of stable atmospheric pressure glow discharges (APGDs) were generated in contact with flowing liquid cathode. As an anode, an argon microjet or a metallic electrode were applied. Both discharges were operated in the ambient air atmosphere at the supplied power lower than 30 W. Different atomic and molecular species were excited in the core of these discharges. The emission spectra of investigated APGDs were dominated by OH, NH, NO, and N_2 bands. In addition, weak atomic O and H emission lines were identified. In order to evaluate the spectroscopic properties of APGD sources used, optical temperatures, including excitation, vibrational and rotational temperatures, as well as the electron number density were determined and compared. Mechanisms of processes occurred in both discharges, responsible for the excitation of atoms and molecules, were also discussed. Water and artificial wastewater after treated by discharges were investigated. Concentrations of species formed due to discharge interaction with solution and degradation effects of wastewater components were measured. The both APGDs with respect to the indication of their possible application for the water purification processes were evaluated.

1. Introduction

Cold atmospheric plasmas (CAPs) generated in and in contact with liquids are frequently applied in the environmental protection engineering [1,2]. It is possible to apply such CAPs in water cleaning, sterilization and environmental remediation processes [1-3]. So far, different constructions of CAP sources, e.g., dielectric barrier discharges (DBDs), atmospheric pressure glow discharges (APGDs), atmospheric plasma jets (APJs), gliding arc or corona discharges [3-7], have successfully been employed in the wastewater treatment processes. Among them, APGD generated in and in contact with liquids is established to generate various oxygen and nitrogen chemically active species, i.e., H_2O_2 and O_3 molecules, OH, H, O_2H, NO and O radicals, as well as the UV irradiation [7,8]. Especially, OH radicals seem to play an important role in the chemical degradation of organic pollutants in wastewater solutions [2].

The main aim of the present work was to elucidate discharge-liquid interactions as well as the production yield of chemically reactive species in the discharge and the liquid phase. Spectroscopic discharge parameters, i.e., optical temperatures and the electron number density, were determined compared in order to clarify what elementary processes exist in APGD sources. The suitability of both APGDs sources in the wastewater purification treatment was also established.

2. Experimental setup

Atmospheric pressure glow discharges (APGDs) were generated in contact with flowing liquid cathode systems (Fig. 1). As the cathode a graphite tube imposed onto a quartz tube (i.d. 1.5-2 mm) was applied [9,10]. Both APGDs were obtained by the direct-current (dc) discharge with a miniature argon gas flow passed through a steel nozzle (i.d. 0.7 mm, see Fig. 1b) or a molybdenum rod anode (o.d. 2 mm, see Fig. 1b). A high voltage (HV) direct current (dc) power supply (Electronic Lab Equipment Engineering, Wroclaw, Poland) with a max. power output of 200 W, working in the current range within 0-400 mA was used. Additionally, a ballast resistor (10 kΩ, 50W), was applied to stabilize the discharge current.

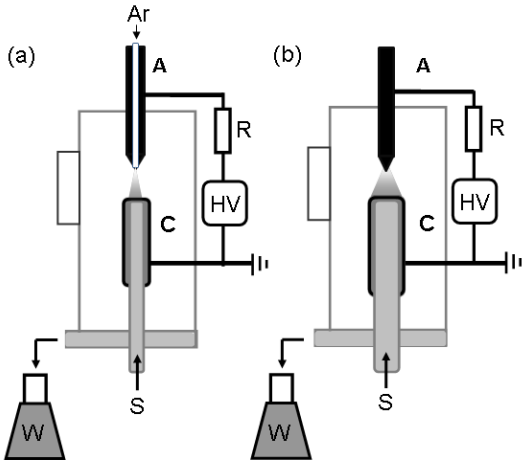


Fig. 1. The experimental set-up for the APGD system containing a) argon microjet-liquid cathode and b) solid anode-liquid cathode (A-anode, C-cathode, R-ballast resistor, HV-high voltage direct current power supply, S-initial solution, W-water solution treated by the discharge).

Both discharges were operated at the atmospheric pressure in the ambient air atmosphere. A peristaltic pump (LabCraft, France) was applied to deliver water sample solutions into the discharge zone Discharge operation conditions are given in Table 1. Water sample solutions, treated by both APGD discharges, were collected into 10-ml glass tubes with stoppers and were directly analyzed by chemical methods of the analysis (see details in the 3.3 and 3.4 sections).

Tab. 1 APGD generation conditions

APGD system	Ar microjet-liquid cathode	Pin electrode-liquid cathode
Discharge atmosphere	Argon in open to air atmosphere	Air at atmospheric pressure
Argon flow rate	up to 300 sccm	-
Discharge current	30 mA	30 mA
Sustaining voltage	1000-1100 V	900-1100 V
Ballast resistor	10 kΩ	
Gap between electrodes	5.0 mm	
Solution flow rate	0.6-3.2 ml min^{-1}	
Liquid cathode	Acidified solutions containing methyl red (MR), $Cr_2O_7^{2-}$ ions and Triton X-45 non-ionic surfactant	

3. Results and discussion

3.1. Emission spectra

It was found that spectra of APGD with argon microjet and solid anode systems were dominated by many emission bands of the N_2 molecule belonging to the second positive system ($C^3\Pi_u$-$B^3\Pi_g$), bands of the OH radical belonging to the $A^2\Sigma$-$X^2\Pi$ system, i.e., (1-0) and (0-0) band heads at 281.1 and 306.4 nm, bands of the NO molecule belonging to the γ-system ($A^2\Sigma^+$-$X^2\Pi$) in the 200-270 nm spectral region and the band of the NH molecule (the $A^3\Pi$-$X^3\Sigma^-$ system) with the band head at 336.0 nm [9,10]. Atomic hydrogen lines of the Balmer series (H_α, H_β and H_γ at 656.2, 486.1 and 434.1 nm, respectively) in addition to atomic oxygen lines (O I) at 777.2, 777.4 and 844.6 nm were also detected in both discharges. Strong emission lines of Ar I in the spectral range 650-800 nm and weak emission bands of the N_2^+ molecule at 391.4 and 427.3 nm belonging to (0-0) and (1-0) $B^2\Sigma^+_u$-$X^2\Sigma^+_g$ transition system were identified in case of the APGD system with the argon microjet [9]. It should be noted that intensities of NH, NO and N_2 molecular band heads observed for the argon microjet APGD source were higher in comparison to those obtained with the APGD system generated between the solid anode and the liquid cathode. This discrepancy may indicate that, in case of the argon microjet APGD system, metastable states of argon (Ar_m) with energy ~11 eV probably participate in the production of

NH, NO and N_2 excited states [9]. Emission intensities of OH band heads as well as O I and H lines were found to be comparable for both APGD systems studied.

3.2. Spectroscopic discharge parameters

Optical spectroscopic discharge parameters, i.e., excitation (T_{exc}), vibrational (T_{vib}) and rotational (T_{rot}) temperatures as well as the electron number density (n_e), for both investigated discharge systems are presented in Table 2.

Tab. 2. Spectroscopic discharge parameters determined in Ar microjet-liquid cathode [9] and pin electrode-liquid cathode [10] systems measured in the near cathode region.

	Ar microjet-liquid cathode	Pin electrode-liquid cathode
T_{exc}(Ar), K	7400-7800	-
T_{exc}(H), K	11000-15000	3100-4200
T_{vib}(OH), K	2900-3400	3800-4200
T_{vib}(N_2), K	3400-4000	3100-4600
T_{rot}(OH), K	2000-2600	2700-4100
T_{rot}(N_2), K	1600-1950	1700-2100
n_e, cm^{-3}	$(2.5\text{-}11)\times10^{14}$	$(3.4\text{-}6.8)\times10^{14}$

As can been seen, the excitation temperature as determined from H atoms for the discharge system with the argon microjet acting as the anode was higher as compared to this evaluated for the discharge system with the pin electrode. Additionally, the excitation temperature of Ar atoms for the first discharge system was also relatively high. This could be associated with the presence of metastable Ar states (Ar_m) in the discharge system with the argon microjet and their possible contribute to the transfer of the energy [9]. On the other hand, lower vibrational and rotational temperatures were noted for this APGD source and a possible explanation of this could be processes leading to a stronger disequilibrium of this type of the discharge. The electron number density measured in APGD with the argon microjet was established to be comparable or higher than in APGD system with the pin electrode. This could be related to an additional source of free electrons in the discharge system with the argon microjet possibly due to the participation of metastable states of argon (Ar_m) in different collisional reactions [9]:

$$Ar_m + e = Ar^+ + 2e,\ Ar_m + Ar_m = Ar^+ + Ar + e,\ Ar_m + Ar_m = Ar_2^+ + e \quad (1)$$

3.3. The analysis of the composition of water solutions treated with APGD systems

The composition of water solutions treated with the discharge and directly collected from the waste reservoir was analyzed. The concentrations of nitride (NO_2^-) ions was determined spectrophotometrically (Metertek, SP-850) with rivanol method, while an Orion ion selective electrode was used to measure the concentration of NO_3^- ions. The concentration of hydrogen peroxide (H_2O_2) was measured by means of the spectrophotometric method with metavanadate ammonium in the acid medium. The Nessler's reagent was applied for the spectrophotometric determination of the concentration of ammonium (NH_4^+) ions.

Hydrogen peroxide (H_2O_2) as well as nitrate (NO_3^-) and traces of nitrite (NO_2^-) and ammonium (NH_4^+) ions were identified in water solutions treated by the discharge. It should be noted that H_2O_2 molecules and NO_2^-, NO_3^- and NH_4^+ ions were not detected in untreated water solutions. Additionally, an increase in the acid concentration of discharge treated water solutions was observed. The following species: H_2O_2, NO_2^- and NO_3^- have recently been identified by Shimizu *et al.* [11] in a water solution treated by an APGD system sustained in the air atmosphere. The maximum concentrations of H_2O_2 as well as NO_3^-, NO_2^- and NH_4^+ ions in water solution treated by both APGD systems under different experimental conditions are collected in Table 3.

It can be presumed that the main sources of nitrite and nitrate ions were nitric oxide (NO) and nitric dioxide (NO_2), respectively, which reacted with OH radicals in the gaseous phase of the discharge according to the following reactions [12,13]:

$$NO + OH = HNO_2 \quad (2)$$

$$NO_2 + OH = HNO_3 \quad (3)$$

Tab. 3. The concentrations of H_2O_2 and NO_3^-, NO_2^- and NH_4^+ ions in water solutions treated by APGDs

Species	Concentration, mg l^{-1}	
	Ar microjet-liquid cathode	Pin electrode-liquid cathode
H_2O_2	20	30
NO_3^-	260	140
NO_2^-	0.3	0.2
NH_4^+	4	1

H_2O_2 molecules were likely to be produced in oxidation processes of water molecules or species originated from them [14], e.g.:

$2H_2O^+ = H_2O_2 + 2H^+$ (4)

$2H_2O^* = H_2O_2 + H_2$ (5)

$OH + OH = H_2O_2$ (6)

Heterogeneous reactions, taking place on the reactor wall or the steel nozzle, were presumably responsible for the production of NH_3 molecules. In this process, NH and H radicals (identified in emission spectra of both discharges) may also play an important role [15,16]:

$NH_x + H = NH_{x+1}$, where x=0-2 (7)

Resulting NH_3 molecules could be the source of NH_4^+ ions.

3.4. The application of APGD sources in the water purification process

The application of APGD sources in the wastewater treatment process was tested in case of water solutions containing an organic dye, i.e., methyl red (MR, $C_{15}H_{15}N_3O_2$), very toxic Cr(VI) ions (added as $Na_2Cr_2O_7$) and a non-ionic surfactant (Triton X-45, $C_{14}H_{22}O(C_2H_4O)_n$, n=4.5).

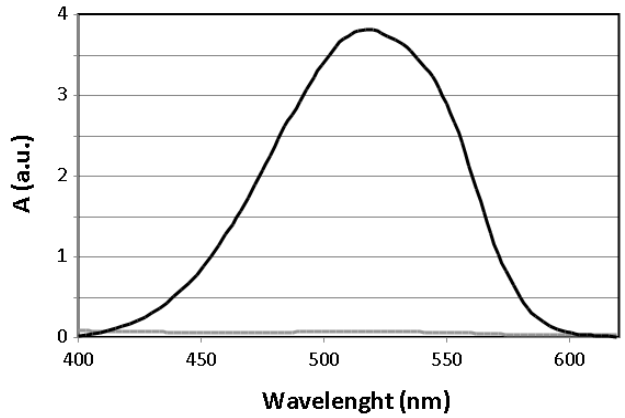


Fig. 2. The absorption spectra of methyl red (MR) in the spectral range 400-620 nm (black line – spectra of the untreated MR dye containing water solution, grey line – spectra of the discharge treated MR dye containing water solution).

The decomposition of the methyl red dye and the Triton X-45 surfactant was verified by means of UV-Vis spectrophotometry, using Thermo Scientific GENESYS 10 Scanning UV/Visible spectrophotometer (see Fig. 2). The concentration of Cr(VI) ions in water samples was measured spectrophotometrically, applying the reaction of Cr(VI) ions with 1,5-diphenylcarbazide in acetone. The degradation efficiency of a pollutant (η) was calculated using the following equation:

$\eta=(C_o-C_P)/C_o \times 100\%$ (8)

where C_o is the concentration of the pollutant in the untreated water solution, and C_P – the concentration of the pollutant in the water solution treated by the discharge. In case of water solutions containing MR dye and Triton X-45 surfactant, values of the absorbance of both pollutants in untreated (A_o) and discharge treated (A_P) water solutions were taken for the determination of the degradation efficiency instead of the concentration.

As can been seen from Table 4, the efficiency of the degradation of selected chemical pollutants were better than 85% for both discharges used. Although overflowing liquid cathodes were applied in both

discharge systems and thus the contact of the discharge with solutions was relative short, it seems that both APGDs are very promising in an efficient on-line degradation of polluted water samples.

Tab. 4 The degradation efficiency of pollutants (MR dye, Cr(VI) ions, Triton X-45 surfactant) in water solutions treated by APGD systems (the concentration of pollutants: MR dye: 25 mg l^{-1}, Cr(VI) ions: 100 mg l^{-1}, Triton X-45 surfactant: 145 mg l^{-1})

Chemical pollutant	Degradation efficiency, %	
	Ar microjet-liquid cathode	Pin electrode-liquid cathode
MR dye	97	99
Cr(VI) ions	85	93
Triton X-45 surfactant	97	98

4. Summary and conclusions

Two kinds of APGD sources, i.e. Ar microjet anode-flowing liquid cathode and pin anode-flowing liquid cathode, were studied and compared in reference to their spectroscopic discharge properties and the production yield of chemically active species in the gas-liquid interface. The following species: OH, NH, NO, N_2, H and O were excited in both discharges. Hydrogen peroxide in addition to nitrite, nitrate and ammonium ions were identified in water sample solutions treated by these discharges as a result of chemical reactions occurred due to the interaction of water solutions with discharges. Additionally, a growth of the H_3O^+ concentration (and consequently a drop of pH) in the liquid phase was noted for both APGD systems. The degradation efficiency of pollutants studied (methyl red dye, Cr(VI) ions and Triton X-45 surfactant) was found to be better than 85%. Results presented here indicate that both APGD systems can be successfully applied for the on-line continuous flow chemical degradation of different organic and non-organic species in wastewater solutions.

5. References

[1] Yang Y, Cho Y I and Friedman A 2012 *Plasma discharge in liquid. Water treatment and applications* CRC Press Boca Raton.
[2] Sommers B S, Gucker S N, Blankson I M and Adamovsky G 2012 *IEEE Trans. Plasma Sci*. **40** 1311.
[3] Yan-hong Bai, Jie-rong Chen, Xiao-yong Li and Chun-hong Zhang 2011 *Rev. Environ. Contam. Toxicol.* **201** 117.
[4] Julak J, Scholtz V, Kotucova S and Januskova O 2012 *Phys. Medica* **28** 230.
[5] Hsu-Hui Cheng, Shiao-Shing Chen, Yu-Chi Wu and Din-Lit Ho 2007 *J. Environ. Eng. Manage*. **17** 427.
[6] Ke Z, Huang Q, Zhang H and Yu Z 2011 *Environ. Sci. Technol.* **45** 7841.
[7] Bogaerts A, Neyts E, Gijbels R and van der Mullen J 2002 *Spectrochim. Acta, Part B* **57** 609.
[8] Ikawa S, Kitano K and Hamaguchi S 2010 *Plasma Process. Polym.* **7** 33.
[9] Jamroz P, Zyrnicki W and Pohl P 2012 *Spectrochimica Acta, Part B,* in press doi:10.1016/j.sab.2012.06.008
[10] Jamroz P and Zyrnicki W 2011 *Plasma Chem. Plasma Process.* **31** 681.
[11] Shimizu T, Iwafuchi Y, Morfill G E and Sato T 2011 *New J. Phys.* **13** 053025.
[12] Chen Q, Li J, Saito K and Shirai H 2008 *J. Phys. D: Appl. Phys*. **41** 175212.
[13] Chen Q, Saito K., Takemura Y and Shirai H. 2008 *Thin Solid Films* **516** 6688.
[14] Mottaleb M A, Yang J S and Kim H Y 2002 *Appl. Spectrosc. Rev.* **37** 247.
[15] Jauberteau J L, Jauberteau I and Aubreton J 2002 *J. Phys. D: Appl. Phys.* **35** 665.
[16] Kinoshita Y., Okumura N, Takashima K, Katsura S and Mizuno A 2004 *Prepr. Pap. Am. Chem. Soc. Div. Fuel Chem*. **49** 460.

6. Acknowledges

The work was financed by a statutory activity subsidy from the Polish Ministry of Science and Higher Education for the Faculty of Chemistry of Wrocław University of Technology.

OZONIZERS OF UNCONVENTIONAL GAS FLOW ORGANIZATION

Sławomir Jodzis

Warsaw University of Technology, Faculty of Chemistry, Noakowskiego 3, 00-664 Warszawa
e-mail: jodzis@ch.pw.edu.pl

Two kinds of ozonizers through which gas flowed with increasing linear velocity were compared. High ozone concentrations and ozone production were obtained in oxygen. In the simple surface discharge arrangement, in which the metal mesh adjacent to the ceramic dielectric was used, similar effects as in more complicated systems were obtained. In one-side cooling reaction space the high ozone concentrations and high energy efficiencies of the process, even at 25ºC, were obtained.

1. Introduction

In the course of the studies on improvement of the efficiency of ozone production under barrier discharge conditions it was stated that the main reason causing the ozone decomposition is a high temperature of a gas in the microdischarge channels [1]. This temperature depends on both the energy delivered into the channels, as well as the temperature of the cooling liquid. Therefore, to prevent the ozone decomposition the temperature of the gas should be quickly lowered directly in the microdischarge channel, immediately after the occurrence of the desired reactions. Besides the reducing the cooling liquid temperature, which is the simplest way, the gas flow of a linear velocity increasing along the ozonizer was forced. The change in gas linear velocity was obtained in Otto-type ozonizers of the circular symmetry, through which gas flows towards the device axis [2-5].

2. Experimental

Fig. 1 depicts the cross-section of an ozonizer with circular symmetry. The ozonizer is equipped with a removable H.V. discharge element. The gas was introduced through the inlets located outside the ozonizer body, then was flowed out into the ring-shaped channel in the reactor lid. From there gas was directed through the system of 60 openings towards the middle of the reactor and was removed through the channel in the voltage supplying element. Experiments were carried out using an alumina plate with diameter of 100 mm and the thickness of 1 mm. The ceramic material with a significant electric strength and a stable permittivity ($\varepsilon = 9.1$) was used. The thickness of the plate facilitated the heat transfer from the reaction space. The bottom side of dielectric (grounded electrode) was cooled with water (0, 25 and 50^{o}C).

Two kinds of discharge elements based on ceramic plate were used (Fig. 2): the former with sputtered structure of electrodes and the latter with a mesh electrode adjacent to the ceramic dielectric surface. The first discharge element (i.e. actuator, Fig. 2a) has concentric strips of 1 mm thickness on the active side of the ceramic plate. The distances between them are 2 mm thick. On the reverse side, an induced electrode was made in the form of a circle with a 90 mm diameter. The electrodes were made by several consecutive depositions of aluminum through a mask [4]. The induced electrode was grounded by the metal wall of the cooling chamber. The total volume of the reaction space in ozonizer with an actuator was ca. 13 cm^3. The linear velocity of the gas in the reaction space varied and equalled (under normal conditions) from 0.005–0.03 m/s (at 10 Ndm^3/h) to 0.04–0.28 m/s (at 80 Ndm^3/h).

The second discharge element (Fig. 2b) was made of metal gauze (brass, mesh 12, wire diameter 0.5 mm) mounted on thin disk of diameter 80 mm. The gauze wire terminals were wrapped around the edge of disk in order to eliminate the local corona effect. The ceramic plate and the mesh were located in the reactor in such a way, to limit the space through which gas could flow, up to approximately 1 mm (the mesh thickness) [6]. The gas flowed through the reaction zone with variable linear velocity

(from ca. 0.016 up to 0.16 m/s for 10 Ndm^3/h and from ca. 0.06 up to 0.6 m/s for 40 Ndm^3/h), as a result of changing cross-section area of the reaction space. Because of the gauze presence in discharge space the gas in the region of wires changed its direction repeatedly. Besides the main component of gas velocity (in radial direction) the dynamic components (in orthogonal directions) always occur, which causes the intensification of gas mixing. The total volume of the reaction space was 5 cm^3 and ca. 0.5 cm^3 was occupied with a mesh. However, not the entire volume of the space was used similarly. There are specific places in the reaction space, where the mesh wires adhere to the ceramic plate. The discharge develops on the metal-dielectric border and forms a system of regularly located "spots". The amount of discharge spots is constant (ca. 1400). Their size depends on the discharge power. When the power rises, the discharge develops also along the mesh wires. Since the wires are very close to each other, the glow around them produces a very homogeneous discharge region. The gas flows through this discharge and the ones on the dielectric surface. This way, the process of gas mixing between the channels and their surroundings was intensified. As a result of gas mixing, the effect of gas cooling in the channels, as well as the reduction of ozone concentrations in the channels was obtained, which inhibits ozone decomposition process.

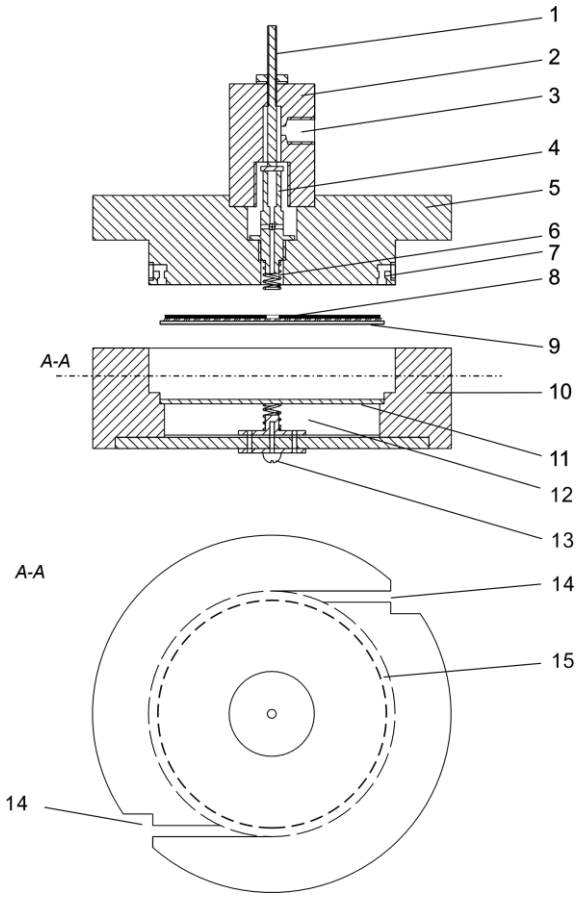


Fig 1. Cross-section of the ozonizer. In the A-A cross-section the idea of gas feeding system is presented; 1 – high voltage clamp, 2 – insulator, 3 – outlet of the post-reaction gas, 4 – gas ejector and voltage supply element, 5 – reactor lid, 6 – contact spring, 7 – openings through which the gas enters the reaction space, (8+9) – removable discharge element, 8 – sputtered electrode or metal mesh, 9 – ceramic plate, 10 – main body of the reactor, 11 – wall of the cooling chamber, 12 – cooling chamber, 13 – grounding clamp, 14 – gas inlet channels, 15 – collecting ring.

The studies were carried out in pure oxygen (99,999 %). The gas flow-rates of 10, 20, 40 and 80 Ndm^3/h were used. The concentration of ozone was measured with BMT-963 VENT. The ozonizer was supplied with an alternating current of up to 12 kVpp. The discharge power was evaluated with a

TDS3032 oscilloscope equipped with P6015 H.V. probe and a current probe P312 with a TCPA300 amplifier (Tektronix). Experiments were carried out at constant flow rates and increasing power.

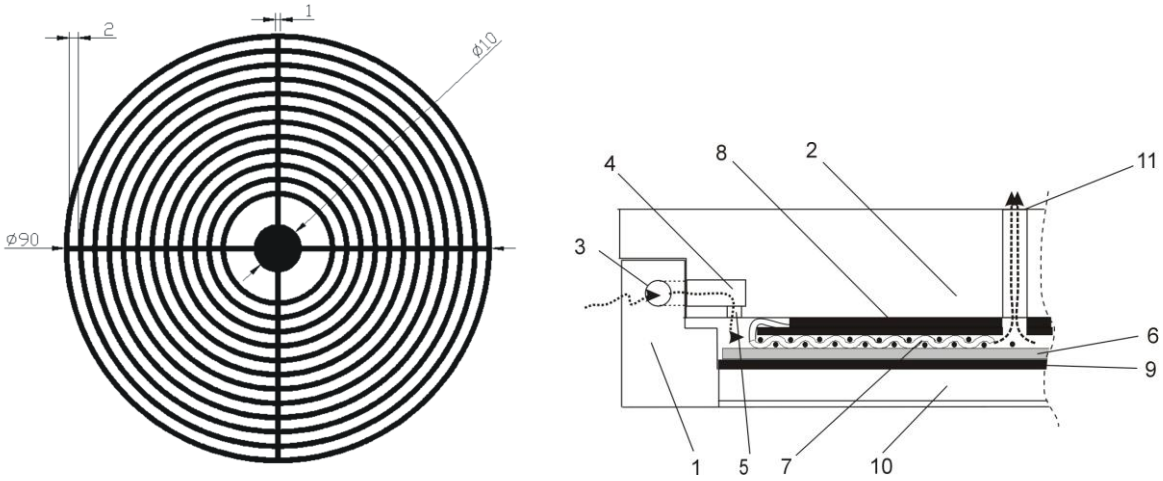


Fig. 2. Discharge elements: a) concentric strip electrode on the actuator surface, b) scheme of reaction space operating with mesh-ceramic plate system. The arrows depicts a way of the gas flow; 1 – main body of the reactor, 2 – reactor lid, 3 – gas inlet channels, 4 – collecting ring, 5 – openings through which the gas enters the reaction space, 6 – ceramic plate, 7 – mesh, 8 – metal plate, 9 – wall of the cooling chamber, 10 – cooling chamber, 11 – outlet of the post-reaction gas.

3. Results and Discussion

Table 1 presents the ozone concentrations and yields (maximum values) obtained in both kinds of ozonizers at 0, 25, and 50°C. Under those conditions energy efficiencies were also calculated.

Tab. 1. Comparison of ozone concentrations and yields (maximal values). The energy efficiencies and specific energies were calculated on the basis of power necessary to obtain maximum concentration.

		Ozonizer with an actuator			Ozonizer with a mesh-dielectric system		
		0°C	25°C	50°C	0°C	25°C	50°C
10 Ndm^3/h	c, g/Nm^3	123.8	102	83.7	132.8	100	70.6
	m, g/h	**1.24**	**1.02**	**0.84**	**1.33**	**1.00**	**0.71**
	η, g/kWh	30.1	28.5	23.4	44.3	53.5	46.8
	P/V, Wh/Ndm^3	3.5	3.0	3.0	3.0	1.87	1.51
20 Ndm^3/h	c, g/Nm^3	106.9	93.1	75.2	117.8	88.0	59.0
	m, g/h	**2.14**	**1.86**	**1.50**	**2.36**	**1.76**	**1.18**
	η, g/kWh	46.4	40.5	37.0	65.5	69.9	58.2
	P/V, Wh/Ndm^3	2.25	2.25	2.0	1.75	1.39	1.23
40 Ndm^3/h	c, g/Nm^3	82.2	72.5	59.4	98.8	68.1	46.7
	m, g/h	**3.29**	**3.00**	**2.38**	**3.95**	**2.72**	**1.87**
	η, g/kWh	71.7	63.3	52.1	85.8	89.3	61.6
	P/V, Wh/Ndm^3	1.13	1.13	1.13	1.13	0.85	0.75
80 Ndm^3/h	c, g/Nm^3	54.2	50	44.6			
	m, g/h	**4.34**	**4.00**	**3.57**			
	η, g/kWh	85.6	87.9	70.6			
	P/V, Wh/Ndm^3	0.63	0.56	0.63			

Fig. 3 depicts maximum ozone concentrations obtained in both ozonizers under process conditions (flow rates 10-80 Ndm^3/h, temperatures 0-50°C). The ozonizer operating with an actuator has a more stable temperature characteristics. Ozone concentration decreases slowly with temperature rising, independently on the gas flow rate. When mesh-dielectric discharge element was used the ozone concentrations were significantly higher at low temperatures, however, they decreased faster.

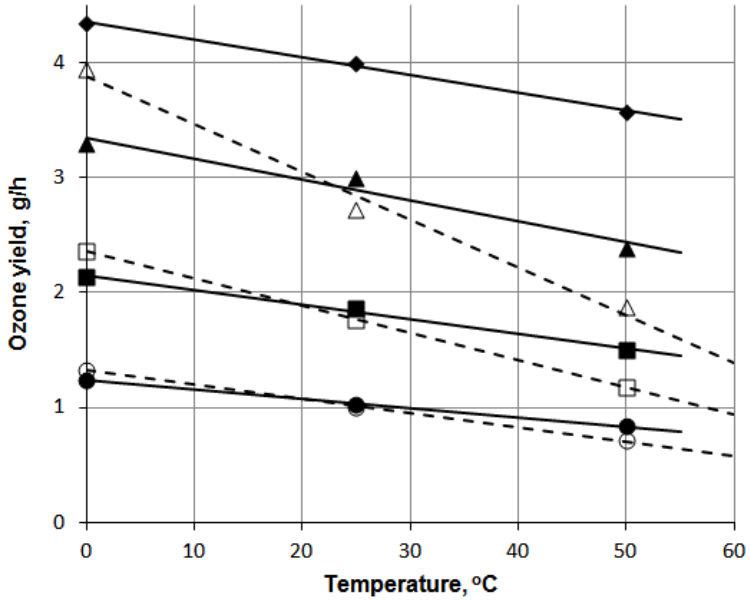


Fig. 3. Maximum ozone yields vs. temperature of cooling liquid; actuator (solid lines), metal mesh-dielectric system (dashed lines); oxygen flow-rates: ○,● – 10 Ndm^3/h, □,■ – 20 Ndm^3/h, Δ,▲ – 40 Ndm^3/h, ♦ – 80 Ndm^3/h.

The reason of such profitable results is suspected in two main parameters: the nature of the discharge obtained and the gas through the discharge space flow arrangement. The discharge action mechanism is not entirely explained. It seems that energy dissipation in the significant part of discharge space has an important meaning. The discharge modified in such a way occurs under low voltages, lower than that in typical DBD ones. As a result, the primary electrons energy should be more homogeneous. When the average energy of the electrons generated during the discharges is somewhat higher than 6 eV, they have only a minimal energy excess over that necessary for O_2 dissociation. Then, in the discharge zones less heat is produced, and the gas temperature should be significantly lower. Also, the secondary electrons should have a lower energy. It can limit the ozone decomposition in reactions just with participation of low energy electrons:

$$O_3 + e \rightarrow O + O_2 + e \qquad (1)$$

Therefore, the change in discharge character, due to which the amount of energy converted into heat is limited, can cause that both, ozone formation and decomposition rates in discharge zones, should be lower. And, since ozone decomposition rate to a higher degree diminishes with the temperature decrease, ozone concentration could be high.

Undoubtedly, the arrangement of the gas flow through the reaction space also has an important effect on the results obtained. Due to the presence of the metal mesh the gas is mixed, what improves both, heat and mass exchange. Since the mesh is a H.V. electrode, in the places where discharges occur, locally strong disturbances of the gas flow occur [e.g. 7,8]. The gas swirls, formed near the wires, are an additional element intensifying the gas mixing. The local micro-mixing of oxygen atoms and particles improves the efficiency of O consumption in reaction:

$$O + O_2 + M \rightarrow O_3 + M \qquad (M = O, O_2 \text{ or } O_3) \qquad (2)$$

and moreover, it limits the recombination of atomic oxygen:

$$O + O + M \rightarrow O_2 + M \quad (3)$$

The intensive gas mixing causes also faster diffusion of newly formed ozone particles into the gas stream, due to which the probability of reaction occurrence decreases:

$$O_3 + O \rightarrow O_2 + O_2 \quad (4)$$

Therefore, improving the gas mixing could cause the high efficiency of the process. Additionally, because in the ozonizers tested the linear velocity of the gas increases with increasing in ozone concentrations in the post-reaction gas stream, also the reducing of the gas residence time in the discharge end zones was obtained, what protects the ozone included against the decomposition.
Relatively low energy efficiencies of the process result from the usage of single-side cooling of the actuator. However, the ozonizer with a small electrode surface area enables to obtain a significant ozone yield. The ozone production obtained at 25ºC was only slightly smaller than that at 0ºC, especially at moderate discharge powers.

4. Summary

It was found that both ozonizers enable to obtain the high ozone concentrations in oxygen. In the simple discharge arrangement, in which the metal mesh adjacent to the ceramic plate was used, similar effects as reported in case of more complicated discharge systems were obtained. In spite of only one-side cooling of the reaction space the high ozone concentrations and high energy efficiencies of the process, even at 25ºC, were obtained. Because the reaction space was only one-side cooled, the results could probably be improved when a cooled H.V. electrode was applied. An essential effect on the results obtained in the presented ozonizer has a manner of the gas flow through the discharge zone. Since the process occurred in low volume reaction space, the results obtained are particularly interesting. The studies aiming to improve the intensity of heat transfer and ozone concentration obtained are in progress.

Acknowledgements

This study was financially supported by Warsaw University of Technology

5. References

[1] Jodzis S 2011 *Ind. Eng. Chem. Res*. ***50*** 6053–6060.
[2] Jodzis S 2010 *Int. Symp. on High Pressure Low Temp. Plasma Chemistry* Hakone XII, 12-17 September, Trečianske Teplice 301-305.
[3] Jodzis S and Kowalska A 2009 *Prz. Elektrotechniczny (Electrical Reviev)* ***85****(5)* 118-121.
[4] Jodzis S, Smoliński T and Sówka P 2011 *IEEE Trans. Plasma Sci.* ***39****(4)* 1055-1060.
[5] Jodzis S 2011 *Przem. Chem.* ***90****(10)* 1904-1908.
[6] Jodzis S 2012 *Ozone Sci. & Eng*. accepted.
[7] Moreau E 2007 *J. Phys. D: Appl. Phys.*, **40** 605–636.
[8] Pons J, Moreau E, and Touchard G 2005 *J. Phys. D: Appl. Phys.*, **38**(19) 3635–3642.

VISUALISATION OF UNDERWATER PULSED DISCHARGE

S. Kanazawa[1], T. Sato[2], M. Kocik[3] and J. Mizeraczyk[3]

[1]*Department of Electrical and Electronic Engineering, Oita University, Japan*
[2]*Institute of Fluid Science, Tohoku University, Japan*
[3]*Institute of Fluid Flow Machinery, Polish Academy of Sciences, Poland*
E-mail: kocik@imp.gda.pl

In this study, Schlieren photography technique has been applied for the visualization of the pressure field of a single-shot underwater pulsed discharge. A needle-to-plane electrode configuration submerged in distilled water was used. The detailed time- and space-resolved observation of both streamers and pressure waves was performed. As a result, several phenomena, such as the phase change prior to the initiation of the discharge, primary and secondary streamers propagation, shock wave generation, and the bubble formation, were observed. From these observations, a scenario of multiple events from pre-breakdown to post-discharge was proposed.

1. Introduction

Recently, liquid-related electrical discharges, such as discharges in water or discharges on the water surface, have been widely studied for environmental and biomedical applications as well as nanomaterial processing [1, 2]. However, the underwater discharge mechanisms are more complicated compared to the discharge in air. In addition, several phenomena, such as the radical formation, UV radiation, and shock wave generation, are involved in the underwater discharge. Although the discharge observation based on the optical emission is widely performed [3-5], the obtained information is limited on the streamer propagation stage. To clarify the initiation and post-discharge phenomena, another optical observation, such as shadow/Schlieren imaging and Mach-Zehnder interferometry, has been performed [6-8]. In this study, Schlieren photography, which measures density gradient in the water, was used for visualization of the pressure field of underwater discharge. To avoid the influence of pre-discharge, a single-shot pulsed discharge was used instead of repetitive pulsed discharge and liquid-gas dynamics was observed from the initiation to after the extinction of the discharge. Simultaneously with Schlieren imaging, the streamer image was also obtained to investigate these relations.

2. Experimental set-up

A laser Schlieren imaging technique [9] was used to study the liquid-gas dynamics in the discharging reactor. KrF excimer laser (Lambda Physik, COMPex 150, λ=248 nm) was used as a pulsed light source. A needle-to-plane electrode configuration submerged in distilled water (3 μS/cm) was used. A stainless-steel needle (0.31 mm in inner diameter and 0.57 mm in outer diameter) with an insulating cover was used as the powered electrode, while a brass plate (70 mm in diameter) was used as the grounded electrode. The tip of needle was protruded 0.5 mm from the insulating cover in order to enhance the electric field at the tip of needle electrode. The needleplane gap was fixed at 40 mm. Fig. 1 shows a pulsed high-voltage circuit using a MOS-FET switch (Behlke, HTS 651-03-LC) for generating an underwater pulsed discharge. A manual trigger pulse generated by a function generator (NF, WF1974) was used to trigger a single-shot positive pulsed high-voltage and was supplied TTL signal to a delay generator (Stanford Research, DG535) for the trigger of the laser and the camera. Voltage and current waveforms were recorded using a high-voltage probe (Iwatsu, HV-P06) and a current monitor (Pearson, 4100), respectively. The ICCD camera (Andor, i-Star) was used to obtain Schlieren images at various time delays between the laser pulse and the pulsed high-voltage. The time relationship between the applied voltage pulse, discharge current pulse, laser pulse, and gate opening time of the ICCD camera was monitored with a digital oscilloscope (Tektronix, TDS 5104). Also a digital camera (Nikon, D90) was used to capture the streamer images. The view angle of the digital camera was set to be ca. 15 degrees.

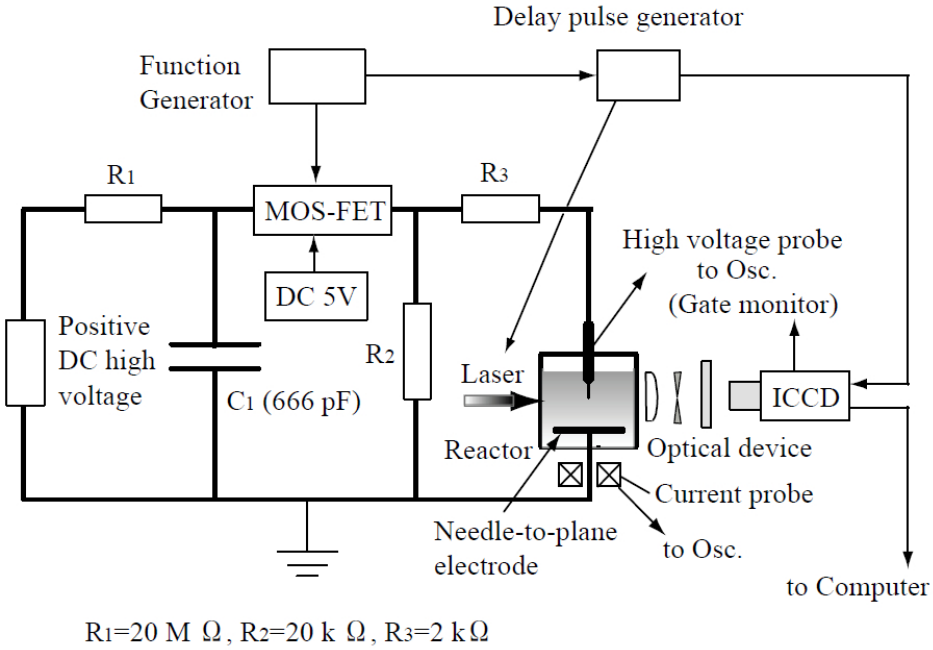


Fig. 1. Electrical circuit for generating pulsed high-voltage.

3. Results

A. Characteristics of underwater discharge

Fig. 2(a) shows the typical waveforms of the applied pulsed voltage and the current at early time. Before the discharge inception, the displacement current appears at the rising edge of the pulse. It can be considered that a certain kind of phase change occurs prior to the initiation of the discharge. After a stochastic time delay, primary streamer appears, followed by secondary streamer. The corresponding primary streamer image is shown in Fig. 2(b). While Fig. 3(a) shows the waveforms of the applied pulsed voltage and the current in terms of a different time scale. In this experiment, typical discharge current pulse reaches ~5 A at 23 kV. After the extinction of the secondary streamer propagation, the re-illumination can be observed within a single-shot pulsed high-voltage application.

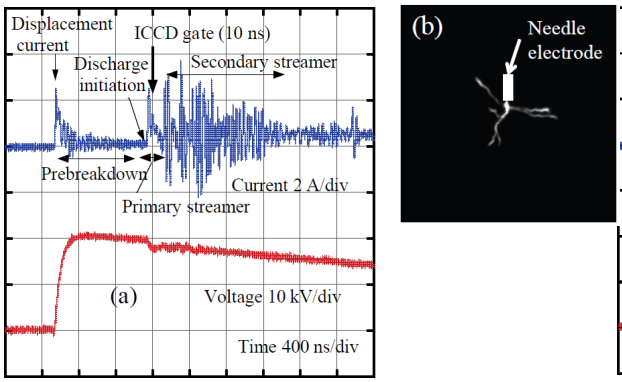


Fig. 2. (a) Applied voltage and current waveforms at early time. (b) Corresponding primary streamer image captured at instant A in figure (a).

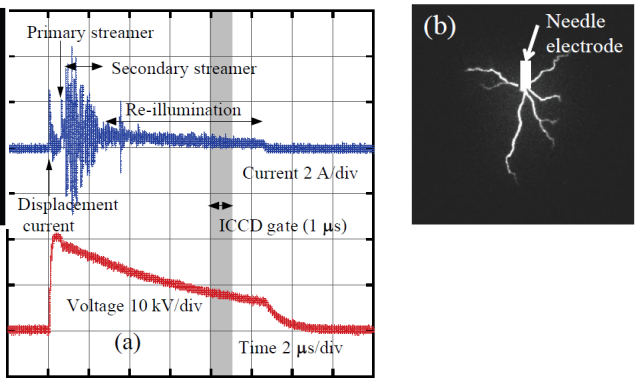


Fig. 3. (a) Applied voltage and current waveforms. (b) Corresponding secondary streamer image captured by light emission through the re-illumination stage (gray colored period in figure (a)).

The re-illumination occurs only for low conductivity liquid [10], especially for dielectric liquids such as oil [11]. This phenomenon is due to the charge deposition on the gas side of the gas/liquid interface left by the secondary streamer. The emission intensity of the re-illumination is weaker than that of secondary streamer. Since the part of streamer channel still exhibits weak light emission during the stage of re-illumination, we can follow the trace of the secondary streamer as shown in Fig. 3 (b).

B. Schlieren images with streamers

Fig. 4 shows the typical temporal and spatial evolution of the Schlieren images for various delay times after the application of the high voltage pulse. Each image presented in Fig. 4 was selected from a set of different observation at the same conditions (applied voltage 23 kV, pulse duration 10 μs, ICCD gate time 300 ns). At first, the appearance of opaque region with a spherical shape can be observed at the tip of the needle electrode before the initiation of the discharge as shown in Fig. 4(a). The extent of this region increased with time. In this region, several mechanisms have been discussed for the discharge initiation [8, 10, 12, 13]: a low density region (including the formation of microbubbles), phase instabilities/phase change prior to electron avalanches. In addition, the microbubbles may pre-exist inside this region, resulting the electron avalanching in gas bubbles. After the inception, primary streamers with a tree like structure appear and then secondary streamers with a filamentary structure are observed. Especially, a fine filamentary structure is clearly seen in Fig. 4(b).

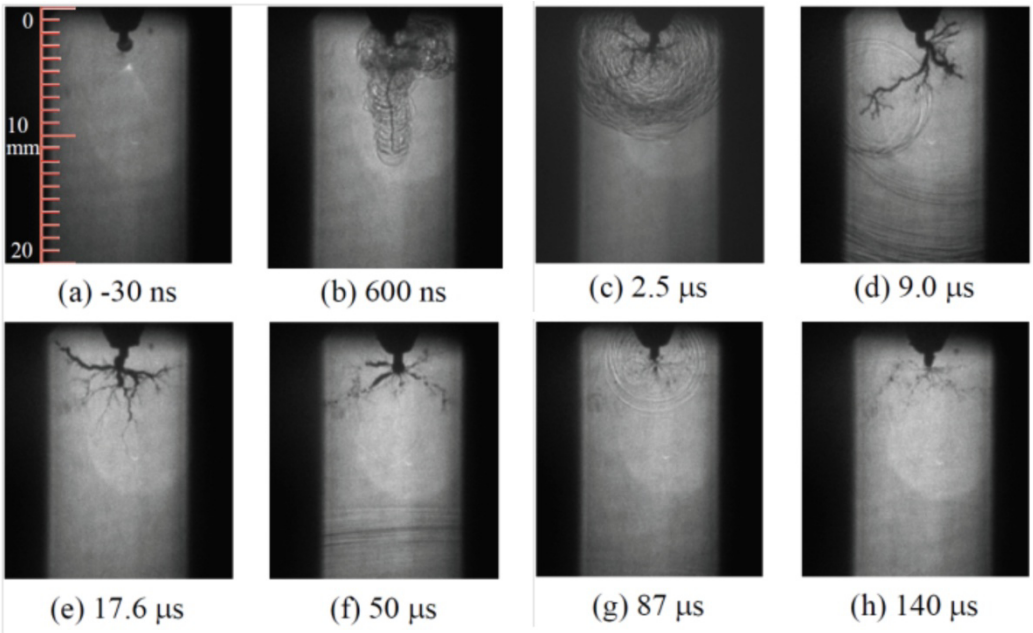


Fig. 4. Time evolution of Schlieren images. (applied voltage: 23 kV, pulse duration: 10 μs, discharge current:4-6 A, needle-to-plane electrode, gap: 40 mm, distilled water).

According to An et al. [7], the streamer channel radius increases proportional to t1/2 at late times. Moreover, the several shock waves appear with the streamer propagation as shown in Fig. 4(b). The reason for this multiple shock wave generation is due to the step-like streamer propagation similar to the stepped leader of a lightning. As a time elapses, the outgoing shock wave is often generated from the tip of the needle electrode (Fig. 4(c)). A spherical wave is also created at the node of streamer branching, and by superposition of all of the waves a complex wave pattern is generated (Fig. 4(d)). On the other hand, tracks of streamer propagation near the power electrode become gaseous channels and those diameters become thicker than that of secondary streamer (Fig. 4(e)). Although the applied pulsed voltage diminishes by ~14 μs, the shock wave is still actively expanding and then reflecting by the plane electrode as shown in Fig. 4(f). On the post-discharge stage, the gas channels are disrupted and develop into gas bubbles which grow and decay, causing the generation of bubble wave (Fig. 4(g)). Finally the trace of streamers fades away in time and several disrupted bubbles are sustained in liquid, moving upward direction (Fig. 4(h)).

Tab. 1. Typical characteristics of underwater discharge modes in needle-to-plane electrode under our experimental conditions.

	Discharge mode		
	Primary streamer	**Secondary streamer**	**Re-illumination**
Shape	Bush-like tree with spherical symmetry	Filamentary with branches	Weak discrete light emission spot or segment
Length	~a few mm	~a few cm	~sub- mm
Channel width	~250 μm	~350 μm	~250 μm
Velocity	100 m/s ~ a few km/s	~30 km/s	Stationary
Current	~2 A	1~10 A	~1 A
Mechanism*	Electron avalanche in low density region	Field induced dissociation and ionisation	Ignition by the deposited charge such as DBD

*The possible mechanism is described.

4. Discussion

The characteristics of the observed discharge mode in the present study are summarized in Table I. Fig. 5 depicts a plausible scenario of multiple events from prebreakdown to post-discharge. In the pre-breakdown regime, one possible mechanism for the instability initiation is modification of electric field with a sharp variation in permittivity near the powered electrode [12]. Since the change of permittivity or density variation leads to a change in refractive index in water, therefore we can observe this effect as the generation of opaque region by the Schlieren photograph. Although the influence of the thermally generated bubbles is negligible because the duration for the initiation of breakdown in liquids is too short to create a new bubbles under our experimental condition, pre-existing microscopic gas bubbles within liquids also contribute for the initiation of breakdown in liquids. The opaque region has a spherical shape for our electrode configuration, resulting the generation of primary streamers with tree-like morphology. Electron avalanche in low density region takes place. While secondary streamers propagate beyond the opaque region and a few long filamentary discharge channels create due to the field induced dissociation and ionization at the tip of the streamer head [7]. Large pressures are created at the electrode boundaries and then shock wave generation occurs. The velocity of the shock wave at early time of the discharge reaches 3 km/s.

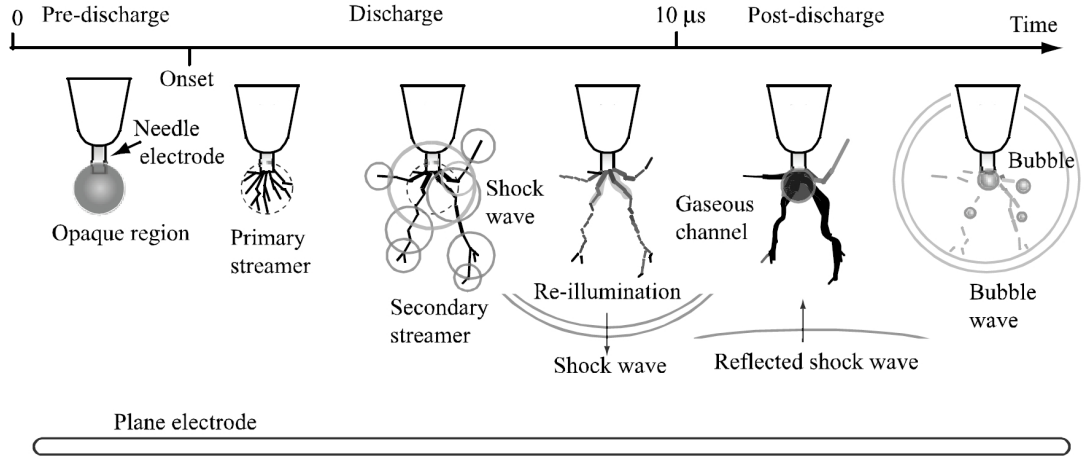


Fig. 5. Illustration of a scenario of multiple events from pre- discharge to post-discharge in underwater discharge. (applied voltage: 23 kV, pulse duration: 10 μs, discharge current: ~ 5 A, needle-to-plane electrode, gap: 40 mm, distilled water).

According to the Hugoniot equation [14], very large pressures on the order of GPa can be created during the secondary streamer propagation period. The charge accumulation occurs at the interface

between gas and liquid, causing the re-illumination. Moreover, we can observe thick trunks in Schlieren images after the propagation of secondary streamers. Those diameters are about twice as large as streamers. Internal heating may be occurred during the whole period of the discharge, gas bubbles is generated as shown in Figs. 4(d)–(f). The generation of the bubble wave is due to the bubble's rebound, such as its growth and collapse. To further investigate the detail phenomena for underwater discharge, a more precise measurement using Mach-Zehnder interferometry is now in progress separately.

5. Conclusion

The commonly observed phenomenon of underwater discharge generated by a single shot pulsed high-voltage was investigated experimentally. A definite sequence of events starting with the generation of lower density region, followed by breakdown, the primary streamer, rapidly expanding stepped secondary streamers and re-illumination as a typical discharge mode, shock wave propagation, localized cavitation at the trace of streamer propagation, and eventual bubble collapse was observed by using Schlieren photography.

6. References

[1] B. R. Locke, M. Sato, P. Sunka, M. R. Hoffmann, and J. S. Chang, "Electrohydraulic discharge and nonthermal plasma for water treatment," Industrial & Engineering Chemistry Research, vol. 45, pp. 882-905, 2006.

[2] P. Bruggeman and C. Leys, "Non-thermal plasmas in and in contact with liquids," Journal of Physics D-Applied Physics, vol. 42, 053001, 2009.

[3] J. S. Clements, M. Sato, and R. H. Davis, "Preliminary investigation of prebreakdown phenomena and chemical reactions using a pulsed high-voltage discharge in water," IEEE Transactions on Industry Applications, vol. IA-23, pp. 224-235, 1987.

[4] S. Kanazawa, Y. Abe, Y. Kihara, M. Kocik, and J. Mizeraczyk, "Time evolution of pulsed streamer discharge in water," IEEE Transactions on Plasma Science, vol. 36, pp. 922-923, 2008.

[5] B. Sun, M. Sato, and J. S. Clements, "Optical study of active species produced by a pulsed streamer corona discharge in water," Journal of Electrostatics, vol. 39, pp. 189-202, 1997.

[6] S. Katsuki, K. Tanaka, T. Fudamoto, T. Namihira, H. Akiyama, and H. Bluhm, "Shock wave due to pulsed streamer discharges in water," Conf. Record of the 26th International Power Modulator Symposium 2004 and 2004 High-Voltage Workshop, pp. 607-610, 2004.

[7] W. An, K. Baumung, and H. Bluhm, "Underwater streamer propagation analyzed from detailed measurements of pressure release," Journal of Applied Physics, vol. 101, 2007.

[8] K. Schoenbach, J. Kolb, S. Xiao, S. Katsuki, Y. Minamitani, and R. Joshi, "Electrical breakdown of water in microgaps," Plasma Sources Science & Technology, vol. 17, 024010, 2008.

[9] R. Ono and T. Oda, "Visualization of streamer channels and shock waves generated by positive pulsed corona discharge using laser schlieren method," Japanese Journal of Applied Physics Part 1-Regular Papers Short Notes & Review Papers, vol. 43, pp. 321-327, 2004.

[10] P. H. Ceccato, O. Guaitella, M. R. Le Gloahec, and A. Rousseau, "Time-resolved nanosecond imaging of the propagation of a corona-like plasma discharge in water at positive applied voltage polarity," Journal of Physics D-Applied Physics, vol. 43, 175202, 2010.

[11] O. Lesaint and G. Massala, "Positive streamer propagation in large oil gaps - Experimental characterization of propagation modes," IEEE Transactions on Dielectrics and Electrical Insulation, vol. 5, pp. 360-370, 1998.

[12] R. P. Joshi, J. Qian, K. H. Schoenbach, and E. Schamiloglu, "Microscopic analysis for water stressed by high electric fields in the prebreakdown regime," Journal of Applied Physics, vol. 96, pp. 3617-3625, 2004.

[13] J. Qian, R. P. Joshi, J. Kolb, K. H. Schoenbach, J. Dickens, A. Neuber, M. Butcher, M. Cevallos, H. Krompholz, E. Schamiloglu, and J. Gaudet, "Microbubble-based model analysis of liquid breakdown initiation by a submicrosecond pulse," Journal of Applied Physics, vol. 97, 113304, 2005.

[14] K. Nagayama, Y. Mori, K. Shimada, and M. Nakahara, "Shock Hugoniot compression curve for water up to 1 GPa by using a compressed gas gun," Journal of Applied Physics, vol. 91, pp. 476-482, 2002.

DEGRADATION OF UNDECANE AND TOLUENE IN AIR BY WATER FALLING FILM DBD REACTOR

Vesna V. Kovačević[1], Ronny Brandenburg[2], Bratislav M. Obradović[1],

Goran B. Sretenović[1] and Milorad M. Kuraica[1]

[1]*University of Belgrade, Faculty of Physics, Studentski trg 12-16, 11000 Belgrade, Serbia*

[2]*Leibniz Institute for Plasma Science and Technology (INP Greifswald), Felix-Hausdorff-Str. 2, D-17489 Greifswald, Germany*

E-mail: vesna@ff.bg.ac.rs

Application of coaxial dielectric barrier discharge (DBD) reactor for treatment of hydrocarbons in air was studied. This configuration of DBD offers to operate the plasma with and without water falling film at one of the electrodes. Thus it can act as a discharge reactor and as a scrubber for soluble compounds in a gas phase, simultaneously. Reactor efficiency was tested on two water insoluble hydrocarbons, namely undecane and toluene as typical VOC. The diagnostics of treated gas was performed by FID analyzer and FTIR spectroscopy. Conversion efficiencies of undecane and toluene with regard to specific energy density and presence of the water in the reactor are presented. In both cases CO_2, CO and HCOOH were identified as the main products of hydrocarbon degradation. Besides these species HNO_3, N_2O and O_3 were formed in the plasma. The results show that in plasma processes it is possible to convert non-soluble pollutants into soluble-ones. The absence of formic acid and nitric acid absorption bands in the FTIR spectra of gas treated in the discharge with water demonstrate that the presence of flowing water inside the reactor improves the gas cleaning process. A synergy between plasma and water scrubbing at atmospheric pressure and room temperature is demonstrated and offers high potential for industrial application.

1. Introduction

In view of the increasingly strict legislation for pollution control and evident environmental and health effects, abatement of volatile organic compounds (VOCs) in industrial exhaust gases and indoor environment has been extensively studied. According to the classification of World Health Organization VOCs include all organic compounds with boiling temperature in the range of 50-260°C, excluding pesticides [1]. VOCs are regarded as the main causes of many environmental problems (ozone layer depletion, contribution to global warming, etc.). The health effects of exposure to VOCs range from sensory irritation to toxic effects (neurotoxic, organotoxic and carcinogenic effects) [2]. VOCs are released into the atmosphere principally from vehicle exhausts, petrol refining and fuel storage, gasoline, solvents, wood preservatives, glues and lacquers. In industrial large volume sources, like paper and pharmaceutical industry or wood and food processing, emissions of VOCs are usually diluted. Conventional technologies used for VOCs removal based on thermal incineration are not economical for large gas flow rates and low concentrations of VOCs [3].

Non-thermal plasma (NTP) technologies, mostly based on dielectric barrier and pulsed corona discharges or electron beam injection, have been recognized as promising methods for pollution control and offer the possibility to overcome difficulties encountered in other alternative VOC treatment methods (biofiltration, adsorption, low temperature catalysis, etc.). Highly reactive species (like free radicals) generated in NTPs initiate chemical reactions and pollutant decomposition at atmospheric pressure and room temperature, while conventional methods based on thermal incineration require the heating of the entire gas stream [3, 5]. In industrial processes NTP is usually combined with catalyst, adsorbents or scrubbing. The simultaneous use of gas discharge and scrubbing (hybrid process) for the removal of VOCs has already been described in [3, 6]. The by-products of

plasma treated VOCs are usually soluble compounds and can be easily removed by water scrubbing. Complete oxidation of hydrocarbons to CO_2 and H_2O consume more plasma generated oxidizers and therefore has higher energy requirements than conversion of the non-soluble compounds into soluble ones. Plasma-water scrubbing approach enables significant reduction of VOC removal energy costs as well as the complete elimination of plasma treatment by-products. Such a solution, where organic compounds are converted from gas to liquid phase, is acceptable for the industries where the amount of polluted water from other sources is large and water cleaning is required anyway [3].

A novel water falling film dielectric barrier discharge has been developed and investigated for water purification [7-11]. This configuration of DBD offers to operate the plasma with and without water falling film at one of the electrodes and recently it has been applied for "dry" cleaning (without water film) of flue gases in a coal-combustion power plant [12]. It is featured by a very compact design which enables plasma treatment of gases and absorption of soluble compounds by water film in a single reactor. This contribution presents application of this reactor for removal of volatile organic compounds (VOCs). The motivation is to demonstrate the synergetic effect of simultaneous NTP-treatment and scrubbing for the degradation of undecane and toluene as water-insoluble VOCs.

2. Experimental set-up

A schematic overview of the experimental set-up is given in Fig. 1. The reactor consists of two electrodes and a dielectric barrier, placed concentrically. The dielectric is a quartz tube with the inner diameter of 26 mm, length of 500 mm. The inner electrode is made of stainless steel with an external diameter of 20 mm and a length of 500 mm. An outer electrode made of aluminum foil (length 400 mm) is wrapped around the quartz tube. When the discharge source works as water falling film reactor, water flows up through the vertical hollow cylindrical electrode and flows down making a thin film over the electrode. Water flows from the reservoir through the discharge by means of a peristaltic pump, with a flow rate of 100 mL/ min. The low frequency ac power supply used in this study consists of a high voltage transformer and a frequency inverter. For this reactor configuration optimal operating conditions are found to be at a frequency of 300 Hz. The DBD is generated within ~ 3 mm gap by applying voltage of up to 20 kV. The inner electrode is grounded via a capacitor of 470 nF and the outer electrode is connected to power supply. Electrical parameters were measured using a digital oscilloscope Tektronix DPO 4104 (1 GHz bandwidth, 5 GSamples/s) and a high voltage probe Tektronix P6015A. Lissajous figures were used for the determination of energy dissipated into the plasma in one period of the applied voltage [13].

The mixture of air and undecane ($CH_3(CH_2)_9CH_3$) was prepared by bubbling of compressed air through a sample of liquid undecane which was heated in a water bath, kept at temperature t= 40°C. The gas stream containing undecane was diluted with the second gas stream of compressed air in order to obtain the desired concentration of undecane in the total air flow through the reactor. The efficiency of coaxial DBD for removal of undecane in air was evaluated for gas flow rate of 800 L/h and initial concentration of undecane measured with FID at the exit of the reactor was 55 ppm of undecane. In experiment with water present in the discharge initial concentration of undecane was somewhat lower as 40 ppm. Prior to experiment, possible absorption of undecane by circulating water in the discharge was checked and it was proved that absorption doesn't occur.

Gas containing toluene ($C_6H_5CH_3$) was prepared by mixing synthetic air (80% nitrogen, 20% oxygen) and toluene from test gas cylinder (50 ppm of toluene in nitrogen, Air Liquide). Toluene degradation was studied for two initial concentrations (20 ppm and 40 ppm) of toluene in synthetic air. All measurements were performed in the dry reactor without water and with water circulating in the discharge. For experiment with 20 ppm of toluene gas flow rate was 900 L/h, and in the case of 40 ppm toluene in synthetic air gas flow rate was 300 L/h.

IR analysis of gas composition was performed with FTIR spectrometer Bruker Alpha (Bruker Optik GmbH, Germany). Also, Gasmet CR-2000 (Ansyco, Germany) FTIR spectrometer was used for online quantitative gas analysis. For continuous monitoring of the concentration of total hydrocarbons in the plasma treated gas, flame ionizing detector FID TESTA 2010T (TESTA GmbH, Germany) was used. The study of Hoeben et al. [14] showed that the standalone (integral carbon) FID analyser is a simple and robust instrument for determination of lower limit conversion levels of hydrocarbon target

compounds, especially suitable for environments where GC- MS cannot operate or is not available. Conversion of undecane and toluene was determined by FID analyzer using measured initial concentration of total hydrocarbon (C_{in}) at the exit of the reactor and concentration of total hydrocarbon as a function of specific energy density (C_{out})(SED was derived from the discharge power and gas flow, and was varied by changing the voltage amplitude).

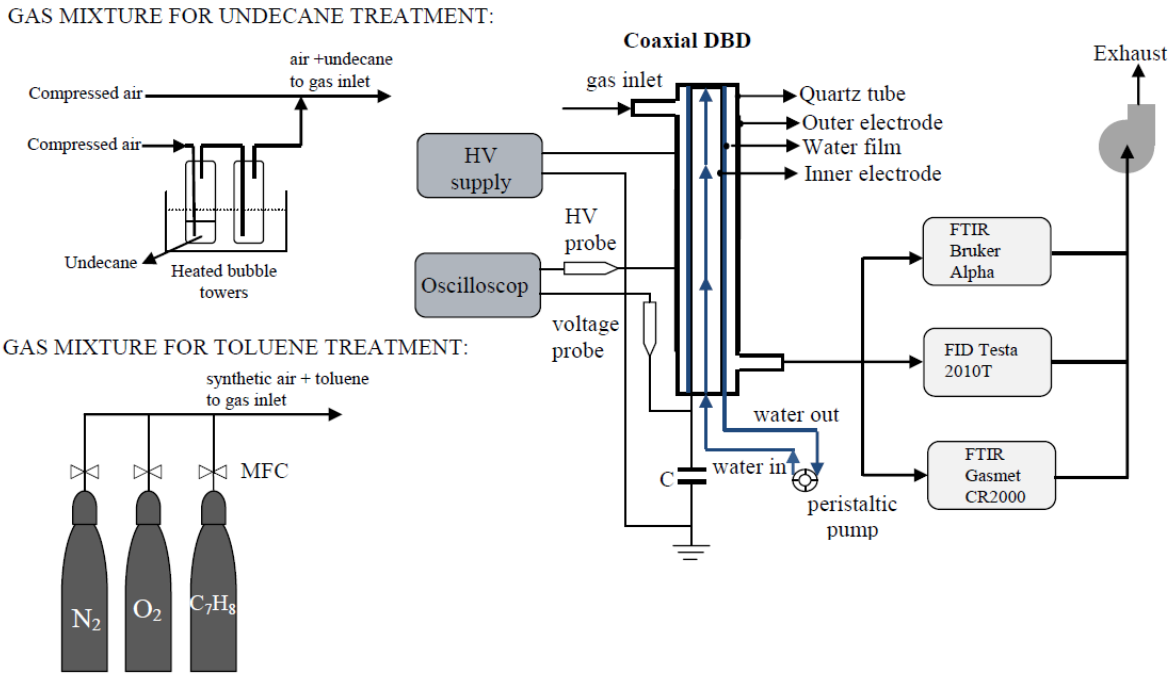


Fig. 1. Schematic overview of experimental setup

3. Results and discussion

Conversion efficiencies of undecane and toluene with regard to SED and presence of water in the reactor are presented in Fig. 2. In the discharge without water undecane conversion was at level of 87% at a specific energy density of 83 J/L, while the same conversion level in discharge with water was reached at 112 J/L. Toluene conversion level of 97% in dry reactor was reached at specific energy density of 28 J/L, while for the 97% conversion in the reactor with water film 43 J/L are needed. In the experiment with higher initial concentration of toluene (40 ppm) for the same conversion level of

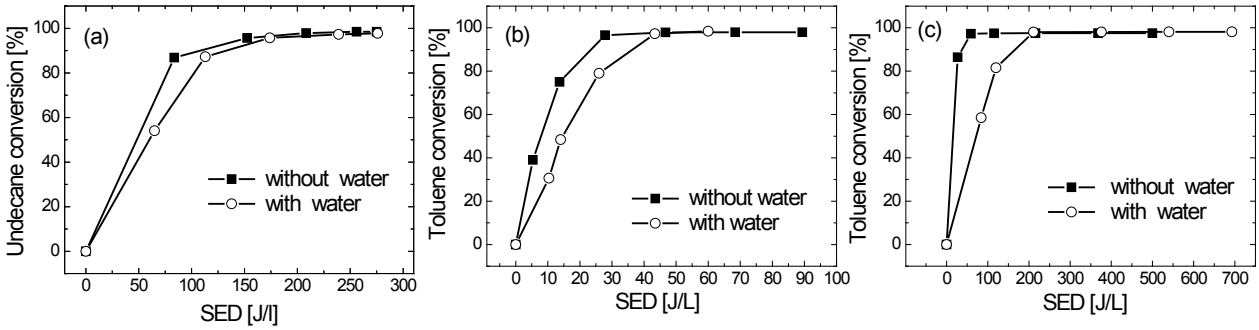


Fig. 2. Conversion efficiency of: a) undecane, b) 20 ppm toluene, c) 40 ppm toluene with and without water film in the reactor

97% a specific energy density of 59 J/L was needed, and in discharge with water SED increased to 210 J/L. It was found that conversion efficiency of tested VOCs increases with an increase of SED, but presence of water film in the discharge to some extent reduces the efficiency compared with results obtained for dry gas stream.

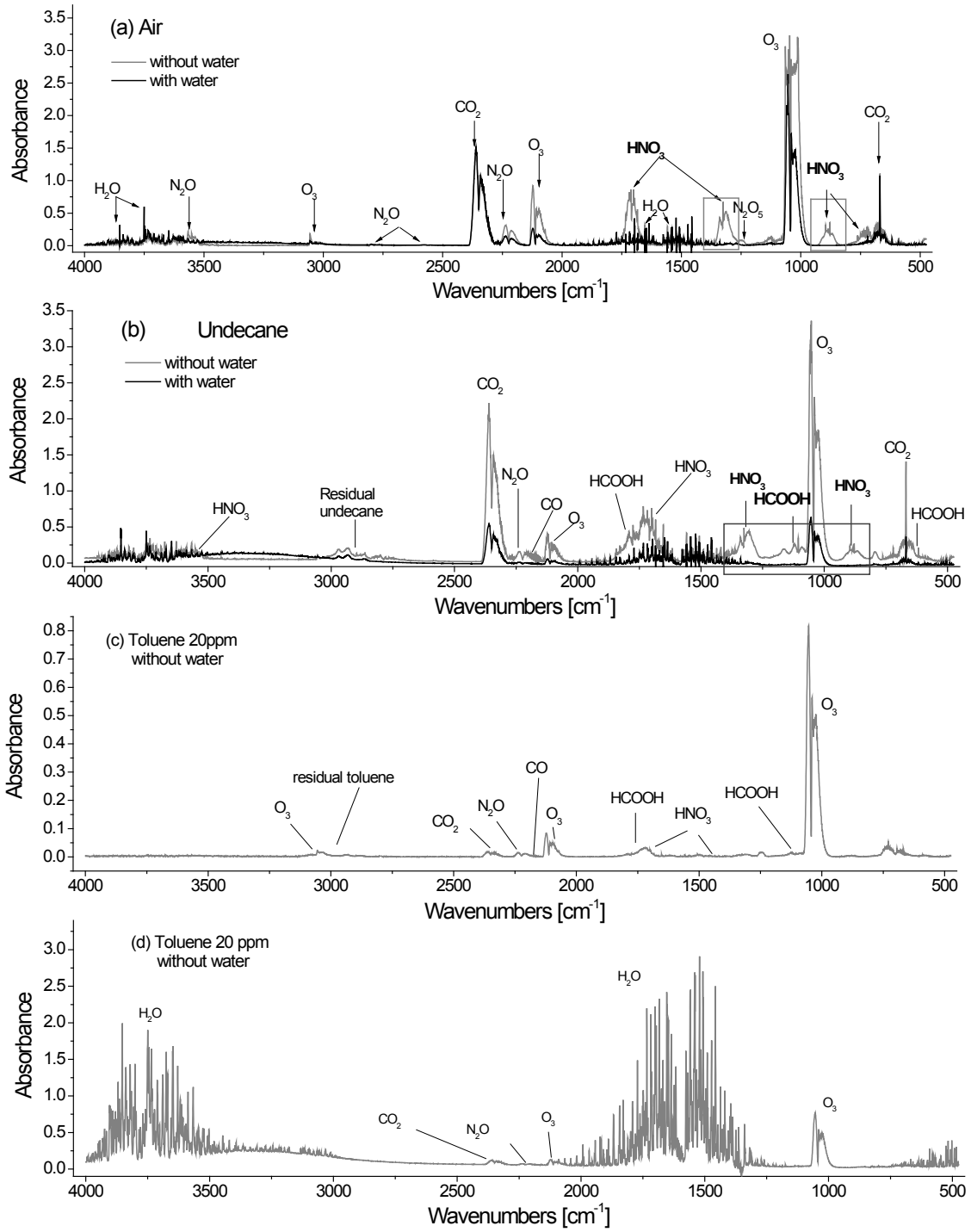


Fig. 3. FTIR spectra of the gas flowing out of the reactor after plasma treatment: (a) air, (b) undecane, (c) and (d) 20 ppm of toluene in synthetic air, with and without water.

Although the presence of water has a bit adverse effect on energy consumption, the FTIR analysis showed that its presence enhances the gas cleaning process and the elimination of plasma treatment by-products. Examples of FTIR spectra obtained in air/undecane and air/toluene mixtures are presented in Fig. 3. Analysis has shown that the major degradation products of tested organic compounds are CO_2, CO and formic acid (HCOOH). Also evident are absorption bands of O_3, HNO_3 and N_2O, formed in the background gas. In Fig. 3a and 3b the absence of HNO_3 and HCOOH bands in plasma with water can be clearly observed (framed part). Such behavior is not obvious in the case of toluene because of the lower initial concentrations which result in lower concentration of by-products. The scrubbing of soluble by-products from the gas phase by water film inside the plasma reactor significantly improves the pollution control processes where plasma converts non-soluble pollutants into soluble ones.

Acknowledgements

This work is supported by the Ministry of Education and Science of the Republic of Serbia (projects No. 171034 and No. 33022) as well as transnational project "PlasTEP – Dissemination and fostering of plasma based technological innovation for environment protection in the Baltic Sea region "part-financed by the European Union (European Regional Development Fund)." The technical assistance of Wolfgang Reich, Helge Grosch and Tomas Hoder is highly appreciated.

4. References

[1] WHO (World Health Organization), 1989. Indoor air quality: organic pollutants. Euro Reports and Studies No. *11 I* . Copenhagen: World Health Organisation, Regional Office for Europe.
[2] European Collaborative Action 'Indoor Air Quality and Its Impact on Man, 1997. Total volatile organic compounds (TVOC) in indoor air quality investigations. Report No 19. EUR 17675 EN. Luxembourg: Office for Official Publications of the European Community
[3] Fridman A, 2008 Cambridge University Press: Cambridge, UK.
[4] Van Veldhuizen E M, 2000 Nova Science Publishers: New York.
[5] Kim H H, 2004 *Plasma Process. Polym.* **1** 91.
[6] Tak G, Gutsol A, Fridman A, 2005 *17th Int. Symposium on Plasma Chemistry (ISPC-17)* 1128.
[7] Kuraica M M, Obradović B M, Manojlović D, Ostojić D R and Purić J, 2004 *Vacuum* **73** 705.
[8] Manojlović D, Ostojić D R, Obradović B M, Kuraica M M, Krsmanović V D and Purić J, 2007 *Desalination* **213** 116.
[9] Manojlović D, Popara A, Dojčinović B P, Nikolić A, Obradović B M, Kuraica M M and Purić J, 2008 *Vacuum* **83** 142.
[10] Dojčinović B P, Manojlović D, Roglić G M, Obradović B M, Kuraica M M and Purić J, 2009 *Vacuum* **83** 234.
[11] Dojčinović B P, Roglić G M, Obradović B M, Kuraica M M, Kostić M M, Nešić J and Manojlović D D, 2011 *Journal of Hazardous Materials* **192** 763.
[12] Obradovic B M, Sretenovic G B and Kuraica M M, 2011 *Journal of Hazardous Materials,* **185** 1280.
[13] Falkenstein Z and Coogan J J 1997 *J. Phys. D: Appl. Phys.* **30** 817.
[14] Hoeben W F L M, Beckers F J C M, Pemen A J M, van Heesch E J M and Kling W L, 2012 *J. Phys. D: Appl. Phys*. **45** 14.

ANTIMICROBIAL ACTIVITY OF SODIUM CHLORIDE SOLUTION TREATED IN WATER FALLING FILM DBD REACTOR

Vesna V. Kovačević[1], Mareike Hänsch[2], Ronny Brandenburg[2], Thomas von Woedtke[2], Bratislav M. Obradović[1], Goran B. Sretenović[1] and Milorad M. Kuraica[1]

[1]*University of Belgrade, Faculty of Physics, Studentski trg 12-16, 11000 Belgrade, Serbia*

[2]*Leibniz Institute for Plasma Science and Technology (INP Greifswald), Felix-Hausdorff-Str. 2, D-17489 Greifswald, Germany*

E-mail: vesna@ff.bg.ac.rs

Inactivation of aquatic microorganisms by indirect and direct air plasma treatment using water falling film dielectric barrier discharge (DBD) reactor was investigated. In this reactor the circulating liquid is a part of discharge electrode configuration. Thus the liquid is directly exposed to radiation and reactive species like ozone, radicals, ions and electrons. Suspension with high concentration of microorganisms (range 10^7-10^9 cfu·ml^{-1}) *Escherichia coli* and *Staphylococcus aureus* have been used to investigate the antimicrobial effect. In indirect treatment NaCl solution was treated by plasma with different exposure times and microorganisms were added to the stock suspension immediately after the treatment. Complete inactivation of *E. coli* was achieved with NaCl solution treated by plasma for 30 min, while for *S. aureus* it was 40 min. In direct plasma treatment of NaCl solution containing suspended microorganisms, complete inactivation of *E. coli* and *S. aureus* were achieved after 2 min and 1 min of plasma treatment, respectively. Furthermore a significant acidification (pH<2) of plasma treated NaCl solution was measured. FTIR analysis of air flowing out of the reactor showed that in plasma treated air without the presence of water O_3, N_2O and HNO_3 were produced in the discharge, while the absence of HNO_3 absorption bands is evident when water is circulating in the discharge region.

1. Introduction

In recent years much attention has been devoted to development of non-thermal plasma (NTP) applications in life-science (bio-decontamination, wound healing, treatment of cancer cells, etc.). Non-thermal atmospheric-pressure discharges, particularly in air, are very effective and convenient in deactivation of micro-organisms. NTPs in air are an effective source of active species, such as radicals, ions, excited atoms and molecules, UV radiation and so on, which are able to deactivate, kill, or even completely disintegrate bacteria, viruses, and other microorganisms without any significant temperature effects [1]. Plasma induced inactivation of microorganisms was demonstrated by plasma treatment of liquids where liquid is in direct or close contact with plasma [2, 3], and by plasma treatment where the plasma is in close proximity to a liquid, but without direct contact [4, 5]. In plasma treated liquid, under atmospheric air conditions, acidification as well as generation of low-molecular chemical species such as nitrate (NO_3^-), nitrite (NO_2^-) and hydrogen peroxide (H_2O_2) have been identified [6, 7]. Research results highlight the complexity of plasma-liquid interactions and hypothesize that reactive nitrogen and reactive oxygen species generated in plasma both play a key role for antimicrobial activity of plasma treated liquids.

In this work we tested application possibilities of hybrid gas-liquid DBD reactor for inactivation of aquatic microorganisms. Application of water falling film DBD has been already investigated for water purification [8-12]. In this reactor configuration chemically active species generated in plasma can easily get into the water which forms a falling film at one of the electrodes.

2. Experimental set-up

Experimental set up is shown in Fig. 1. The cylindrical reactor consists of two glass tubes and electrodes, placed concentrically. The inner glass tube, with a diameter of 20 mm, has double walls and it's silverised on the inner side. The silver layer served as the grounded inner electrode. The outer glass tube, with the inner diameter of 29 mm and length of 600 mm, was wrapped with an aluminum foil of a length of 380 mm. The aluminum foil was connected to the high voltage.

When the discharge source works as a falling film reactor, water flows up through a vertical hollow inner glass tube and flows down making a thin film over the inner electrode. Water flows from the reservoir through the discharge by means of peristaltic pump, with a flow rate of 100 mL/ min. All measurements were done for a discharge reactor operating at atmospheric pressure in flowing air with a gas flow rate of 2 L/min. In this way water becomes a part of discharge electrode configuration and plasma is generated between the glass and the water layer.

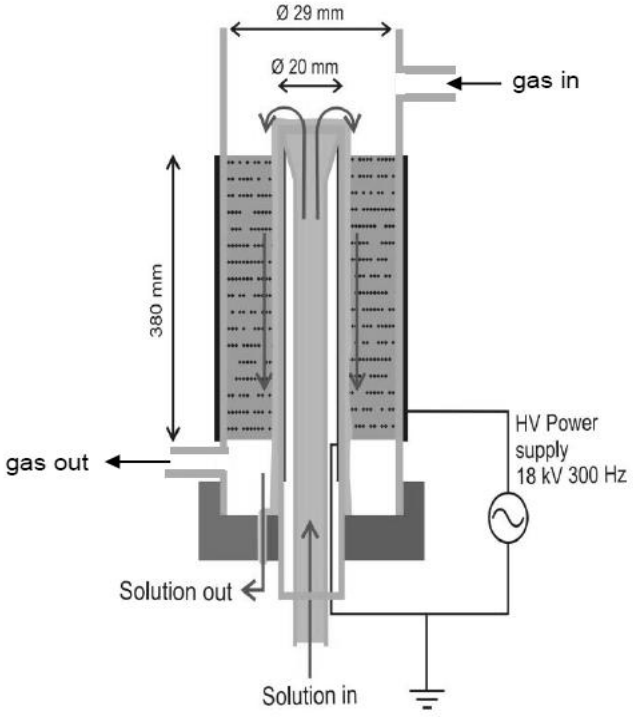


Fig. 1. Coaxial water falling film DBD

The low frequency ac power supply used in this study consists of a high voltage transformer and a frequency inverter. For this reactor configuration optimal operating conditions are found to be at frequency of 300 Hz. The filamentary barrier discharge is generated within 4.5 mm gap between the inner and the outer glass tubes by applying voltage of 18 kV amplitude. Electric parameters were measured using a digital oscilloscope Tektronix DPO 4104 (1 GHz bandwidth, 5 GSamples/s) and a high voltage probe Tektronix P6015A. Lissajous figures (Q-U graphs) were used for determination of electric power of the discharge [13]. To obtain these graphs a capacitor of 470 nF was connected in series with the discharge. In this study electrical power of 43 W was dissipated into the plasma in all experiments.

Online FTIR analysis of gas exiting the reactor was performed with the Bruker Alpha FTIR gas analyser using a 4.9 m long gas cell. For pH measurement of treated liquid a pH meter (WTW GmbH, Germany) and a semi-micro pH electrode (SENTEK P13, Sentek Ltd., UK) were used.

In order to investigate inactivation of microorganisms with water falling film DBD indirect and direct treatments of microorganisms were applied. In this study *indirect treatment* refers to a plasma treatment of liquid without microorganisms, which is added to microorganism stock suspension immediately after the plasma treatment. *Direct treatment* refers to a plasma treatment of liquids containing suspended microorganisms.

As test microorganism overnight cultures of *Escherichia coli* NTCC 10538 and *Staphylococcus aureus* ATCC 6538 (Institute of Hygiene and Environmental Medicine, University of Greifswald, Germany) were diluted using sodium chloride solution (NaCl 0.85 %; 8.5 g NaCl per 1000 mL water) to get concentrations of 10^7- 10^9 colony forming unites per milliliter (cfu · ml^{-1}). For indirect plasma treatment 100 ml of sodium chloride solution without bacteria were treated. Starting volume of 100 ml was circulating in water falling film DBD reactor. Samples of treated solution were taken every 10 min. within 60 min. of total treatment time and immediately added to culture tubes containing *E. coli* and *S. aureus* stock suspension (exposure time 15 min), respectively. For direct plasma treatment 100 ml of *E. coli* and *S. aureus* stock suspensions were treated, respectively, in water falling film DBD for different times (1-15 min.). The number of viable microorganisms (cfu · ml^{-1}) was estimated by the surface-spread plate count method using aliquots of serial dilutions of microorganism suspensions according to the European Pharmacopoeia. Detection limit of this procedure was 10 cfu · ml^{-1}. Inactivation kinetics of microorganisms is depicted in semi-logarithmic plots. If the number of microorganisms fell below the detection limit, i.e. no viable microorganisms have been found, these values in the diagrams are set at 5 cfu · ml^{-1}.

3. Results and discussion

Influence of plasma treated NaCl solution on inactivation of *E. coli* and *S. aureus* is shown on Fig. 2. The results show that the inactivation of *E. coli* is found to be more efficient than inactivation of *S. aureus*. Complete inactivation of *E. coli* was achieved with NaCl solution treated in plasma for 30 min. This corresponds to 8 log order reduction of *E. coli* with specific energy density of 878 kJ/L. *S. aureus* is more resistant to external influences in general compared to *E. coli*. Complete inactivation of *S. aureus* is reached with NaCl solution treated in plasma for 40 min. In the case of *S. aureus* 8 log order reduction was obtained with specific energy density of 1263 kJ/L.

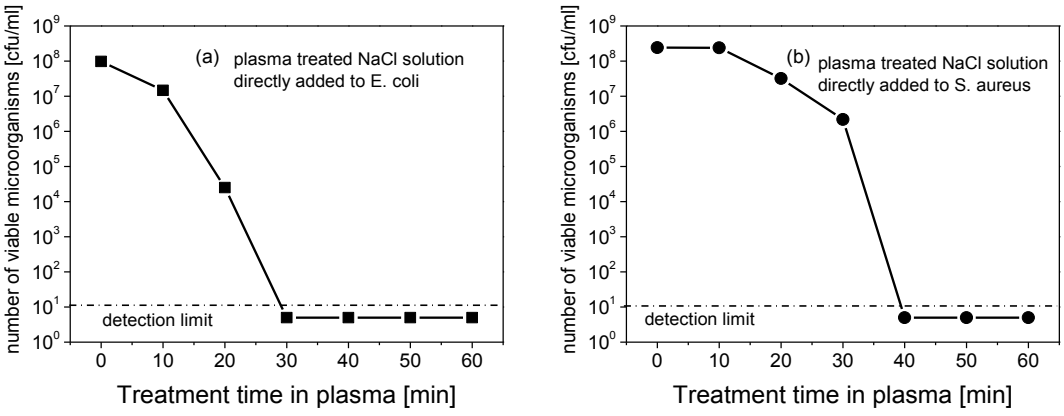


Fig. 2. Influence of plasma treated NaCl solution on inactivation of (a) *E. coli* and (b) *S. aureus*

The change of pH of treated NaCl solution during the plasma treatment is shown in Fig 3. First 10 min of treatment in the discharge resulted in a steep decrease of pH from 7 to less than 3, this is followed by a further slight decrease and pH value less than 2 was recorded after 60 min of treatment. It has been reported by several groups that in the case of water disinfection by plasma treatment, antimicrobial plasma effects correlated at least partially with pH decrease of liquids, i.e. acidification. Air plasma treated water becomes acidic and contains active species nitrite (NO_2^-), nitrate (NO_3^-) and hydrogen peroxide (H_2O_2). In air plasma reactive nitrogen and oxygen species are generated in gas phase and dissolved in plasma-liquid interactions. Dissolution of these reactive species leads to the acidification of the liquid exposed to the plasma. This is also confirmed in one configuration of water falling film DBD where water was treated with air plasma and concentrations of nitrite, nitrate and hydrogen peroxide were measured using spectrophotometric methods [14]. In order to better understand plasma-liquid interactions FTIR spectra of air flowing out of the reactor were recorded in dry rector without water and while water was circulating in the reactor, Fig. 4.

FTIR analysis showed that in plasma treated air without the presence of water in the discharge O_3, N_2O and HNO_3 were produced. When water circulation through the discharge is switched on, the absence of HNO_3 absorption bands is evident. These results indicate that species generated in gas phase can diffuse and interact with water, which further leads to chemical reactions in water and production of new species.

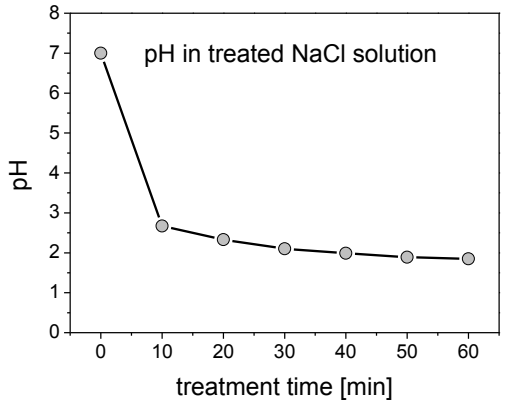


Fig. 3. The pH of NaCl solution dependent on plasma treatment time

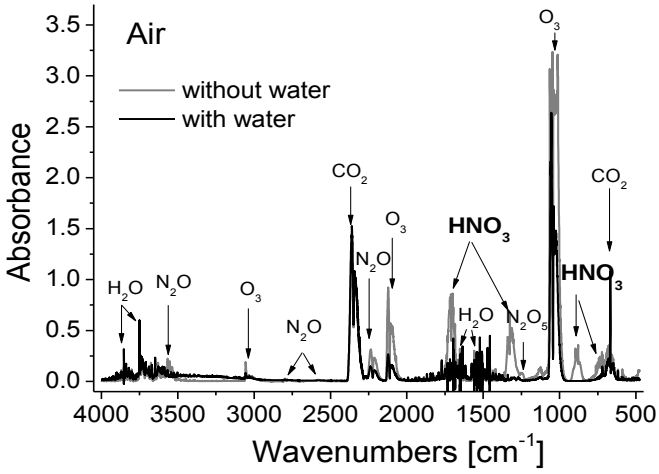


Fig. 4. FTIR spectra of air treated in water falling film reactor without water and with water

Inactivation kinetics of *E. coli* and *S. aureus* in suspensions directly exposed to plasma dependent on plasma treatment time is shown on Fig. 5. After 1 min of plasma treatment 6 log reduction in *E. coli* viability was measured. Complete inactivation of *E. coli* was achieved after 2 min of plasma treatment. In this experiment complete inactivation of *E. coli* corresponds to 9 log order reduction achieved with specific energy density of ~ 52 kJ/L. Initial concentration of *E. coli* was somewhat higher than initial concentration of *S. aureus.* Complete inactivation of *S. aureus* was accomplished after 1 min of plasma treatment which corresponds to 7 log order reduction with specific energy density of ~ 25 kJ/L.

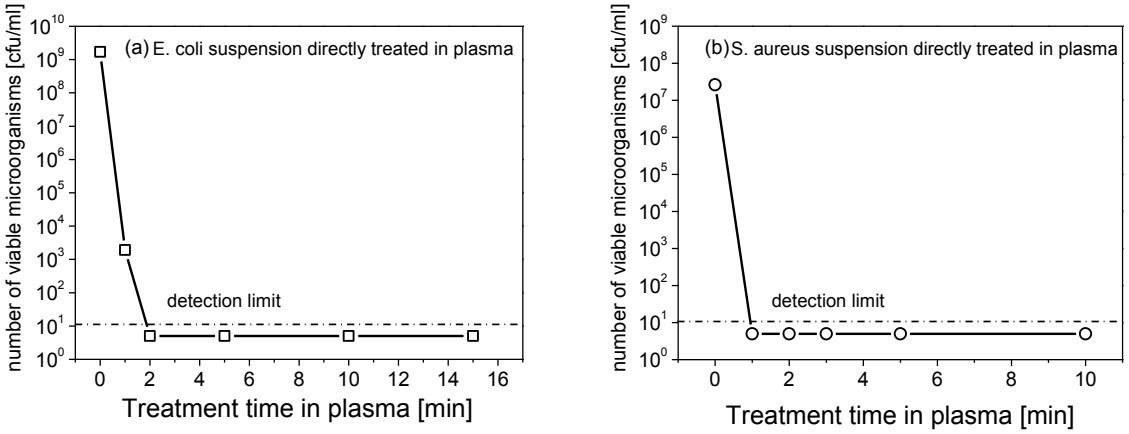


Fig. 5. Concentrations of (a) *E. coli* and (b) *S. aureus* in suspensions treated in plasma as a function of plasma treatment time

Taking into account that initial concentration of *E. coli* was higher than that of *S. aureus* for almost 2 log orders, it could be sad that under the studied experimental conditions it takes approximately 1 min of direct treatment for 7 log order reduction of *S. aureus* or *E. coli*, which corresponds to specific energy density of 25 kJ/L. Inactivation of *E. coli* and *S. aureus* in indirect and direct plasma treatment as a function of specific energy density is given in Fig. 6 and Fig. 7, respectively.

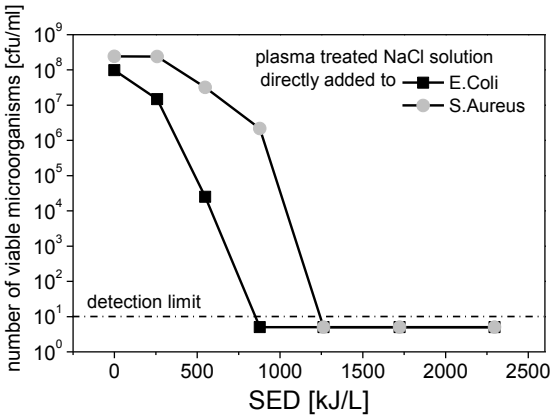


Fig. 6. Inactivation of *E. coli* and *S. aureus* in indirect plasma treatment as a function of SED

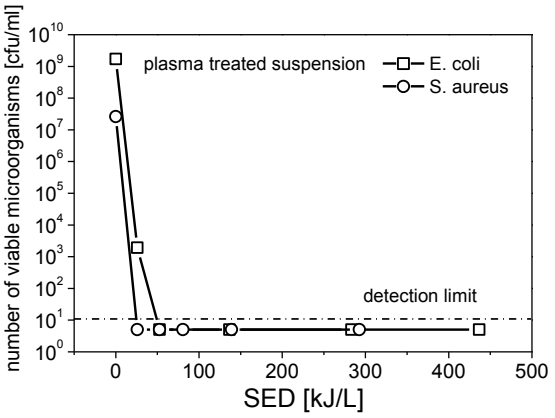


Fig. 7. Inactivation of *E. coli* and *S. aureus* in direct plasma treatment as a function of SED

Regarding the energy efficiencies the water falling film DBD exhibits highly efficient antimicrobial activity comparing to some results reported in literature where the liquid containing microorganisms is in direct contact with the plasma [3]. It took around 40 min to achieve five-log order reduction for *E. coli*, which corresponds to 120 J/ml according to data reported in [3]. Although, the energy consumption for indirect treatment reported in this paper is significantly higher than one for direct treatment, biological effects of plasma-activated water and antibacterial effectiveness for a period of up to 7 days after plasma treatment [5] make it important in plasma bio-decontamination (antimicrobial treatment of various surfaces, medical instruments and equipment, different food products, etc.) processes.

Acknowledgements

This work is supported by the Ministry of Education and Science of the Republic of Serbia (projects No. 171034 and No. 33022) as well as the transnational project "PlasTEP" (part-financed by the European Union (European Regional Development Fund)).

4. References

[1] Fridman A, 2008 Cambridge University Press: Cambridge, UK.
[2] Chen C W, Lee H M and Chang M B, 2008 *IEEE Trans. Plasma Sci.* **36** 215.
[3] Liu F et al. 2010 *Plasma Process. Polym.* **7** 231.
[4] Oehmigen H et al. 2010 *Plasma Process. Polym.* **7** 250.
[5] Traylor M J et al, 2011 *J. Phys. D: Appl. Phys.* **44** 472001.
[6] Von Woedtke T et al. 2012 *NATO Science for Peace and Security Series A: Chemistry and Biology* **1** 67.
[7] Oehmigen H et al. 2011 *Plasma Process. Polym.* **8** 904.
[8] Kuraica M M, Obradović B M, Manojlović D, Ostojić D R and Purić J, 2004 *Vacuum* **73** 705.
[9] Manojlović D, Ostojić D R, Obradović B M, Kuraica M M, Krsmanović V D and Purić J, 2007 *Desalination* **213** 116.
[10] Manojlović D, Popara A, Dojčinović B P, Nikolić A, Obradović B M, Kuraica M M and Purić J, 2008 *Vacuum* **83** 142.
[11] Dojčinović B P, Manojlović D, Roglić G M, Obradović B M, Kuraica M M and Purić J, 2009 *Vacuum* **83** 234.
[12] Dojčinović B P, Roglić G M, Obradović B M, Kuraica M M, Kostić M M, Nešić J and Manojlović D D, 2011 *Journal of Hazardous Materials* **192** 763.
[13] Falkenstein Z and Coogan J J 1997 *J. Phys. D: Appl. Phys.* **30** 817.
[14] Kovačević V V et al. 2011 *The Fourth Central European Symposium on Plasma Chemistry (CESPC 4)*

STABILIZATION OF A LEAN METHANE–AIR FLAME USING TRANSIENT SPARK DISCHARGE

M. Janda[1], Z. Machala[1], D. A. Lacoste[2], G. D. Stancu[2], C. O. Laux[2]

[1]*Faculty of Mathematics, Physics and Informatics, Comenius University, Mlynská dolina, 84248 Bratislava, Slovakia*

[2]*Laboratoire EM2C, CNRS-UPR288, Ecole Centrale Paris, 92295 Châtenay-Malabry, France*

E-mail: machala@fmph.uniba.sk

Reducing NOx emissions from combustion processes can be achieved by decreasing the combustion temperature while operating at sub-stoichiometric (lean) conditions. However, there is a limit at which flame becomes unstable. It was found that this limit can be significantly improved and the lean flame can be stabilized using high frequency (~kHz) nanosecond repetitively pulsed (NRP) discharge. NRP discharges generate reactive plasma with high energy efficiency. We tested a DC-driven self-pulsing transient spark (TS) discharge for the stabilization of a lean premixed methane-air flame and compared the stabilizing effect with that of the NRP discharge. We found a very similar stabilizing effect to that of NRP discharge at lower discharge power and with low-cost DC power supply.

1. Introduction

Reducing pollutant emissions in combustion engines has become a major issue because of new environmental regulations. Various electrical discharges have been successfully applied for the removal of NO_x from exhaust gases. However, it is more efficient to prevent their formation during the combustion process. In a flame, the production of nitric oxides NO_x is strongly related to the flame temperature [1]. Since this temperature is directly related to the fuel equivalence ratio Φ, one way to reduce this temperature is to burn the fuel in lean conditions [2]. However, in these conditions, the flame becomes unstable and can eventually extinguish. Stabilizing the lean flame is an issue that can be well addressed by using non-thermal plasma discharges applied directly in the flame , as successfully demonstrated by using nanosecond repetitively pulsed (NRP) discharges with premixed propane-air [2, 4] or methane-air [5] flames. Methane-air flames are employed in a great number of applications involving natural gas turbines. A review of additional work in this area is provided in [3].
In this paper, we compare the effects of NRP discharges and self-pulsed transient spark (TS) discharges on the stability of a CH_4-air flame.

2. Experiment

A NRP discharge was produced by a FID FPG 10-30MS generator, between two metal electrodes. The TS discharge was produced by supplying a high DC voltage through a resistor of 700 kΩ placed in series between the DC power supply and the gap to reduce the voltage after the current pulse. A capacitor C=500 pF was added in parallel of the discharge gap in order to increase the energy delivered to the plasma.
The plasma discharge (either NRP or TS) is located in the combustion zone between the two stainless steel electrodes separated by a 5 mm gap. A bluff body (10 mm in diameter) is used as a cathode and creates a recirculation zone. The premixed CH_4-air burner is presented in Fig. 1 along with the experimental set-up. The flow rates of air and methane are controlled by Bronkhorst High-Tech EL-FLOW electronic flow meters. Voltage measurements are made with a Lecroy PPE 20-kV high-voltage probe, and current measurements are made with a Pearson Electronics 6585 probe, with a Lecroy WavePro 7000 oscilloscope. The flame without or with the discharge is photo and video-documented by Olympus E410 and Nikon 7000 digital cameras.

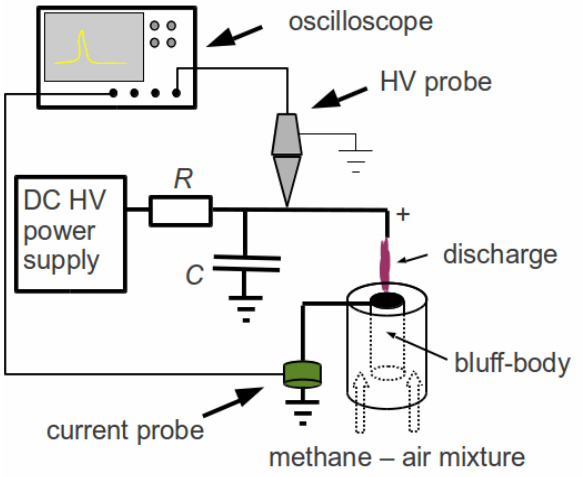


Fig. 1. Schematic of the experimental set-up.

3. Results and discussion

3.1. NRP and TS discharges

Nanosecond repetitively pulsed (NRP) discharges in air and combustion mixtures have been extensively studied at Ecole Centrale Paris [6]. The applied electric pulse has a duration of about 10 ns and an amplitude of several kilovolts. The typical NRP voltage and current pulse are shown in Fig 2a. Depending on the pulse voltage, we can obtain three different regimes: corona, glow, and spark [6]. The frequency is fixed at f = 30 kHz, which results in less electric power consumed by the plasma discharge as compared to a continuous (pulse-less) discharge. Only the spark NRP regime can stabilize a lean flame. There is a significant increase in the energy provided to the discharge at the transition between the two main regimes (glow and spark). However, even at the highest voltage allowed by the experimental setup, the energy provided to a single nanosecond pulse is only 1.6 mJ, which corresponds to an average power of only 48 W at a 30-kHz repetition frequency. This represents less than 1% of the power of the flame.

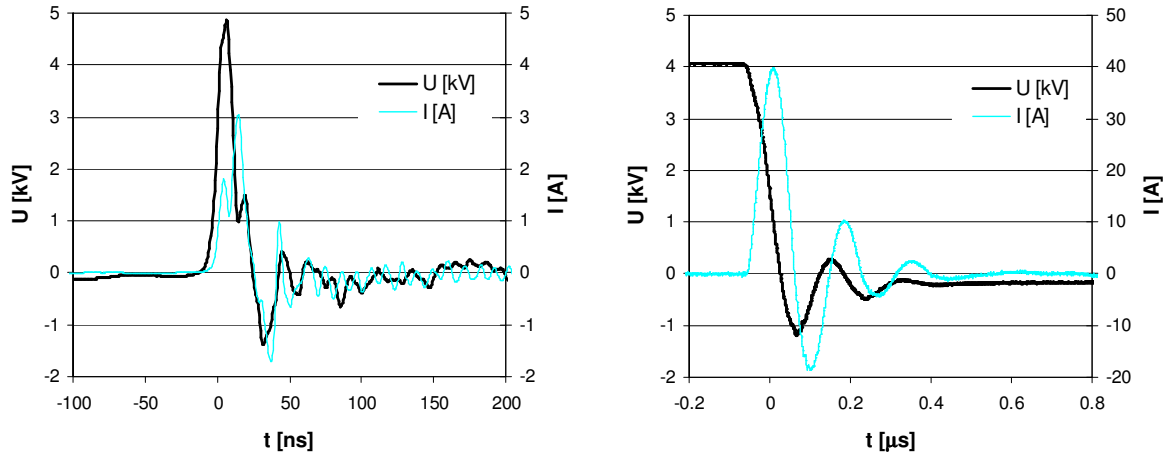
The transient spark (TS) is a spontaneous streamer-to-spark transition pulsed discharge generated by a high DC voltage. It has been extensively studied at Comenius University in Bratislava, especially in air [7-10], air with sprayed water for bio-decontamination applications [11-12], air with VOC for flue gas cleaning [13], and N_2-CO_2-H_2O mixtures [14]. The details of its electrical and optical emission characteristics can be found in [8-10]. Here we show the typical voltage and current pulse waveforms when operated in the CH_4-air combustion flame with a capacitor C=500 pF inserted in the circuit (Fig. 2b).

With the NRP discharge, the higher the pulse voltage, the more luminous and powerful the discharge. On the contrary, the TS is a pulsed discharge with spontaneous pulses determined by the streamer-to-spark transition process. The electrical characteristics of the TS are influenced by the flame, and vice versa, the flame is influenced by the discharge. With the TS, the frequency increases with the applied voltage, but the discharge is not necessarily more luminous or powerful. In fact, single pulses occur at lower breakdown voltage and have a lower current amplitude with increasing frequency.

Our goal was to maximize the power delivered to the plasma. We kept the mean discharge current at 6 mA (the limit of the DC power supply), which resulted in a TS repetition frequency f ~2.5 kHz. Fig. 3 shows the TS breakdown voltage U_{TS} as a function of the CH_4-air equivalence ratio Φ (Φ=1 corresponds to stoichiometry) and the gas flow rate Q. U_{TS} decreases with increasing Φ, especially at low Q. This is due to an increase of the gas temperature: because the flame is more energetic with higher Φ, the higher gas temperature results in a lower gas density N, hence a lower electric field or lower voltage is sufficient to keep the same reduced electric field E/N. At higher flow rates, there is less gas heating, and the effect is not as strong. The current pulse maximum similarly decreases with

increasing Φ. On the contrary, the frequency f increases with Φ (i.e. rising temperature) and decreasing U_{TS} voltage.

The energy per pulse has the same decreasing trend as U_{TS} with increasing Φ, especially for low Q, since it is determined by the discharging capacity C and can be calculated as $E_{pulse} = ½ CU_{TS}^2$. The E_{pulse} values are between 4.5 and 6.5 mJ. This calculation was confirmed by determining E_{pulse} from the measured voltage and current waveforms. Finally, the TS power (Fig. 4), calculated as $P=f E_{pulse}$, is also a function of Φ. Similar to U_{TS} and E_{pulse}, the power decreases with increasing Φ and it is only partly compensated by the increasing f. This TS behavior is suitable for flame stability enhancement: there is more power delivered where it is more needed - close to the flame stability limit.



(a) (b)

Fig. 2. Typical voltage and current pulse waveforms of (a) NRP discharge and (b) TS operated in the CH_4-air premixed flame at total gas flow Q=4 Nm^3/h and Φ=0.8.

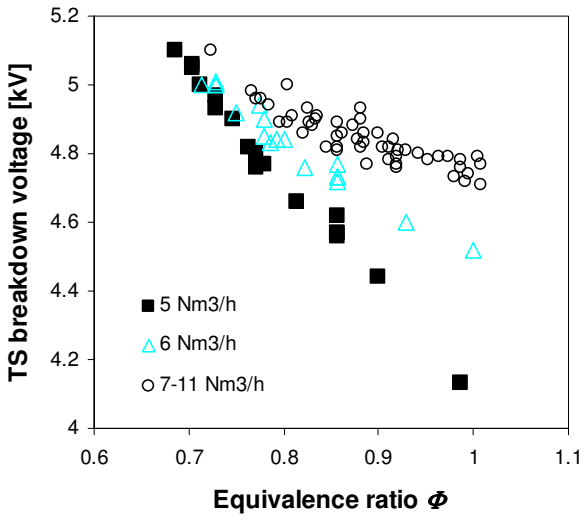


Fig. 3. TS breakdown voltage U_{TS} as a function of the equivalence ratio Φ and gas flow rate Q.

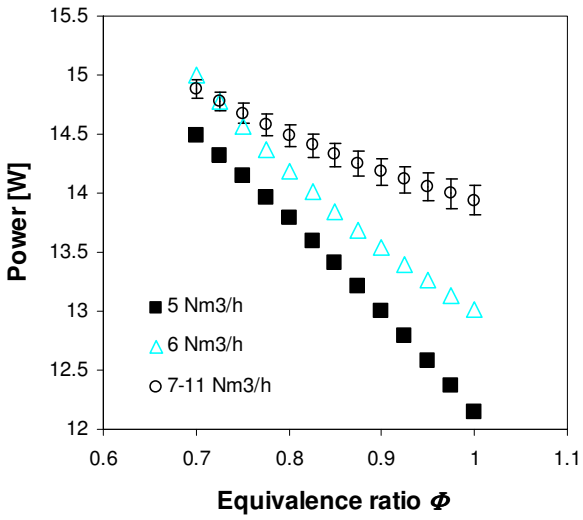


Fig. 4. TS power as a function of the equivalence ratio Φ and gas flow rate Q.

3.1. NRP and TS effect on flames

By decreasing the methane flow rate at a constant total CH_4-air flow rate, i.e. by decreasing the equivalence ratio Φ, four flame regimes are usually observed before the flame blows out:

1) stable V-shaped flame;
2) intermittent flame;
3) unstable flame;
4) pilot flame (confined to the recirculation zone).

Fig. 5 shows the photographs of the combustion flame without TS at the stability limit between stable and intermittent flame (Φ=0.7) and stabilized with TS.
Fig. 6 shows the extended domain of flame stability when using the TS discharge. With the TS discharge, a stable flame can be operated with lower Φ. The stabilizing effect of TS was found to be very similar to the effect of the NRP discharge (spark regime) [5], as shown in Fig. 7. Approximately an 11% decrease in the lean extinction limit is obtained with both types of discharges. The data in Fig. 7 are normalized to the value of Φ corresponding to the transition between stable and unstable flame at Q=9 Nm^3/h without plasma. This normalization was needed for comparison, since the NRP experiments were performed earlier and the flame conditions were not absolutely identical with the TS experiments.



Fig. 5. Photographs of the CH_4-air premixed flame without and with TS discharge at Φ=0.7 (stability limit without discharge) and gas flow rate Q=4 Nm^3/h, photo exposure time 2s, ISO 100, f 5.6.

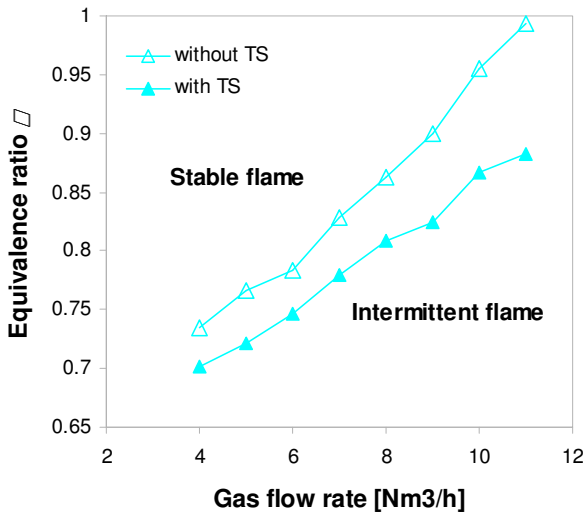


Fig. 6. Stabilizing effect of TS discharge on lean CH_4-air flame.

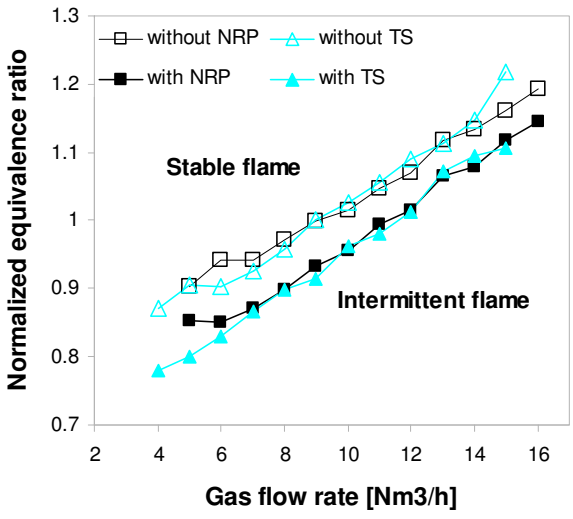


Fig. 7. Comparison of the stabilizing effect of NRP and TS discharges on lean CH_4-air flame.

4. Summary

The lean extinction limit of a premixed CH_4-air combustion flame can be lowered by applying non-thermal plasma discharges in the flame. In this comparative study we demonstrated the lean extinction limit can be decreased by ~11% using high frequency (~30 kHz) nanosecond repetitively pulsed discharge with ~48 W discharge power, as well as with a DC-driven self-pulsing transient spark (TS) discharge of ~2.5 kHz and ~12-15 W power. Besides lower power, the advantage of TS discharge is the use of low-cost DC power supply. On the other hand, NRP discharges with low-jitter, regular 10 ns pulses makes it much easier to study kinetic and thermal effects with complex nanosecond time-resolved optical diagnostics.

5. Acknowledgments

This work was supported by Slovak Research and Development Agency SK-FR-0038-09 and Slovak grant agency VEGA 1/0998/12, and by the ANR project PLASMAFLAME

6. References

[1] Lefebvre A H 1999 *Gas Turbine Combustion*, Philadelphia, PA: Taylor & Francis.
[2] Pilla G, Lacoste D A, Veynante D and Laux C O 2008 *IEEE Trans. Plasma Sci.* **36** 940.
[3] Starikovskaia S M 2006 *J. Phys. D: Appl. Phys.* **39** R265
[4] Pilla G, Galley D, Lacoste D A, Lacas F, Veynante D, and Laux C O 2006 *IEEE Trans. Plasma Sci.* **34** 2471.
[5] Pham Q L L, Lacoste D A and Laux C O 2011 *IEEE Trans. Plasma Sci.* **39** 2264.
[6] Pai D Z, Lacoste D A and Laux C O 2010 *J. Appl. Phys.* **107** 093303.
[7] Machala Z, Jedlovksý I and Martišovitš V 2008 *IEEE Trans. Plasma Sci.* **36** 918.
[8] Janda M and Machala Z 2011 *IEEE Trans. Plasma Sci.* **39** 2246.
[9] Janda M, Martišovitš V and Machala Z 2011 *Plasma Sources Sci. Technol.* **20** 035015.
[10] Janda M, Machala Z, Niklová A and Martišovitš V 2012 *Plasma Sources Sci. Technol.* **21** 045006.
[11] Machala Z, Jedlovský I, Chládeková L, Pongrác B, Giertl D, Janda M, Šikurová L and Polčic P 2009 *Eur. Phys. J. D* **54** 195.
[12] Machala Z, Chládeková L and Pelach M 2010 *J. Phys. D: Appl. Phys.* **43** 222001.
[13] Machala Z, Morvová M, Marode E and Morva I 2000 *J. Phys. D: Appl. Phys.* **33** 3198
[14] Janda M, Machala Z, Morvová M and Morva I 2008 *Orig. Life Evol. Biosph.* **38** 23.

BIOFILM INACTIVATION ON TEETH AND PLASTIC SURFACES WITH DC CORONA DISCHARGES

Zuzana Šipoldová[1], Zdenko Machala[2]
[1]*Division of Biomedical Physics,*
[2]*Division of Environmental Physics,*
Faculty of Mathematics, Physics and Informatics, Comenius University, Slovakia
E-mail: machala@fmph.uniba.sk

A cold plasma of DC corona discharges: positive streamer corona and negative Trichel pulses was used for bio-decontamination of *Streptococci* biofilm on plastic and teeth surfaces. Enhancement of plasma biocidal effects by was investigated. Electro-spraying of water through a hollow needle high-voltage electrode significantly increased the bacterial reduction up to 4 logs with both types of samples. Analysis of tooth surfaces after plasma treatment was carried out by Fourier transform infrared spectroscopy (FTIR) did not show any chemical changes on plasma treated teeth.

1. Introduction

Biological decontamination of thermo-sensitive materials by non-equilibrium plasma has been widely studied recently. The plasma found applications e.g. in dentistry [1] in biofilm decontamination and teeth whitening [2]. Various contamination agents can be efficiently treated by plasma, for example: fungi, yeasts, bacteria, etc. Even resistant bacterial species (e.g. MRSA), biofilms and bacterial spores, which are not easily decontaminated by conventional chemical agents could be eliminated by plasma [3-5].

Plasma chemical effect on a bacterial cell membrane is highly dependent on the amount of water. The highest biocidal effect was found on moist samples but a large amount of water causes a dilution effect [6]. Electrostatic spraying [7-8] of water on a sample with a small flow rate could possibly have the same effect as a sample moistening before decontamination [3].

Recently, we have been working on decontamination of bacterial spores [3]. Then, we started testing another very resistant bacterial community – a bacterial biofilm. Human tissues support complex microbial communities growing as biofilms that can cause a variety of infections. As a result of an increased use of implanted medical devices and long-term catheters, the incidence of biofilm-associated diseases is increasing. Bacteria in biofilms exhibit increased tolerance towards commonly used antimicrobial agents and cold air plasma can be an alternative method for disinfection and sterilization of these thermo-sensitive materials. Plasma used for biofilm decontamination has been relatively little tested so far and is capable to disinfect dental plaque or caries and so might become an attractive painless alternative to teeth drilling.

In our work we are interested in decontamination of oral *Streptococci* biofilms cultivated on extracted teeth surface and plastic surfaces. We investigated the influence of electrostatic water spraying through the discharge on the bacterial reduction.

2. Methodology

2.1. Experimental set-up

The experimental set-up consisted of a DC high-voltage (HV) power supply and a discharge chamber placed in a Faraday cage. The treated samples were placed on the grounded electrode. The voltage was measured with a HV probe Tektronix P6015A and the current was measured on a 50 Ω grounded resistor connected through a coaxial cable to the digital oscilloscope Tektronix TDS 2024 (Fig. 1).

The discharge chamber contains a sharp hypodermic injection needle as a HV electrode opposite to a grounded stainless steel mesh or a copper plate. In some experiments, tap water was electro-sprayed on the samples. Water was pumped by an injection pump (SyringePump NE-300) with adjustable flow rate, through the HV electrode (specially modified for electro-spraying) and the discharge.

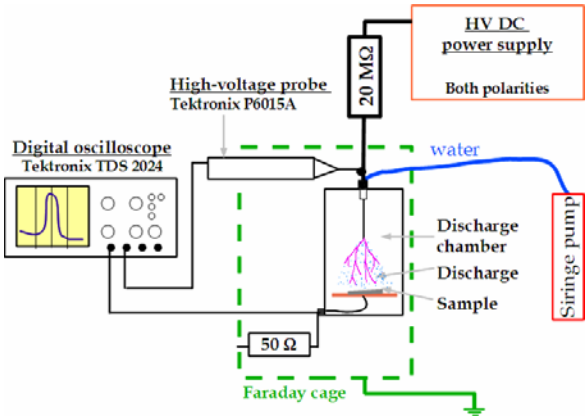


Fig. 1. Schematic of discharge set-up for corona on teeth or plastic surfaces.

2.2. Discharges used

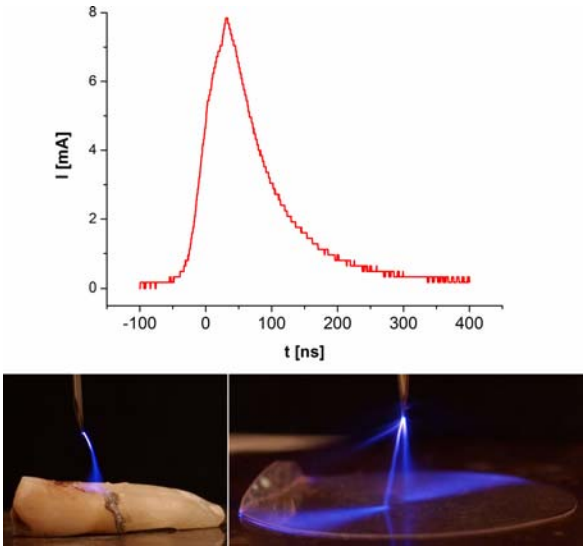


Fig. 2. The oscilloscopic record of positive streamer current pulse (U = 11.6 kV, f = 11.4 kHz, I_{max} = 23 mA) and the related photos on teeth and plastic surfaces.

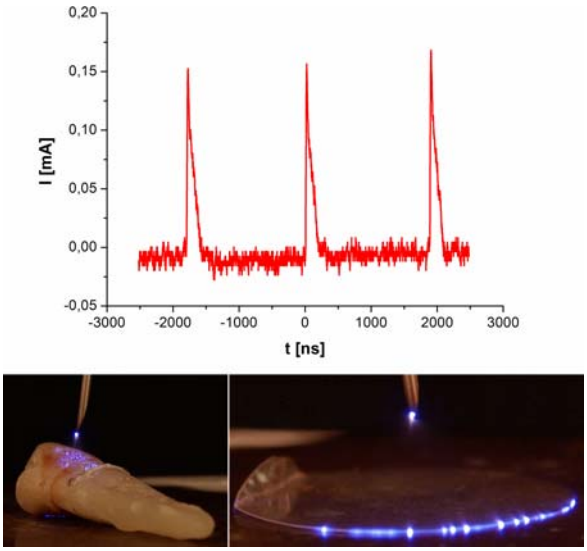


Fig. 3. The oscilloscopic record of the current of negative Trichel pulses (U = 6.88 kV, f = 550 kHz, I_{max} = 0.17 mA) and the related photos on teeth and plastic surfaces

Positive streamer corona was supplied with a HV from 4 to 8 kV for teeth and 5 - 8 kV for plastic samples. On teeth samples, there were streamers with frequency ~20 kHz and maximum amplitude up to 74 mA without water spraying, and ~10 kHz and up to 40 mA with spraying on the sample. On plastic samples, positive corona forms current pulses (streamers) with frequency 4-20 kHz and maximum amplitude up to 150 mA for the lowest frequencies (Fig. 2).

Negative Trichel pulses were supplied with a HV from -4 to -7 kV for both types of samples. On teeth, this HV with water spraying formed current pulses with frequencies ~100 kHz and amplitudes ~5 mA, and without spraying 0.25-2 MHz and 0.8 mA, respectively. On plastic samples, the mean frequency 60 kHz and current amplitude up to 9 mA were measured in streamers with spraying, while without water spraying ~180 kHz and <2.4 mA (Fig. 3).

2.3. Experimental procedure

The biofilm was produced by Viridans group of genus *Streptococcus* taken from oral microflora of three volunteers.

Sample preparation. The extracted human teeth were disinfected in 3% H_2O_2, than rinsed with sterile distilled water and dried. The polypropylene plastic samples (1.5×1.5 cm squares) were decontaminated under UV C lamp (λ = 254 nm, P = 11.2 W) from both sides.
Streptococci biofilm was prepared from a culture and cultivated on *Streptococci* selective agar (*Biolife*). The overnight culture was produced from selected colonies. On the next day, we cultivated 24 hour biofilm on teeth in the test tubes and on plastic samples in a special receptacle. After 24 hours biofilm cultivation on plastic and teeth surfaces, the samples were rinsed in sterile physiological solution to remove unattached bacteria.
Sample treatment in the discharges. In the experiments *without water spraying*, the teeth or plastic samples were put on a sterile copper plate. The teeth were treated for 1.5, 3, 5 and 10 minutes and plastic samples for 2 minutes in the discharge. In the experiments *with water spraying*, the samples were put on a stainless-steal mesh. The plastic samples were treated for 2 min and teeth for 5 min. Tap water was sprayed from the needle HV electrode through the discharge with flow rates 0.01 and 0.05 mL/min. After the treatment, the samples were put in test tubes with a sterile physiological solution.
Cultivation of samples. The samples in test tubes were placed in an ultrasound cleaner for 20 min to detach biofilm from surfaces of the samples. We used Vortex Classic for homogenization of the samples. Each sample diluted in the saline solution was spread on agar in three Petri dishes. The Petri dishes with inoculated bacteria were cultivated overnight at 35ºC. Reference samples were prepared in the same way without exposure to the plasma.
Results evaluation. Efficiency of plasma decontamination was determined as a decadic logarithm from the number of bacteria in the reference sample divided by the number of bacteria in the treated sample. All statistical tests were made at the level of significance 5%.

2.4. ATR FTIR analysis

Teeth were analysed by the ATR FTIR spectrometer (*BRUKER optics VECTOR 22* with ATR crystal: diamond/ZnSe) after being lyophilized (in lyophilizator *GT2 LEYBOLT - HERAEUS*) under vacuum of 1 - 3 hPa. After desiccation, the teeth were fixed in the 10% formalin solution used for biopsy and necropsy. The teeth were cut in halves longitudinally on a diamond saw microtome (*LEICA SP1600*).
FTIR spectra were measured on reference samples in the region of enamel on the cut side. One spectrum was obtained by averaging of 10 scans with the resolution of 2 cm^{-1}. The same half-tooth was exposed to the discharge for 10 minutes without electrostatic spraying. Immediately after the discharge exposure, FTIR spectrum was measured again at the same place of the tooth. This procedure was applied for positive streamer corona (P_{mean} = 105 mW) and negative Trichel pulses (P_{mean} = 17 mW) on two different halves for two teeth. The differences in intensity of spectra were caused by different contact pressure of the teeth sample on the crystal of ATR FTIR device. Due to this, spectra were normalized on the highest peak.

3. Results and discussion

3.1. Teeth

Fig. 4 shows $\log_{10}$ reduction results on teeth surfaces. Reduction of bacterial population tends to increase with the extension of the exposure time. For 10 min exposure time, the positive corona was more efficient in decontamination than the negative corona, although this difference was marginally significant ($p = 0.06$). For 5 min exposure time, the negative corona performs greater bactericidal effect than the positive one ($p = 0.035$). We did not find significant difference between the positive and the negative corona in exposure times 3 and 1.5 minutes. Nevertheless, 10 min exposure significantly enhanced the bactericidal effect with respect to shorter exposures. These experiments were performed in 14 series with average number of the contaminated teeth samples 8.
Fig. 5 contains box plots of $\log_{10}$ reduction with water spraying. The positive streamer corona with water flow rate 0.05 mL/min (3.15 log) and negative corona with the water flow rate 0.01 mL/min (3.16 log) were the most efficient. Unlike the positive corona, the negative corona demonstrated no significant difference between the flow rates 0.01 and 0.05 mL/min. The negative corona was significantly more efficient than the positive corona in water flow rate 0.01 mL/min. The electro-spraying of water significantly enhanced the plasma bactericidal effect with both polarities. Corona decontamination without water spraying reduced the bacterial population by ~1 log only.

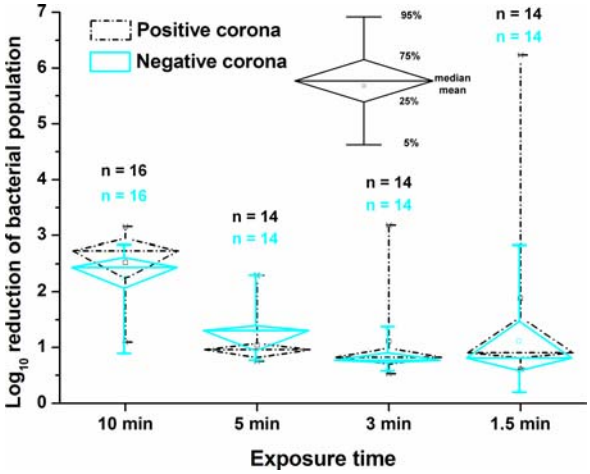


Fig. 4. Reduction of bacterial population on teeth for different exposure times to the corona discharges (n is number of repeated experiments).

3.2. Plastic surfaces

Fig. 6 contains box plots of $\log_{10}$ reduction of bacterial population with/without water spray on plastic surfaces. Differences in $\log_{10}$ reduction between the positive and the negative corona discharges were not significant at all three flow rates tested. The electro-spraying significantly increased $\log_{10}$ reduction of bacterial population ($p < 0.0001$). For the positive corona, the difference between flow rate 0.05 and 0.01 mL/min is marginally significant ($p = 0.0531$), with 0.01 mL/min more efficient. For the negative corona, there is no significant distinction between the two flow rates.

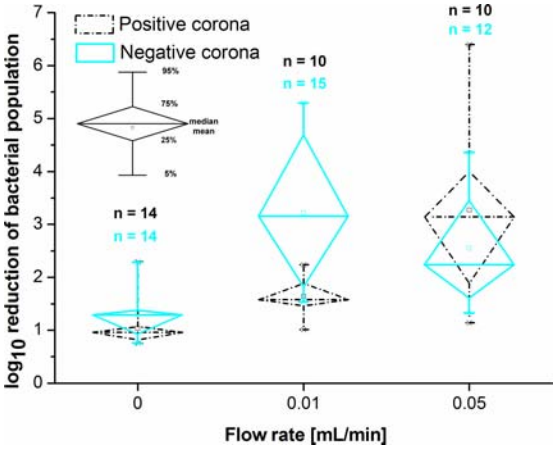


Fig. 5. Reduction of bacterial population on teeth by corona discharges with water electro-spraying for various flow rates (exp. time 5 min)

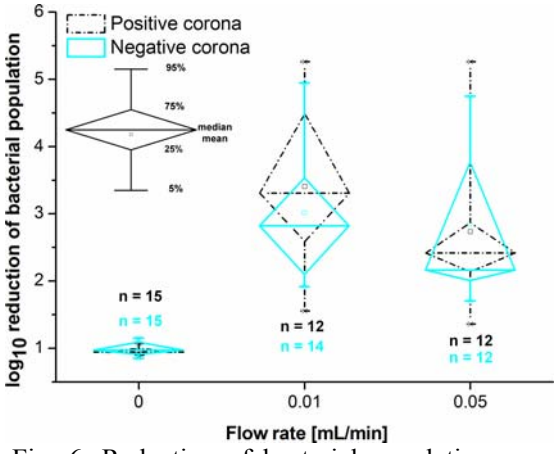


Fig. 6. Reduction of bacterial population on plastic samples by corona discharges with electro-spraying for different flow rates (exp. time - 2 min)

3.2. ATR FTIR spectroscopy of teeth

Typical ATR FTIR spectra measured on teeth samples before and immediately after 10 min plasma treatment are presented in Fig. 7a (positive) and 7b (negative).

The most significant absorption band has maximum around 1000 cm^{-1} and it is hiding the band 960 cm^{-1} which is associated with phosphate ion. The band 870 cm^{-1} corresponds to carbonate ion. Peaks 1410 and 1450 cm^{-1} are other bands of carbonate ion. Enamel and dentine contains, except for inorganic hydroxyapatite, organic component (mainly collagen). Therefore, we have determined the peak with maximum 1550 cm^{-1} as amide II (-CO-NH-) and the peak 1655 cm^{-1} as amide I (-CO-NH_2) groups. The broad band in the region 2500 to 3700 cm^{-1} is associated with intermolecular hydrogen bonds in polymers. [9-10]

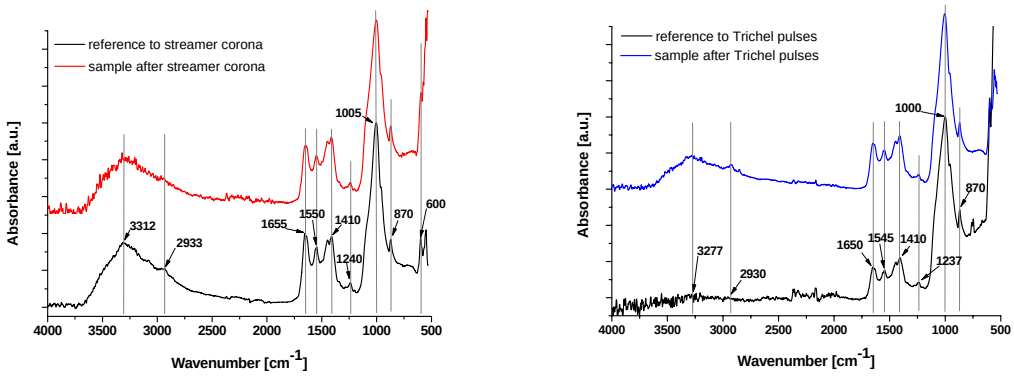


Fig. 7. ATR FTIR spectra of the tooth samples after: a) positive streamer corona b) negative Trichel pulses with their respective references (black).

4. Conclusions

We tested the bactericidal ability of cold plasma of positive streamer corona and negative Trichel pulses on extracted human teeth and plastic surfaces contaminated with bacterial *Streptococci* biofilm. The corona discharge reduced bacterial population in biofilm by 1 - 1.5 orders of magnitude in exposure time 2 min on plastic surfaces and 5 min on teeth surfaces. On teeth, the positive corona in exposure time 10 min was the most efficient, resulting in bacteria population reduction by 2.73 logs. Electro-spraying of water through the plasma significantly enhanced these effects. In the same exposure times, up to 3 - 3.5 log reduction of bacterial population in biofilm was reached. Plasmas in air-water environments form reactive oxygen and nitrogen species that seem responsible for this enhancement [11]. In addition, the electro-spraying resulted in a reduction of the energy consumption. We found that corona discharges of both polarities are able to effectively reduce bacterial population of the biofilm on different surfaces and therefore can be used as an alternative to chemical and mechanical bio-decontamination methods currently used in medicine and dentistry. The FTIR spectra of the plasma treated teeth surfaces did not show any chemical changes, which is encouraging for dental applications.

5. Acknowledgements

This work was supported by Slovak Grant Agency VEGA 1/0668/11.

6. References

[1] C. Jiang, C. Schaudinn, D. E. Jaramillo, M. A. Gundersen, and J.W. Costerton, "A sub-microsecond pulsed plasma jet for endodontic biofilm disinfection," in *Plasma for Bio-Decontamination, Medicine and Food Security* (Z. Machala et al., eds.), NATO Science for Peace and Security Series A: Chemistry and Biology, 179-190, Springer, 2012.
[2] H. Lee, G. Kim, J. Kim, J. Park, J. Lee, and G. Kim 2009 *J Endodontics* **35** 587.
[3] Z. Šipoldová and Z. Machala 2011 *IEEE Trans. Plasma Sci*. **39** 2970
[4] M. H. Lee, B. J. Park, S. C. Jin, D. Kim, I. Han, J. K. Soon, et al. 2009 *New J. Phys.* **11**.
[5] S. Salamitou, M.J. Kirkpatrick, H.M. Ly, G. Leblon, E. Odic and M.S. DuBow 2009 *Biotechnology* **8** 228.
[6] D. Dobrynin, G. Fridman, G. Friedman, and A. Fridman, 2009 *New J. Phys.* **11**.
[7] H.-H. Kim, J.-H. Kim, and A. Ogata 2011 *J. Aerosol Sci.* **42** 249.
[8] B. Pongrác and Z. Machala 2011 *IEEE Trans. Plasma Sci*. **39** 2664.
[9] W. Hędzelek, R. Wachowiak, A. Marcinkowska, L. Domka 2008 *Acta Phys. Polonica A* **114** 471.
[10] S. Cavalu and A. Pirte 2010 *J. Optoelectronics Biomed. Mat.***1** 5.
[11] Machala Z., Lukeš P., Tarabová B., Špetlíková E., Šikurová L., Hensel K., *Bactericidal effects in water sprayed through transient spark in air and related formation of ROS and RNS*, 8th International Symposium on Non-thermal Plasma Technology for Pollution Control ISNTP-8, Camaret (France), June 25-29, 2012

PULSED CORONA DISCHARGE FOR THE DEGRADATION OF METHYLENE BLUE IN WATER

Monica Magureanu[1], Corina Bradu[2], Daniela Piroi[1], Nicolae Bogdan Mandache[1], Vasile Parvulescu[2]

[1]*National Institute for Lasers, Plasma and Radiation Physics, Department for Plasma Physics and Nuclear Fusion, Atomistilor Str. 409, 077125 Magurele-Bucharest, Romania*
[2] *University of Bucharest, Department of Organic Chemistry, Biochemistry and Catalysis, Bd. Regina Elisabeta 4-12, 030016 Bucharest, Romania*
E-mail: monimag@infim.ro

A pulsed corona discharge generated above water was studied for the degradation of organic pollutants in liquids. As target compound an organic dye, methylene blue (MB) was chosen. The formation of hydrogen peroxide (H2O2) in the plasma treated liquid was investigated as well. It was found that the concentration of H2O2 generated in water increased with plasma exposure time, reaching 200 mg/L after 30 min treatment. Less H2O2 was detected in the MB solution, indicating chemical reactions with MB and its degradation intermediates. The MB solution was decolorized after approximately 10 min treatment, evidencing the rapid degradation of the dye. However, MB was not mineralized for such short treatment duration, as indicated by TOC measurements. The addition of $FeCl_2$ had a favourable effect on MB degradation, which was accelerated in its presence.

1. Introduction

Synthetic organic dyes are extensively used in textile, paper, leather and plastics industries. Significant amounts of dyes are discharged into water streams from industrial effluents, estimated in some works to 1–2% in production and 1–10% in use [1], while other authors report even higher figures, 10-20% [2]. The toxicity of some organic dyes in the environment has been investigated by specific biological tests [3,4]. Most of these chemical compounds are not degraded in conventional wastewater treatment plants due to high chemical stability and low biodegradability [1,5]. Physico-chemical treatment (such as adsorption, coagulation, filtration and ion exchange) can lead to effective decolorization of dye wastewater, but has limitations related to formation of sludge and/or the necessity to regenerate adsorbent materials [1]. Advanced oxidation processes (AOPs) have been also studied for the degradation of dyes [6,7]. It was suggested that plasma might be useful as a pre-treatment step to decompose the target compounds into less stable molecules with reduced size, so that the resulting effluent is more amenable to classical water treatment techniques [8,9]. Electrical discharges in water and at the interface between gas and water produce various oxidizing species, such as hydroxyl radicals (OH), atomic oxygen (O), ozone (O_3), hydrogen peroxide (H_2O_2) etc, as well as UV light and shock waves [10-13], all these being effective for the degradation of chemical and biological pollutants.

In the present work a pulsed corona discharge above water was used for the degradation of methylene blue (MB), a heterocyclic aromatic chemical compound with the formula $C_{16}H_{18}N_3SCl$ belonging to the phenothiazine family. The formation of hydrogen peroxide in water and in the treated solution has been determined as a function of plasma treatment time. The effect of $FeCl_2$ addition (by Fenton reaction) on MB degradation by plasma was examined. The post-treatment evolution of the concentrations of MB and H_2O_2 has been followed in the absence and in the presence of $FeCl_2$.

2. Experimental arrangement

The plasma reactor consisted in a Plexiglas vessel of 125 mm length, 83 mm width and 7 mm height, which contains 35 mL aqueous solution. An array of 13 copper wires (wire diameter 100 μm; distance between adjacent wires 6 mm) was used as high voltage electrode. This electrode was placed at approximately 5 mm above the solution. The ground electrode was an aluminium tape placed on the bottom of the vessel.

The discharge was operated in pulsed mode. High voltage pulses were generated by discharging a capacitor of 6 nF by means of a spark-gap switch operating in self-breakdown mode. The discharge voltage was measured with a high voltage probe (Tektronix P6015) and the discharge current was measured using a current probe (Tektronix P6021) and a current transformer (CT-5).
The experiments were performed for an initial concentration of MB in solution of 50 mg/L. The dye was dissolved in distilled water and the conductivity was adjusted to 250 μS/cm by adding NaCl. The initial pH of the solution was 6.
The solution was analysed by UV-visible absorption spectroscopy using a Varian Cary 100 apparatus, in the wavelength range 190-800 nm. The concentration of the dye in solution was determined from the absorption maximum at 668 nm, which was also used for the calibration curves. The concentration of H_2O_2 formed in solution as a consequence of plasma treatment was measured by a colorimetric method based on the reaction of H_2O_2 with $Ti(SO_4)_2$ [14]. The ionic species generated during plasma treatment, were quantified by ion-exchange chromatography, using a Varian ProStar apparatus equipped with a conductivity detector.

3. Results and discussion

The discharge consists in numerous plasma filaments which propagate from the wires towards the solution surface. In the present work a small gap between the wires and the liquid surface was used in order to generate a uniform distribution of the plasma filaments in the discharge gap. This leads to the uniform distribution of the plasma-generated active species above the liquid surface, which is important for the transfer of these active species from the gas phase to the solution [15].
Typical waveforms of the discharge voltage and discharge current are shown in Fig. 1.

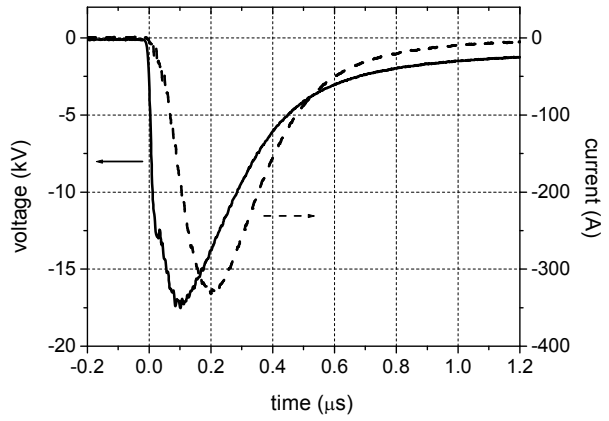


Fig. 1. Waveforms of the discharge voltage and current after 2 min plasma treatment.

Voltage pulses with amplitude of 17 kV were used in the experiments. The duration of the voltage pulses varies in time, decreasing from 310 ns (FWHM - full width at half maximum) after 2 minutes plasma exposure to 225 ns after 15 minutes plasma treatment. The current pulses become also narrower with treatment time, while their amplitude increases from 331 A after 2 minutes to 486 A after 15 minutes plasma exposure. These temporal changes in the electrical characteristics of the discharge are due to the continuous increase in solution conductivity. A similar effect of the electrical conductivity on the current pulses was reported in [16] for experiments performed in point-to-plate corona above water, discharges in gas bubbles and discharges generated directly in water. The energy per pulse, calculated by integrating the product of current and voltage over the pulse duration, was around 1.1 J.
The evolution of solution pH and conductivity as a function of plasma treatment time, as well as the temperature increase of the solution are shown in Fig. 2. The solution temperature increases almost linearly with treatment time, reaching 47 ^oC after 10 min plasma exposure. The solution conductivity shows also a continuous increase with treatment time, reaching 714 μS/cm after 15 minutes plasma treatment time. The solution pH decreases abruptly soon after plasma is ignited and afterwards is gradually reduced to 3.2 after 15 minutes treatment. Similar evolutions of the solution conductivity and pH were reported for discharges generated directly in water [17] and for discharges at the water-gas interface [8]. Acid effects induced in water by electrical discharges were related to the formation of nitrogen oxides in the gas phase, which dissolve into the liquid leading to nitrite and nitrate ions and further to nitric acid, nitrous acid and peroxynitrous acid (ONOOH) [18]. In the present experiments, the formation of the nitrate ions was evidenced by ion-exchange chromatography. The concentration of NO_3^- ions in the MB solution reached 1.71 mM after 15 minutes plasma exposure. Similar levels were detected in blank experiments carried out in water, suggesting that NO_3^- was not generated from

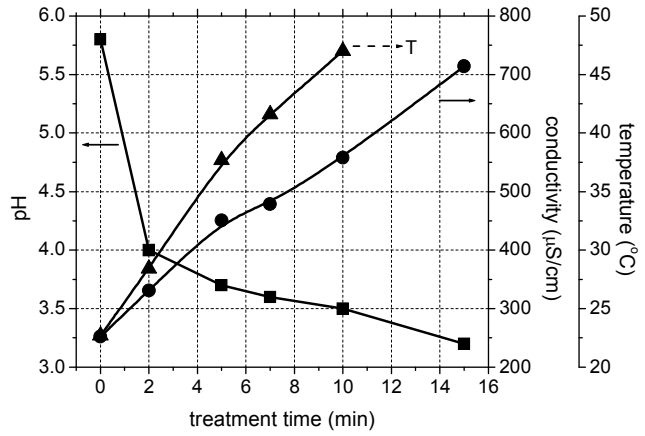


Fig. 2. Conductivity, pH and temperature of the MB solution as a function of plasma treatment time.

the nitrogen in the MB molecule. Considering that the experiments were performed in oxygen, it can only be assumed that the NO_3^- originates mainly from nitrogen in air, which was dissolved in water and adsorbed in the walls of the plasma reactor. Nitrite was not detected in the solution; even if NO_2^- is formed, it is likely to be rapidly oxidized to nitrate.

Another contribution to the decline of solution pH might be the formation of acid reaction products as a result of MB degradation. Formic acid was detected in the present experiments, probably as a result of side chains oxidation. Small amounts of sulfate (SO_4^{2-}) were also produced, supporting the cleavage of the C-S bond. These compounds might be also responsible for both pH decrease and conductivity growth.

The concentrations of H_2O_2 generated in water and in the MB solution subjected to plasma treatment are shown in Fig. 3 as a function of treatment time. After 30 minutes plasma exposure, the H_2O_2 concentration in water reached 202 mg/L, which corresponds to an energy yield for H_2O_2 generation of 0.47 g/kWh. The data summarized in a recent review [11] for discharges above liquids range mostly below 1 g/kWh. The authors suggested that mass transfer and the contact area between plasma and liquid are the limiting factors of the energy yield for H_2O_2 formation by plasma [11].

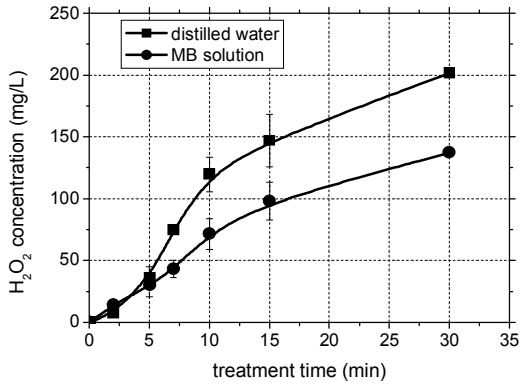


Fig. 3. Concentration of H_2O_2 generated in water and in the MB solution as a function of plasma treatment time.

The concentration of H_2O_2 generated in the MB solution was lower than in water, reaching only 137 mg/L after 30 min plasma treatment. This result is most likely due to reactions of MB molecules and degradation products resulting from MB decomposition either with OH radicals, leading to formation of less H_2O_2, or with H_2O_2 itself.

The UV-visible spectra of the untreated MB solution and of the solutions treated by plasma for durations up to 15 minutes are shown in Fig. 4. The absorption maxima in the visible range (660 nm and 610 nm) and in the UV spectral region (291 nm and 246 nm) decreased with increasing treatment time and the solution became colorless after 10 min plasma exposure. Meanwhile, another absorption band appears in the UV region, with a maximum below 210 nm, which initially increases (up to 5 min treatment) and then remains approximately constant. This suggests the degradation of MB and the formation of reaction products which are more difficult to decompose by plasma during this time interval. Carboxylic acids and H_2O_2 absorb also in this region. Total organic carbon (TOC) measurements also show that although color removal was fast, MB was not mineralized in the present experiments.

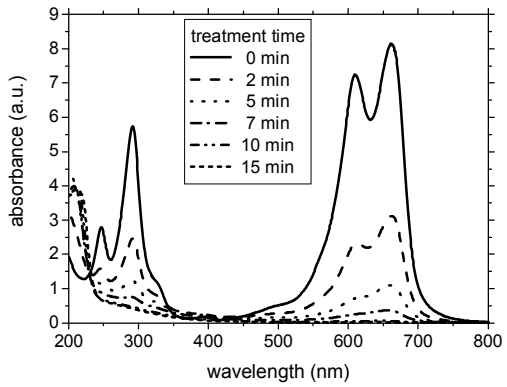


Fig. 4. UV-visible spectra of MB aqueous solution, untreated and treated by plasma up to 15 min.

The chemical mechanism responsible for MB degradation using plasma is not entirely understood. Reactions with ozone are important in case of discharges at the interface between gas (air or oxygen) and liquid, where O_3 is formed in high concentration [7,19-21]. Reactions with OH radicals are also very important, considering the high reactivity of OH for organic compounds [21,22]. Hydroxyl radicals can be produced by the reaction of ferrous ions with H_2O_2 (Fenton's reaction), so the addition of Fe was found beneficial for the degradation of pollutants in water, including MB [23]. In the present experiments $FeCl_2$ (5 mg/L) was added to the MB solution. It was found that the decrease of MB concentration is slightly faster in the presence of $FeCl_2$: 98% of the MB in solution was removed after 5 min plasma treatment in the presence of $FeCl_2$, as compared to 91% without $FeCl_2$. Therefore, it appears that the addition of Fe had indeed a favorable effect on MB decomposition.

Fig. 5 shows the post-plasma evolution of the concentration of H_2O_2 generated in water and in the MB solutions (with and without $FeCl_2$) treated by plasma for 15 minutes (left graph) as well at the evolution of the MB concentration after 2 minutes plasma treatment (right graph). The MB concentration decreased significantly in the first 3 h after plasma treatment and later on showed a slower reduction, so that after 24 h the amount of MB was reduced to almost half of the value measured immediately after plasma treatment. Other authors have also reported a considerable decline in the absorbance of organic dyes solutions, even for several days after plasma treatment [8,24]. Post-discharge reactions were discussed in [25], where the essential role of nitrous and peroxonitrous acids was emphasized. Reactions with O_3 or H_2O_2 which persist in solution after plasma exposure may also contribute to the post-plasma reduction of MB concentration. The amount of H_2O_2 generated in the liquid also diminished in time. This decrease amounts to less that 10% in case of distilled water, in the absence of MB after 18 h from the plasma exposure, but becomes significant (above 50%) in the MB solution. After 15 min plasma treatment MB was completely removed, but organic reaction products persist in the solution and are responsible for the decrease in H_2O_2 concentration shown in Fig. 5.

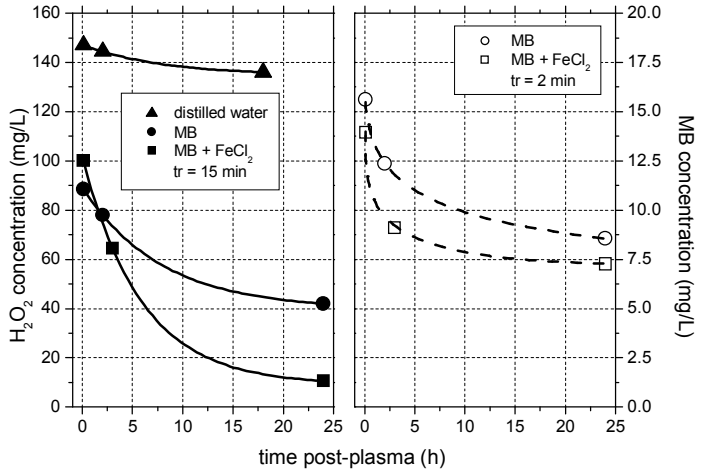


Fig. 5. Post-plasma evolution of the H_2O_2 and MB concentrations (tr – plasma treatment time).

4. Summary

A pulsed corona discharge above water was investigated for the degradation of organic pollutants in liquids. As target compound, the organic dye methylene blue was chosen. MB was removed, i.e. the solution became colorless after approximately 10 min plasma treatment. However, MB was only partially degraded and not mineralized for such short treatment duration. The addition of $FeCl_2$ as catalyst accelerated MB degradation to some extent due to Fenton's reaction.

Hydrogen peroxide was formed as a consequence of plasma treatment, its concentration reaching 200 mg/L in water after 30 min plasma exposure and only 137 mg/L in the MB solution. This suggests that reactions of H_2O_2 with MB and its degradation products take place.

Post-plasma chemical reactions of MB and its degradation products with active species which persist in the aqueous solution were evidenced by the continuous decrease of MB and H_2O_2 concentrations for a long time (24 h) after the discharge was stopped.

Acknowledgment

This work was supported by a grant of the Romanian National Authority for Scientific Research, CNCS – UEFISCDI, project number PN-II-RU-TE-2011-3-0015. D. Piroi acknowledges financial

support from POSDRU/88/1.5/S/56668.

References

[1] Martinez-Huitle C A and Brillas E 2009 *Appl. Catal. B: Environ*. **87** 105.
[2] Ji F, Li C, Zhang J and Deng L 2011 *Desalination* **269** 284.
[3] Sharma K P, Sharma S, Sharma S, Singh P K, Kumar S, Grover R, and Sharma P K 2007 *Chemosphere* **69** 48.
[4] Ulson de Souza S M A G, Forgiarini E, and Ulson de Souza A A 2007 *J. Hazard. Mater*. **147** 1073.
[5] Ramalho T C, Carvalho H W P, Batista A P L, Pérez C A, and Gobbi A L 2009 *J. Mater. Sci*. **44** 1029.
[6] Sivalingam G, Nagaveni K, Hegde M S, and Madras G 2003 *Appl. Catal. B: Environ*. **45** 23.
[7] Turhan K, Durukan I, Ozturkcan S A, and Turgut Z 2012 *Dyes and Pigments* **92** 897.
[8] Dojcinovic B P, Roglic G M, Obradovic B M, Kuraica M M, Kostic M M, Nesic J, and Manojlovic D D 2011 *J. Hazard. Mater*. **192** 763.
[9] Magureanu M, Piroi D, Mandache N B, and Parvulescu V 2008 *J. Appl. Phys*. **104** 103306.
[10] Lukes P, Clupek M, Babicky V, Janda V, and Sunka P 2005 *J. Phys. D: Appl. Phys*. **38** 409.
[11] Locke B R and Shih K-Y 2011 *Plasma Sources Sci. Technol*. **20** 034006.
[12] Bruggeman P and Schram D C 2010 *Plasma Sources Sci. Technol*. **19** 045025.
[13] Lukes P, Clupek M, Babicky V, and Sunka P 2008 *Plasma Sources Sci. Technol*. **17** 024012.
[14] Eisenberg G M 1943 *Ind. Eng. Chem. Anal. Ed*. **15** 327.
[15] Grabowski L R, van Veldhuizen E M, Pemen A J M, and Rutgers W R 2006 *Plasma Chem. Plasma Process*. **26** 3.
[16] Shih K-Y and Locke B R 2010 *Plasma Chem. Plasma Process*. **30** 1.
[17] Dang T H, Denat A, Lesaint O, and Teissedre G 2008 *Plasma Sources Sci. Technol*. **17** 024013.
[18] Brisset J-L, Benstaali B, Moussa D, Fanmoe J, Njoyim-Tamungang E 2011 *Plasma Sources Sci. Technol*. **20** 034021.
[19] Magureanu M, Piroi D, Gherendi F, Mandache N B, and Parvulescu V 2008 *Plasma Chem. Plasma Process*. **28** 677.
[20] Magureanu M, Mandache N B, and Parvulescu V I 2007 *Plasma Chem. Plasma Process*. **27** 589.
[21] Grabowski L R, van Veldhuizen E M, Pemen A J M, and Rutgers W R 2007 *Plasma Sources Sci. Technol*. **16** 226.
[22] Velikonja J, Bergougnou M A, Castle G S P, Cairns W L, and Inculet I I 2002 *Ozone Sci. Eng*. **24** 159.
[23] Dutta K, Mukhopadhyay S, Bhattacharjee S, and Chaudhuri B 2001 *J. Hazard. Mater*. **B84** 57.
[24] Moussa D, Doubla A, Kamgang-Youbi G, and Brisset J-L 2007 *IEEE Trans Plasma Sci*. **35** 444.
[25] Brisset J-L, Moussa D, Doubla A, Hnatiuc E, Hnatiuc B, Kamgang Youbi G, Herry J-M, Naitali M, Bellon-Foantaine M-N 2008 *Ind. Eng. Chem. Res*. **47** 5761.

DEPOSITION OF THIN LAYERS CONTAINING TITANIUM AND BARIUM WITH THE USE OF DIELECTRIC BARRIER DISCHARGE PROPERTIES

Małgorzata Majdak[1], Teresa Opalińska[1], Bartłomiej Wnęk[1]

[1]*Tele & Radio Research Institute*
03-450 Warsaw, Ratuszowa 11
E-mail: malgorzata.majdak@itr.org.pl

Two different methods of deposition of thin layers containing titanium and barium with the use of dielectric barrier discharge properties were developed. The first was carried out in two stages. The first stage consisted in transferring compounds containing titanium and barium from the vapour of the organic precursor on the substrate made of copper, while the second stage involved the etching of the organic layer in oxygen. The second method consisted in transferring titanium and barium on the copper substrate from the ceramic plate made of barium titanate, which was one of the electrodes during the plasma process. The results of analysis obtained by SIMS showed directly that both methods gave a positive result in the deposition of the thin layers containing a certain amount of titanium and barium on the surface of the copper plate. However, more effective method was that involving the properties of discharge with the ceramics as one of the electrodes. FTIR study of the layers prepared from the organic precursor indirectly showed that layers deposited on the copper plate contained compounds of barium and titanium. FTIR study also revealed that during the process of etching in oxygen, the organic layer was decreased, but it was not completely removed.

1. Introduction

The topic of this paper concerns the search for new methods and technology in the preparation of materials that are used in electronics. The miniaturization of microelectronic devices such as multilayer ceramic capacitors, requires reducing the size of these devices building [1, 2]. For this reason, the interest in receiving the various nanolayers grows. Materials such as $BaTiO_3$ or $Ba_xSr_{1-x}TiO_3$ (BST) are primarily used in the capacitors due to its high dielectric constant [2-4]. Barium titanate is a promising material in the manufacture of integrated optoelectronic devices such as non-volatile RAM (random-access memories), thin-film capacitors and infrared sensors. These devices require the use of high-quality thin layers of $BaTiO_3$ [3] with a high degree of crystallization and a smooth layer of $BaTiO_3$ [4].

The purpose of this study was to determine whether the new method that uses the properties of dielectric barrier discharge may be used as a method of preparing thin layers containing titanium and barium on the substrate. The desired layers were planned to be obtained in two different ways using the properties of dielectric barrier discharge. The first one (method I) was based on transferring the titanium and barium ions from the organic precursor on the copper substrate. The second way (method II) consisted in transferring compounds of titanium and barium from a ceramic plates made of barium titanate on the copper substrate.

2. Experimental conditions

The experimental setup consisted of: a working gas vessel (argon or oxygen), a mass flow controller, a bubbling washer with the organic precursor, a plasma reactor and the power supply. Argon flow rate amounted to 0.06 - 0.28 Nl/min and that of oxygen 0.50 - 1.67 Nl/min. Experiments were carried out in 20, 30, 45 or 60 minutes. The discharge was generated with frequency of 50 kHz.

Thin films were prepared by means of two methods. The first one consisted in preparing a thin layer containing titanium and barium with the use of precursor of Ti^{4+} and Ba^{2+} ions. The precursor was the organometallic compound - tetrahydrofurfuryl barium and titanium (IV) oxide ($C_{30}H_{54}BaO_{12}Ti$ - Sigma-Aldrich). The precursor was used as a solution with tetrahydrofururyl alcohol and ethanol.

The process consisted of two stages. In the first stage, the working gas (argon) flowing through the bubbling washer with the precursor, washed away the organometallic compound and delivered

it to the discharge zone. There was a discharge generated between the metal surface of the high-voltage electrode and the surface of the dielectrics mounted to the grounded electrode. In the second stage, the obtained layer was etched in the discharge generated in the atmosphere of a mixture of argon and oxygen. A few additional materials were used as the dielectric barriers. They were: polyimide (PI), polycarbonate (PC) and acrylic glass (PMMA).
The second method consisted in generating the discharge in argon between the high-voltage copper electrode and the grounded electrode made of $BaTiO_3$.

Tab. 1. The experimental parameters.

Sample	**Method / stage**	**VAr [Nl/min]**	**Dielectric**	**t [min]**
Cu 1	I / 1	0,06	PC	20
Cu 2	I / 1	0,28	PMMA	45
Cu 3	I / 1+2	0,14	PI	45
Cu 4	II	0,20	$BaTiO_3$	45
Cu 5	I / 1	0,12	PI	45

Two different methods were used to analyse the obtained layers: the infrared spectroscopy with Fourier transformation (FTIR) and the secondary ion mass spectrometry (SIMS). The research carried out by FTIR was performed by means of Nicolet FTIR spectrometer (ThermoScientific IS10 company), equipped with the ATR (attenuated Total Reflectance - the method of total internal reflection) with a ZnSe crystal. Number of scans was 64, the spectra were measured with resolution of 4 cm^{-1}. The research carried out by SIMS was performed using secondary ion mass spectrometer - SAJW-05. The etching with Ar^+ ions was performed with the energy of 3 keV. The analysis of profiles were performed at 0-3 microns of depth and additionally at 0 - 100 nm of depth. The depth of the crater was measured with the needle profilometer Alpha-step 100 Tencor.

3. Results and Discussion

Figure 1 presents the results of SIMS analysis of the samples Cu1, Cu2, Cu3 and Cu4. The signals are shown as quotients of the secondary ion currents of individual elements to the current of the copper ions. These signals decrease with the depth of etching by Ar^+ primary ion beam.

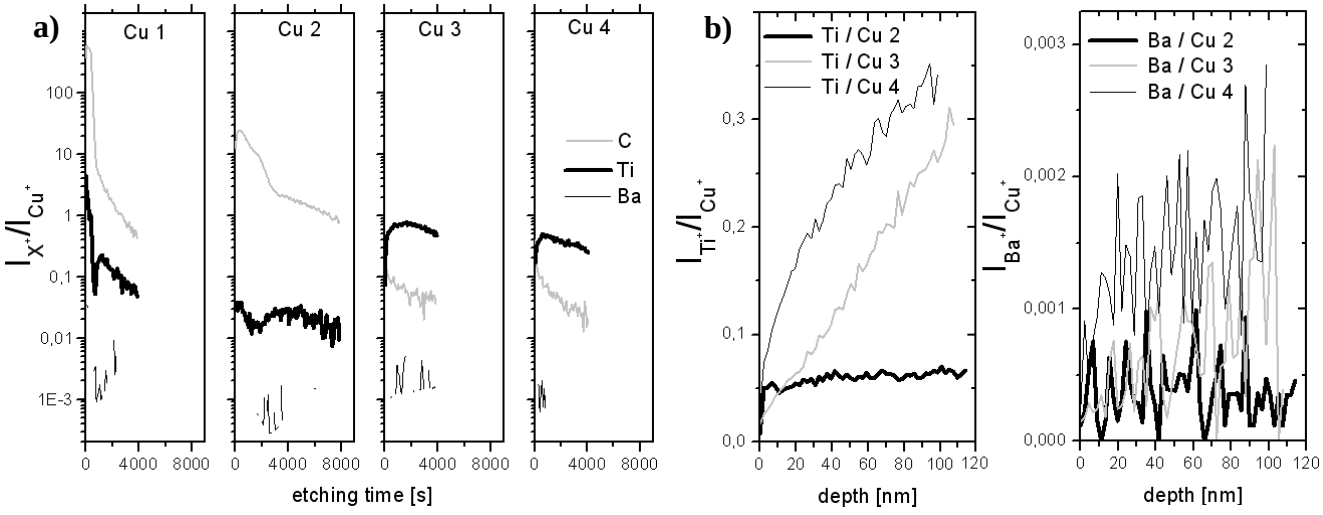


Fig. 1. The results of the SIMS profile analysis presented as ratio of ion current to the currents of the copper ion: a) versus the etching time (0-3 microns), b) versus the depth of etching (0-100 nm).

Both Cu1 and Cu2 samples contain a layer of carbon. The carbon deposited on the surface of the copper substrate comes from the organic layer, which was formed during the plasma process carried out by means of the method I. For these two samples, only the first stage of the method I was

performed. It seems that the organic layer on the surface of the Cu1 sample is dense in comparison with that of the Cu2 sample, on which the organic layer is thicker, but also more porous, so the other analysed elements may be seen through it. The Cu3 sample was also treated with the method I, but in this case, both steps of the process were completed - the reaction with the precursor and plasma etching in oxygen.
The organic coating of the Cu3 sample is much thinner in comparison with those of the Cu1 and Cu2 samples, which indicates that the plasma reaction in oxygen resulted in partial etching of this layer. The Cu4 sample was treated in argon with the use of the method II, in the discharge with the ceramic barrier. The layers on the Cu3 and Cu4 samples contain a lot more of titanium in comparison with the layer on the Cu2 sample. All the samples contain a small amount of barium.
The additional SIMS study was performed to analyse the profile in the range of 0-100 nm (Figure 1b). In this analysis three ionic currents of Cu^+ Ti^+ and Ba^+ were examined. Three samples were analyzed: Cu2, Cu3 and Cu4. The Cu4 sample contained the most of both elements, barium and titanium, what improves the positive effect of the surface modification in the plasma and confirms the effectiveness of this method in the process of depositing a thin layer containing titanium and barium on the chosen substrate. Basing on these results, it can be concluded, that both, method I and method II gave a positive result in the deposition of the thin layer containing certain amounts of Ti and Ba on the copper substrate. However, the method II occured more effective.
FTIR was used to determine the composition of the organic layer obtained on the copper substrate during the experiment carried out with the use of method I. The Cu5 sample – the sample after processing with the use of the first stage of the method I and the Cu3 sample – the samples after processing with the use of both stages of method I, were examined. The organic layer formed on the copper substrate should contain functional groups that are present in the precursor solution and possibly groups of derivatives, which could be formed from the decomposition of the specific compounds. Figure 2 presents the IR spectra of ethyl alcohol and tetrahydrofurfuryl alcohol. For a comparison, Figure 3 presents the spectra of the organic layers that were obtained on a copper substrate by means of the method I in stage 1 (Table 1).

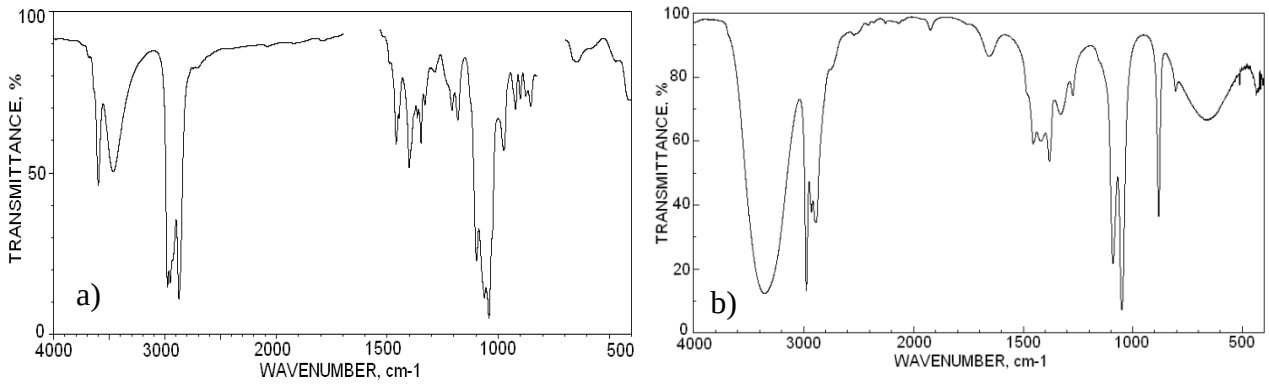


Fig. 2. The IR spectra of a) tetrahydrofurfuryl alcohol [5]; b) ethyl alcohol [5].

The spectrum of tetrahydrofurfuryl barium and titanium oxide (precursor) should look similarly to the spectrum of tetrahydrofurfuryl alcohol - solvent, since both compounds are structurally similar and have the same functional groups, excluding the OH group, which is not present in the precursor molecule. Comparing the spectra of three substances it is easy to see that they have some common features - the main group at the same wave numbers. Each of these spectra contains a group of ~ 3500cm^{-1}, which corresponds to the OH group present in alcohol. The other similar features are: 2800-2900cm^{-1} signals, that correspond to the aliphatic CH carbon atoms that are not bound with unsaturated bonds. Groups occurring at 1400-1500cm^{-1}, could not be identified on the basis of tables of specific bonds.

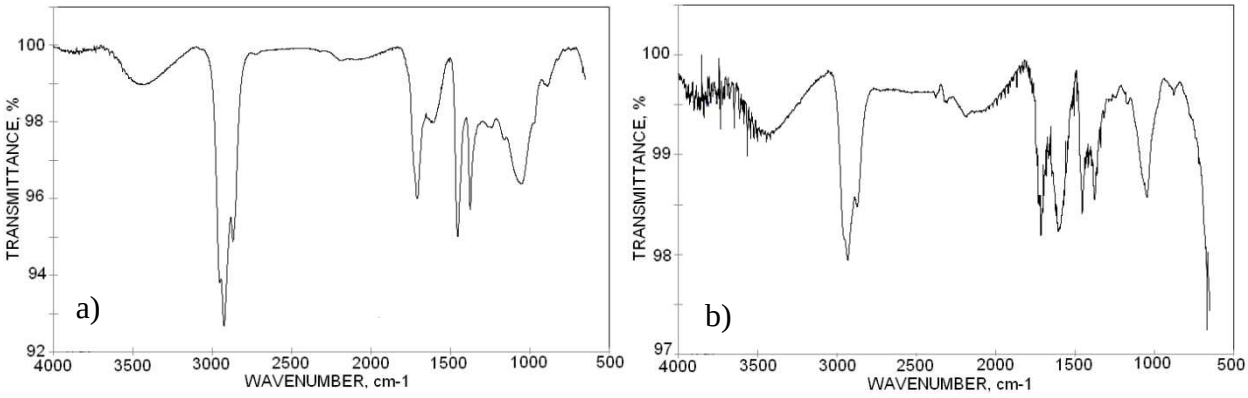


Fig. 3 The IR spectra of the layers obtained on the copper substrate: a) the sample after processing with the use of the first stage of the method I - Cu 5, b) the sample after processing with the use of both stages of method I -Cu 3.

However, these are probably the groups corresponding with the unsaturated C-C bonds. The other similar features are 1000-1100cm^{-1} signals, that correspond to CO groups in primary alcohols (and ethers. It is supposed that this group is higher for tetrahydrofurfuryl alcohol (Fig. 2a), because it contains the oxygen bound in the ether group COC in its molecule. Similar in shape is the spectrum of the Cu5 sample (Fig. 3a), that may indicate the presence of ether groups in the surface layer of the sample.

The new groups for wave numbers ~ 1600-1700cm^{-1}, which are not present in the spectrum of any of the solvents, were in the spectrum of the layer obtained in plasma.

To identify these groups we had to refer to the example of two compounds similar in structure: ethyl alcohol (C_2H_5OH) and the other in which hydrogen atom is replaced with sodium (C_2H_5ONa) [5]. It was noticed that the C_2H_5ONa spectrum included additional groups for wavenumbers ~ 1600-1700cm^{-1}. The signal at this point, probably corresponds with CO combined with oxygen, which is bonded ionically with sodium cation. That caused a shift of this signal toward the higher wavenumbers. A similar situation occurs when we consider the structure of the precursor and tetrahydrufurfuryl alcohol. The precursor cations Ba^{2+} and Ti^{4+} are bonded to the oxygen atom. A similar oxygen atom in the molecule, is related to the hydrogen atom in the solvent molecule. Thus, the spectrum of the precursor should contain the additional spectrum with the wavenumber ~ 1600-1700cm^{-1}. This group is observed in the spectrum of the Cu 5 sample (Fig. 3a), indicating that the precursor had evaporated from the bubbling washer during the process and was deposited on the copper substrate. The presence of oxidised groups corresponding with the cations Ba^{2+} and Ti^{4+}, indicates the presence of these cations in the examined layer.

Comparing the spectrum of the Cu5 (Fig. 3a) and Cu3 (Fig. 3b) samples, we can see that they are similar. But there are differences both in the signal level and in the shape of the signals corresponding to the groups combined with oxygen. It is supposed that the signal corresponding to the groups CH (2800-2900cm^{-1}) decreased in comparison with the CO signal (1000-1100cm^{-1}).

This indicates that the oxygen plasma partially removed the organic layer from the substrate and left a layer containing inorganics in the form of barium and titanium. The growth of CO signals combined with oxygen ion, shows an enrichment of the obtained layer in oxygen. Based on the results, it may be concluded that the obtained layers contain barium and titanium.

4. Conclusions

On the basis of the test results it can be stated that it is possible to obtain a layer containing titanium and barium on the copper substrate with the use of dielectric barrier discharge at atmospheric pressure. The results of analysis by the secondary ion mass spectrometry (SIMS) showed directly that both method I and method II gave positive results in the deposition of a certain amount of compounds containing barium and titanium. However, method II turned out to be more effective in obtaining this

kind of thin layer - the reaction with the use of barium titanate ceramics. . By contrast, the results of the analysis by FTIR allow us to indirectly draw conclusions about the contents of the required elements in the examined layers obtained by the method I. The FTIR study showed that the layer deposited on a copper substrate contained the group-CO combined with the oxygen connected with metal ion binding . The only metals in the solution are barium and titanium, so it can be concluded that the obtained layer had to contain these elements. FTIR study also showed that the oxygen etching in the method I resulted in decrease of the organic layer. Barium and titanium can be found on the plasma modified surface but they are dispersed in the organic phase.

Acknowledgement
This work was supported by the Tele & Radio Research Institute Statutory Fund.

1. References

[1] Suzuki K and Kijima K 2004 *Materials Letters* **58** 1650– 1654
[2] Purwanto A, Wang W N, Lenggoro I W and Okuyama K 2007 *Journal of the European Ceramic Society* **27** 4489–4497
[3] Craciuna V and Singh R K 2000 *Applied Physics Letters* **76** No 14
[4] Gonzalo J G´omez San Rom´an R Perrière J Afonso C N P´erez Casero R 1998 *Applied Physics A 66 Materials Science & Processing* 487–491
[5] www.webbook.nist.gov

OBSERVATION OF DYNAMIC BEHAVIOR OF GLIDING ARC DISCHARGE

Fumiaki Mitsugi[1], Jin Furukawa[2], Tamiko Ohshima[3], Hiroharu Kawasaki[3], Toshiyuki Kawasaki[4], Shin-ichi Aoqui[5], Henryka D. Stryczewska[6]

[1] *Graduate school of science and technology, Kumamoto University, 2-39-1 Kurokami, Kumamoto, 860-8555, Japan*
[2] *Imaging division, Photron Limited, 9-8 Nozaki, Osaka, 530-0055, Japan*
[3] *Department of electrical and electronics engineering, Sasebo National College of Technology, 1-1 Okishin, Sasebo, 857-1171, Japan*
[4] *Department of Mechanical and Electrical Engineering, Nippon Bunri University, 1727 Ichigi, Oita, 870-0397, Japan*
[5] *Department of computer and information sciences, Sojo University, 4-22-1 Ikeda, Kumamoto, 860-0082, Japan*
[6] *Institute of Electrical Engineering and Electrotechnologies, Lublin University of Technology, 38A Nadbystrzycka St, 20-618 Lublin, Poland*
E-mail: mitsugi@cs.kumamoto-u.ac.jp

In this work, we report on time-resolved dynamic behavior of gliding arc discharge plasma using comparison of obtained results between high-speed camera photographs and the corresponding electric properties. For a gliding arc discharge in Ar 20 L/min, the plasma path became complex with gliding due to turbulence gas and reconnections for plasma path were observed. The applied voltage was decreased and small pulsed current flowed at the moment of the reconnection.

1. Introduction

There has been much interest in gliding arc discharge plasma[1] due to its potential for pollution control[2-5], material processing, surface treatment and biological application[6-8]. The gliding arc discharge can realize high electron temperature, electron density and low gas temperature which no thermal or non-thermal plasma can satisfy. The gliding arc discharge starts from breakdown of atmospheric gas at the shortest gap between two divergent electrodes under DC or AC power source and it glides along the same direction as the gas flow. The fundamental studies such as electrical properties, temperature distribution[9,10], power supply[11,12], electrode geometry[13], optical emission spectroscopy[14-16] and acoustic emission[17] have been done. The dynamic behavior of the gliding arc discharge[18] becomes rather complex especially in turbulent gas flow, however, time-resolved analysis for the behavior of the plasma with the simultaneous measurement of the corresponding electric properties has not been investigated. Therefore, in this work, we report on time-resolved dynamic behavior of the gliding arc discharge plasma in turbulence gas using comparison of obtained results between high-speed camera photographs and the corresponding electric properties.

2. Experimental Setup

Fig.1 shows the schematic diagram of a dynamic measurement system for gliding arc discharge. Two knife edge-shaped electrodes are made of iron and their shortest gap was adjustable (3-6 mm). The electrodes were set inside an acrylic chamber. Outlet of a gas supply was placed at the bottom of the acrylic chamber. The gas flow rate was controlled by a digital flow instrument. High voltage (sine

wave, 60 Hz) was applied between the two electrodes with a high-voltage transformer (VIC international, 120:1). The amplitude was adjusted with a voltage slide autotransformer (TAMABISHI, S-130-39). Applied voltage waveform during discharge was observed with a high-voltage probe (IWATSU, HV-P60). Discharge current waveform was measured by clamping a current sensor (Tektronix). The both waveforms were captured with a digital oscilloscope. Time-resolved digital photographs for a gliding plasma were recorded by a high speed digital camera (Photron, FASTCAM SA1.1) with the frame rate of 54,000 frames per second and 320 x 256 pixels. The observation time for the digital oscilloscope and the high speed camera were synchronized by an external trigger signal.

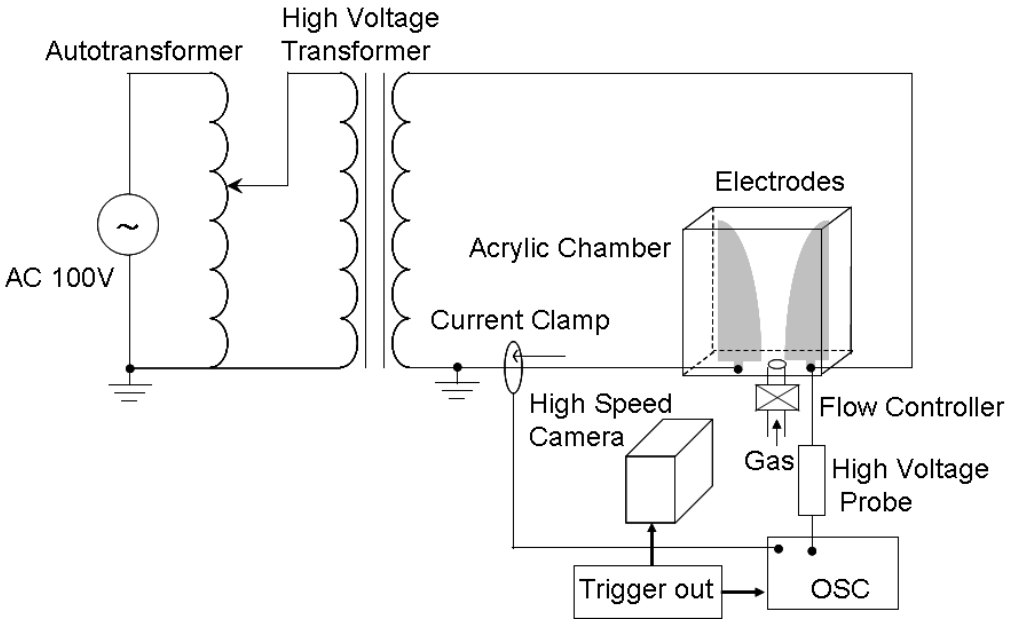


Fig. 1 Experimental setup for measurement of dynamic behavior of gliding arc discharge.

3. Results and Discussion

Gliding arc plasmas in different gases of He, N_2 and Ar with various flow rate (10-50 L/min) were observed. Here, we show typical results. Fig.2 shows waveforms of applied voltage and discharge current during period of approximately one cycle for a gliding arc discharge in He (10 L/min) with the corresponding high speed camera photographs. Exposure time of the each photographs was about 19 us (about 900 photographs per one cycle of applied voltage). As can be seen from Fig.2, the phase of the displacement component of the current waveform was advanced by about 90 degrees from the applied voltage because the influence of the reactance of the capacitance component between the electrodes was remarkable. A breakdown of He occurred at 1.5 kV and the shortest gap (6 mm) with a large discharge current and rapid voltage drop at 2.4 ms. The applied voltage increased with gliding of the arc plasma and next breakdown appeared at the shortest gap (4.4 ms). The arc plasma glided to upper side with recovery of the applied voltage due to the increase of the impedance of the plasma ,which was caused by the increased plasma path, until 11.0 ms. Almost same tendency as the above mentioned behavior was observed in case of the opposite polarity of the applied voltage. However, polarity dependence was confirmed from the evidence that strong optical emission appeared at a positive electrode along the edge. Rather different dynamic behavior was observed for gliding arc discharges in Ar with the increased flow rate (20 L/min). The results were shown in Fig.3. A breakdown of Ar occurred at 4.7 ms (4.5 kV) and gliding of the arc began after that. The gliding of the arc continued until around 11 ms with the almost the same gliding speed as the gas flow. Complex dynamic behavior of the gliding arc plasma path was induced because of the turbulent gas flow. During the complex gliding of the arc, reconnections of the arc path were able to be found out at

around 5.7, 8.0 and 10.3 ms as can be seen in Fig.3. It was also revealed that small voltage drop and pulsed current were caused at the same time as the reconnections. The arc disappeared at 11.1 ms at upper region where the arc impedance increased with the arc length. Immediately after the disappearance of the arc, vibration of the applied voltage was observed.

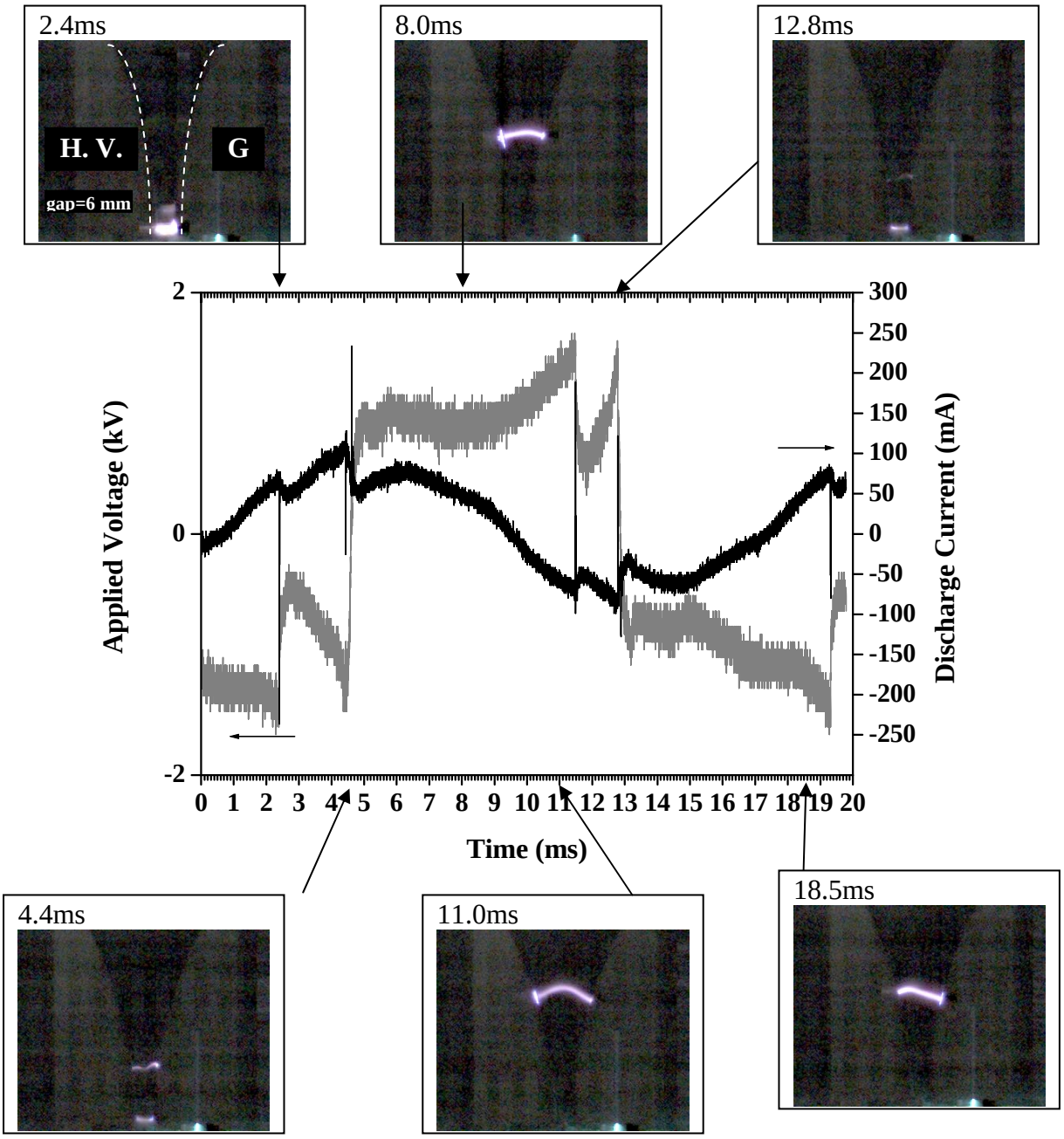


Fig. 2 Waveforms of applied voltage and current for a gliding arc discharge in He (10 L/min) with the corresponding high speed camera photographs.

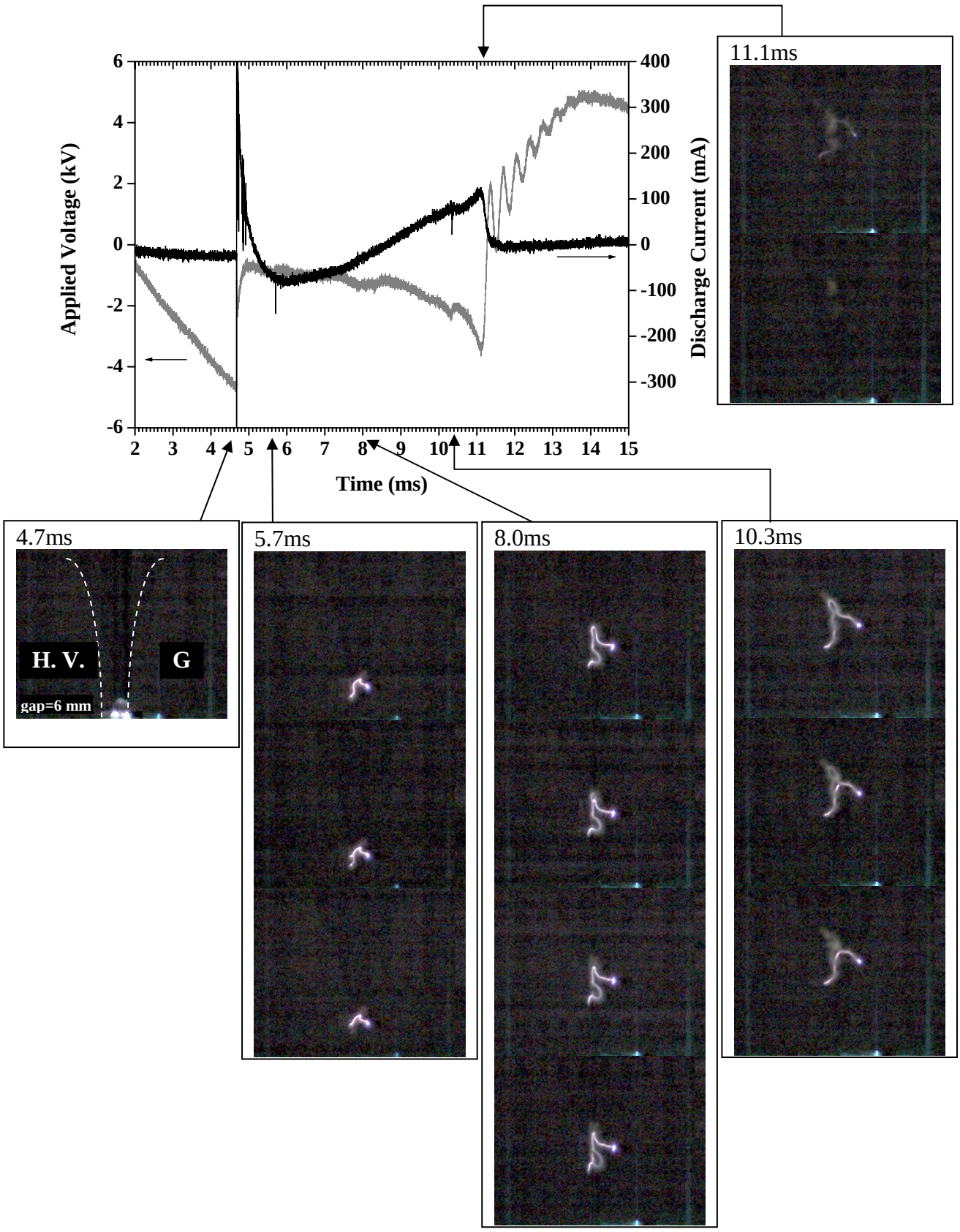


Fig. 3 Waveforms of applied voltage and current for a gliding arc discharge in Ar (20 L/min) with the corresponding high speed camera photographs.

4. Summary

Time-resolved dynamic behavior of gliding arc discharge plasma was investigated using comparison of obtained results between high-speed camera photographs and the corresponding electric properties. For a gliding arc discharge in He gas flow, relationship between electric properties and plasma behavior was well mapped. In addition, polarity effect was confirmed around the edge of a electrode. For a gliding arc discharge in Ar 20 L/min, the plasma path became complex with gliding due to turbulence gas and reconnections for plasma path were observed. The applied voltage was decreased and small pulsed current flowed at the moment of the reconnection.

5. References

[1] A. Fridman, S. Nester, L. A. Kennedy, A. Saveliev and O. Mutaf-Yardimci, Gliding arc discharge, Progress in Energy and Combustion Science, 25 (1999), 211-231

[2] M. Mlotek, J. Sentek, K. Krawczyk and K. Schmidt-Szalowski, The hybrid plasma-catalytic process for non-oxidative methane coupling to ethylene and ethane, Applied Catalysis A: General, 366 (2009), 232-241

[3] K. Krawczyk, B. Ulejczyk, H. K. Song, A. Lamenta, B. Paluch and K. Schmidt-Szalowski, Plasma-catalytic reactor for decomposition of chlorinated hydrocarbons, Plasma Chemistry and Plasma Processing, 29 (2009), 27-41

[4] Z. Bo, J. Yan, X. LI, Y. Chi, K. Cen, Nitrogen dioxide formation in the gliding arc discharge-assisted decomposition of volatile organic compounds, Journal of Hazardous Materials, 166, (2009), 1210-1216

[5] L. Yu, X. Li, X. Tu, Y. Wang, S. Lu and J. Yan, Decomposition of Naphthalene by dc Gliding Arc Gas Discharge, Journal of Physical Chemistry A, 114 (2010), 360-368

[6] R. Burlica, R. G. Grim, K. –Y. Shih, D. Balkwill, B. R. Locke, Bacteria inactivation using low power pulsed gliding arc discharges with water spray, Plasma Processes and Polymers, 7, (2010), 640-649

[7] R. Burlica, K. –Y. Shih, B. R. Locke, Formation of H2 and H2O2 in a water-spray gliding arc nonthermal plasma reactor, Industrial and Engineering Chemistry Research 49 (14) (2010), 6342-6349

[8] C. M. Du, Y. W. Sun, X. F. Zhuang, The effects of gas composition on active species and byproducts formation in gas-water gliding arc discharge, Plasma Chemistry and Plasma Processing 28 (4) (2008) 523-533

[9] J. Diatczyk, H. D. Stryczewska and G. Komarzyniec, Modeling of the Temperature Distribution in Arc Discharge Plasma Reactor, Journal of Advanced Oxidation Technologies, 9(2), (2006), 174-177

[10] H. D. Stryczewska, J. Diatczyk, J. Pawlat, Temperature distribution in the gliding arc discharge chamber, Journal of Advanced Oxidation Technologies, 14(2), (2011), 276-281

[11] G. Komarzyniec, J. Diatczyk and H. D. Stryczewska, Arc plasma reactor power system with 5-limb transformer, Journal of Advanced Oxidation Technologies, 9(2), (2006), 178-181

[12] G. Komarzyniec, H. D. Stryczewska and J. Diatczyk, The influence of power source parameters on the gliding arc characteristics, Przeglad Elektrotechniczny, 84(7), (2008), 60-63

[13] Z. Bo, J. H. Yan, X. D. Li, Y. Chi, B. Cheron, K. F. Cen, The dependence of gliding arc gas discharge characteristics on reactor geometrical configuration, 27, (2007), 691-700

[14] H. D. Stryczewska, G. Komarzyniec and J. Diatczyk, Technological features of gliding arc discharges plasma, Przeglad Elektrotechniczny, 84(7), (2008), 170-173

[15] J. Diatczyk, G. Komarzyniec and H. D. Stryczewska, Spectroscopic diagnostic of non-thermal plasma generated in gliding arc discharge plasma reactor, Przeglad Elektrotechniczny, 84(5), (2008), 309-311

[16] J. Diatczyk, H. D. Stryczewska and G. Komarzyniec, Diagnostic of the gliding arc discharge plasma's non-equilibrium, Przeglad Elektrotechniczny, 86(5), (2010), 298-300

[17] F. Mitsugi, T. Ikegami, S. Aoqui, Y. Tashima, H. Kawasaki, T. Nakamiya, Y. Sonoda, H. D. Stryczewska, Application of optical wave microphone to gliding arc discharge, 88 (6) (2012) 105-107

[18] X. Tu, H. J. Gallon, J. C. Whitehead, Dynamic behavior of an atmospheric argon gliding arc plasma, IEEE transactions on plasma science 39(11) 2900-2901

A TOMOGRAPHIC VISUALIZATION OF ELECTRIC DISCHARGE SOUND FIELDS IN ATMOSPHERIC PRESSURE PLASMA USING LASER DIFFRACTION

T. Nakamiya[1], Y. Iwasaki[1], F. Mitsugi[2], T. Ikegami[2], R. Tsuda[1], and Y. Sonoda[1]

[1]*Graduate School of Industrial Engineering, Tokai University, 9-1-1,Toroku Higashi-ku, kumamoto, Japan 862-8652*

[2]*Graduate School of Science and Technology, Kumamoto University, 2-39-1, Kurokami Chuo-ku, Kumamoto, Japan 860-0082*

E-mail:nakamiya@tokai.ac.jp

Abstract

The characteristics of Dielectric Barrier Discharge (DBD) are mainly examined by applied voltage, discharge current, and luminescence of discharge. There is little research paper that uses the discharge sound to examine the electrical discharge phenomenon such as DBD. We have examined the sound signals which are emitted from the discharge area. Because the sound signals contain about the information of discharge and atmospheric condition around the discharge.

1. INTRODUCTION

DBD (Dielectric Barrier Discharge) is widely used for ozone synthesis, pollution control including the removal of the environmental pollutant, surface modification, biomedical application and so on. Future applications may include their use in greenhouse gas control technologies. In addition, recently, coplanar type surface discharge, which is one of the DBD, has been researched as a plasma actuator which applies the ionic wind originated from the discharge. DBD can provide non-equilibrium plasma conditions at atmospheric pressure.

The characteristics of the DBD operated in atmospheric pressure are investigated. Applied voltage, current and the electrical discharge sound of DBD are measured, and examined the relationship between the micro discharge and the acoustic properties. The understanding of acoustic properties may give more detailed knowledge of the electric discharge phenomenon.

However, it's not easy to detect the sound signal in plasma reactor by the conventional condenser microphone technique. Therefore, we have developed a new diagnostic method, in which sound wave is measured by an optical sensor based on a Fraunhofer diffraction effect between the sound wave and laser beam. The light diffraction technique, which we call the "Optical Wave Microphone (OWM)" technique, is an effective sensing method to detect the sound and is flexible for practical uses as it involves only a simple optical lens system. This technique is also very useful to detect the sound wave without disturbing the sound field. Moreover, OWM can be applied for the visualization of sound field by computerized tomography (CT) because the ultrasmall modulation by the sound field is integrated along the laser beam path.

2. PRINCIPLES OF OWM-CT

The fundamental optical setup of the Fraunhofer diffraction measurement is shown in Fig. 1, where the laser beam is assumed to be of Gaussian type. x and z directions are defined as the forward directions of the laser beam and the sound wave, respectively. y directions is taken to be perpendicular to the propagated directions of laser beam and sound wave. x_f, y_f and z_f are defined as the location coordinates of the back focal plane (detection plane). When the incident probing laser beam crosses the sound wave as shown in Fig. 1, the diffracted waves are generated. They propagate with the penetrating beam through the Fourier optical system and reach the observing plane, which is set at the Fraunhofer diffraction region or in the back focal plane of the first receiving lens. The diffracted optical waves are homodyne-detected there by using the penetrating optical wave as a local oscillating power. The intensity of diffracted waves of higher orders is much smaller than that of the first order wave and can be neglected. We are calling this setup the OWM system. The spatial intensity (I_{ac}) of the resultant optical field at the back focal plane is given by the following equation [1-4].

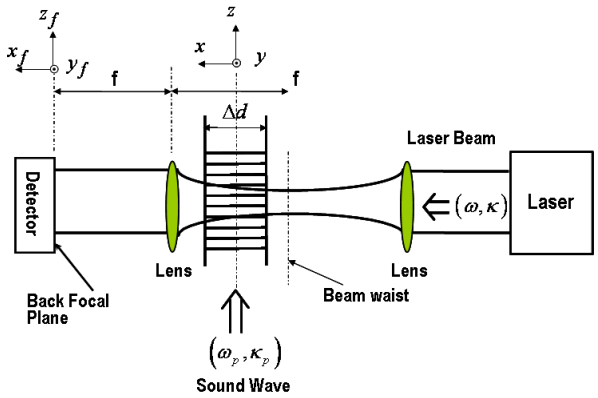


Fig. 1. Schematic representation of OWM.

$$I_{ac} = I_0 \Delta\phi_0 \left[\exp\left\{-\left(u^2 + (u-n)^2\right)\right\} - \exp\left\{-\left(u^2 + (u+n)^2\right)\right\} \right] \sin \omega_P t \qquad (1)$$

Where $I_0 = \left(2P_0 / \pi {W_f}^2\right) \exp\left[-2\left(y_f / W_f\right)^2\right]$,

$\Delta\phi_0 = \kappa_i \Delta\mu_0 \Delta d = \kappa_i \left(\mu_0 - 1\right) \Delta d \Delta p / \gamma p$,

$u = x_f / W_f$: the normalized x-coordinate in the back focal plane, $n = k_p W_0 / 2$: the normalized wave number, W_f : the beam size in the focal plane, $k_p \left(= 2\pi / \lambda_p\right)$: the wave number of sound wave, λ_p : the wavelength of sound wave, W_0 : the spot size, ω_P : the angular frequency of sound wave, P_0 : the total incident power, $k_i \left(= 2\pi / \lambda_i\right)$: the wave number of incident beam, λ_i : the wave length of probing beam, μ_0 : the reflective index of air, Δd : the width of sound wave, Δp : the intensity of sound wave, γ : the specific heat ratio, p : the atmospheric pressure

In the case where λp is much more and n is less than 1, Eq.(1) can be approximated by

$$I_{ac} = 4 I_0 \Delta\phi_0 \exp(-2u^2) un \sin \omega_P t \qquad (2)$$

Because $n = k_p W_0 / 2 = W_0 \omega_P / 2 v_p = \pi W_0 f_p / v_p$, where v_p is the sound velocity and f_p is the frequency of sound wave, Eq. (2) indicates that I_{ac} is proportional to f_p and $\Delta p \Delta d$ [5,6]. The diffraction pattern of the first order appears along z direction, and it consists of two simultaneous waves on the + z and - z axes with temporal phases opposite to each order. If the interaction length (L) between the laser beam and the sound field is long, Eq. (2) is rewritten as

$$I_{ac} = 4 I_0 \exp(-2u^2)\, unk_i (\mu_0 - 1) / \gamma p \sin \omega_P t \int_L \tilde{p}(\rho) d\rho \qquad (3)$$

where $\tilde{p}(\rho)$ is the sound pressure distribution along the ρ axis [5,6].

Incidentally, CT method can reconstruct a cross-sectional image using projected data from 0 to 180 degrees. Figure 2 shows the relation between $x-y$ and $x'-y'$ coordinates. Here, the two-dimensional sound $S(x, y)$, with the propagation direction perpendicular to the $x-y$ plane, is the subject of our present analyses. If the output voltage signal of the OWM is proportional to I_{ac} or $\Delta p \Delta d$ is normalized by the maximum signal amplitude, the detected signal, i.e., the projected data $D(\rho, \theta)$ along the interaction length (L) between the laser beam and the sound field, can be written as

$$D(\rho, \theta) = \int_{-\infty}^{\infty} \int_{-\infty}^{\infty} S(x, y)\, \delta(x \cos\theta + y \sin\theta - \rho) dx dy \qquad (4)$$

θ: rotated angle from $x-y$ coordinates to $x'-y'$ coordinates.

The reconstruction image can be obtained by inversely projecting the data to the $x-y$ coordinates, in

which the filtered back-projection method and Lamp filter function are used as the reconstruction algorithm [7].

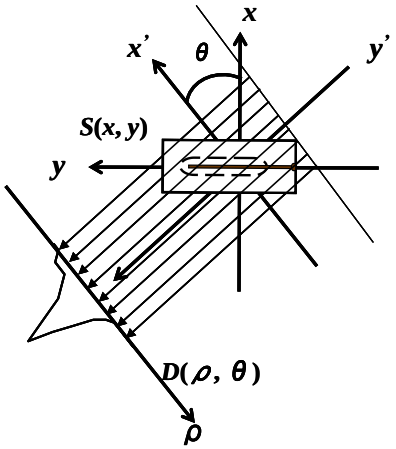


Fig. 2. Top view of electrodes module and relation between the coordinates of (x, y) and (x', y').

3. EXPERIMENTAL SETUP

Figure 3 shows the experimental setup to detect the sound signal from coplanar DBD using OWM-CT. When the high voltage ($7kV_{p\text{-}p}$: peak to peak voltage, 10 kHz) is applied to the electrodes in atmospheric pressure, the discharge and sound signal is generated. The coplanar DBD is generated ozone with the rate of approximately 15 mg/h and the main atmosphere around the sound detector is air and ozone. The discharge current is measured through a shunt resistance (50 ohm) in series with the grounded electrode. The applied voltage, discharge current and acoustic signal of coplanar discharge are stored in the digital oscilloscope (Tektronix TDS3034). The acoustic signal is measured by using both OWM and condenser microphone (Rion, UC-29, 20-100 kHz). To obtain projection data for CT analysis, the sound field was rotated in the θ direction and moved toward the y direction. The rotation step angle was set to 10 degrees from 0 to 180 degrees, and the driving range in the y direction was from y = -17 mm to 17 mm with the step length of 2 mm. To obtain projection data for CT analysis, the sound field was rotated in the direction and moved toward the direction. The rotation step angle was set to 10 degrees from 0 to 180 degrees, and the driving range in the direction was from -17 mm to 17 mm with the step length of 2 mm.

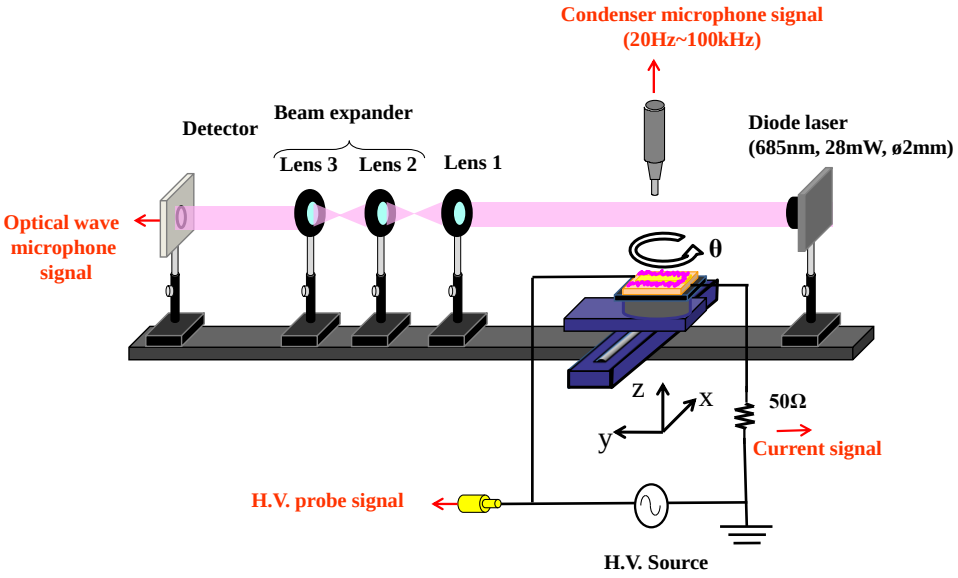


Fig. 3. Experimental setup to detect the sound of coplanar DBD using OWM-CT.

The photo and schematic of the electrodes are shown in Fig. 2. The main part of coplanar DBD is a high-purity Al_2O_3 ceramic substrate (15 mm in width, 37 mm in length, and 1.25 mm in thickness) and is also used as the dielectric. The discharge system consists of two electrodes buried under Al_2O_3 ceramic substrate. The distance between the electrodes is 220 μm. HV electrode (1.25 mm in width, 29.5 mm in length, and 10 μm in thickness) of the surface and a grounded electrode (6 mm in width, 24.5 mm in length, and 10 μm in thickness) inside the substrate are printed by a plasma spray coating method. This type device is used for ozonizer. The discharge plasma is generated on the surface.

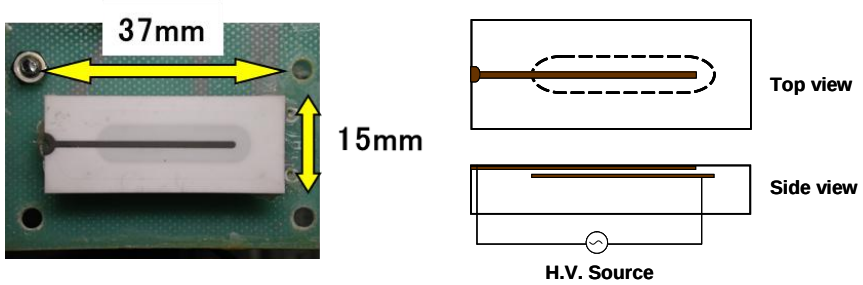
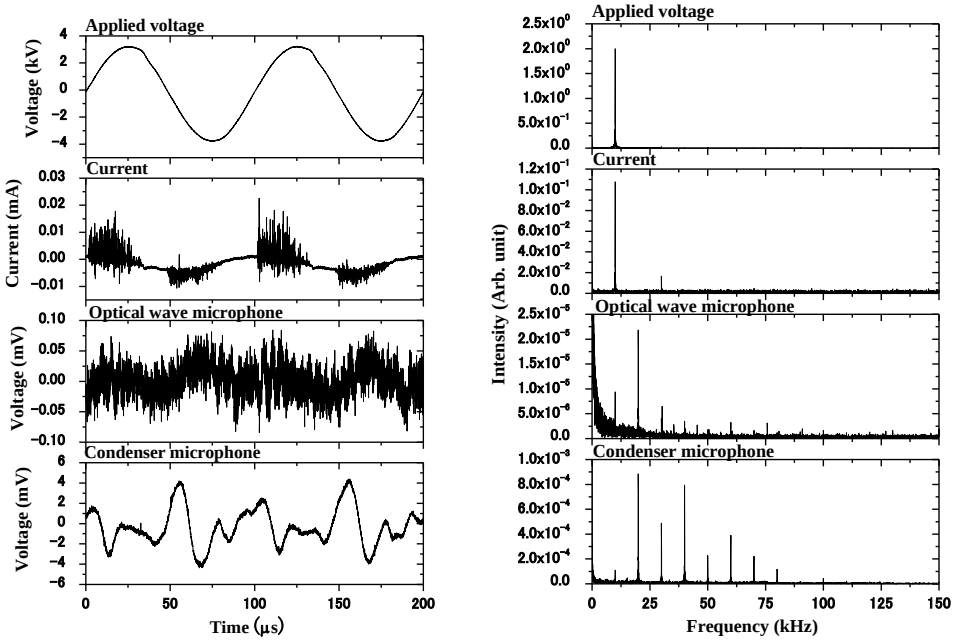


Fig. 4. Photo and schematic of the electrodes module.

4. Results

Figure 5(a) shows the time-resolved waveforms obtained from applied voltage, discharge current that flows in resistance, OWM and condenser microphone in air. When the high voltage of $7kV_{p\text{-}p}$ with the frequency of 10 kHz is applied to the electrodes, the typical DBD current wave form appears. The current of coplanar DBD is composed of two components. The first component is a displacement current due to the dielectric between both electrodes. The second component is glow type discharge current. In micro discharges, it corresponds to the drift of ions between both electrodes. It is obvious that the discharge emits the ultrasonic wave because the result obtained by the condenser microphone shows the typical wave form of compressional wave. The waveform of OWM seems to be contained high frequency components. The generation time of the discharge current and the sound signals are fairly in good agreements.



(a) (b)

Fig. 5. Voltage waveforms (a) and FFT results (b) obtained from high voltage probe, shunt resistance, OWM and condenser microphone. The frequency of applied voltage is 10 kHz.

Figure 5(b) shows the FFT spectra of voltage wave forms obtained from high voltage probe, shunt

resistance, OWM and condenser microphone in air. The frequency range of FFT analysis is shown from 0 to 150 kHz. The coplanar DBD occurs two times in a cycle of applied voltage. The FFT result for the current shows that the large peak appears at 10 kHz which corresponds to the frequency of the applied voltage due to the relatively large displacement current. The FFT result for OWM contains many frequency components such as 10, 20, 30, 35, 40, 45, 50, 60, 75, 90, 100, 130 and 150 kHz. These values are almost same with the harmonics frequency of applied voltage. This result may be shown that the electric wind, which is due to the migration of ions inside plasma, is produced or/and the discharge device is vibrated by the applied voltage. The FFT result of the condenser microphone shows that the main frequency components are 10, 20, 30, 40, 50, 60, 70, 80 and 100 kHz. The condenser microphone is not able to detect the high frequency components that OWM have detected, because OWM is more sensitive compared with the condenser microphone at the high frequency region.

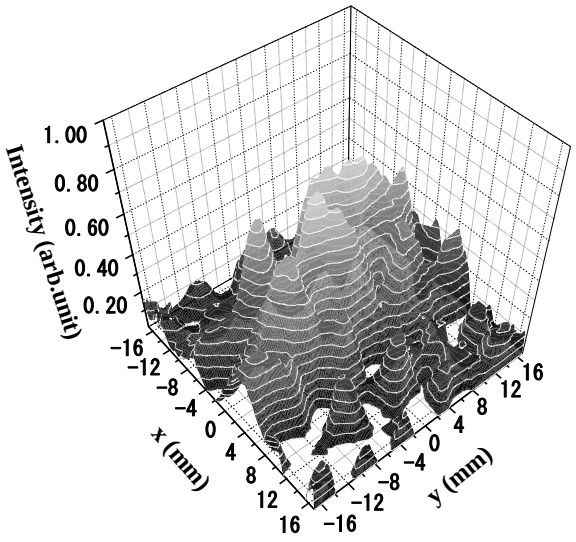


Fig. 6. Reconstructed distribution of the discharge sound in the $x-y$ plane at 10 kHz.

Figure 6 shows a reconstructed distribution of the discharge sound field on the $x-y$ plane. The applied voltage is 7 $kV_{p\text{-}p}$ and the frequency of applied voltage is 10 kHz. The proving laser of OWM is 2 cm away from the surface of coplanar electrodes. Therefore, the coordinate of z axes becomes 2cm. The dominant peak is located at $x=1.21\,\text{mm}$, $y=-3.33\,\text{mm}$. This result shows that the strong pressure area is located around the electrodes.

5. Conclusions

The sound signal generated by the coplanar DBD was detected by the OWM-CT and the condenser microphone, and the discharge sound was analyzed. The strong pressure area is appeared around the electrodes. The sound signal from discharge device may be useful to examine discharge current and atmospheric condition around discharge electrodes.

Acknowledgement

This work was supported by Grant-in-Aid for Scientific Research (23560510), the Japan Science and Technology Agency (15-138) and the Research and Study Project of Tokai University Educational System General Research Organization.

References

[1] Evans D E, von Hellermann M and Holzhauer E, Plasma Phys. Control Fusion, 1982, **24**, 819.
[2] Sonoda Y, Suetsugu Y, Muraoka K and Akazaki M, Plasma Phys. Control Fusion 1983, **25**, 1113.
[3] Nakamiya T, Sonoda Y, Ikegami T, Mitsugi F, Ebihara K and Tsuda R, PRZEGLĄD ELEKTROTECHNICZNY (Electrical Review) 5/**2009**, 143.
[4] Nakamiya T, Mitsugi F, Suyama S, Ikegami T, Ebihara K, Sonoda Y, Iwasaki Y, Aoqui S, Henryka Stryczewska and Joanna Pawlat , PRZEGLAD ELEKTROTECHNICZNY (Electrical Review), **1/2011**, 249-253.
[5] Sakoda T and Sonoda Y, Acoust. Sci. & tech., **29(4)**, 295-299.
[6] Nakamiya T, Iwasaki Y, Mitsugi F, Kozai R, Ikegami T, Sonoda Y, and Tsuda R, Journal of Advanced Oxidation Technologies, **14 (1)**, 63-70, 2011.
[7] Gonzalez R C and Woods R E, Digital Image Processing; Pearson Education, NJ, 2008.

SPATIO-TEMPORALLY RESOLVED DENSITY OF NITROGEN METASTABLES IN BARRIER DISCHARGES

Sebastian Nemschokmichal, Jürgen Meichsner

Institute of Physics, University of Greifswald, Felix-Hausdorff-Str.6, 17489 Greifswald
E-mail: nemschok@physik.uni-greifswald.de

The density of $N_2(A^3\Sigma_u^+, v=0)$ metastables was measured by laser induced fluorescence (LIF) spectroscopy in filamentary and diffuse nitrogen barrier discharges at 500 mbar. The absolute density calibration was performed by the comparison of the LIF signal with Rayleigh scattering and results in densities in the range of 10^{13} cm^{-3}. The time dependence of the metastables density and their axial density profiles within the 1 mm gap are presented. The time dependence confirms the delay of the metastables production with respect to the discharge current. The axial profiles differ strongly comparing both half cycles and the discharge modes, respectively.

1. Introduction

Barrier discharges at atmospheric pressure can operate in two different discharge modes, the filamentary and the diffuse mode. In pure nitrogen, the diffuse Townsend-like discharge can be observed [1]. A transition into the filamentary mode can be forced by adding about 500 ppm oxygen, well known as an effective quencher of nitrogen metastables. Hence, the transition between both modes depends on the nitrogen metastables density [2,3]. The metastables are able to release electrons by Penning-ionization in the volume or by exoemission at the dielectric surfaces. To clarify the importance of both processes a new discharge cell was designed to measure the density of the $N_2(A^3\Sigma_u^+)$ metastables together with surface charges and the optical emission [4,5,6]. Here, the focus is directed on the determination of metastables by laser induced fluorescence spectroscopy.

2. Experimental setup

The investigated discharge cells are sketched in figure 1. Both consist of an aluminium mirror at the bottom with a BSO ($Bi_{12}SiO_{20}$) crystal on it and a glass plate as the second dielectric on top. The gap distance between both amounts 1 mm. The electrode on top of the glass plate is in the first configuration pin-like shaped at the central axis of the discharge cell and in the second configuration realized by a conductive ITO layer. The former setup fixes single microdischarges in the centre whereas the latter allows the investigation of the diffuse discharge mode in the entire volume. The combination of the aluminium mirror, the BSO crystal and the transparent ITO layer on the glass plate was choosen for the measurement of surface charges in an identical discharge cell. The discharges were ignited at a pressure of 500 mbar using sinusoidal voltages between 7 and 12.5 kV_{pp} (at 2 and 5 kHz).

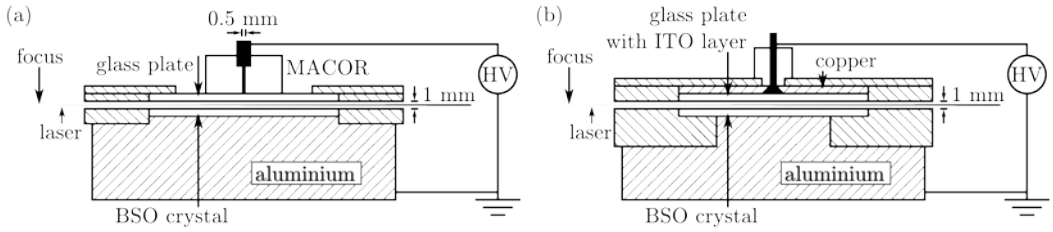


Fig. 1: Cross section of the discharge cells used for the (a) filamentary and (b) diffuse discharge mode.

For the detection of $A^3\Sigma_u^+, v=0$ metastables by laser induced fluorescence (LIF) spectroscopy a Nd:YAG pumped dye laser (dye: pyridine 1, linewidth: 0.6 cm^{-1}, pulse energy: < 5 mJ) was focussed by a cylindrical lens to pass the discharge gap. The laser excited the 0-3 transition from the $A^3\Sigma_u^+$ to

$B^3\Pi_g$ state of nitrogen at 687.44 nm. Perpendicular to the laser beam, the fluorescence at 762 nm from the $B^3\Pi_g, v=3$ to $A^3\Sigma_u^+, v=1$ transition was imaged to a monochromator and a photomultiplier tube. The electrical pulse was recorded by a fast oscilloscope. Besides the LIF, the time dependent signal from Rayleigh scattering in CO_2 was measured at 687 nm for the absolute density calibration.

3. Absolute density calibration

The absolute density calibration is based on the comparison of the time dependent LIF signal with the Rayleigh signal. As known, the LIF signal is delayed with respect to the laser pulse due to the finite effective lifetime of the excited state, in this case the $B^3\Pi_g, v=3$ state. In contrast, Rayleigh scattering takes place immediately without any delay. Hence, the LIF signal is shifted in time with respect to the Rayleigh signal. Both signals are plotted in figure 2 for a pressure of 500 mbar.

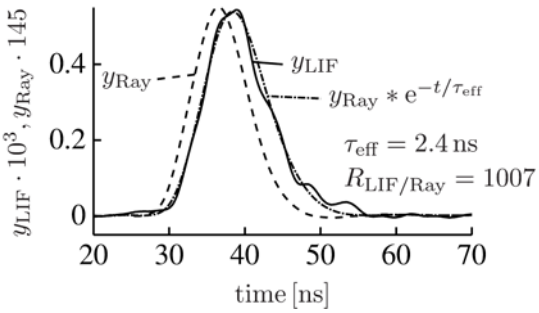


Fig. 2: Time dependent Rayleigh and LIF signal as well as the fitted convolution of the Rayleigh signal with an exponential decay to the LIF signal.

The temporal shift of both signals is well visible. A detailed calculation shows that the LIF signal is the convolution of the Rayleigh signal with an exponential decay:

$$u_{\mathrm{LIF}}(t) = R_{\mathrm{LIF/Ray}} A_{B_3 \to A_1} \left(u_{\mathrm{Ray}} * \Theta(t) \exp\left(-\frac{t}{\tau_{\mathrm{eff}}} \right) \right)(t). \qquad (1)$$

The factor $R_{\mathrm{LIF/Ray}}$ is a kind of ratio of the LIF to the Rayleigh signal, $A_{B_3 \to A_1}$ the Einstein coefficient for spontaneous emission and τ_{eff} the effective lifetime of the excited $B^3\Pi_g, v=3$ state. The latter is about 2.4 ns at 500 mbar and $R_{\mathrm{LIF/Ray}}$ is about 1000. To proof this formula, the pressure was varied between 100 mbar and atmospheric pressure. For pressures between 100 and 600 mbar, the effective decay rates τ_{eff}^{-1} depend linear on pressure. Above 600 mbar, the error increased considerably. Using the ratio from the fit, one can calculate the $A^3\Sigma_u^+, v=0$ metastables density by

$$n_{A_0} = n_{\mathrm{Ray}} \frac{T_{\mathrm{Ray}} Q_{\mathrm{Ray}}}{T_{\mathrm{LIF}} Q_{\mathrm{LIF}}} \frac{3}{2} \frac{\sigma_{\mathrm{Ray}}}{\sigma_{\mathrm{LIF}}} R_{\mathrm{LIF/Ray}}. \qquad (2)$$

The constants are the density of the Rayleigh scatterer n_{Ray}, the different optical properties (transmission T, quantum efficiencies Q) at the different wavelengths, and the cross sections σ [7]. The typical densities at 500 mbar are in the range of 10^{13} cm^{-3}.

4. Filamentary discharge mode

The investigation of the filamentary discharge mode was performed with the pin-like electrode on top. In the multi-filamentary mode, the metastables density increases as expected after the ignition of several microdischarges and depletes afterwards. Unfortunately, the microdischarge ignition scatters around the central axis and a lot of them miss the detection volume given by the laser beam. Hence, the investigation of single microdischarges is necessary. The temporal development of the metastables

density after one single microdischarge is shown in figure 3 for the two half cycles (a: pin = anode, b: pin = cathode). Both measurements were performed about 0.2 mm below the glass plate. The delay of 0 µs is actually about 350 ns after the current pulse due to the laser electronics. Hence, the current pulse has been already past at 0 µs and the metastables density increases in the afterglow of the discharge. This indicates a production of metastables from higher molecular states instead of electron impact excitation.

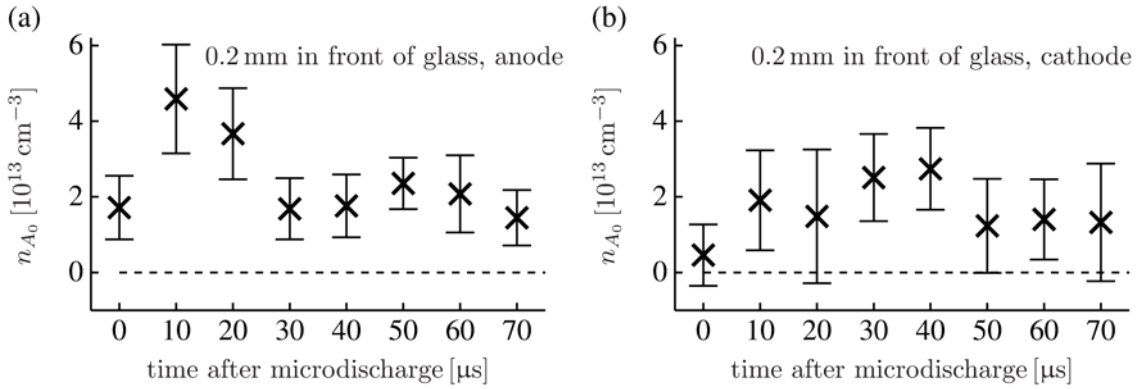


Fig. 3: Time dependence of the $A^3\Sigma_u^+, v = 0$ density in the afterglow of a single microdischarge in front of the (a) anode and (b) cathode. 500 mbar, 2 kHz, 10.50 kV_{pp}.

During the anode phase, the increase in density is very steep up to a value of about 5×10^{13} cm^{-3}, followed by a fast and a slow decay. The fast decay after the maximum is related to the quenching by atomic nitrogen and the pooling reaction in the discharge channel, respectively. For the latter process, densities from 10^{14} to 10^{15} cm^{-3} must be assumed to get time constants of some tens of microseconds as in figure 3 (a). Such values are realistic since the cross section area of the microdischarge channel is clearly smaller than the base area of the detection volume. The temporal development in the cathode phase is much slower. This might correspond to the different electron energies in front of the anode and cathode. As known from optical emission spectroscopy [8], the electron energy in front of the cathode is much larger, but the density is lower. Hence, one can expect the excitation of higher molecular states or ionisation in front of the cathode rather than at the anode. The cascade processes from highly excited species might take more time to produce $A^3\Sigma_u^+$ metastables.

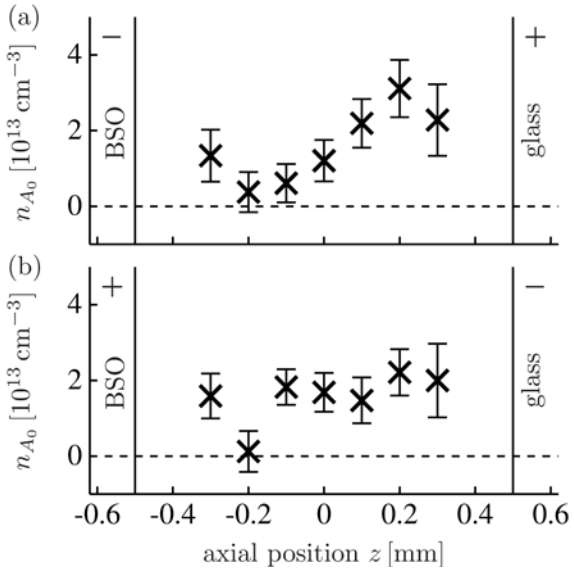


Fig. 4: Axial $A^3\Sigma_u^+, v = 0$ density profiles for the (a) positive and (b) negative half cycle in the filamentary mode at 500 mbar, 5 kHz, 12.50 kV_{pp}, and 30 µs after zero-crossing of the voltage.

Besides the temporal shift of the laser pulse, its vertical position was variable and axial profiles were measured in the multi-filamentary mode. Such profiles are presented in figure 4 for the different half cycles. In the positive half cycle, the metastables density increases toward both dielectrics and has a minimum between the centre and the BSO. Furthermore, the density in front of the anodic glass plate is larger than in front of the cathodic BSO. This underlines the presumption of a larger metastables production in the anode glow in comparison to the cathode. On the other hand, the asymmetric discharge setup might result in a larger focussing of microdischarges in front of the pin-like electrode and therefore a larger metastables density there. In the negative half cycle, the density is nearly constant within the gap. Here, both discussed effects are directed vice versa and might compensate each other. To distinguish them a symmetric setup is necessary.

5. Diffuse discharge mode

The diffuse discharge mode was observed in the discharge cell with two planar electrodes shown in figure 1 (b). The time dependence of the metastables density in the centre is presented in figure 5 in correlation to the applied voltage and discharge current.

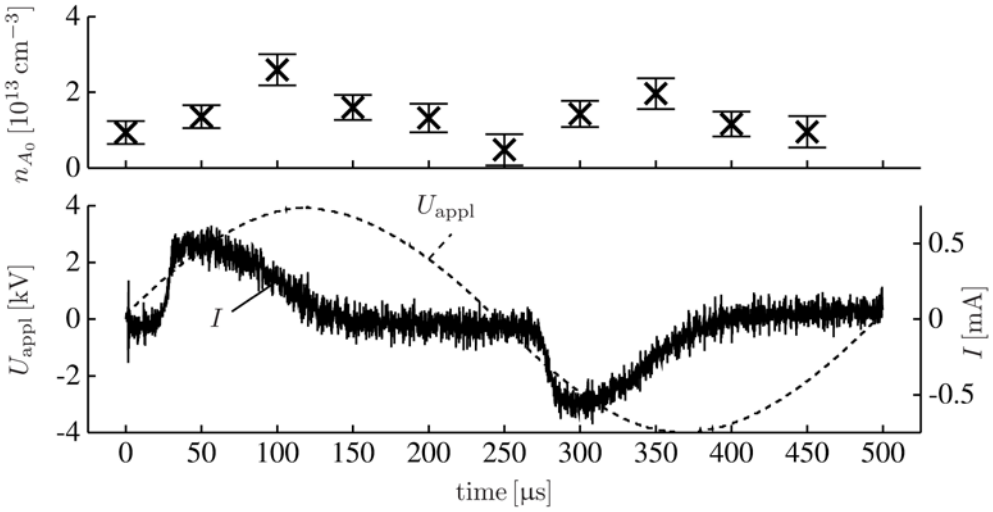


Fig. 5: Time dependent $A^3\Sigma_u^+, v = 0$ density in the centre of the diffuse discharge configuration at 500 mbar, 2 kHz, and 8.00 kV_{pp}.

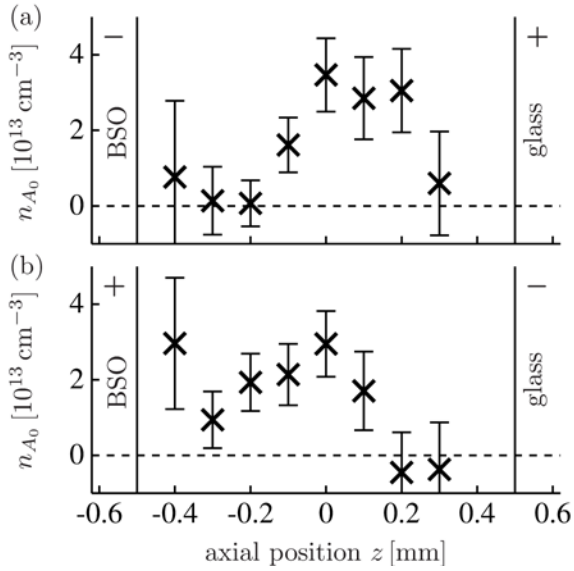


Fig. 6: Axial $A^3\Sigma_u^+, v = 0$ density profiles for the (a) positive and (b) negative half cycle in the diffuse mode at 500 mbar, 2 kHz, 8.00 kV_{pp}, and 125 µs after zero-crossing of the voltage.

It shows an increase in the metastables density in every half cycle during and after the current pulse. As for the filamentary mode, the density maximum does not concur with the current maximum. This is in agreement with optical-optical double resonance (OODR)-LIF measurements in [9] and emission spectroscopy of the NO_γ system [3,9,10]. The NO_γ system is excited by a fast energy transfer from $A^3\Sigma_u^+$ metastables to NO molecules indicating the metastables distribution. The reason for the delay might be as previously discussed a production from higher nitrogen states instead of electron impact excitation. After the maximum the density decreases to a value of about 10^{13} cm^{-3} at the beginning of the next half cycle.
Axial density profiles are presented in figure 6 for the (a) positive and (b) negative half cycle. The density maximum is shifted toward the anode. This corresponds to a maximum of the optical emission of the second positive and first negative system of nitrogen in front of the anode [2] and to the electron density maximum in simulations of the Townsend-like discharge mode [1,2]. In contrast to both, the density in front of the glass plate is nearly zero for the whole period and does not exponentially grow from the cathode to the anode. The reason for this difference might be quenching by etching products released from the dielectrics [10].

6. Conclusions

The laser induced fluorescence spectroscopy of $N_2(A^3\Sigma_u^+)$ metastables in combination with the absolute density calibration by the comparison with Rayleigh scattering was successfully applied to filamentary and diffuse nitrogen barrier discharges. The time dependent density measurements show the well known delay of the metastables density maximum with respect to the current pulse of single microdischarges as well as to the current pulse of the diffuse Townsend-like discharge. The axial density profiles in the filamentary mode differ strongly for the two half cycles. The reasons are probably the asymmetric setup with the pin electrode on top and a larger production of metastables in the anode glow in comparison to the cathode. In the diffuse mode, the spatial density maximum is shifted clearly toward the anode which is in good agreement with optical emission spectroscopy and simulations of the Townsend-like discharge in pure nitrogen.

7. Acknowledgement

The work was supported by the “Deutsche Forschungsgemeinschaft” within the collaborative research center TRR-24, project B11.

8. References

[1] F. Massines, P. Ségur, N. Gherardi, C. Khamphan and A. Ricard, *Surf. Coat. Technol.* **174-175** (2003) 8
[2] R. Brandenburg, V. A. Maiorov, Yu B. Golubovskii, H.-E. Wagner, J. Behnke and J. F. Behnke, *J. Phys. D: Appl. Phys.* **38** (2005) 2187
[3] K. V. Kozlov, R. Brandenburg, H.-E. Wagner, A. M. Morozov and P. Michel, *J. Phys. D: Appl. Phys.* **38** (2005) 518
[4] M. Bogaczyk, H.-E. Wagner, operation modes in barrier discharges: discharge development and surface charge accumulation, this issue
[5] M. Bogaczyk, S. Nemschokmichal, A. Zagostin, G. B. Sretenović, J. Meichsner, H.-E. Wagner, *J. Adv. Oxid. Technol.* **15** (2012), accepted
[6] M. Bogaczyk, S. Nemschokmichal, R. Wild, L. Stollenwerk, R. Brandenburg, J. Meichsner, H.-E. Wagner, *Contrib. Plasma Phys.*, accepted
[7] S. Nemschokmichal, F. Bernhardt, B. Krames and J. Meichsner, *J. Phys. D: Appl. Phys.* **44** (2011) 205201
[8] K. V. Kozlov, H.-E. Wagner, R. Brandenburg and P. Michel, *J. Phys. D: Appl. Phys.* **34** (2001) 3164
[9] G. Dilecce, P. F. Ambrico and S. De Benedictis, *Plasma Sources Sci. Technol.* **16** (2007) 511
[10] N. Gherardi, G. Gouda, E. Gat, A. Ricard and F. Massines, *Plasma Sources Sci. Technol.* **9** (2000) 340

FORMATIONS OF NEGATIVE ION IN SF_6/N_2 MIXTURES

Yui Okuyama[1,2], Martin Sabo[1], Haruo Itoh[2] and Štefan Matejčík[1]

[1] *Department of Experimental Physics, Comenius University,Mlynska dolina F2,84248 Bratislava, Slovakia*

[2]*Graduate school, Chiba Institute of Technology, 2-17-1, Tsudanuma, Narashino, Chiba, 275-0016, Japan*

E-mail: Stefan.Matejcik@fmph.uniba.sk

The formation of negative ions initiated by the interaction of thermal electrons in N_2 containing a small admixture of SF_6 was studied by ion mobility spectrometry/mass spectrometry (IMS/MS) at atmospheric pressure. We identified negative ions by this technique, and the results are illustrated as two-dimensional (2D) IMS-MS spectra. We observed four peak mobilities at 2.43, 2.32, 2.08 and 1.99 $cm^2/V•s$ in the ion mobility spectra, which were identified as the ion species $HF_2^-(HF)_n$, $NO_3^-(HF)_n$, SF_5^- and SF_6^- from the mass spectra, respectively. Moreover, the ions separated again to $F^-(HF)_n$ (m/z=39, 59 and 79) , $NO_3^-(HF)_n$ (m/z=62, 82 and 102), SF_5^- (m/z=127) and SF_6^- (m/z=146) according to the mass spectra. We also detected the negative ions SOF_4^- and $SF_6^-(HF)$ in the mass spectra.

1. Introduction

The use of SF_6 has been restricted because of its high global warming potential. However, SF_6 is an excellent gas medium for use in electrical engineering, for example, for gas insulation in high-voltage power apparatus and etching in semiconductor processes. SF_6 has already been investigated for about 40 years in order to accumulate fundamental data on the compound [1-3]. In the present work, we used ion mobility spectrometry-mass spectrometry (IMS-MS) [4] to study the formation of negative ions by the interaction of thermal electrons in N_2 with a small amount of SF_6 and during the subsequent ion-molecule reactions.

There are many papers describing the mobility of negative ions formed from SF_6 as the parent gas [5-9], and mass spectrometers have often been used in such studies [10, 11]. These studies were carried out at a low pressure and high reduced electric field *E*/*N*. Studies on the mobility of negative ions formed from SF_6 in N_2 [12, 13] without mass analysis of the ions have also been reported.

In the present work, we measured the zero-field mobilities of negative ions formed in SF_6/N_2 mixtures (30-180 ppm SF_6) at atmospheric pressure. Additionally, we obtained two-dimensional used later 2D IMS-MS spectra and identified ions from their ion mobility and mass to charge ratio (m/z).

2. Experimental Setup

We applied IMS-MS [4] to investigate the formation of negative ions in SF_6/N_2 mixtures in this experiment. The IMS apparatus was operated at ambient pressure in negative ion mode. The negative ions were formed by corona discharge (CD). A detailed description of CD-IMS was given in our previous work [4]. The IMS apparatus was interfaced with a 100μm pinhole to enable differential pumping between the ion drift tube and mass spectrometer. The ions that passed through the pinhole were guided by an ion optics (IO) system located in the vacuum chamber. Ions were accelerated in the time-of-flight (TOF) mass spectrometer in the third vacuum chamber. The drift tube of the TOF mass spectrometer was constructed from a stainless-steel perforated tube of total length 547mm. A multi-channel plate (MCP) (Tectra) was used as an ion detector. The ions were incident to the TOF mass spectrometer and had a period of 25μs and pulse width of 10μs.

The CD-IMS/TOF instrument was able to operate in three modes; in single IMS mode, in single-TOF mode when the shutter grid of the IMS apparatus was fully open and in the 2D mode using both spectrometers operating synchronically.

A negative CD between a wire and plane electrodes was maintained in high-purity N_2 to produce thermal electrons. The electrons then entered the drift tube containing N_2 and a small admixture of SF_6. The electrons reacted with SF_6 in the reaction region including the drift tube to form negative ions. We used high-purity gaseous N_2 (99.999%, Linde) and SF_6 (99.75%, Sigma-Aldrich).

3. Results

3.1 Two-dimensional IMS-MS map

Figure 1 shows a 2D IMS-MS spectrum of negative ions formed by thermal electron attachment to SF_6 and subsequent ion-molecule reactions in the drift tube of the IMS apparatus. We detected four different groups of ions, $F^-(HF)_n$ (n = 0, 1, 2), $NO_3^-(HF)_n$ (n = 0, 1, 2), SF_5^- and SF_6^-, in this map. The spectrum obtained from IMS is shown on the left vertical axis and the mass spectrum is shown on the top horizontal axis. We combined these spectra to obtain the 2D map observed using TOF signals. From this map, we determined the mobility peaks and m/z ratios of ions. In this way, we could identify each ion species. The 2D map shows that the peaks in the IMS spectrum are usually due to several clusters of ions. In the results, there are three sharp peaks ($HF_2^-(HF)_n$, SF_5^- and SF_6^-). Only the $NO_3^-(HF)_n$ clusters did not correspond to an independent peak in the IMS spectrum. We describe the peaks in the IMS spectrum in detail in the next section.

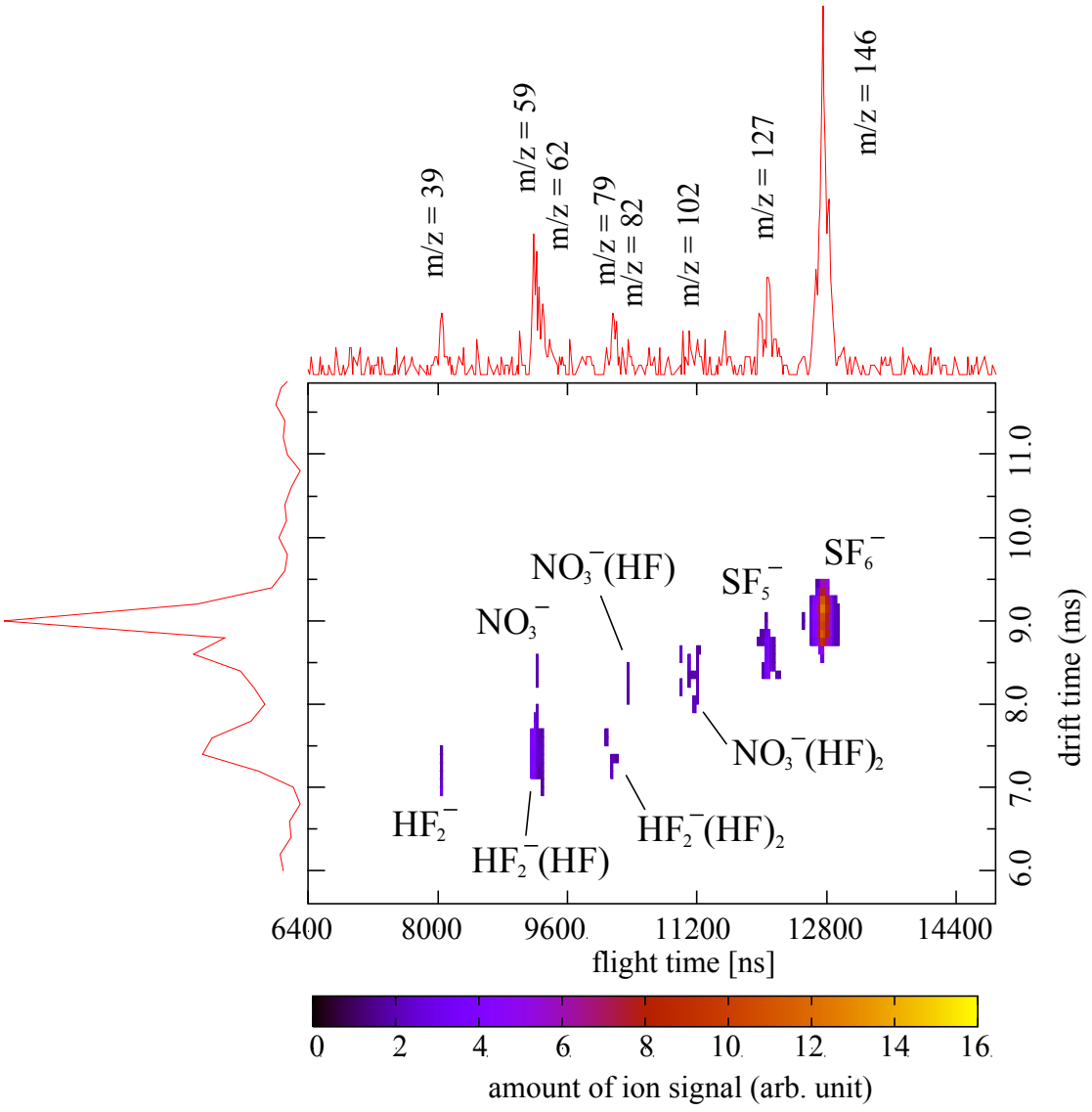


Fig. 1. Two dimensional IMS-MS map of negative ions observed in SF_6/N_2 mixture.

3.2 Negative ion formation

Figure 2 shows the mass spectrum measured with an open shutter grid, i.e., no use of IMS. In this way, we were able to obtain a mass spectrum with a better signal to noise ratio. From this spectrum, we identified ten types of ions with m/z of 39, 59, 62, 79, 82, 102, 124, 127, 146 and 166. The ion having m/z=146 is SF_6^-, which is the dominant ion in the SF_6/N_2 mixture. The ion with m/z=166 was assigned

to $SF_6^-(HF)$. In the mass spectrum we detected the HF cluster ions $HF_2^-(HF)_n$ (n = 0, 1, 2) (m/z of 39, 59 and 79) and $NO_3^-(HF)_n$ (n = 0, 1, 2) (m/z of 62, 82 and 102). The ions with m/z of 124 and 127 were assigned to SOF_4^- and SF_5^-, respectively.

We assume that the SF_6^- ions were formed efficiently in the drift region by electron attachment. However, the formation of SF_5^- is less efficient [14, 15]:

$$e + SF_6 \rightarrow SF_6^- \quad (1)$$

$$SF_5^- + F \quad (2)$$

The attachment of dissociated electrons to SF_6 also results in the formation of F^-, F_2^-, SF_4^-, SF_3^- and SF_2^-; however, the thresholds for these reactions are much higher than that of thermal electron attachment [14]. Thus, it is considered that only SF_6^- and SF_5^- were formed by the attachment of thermal electrons.

The HF cluster ions with m/z of 59 and 79 detected in the mass spectrum HF_2^-. Sauers and Harman [16], who observed $HF_2^-(HF)_n$ explained its formation by the following reactions:

$$SF_6^- + H_2O \rightarrow SOF_4^- + 2HF \quad (3)$$

$$F + H_2O \rightarrow HF + OH \qquad 1.1\times10^{-11}\ cm^3/s\ [17] \quad (4)$$

$$SF_6^- + HF \rightarrow HF_2^- + SF_5 \quad (5)$$

$$HF_2^-(HF)_n + HF + SF_6 \rightarrow HF_2^-(HF)_{n+1} + SF_6. \quad (6)$$

The H_2O in reaction (3) was present in trace amounts in N_2 and SF_6 gases, and the HF formed in reaction (3) may have been present in trace amounts in the SF_6 used in this study. Unfortunately, no additional information about the impurities present in SF_6 was available. However, it is plausible that small amounts of H_2O and HF existed in the SF_6 [13]. The negative ion SOF_4^- (m/z=124) was identified from Figure 2, indicating that SOF_4^-, a product of reaction (3), existed in the IMS drift tube.

NO_3^- ions are efficiently formed in gases containing N_2 and O_2. The N_2 used in this study contained 5 ppm O_2, and the air concentration in SF_6 was on the order of 1000 ppm [18]. Owing to high electron affinity of NO_3, NO_3^- ions are very stable. The $NO_3^-(HF)$ ions (m/z 82 and 102) were formed by three body attachment as follows:

$$NO_3^- + HF + N_2 \rightarrow NO_3^-(HF) + N_2 \quad (7)$$

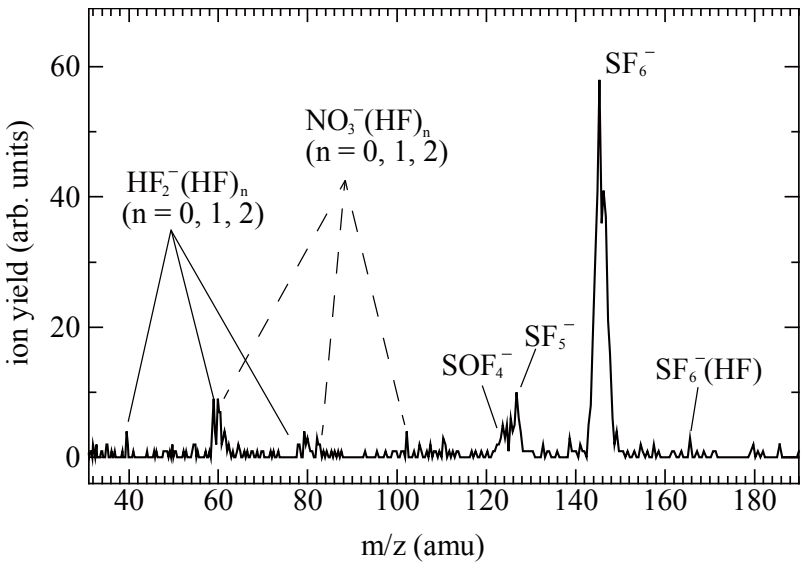


Fig. 2. Mass spectrum observed by TOFMS.

HF exhibits a high dipole moment of 1.826 D [19], similar to that of H_2O; therefore, it can form clusters efficiently. Other reactions that produce $NO_3^-(HF)$ are the reactions of SF_6^- and SF_5^- with HNO_3 [20].

$$SF_6^- + HNO_3 \rightarrow NO_3^-(HF) + SF_5 \qquad 1.9\times10^{-9}\ cm^3/s \quad (8)$$

$$SF_5^- + HNO_3 \rightarrow NO_3^-(HF) + SF_4 \qquad 2.1\times10^{-9}\ cm^3/s \quad (9)$$

The HNO_3 may have been formed from the impurities in SF_6 in this study.

The $SF_6^-(HF)$ cluster ion, which was also observed by Sauers and Harman [16], may have been formed by the clustering reaction

$$SF_6^- + HF + N_2 \rightarrow SF_6^-(HF) + N_2. \qquad (10)$$

3.3 IMS spectra

Figure 3 shows a IMS spectra measured by the conventional at the Faraday plate in the IMS apparatus in N_2 containing a small amount of SF_6 in the drift region. These IMS spectra have a better signal to noise ratio than the IMS spectra generated from the 2D map. The flow rate of N_2 was 1000 ml/min in the drift region and 200 ml/min in the corona region. The flow rate of SF_6 was varied from 0 to 0.18 ml/min (0 to 180 ppm). Four peaks, $HF_2^-(HF)_n$, $NO_3^-(HF)_n$, SF_5^- and SF_6^-, can be observed in Figure 3. In the case of 0 ppm SF_6, only a small NO_3^- peak appeared in the IMS spectra. The intensities of the peaks associated with SF_6^- and $HF_2^-(HF)_n$ strongly depend on the SF_6 concentration.

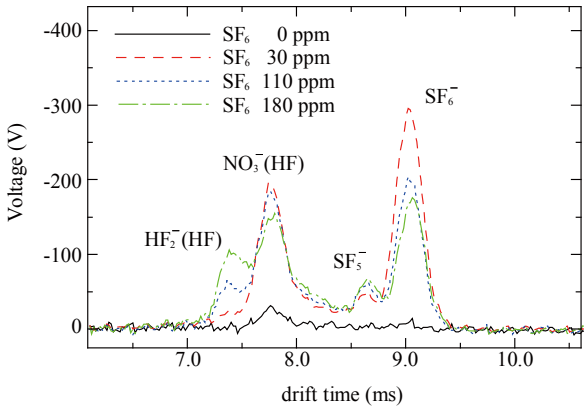


Fig. 3 Ion Mobility Spectra in N_2 with a small amount of SF_6.

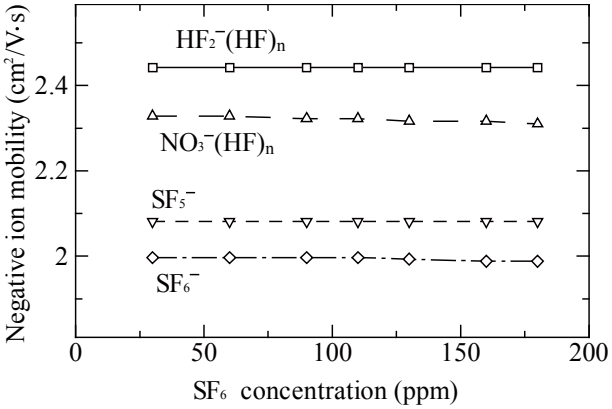


Fig. 4 Negative ion mobilities of $HF_2^-(HF)_n$, $NO_3^-(HF)_n$, SF_5^-, and SF_6^- against SF_6 concentration.

Figure 4 shows the dependence of the reduced mobilities of $HF_2^-(HF)_n$, $NO_3^-(HF)_n$, SF_5^- and SF_6^- on the SF_6 concentration in N_2. The reduced mobilities of $HF_2^-(HF)_n$, $NO_3^-(HF)_n$, SF_5^- and SF_6^- are 2.43, 2.32, 2.08 and 1.99 $cm^2/V•s$, respectively. The measurements were carried out at atmospheric pressure in a reduced electric field E/p_0 of 0.46 V/cm•Torr and the drift length was 8.25 cm. Figure 4 indicates only a very weak dependence of the ion mobilities on the SF_6 concentration. To our knowledge, there is no published data on the mobilities of $HF_2^-(HF)_n$, $NO_3^-(HF)_n$ and SF_5^- in N_2 containing a small amount of SF_6. Only data on the mobility of SF_6^- in the parent gas has been reported [10, 11]. Hinojosa and Urquijo also measured the mobility of SF_6^- in SF_6/N_2 mixtures [12]. In Table 1, reduced mobilities of SF_6^- in N_2 containing small admixture of SF_6 are listed. Hinojosa and Urquijo reported values of 1.89 $cm^2/V•s$ for SF_6^- in SF_6/N_2 mixtures with SF_6 concentrations of 0.02% and 1%. This value is close to the present value for SF_6^-. Lakdawala and Moruzzi also determined the reduced mobility of SF_6^- in a SF_6/N_2 mixture [13]. They reported a value of 1.90±0.05 $cm^2/V•s$ in the N_2 concentration range from 0.03 to 10%. This value is also in good agreement with the present value. However, the present value is slightly higher than the other values. We believe that this could be due to the fact that the SF_6 concentration in N_2 was below 180 ppm, which is considerably less than that in previous studies.

Tab. 1 Reported values of negative ion mobility in N_2 with a little amount of SF_6.

Presenters	mobility μ_0^- ($cm^2/V•s$)	ion species	SF_6 concentrations
present value	1.99±0.05	SF_6^-	0.003 – 0.018 %
Hinojosa and Urquijo	1.89	SF_6^-	0.02 and 1 %
Lakdawala and Moruzzi	1.90±0.05	no description	0.03 - 10 %

4. Conclusions

The formation of negative ions by electron attachment and ion-molecule reactions in N_2 containing a small admixture of SF_6 was studied by IMS-MS at atmospheric pressure. We detected the negative ions $HF_2^-(HF)_n$, $NO_3^-(HF)_n$, SOF_4^-, SF_5^-, SF_6^- and $SF_6^-(HF)$, which were identified using a mass spectrometer. We also determined the zero-field mobilities of $HF_2^-(HF)_n$, $NO_3^-(HF)_n$, SF_5^- and SF_6^- to be 2.43, 2.32, 2.08 and 1.99 $cm^2/V•s$, respectively.

5. Acknowledgment

This work was supported by the Slovak Research and Development Agency, project Nr. APVV-0733-11 and partially by project VEGA 1/0514/12. Y.O. thanks the National Fellowship Program of Slovak republic for support.

6. References

[1] Ed. Christophorou L G and Olthoff J K 2004 GASEOUS DIELECTRICS IX, *KLUWER ACADEMIC / PLENUM PUBLISHERS*
[2] Christophorou L G, Olthoff J K, and Green D S 1997 *NIST Technical Note* 1425
[3] Dutton J 1975 *J. Phys. Chem. Reff. Data* **4** 640
[4] Sabo M, Palenik J, Kucera M, Han H, Wang H, Chu Y, Matejcik S 2011 *Int. J. Mass Spectrom.* **293** 23–27
[5] McAfee K B 1955 *J. Chem. Phys.* **23** 1435
[6] McDaniel E W, McDaniel M R C 1959 *Phys. Rev.* **114** 1028
[7] Fleming I A and Rees J A 1969 *J. Phys. B* **2** 777
[8] Naidu M S and Prasad A N 1970 *J. Phys. D* **3** 951
[9]Y. Nakamura 1988 J. Phys. D 21 67
[10] Patterson P L 1970 *J. Chem. Phys.* **53** 696
[11] Urquijo-Carmona J de, Alvarez I, Martinez H and Cisneros C 1991 *J. Phys. D* **24**, 664
[12] Hinojosa G and Urquijo J de 2003 *J. Phys. D* **36** 2510
[13] Lakdawala V K and Moruzzi J L 1980 *J. Phys. D* **13** 1439
[14] Christophorou L G and Olthoff J K 2001 *Int. J. Mass Spectrom.* **205** 27
[15] Matejcik S, Eichberger P, Plunger B, Kiendler A, Stamatovic A, Mark T D 1995 *Int. J. Mass. Spectrom. Ion Process* **144** L13
[16] Sauers I and Harman G 1992 *J. Phys. D* 25 774-782
[17] Baulch D L, Cox R A, Hampson R F, Kerr J A, Troe J and Watson R T 1984 *J. Phys. Chem. Ref. Data* **13** 1259
[18] Chu F Y 1986 *IEEE Trans. Electr. Insul.* **21** 693
[19] Werner H and Rosmus P 1980 *J. Chem. Phys.* **73**, 2319
[20] Lovejoy E R and Wilson R R 1998 *J. Phys. Chem. A* **102** 2309

FLUORESCENCE OF METHANE INDUCED BY ELECTRON IMPACT

Juraj Országh, Marián Danko, Štefan Matejčík, Anita Ribar

Dept. of Experimental Physics, Comenius University, Mlynska dolina F2, Bratislava, Slovakia
E-mail: orszagh@fmph.uniba.sk

Electron induced fluorescence (EIF) is a reaction where an atom or a molecule is excited by the collision with an electron and subsequently emits a photon during the deexcitation. In our experiment we have focused on the EIF of methane. Its investigation can help with understanding of elementary processes occurring in presence of low energy electrons in atmospheres (Titan), thermonuclear plasma and also provide information on reaction dynamics. Such data are valuable for both experimentalists (optical emission spectroscopy) and theoreticians focused on modelling. The collision of electron with methane molecules leads to production of electronically excited fragments. These can subsequently deexcitate by photon emission. We observed radiation transitions corresponding to Balmer's series, CH fragments A-X, B-X and C-X, CH^+ B-A and CI. In the first phase the emission spectra studied and then the relative excitation curves of individual transitions were measured. From these data the threshold energies were determined by fitting the data by appropriate set of functions. Some of the measured transitions were not measured in the past. The reason seems to be the high sensitivity of our experimental apparatus. Excitations curves and threshold energies were determined for H(6,7,8,9-2) and CH B-X (314.5nm) transitions.

Collisions of electrons with methane play an important role in several areas of physics and chemistry. This arises from the fact that methane is present in planetary atmospheres (like for example Earth, Jupiter or Titan) as well as in the interstellar medium. Moreover, applications can be found for thermonuclear fusion plasmas. Aarts et al. [1] published a paper on radiation of methane fragments. Beenakker et al. [2] were investigating small hydrocarbons, among which methane was as well. They determined the threshold energies of fragments. Radiation from the same fragments as in methane was investigated in paper aimed at electron impact of isoxazole [3] or furan [4].

Using the experimental apparatus described in [5] we are able to obtain results with higher accuracy than in previous studies.

The electron beam is generated by trochoidal electron monochromator and molecular beam is produced by effusive capillary. The collision of electron with a molecule of methane, leads to electronic excitation. Such an excited molecule is unstable and fragments into several excited fragments. These can subsequently deexcitate by photon emission. We observed radiation transitions are Balmer's series H_α (3-2) up to H_η (9-2), CH fragments $A^2\Delta \rightarrow X^2\Pi$, $B^2\Sigma^- \rightarrow X^2\Pi$ and $C^2\Sigma^+ \rightarrow X^2\Pi$, CH^+ $B^1\Delta \rightarrow A^1\Pi$ and CI transition $3s^1P^0 \rightarrow 2p^2\,^1S$. Some of them are marked in the spectrum (Fig. 1).

In the first phase of the investigation we measured the emission spectrum using an electron beam with constant energy. In the Figure 1 a sample spectrum taken at electron energy 50eV can be seen. The bands correspond to various transitions of methane fragments (Balmers series, CH fragments, CH^+ ions or atomic transition of carbon). The rotational lines of the P, Q and R branches of the CH($A^2\Delta \rightarrow X^2\Pi$) (0,0) in the region from 410nm to 450nm wavelength can be seen as well. These were detected by Wasowicz et al. As well [6]. Emission spectra were measured at different electron energies (100eV, 85eV, 70eV, 50eV, 40eV). Some parts of the spectra were compared to theoretical spectra generated by Lifbase and there was very nice agreement with experimentally measured bands.

The second mode of electron induced fluorescence measurement is determination of excitations curves for each transition seen in the spectrum.

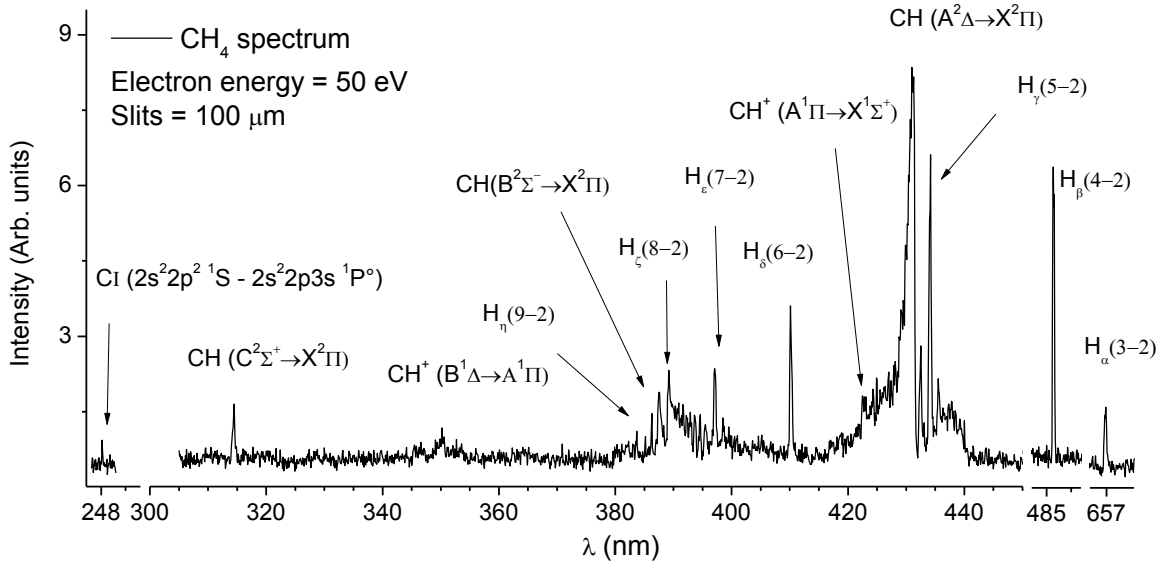


Fig. 1. Example of the measured spectrum. Some lines from Balmer's series as well as P, Q, and R branches of CH (A-X) and C (B-X) can be seen.

After the measuring of excitation curve at the exact wavelength that corresponds to each of the transition, we could determine threshold energy, the energy at which the examined transition starts to be active. Then the results were compared with the values determined by other authors [1][7][8], which is represented in Table 1. Some of the transitions could not been measured before, but due to the high sensitivity of our apparatus, excitation curves and threshold energies were determined for H(6,7,8,9-2) and CH $B^2\Sigma^- \rightarrow X^2\Pi$ (314.5nm) transitions.

Tab. 1. Comparison of first energy thresholds determined experimentally, theoretically and by other authors [1], [7], [8] for individual processes.

	Fragment	Transition	Wavelength (nm)	Threshold energy (eV)				
				Calc.	Present	Motohashi	Aarts	Donohue
1	$CH_3(X)+H^*$	H_α (3-2)	656.9	16.65	17.3±0.15	20.2	21.9±0.5	
2	$CH_3(X)+H^*$	H_β (4-2)	486.4	17.30	18.3±0.15	20.5	21.8±0.5	22
3	$CH_3(X)+H^*$	H_γ (5-2)	434.2	17.61	19.4±0.2	20.7	22.3±0.5	22.6
4	$CH_3(X)+H^*$	H_δ (6-2)	410.1	17.77	19.6±0.2	21		
5	$CH_3(X)+H^*$	Hε (7-2)	397.1	17.868	19.6±0.3			
6	$CH_3(X)+H^*$	H_ζ (8-2)	389.2	17.933	19.7±0.3			
7	$CH_3(X)+H^*$	H_η (9-2)	383.7	17.978	24.3±0.3			
8	$CH(A)+H+H_2$	$A^2\Delta \rightarrow X^2\Pi$	430.9	12.01	12.24	14.2	14.6	13.4
9	$CH(B)+H+H_2$	$B^2\Sigma \rightarrow X^2\Pi$	387.5	12.33	12.6			
10	$CH(C)+H+H_2$	$C^2\Sigma^+ \rightarrow X^2\Pi$	314.5	13.08	13.4			13.9
11	$CI+2.H_2$	$3s^1P^0 \rightarrow 2p^2\ ^1S$	248.2	13.2	20.6			
12	CH^+	$B^1\Delta \rightarrow A^1\Pi$	350.2	26.25	27.6			31.6

In the figure 2 the example of the excitation curve measurement is shown. The curves were fitted by convolution of two functions to determine the threshold value.

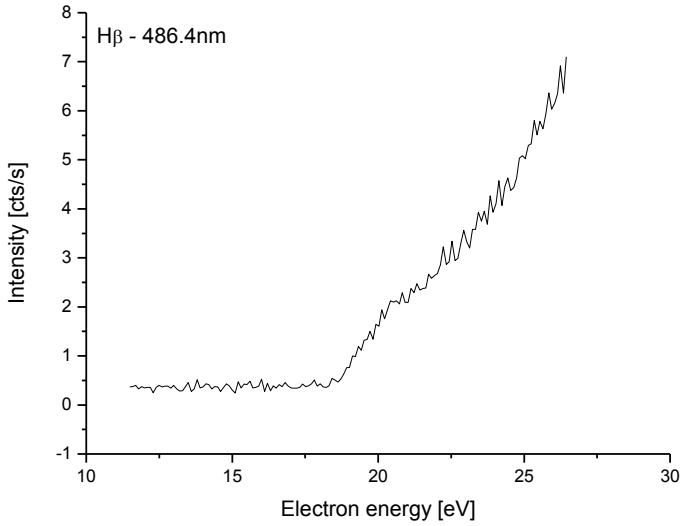


Fig. 2. Example of the measured excitation curve for H_β line.

The electron induced fluorescence of methane was studied by crossed beams method experiment. The spectra at different electron energies were measured and the bands corresponding to individual transitions were identified. For each transition the excitation curve was measured and the threshold for the process was determined by fitting procedure.

References

[1] Aarts J. F.M., Beenakker C.I.M., and De Heer F.J., *Physica* **53**, 32-44 (1971)

[2] Beenakker C.I.M., and De Heer F.J., *Chemical Physics* **7**, 130-136 (1975)

[3] Linert I., Lachowicz I.,Wasowicz T.J., Zubek M., *Chemical Physics Letters* **498**, 27-31 (2010)

[4] Dampc M., Zubek M., *International Journal of Mass Spectrometry* **2777**, 52-26 (2008)

5) Országh, J., Danko, M., Ribar, A., Matejčík, Š., *Nucl. Instr. Meth. B* **279**, 76-79 (2012)

6) Wasowicz, T.J., Kivimaki, A., Dampc, M., Coreno, M., de Simone, M., Zubek, M., *Physical Review A* **83**, 033411 (2011)

7) Motohashi, K., Soshi, H., Ukai, M., Tsurubuchi, S., *Chem. Phys.* **213**, 369-384 (1996)

8) Donohue, D.E., Schiavone, J. A., and Freund, R.S., *J. Chem. Phys* **67**, 769-780 (1977)

PLASMA PARAMETERS AFFECTING DEPOSIT GROWTH DURING ARC CARBON NANOTUBES SYNTHESIS

Grzegorz Raniszewski

Technical University of Lodz
Institute of Mechatronics and Information Systems
ul. Stefanowskiego 18/22, 90-924 Lodz, Poland
E-mail: grzegorz.raniszewski@p.lodz.pl

One of the most effective technique of carbon nanotubes synthesis is a method where an electric arc plasma is used. In this system one of the most important parameters for the process is the arc discharge. Although the synthesis method is well known the thermodynamic phenomena during discharge CNTs synthesis are still under investigation. Plasma composition changes due to temperature and local pressure plasma. Electrons density influences on electrical and thermal parameters of the arc and in effect on temperature. In this paper the process of carbon nanotubes synthesis by plasma arc was presented. The helium-carbon arc parameters were calculated. Catalyst introduction to the plasma was discussed and plasma parameters with different amount of catalyst was compared.

1. Introduction

A common technique for the production of carbon nanotubes is the electric arc discharge method in which graphite electrodes are as a source of carbon. In the arc discharge method electric arc burns between two graphite electrodes in the neutral gas – usually He or Ar. The diameter of the electrodes may vary from 4 to 8 mm for the anode and from 10 mm to flat surface for the cathode. In our system 6 mm anodes and 50 mm cathodes were applied. The temperature in the arc channel axis is about 5000K. This temperature leads to vaporization of graphite anode and forms carbon-gas plasma. Carbon atoms are deposited on the cathode surface as a mixture of different forms of carbon, soot, fullerenes and nanotubes.

During carbon nanotubes synthesis with the arc plasma the essential are: voltage, current, pressure, ambient gas, dimensions of electrodes, electrodes spacing, presence of catalyst and plasma composition. When the metal catalyst is inserted metal molecules determine plasma parameters. In this case single-walled carbon nanotubes instead of multi-walled carbon nanotubes are generated. Thermal processes in the plasma may be a basis for understanding carbon nanotubes growth conditions

Anode and cathode are placed in a hermetic chamber, equipped with the diagnostic windows and the inlet/outlet gas systems. The distance between electrodes – up to 2 mm - ensures generation of a stable arc discharge as an effect of voltage and it is controlled be an automatic control system. The arc current density is set from 0,05 A/mm^2 to 15 A/mm^2. Current density influences on erosion rate and on final product quality. In fact large arc current increases the temperature what leads to thermal destruction of nanoparticles and their vitrification in the cathode deposit. Otherwise lower current may reduce temperature below the boiling point of carbon which prevents the nanoparticles formation. But temperature is not only an effect of voltage but also an effect of plasma arc composition. The study of the basic phenomena occurring in the electric arc plasma allow to understand the thermodynamic factors determining the synthesis of carbon nanotubes. The effect of the plasma arc composition on the arc discharge was investigated for many technological applications but these studies concerned atmospheric plasma, mineral components and argon – air plasma [1]

To remove an oxygen from the set-up the synthesis process begins with repetitive evacuation of the chamber and filling it with inert gas – helium or argon. The control system adjust the pressure to the appropriate level – usually between 0,1 and 0,5 bar. After setting the pressure two electrodes are connected and heated by high current. Then the anode is moved to make a distance between electrodes, current is reduced to set value and the synthesis process begins.

The erosion rate of the anode vary from 6 to 20 mm/min. Over 70% of anode loss is deposited on a relatively cold cathode. In the Fig. 1 is shows typical cathode deposit and its cross-section structure. Two main parts of deposit are hard outer shell and soft core. Soft core is about 30% - 60% of deposit and over a half of this soft core are carbon nanotubes.

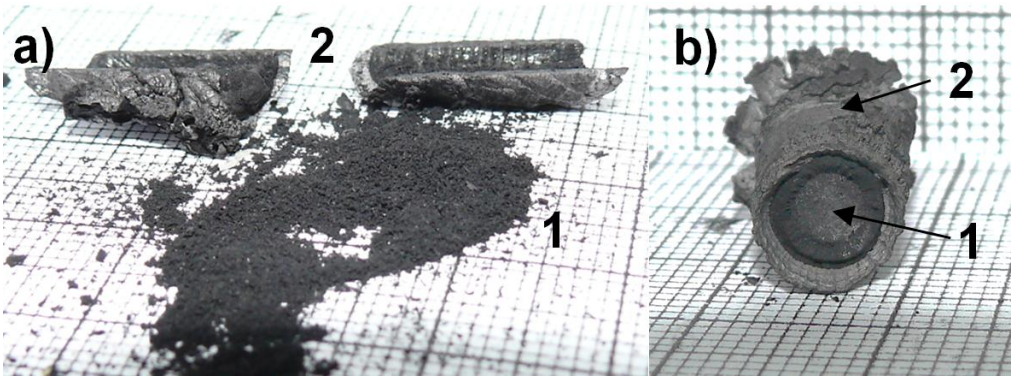


Fig. 1. Cathode deposit where 1 – soft core with nanotubes, 2 – hard shell a) separated parts of deposit b) deposit cross-section.

2. Calculations

Although the process of synthesis is the subject of worldwide research [2-14] and it is already well developed - the exact phenomena that occur in this process are not known. Understanding of all phenomena allows to maximize the efficiency. Determination of thermodynamic parameters (such as the composition of the plasma) is an attempt to provide data for calculation the electrical parameters - such as electrical conductivity, the effective ionization potential, thermal conductivity, etc. This fact will allow to estimate of local temperatures in the areas of synthesis of nanotubes and their environment.

The calculations assume that the arc burns between pure carbon electrodes. Helium is a working gas at a pressure of 0,5 bar. Thereby, produced plasma is composed mainly of electrons (N_e), atoms of graphite (Nc), atoms of gas (N_{He}), ionized graphite (N_c^+) and ionized helium (N_{He}^+). Due to the process temperature (about 5000K) the second and subsequent stages of ionization is negligible. In following calculations the state of local thermodynamic equilibrium (LTE) is assumed. In order to determine the composition of the plasma arc in an atmosphere of carbon-helium Saha-Eggert equation for each component has been used:

$$\frac{N_+ \cdot N_e}{N_0} = S(T) \tag{1}$$

Where:

$$S(T) = 2 \cdot \frac{u_+(T)}{u(T)} \cdot \frac{(2 \cdot \pi \cdot m \cdot k \cdot T)^{3/2}}{h^3} \cdot \exp\left(-\frac{E - E_v}{kT}\right) \tag{2}$$

Because we assume five components plasma we need five equations to determine the plasma compositions. To solve this system of equations can be used Dalton's law:

$$p = (N_{He} + N_{He+} + N_C + N_{C+} + N_e) \cdot k \cdot T \tag{3}$$

The equation for the electron density in the conditions of local thermodynamic equilibrium:

$$N_e = N_{C+} + N_{He+} \tag{4}$$

The equation for the percentage amount of carbon:

$$x = \frac{N_C + N_{C+}}{N_C + N_{C+} + N_{He} + N_{He+}} \tag{5}$$

In equations 1-5 the following designations have been used:

$u_{He}(T)$, $u_{He+(}T)$ – partition function of helium and single ionized helium, respectively.
$u_C(T)$, $u_{C+(}T)$ – partition function of carbon and single ionized carbon, respectively;
m – electron rest mass;
h – Planck's constant;
k – Boltzmann's constant;
E_{He}, E_C - ionization energy for helium and carbon, respectively;
ΔE_{He}, ΔE_C – lowering of ionization energy for helium and carbon, respectively;
T – absolute temperature [K];
$\Delta\chi$ - lowering of ionization energy

Different compositions of carbon-helium plasma have been considered to establish correlation between metal density and electron amounts.

3. Results

Calculations have been conducted for 0,5 up to 5% carbon ratio in helium plasma. Fig. 2 shows concentration of carbon-helium plasma components in function of temperature at the pressure of 0,5 bar. Different compositions of carbon-helium plasma have been considered to establish correlation between carbon density and electron amounts.

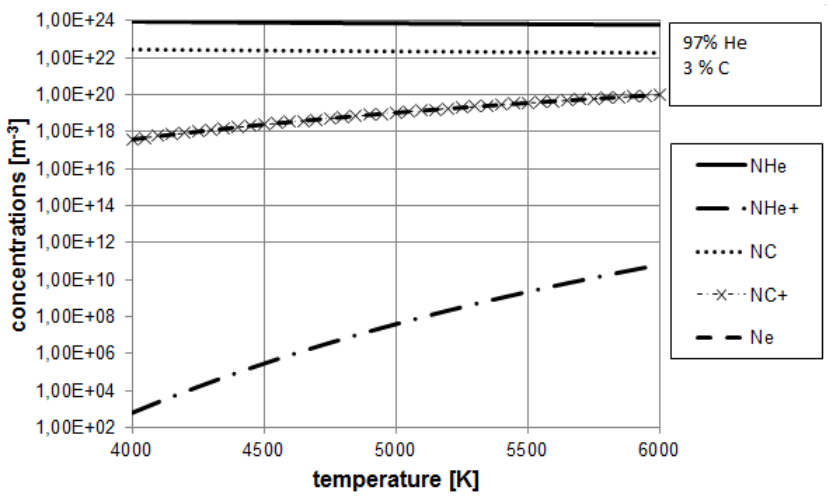


Fig.2. Concentration of plasma components for helium-carbon plasma for 3% amount of carbon.

With the temperature the number of unionized particles decreases leading to the release of the electrons and increase their concentration. More energy leads to higher concentrations of helium ions (NHe+) and carbon ions (NC+). However we can notice that there is much more ions of carbon than ions of helium and there is almost the same concentration of carbon ions as concentrations of electrons (Ne). It means that most of the electrons in electric arc discharge are from electrodes material and ions of carbon are only carriers of building material for nanotubes. In many applications additional element – catalyst – is applied to the process what means additional two components in plasma (neutral catalyst and ions of catalyst). It was proved that the influence of the gas on electron density is minimal so for simplification in the following calculations helium is omitted. Plasma still consists of 5 elements – but instead of helium for calculations additional catalyst is assumed. The most popular element in nanotechnology processes is iron. Fig. 3 plasma composition with iron as a catalyst with 0,1% of Fe, and Fig.4. shows the comparison of influence of iron concentration on electron density.

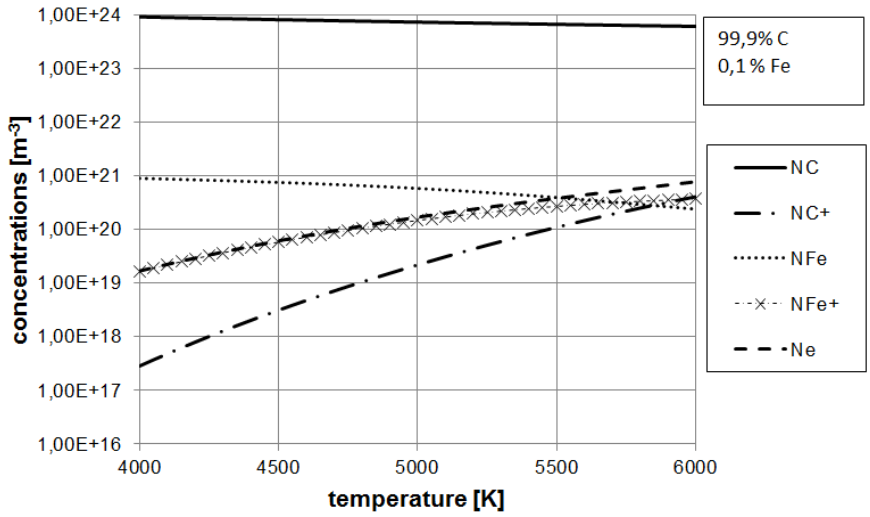


Fig. 3. Concentration of plasma components for carbon-iron plasma for 3% amount of iron

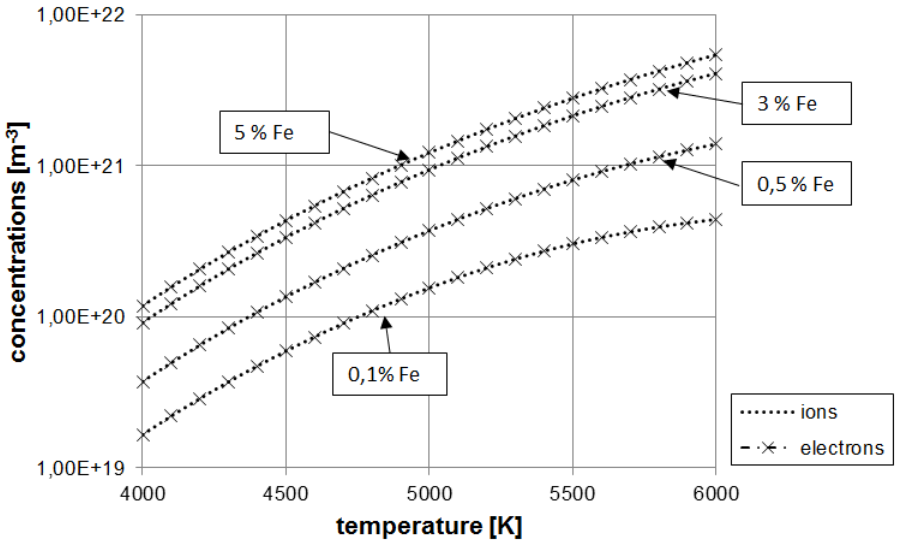


Fig. 4. Comparison of electrons and ions densities for different amounts of iron.

Presence of catalyst e.g. iron strongly changes parameters of synthesis what leads to creation of completely different nanoparticles. The plasma parameters with minimal amount of iron is presented in Fig.3. It can be seen that electron density strongly depends on catalysts presence. That means that electrons for arc formation comes almost entirely from a catalyst.

4. Conclusion

In this paper, we have presented an effect of carbon presence in helium plasma. Double and multiatom gases enable to carry much more thermal energy than in case of one atom gases [15]. It has been estimated that minimal amount of carbon vapour strongly changes plasma composition what results by changing plasma properties. Estimate of influence for these components is connected with calculation of equilibrium and thermodynamics parameters. Additional carbon in the neutral gas in which burns an electric arc change heat transport conditions due to their thermal conductivity. Due to electrons concentrations the resistance and electrical conductivity is changed. In plasma stream with molecular gases there have been created a large amounts of unbounded atoms.

Electric arc stability depends on two factors: source quality parameters and resistance changes during the process. The resistance influence voltage. Additions of iron changes effective ionization potential and in effect conductance. In this paper, we have presented an effect of iron presence in carbon plasma arc. Even 0,1% of metal vapour determine electron quantity in plasma in temperature up to 6000K what is sufficient in the most technologies. Number of electrons influences on electric parameters and thermodynamic state.

The calculation results showed that the addition of a catalyst such as iron increases electron density. This fact improves the conditions for the arc discharge and finally increases chance for maintaining the continuity of the discharge under rapid changes of additional components concentrations in the plasma.

Acknowledgements

The scientific work has been financed from the budget for science in the years 2010-2012 as a research project.

5. References

[1] Raniszewsk G, PhD Thesis, Technical University of Lodz (2009)
[2] Journet C, Bernier P *Appl. Phys. A*, **67**, Issue 1, (1998),1–9
[3] Ebbesen TW, Ajayan PM (1992) *Nature* 358 (6383), 220-222
[4] Kiselev NA, Moravsky AP, Ormont AB, Zakharov DN (1999), Carbon **37** (7), 1093.
[5] Colbert D, Zhang J, McClure S, Nikolaev P, Chen Z, Hafner J, Owens D, Kotula P, Carter C, Weaver J (1994) Science **266** (5188), 1218
[6] Morishita K, Takarada T (1999) J Mater Sci **34** (6), 1169.
[7] Zhao J, Zhang J, Su Y , Yang Z , Wei L, Zhang Y, *J Mater Sci* (2012) **47**, 6535–6541
[8] Zhao X, Ohkohchi M, Wang M, Iijima S, Ichihashi T, Ando Y (1997) *Carbon* **35** (6):775.
[9] Cui S, Scharff P, Siegmund C, Schneider D, Risch K, Klotzer S,Spiess L, Romanus H, Schawohl J (2004) Carbon **42** (5–6), 931.
[10] Mao BD, Kang ZH, Wang EB, Tian CG, Wang CL, Lan Y (2006*) J Nanosci Nanotechnol* **6**(5), 1392
[11] Borisenko DN, Kolesnikov NN, Kulakov MP, Kveder VV, *International Journal of Nanoscience*, **Vol. 1,** Nos. 3 & 4 (2002) 235–246
[12] Tingkai Zhao, Yongning Liu, *Carbon* **42** (2004) 2735-2777
[13] Yudasaka, M.; Kasuya, Y.; Kokai, F.; Takahashi, K.; Takizawa, M.; Bandow, S.; Iijima, S. *Applied Physics A Materials Science & Processing* Volume: **74**, Issue: 3, March, 2002, pp. 377 – 385
[14] Lange, H.; Sioda, M.; Huczko, A.; Zhu, Y.Q.; Kroto, H.W.; Walton, D.R.M. *Carbon* Volume: **41**, Issue: 8, 2003, pp. 1617-1623
[15] Brzeski J (Ed.), Chemia plazmy niskotemperaturowej, Wydawnictwa Naukowo-Techniczne, Warszawa 1987

PLASMA ARC FOR CARBON NANOTUBES SYNTHESIS DEDICATED FOR MEDICAL APPLICATIONS

Grzegorz Raniszewski

Technical University of Lodz
Institute of Mechatronics and Information Systems
ul. Stefanowskiego 18/22, 90-924 Lodz, Poland
E-mail: grzegorz.raniszewski@p.lodz.pl

The article presents the plasma synthesis method of carbon nanotubes using an electric arc discharge. In this method different carbon nanotubes are produced as a cathode deposit growth or are deposed on a various substrates such as silicon, metals and other materials. The examples of applications of carbon nanotubes in medical applications were presented. Conditions required for the synthesis of carbon nanotubes and process parameters were determined. Synthesis of carbon nanotubes with iron was described. Applications of carbon nanotubes for cancer treatment were discussed.

1. Introduction

Nanotechnology is one of the fastest-growing technologies. Carbon nanotubes are widely used in many industry branches – chemical, defence, automotive, food, textile, cosmetics, etc. One of the most promising areas is medicine. Depending on the type of nanoparticles it can be used to improve the sensitivity of diagnostic tools, to manufacture of surgical instruments. They may also be used as carriers for slowly released drugs. Nanoparticles appropriately addressed can detect and deliver chemicals to cancer cells without destroying healthy cells. Combination of nanoparticles with drugs would be a milestone for novelty medicine. These nanoparticles should have many characteristic parameters such as purity, size, shape. The quality of the product, composed mostly of carbon nanotubes (CNTs), depends on parameters of synthesis such as pressure, gas composition, temperature. CNTs possess a one-dimensional nanostructure, which are characterized by high strength, high thermal conductivity, high electrical conductivity and electronic properties ranging from metallic to semiconducting. These graphitic forms can be divided into two main groups: single-walled CNTs (SWNTs) and multiwalled CNTs (MWNTs).
SWNTs are formed by wrapping a one-atom-thick layer of graphite called graphene into a cylinder. Multi-walled nanotubes (MWNT) consist of multiple rolled layers (concentric tubes) of graphite. There are other forms of carbon nano-scale such as the nanohorns, nanowires; several types of fullerenes (Fig.1.).

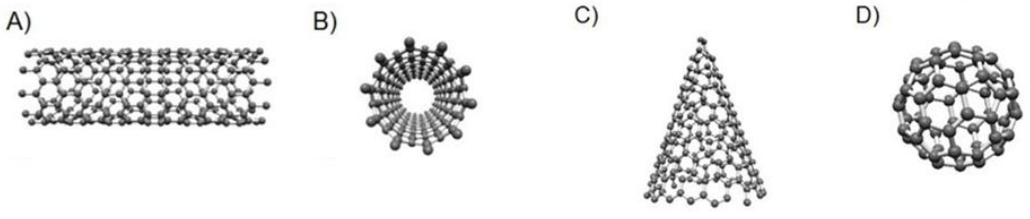


Fig.1. A) SWNT – side view, B) SWNT – top view, C) nanohorn, D) fullerene

The product of synthesis is a mixture of different types of carbon. The research objective is to determine the optimal conditions for creating a product with the desired properties.

2. Medical applications

Progress in the functionalization created many new opportunities for applications including medicine. Worldwide research can be divided into two main groups: diagnostics and treatment. Diagnostic applications exploit new electronic devices containing CNTs, nanoelectroedes, nanomaterials, nanopowders etc. Treatment applications are connected with drugs delivery and release.

CNTs have a large potential as drug delivery systems because their size. A few examples of delivery of therapeutic agents as carrying proteins into the are described in the literature [1]. Wu and coworkers connected CNTs with one of the most effective antimycotic molecules for the treatment of chronic fungal infections – AmB [2]. Disadvantage of AmB is its toxicity and side effects range which may even lead to destruction of healthy cells [3]. The conjugation of AmB to the tubes modulated its therapeutic effect by decreasing mammalian toxicity and increasing the antifugal activity.
SWNTs with a carborane cage can be used for boron capture therapy [4]. Boron Neutron Capture Therapy (BNCT) is a method of cancer treatment, especially for brain tumors. In the BNCT method the boron components are injected into the human body, selectively deposited in tumor tissue. SWNTs improve selectivity and protect healthy cells. Then the patient is irradiated with neutron beam. Particles with a large energy and short range are produced as a result of reaction radiation with boron, thus destroying the local cancer cells but it has limited cellular uptake. Another well-known anticancer molecule used in cancer treatment is methotrexate (MTX), but it has limited cellular uptake. It was proved that it is possible to increase the ability to cross the cell membrane by conjugation CNTs with MTX [5].
Another application of CNTs in cancer therapy is its ability to absorb NIR irradiation [6]. SWNTs with folic acid are taken up by cancer cells which were then destroyed by a laser wavelength of 808nm. Tumor cells with nanotubes are heated and consequently destroyed. CNTs with iron can be heated by RF wave. Carbon nanotubes could be also used to introduce drugs or other substances into human cells, however influence of CNTs on the human body is not known so far.
The specific form of nanocarbon are carbon nanotubes comprised of a single layer of graphitic carbon and exhibits an irregular horn-like shape. These structures are called single walled nanohorns (SWNHs). Dexamethasone and cisplatin are chemotherapy drugs used to treat various types of cancers but they have a lot of side effects as kidney damage, nerve damage, nausea and vomiting, hearing loss, high electrolyte disturbance and strongly decreases the morphology of the blood. Carbon nanohorns can be used to encapsulate these anticancer agents [7, 8]. Drugs can be slowly released into the pathologically changed cells.
There are just a few examples of worldwide research carried out in bionanotechnology area. There are a variety of uses in diagnostics. But both the treatment and diagnosis require a appropriate synthesized nanotubes.

3. Plasma for carbon nanotubes synthesis

Several techniques can be used to synthesize CNTs. The most popular are arc-discharge, chemical vapour deposition (CVD) and laser ablation. The CNTs prepared by all methods are mixtures of different tubes with broad size, chirality, structure and properties with impurities containing mostly amorphous carbon. In our laboratory our research focus on plasma and CVD methods [9-16].
It involves a high-density current flow through a thin graphite rod. The generated heat leads to the graphite evaporation, and then condensation on the walls of the synthesis chamber or on cathode surface. This system was initially used for the production of fullerenes, and then was modified by applying an electric arc. Figure 2 shows the system used in our research.

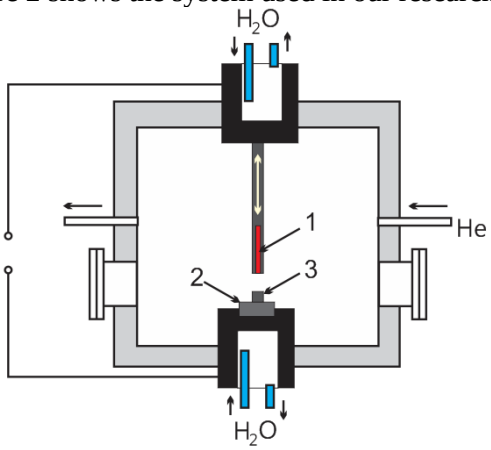


Fig.2. System for arc carbon nanotubes synthesis – 1 – anode with catalyst, 2- cathode, 3 – deposit

In our system the process begins by filling plasma reactor with helium or argon at a pressure 0,5 atm. The electric arc burns between two graphite rods. The distance between rods is constant and is about 1-2 mm. Vapors of carbon move from anode spot, through a short arc column of about 5000K temperature and enter into a cathode zone. Thermodynamic and electrical parameters of cathode region determine the efficiency of the carbon nanotubes synthesis. As soon as the deposition process starts, the local electric field increases due to the formation of micro-roughness on the surface of the cathode. Electron field emission becomes dominant over the thermoelectron emissionA relatively low temperature of the cathode surface allows to starts the process of the CNTs deposition. Physical parameters for short arc plasma for switching devices are described in literature [17]. The synthesis phenomenon in cathode zone is not theoretically elaborated up to now. The phenomenon responsible for the deposit growth is the anode stream [14-16].

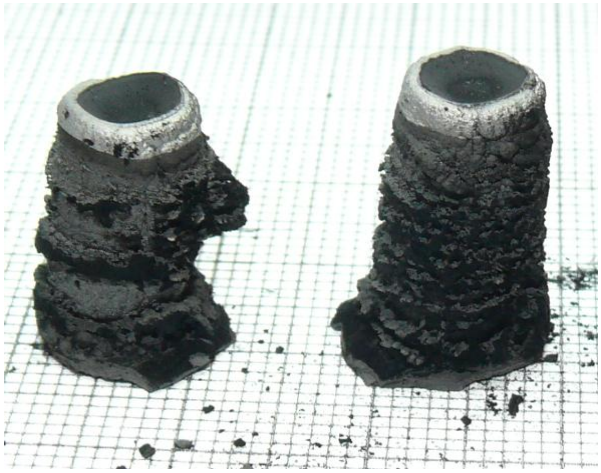


Fig.3. Cathode deposits

The second factor determining the synthesis is thermal destruction of CNTs settled on the surface of the cathode. It is important to maintain a proper temperature process, especially in the deposition sector to avoid CNTs destruction. Therefore anode and cathode should be cooled by water.
A typical cathode deposit has a structure of hard coating (shell) and soft core (Fig.3). The shell is a waste and the core is a product which is composed of a multi-walled carbon nanotubes MWNTs, fullerenes and soot (Fig. 4). It has been estimated that maximum 25% of the anode vapour turns into nanotubes [14-16].
Nanotube formation process depends on many factors including quite a large difference of density and conductivity of electrodes, grain of the graphite, configuration of electrodes, the physical process parameters (current, temperature, pressure, etc.). Conducted research focuses on identifying the key parameters of the synthesis process. The soft core needs purification before using.

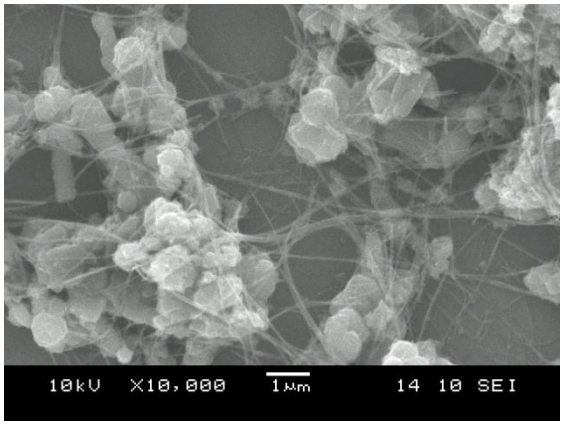


Fig.4. CNTs with impurities from cathode deposit.

4. Carbon nanotubes with iron

Synthesis of carbon nanotubes can be conducted with the presence of a catalyst. The presence of catalysts is also an important condition for receiving SWNTs, which can be found in the soot condensation on the inner walls of the chamber. This changes the appearance of soot, which is no longer loose, and is in the form of thin sheets or tangled threads.

During plasma carbon nanotubes synthesis catalyst may be introduced into the arc in the form of gas (as a ferrocene or pentacarbonyl). Iron may be also applied also in solid form. In this case anode is hollowed and mixture of carbon and iron is placed inside anode. This mixture vaporize due to arc heat and creates a plasma cloud in the synthesis process surroundings. The anode may also be covered with iron. It is also possible to use electrodes made of graphite with iron. Catalyst can also be sputtered on different substrates and placed inside the reaction chamber.

When a microwave plasma is applied catalyst is introduced in gaseous form (pentacarbonyl or ferrocene), or is a placed as a component of substrates where carbon nanotubes growth occures.

Depending on the parameters of the synthesis the iron can be encapsulated inside the nanotubes or attached to the surface. Nanotube with iron can be used in a variety of applications - in particular in medicine for cancer diagnosis and therapy. One of the therapy is described as a Kanzius therapy [18]. It has been patented by ThermMed LLC founded by the inventor of the method - John Kanzius. [19,20] The idea of the therapy is the introduction of metallic nanoparticles to cancer cells and then stimulating them with RF waves. The energy from radio waves creates heat, which destroys a group of cancer cells. This method is still under investigation.

Depending on the type of nanoparticles, they can also be used to improve the sensitivity of diagnostic tools such as the magnetic resonance and it can be a donor for slowly release drugs. It is believed that nanoparticles supplied with ferromagnetic material will be easier to manipulate inside the human body what improve selectivity of the applied therapies.

5. Conclusions

Using arc-discharge method MWNTs without catalyst and SWNTs with yield up to 90% can be easily produced. The main disadvantage is that SWNTs may contain some defects and tubes tend to be short with random sizes and directions. The advantage of this method is low cost and possibility to synthesis in an open air. The discovery of nanotubes has contributed significantly to the development of nanotechnology. Today, it seems that the possibilities of using carbon nanotubes are unlimited. Medicine is an especially promising area for nanotechnology. Although several studies have already been taken it seems that much more remains to be done. The presented article focused on some possible applications especially of ferromagnetic CNTs.

Depending on various electrical parameters of the arc during the synthesis of nanomaterials we can get different levels of purity and quality of the nanotubes. Impurities consist of catalyst residues and amorphous carbon. A large amount of impurities may increase the toxicity of the material. The presence of residual amorphous carbon and trace metals catalysts can affect cell viability. Very important is the size of nanotubes. Smaller particles have larger area and higher toxicity, short nanotubes have less inflammatory response therefore final product needs purification and in many cases subsequent functionalization.

Despite the promising possibility of targeting the use of carbon nanotubes in medicine is associated with a number of issues which require detailed research, such as diagnosis and delivery, methods of preparation, functionalization of nanomaterials, characterization, etc.

Acknowledgements

Scientific work financed from the budget for science in the years 2010-2012 as a research project

6. REFERENCES

[1] Kam NWS, Dai H, *,J.Am. Chem. Soc.* (2005), **127**, 6021-6026

[2] Wu W, Wieckowski S, Patorin G et.al., *Angew. Chem. Int. Ed.* (2005), **44**, 6358-6362

[3] Gruda I, Milette D, Brother M, Kobayashi GS, Medoff G, Brajtburg J, *Antimicrob Agents Chemother*, **35** (1991) 24-28.
[4] Yinghuai Z,. Peng AT, Carpenter K, *J. Am. Chem. Soc*. (2005), **127**, 9875-9880
[5] Postorin G, Wu W, Wieckowski S et. al., *Chem. Commun*., (2006), 1182-1184
[6] Kam NWS, O'Connell M, Wisdom JA et. al., *Proc. Natl Acad. Sci. USA*, (2005), **102**, 11600-11605
[7] Murakami T, Ajima K, Miyawaki K et al., *Mol. Pharm*, 2004, **1**, 399-405
[8] Ajima K, Yudusaka K, Murakami M et al., *Mol. Pharm*, 2005, **2**, 475-480
[9] Kolacinski Z, Wiak S, Raniszewski G, Szymanski L, *Elektronika – konstrukcje, technologie zastosowania*, 2011-**10**, 122-124
[10] Kolacinski Z, Raniszewski G, Szymanski L, *Metal influence on plasma parameters in CNTs synthesis*, 6th International Conference on Surfaces, Coatings and Nano-Structured Materials NANOSMAT 2011, Kraków, 2011
[11] Kolacinski Z, Raniszewski G, Szymanski L, *CNTs Synthesis in a Microwave Plasma*, 22nd European Conference on Diamond, Diamond-Like Materials, Carbon nanotubes and Nitrides, Garmisch-Partenkirchen, Bavaria, Niemcy, 2011
[12] Kolacinski Z, Szymanski L, Raniszewski G, *Synteza nanorurek węglowych metodą CVD z wykorzystaniem plazmy mikrofalowej*, V Krajowa Konferencja Nanotechnologii NANO 2011, Gdańsk, 3-7.07.2011
[13] Kolacinski Z, Szymanski L, Raniszewski G, Druri M, *In-flow continuous CNTs deposition*, 2nd International Conference from Nanoparticles & Nanomaterials to Nanodevices & Nanosystems, Rhodes, Greece, 23 June-3July, 2009, s.91
[14] Kolacinski Z, Mitura S, Szymanski L, Kaczorowski W, *Arc Discharge Parameters Affecting Carbon Nanotubes Growth in the Catalyst Free Environmen*t, 19th European Conference on Diamond, Diamond-Like Materials, Carbon Nanotubes and Nitrides, Sitges, Spain, (2008)
[15] Kołacinski Z, Mitura S, Szymanski L, Kaczorowski W, *Conditions Affecting Carbon Nanotubes Growth in the Arc Discharge*, 1st International Conference from Nanoparticles & Nanomaterials to Nanodevices & Nanosystems, Halkidiki, Grecja, (2008)
[16] Kolacinski Z, Mitura S, Szymanski L, KaczorowskivW, Raniszewski G, *Effective Growth of Carbon Nanotubes in the Arc Discharge*, II Krajowa Konferencja Nanotechnologii, Kraków (2008)
[17] Kolacinski K, *Thermodynamics of short-arc plasma ed.* PWN Warsaw (1989)
[18] Gannon CJ, Cherukuri P, Yakobson BI, Cognet L, Kanzius JS, Kittrell C, Weisman RB, Pasquali M, Schmidt HK, Smalley RE, Curley SA. *Cancer*. 2007 Dec 15;**110**(12):2654-65.
[19] United States Patent No.: US 7,510,555 B2 *Enhanced systems and methods for RF-induced hyperthermia*
[20] United States Patent No.: 4,674,481 *RF electromagnetic apparatus for regionally-focused hyperthermia*

TEMPORAL AND SPECTRAL CHARACTERISTICS OF ATMOSPHERIC PRESSURE PLASMA JET

Jüri Raud, Indrek Jõgi, Matti Laan

Institute of Physics, University of Tartu, Tähe 4, 51010 Tartu, Estonia
E-mail: juri.raud@ut.ee

An investigation of atmospheric pressure argon DBD plasma jet generated at 6 kHz sinusoidal voltage was carried out. On the basis of recorded electrical, optical and spectral characteristics spatio-temporal evolution of plasma jet in negative and positive half-cycles of voltage was studied. It was found that plasma propagation velocity in the positive half-cycle differs in- and outside of the tube considerably while in the negative half-cycle it remained constant up to the distance of 5 mm from the orifice of the tube. The different plasma propagation velocities as well as different shape of light pulses in positive and negative half-cycles outside the tube were found to be in concordance with simulation presented in [1].

1. Introduction

Materials processing needs an inexpensive remote plasma source for producing chemically active species at high concentrations which does not change the morphology and temperature of the treated material. The atmospheric pressure plasma jet (APPJ) is one of the most promising solution for this problem and has been a subject of extensive research [2].

Most of the studies carried out so far deal with APPJ driven in helium e.g. [3-5]. However, from the viewpoint of applications Ar APPJ could be desirable because it is relatively cost effective and allows efficient production of several useful chemical species (like reactive oxygen species).

Our preliminary tests of Ar APPJ influence on the surface of TiO_2 coatings of few nm thickness were promising: the products of plasma jet increased considerably the wettability of TiO_2 coating. This result was one of the reasons which triggered us to a more fundamental study of processes occurring in the Ar plasma jet. As one step in the determination of production paths of active species, the aim of the current work was to connect the evolution of emission from various plasma species with electrical characteristics of plasma jet.

2. Experimental setup

A sketch of setup is shown in figure 1. The discharge was excited in a quartz tube of 0.6 mm inside and 0.8 mm outside diameters. The powered electrode was a 2 mm wide Al foil which was wrapped around the tube. The distance between the electrode edge and the tube orifice was 12 mm. The opposite plane electrode of 100 mm diameter was grounded and it was placed at the distance of 35 mm from the tube orifice. Thus, according to the classification given in [2], our electrode configuration belonged to a DBD plasma jet. A sinusoidal voltage at 6 kHz excited the discharge in Ar flow. The temporal electrical as well as optical characteristics of jet were recorded by using TDS-540B oscilloscope. The voltage was measured with a capacitive voltage divider, C1, C2 and 1:10 probe. The current was determined from the voltage drop on the 50 Ω induction-free resistor R. The distribution of light intensity along the plasma jet was recorded moving fibre F along the 1:1 image produced by f=75 mm quartz lens. The measurements of light distribution along jet axis were carried out with ≈1 mm spatial resolution. Time-averaged spectra in 300-850 nm range as a function of position y were recorded with spectrometers Ocean Optics 4000 (ca 1 nm resolution) and MDR-23 (0.1 nm resolution). Relative spectral sensitivity was determined by using calibrated light source Ocean Optics DH-2000-Cal. Temporal changes of the light intensity emitted from different parts of the jet were recorded separately in the red (further "IR", $\lambda > 680$ nm, photomultiplier tube PMT R5108 with the infrared filter KC19), and blue ("UV", $200 < \lambda < 600$ nm, PMT 1P28A) regions. The rise time of PMT signals was ≤ 2.2 ns.

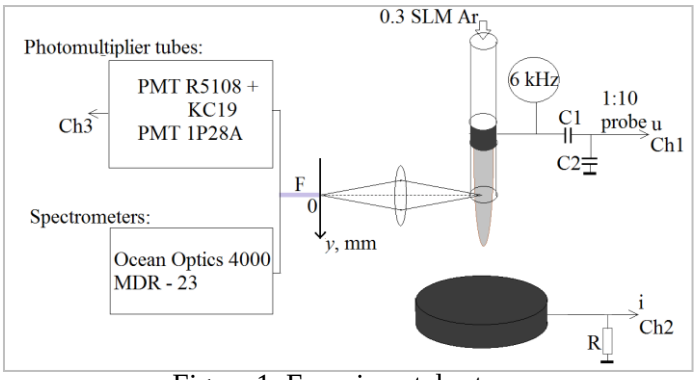


Figure 1. Experimental setup.

Figures presented below take into account the delay times caused by connecting cables and electron transit times through PMT.

3. Results and discussion

To obtain a long and a stable jet channel the gas flow should be laminar. We found that at 0.3 SLM Ar flow rate and at a fixed voltage the jet length outside the tube was the longest. At such a flow the linear gas velocity in the tube was $\approx 2 \cdot 10^4$ mm/s, corresponding Reynolds number $R_e \approx 700$ which is within laminar flow limits.

3.1 Electrical characteristics

All presented results belong to applied voltage $u_{p\text{-}p} \approx 3$ kV. At such voltage the visible part of plasma jet did not hit the opposite electrode. Generally, during a half cycle several short-duration discharge pulses arose. At the used voltage there were two current pulses during negative and positive half-cycles. Figure 2 shows the current, voltage and light waveforms. Because of a low sweep rate the recording does not pass the actual peak values of pulses. It appeared that the current pulses arose at relatively well-fixed times, the time separation of current pulses in the positive half cycle was $\approx$ 15 μs, and in the negative half cycle $\approx$ 30 μs. At the same time the peak values and waveforms of current pulses varied in wide ranges. This circumstance did not allow the averaging of current and light pulses over number of voltage cycles, i.e. our results belong to single shot recordings.

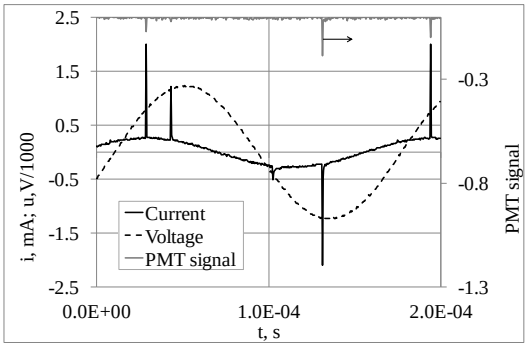


Figure 2. Measured waveforms of current, voltage and light signals.

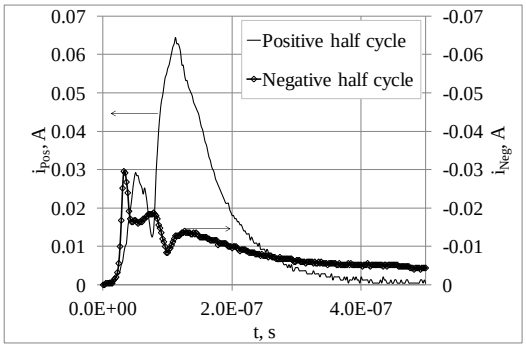


Figure 3. Current pulses at positive and negative half cycle.

In case of both half cycles the sweeps of oscilloscope were triggered from the current pulse of the corresponding half cycle. The same condition of current peak value, $0.028 < |i_{trigger}| < 0.03$ A was used for triggering of both polarities of current pulses. Following results belong to the first pulses of both half cycle polarities. Typical current pulses are presented in figure 3. The positive current pulse had two-humped structure and its half-width was $\approx$ 200 ns. The waveform of negative current pulse was more complicated and it has remarkably longer duration.

3.2 Optical measurements

Figure 4 shows time averaged spectra. At $\lambda > 650$ nm all lines except very weak atomic O line (λ=777. 4 nm) belonged to Ar. The bands recorded in the spectral region 300-400 nm belonged to OH

(A-X) and N_2 (C-B) transitions (figure 4 insets). Inside the tube Ar and OH spectra were dominating. Outside the tube (figure 4B) N_2 (C-B) bands appeared besides the OH (A-X) band. The most intensive bands among them belonged to the vibrational transitions 0-0 (bandhead at 337.1 nm), 1-0 (315.9 nm), 1-2 (353.7 nm), 0-1 (357.7 nm) and 0-2 (380.5 nm).

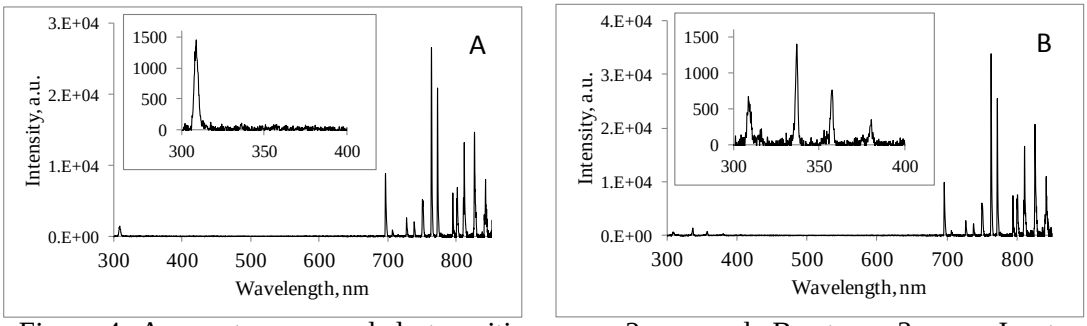


Figure 4. A- spectrum recorded at positions y = -2 mm and B- at y = 3 mm. Insets: spectra in the wavelength range λ = 300 – 400 nm.

Figure 5 presents the intensity dependence of characteristic line (bandheads) on coordinate y. Intensities of all Ar lines depended on y- coordinate similarly to λ = 763.5 nm (figure 5). The intensities of OH band in turn followed the same main trends as Ar lines. Inside the tube N_2(C-B) bands were very weak, but outside the tube in the UV region their radiation became dominating.

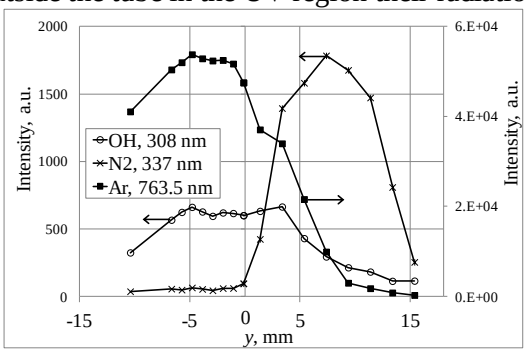


Figure 5. Intensity distribution of Ar line and OH, N_2 bandheads along the jet axis.

Rotational temperature was estimated on the basis of rotational spectra of OH(A-X, 0-0) and N_2(C-B, 0-1). Within limits of experimental uncertainties the rotational temperatures coincided. Inside the capillary the temperature was almost constant, $T \approx 330$ K, while outside the rotational temperature increased with the coordinate y and reached the value $T \approx 380$ K.

Figure 6 shows typical IR light pulses belonging to positive half-cycle.

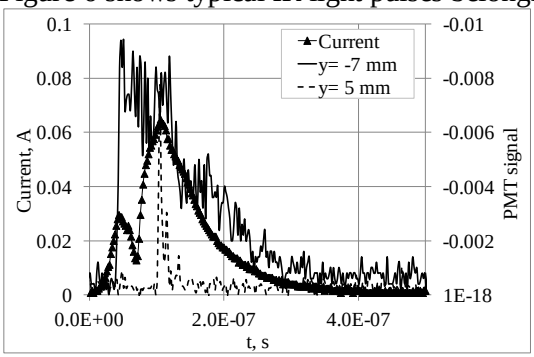


Figure 6. Current and IR light pulses in the positive half cycle at positions y=-7 mm and y=5 mm.

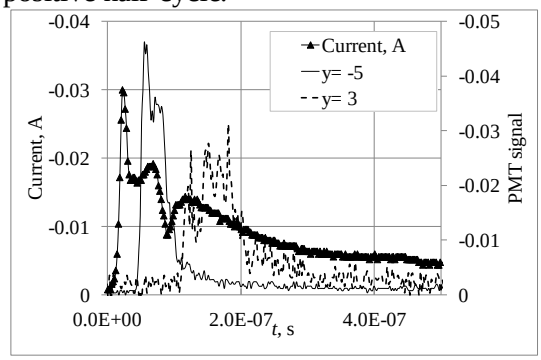


Figure 7. Current and IR light pulses in the negative half cycle at positions y=-5 mm and y=3mm.

The light pulses recorded inside and outside of the tube arose at different times and their waveforms differed considerably. The rise of the light pulses inside the tube occurred during the first hump of the current. The half-width of light pulses inside the tube decreased along jet from ≈ 200 ns near the electrode to ≈ 10 ns near the orifice of the tube. The development of the jet channel outside the tube

was related to the second hump of the current. The half-width of pulses outside the tube were ≈ 6 ns and they did not depend on the coordinate *y*.

Figure 7 shows IR light pulses belonging to negative half-cycle. Development of light pulse inside the tube is observable during the first two humps of the current. At the same time the development of jet channel outside the tube is related to the third hump of the current. Differently from positive half-cycle the half-width of light pulses inside the tube were almost constant, ≈30 ns, while outside the tube the half-width increased with coordinate *y* reaching ≈300 ns value at the distance *y* = 6 mm. The development of jet channel outside the tube in the positive half-cycle is similar to the cathode directed streamer while in the negative half-cycle to that of the anode directed streamer [1]. Regularities of light pulses observed outside the tube indicate that the electric field magnitude as well as its spatial distribution in the positive half-cycle differs considerably from that in the negative one. This finding is consistent with the results of modelling presented in [1].

Figure 8 shows the position of the leading edge of IR light pulse as a function of time in the negative and positive half-cycles. The slopes of the dependences give the propagation velocity of plasma plume.

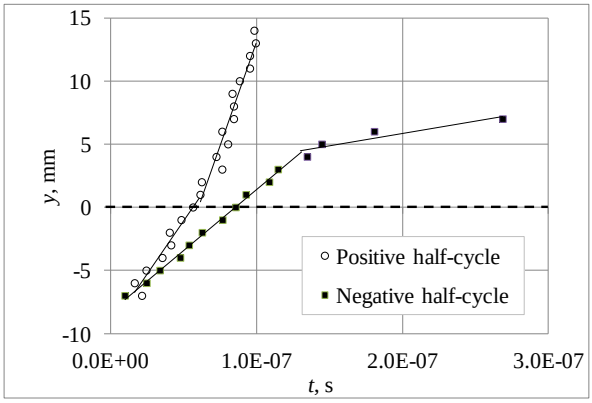


Figure 8. The position of the leading edge of IR light pulse as a function of time in the negative and positive half cycles.

In the positive half-cycle the velocity inside the tube was $v = 1.7 \cdot 10^8$ mm/s and increased outside the tube to $v = 3.3 \cdot 10^8$ mm/s. In the negative half-cycle the velocities were lower: inside the tube and up to the position $y = 5$ mm $v = 9.6 \cdot 10^7$ mm/s, for positions $y > 5$ mm velocity decreased, $v = 2 \cdot 10^7$ mm/s. Another remarkable difference is that in the negative half-cycle the light pulse developed to the smaller distance.

Table 1 gives propagation velocity of plasma plume at positive and negative half cycles, found by other authors.

Table 1. Propagation velocity of plasma plume.

Electrode configuration	Waveform of voltage	Gas	Polarity	Recording position	Velocity, $v/10^8$ mm/s	Reference
Single rod electrode inside the tube	4 kHz, sin Pulsed DC	He	+ +	Outside Outside	Max: 1.25 Max:: 2.5	[3]
Two ring electrodes inside the tube	Pulsed DC	He	+ +	Inside Outside	1-0.6 Max: 2	[5]
Single rod electrode inside the tube	Pulsed DC	He	+ - + -	Inside Inside Outside Outside	0.3 0.3 Max: 1.5 Max: 0.7	[4]
Two DBD electrode	Pulsed DC	5% Ar/He	+	Outside	5.5	[6]
Concentric tubular electrodes	Pulsed DC	1%O_2/He	+ -	Outside Outside	Max: 5.3 Max: 4	[7]

According to the table velocities determined in different experiments have the same order of magnitude. The variations of velocities could be caused by different jet configurations, applied voltage waveforms, gas compositions etc. A common trend is that the pulse velocity is lower inside the tube compared to that of outside. Besides, outside the tube the velocity is higher in the positive half-cycle than in the negative one. Compared to the table data, velocities found in the present work were inside the tube higher at both half-cycles. This discrepancy could be explained by a smaller inside diameter of tube in our experiments. Indeed, according to the modelling and experiments carried out in [8] the discharge velocity inside the tube increases with the decrease of the tube diameter. Outside the tube the velocities found in our experiments were within the limits of velocity values presented in the table. The result that in the negative half-cycle the velocity of discharge propagation was lower as well as the discharge channel length was shorter than they were in the positive half-cycle matches with the results of modelling presented in [1].

4. Conclusion

In this work spatio-temporal characteristics of atmospheric pressure plasma jet were studied. Electrical, optical and spectral characteristics as well as spatio-temporal evolution of jet channel on both half-cycles of voltage in- and outside of the tube were recorded.

The main results of the study are:

- Spectrally determined rotational temperature of the jet channel did not exceed 380 K.
- The relationship has been established between the light pulses developing in- and outside of the tube and the different parts of current pulses.
- Considerably different waveforms of light pulses belonging to positive and negative half-cycle indicate a different spatial distribution of electric field.
- In the positive half-cycle the characteristics of the light pulse development are typical to that of cathode directed streamers while in the negative half-cycle to that of anode directed streamer.

Acknowledgements

The study is supported by Estonian Science Foundation, grant no. 9310.

5. References

[1] Naidis G V 2011 *Appl. Phys. Lett.* **98** 141501.

[2] Lu X, Laroussi M and Puech V 2012 *Plasma Sources Sci. Technol.* **21** 034005.

[3] Xiong Q, Lu, X P, Ostrikov, K, Xian,Y, Zou C, Xiong, Z and Pan Y 2010 *Phys. Plasmas* **17** 043506.

[4] Xiong Z, Lu X, Xian Y, Jiang Z and Pan Y 2010 J. Appl. Phys. **108** 103303.

[5] Mericam-Bourdet N, Laroussi M, Begum A and Karakas E 2009 J. Phys. D: Appl. Phys. **42** 055207.

[6] Sands B, Ganguly B and Tachibana K 2008 *Appl. Phys. Lett.* **92** 151503.

[7] Jiang C, Chen M T and Gundersen M A 2009 *J. Phys. D: Appl. Phys.* **42** 232002.

[8] Jansky J, Delliou P, Tholin F, Tardiveau P, Bourdon A and Pasquiers S 2011 *J. Phys. D: Appl. Phys.* **44** 335201.

ANTIMICROBIAL PROPERTIES OF SULFUR CONTAINING COATINGS

Zenobia Rżanek-Boroch, Paulina Dziadczyk, Danuta Czajkowska,
Krzysztof Krawczyk, Wojciech Fabianowski
Warsaw University of Technology, 00-664 Warszawa, Noakowskiego 3
E-mail: rzanek@ch.pw.edu.pl

Studies concerned the elaboration of a plasma method of coating deposition on the surface of organic substances characterized by antimicrobial properties

1.Introduction

Sulfur dioxide (SO_2) is a preservative used mainly for food of low pH, e.g.: juices and fruit drinks, in the production of wine and for maintaining freshness of dried fruits (raisons, peaches, apricots, apples), vegetables and ready-made potato products. It is used in the production of wine, since it controls the microorganisms (bacteria, yeast and fungi) dangerous for fruit juice and wine, moreover, it has oxidative properties [1-4]. It prevents also the development of mold on grapes kept for several months in cold-stores, which before sale are saturated with sulfur dioxide [5]. Packaging is sought, which would prevent grapes against spoiling and fast liberation of saturated SO_2 [6]. In order to limit the amount of SO_2 used as preservative, studies are carried out on obtaining active packaging of antimicrobial properties.

2. Experimental part

The process was carried out under atmospheric pressure, in barrier discharge powered with impulse current of 400 Hz frequency. The used for this laboratory reactor consisted of a cylindrical rotating electrode (on which the film was placed) and a glass body with a high-voltage electrode, covering only a small part of the reactor's wall (Fig. 1).

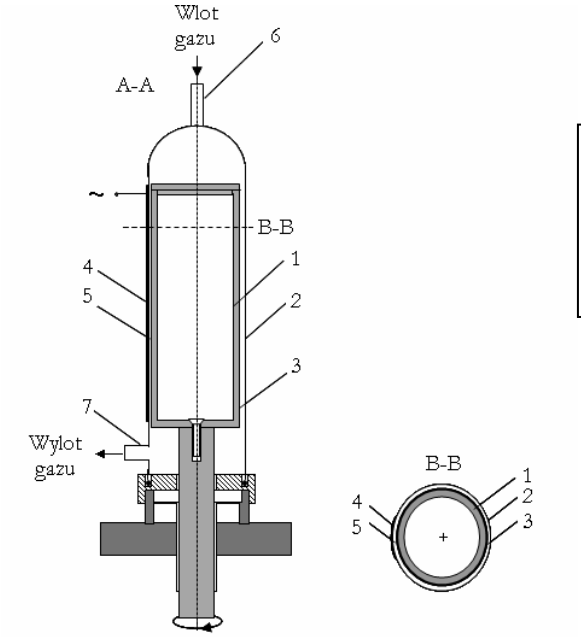


Fig.1. Scheme of the reactor [7]
A-A vertical section, B-B horizontal section;
1 – rotating electrode, 2 – glass body, 3 – film,
4 – HV electrode, 5 – discharge gap (2 mm)
6, 7 – inlet and outlet pipes, respectively

Due to the rotational motion of the inner electrode, the film placed on its surface moved through the discharge zone. The real residence time of the film in the discharge zone, which depends on the width of the electrode on the outside reactor's wall, was ten-times smaller than the time of carrying out the process.

The polyamide side of the polyamide-polyethylene film [quickly welded laminate (27-37% PA, 63-73% PE) of 53 µm thickness (product of PPH Gąsior Sp. z o.o.) was subjected to plasma modification. Technical grade sulfur oxide (IV) of Multax or/and sodium oxide (80% Na_2O of Sigma-Aldrich, cat. No. 645613) were the precursors of plasma deposited coatings. The process was carried out in the atmosphere of argon (Multax). Plasma modification was carried out in three different ways:

1. plasma etching of the film surface with a mixture of argon and sulfur dioxide of SO_2 concentrations from 0.1% to 1.4%.
2. deposition of coatings containing sodium delivered to the reactor by sodium oxide sublimation at: ca. 300 °C, ca. 450 °C, ca. 530 °C, ca. 640 °C.
3. deposition of coatings from the mixture Ar + (0.1%−1.4%)SO_2 + Na_2O sublimed at 300 °C.

The coatings thus obtained were subjected to wetting angle and bacterial studies as well to water vapor permeability determination.

Wetting angle

To determine, whether the deposited substance was incorporated into the film, or only adsorbed on its surface, the wetting angle was measured twice, immediately after plasma modification, and then after three days. Distilled water was used as the wetting agent (Fig. 2).

Water vapor permeability studies

Water vapor permeability studies were carried out to determine whether the film is not destroyed as a result of plasma modification. Water vapor permeability was determined by the weighing method [8].

Bacteriological studies

Bacteriological studies were carried out on bacteria strains of *Staphylococcus aureus* of the Gram-positive group and *Salmonella* of Gram-negative group. The concentrations of both bacteria strains was 10^8 CFU/ml. The TSB medium (CASO bullion of Merck) was used for bacteria proliferation.

Studies were carried out as follows:

1. From each film samples were prepared of ca. 1 cm^2 dimension, which were placed in sterilized tubes,
2. To each tube, 5 ml of the medium and 0.1 ml of the bacteria suspension were introduced,
3. The samples prepared were kept for three days in an incubator at 37 °C,
4. After 24 h, absorbance was measured to determine bacteria development,
5. Absorbance measurement was carried out at 521 nm wavelength,

Absorbance measurement of samples was utilized to determine the degree of inhibition of the film plasma modified. The degree of inhibition of bacteria development was calculated from the formula:

$$S_i = \left(1 - \frac{A_i}{A_0}\right) \cdot 100\%$$

S_i- degree of inhibition, A_i- absorbance of the sample studied, A_0- absorbance of the sample with the crude film.

3. Results and discussion

Results of the wetting angle measurements.

During film modification a decrease in the wetting angle from 87° of the pristine film to 40° of the film plasma modified in argon was observed. Moreover, it was noticed that the wetting angles values were maintained at a constant level after three weeks.

For consecutive mixtures, in which SO_2 was added in an amount of from 0.7% to 1.4% or Na_2O sublimed at 300 – 640 °C, a decrease in the wetting angle values during carrying out the process from 44° to 15° was observed, with an increasing tendency after 3 weeks. Small increases in the wetting angle may prove that some of SO_2 or deposited Na_2O desorb from the film surface.

The temperature of sodium sublimation did not have an essential effect on the wetting angle value, despite that the amount of sodium introduced increases.

The wetting angles for samples modified in $Ar+SO_2+Na_2O$ mixtures, in which SO_2 concentrations was from 0.1% to 1.4%, and Na_2O sublimation proceeded at 300 °C, decreased with an increase in the SO_2 content. It can be assumed that at larger concentrations, SO_2 reacted with the polymer, which resulted in a decrease in the wetting angle after three weeks.

Results of bacteriological studies.

Bacteriological studies on strains of *Salmonella* bacteria of Gram-negative group and *Staphylococcus aureus* of Gram-positive group, of 10^8 CFU/ml concentrations, were carried out for consecutive series of experiments. The results of studies of the degree of inhibition show that plasma modified films considerably better inhibited the *Salmonella* bacteria growth than that of *Staphylococcus aureus* bacteria (Figs. 2, 3).

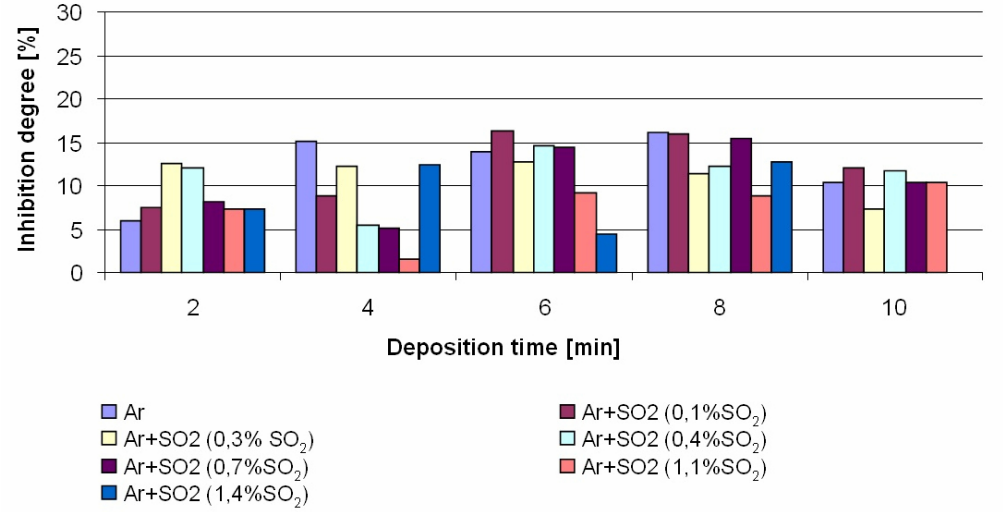


Fig. 3. Dependence of the degree of Salmonella bacteria development inhibition on the time of the film plasma modification in the Ar + (0-1.4%) SO_2 mixture.

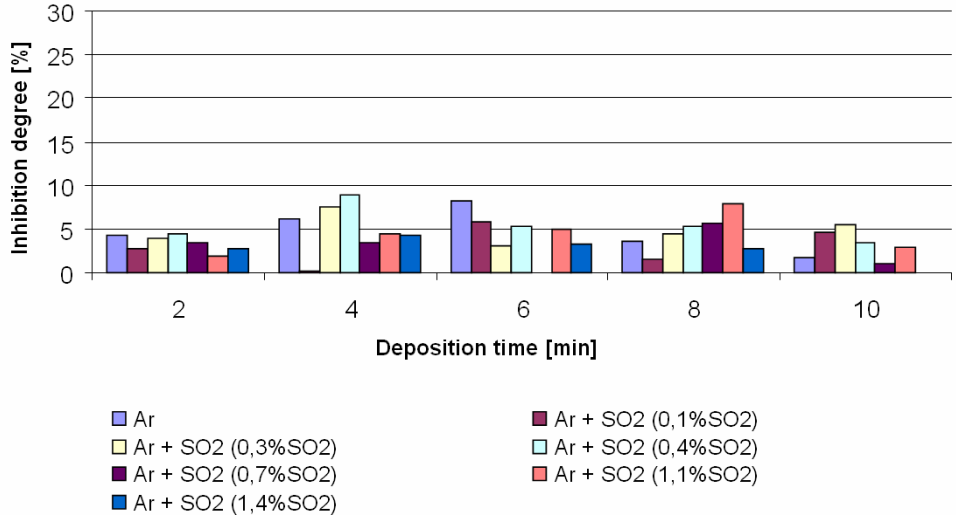


Fig.4. Dependence of the degree of Staphylococcus aureus bacteria development inhibition on the time of the film plasma modification in the Ar + (0-1.4%) SO_2 mixture

The obtained degree of inhibition values for *Salmonella* bacteria are higher and are equal to 16%, than those for *Staphylococcus aureus* bacteria (ca. 8%) (Figs. 3, 4).

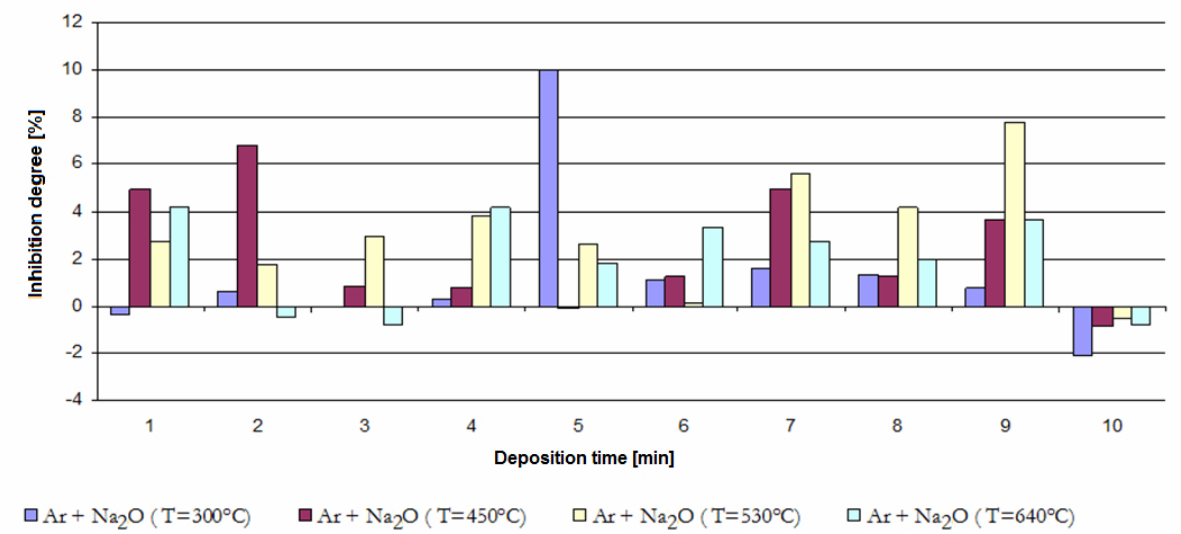


Fig. 5. Dependence of the degree of inhibition for *Salmonella* bacteria of samples of films modified in a mixture: Ar+Na_2O sublimed at 300, 450, 530 and 640 °C.

The results obtained for plasma deposited coatings from mixtures: Ar + Na_2O sublimed at 300, 450, 530 and 640 °C are little consistent and the degrees of inhibition are low. However, these coatings show much higher degrees of inhibition for *Salmonella* bacteria than that deposited from mixtures: Ar + (0.1 - 1.4%) SO_2 + Na_2O sublimed at 300 °C.

Sodium content in coatings

For selected samples, modified for 6 minutes, sodium content studies were carried out by means of the AS30 Carl Zeiss Jena apparatus. Atomization of the ashes sample occurred in the burner's flame, to which air as the oxidative gas and acetylene as the combustible gas were introduced. On the basis of these studies it was found that the sodium content in the coatings increases slightly with a rise of sublimation temperature, and is equal to 2.7 – 3.3 µg/cm^2 for temperatures of the 300 – 640 °C range. Studies showed that the plasma unmodified film contained also a small amount of sodium (1.2 µg/cm^2).

The greatest amount of sodium of ca. 6 µg/cm^2 was introduced from the mixture Ar+0,1% SO_2 +Na_2O sublimed at T_s = 600 °C. It should be believed that the presence of even a small (0.1%) amount of SO_2 causes bounding of considerable amount of sodium, which definitely does not affect favorably the anti-microorganisms properties of the films obtained.

Sulfur content in samples

For selected samples of plasma modified films, sulfur content measurements by means of induction-conjugated plasma were performed, in two series with 7 repeating (ICP – OES Integra XL; GBC Scientific Equipment for two lines of sulfur: 182.0 nm and 182.6 nm. Studies were carried out by two methods:

- in the first one the samples were burned in oxygen and the vapors were absorbed in a hydrogen peroxide solution, which corresponds to the determination of the total sulfur content in the film,
- in the second one sulfur was extracted from the samples with a hydrogen peroxide solution assisted with microwaves, which can correspond to the content of sulfur not permanently linked to the film material.

In Table 2 is presented the average of the results of measurements carried out in two series with 7 measurement repeating, for each sulfur line. For determination of sulfur content the standard curve method was applied.

On the basis of the results presented it was found that there is no explicit relationship between the SO_2 concentration in the reaction gases and the amount of sulfur on the surface or that introduced to the polymer.

Tab. 2. Sulfur content in samples

Type of modification	Total sulfur content in film [µg/g]	Non-linked sulfur[µg/g]
Unmodified film	76	17
Ar + 0.1% SO_2	620	32
Ar + 0.7% SO_2	1190	155
Ar + 1.4% SO_2	860	62
Ar + 0.1% SO_2 + Na_2O (T_s=600°C)	480	30

Results of water vapor permeability

On the basis of bacteriological studies, film samples were selected, for which water vapor permeability studies were carried out. Studies were carried out to be assured that during plasma processing the film was not destroyed. The highest sealing degree was achieved by the unmodified film in the mixture Ar+Na_2O (T_s = 530°C) (61%) and in Ar+0.1%SO_2+Na_2O (T_s = 600°C) (54%). In a majority of cases an increase in the sealing degree is observed after the third day even up to 96%, which may be caused by swelling of the deposited coatings under the influence of moisture (Fig.6)

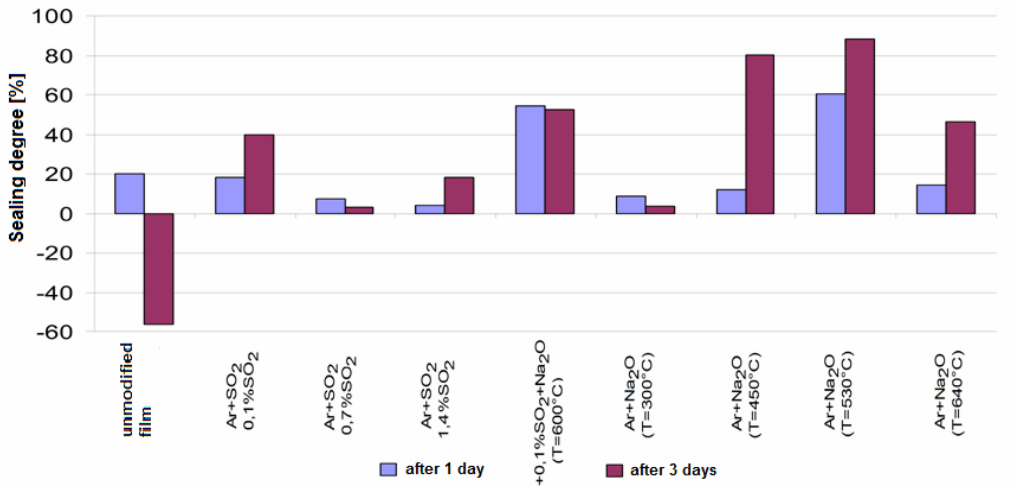


Fig. 6. Dependence of the sealing degree of the film towards water vapor on the type of modification; modification time of particular films = 6 min.

4. Conclusions

1. Sulfur or sodium containing coatings characterized by antimicrobial properties can be obtained by the PE-CVD method under atmospheric pressure.
2. The highest degree of inhibition of 16% for *Salmonella* bacteria of group Gram (-) and that of 8% for *Staphylococcus aureus* bacteria of group Gram (+), were achieved for films with a sulfur containing (620 – 1190 µg/g) deposited from mixtures: Ar+0.1% SO_2 and Ar+0.7% SO_2.
3. Samples containing about 3 µg/g of sodium deposited from a mixture Ar+Na_2O sublimed at 300°C showed, with respect to *Salmonella* bacteria of group Gram (-), the inhibition degree of up to 10%.
4. Plasma deposited coatings were characterized by sealing properties towards water vapor, maximally at the level of 60%.
5. The films thus obtained may find application as packaging of food products.

5. References

1]. Ribe´reau - Gayon P, Glories Y., Maujean A., Dubourdieu D., Handbook of enology: the chemistry of wine stabilization and treatments, J. Wiley, Chichester, 2006, vol 2.
[2] Santos M. C., Nunes C.,. Saraiva J. A,. Coimbra M. A, Conference material: European Food Research and Technology, Portugal Aveiro 2011, p. 1.
[3]. Ribe´reau - Gayon P, Dubourdieu D., Done`che B., Lonvaud A., *Handbook of enology: The microbiology of wine and vinifications,* vol 1, 2nd edn. Wiley, Chichester, 2006.

This work was financially supported by National Science Center - 1376/B/H03/2011/40

ETHANOL CONVERSION IN THE DC ATMOSPHERIC PRESSURE AIR GLOW DISCHARGE

V.I. Arkhipenko, A.A. Kirillov, L.V. Simonchik, S.M. Zgirouski

B.I. Stepanov Institute of Physics of NAS of Belarus
e-mail: simon@imaph.bas-net.by

Three-electrode system is proposed for creation of the non-self-sustained large volume glow discharges in different atmospheric pressure gas mixtures. Special designs of plasma reactors are considered. Positive column of the non-self-sustained atmospheric pressure glow discharge at the length of about 15 mm is used to facilitate ethanol conversion into syngas. In the experiment, for example, with heated working gas mixture at the input, containing about 57% of air, 30% of ethanol vapor and 13% of water vapor, after plasma conversion the outlet mixture consists of about 36 % H_2, 23% CO, 1.2% CH_4, 0.8% C_2H_2, 1.0% CO_2, 0.3 % C_2H_5OH and about 8% H_2O. Conversion efficiency is about 95%. Hydrogen output is about 1.2 liter per minute. The energy cost-effectiveness ratio defined as the ratio of the energy release at the syngas burning to the electrical energy costs for the plasma maintenance is about 1.85.

1. Introduction

At the present one of the most important energy problems is to find alternative energy sources that would allow some to abandon the traditional hydrocarbon fuels such as gasoline, kerosene, methane, which are produced from oil and natural gas. The reserves of the latter on Earth are limited. In this connection, the use of vegetable origin fuels: biodiesel, biokerosene and ethanol has increased. However, in comparison with the "oil" these fuels have some properties that present certain difficulties to use them effectively. The main reasons are the low speed of combustion propagation and a variability of the component composition. A possible way to eliminate the mentioned above drawbacks of unconventional fuels can be an additive of free hydrogen into the fuel mixture, which leads to an increase in its combustion rate. Hydrogen can easily flare up and provide a sufficiently large velocity of combustion wave propagation. However, the problems of storage and transportation of hydrogen appear. The way to solve these problems would be to use the bio-fuels as a source of hydrogen of the needed amount in the place of its direct utilization. Among hydrocarbon fuels ethanol is the most promising, because it can be obtained from various sources, for example, from industrial waste or biomass. At the same time, a relatively low amount of pollutants such as nitrogen oxides is allocated with its burning, because the methane molecules in the presence of nitrogen oxides are restored back to nitrogen.

A plasma-chemical method is a promising way to generate hydrogen directly before biofuel burning. It consists in the reforming of fuel into syngas with the support of non-equilibrium plasma. The main advantages of technologies based on the use of non-equilibrium plasma, include the acceptable regimes of operation (atmospheric pressure, low gas temperature), quick start, compact plasma systems, etc. Different types of atmospheric pressure discharges (corona, spark, a barrier, gliding arc at DC, AC and pulsating current of different frequency bands) are proposed as plasma sources for these purposes [1, 2]. In the present work a DC non-self-sustained glow discharge at atmospheric pressure supported by self-sustained normal glow discharge in the three-electrode system described in [3, 4] is proposed to use for the conversion of ethanol into syngas.

2. Plasmachemical reactor and diagnostics of conversion products

The design of plasma-chemical reactor is based on the three-electrode system, which was used in [3, 4] for generation of volumetric glow discharges in various atomic and molecular gases. The reactor consists of three-sectional (A, B and C) discharge chamber 1 (Fig. 1, *a*). In the section A, there are both a cooled tungsten cathode 2 (6 mm diameter rod with a working part rounded at radius of 3 mm) and copper anode 3 (plate thickness of about 1 mm) located at the distance of 2 mm. Power supply U1 (output voltage of 1500 V, the ballast the resistance R1 ~ 1200 Ω) is used to ignite a self-sustained glow discharge at a current of 200 mA between these electrodes. The air flow with the rate up to 1 liter per minute was provided through the section A. Air output takes place through the hole (diameter

2 mm) in the center of electrode 3 into section C (quartz tube 5 at the diameter of 10 mm and 15 mm long), which is located under the this hole.
The discharge in section A served as a plasma cathode for the non-self-sustained discharge in section C. For this purpose at the far end of the tube 5 an additional electrode 4 was placed, which is powered

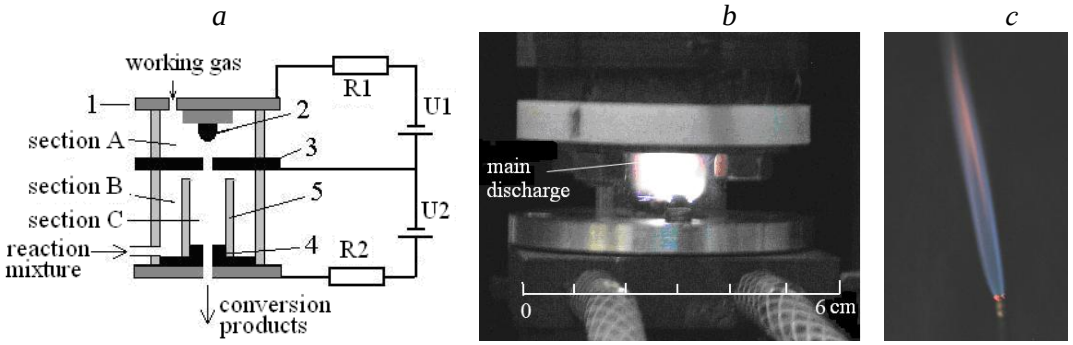


Fig. 1. Schematic of plasmachemical reactor (*a*) and photos of discharge during ethanol conversion (*b*) and flame at the reactor ouput (*c*).

from the second power supply U2 (4000, R2 ~ 10000 Ω) in such manner that this electrode polarity is positive relative to electrode 3. Thus, the electrode 4 is the second anode. Mixture of ethanol and water is fed into the chamber together with air flow with rate less than 0.5 liter per minute using the same input canal. Ethanol and water evaporate due to the heating of electrode 4 by the discharge and air-vapor mixture spreads along the section B. Then the mixture is mixed with the gas flow from section A and is directed into section C. At discharge current of about 130 mA the positive column plasma fills almost the whole volume of the section C (Fig. 1, *b*). The yield of gases from section C takes place through the hole (diameter of 2 mm) in the anode 4 (Fig. 1, *a*) into a copper tube (internal diameter 3 mm). In Fig. 1, *c* a photograph of the plume of exhaust gases combustion at the end of the tube (bottom of the photo) is presented. The length of the flame can reach up to 10 cm, while its color is blue.
The composition of conversion products of the mixture after processing in a plasma reactor was determined by infrared (IR) absorption spectroscopy method. For this purpose, we used infrared spectrometer NEXUS (Thermo Nicolet). The absorption spectra were recorded in the range 400–4000 cm^{-1} with the resolution of 2 cm^{-1}. A triangular apodization function was chosen, which leads to

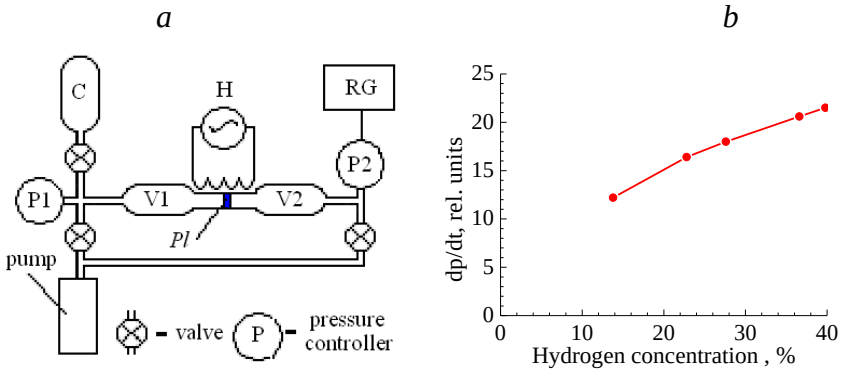


Fig. 2. Schematic of system for the hydrogen collection. Pl – palladium inlet valve, V1 and V2 – volumes, C – cylinder, H – heater, RG – leakage recorder, *Pl* – palladium membrane.

the line diffraction contours. For spectroscopic analysis the exhaust gases from the plasma-chemical reactor were pumped through 5- centimeter cuvette, which was previously heated up to 110 ºC in order to prevent condensation of water and alcohol vapors.
The main component of the alcohol conversion, as it will be shown in the following section, is hydrogen. Determination of its presence in the reactor exhaust by means of infrared spectroscopy is not possible. To determine the concentration of hydrogen we used the method based on the inleakage of hydrogen through palladium membrane into previously evacuated volume [6].

Schematic diagram of the setup is shown in Fig. 2, *a*. It consists of two volumes V1 and V2 divided by the palladium membrane. These volumes were previously evacuated by forepump. Palladium membrane was heated by the heater H. Then, the volume V1 was filled by the gas mixture collected at the reactor outlet. Hydrogen penetrates through the membrane into volume V2. At the same time, the pressure growth rate *dp/dt* in this volume is registered by recorder RG. The same operations of the evacuation, filling and leakage through palladium membrane were performed for nitrogen-hydrogen mixtures with known percentage of hydrogen. Comparing the leakage rates through palladium membrane for both the reactor mixture and mixtures with known hydrogen concentration we can determine a quantity of hydrogen in reactor exhaust using previously plotted calibration dependence (Fig. 2, *b*).

3. Results and discussion

For the conversion in the experiment, we used the mixture of ethanol (85%) with water (15%). When alcohol and water pass through the heated (> 100 ^{o}C) anode 4 they evaporate. Alcohol and water vapors with concomitant air at a flow rate of about 0.5 liter per minute spread along section B. Then this mixture is mixed with the gas flow (about 0.3 liter per minute) from section A and resulting reaction mixtute is directed into section C. If we have at the input of the reactor the of alcohol-water mixture rate of 1.25 ml/min , the reaction mixture composition in section C can be estimated as follows: 57% of air, 30% of ethanol vapor and 13% of water vapor. Parameters of the discharges: sustaining discharge in section A – voltage applied to the electrodes 2 and 3 is 380 V at discharge current of 0.15 A, which corresponds to the electrical power of 50 W; the main discharge in a ethanol-water-air mixture in section C – discharge current equal to 0.13 A at the voltage across the electrodes 3 and 4 in 1500 V and, accordingly, the power was about 200 W.

Intense vibrational-rotational bands of ethanol (900, 1050, 1250, 1400, 2950 and 3700 cm^{-1}), water vapor (1600 cm^{-1}, 3750 cm^{-1}), and much weaker bands of carbon dioxide molecules as a component of the used ambient air in the laboratory are only observed in the IR absorption spectrum (Fig. 3, *a*) of initial reaction mixture. The spectra were recorded by heating the infrared spectrometer cuvette up to 110 °C.

After processing in a plasma the new bands of CH_4 (3100 cm^{-1}), CO (2200 cm^{-1}), C_2H_2 (750 and 3300 cm^{-1}) and CO_2 (740 and 2400 cm^{-1}) are observed (Fig. 3, *b*) in the spectrum of the mixture leaving the reactor. The weak intense absorption bands of ethanol and water present in the spectrum as well.

Excluding the ethanol, mole fractions of all infrared active components in the exhaust mixture were determined by comparison of the registered spectrum with calculated one. These spectra in the range of 2000 cm^{-1}–2400 cm^{-1} are shown in Fig. 4. The calculation of absoption spectrum was fulfilled using the data base of Hitran [5]. The absorption in the range of 2000 cm^{-1}–2250 cm^{-1} is determined by the CO molecules and we observed the resolved rotational line structure. In the range of 2250 cm^{-1}–2250 cm^{-1}, the absorption is defined by carbon dioxide molecules and due to smaller (compared to CO) distance between the rotation lines of CO_2 this band is unresolved. As one can see, there is a good agreement between experimental and calculated data. The molar concentrations of conversion

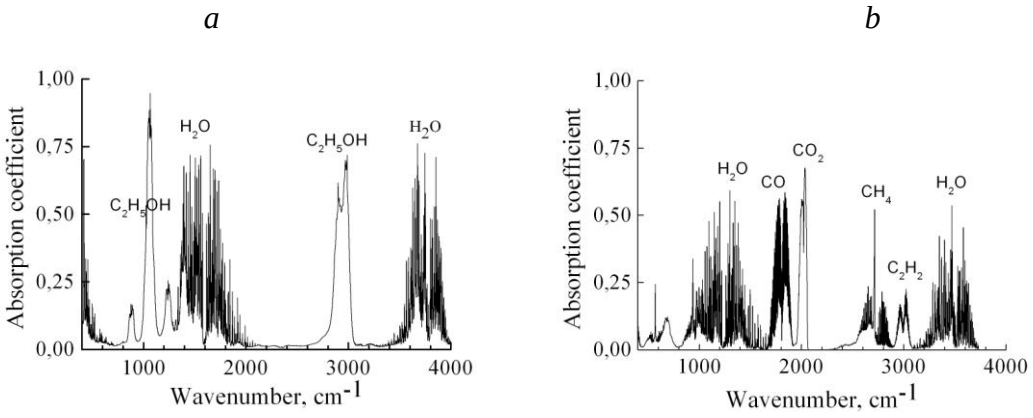


Fig. 3. Absorption IR-spectra of mixtures at the inlet (a) and outlet (b) of plasma reactor.

products defined in this way are presented in Tab. 1. The mole fraction of ethanol was determined by experimental calibration curve of absorption, ploted using the gas mixtures with known concentrations of alcohol.

As it follows from the examination of the IR absorption spectra (Fig. 3, *b*) of the ethanol conversion products the additional gas components with a noticeable percentage which could appear in the IR

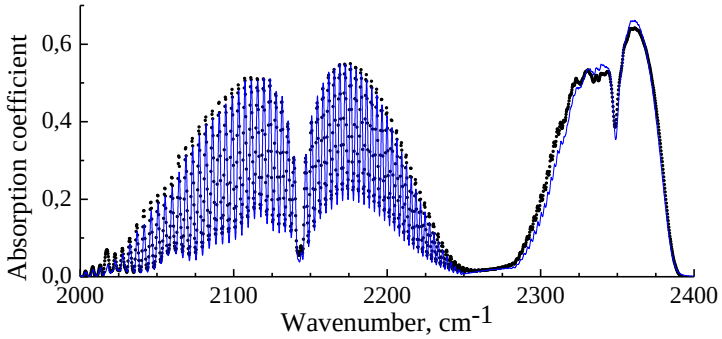


Fig. 4. Experimental (doted) and calculated (solid) absorption IR-spectra of CO and CO_2.

spectra are absent. In addition to the above-mentioned IR active components leaving the reactor the exhaust mixture contains, of course, the homonuclear molecules of hydrogen, nitrogen and oxygen. The definition of their mole fractions with the help of IR spectroscopy is not possible. Mole fractions of these components were calculated taking into account the composition of reaction mixture at the inlet of the reactor and the mole fractions of IR active components in the exhaust products determined experimentally. Furthermore, the mole fraction of hydrogen in the exhaust mixture can be compared with the amount of hydrogen determined experimentally by the rate of hydrogen leakage in a given volume through the palladium membrane (see Section 2). It is about 30%.

So, we know the molar concentration of carbon components, that allow us to determine the number of carbonaceous molecules leaving the plasma reactor during one minute and distribute between them the number of carbon atoms containing in the input reaction mixture. Now, knowing the ratio of molar concentrations of water and carbon-containing component, it is easy to get the number of water molecules. Then, taking into account an equality of the number of hydrogen , oxygen and nitrogen atoms in the inlet and outlet mixtures one can easily calculate the number of relevant molecules leaving the plasma reactor per unit time, and determine the appropriate molar concentrations, which are as follows: $\{H_2\}$ = 36%, $\{O_2\}$ = 0.1%, $\{N_2\}$ = 21%. Summing over the molar concentrations of all gas components leaving the reactor, we obtain 91.4% instead of 100%. It can indicate that the corresponding experimental data used in estimations have been obtained with some error.

Tab. 1. Mole fraction of the main components in the inlet and outlet mixtures.

inlet mixture		outlet mixture		
			experiment	estimation
Ethanol	30%	C_2H_5OH	0.3%	
Water	13%	H_2O	8%	
air	57%	CO	23%	
		CO_2	1,0%	
		CH_4	1,2%	
		C_2H_2	0,8%	
		H_2	30%	36%
		O_2		0.1%
		N_2		21%

Productions of ethanol conversion products are G(H_2) = 1.2 l/min, G(CO) = 0.75 l/min, G (CH_4) = 0.04 l/min and G (C_2H_2) = 0.025 l/min. The totel production of the syn-gas is 2.0 l/min. Let's define the conversion efficiency of ethanol into hydrogen by the following expression

$$\eta\ \mathrm{H_2} = \frac{\text{number of H-atoms in generated hydrogen molecules } \mathrm{H_2}}{\text{number of H-atoms in ethanol molecules}}, \quad (1)$$

According to (1) we obtain $\eta(H_2)$ = 88%. Similarly one can determine the coefficients of ethanol conversion into hydrogen, methane and acetylene, and calculate the total of ethanol conversion coefficient, which is 95%. Energy efficiency is determined by the formula

$$\alpha = \frac{\text{energy release at the burning of } \mathrm{H_2},\ \mathrm{CO},\ \mathrm{CH_4},\ \mathrm{C_2H_2}}{\text{total electric energy for plasma maintenance}}. \quad (2)$$

Taking into account that the total electric power needed for the maintenance of both the self-sustained and non-self-sustained discharges is about 250 W, we obtain α = 1.85. As a result, the energy costs per molecule of hydrogen are approximately 3 eV.

4. Conclusions

Thus, the results of performed experiments show that it is possible to create a compact effective source for the syn-gas production operating at comparably low electrical power consumption of 200-300 W and at relatively low voltages (less than 4000 V).

Conversion efficiency reaches about 95%. Hydrogen production is about 1.2 liters per minute; the syn-gas production is 2 liters per minute. Energy efficiency, defined as the ratio of the energy released during combustion of the syn-gas to the electricity consumed for the discharges maintenance is about 1.85. The energy costs per molecule of hydrogen are approximately 3 eV. It should be noted that the described conditions of the reactor operation are not optimal. Therefore the further improvement of its design and the selection of the reaction mixtures is required.

The work was supported by BRFFR-SFFRU (grant T11K-034).

5. References

[1] Deng X., J. Sun, Sh. Yu et al. 2008 *International Journal Of Hydrogen Energy* 33 1008.
[2] Fridman A. 2008 Plasma Chemistry, Cambridge: Cambridge University Press, 980p.
[3] Arkhipenko, V.I., Kirillov, A.A. et al. 2009 *IEEE Trans.Plasma Phys*. 37 1297.
[4] Arkhipenko, V.I., Kirillov, A.A. et al. 2011 *IEEE Trans.Plasma Phys*. 39 1297.
[5] http://www.cfa.harvard.edu/hitran/
[6] Arkhipenko, V.I., Kirillov, A.A. et al. 2009 Proc. 19th International Symposium on Plasma Chemistry (ISPC), Bochum, Germany, July 26–31, 2009, http://www.ispc-conference .org/ispcproc/papers/572.pdf.

SPECTROSCOPIC STUDY OF HELIUM DBD PLASMA JET

Goran B. Sretenović, Ivan B. Krstić, Vesna V. Kovačević, Bratislav M. Obradović and Milorad M. Kuraica

University of Belgrade – Faculty of Physics, Belgrade 11000, P.O. Box 44, Serbia
E-mail: sretenovic@ff.bg.ac.rs

Atmospheric-pressure helium plasma jet has been studied by optical emission spectroscopy and electrical measurements. Streamer/bullet properties of the plasma jet are observed in the positive voltage half cycle, while in the negative jet operates more as a glow-like atmospheric pressure discharge. This is revealed by spatially resolved measurements of intensity distribution of typical excited species and by electric field measurements based on Stark polarization spectroscopy. Obtained radial distribution of the axial electric field of the bullet shows that the ring-shaped structure of the light emission is a consequence of such electric field distribution.

1. Introduction

The rising field in the applied plasma physics is development of plasma sources favourable for biomedical applications. Understanding of the mechanisms of interaction between plasma and living organisms is a challenge from the fundamental and technological points of view. Promising applications in medicine are electro-surgery, dentistry, skin care and sterilization of heat sensitive medical instruments [1]. Non-equilibrium properties of non-thermal plasmas like hot electrons with energies of several eV, and cold neutral gas and ions, represent a big advantage. The energetic electrons are able to produce oxygen and nitrogen reactive species (RONS) [2, 3]. RONS are important in medical applications and in some cases they could have a key role in some important existing and emerging therapies. Beside the chemically active species, non-thermal plasma provides UV radiation and usually appears with high electric field which can also find biomedical application such as tumour treatment [4]. Gas temperature of atmospheric-pressure plasmas remains near room temperature, so it does not cause thermal damage to heat sensitive cells and living tissue. Due to high frequency of collisions between electrons and heavy particles at atmospheric pressure, the electrons lose their energy in a short period. Therefore, at atmospheric pressure, the electric field required to initiate the discharge is high, in order of tens of kV/cm. This fact limits discharge gaps for most atmospheric pressure discharges to values from mm for dielectric barrier discharge to several cm for corona discharge [5]. Short discharge gaps reduce the size of objects to be directly treated. Indirect treatment by the effluent of the plasma has disadvantage due to short lifetime of most of reactive species which do not reach the objects of treatment. Also, in the indirect treatment, the object is not exposed to the high electric field. Those problems are overcome by designing of several types of plasma jet [5]. Classification methods of non-thermal plasma jets could be based on the type of the feeding gas or on the electrode configuration. Consequently, the noble gas plasma jets, the nitrogen plasma jets and the air plasma jets are in use [5]. On the other hand, dielectric-free electrode (DFE) jets, dielectric barrier discharge (DBD) jets, DBD-like jets and single electrode jets are recognized on the basis of the electrode configuration arrangement [5]. Further, plasma jets could be divided into linear field jets and cross field jets, according to the direction of the gas flow in comparison to the applied electric field orientation [6]. At the end, the shape and the frequency of the feeding voltage signal can be used as a classifying factor, so there are: RF plasma jets, low frequency plasma jets, DC plasma jets, pulsed plasma jets etc. Fast imaging of the plasma jets revealed its discrete structure [7]. It was shown that the plasma plume, which appears continuous to the naked eye, is made of fast mowing plasma structures. Depending on the jet construction and feedings, the velocity of the luminous moving train is in range of $1.5 \cdot 10^4$ m/s - $1.5 \cdot 10^5$ m/s [5]. These values of speed are several orders of magnitude higher than value of velocity of the gas flowing through the electrode system. Also, they are higher than electron and ion drift velocities. So, the explanation for propagation mechanism of the plasma bullet could be Dawson's photon-ionization theory, as proposed in [8]. Measurements of the axial electric field of the plasma jet operating in the bullet mode brought results compatible to Dawson's photon-ionization theory and pointed out the streamer nature of the plasma bullet [9].

The aim of this work is a diagnostic of helium, linear field, low frequency DBD plasma jet. Results of space resolved spectroscopic measurements are presented. Excitation mechanisms of some excited species are discussed based on the intensity distribution of several atomic lines and molecular bands. Radial intensity distributions of He I 492.1 nm line obtained by Abel inversion of measured lateral profiles are used for electric field determination based on Stark polarization spectroscopy.

2. Experimental set-up

Discharge device considered in this study is dielectric barrier discharge plasma jet. It consists of a glass tube 2 cm in length (2 mm inner diameter, 3 mm outer diameter) with a 1 cm wide copper electrode wrapped tightly around it at the distance of 1 cm from the tube nozzle. A second grounded copper electrode is placed 1 cm downstream from the nozzle. The helium flow (99.996%) through the tube was 5 l/min. Helium flowed into the ambient air. A laboratory-built power supply operated at 12 kHz, able to provide high voltage sinusoid signal with variable amplitude up to 20 kV, was connected to the wrapped electrode. The applied voltage was measured using P6015A Tektronix high-voltage probe and a Rogowsky coil placed between the grounded electrode, and the grounding point was used for current measurements as presented in Figure 1. A Tektronix TDS 2024B digital storage oscilloscope (200MHz, 2 GS/s) was employed to record voltage and current signals.

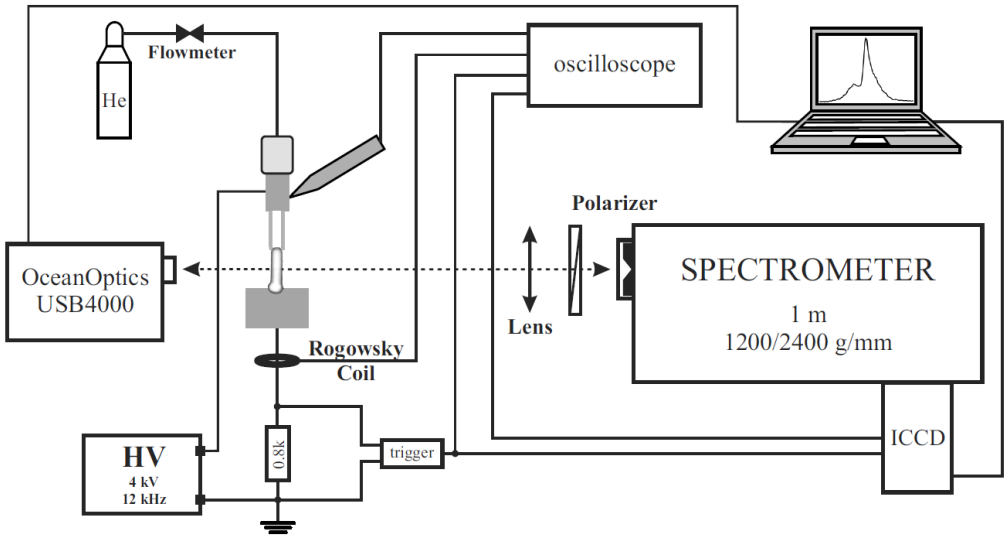


Fig. 1. Experimental set-up.

For a space resolved emission measurements, projection optics was used to project the whole plasma jet onto the entrance slit of a 1m spectrometer (SOLAR TII, model MSDD 1000) with 1200 g/mm diffraction grating. Radiation from the jet was detected using an ICCD (PI-MAX2, Princeton Instruments) with 1024×1024 pixels, size of the pixel 13 μm. ICCD was triggered using time delayed pulse signal from the non-inductive 800 Ω resistor inserted between grounded electrode and the grounding point as shown in Figure 1. Each recorded image is made of 50 accumulations, each of 50000 gates per exposure. The gate was triggered at the beginning of the current peak with duration of 5 μs. Resolution of spectral apparatus was 10.8 pm/pixel. With an entrance slit of 30 μm full width at the half of maximum (FWHM) of corresponding instrumental profile was 0.035 nm.

3. Results and discussion

Fig. 2(a) presents recorded current and voltage signals of the plasma jet. It is obvious that each half cycle is characterized by one strong current peak, typical for some types of the dielectric barrier discharges. Magnitude of the current is significantly higher in the positive half cycle then in the negative one which implies two different operational regimes of the plasma jet in the each half cycle. In the positive half cycle, grounded, copper electrode acts as a cathode and powered electrode wrapped around the glass tube as an anode. In that half period cathode directed streamers – bullets appear. Plasma bullets tend to form in the positive half cycle and their appearance is rear in the negative half cycle [10].

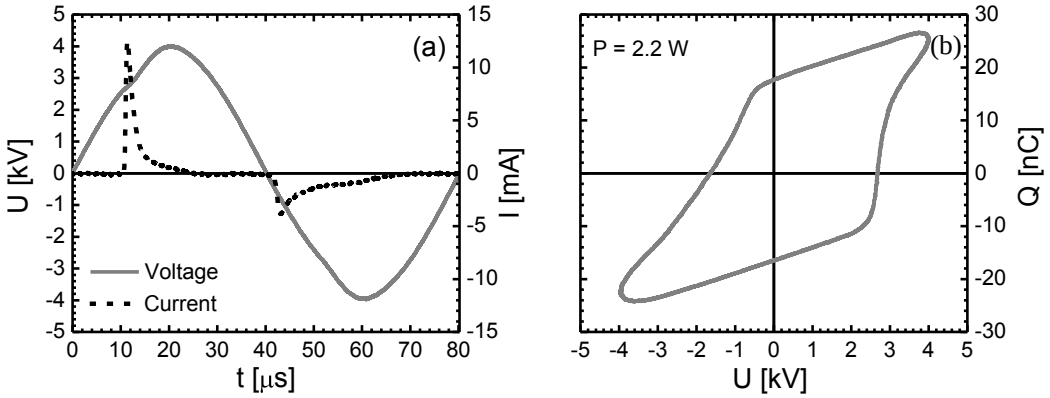


Fig. 2. (a) Current and voltage signals of the plasma jet operating in the bullet mode. (b) Lissajous figure (Q-U plot) showing dissipated power.

Charge versus voltage (Q–U) plot, i.e. Lissajous figures, can be used for determination of the charge transferred through the discharge gap and the energy dissipated into the gap by geometrical analysis. As can be seen from the Fig. 2(b) Lissajous figure is asymmetrical due to the asymmetric arrangement of the discharge. Low discharge power of about 2 W is characteristic for the bullet mode and in agreement with measurements presented in other studies [10].

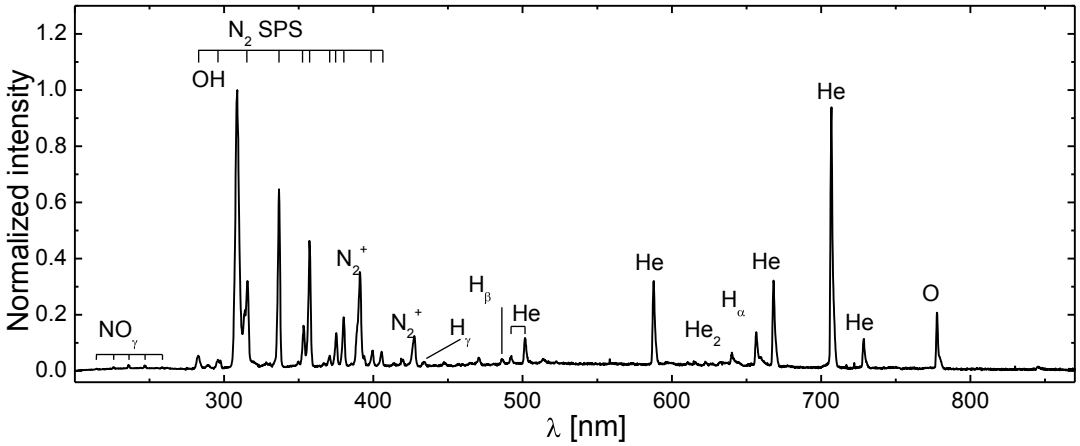


Fig. 3. Optical emission spectrum of DBD plasma jet.

The easiest way to detect species in the discharge is to record overview spectrum. An overview spectrum in the UV-visible-near IR range (200 – 900 nm) is presented in Fig. 3. As can be seen from the presented spectrum NO-γ system, nitrogen second positive system – N_2 (C-B), OH (A-X), nitrogen first negative system - N_2^+ (B-X) and some O I, H I and He I lines could be detected. Atomic oxygen, hydroxyl radical and NO are some of the most important reactive species in plasma medicine applications. Presence of atomic oxygen directly points out the presence of the ozone, and vice-versa which is also important factor for such applications. Relatively high intensity of the N_2^+ (B-X) comes from the resonant reaction channel between metastables of helium and nitrogen in the ground state, which produce very effective excited ions $N_2^+ (B^2\Sigma_u^+)_{v'}$. This so called Penning process is followed by the emission of the first negative system. The second positive system of nitrogen is mainly produced by direct electron excitation. The spatially resolved intensity distributions of the 1 cm DBD plasma jet are presented in Fig. 4. This figure shows the normalized intensities of some lines and bands for positive and negative current peaks. The intensity distributions of the He I line at 706 nm, oxygen line at 777 nm, H_β line at 486 nm, OH band in the range of 306-309 nm, and nitrogen second positive system (SPS) and first negative system (FNS) at 337 nm and 391 nm respectively.

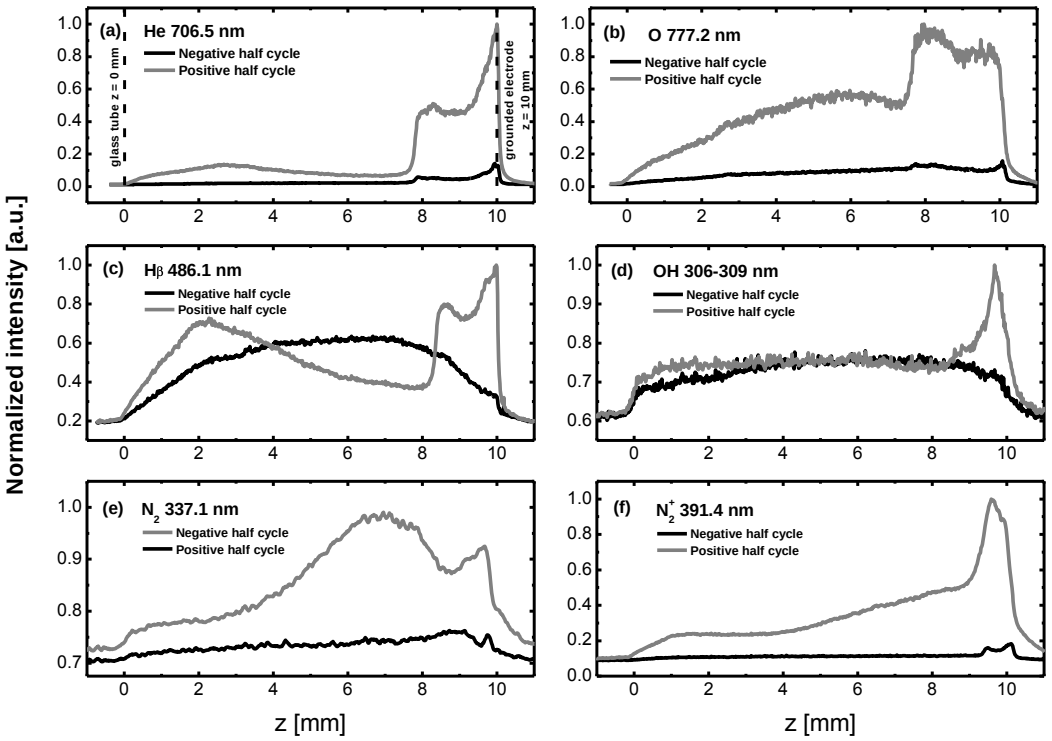


Fig. 4. Spatially resolved intensity distributions of various emissions for the positive and the negative current peaks of the jet.

Depending on the excitation mechanism of radiative states, two groups of lines/bands can be distinguished: direct excitation by energetic electrons and indirect excitation involving metastables. First group (He 706 nm and N_2 SPS 337 nm) correspond to the high electric field and electron density and its appearance follows the current pulse. The second group (O 777 nm, H_β 486 nm, OH 306-309 nm and N_2^+ 391 nm) is usually delayed in respect to the current pulse due to the necessary preceding dissociation or ionization of existing species and participation of metastables in these processes [11]. He 706 nm line is the fingerprint of high energetic electrons i.e. high electric field. From the Fig. 4(a) enormous difference between intensities for the positive and the negative current peaks suggests significant existence of energetic electrons only for the positive current peak, while for the negative one the intensity of the line is non-negligible only near the grounded electrode – instantaneous anode.

Optical emission spectroscopy technique based on the application of the polarization-dependent Stark splitting and shifting of He I 492 nm line, and its forbidden counterpart is used for electric field measurements. Following the methods demonstrated in [12, 13], axial electric field in the space between the glass tube and the grounded electrode is determined. Examples of typical π-polarized spectra of He I 492 nm line recorded for the positive and negative current peak are shown in Fig. 6. According to [12], with the polarizer mounted with its axis parallel to the external field three components are detected: allowed line, its forbidden counterpart and a field-free component (ff) originating from the area where the electric field is negligible. Spectral lines are fitted with pseudo-Voigt profiles in order to estimate peak-to-peak distance between the forbidden and allowed counterparts according to which the electric field is determined. For the positive current peak of the plasma jet the ff component is Van der Waals broadened while the forbidden and allowed lines are broadened predominantly due to the overlapping of shifted spectral lines emitted by atoms placed at various positions in the streamer head electric field. The measured electric field distribution along the discharge axis actually represents time integrated electric field in the head of the streamer propagating along the axis.

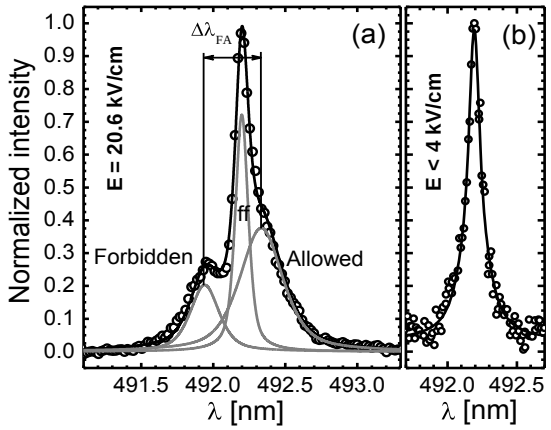


Fig. 6. Typical π-polarized spectra of He I 492.19 nm line recorded from the plasma jet for (a) positive and (b) negative current pulse.

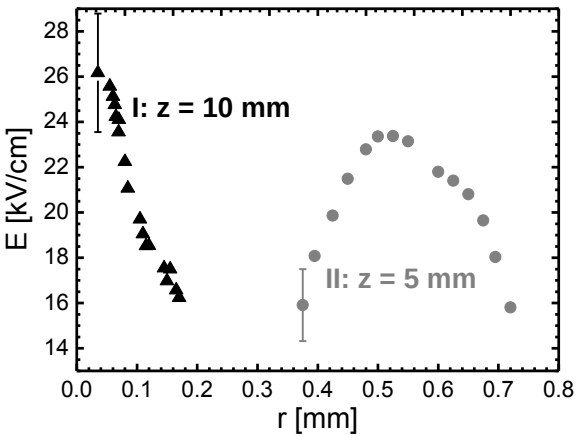


Fig. 7. Radial distribution of the axial electric field in the plasma jet at two characteristic axial positions.

Concerning the negative current peak, measurements were performed also - see Figure 6(b). As shown at Figure 6(b) substantial splitting of the line is not observed, which implies low electric field strength along the jet for the negative current peak. Method used for electric field determination is suitable for electric field strength down to 3-4 kV/cm, depending on the signal to noise ratio of the recorded line. According to this, electric field strength of the jet, for the negative current peak for given experimental conditions, is lower than 4 kV/cm, which is in agreement with modelling results presented in [7]. In order to estimate radial distribution of axial electric field of the plasma bullet at different positions in the plasma jet, lateral profiles of the plasma jet for the positive current pulse are recorded and the Abel inversion procedure was applied. Then, fitting of line profiles resulted in the electric field strength distribution data. Radial distribution of axial electric field has the ring shaped structure at the middle of plasma jet (z = 5 mm), see Figure 7. Near the grounded electrode the electric field reaches maximal value of 26 kV/cm at the axis (z = 5 mm), while in the middle of the jet maximum is off-axis with values up to 23 kV/cm. These experimentally obtained results also confirm modelling outcomes, and calculations presented in [15, 16].

Acknowledgements This work is supported by the Ministry of Education and Science of the Republic of Serbia through the Project No. 171034 and the Project No. 33022.

4. References

[1] Park G Y et al. 2012 *Plasma Sources Sci. Technol.* **21** 043001
[2] Kong M G et al. 2009 *New J. Phys.* **11** 115012
[3] Graves D B 2012 *J. Phys. D: Appl. Phys.* **45** 263001
[4] Nuccitelli R et al. 2009 *Int. J. Cancer* **125** 2
[5] Lu X, M Laroussi and Puech V 2012 *Plasma Sources Sci. Technol.* **21** 034005
[6] Law V J and Anghel S D 2012 *J. Phys. D: Appl. Phys.* **45** 075202
[7]Teschke M, Kedzierski J, Finantu-Dinu E G, Korzec D and Engemann J 2005 *IEEE Trans. Plasma Sci.* **33** 2
[8] Lu X and Laroussi M 2006 *J. Appl. Phys.* **100** 063302
[9] Sretenović G B, Krstić I B, Kovačević V V, Obradović B M and Kuraica M M *Appl. Phys. Lett.*, **99** 161502
[10] Walsh J L, Iza F, Janson N B, Law V J and Kong M G *J. Phys. D: Appl. Phys.* **43** 075201
[11] Navrátil Z, Brandenburg R, Trunec D, Brablec A, St'ahel P, Wagner H-E and Kopecký Z 2006 *Plasma Sources Sci. Technol.* **15** 1
[12] Kuraica M M and Konjević N 1997 *Appl. Phys. Lett.* **70** 1521
[13] Obradović B M, Ivković S S and Kuraica M M 2008 *Appl. Phys. Lett.* **92** 191501
[14] G. V. Naidis 2011 *Appl. Phys. Lett.* **98** 141501
[15] G. V. Naidis 2010 *J. Phys. D: Appl. Phys.* **43** 402001
[16] G. V. Naidis 2011 *J. Phys. D: Appl. Phys.* **44** 215203

MECHANISM OF 4-CHLOROTOLUENE DECOMPOSITION IN AIR MIXTURE IN AN ELECTRON BEAM GENERATED NON-THERMAL PLASMA REACTOR

Yongxia Sun[1], A.G.Chmielewski[1,2]

[1] *Institute of Nuclear Chemistry and Technology, Dorodna 16, 03-195 Warsaw, Poland*
[2] *Warsaw University of Technology, Department of Chemical and Process Engineering, Warsaw , Poland*
E-mail: y.sun@ichtj.waw.pl

4-chlorotoluene decomposition in air mixture in an electron beam generated non-thermal plasma reactor was investigated. Chlorobenzene, chlorobenzaldehyde , chlorobenzyl alcohol and chlorobenzoic acid were identified as 4-chlorotoluene degradation products by using a GC-MS. Mechanism of 4-chlorotoluene decomposition in air mixture in an electron beam generated non-thermal plasma reactor was proposed. OH radicals play a main role for 4-chlorotoluene decomposition.

1. Introduction

Volatile organic compounds (VOCs) , which are emitted from fossil–fuel power stations [1], waste incinerators [2], chemical factories, etc. are very harmful to the environment and human health. It can cause ozone depletion in stratosphere and ozone formation in troposphere. In urbanized area, VOCs are emitted into atmosphere by mainly anthropogenic sources. About 40% ozone produced photochemically might contribute to emission of aromatics, mainly toluene [3]. Moreover, recent studies reported that chlorinated benzenes or phenols are suspected as precursors for dioxins emission [4]. Therefore, VOCs must be treated before they are discharged into atmosphere.

VOCs removal from gas phase has been studied in recent years. Toluene destruction by using non-thermal plasma(NTP) [5,6], NTP combined with catalyst [7], electron beam (EB) [8-10] and electron beam combined with catalyst technology [11] has been studied extensively in recent years. However very few work has been reported for 4-chlorotoluene (4-CTO) removal in gas phase [12]. Dechlorination of chlorotoluene in aqueous solution was studied, toluene [13] and benzene [14] were reported as dechlorination products.

Radical species formed inside the non-thermal plasma rector can oxidatively destroy organic pollutants present in gas phase. EB technology is one of the most promising NTP technologies. It can simultaneously decompose multiple pollutants in gas phase [15] at a relatively low energy consumption. In this work we studied 4-chlorotoluene degradation under EB radiation, in the meantime its degradation mechanism was proposed.

2. Experimental

2.1 Preparation model gas containing 4-chlorotoluene

The set up for preparation model gas of 4-chlorotoluene (CTO) was similar to that described in our previous work [16]. 4-Chlorotoluene model gas was prepared by bubbling synthesized air (≥99.995% purity; 21% O_2, N_2 as balance gas; $CO_2 \leq 1$ ppm, BOC gas company, Poland) into liquid 4-chlorotoluene (4-chlorotoluene, Purity 98% without further purification, provided by Sigma-Aldrich company, Germany). A temperature of 4-chlorotoluene was set to be 21°C with a water bath (type LW, manufactured by WSL Bytom company, Poland). The concentration of 4-chlorotoluene in the model gas was adjusted by controlling air flow rate by means of valve and rotameters. The model gas of 4-chlorotoluene was introduced into four connected Pyrex glass reactors by parallel connections . Active carbon adsorbents were connected at the outlet of glass reactors before the model gas was discharged into the atmosphere. When concentration in glass reactors became constant, the glass reactors were sealed with the stopcocks. The water concentrations in the model gas mixture were measured by a HM141 humidity and temperature indicator (Vaisala company, Finland). Water concentration in gas

mixture was 56 ppm. Experiments were carried out at ambient temperature condition and 1 bar atmospheric pressure.

2.2 An accelerator applied for plasma generation in the reactor

A pulsed electron beam accelerator ILU-6 (2.0 MeV max, 20 kW max) was used to generate plasma inside glass reactors. Irradiation set up can be referred to our previous work [16]. Pyrex glass reactors were put under scan horn of the accelerator for irradiation. Irradiation condition was described as follows: 2 Hz (pulse repetition rate), 2 MeV (energy) and 60 mA (pulse current). The absorbed dose (kGy, 1 kGy = 1 kJ/kg) inside glass reactors was measured by a cellulose triacetate (CTA) film dosimeter and was recalculated based on an empirical formula obtained between $\text{dose}_{(CTA)}$ and $\text{dose}_{(N_2O)}$ [17]:

$$\text{dose}_{(N_2O)} = 2.897 * \text{dose}_{(CTA)} \quad (1)$$

2.3 Analytical methods

Concentrations of 4-chlorotoluene (4-CTO) before and after irradiation contained inside the reactos were measured by a gas chromatography (GC-17A, Shimadzu Corporation, Japan) equipped with a flame ionizing detector (GC-FID). A capillary column (Supercowax^{TM}-10, 30m × 0.32mm × 0.25μm, Supelco Company, USA) was used. Stock solutions of 4-chlorotoluene (200 μg/ml in methanol, AccuStandard company, USA) were used for preparation calibration curves. Analytical condition for 4-chlorotoluene concentration measurement was given as follows: column temperature was kept at 40°C for 1 min, then increased to 160°C at 20°C/min; injector temperature was 100°C and detector temperature was 250°C; Injection mode was split, split ratio was 40:1. The injection volume of 4-chlorotoluene air mixture was 1 mL.

By-product analysis after electron beam radiation were carried out in this work. Analytical method for by-products identification was improved based on our previous work [12]. A gas chromatography equipped with a mass detector (GCMS-QP 5050A, Shimadzu Corporation, Japan) and a HP-5MS column (30m × 0.25mm × 0.25μm, Agilent technologies Incorporation, USA) were used to identify by-products. Gas phase by-products of 4-chlorotoluene degradation were analyzed by direct injecting 250 μl gas mixture into the GC-MS, GC-MS analytical condition was given as follows: the oven was held at 40°C for 1 minute, then programmed at 5°C/min to 140°C, then 10°C/min to 270°C and held at 270°C for 1 minute. Injector temperature was 210°C and detector temperature was 280°C. Solid phase by-products formed from 4-chlorotulene degradation were analyzed according to the following procedures: 5 ml CH_3OH was used to wash the glass reactors which contained the by-products to obtain solution I , then this solution I was concentrated to approximately 0.3 ml by using a micro-extractor under continuously blowing high purity N_2 (99.995% purity, BOC gas company, Poland) to obtain solution II. 1 μL of the concentrated extract solution II was injected. The analytical condition was given as follows: the oven was held at 40°C for 1 minute, then programmed at 3°C/min to 139°C, then 10°C/min to 269°C and held at 269°C for 1 minute. Injector temperature was 210°C and detector temperature was 280°C. Electron impact ionization mode of MS was applied, 70 eV energy was used.

2.4 Dose dependence of removal efficiency or decomposition efficiency

In radiation process, it is very important to consider energy consumption for degradation of pollutants, how much energy (unit: kJ) is consumed/absorbed to decompose amount of pollutants in the base gas (unit: kg). Energy absorbed by per amount of gas is defined as a term of dose, unit is kGy.

1 kGy = 1 kJ/ kg.

Removal efficiency or decomposition efficiency of organic pollutants is defined as R

$$R = (C_0 - C_i) / C_0 \quad (2)$$

where C_0 is initial concentration of organic pollutants, unit: ppm (v/v); C_i is concentration of organic pollutants at i kGy absorbed dose, unit: ppm (v/v)

3. Results and discussions

3.1 Decomposition efficiency of 4-chlorotoluene vs. dose

Decomposition efficiency of 4-chlorotoluene versus dose in an air mixture was studied in an electron beam generated non-thermal plasma reactor and results were presented in figure 1. Water vapor concentration in an air mixture was 58 ppm (v/v). It can be seen that decomposition efficiencies of 4-chlorotoluene increase with the absorbed energy increasing.

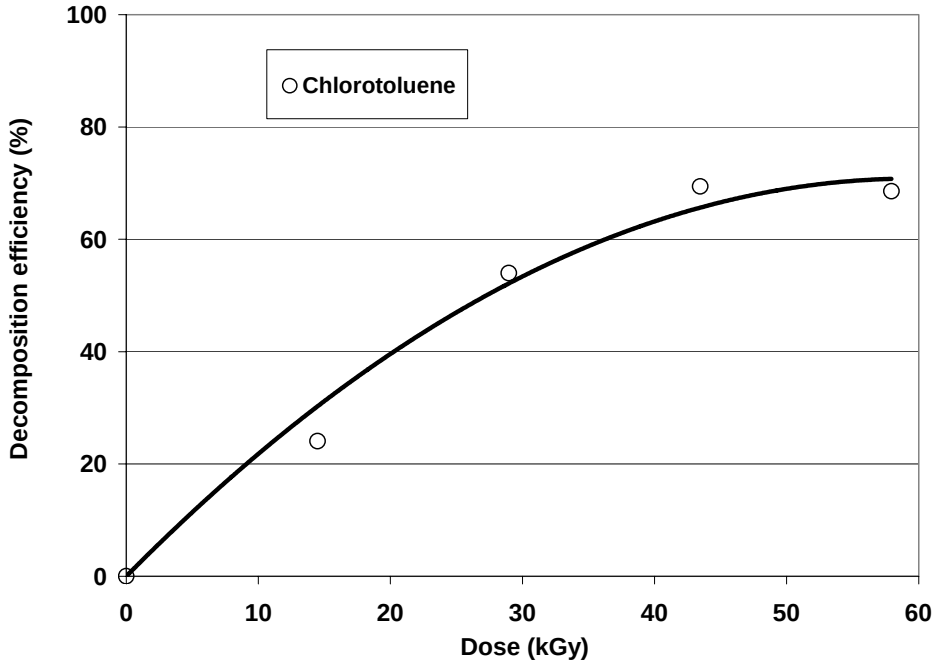


Fig. 1. A dependence of the removal efficiency of 4-chlorotoluene on the dose absorbed under EB radiation (initial concentration of 4-chlorotoluene was 51.9 ppm)

3.2 By-products

In order to obtain information of by-products formed from 4-chlorotoluene degradation, high inlet concentration of 4-chlorotoluene (275.9 ppm) in an air mixture was studied at 57.94 kGy absorbed dose. About 26.46% 4-chlorotoluene was decomposed.

The GC-MS chromatograms of the gas phase and solid phase by-product of 4-chlorotoluene degradation in air mixture under electron beam radiation were presented in Fig.2a and Fig. 2b, respectively.

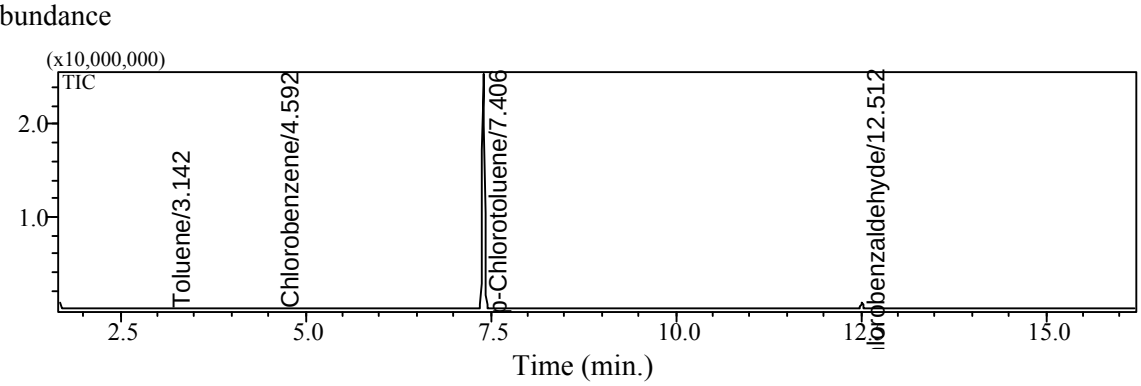


Fig. 2a A GC-MS chromatogram of gas phase by-product of 4-chlorotoluene degradation in air mixture

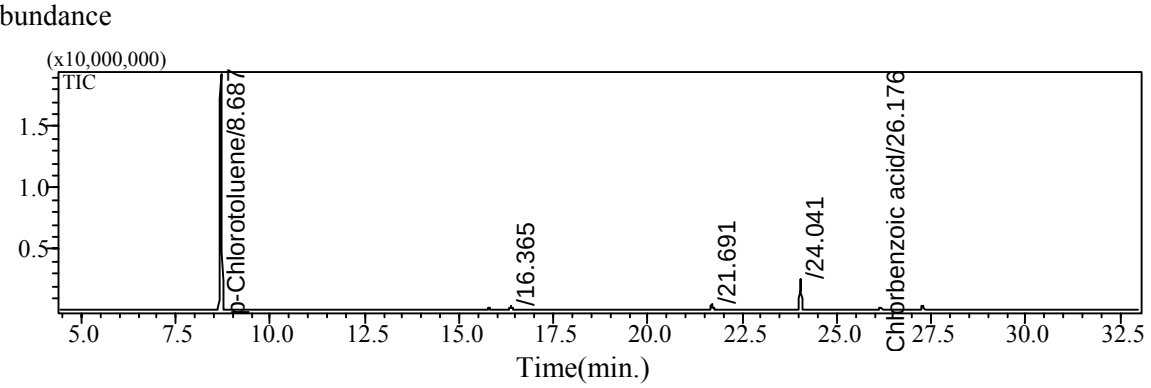


Fig. 2b A GC-MS chromatogram of solid phase by-product of 4-chlorotoluene degradation in air mixture

Compounds eluted in Fig. 2b at retention time 16.365, 21.691, 24.041min., respectively, were identified as 4-chlorobenzaldehyde, 4-chlorobenzyl alcohol, 1-chloro-2-(dimethoxymethyl)benzene. Toluene was also detected in the 4-chlorotoluene air mixture before irradiation. Toluene presence was due to impurity of 4-chlorotoluene. The by-products of 4-chlorotoluene degradation in air mixture are chlorobenzene (C_6H_5Cl), 4-chlorobenzaldehyde ($Cl\text{-}C_6H_4\text{-}CHO$), 4-chlorobenzyl alcohol ($Cl\text{-}C_6H_4\text{-}CH_2OH$), 4-chlorobenzoic acid ($Cl\text{-}C_6H_4\text{-}COOH$) and 1-chloro-2-(dimethoxymethyl)benzene.

3.3 Mechanism

Irradiation a low-humidity air mixture containing 4-chlorotoluene ($\mathbf{Cl}\text{-}C_6H_4CH_3$) by an electron beam accelerator leads to a formation of $^{\bullet}OH$ radicals. $^{\bullet}OH$ radicals react subsequently with 4-chlorotoluene by hydrogen abstraction from the methyl group resulting in a formation of benzyl radicals (reaction R1). In the presence of oxygen the respective peroxyl radicals derived from benzyl radicals are formed (reaction R2). The peroxyl radicals undergo further recombination resulting in the formation of oxyl radicals, molecular oxygen (reaction R3a) and tetraoxide (reaction R3b). This tetraoxide intermediate decomposes according to the Russel-mechanism (reaction R4). Chlorobenzaldehyde ($Cl\text{-}C_6H_4\text{-}CHO$), chlorobenzyl alcohol ($Cl\text{-}C_6H_4\text{-}CH_2OH$) and oxygen are formed. $RC_6H_4CH_2O^{\bullet}$ reacts with O_2 to form chlorobenzaldehyde (reaction R5).

$OH + Cl\text{-}C6H_4\text{-}CH_3 = H_2O + Cl\text{-}C_6H_4CH_2^{\bullet}$ (R1)

$ClC_6H_5CH_2^{\bullet} + O_2 = Cl\text{-}C_6H_4CH_2(O_2)^{\bullet}$ (R2)

$2Cl\text{-}C_6H_4CH_2(O_2)^{\bullet} = 2Cl\text{-}C_6H_4CH_2O^{\bullet} + O_2$ (R3a)

$2Cl\text{-}C_6H_4CH_2(O_2)^{\bullet} = (Cl\text{-}C_6H_4CH_2O_2)_2$ (R3b)

$(Cl\text{-}C_6H_4CH_2O_2^{\bullet})_2 = \mathbf{Cl\text{-}C_6H_4CHO} + \mathbf{Cl\text{-}C_6H_4CH_2OH} + O_2$ (R4)

$Cl\text{-}C_6H_4CH_2O^{\bullet} + O_2 = \mathbf{Cl\text{-}C_6H_4CHO} + HO_2$ (R5)

$Cl\text{-}C_6H_4CHO$ might undergo further reaction R6 resulting in formation of chlorobenzoic acid ($Cl\text{-}C_6H_4\text{-}COOH$). Chlorobenzoic acid will release CO_2 to form chlorobenzene (R7).

$Cl\text{-}C_6H_4CHO + O = \mathbf{Cl\text{-}C_6H_4COOH}$ (R6)

$\mathbf{Cl\text{-}C_6H_4COOH} = \mathbf{Cl\text{-}C_6H_5} + CO_2$ (R7)

It is not clear how 1-chloro-2-(dimethoxymethyl)benzene was formed from 4-chlorotoluene degradation.

4. Conclusions

4-chlorotoluene in air mixture can be decomposed in an electron beam generated plasma reactor. The decomposition efficiency of 4-chlorotoluene increases with the absorbed dose. Chlorobenzene,

chlorobenzaldehyde , chlorobenzyl alcohol and chlorobenzoic acid were identified as 4-chlorotoluene degradation products. OH radicals play a main role for 4-chlorotoluene decomposition.

Acknowledgments

This work was funded by "PlasTEP: Dissemination and fostering of plasma based technological innovation for environment protection in BSR" (Project No #033 of the Baltic Sea Region Program 2007-2013) and this financial support is greatly appreciated.

5. References

[1] Fernández-Martínez G, López-Mahía P, Muniategui-Lorenzo S, Prada-Rodríguez D and Fernández-Fernándze E 2001 *Atmos. Environ.* **35** 5823.
[2] Jay K and Stieglitz L 1995 *Chemosphere* **30** 1249.
[3] Derwent R G, Jenkin M E and Saunders S M 1996 *Atmos. Environ.* **30** 181.
[4] McKay G 2002 *Chem. Eng. J.* **86** 343.
[5] Chang C L and Lin T S 2005 *Plasma Chem Plasma P.* **25** 227.
[6] Guo Y F, Ye D Q, Tian Y F and Chen K F 2006, *Plasma Chem Plasma P*. **26** 237.
[7] Subrahmanyam Ch, Magureanu M, Renken A and Kiwi-Minsker L 2006 *Appl. Catal. B-Environ.* **65** 150.
[8] Han D H.,Stuchinskaya T, Won Y S, Park W S and Lim J K 2003, *Radiat. Phys. Chem*. **67** 51.
[9] Hashimoto S, Hakoda T, Hirata K and Arai H 2000 *Radiat. Phys. Chem.* **57** 485.
[10] Sun Y, Chmielewski AG, Licki J, Bułka S and Zimek Z 2009 *Radiat. Phys. Chem.* **78** 721.
[11] Kim K J, Kim J C, Kim J and Sunwoo Y 2005 *Radiat Phys Chem* **73** 85.
[12] Sun Y, Chmielewski A G, Bułka S and Zimek Z 2008 *Chem. Listy* **102** s1524.
[13] Janiak T 2008 *Appl. Catal. A-Gen.* **335** 7.
[14] Haines B M, Gland J L 2008 *Surf. Sci.* **602** 1871.
[15] Sun Y, Chmielewski A G, Licki J, Bułka S and Zimek Z 2003 *Radiat. Phys. Chem.* **67** 555.
[16] Sun Y, Chmielewski A G, Bułka S and Zimek Z 2006 *Plasma Chem. Plasma P.* **26** 347.
[17] Sun Y 2005 *Radiation Induced Decomposition of Selected Chlorinated Hydrocarbons in Gaseous Phase*. Ph.D thesis, Warsaw, Poland.

SECONDARY IONIZATION COEFFICIENT OF DIELECTRIC ELECTRODE MATERIALS

Susumu Suzuki[1], Yasuhide Kashiwagi[2], Haruo Itoh[1]

[1]*Chiba Institute of Technology*
[2]*Kisarazu National College of Technology*
E-mail: susumu.suzuki@it-chiba.ac.jp

Investigation is carried out to determine the secondary ionization coefficient γ of a CaO film electrode taking into account the difference between the breakdown voltages in the first, second and stationary states. The voltage and charge waveforms vary with repeated measurements. If the CaO film electrode serves as the cathode, the breakdown voltage gradually decreases, becoming almost constant after several breakdowns. It is thus confirmed that the γ of the CaO film electrode in the stationary state is higher than that in the first breakdown. The results suggest a difference in γ between breakdown originating from some changes accumulated on the CaO film electrode.

1. Introduction

Dielectric barrier discharge (DBD) is widely utilized in many fields, such as plasma display panels, ozonizers and excimer lamps. The selection of its dielectric material is important from the following points, such as the decrease in and stabilization of the starting voltage at the gaps, the deterioration and lifetime of the electrode material and the secondary electron emission characteristic of the material. In particular, the secondary ionization coefficient γ is necessary for DBD investigation and the design of discharge gap on the based of numerical simulation.

We have determined γ from breakdown voltage using the sequential procedure mentioned by Auday et al.[1]. Furthermore, the breakdown voltage V_s between the MgO film and stainless steel electrodes (SUS) was measured to be AC 2 kHz, and γ was estimated using Townsend's criterion[2]-[6].

In this paper, we describe γ of CaO that is expected to serves the protective film of metal electrodes in the next-stage PDP. We observe in this study the breakdown voltage in the first, second and stationary states. We also observe waveforms of surface voltage on CaO films and the electric charge produced by discharge by inducing repeated discharges at a gap. If a CaO film serves as the cathode, breakdown voltage decreases gradually with discharge repetition, and after several discharges, breakdown voltage becomes almost constant. This means that the initial γ of a dielectric material is smaller than γ during discharge in the steady state. Moreover, it is also confirmed that the secondary ionization coefficient γ of a CaO film electrode is smaller than those of other dielectric materials determined by the authors until now.

2. Experimental apparatus and method

Figure 1 shows the schematic diagram of the experimental apparatus. The sinusoidal voltage generated by a signal generator and amplified by a high-speed bipolar power supply is applied to a stainless steel electrode. A parallel-plate gap consists of a stainless steel electrode shaped as a cylinder with a diameter of 20 mm and the

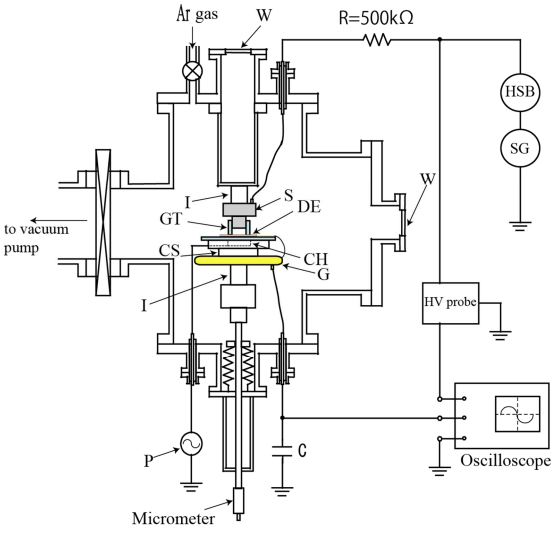


Fig. 1 Schematic diagram of experimental setup. SG: Signal generator, HSB: High-speed bipolar power supply, S: Stainless steel electrode, DE: Dielectric electrode, CH: Ceramic heator, CS: Ceramic spacer, G: Gold film electrode, I: Insulator, W: Quartz window, GT: Glass tube, P: Power supply for ceramic heator.

surface of the CaO film electrode. The stainless steel electrode is installed in a glass tube. The waveform of applied voltage is monitored using an oscilloscope through a potential divider with the probe. At the same time, the accumulated charge on the CaO film electrode is detected by the capacitor C connected between the CaO film electrode and the ground. In preparation for the experiment, the CaO film electrode is heated using a ceramic heater for at least 2 h at 400℃, in accordance with the experiment of Shiokawa et al. [7], and the discharge chamber is evacuated to vacuum using a turbomolecular pumping system. The purity of the Ar used is 99.9995%.

3. Experimental results and discussion

3.1 Breakdown voltage

After the chamber is evacuated using the turbomolecular pump, Ar gas is introduced into the chamber and sinusoidal voltage is applied between the electrodes. Figure 2 shows the result of the waveforms for the first and second discharges, which started in a positive polarity. The waveforms in Figure 2 (a) are the applied voltage $V(t)$ and the accumulated charge q (t) of the CaO film electrode. Those Figure 2 (b) are gap voltage V_g (t) and the surface voltage $V_w(t)$ of the CaO film electrode. During the application of a positive voltage, the CaO film electrode serves as the cathode. Therefore, the breakdown voltage V_s was determined from the gap voltage V_g (t) in Figure 2 (b) at the time A, which is the buildup time of $q(t)$ in Figure 2 (a). The buildup of $q(t)$ is almost vertically; however, the second breakdown at the time C is slower than the first one at the time A. Moreover, the position of the first starting voltage at the time A is placed at the back of the peak in the positive half-period; however, the position of the second starting voltage shifts to the front of the peak at the time C with repeated measurements. Breakdown voltage decreases gradually, and after several breakdowns, becomes almost constant and appears in a constant phase; it is thus considered to be in the stationary state.

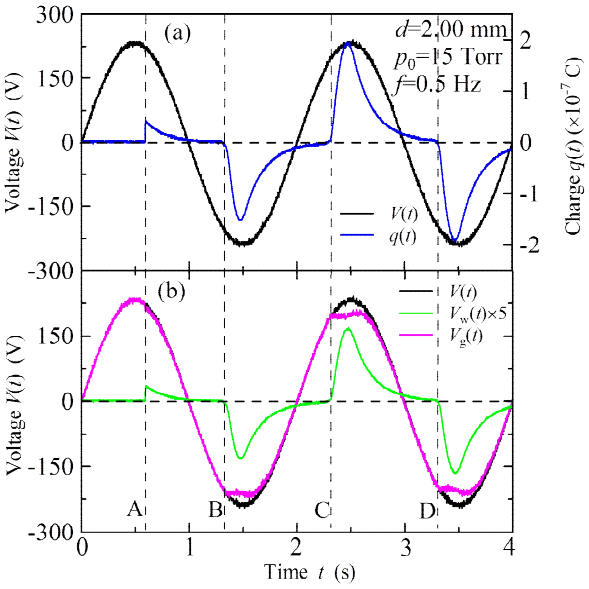


Fig. 2 Voltage and charge waveforms. (d = 2.00 mm, p_0 = 15 Torr, f = 0.5 Hz)

Figures 3 and 4 show expanded figures in the vicinity of the times A and B, which are the first starting voltages in the positive and negative polarities in Figure 2 (b), respectively. The waveform of V_w (t) increases and the gap voltage V_g (t) decreases slightly.

Figures 5 and 6 show the discharge currents at the times A and B calculated from $q(t)$, respectively, as shown in Figure 2. The current is a single pulse during buildup at the time A. In contrast, the buildup

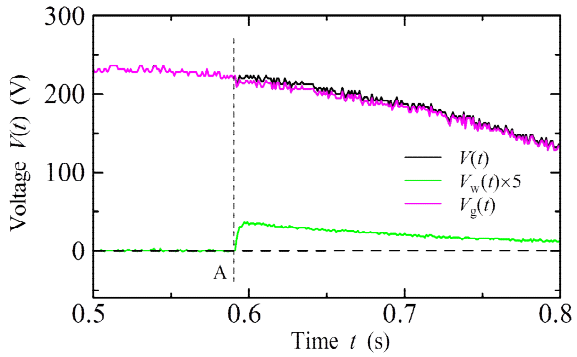


Fig. 3 Enlarged in the vicinity of A of Fig. 2(b) of voltage waveforms.

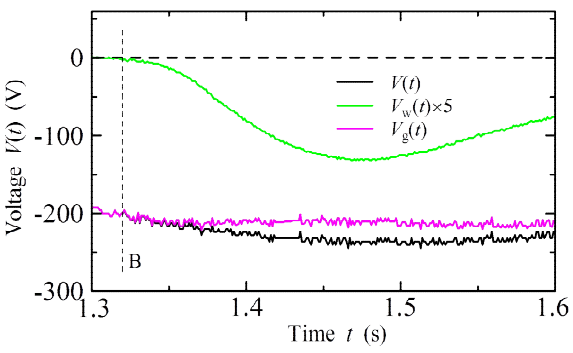


Fig. 4 Enlarged in the vicinity of A of Fig. 2(b) of voltage waveforms.

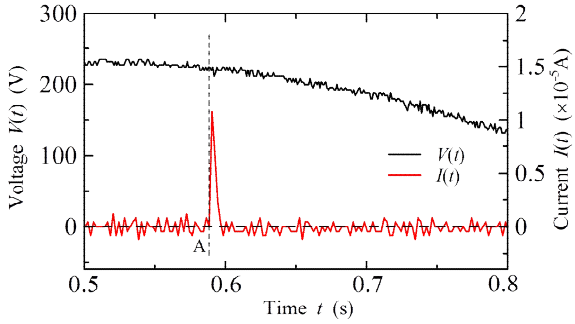


Fig. 5 Current in the vicinity of A of Fig. 2.

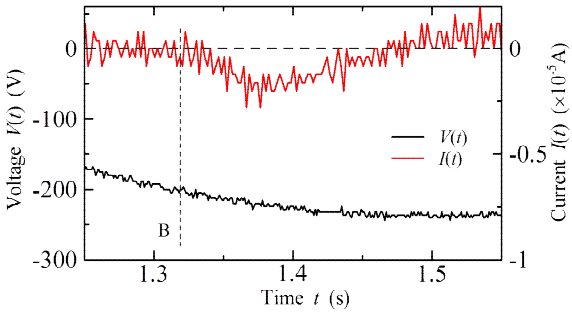


Fig. 6 Current in the vicinity of A of Fig. 2.

of current at the time B is slower.

In contrast, Figure 7 shows an example of the first discharge generated at the time A when the stainless steel electrode serves as the cathode. The first discharge voltage of the time A is higher than the second discharge voltage of the time C. In addition, it is understood that the amplitude of $q(t)$ at the time C is larger than that at the time A. $q(t)$ on the CaO at B and D is almost of the same amplitude. The buildup time of $q(t)$ at the time A is almost the same as that at the time B. The position of the buildup of $q(t)$ at the time A is at the back of the peak of the applied voltage as shown in Figure 2, and the position of the second starting voltage shifts to the front of the peak of the applied voltage.

Figures 8 and 9 show expanded figures in the vicinity of the times A and B of the starting voltages in the first positive and negative polarities in Figure 7 (b), respectively. The waveform of the gap voltage V_g (t) decreases simultaneously with the charge $q(t)$ buildup according to the buildup. The charge waveform has an extremely small amplitude so that the first discharge is generated on the stainless steel electrode side, as shown in Figure 7.

Figure 10 shows the breakdown voltage against p_0d, where p_0 is the gas pressure at 273 K and d is the gap length. The V_s values of the CaO film electrode and stainless steel electrode, both of which serve as the cathode, are shown by the solid and dotted lines in the stationary state, respectively. These value are determined by averaging the breakdown voltage. The closed circles ●, open circles ○ and squares □ are values of the first, second and third breakdown

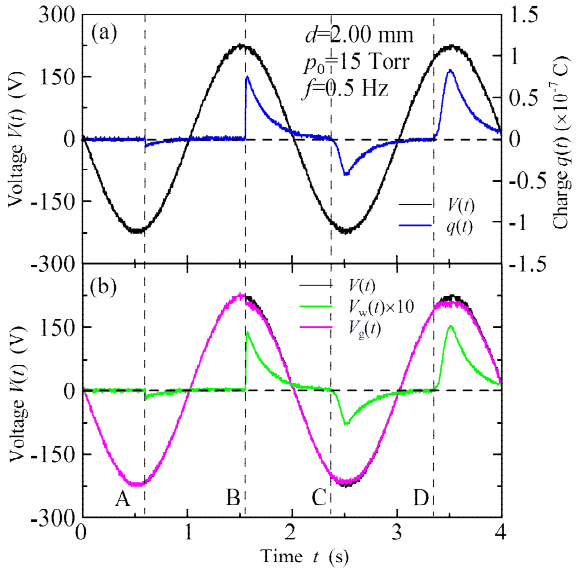


Fig. 7 Voltage and charge waveforms. (d = 2.00 mm, p_0 = 15 Torr, f = 0.5 Hz)

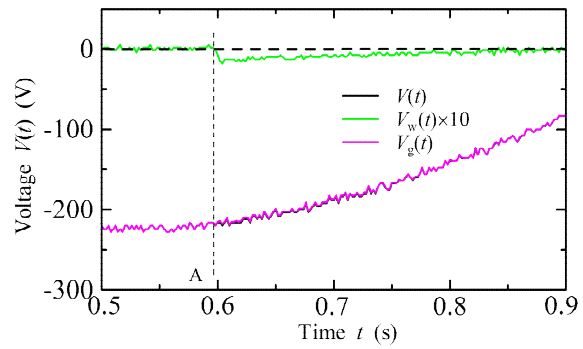


Fig. 8 Enlarged in the vicinity of A of Fig. 5(b) of voltage waveforms.

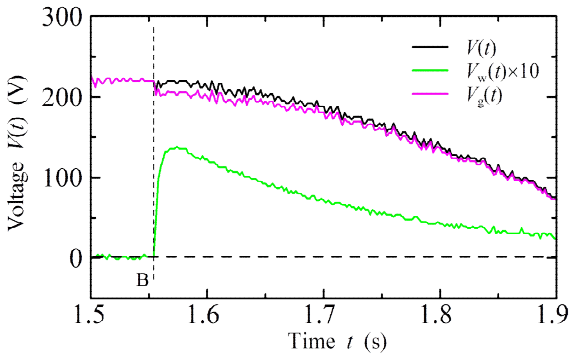


Fig. 9 Enlarged in the vicinity of B of Fig. 5(b) of voltage waveforms.

Voltages, respectively, as shown in Figures 2 and 7. The first V_s is highest, and the second and third ones are lower.

Figure 11 shows the detailed variation in the breakdown voltage V_s with repeated measurements for each gas pressure. The V_s values of the CaO film and stainless steel electrodes are shown by ○ and △, respectively. When the CaO film serves as the cathode at any gas pressure, the first V_s is highest. In contrast, the V_s fluctuates when the stainless steel electrode serves as the cathode.

The reason for the first V_s of the CaO film being highest is considered to be the nonaccumulation of charges on the dielectric electrode. This is supported by the notion that the first buildup of $q(t)$ is faster compare with the following breakdown, so that it is considered under an overvoltage condition. After the first time, charges accumulate on the CaO film and are introduced into lower breakdown voltage and slow buildup of $q(t)$. However, if a certain charge attaches on CaO at once, it can perform as a source of the initial electron.

Figure 12 shows the variation of buildup time of discharge current. The first buildup time in the case of the CaO film electrode is about 2 ms. This value is shorter than that in the case of the stainless steel electrode which is typically almost 26 ms. After several breakdowns with repeated measurements, the buildup time becomes constant in both cases. In particular, the first buildup time in the case of the CaO film electrode is about tenfold shorter than the second buildup time.

3.2 Secondary ionization coefficient

Figure 13 shows the secondary ionization coefficient γ of the CaO film electrode determined from the data in Figure 10. It is understood that the first γ is smallest compared with second, third and the average γ's. It is considered that a higher voltage is needed for the first discharge, and thus, it is assumed that the buildup times of discharge current and charge shorten.

Figure 14 shows the variation in γ with repetition time for the CaO film and the stainless steel electrodes at a gap length d = 2.00 mm and a gas pressure p_0 = 30 Torr. The first γ is small, but increases toward a constant value with repeated measurements. Moreover, the reduced electric field E/p_0 decreases toward a definite value with repeated measurements. From such a result, the first discharge, when the CaO film serves as the cathode, lacks an initial charge for the initiation of breakdown. However, if electrical discharge starts

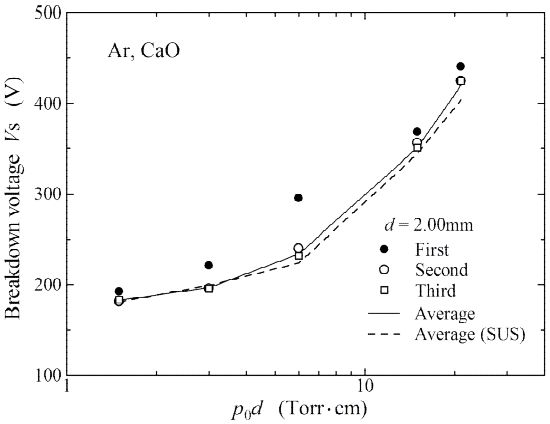


Fig. 10 Paschen curve.

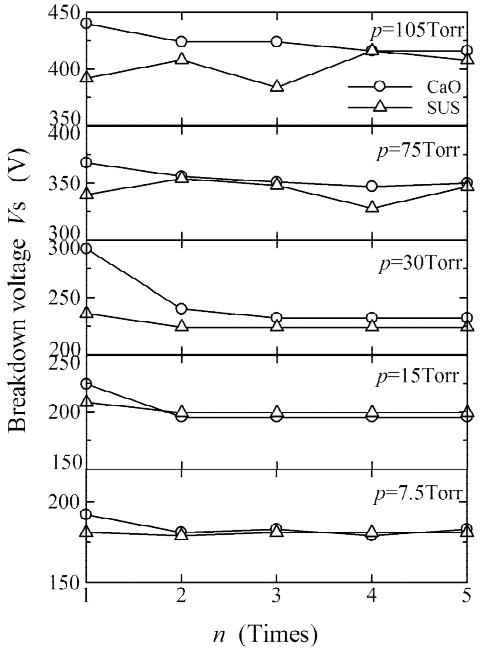


Fig. 11 Variation of breakdown voltage by repeated measurement.

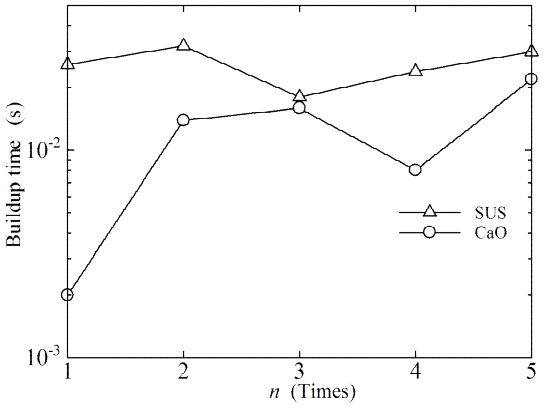


Fig. 12 Variation of rise time by repeated measurement.
(d = 2.00 mm, p_0 = 15 Torr, f = 0.5 Hz)

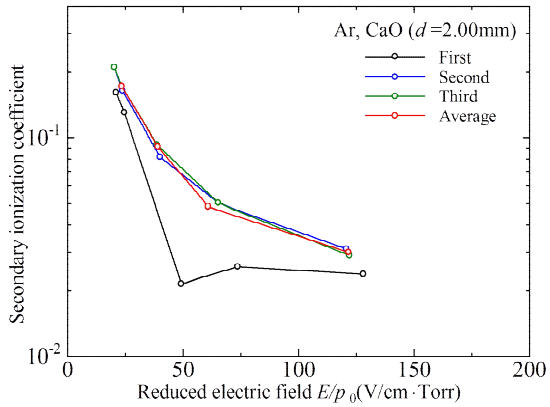


Fig. 13 Secondary ionization coefficient.

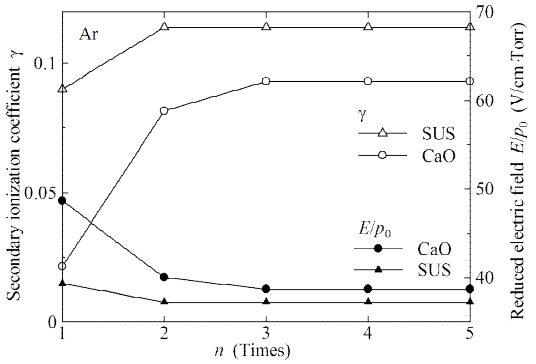


Fig. 14 Variation of secondary ionization coefficient by repeated measurement.
(d = 2.00 mm, p_0 = 30 Torr, f = 0.5 Hz)

at once, residual charges on the surface contribute to maintaining lower starting voltage of the discharge as the source of initial electrons. Therefore, this process should be called as electron release from CaO or as the restart of the electron from CaO rather than electron emission from a bulk in CaO. This result proves the discussion in our previous paper that the pattern of the self-organized hexagon is formed with the residual charge on the dielectric surface in He/Xe mixture by time-resolved photographs [8].

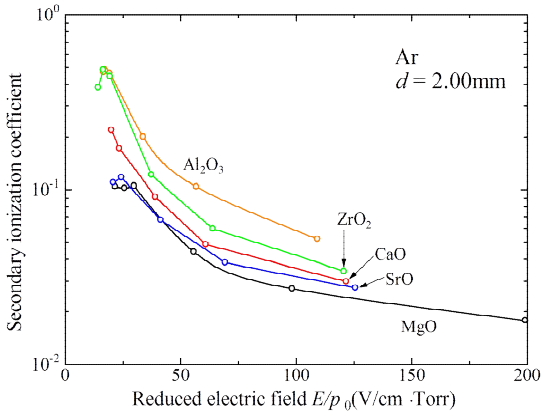


Fig. 15 Secondary ionization coefficient.

Figure 15 shows the γ of the CaO film electrode together with those obtained in our previous investigation [6]. These correspond to the stationary state of discharge and thus could be considered averages. In the range of measured E/p_0 values, the γ values of CaO is smaller than those of $A1_2O_3$ and ZrO_2, however it is larger than those of SrO and MgO.

4. Conclusions

We found that if no charge is on the surface dielectric electrode, then the secondary ionization coefficient γ is low compared with the stationary discharge condition. This suggests that the accumulated charge plays a role as the source of electron for restart of the discharge.

5. Acknowledgment

This work was supported by MEXT-Supported Program for the Strategic Research Foundation at Private Universities, 2008-2012.

6. References

[1] G.Auday, Ph. Guillot and J.Galy 2000 *J. Appl. Phys.*, 88, 4871-4874.
[2] S.Suzuki and H.Itoh 2004 *Jpn.J.Appl.Phys.*, 43, 10, 7234-7239.
[3] S.Suzuki and H.Itoh 2007 *Jpn.J.Appl.Phys.*, 46, 1129-1136.
[4] S.Suzuki, K.Konno and H.Itoh2009 *IEEJ Trans. FM*, **129**, 909-914. (in Japanese)
[5] K.Kashiwagi, S.Suzuki and H.Itoh 2011 *IEEJ Trans. FM*, Vol.131, 7, pp.547-552. (in Japanese)
[6] S.Suzuki, T.Sekizawa, Y.Kashiwagi and H. Itoh 2011 *Jpn. J. Appl. Phys.*, 50, 106002(6 pages).
[7] A.Shiokawa, Y.Takada, R.Murai and H.Tanaka 1999 *Proc. of IDW '99*, 519-522.
[8] H.Itoh, K.Kobayashi, K.Teranishi, N. Shimomura and S. Suzuki 2011 *IEEE Trans. Plasma Science*, 39, 11, 2204-2205.

MAGNETIC FIELD CONTROLLED CNTS SYNTHESIS IN AN ELECTRICAL ARC

Lukasz Szymanski, Grzegorz Raniszewski, Zbigniew Kolacinski

Technical University of Lodz, Institute of Mechatronics and Information Systems,
18/22 Stefanowskiego Street, 90924 Lodz, Poland

E-mail: lukasz.szymanski@p.lodz.pl

The paper presents the research results of carbon nanotubes synthesis in different electric arc parameters and the chamber atmosphere. In order to improve the efficiency of the system the external magnetic field was applied. The field had been used to produce a stable, rotating arc in the cathode region. It allowed creation of an intense and uniform jet of vapor which was generated in the anode spot and flowing to the cathode region ensuring effective mass transfer. Due to the magnetic field generated by external coil or permanent magnets it was possible to stabilize the arc cathode region temperature. The arc channel temperature in this region appeared to be crucial for synthesis and quality of the CNTs.

1. Introduction

The carbon electric arc was a primary processing method that was developed for nanomaterials synthesis. The plasma reactor consisted of DC supplied two graphite electrodes prepared to generate an electric arc in a chamber of a low pressure helium atmosphere. The gas present in the plasma chamber does not react with carbon being the material of the electrodes. The effect of high temperature in the arc discharge channel leads to the moving of graphite material as the vapor jet generated in the hot anode spot to the relatively cool cathode surface. This in turn results in erection and growing of the cathode carbon deposit. This deposit forms a graphite root which has a hard outer shell and a soft inner core filled with carbon nanotubes (CNTs). The quality of these nanotubes and the degree of contamination with soot depend strongly on temperature of the anode spot where carbon sublimation takes place and the temperature of the near cathode arc channel region where the synthesis of CNTs appears.

2. Reactor concept and research

Synthesis of CNTs followed in a steel chamber in the electric arc discharge, which burned between two electrodes in an atmosphere of helium at low pressure (from 0.2 to 0.6 bar). The gas in the chamber doesn't react with the carbon being the material of the electrodes. The temperature in the discharge leads to the formation of graphite cathode deposits. The carbon material moving directly from the hot anode spot to cathode surface. To improve the efficiency synthesis the external magnetic field was used to produce a stable-rotating arc.

This concept allowed to create an intense and steady stream of vapour, which was transferred from the anode to the cathode, in order to ensure the effective mass flow of the material. This field was produced by applying a DC-powered magnetic coil mounted axially on the cathode rod. Fig.1 shows the reactor concept and Fig. 2 shows view inside the chamber.

The system was equipped with a gas pressure regulator. The vacuum can be adjusted with an accuracy of 1 hPa (0.01 Bar). This was made possible through the control valve with a vacuum pump and helium metering valve. The arc voltage was adjusted through the system measuring and regulating distance between the electrodes. In order to determine the relation between the growth of CNTs and the arc parameters (determining the processing conditions in the chamber) the following parameters were measured and adjusted: current and voltage of the electric arc, the pressure inside the chamber, current flowing in the magnetic coil. Circuit parameters during the tests were adjusted automatically by the PLC driver, to obtain the optimal rotation of the arc on the cathode surface (area

about 2 cm^2). Anode rod diameter used during the tests was 6 mm. Fig. 3 shows a photo of the synthesis chamber.

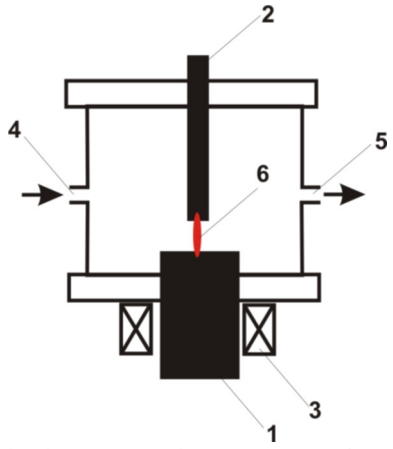


Fig. 1. Concept of reactor (1 – cathode, 2 – anode, 3 – magnetic coil, 4 - gas inlet, 5 – gas outlet, 6- electric arc)

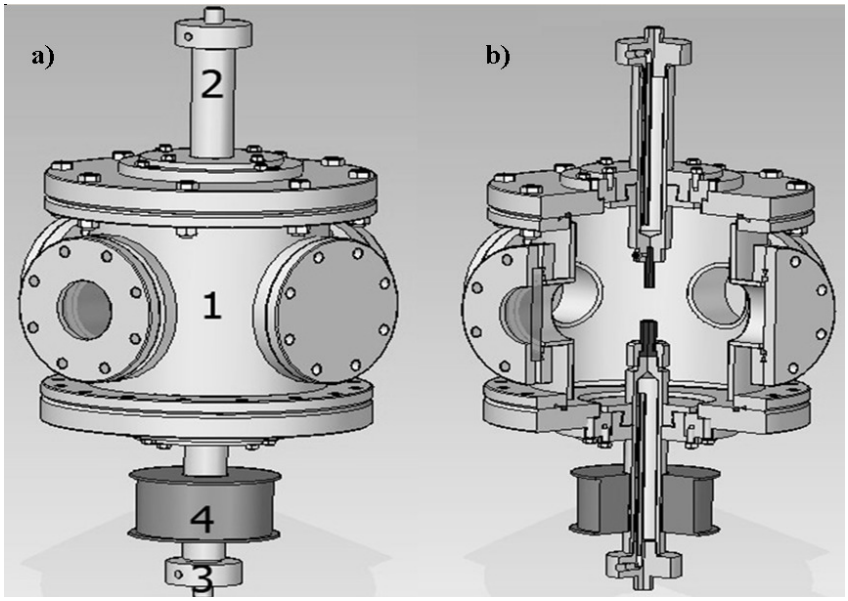


Fig.2. Reaction chamber (left hand side – a) and view inside the chamber (right hand side – b) (1 – chamber, 2 – anode, 3 – cathode, 4 – magnetic coil).

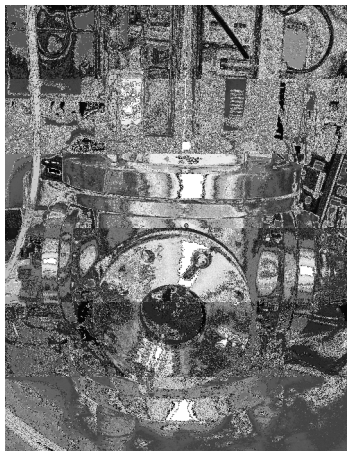


Fig. 3. Photo of the CNTs synthesis chamber

3. Arc burning conditions

All the tests were guided by the equation describing the optimal conditions in the chamber for synthesis of carbon nanotubes obtained in the helium plasma defined by Przemyslaw Byszewski [1]. The area of efficient synthesis of nanotubes in the helium-carbon arc plasma is situated above the curve described a common function of the pressure (p) and the current arc (i):

$$(p + p_o)(i - i_0) = c_o \quad (1)$$

where:

p_o = - 0,3 atm, i_o = 40 A, c_o = 12,7 A·atm.

In laboratory tests we have defined and checked the range of currents depended on pressure in the chamber for electrodes with a diameter of 6 mm (Tab.1). The optimal synthesis conditions determines the curve in Fig. 4.

Tab. 1. Optimal conditions of arc current and pressure in the arc chamber for CNTs synthesis.

Chamber pressure Bar	Arc current A	Chamber pressure Bar	Arc current A
0,15	68,22	3,95	43,02
0,30	61,17	4,10	42,92
0,46	56,93	4,26	42,82
0,61	54,11	4,41	42,73
0,76	52,10	4,56	42,65
0,91	50,58	4,71	42,57
1,06	49,41	4,86	42,49
1,22	48,47	5,02	42,42
1,37	47,70	5,17	42,35
1,52	47,06	5,32	42,29
1,67	46,51	5,47	42,23
1,82	46,05	5,62	42,17
1,98	45,64	5,78	42,12
2,13	45,29	5,93	42,07
2,28	44,98	6,08	42,02
2,43	44,70	6,23	41,97
2,58	44,46	6,38	41,92
2,74	44,23	6,54	41,88
2,89	44,03	6,69	41,84
3,04	43,85	6,84	41,80
3,19	43,68	6,99	41,76
3,34	43,53	7,14	41,73
3,50	43,39	7,30	41,69
3,65	43,26	7,45	41,66
3,80	43,14	7,60	41,63
3,95	43,02	7,75	41,60

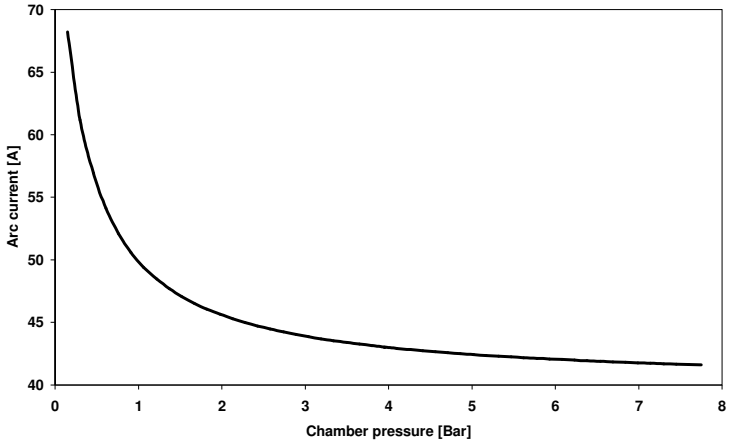


Fig. 4. Conditions of optimal synthesis of nanotubes.

4. Magnetic field measurement

A series of measurements of magnetic field in the reactor chamber were done with the Gaussmeter (Hirst GM04). Sample measurements of the magnetic field strength (for the coil current 20 A) around the cathode are shown in Fig. 5.

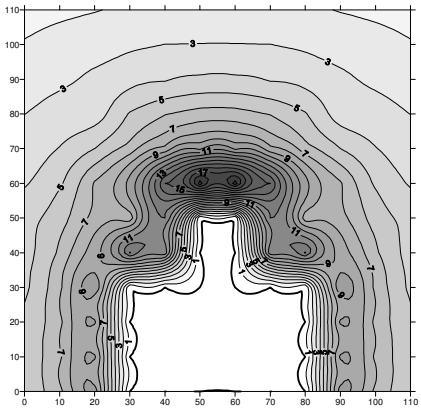


Fig. 4. Magnetic field around the cathode (in mT). Isolines show the location of the same field strength).

5. Test results

The final product is a mixture of carbon nanotubes, amorphous carbon, carbon black, graphite, etc. (Fig. 5) with different proportions, depending on process conditions. Therefore, in order to analyze the final product the purification and characterization are required.

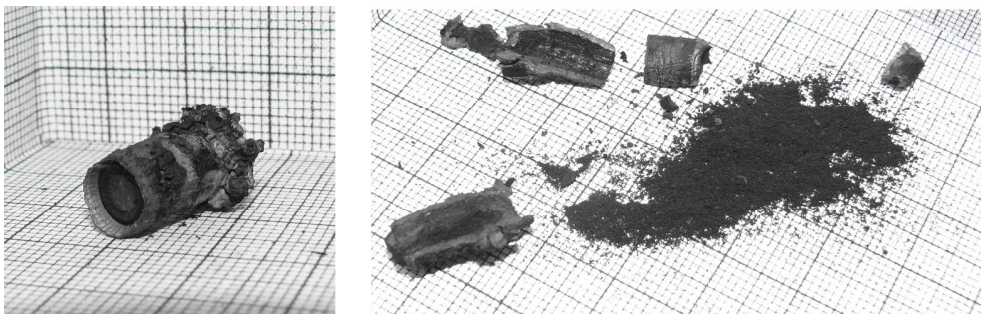


Fig. 5. Sample photo of the cathode deposit (whole deposit - left hand side and separated parts - right hand side).

Cathode deposits contained several to tens percent of carbon nanotubes, carbon black and the catalyst particles. Most of the samples were pre-treated by burning at a temperature of 450^0C in air for 2 hours to remove carbon black, fullerenes and nanotubes with defect. The residue after burning remained the nanotubes with good conformation and oxidized catalyst. At the SEM images it is possible to observe an improve of the quality of the deposit after the pretreatment operation (Fig. 6).

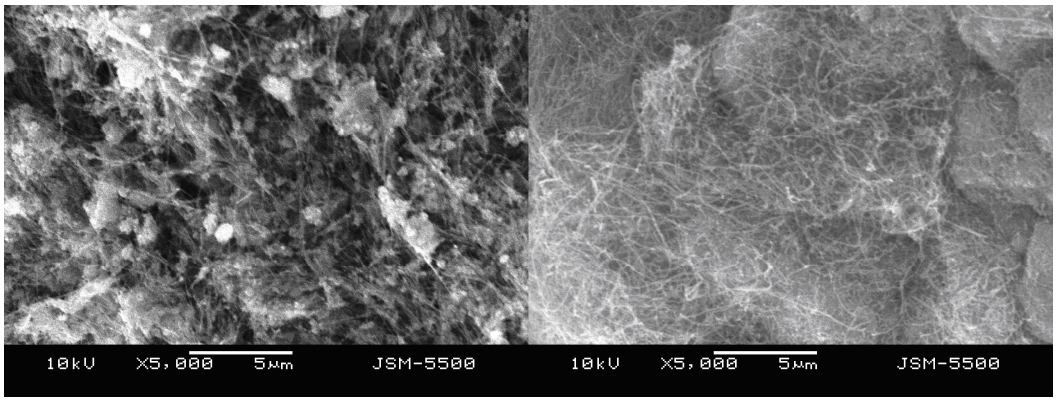


Fig. 6. - MWNTs nanotubes before pretreatment (left hand side) and after (right hand side)

In order to remove the iron III oxide (from nanotubes with the iron catalyst) milligrams of sample was heated in strong hydrochloric acid (36%). In our research a visible aggregation of CNTs followed in the acidic environment and therefore the reagent access to the interior of "clusters" was very difficult. The effective operation of elution Fe_2O_3 should be at least 20 - 25 hours or longer. Control of elution was carried out from time to time by applying a few drops of suspension on a porcelain plate. After the spot has dried the pellet was carefully washed with water. The plate was then heated in gas burner flame. Orange-brown traces indicated the presence of iron. Because in many samples after washing from Fe_2O_3 and burning the white precipitate was yet identified in the following etching trials we used hydrofluoric acid, which was able to dissolve the compounds iron and silicon. The reactions were made at a temperature 50^0C for 16 hours. The results were better than cleaning deposit with hydrochloric acid (Fig. 7).

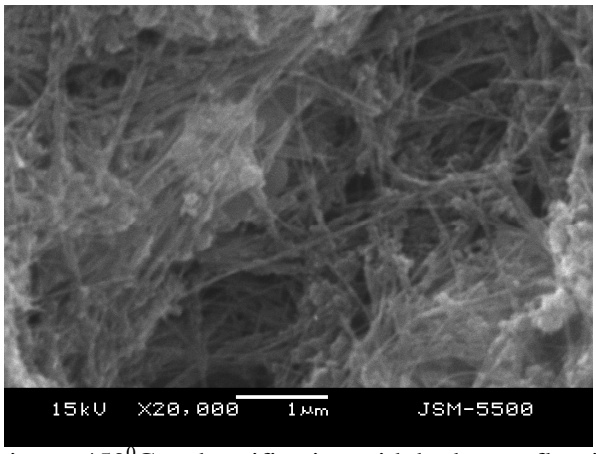


Fig. 7. MWNTs after burning at 450^0C and purification with hydrogen fluoride

At the end of elution of the catalyst slurry was filtered at low vacuum through a Schoot`s glass filter. The sizes of nanotube aggregates were so large that they had not passed through the pores of the filter G1 (100 -160 μm). The resulting filtrate was completely clear and colorless. The precipitate on the filter was repeatedly washed with small amounts of distilled water to completely neutralize the filtrate. Next it was dried in air and then in an oven at 120^0C for 2 hours. After drying the sludge layer was cracked, fragile and easily separated from the filter.

6. Conclusion

The results of this research show that the distance between the electrodes has a significant influence on the diameter and purity of synthesized carbon nanotubes. It has been proved that with the distance between the electrodes increase the purity of the sample was better (the synthesis efficiency increases). It was expected linear relationship between the distance of electrodes and the arc voltage. However it appeared that the change in arc voltage isn't always proportional to the difference change in distance between the electrodes. The proportional relationship is true only for large distances between electrodes. Wear of the carbon anode with a diameter of 6 mm was in the range from 8 to 25 mm/min. During the synthesis of CNTs it was possible to convert up to 80% of the anode material in the cathode deposit. 30% of these 80% was a hard crust. The rest consisted of a soft material made from up to two thirds of nanotubes and 1/3 of of carbon black and fullerenes.

ACKNOWLEDGEMENTS

The work was supported by the by Polish Ministry of Science and Higher Education Grant N510 390138 in 2010-2012.

7. References

[1] Huczko A., Nanorurki węglowe, Bel Studio, Warszawa 2004, ISBN 83-88442-86-4, pp. 159

COMPACT PLASMA SYSTEM FOR ORGANIC COMPOUNDS DECOMPOSITION

Lukasz Szymanski

Technical University of Lodz, Institute of Mechatronics and Information Systems,
18/22 Stefanowskiego Street, 90-924 Lodz, Poland

E-mail: lukasz.szymanski@p.lodz.pl

The aim of the paper is to study a stream rate and quantity of organic fluid waste production by an average analytic chemical laboratory, to find out the required conditions of its thermal treatment in electric arc plasma and to demonstrate a concept of compact system able do utilize from one to a few kilograms of reagent per hour. The main part of the device is the plasma reactor equipped with the electrode spacing adjustment actuator and the power and flow control unit. The collected wasted solvents must be filled in the container feeding the reactor. The gasified waste is heated in the reactor space and must pass across the plasma column going to the compact chlorine absorber and catalytic oxidizer.

1. Introduction

In a chemical analytic laboratory practice small amounts of diverse reagents, mostly liquid organic substances are used for many purposes such as chromatography. They are the chlorinated solvents, solvents from the group of alcohols, esters, and aliphatic or aromatic hydrocarbons. Annually particular analytic laboratory have been using from several to a dozen of tones of those reagents, which as containing some dirt must be qualified as the waste. Small daily production rate of those wastes (rating from several to some tens of kilograms) must be collected and temporary stored before transportation to a place of utilization. The cost of building and exploitation fulfilling the suitable requirements of store-house is in this process the financial largest burden.

The avoidance of stockpiling and transportation of those waste is the economic challenge in the procedure of utilization of the used reagents. So far any device able to utilize those wastes “in situ” where they are produced had not been offered. Such device had to be placed in/or close to the laboratory and may be working in measure of the need (batch mode) on principle how the office document shredder.

The aim of the paper is to study a stream rate and quantity of organic fluid waste production by an average analytic chemical laboratory, to find out the required conditions of its thermal treatment and to demonstrate a concept of compact device PDUCR (Plasma Destructor of Used Chemical Reagents) able do utilize from one to a few kilograms of reagent per hour.

2. Reactor concept

Thermal plasma in the state of LTE (Local Thermodynamic Equilibrium) or near LTE (in a reduced pressure) can be an efficient medium for breaking bonds of unwanted molecular chains. It can be used for gas and fluid waste destruction into valuable friendly products. In the field of gas and fluid waste treatment plasma reactor with cylindrical and divergent channels have been used in the laboratory testing. This kind of reactor have been successfully used in thermal destruction of fluid chemical reagents. The device will be able do utilize from one to a few kilograms of reagent per hour.

In Fig.1. the compact device PDUCR and required installation are presented. The main part of the device is the plasma reactor (1) equipped with the adjustment actuator (2) and the power and flow control unit (5). The collected wasted solvents must be filled in the container (4) feeding the reactor (1). The off gas must be flowing through compact chlorine absorber and catalytic oxidizer (3) before fan (6) cools it down admixing with ambient air. PDUCR will be supplied in the inert gas delivered from the bottle (7) in the slow rate and atmospheric pressure. Fig. 2. shows a photo of the reactor with actuator and catalytic oxidizer only (numbered as 1 in Fig. 1.).

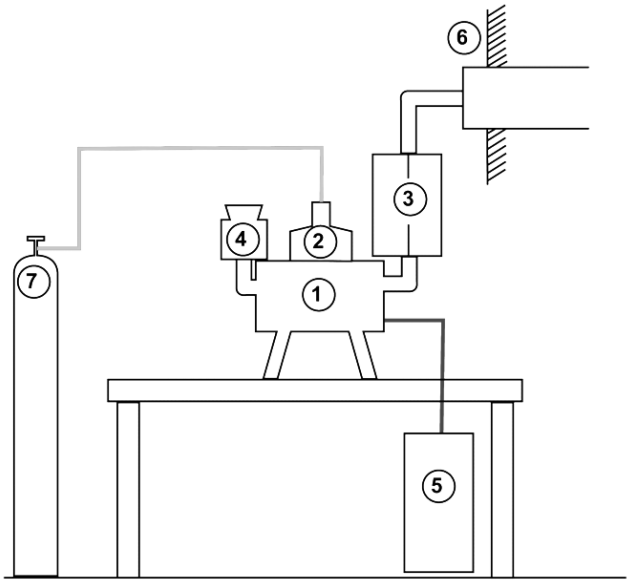


Fig. 1. PDUCR installation (parts numbered described in the text)

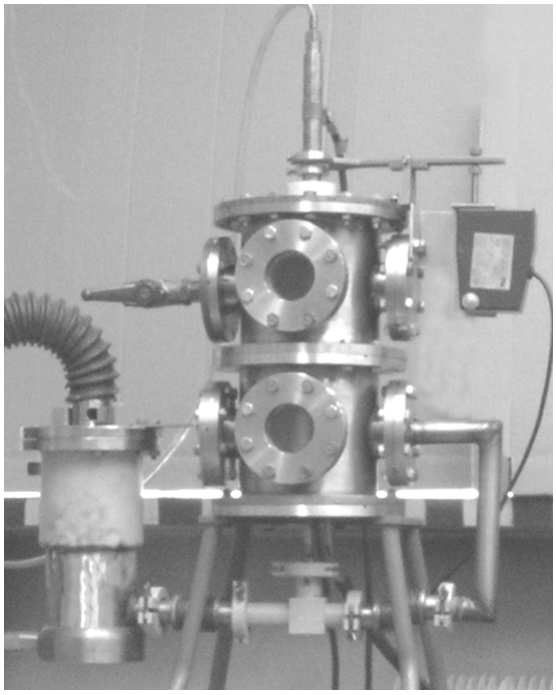


Fig. 2. Photo of parts of system (reactor with actuator and catalytic oxidizer).

3. Simulation of the course of reaction

To find the most effective conditions for these waste destruction in the thermal plasma, the thermochemical calculations have been done before the PDUCR designing and employing it in the experiment. A major advantage of plasma processing is that the heat input may be accomplished in an atmosphere of any desired composition and reactivity. In practice there are only a few variations of chemical strategies available for thermal processing i.e. pyrolysis, oxidation, reaction with hydrogen and water. To optimize the conditions of the reaction we have calculated the decomposition of solvents within the range of temperatures from 400 to 2400K using the CHEMSAGE program based on the minimization of Gibb's free energy [1].

The results of the quantitative and parametric analysis of the chemical reagents waste stream shown that the organic solvents may be selected as the representative stream of wastes to demonstrate the treatment process in the device - PDUCR. The organic solvents after pyrolytical treatment produce similar gaseous products mainly hydrogen, carbon monoxide and if the solvents contain chlorine - hydrochloric acid. Those we decided to choose methanol being typical solvent used in fluid chromatography and representing alcohols, ketons and esters.
In Figures 3 and 4 the results of thermochemical calculations presenting the methanol decomposition are presented.

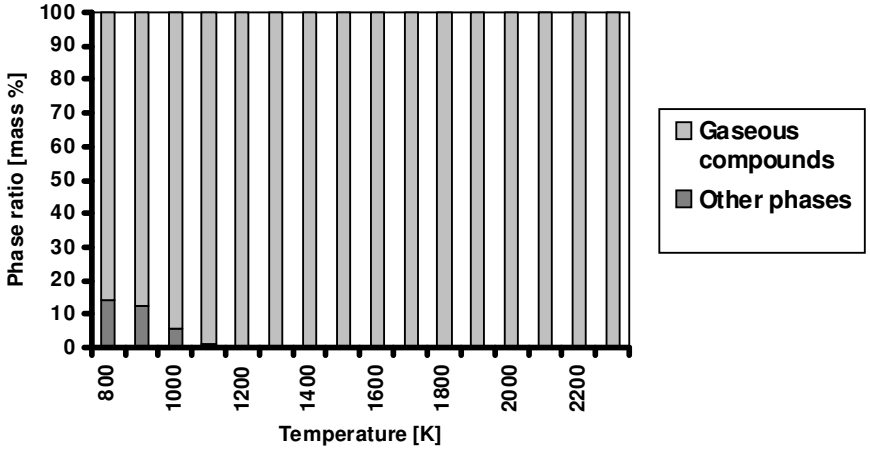


Fig.3. Phase ratio of methanol during its thermal decomposition

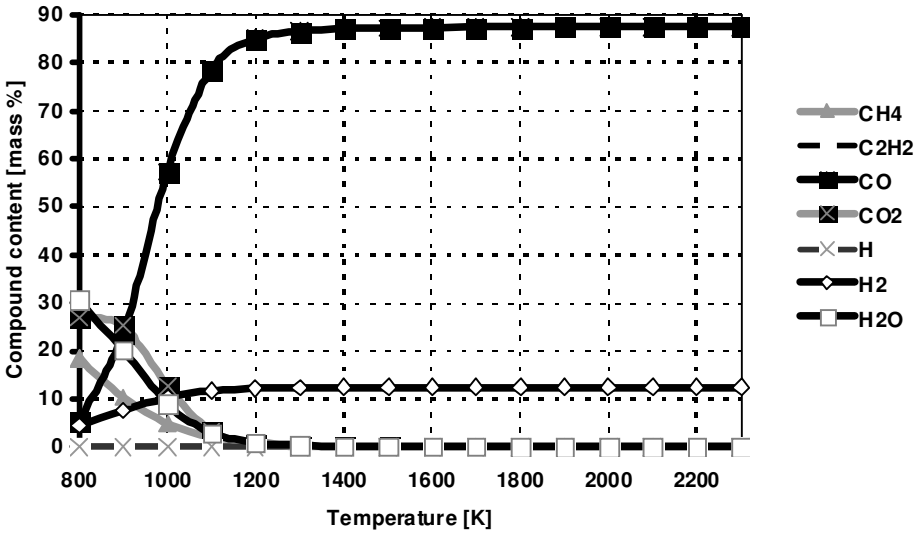


Fig. 4 Thermal decomposition of methanol gaseous fraction

It can be seen in Fig. 3 that 1200K of temperature is required to convert the whole volume of the fluid into gas phase. This is because the soot is formed in the temperature range bellow 1200K. Up to 1200K the soot is only partially oxidized but crossing over the 1200K nearly all soot particles are oxidized to form carbon monoxide. Considering the Fig. 4 results we can notice that also the mass ratio of methane and carbon dioxide decreases and disappears crossing the threshold point (1200K). All of those is done due to steam generated from the water self extraction in the alcohol that works as oxidant.

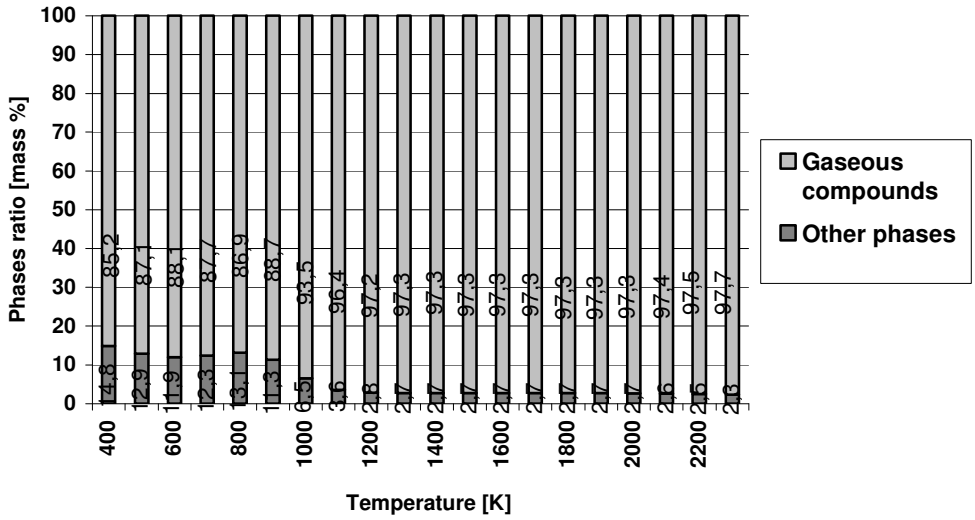


Fig.5 Phase ratio of methanol (66%) admixed with carbon tetrachloride (34%) during thermal decomposition

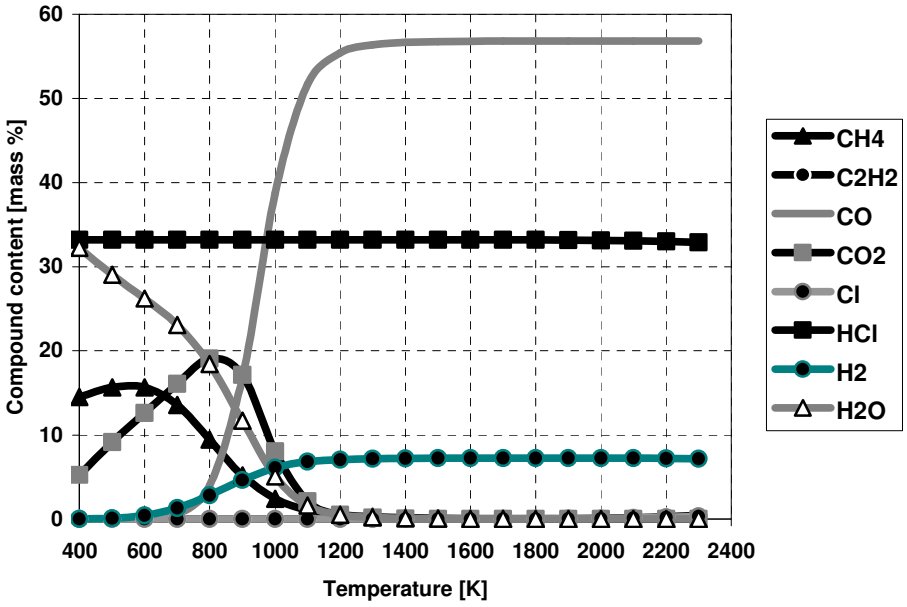


Fig. 6 Thermal decomposition of gaseous fraction of methanol and carbon tetrachloride mix (66%/34%)

However solvents may contain chlorine. The ratio of solvents with chlorine to the solvents without chlorine amounts 1/4 for general laboratories up to 1/3 for university laboratories. We have assumed in our calculations the worst case in which the admixed solvent amounts 34% and that it is very reach in chlorine so we selected carbon tetrachloride.

In Figs. 5 and 6 you can see the phase ratio and thermal decomposition of gaseous fraction of methanol and carbon tetrachloride mix (66%/34%). In this case the mixed solvent is so rich in carbon so after 1200K threshold the residue of 2.7 weight % of soot remains. In such extreme conditions a little volume of water should be added to avoid sooting that allows keeping the installation clean.

In Fig. 6 the thermal decomposition of gaseous fraction of methanol and carbon tetrachloride mix (66%/34%) is presented. We can see here 33 weight % of hydrochloride that must be converted into salt before hydrogen and carbon monoxide burning.

4. Conclusion

The PDUCR is now tested to find out its technical performance. PDUCR is dedicated for analytic chemical laboratories to make utilization of spent reagents in place of their formation. Such solution is essential economically as it allows to avoid of stockpiling and transportation of those waste before utilization of spent reagents. PDUCR is able to utilize those wastes “in situ” where they are produced. It can be placed in/or close to the laboratory and may be working in measure of the need (batch mode) on principle how the office document shredder.

ACKNOWLEDGEMENTS

The scientific work has been financed by Polish Minister of Science and Higher Education, executed within the framework of the Multi-Year Program entitled "Development of innovativeness systems of manufacturing and maintenance 2004-2008".

5. References

[1] K. Cedzyńska, Z. Kołaciński: “Plasma Destruction of Toxic Chloroorganic Wastes Towards Zero Residues”, Journal of Advanced Oxidation Technologies ISSN 1203-8407 Science & Technology Network, Inc. J. Adv. Oxid. Technol. Vol. 7, No. 1, 2004.

CARBON NANOTUBES DEPOSITION USING ATMOSPHERIC PRESSURE GLOW BARRIER DISCHARGE IN ARGON WITH ACETYLENE ADMIXTURE

Marek Elias[1,2], Petr Kloc[1], Ondrej Jasek[1,2], Vera Mazankova[1], David Trunec[1], Lenka Zajickova[1,2]

[1]*Department of Physical Electronics, Faculty of Science, Masaryk University, Kotlarska 2, 611 37 Brno, Czech Republic*

[2]*Plasma Technologies, CEITEC - Central European Institute of Technology, Masaryk University, Kotlarska 2, 611 37 Brno, Czech Republic*

E-mail: trunec@physics.muni.cz

Atmospheric pressure glow barrier discharge in argon with acetylene admixture was used for carbon nanotubes deposition. It was shown that initially filamentary dielectric barrier discharge burning in pure argon at atmospheric pressure can be converted into homogeneous discharge by an acetylene admixture. Using fast ICCD camera it was proven that this homogeneous discharge is an atmospheric pressure glow discharge. The discharge was studied by electrical measurements and optical emission spectroscopy. The optimum conditions for carbon nanotubes deposition were searched, the deposited carbon nanotubes were studied by scanning electron microscopy.

1. Introduction

Dielectric barrier discharges (DBDs) burning at atmospheric pressure in filamentary form are widely used in industrial applications [1]. Homogeneous DBDs, which were discovered in late nineteen eighties and nineties, brought new possibilities of DBD applications. A homogeneous DBD can be obtained in helium or neon and this type of DBD is called atmospheric pressure glow discharge (APGD) [2,3]. Another type of homogeneous DBD can be obtained in nitrogen and this discharge type is called atmospheric pressure Townsend-like discharge (APTD) [4].The uniformity of the plasma favours these discharge types also for thin film deposition techniques such as plasma enhanced chemical vapour deposition (PECVD) [5-9].

APGD in the mixture $He/H_2/CH_4$ was also used for carbon nanotubes (CNTs) deposition by Nozaki et. al. [10]. Latter, Nozaki et. al. [11] developed atmospheric pressure radio-frequency discharge (APRFD) for CNTs deposition. APRFD is driven by radio-frequency (13.56 MHz) power source, it uses metallic electrodes only and it burns again in the mixture $He/H_2/CH_4$.

In this paper an APGD in argon with admixture of acetylene was studied and it was used for CNTs deposition. Firstly, the discharge was studied using electrical measurements, by fast ICCD camera and by optical emission spectroscopy. Secondly, the discharge was used for CNTs deposition and the optimum deposition conditions for CNTs deposition were searched.

2. Experimental

The experiments were carried out in a metallic discharge reactor with the dimensions 500 mm × 500 mm × 500 mm. The bottom electrode was circular with diameter of 40 mm, the upper electrode was circular with a diameter of 36 mm. The upper electrode was covered with quartz glass, 1.8 mm in thickness, the bottom electrode was covered by aluminium nitride plate with dimensions 50 mm × 70 mm × 0.6 mm. The bottom electrode was attached to a heater and its temperature could be elevated up to 750°C. The electrode temperature was measured by a thermocouple. The CNTs were deposited on silicon substrates with dimensions 15 mm × 10 mm × 0.5 mm. The discharge gap between the substrate and the upper electrode was set to 1.75 mm.

Before starting the experiments the discharge chamber was pumped down to a pressure of 20 Pa and then filled up with argon to a pressure of 101 kPa. In the case of substrate heating the heater

temperature was set to 300°C during the filling and after reaching the pressure of 101 kPa the heater temperature was increased up to 750°C.
The argon flow was set to 7 slm and an acetylene flow of 15 sccm was added. Atmospheric pressure during the deposition was maintained by slight pumping. At the CNTs deposition also the hydrogen flow of 100 sccm was added. The hydrogen admixture suppressed the graphite soot deposition on electrodes and it improved the quality of deposited CNTs. The deposition time was 15 min. A high voltage power supply with frequency of 6.8 kHz and applied voltage of 2.6 kV (peak-to-peak) was used for discharge generation.
Jobin Yvon FHR 1000 spectrometer with a CCD detector (focal length 1 m, grating 2400 gr/mm) was used for optical spectroscopy in the UV/VIS spectral range (300 - 750 nm). To obtain the optical spectra from the weakly glowing discharge the 7 cm diameter lens was attached to the side window and this lens focused the light from the discharge to the input of the optical fibre. Temporally and spatially resolved, but spectrally unresolved, measurement of discharge emission was carried out with an intensified CCD camera PI-MAX1024RB-25-FG-43 (Princeton Instruments), controlled by a ST-133 controller and working in image mode. The camera was synchronized with the applied voltage. The applied voltage and discharge current were recorded by the digital oscilloscope HP 54820A Infinium (500 MHz, 2 GSa/s).

3. Results

The discharge diagnostics was done by electrical measurement and optical emission spectroscopy. The dependence of ignition voltage on admixture concentrations is shown in figure 1. It can be seen that a small admixture of acetylene (up to 1%) to argon significantly decreases the ignition voltage for such mixture in comparison with ignition voltage for pure argon. This is due to Penning ionization of acetylene molecules by argon metastables. The ionization potential of acetylene is 11.40 eV, the energy of argon $1s_5$ metastable is 11.55 eV, thus the Penning ionization of acetylene is possible. On the other hand, the ionization potential of methane is 12.61 eV, thus the Penning ionization of methane by argon metastables is not possible. Therefore no significant decrease of ignition voltage was observed after adding of methane to argon, see again figure 1.

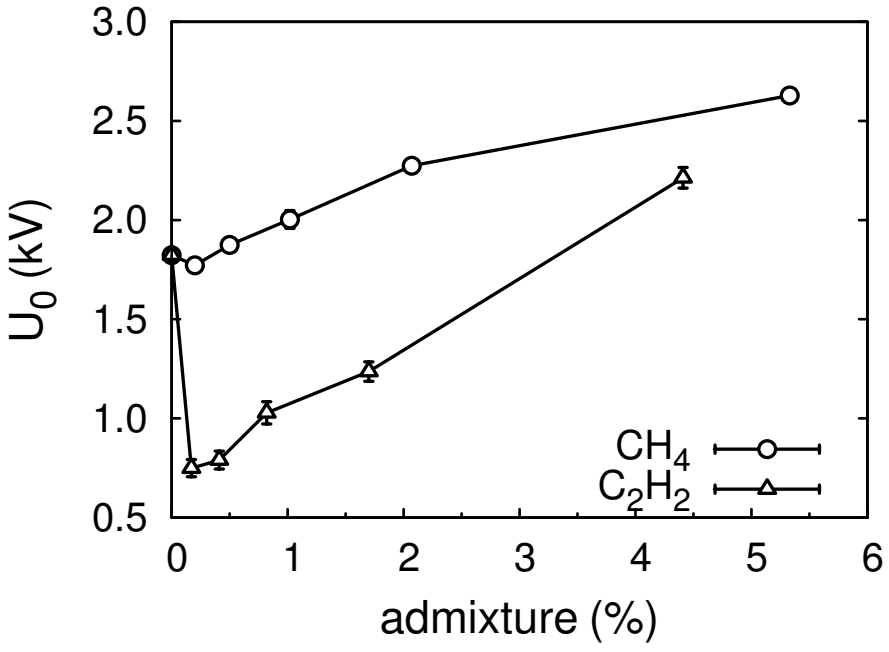


Fig. 1. The dependence of ignition voltage U_0 on admixture concentrations.

The discharge current in the argon DBD consists of sharp current peaks, whereas the discharge current in APGD in argon with acetylene admixture has the form of broad peaks superimposed by many

smaller and shorter peaks, see figure 2. This current course indicates that the discharge does not

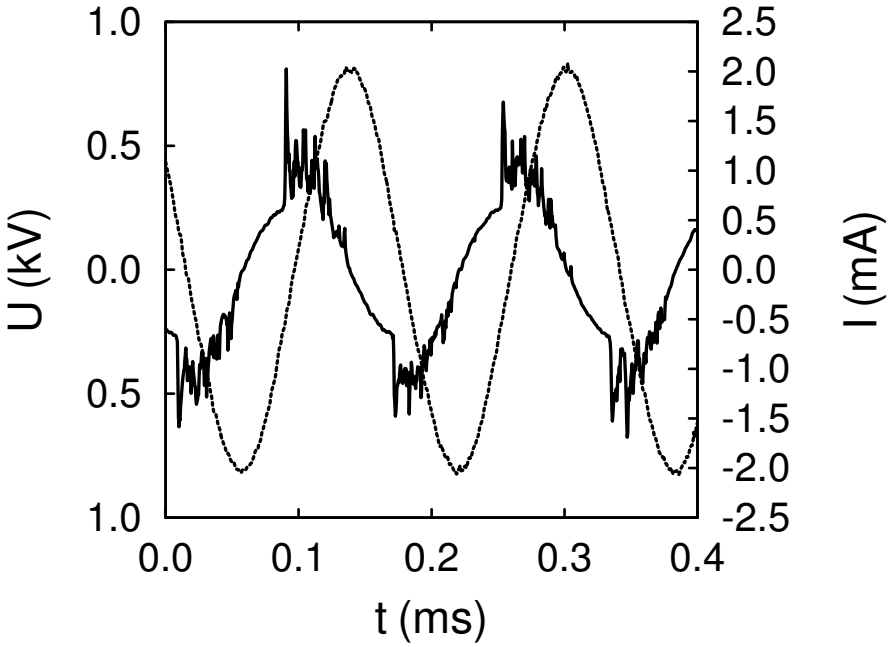


Fig. 2. The time dependence of applied voltage and discharge current in APGD in argon with 0.41% admixture of acetylene. Full line – discharge current, dotted line – applied voltage.

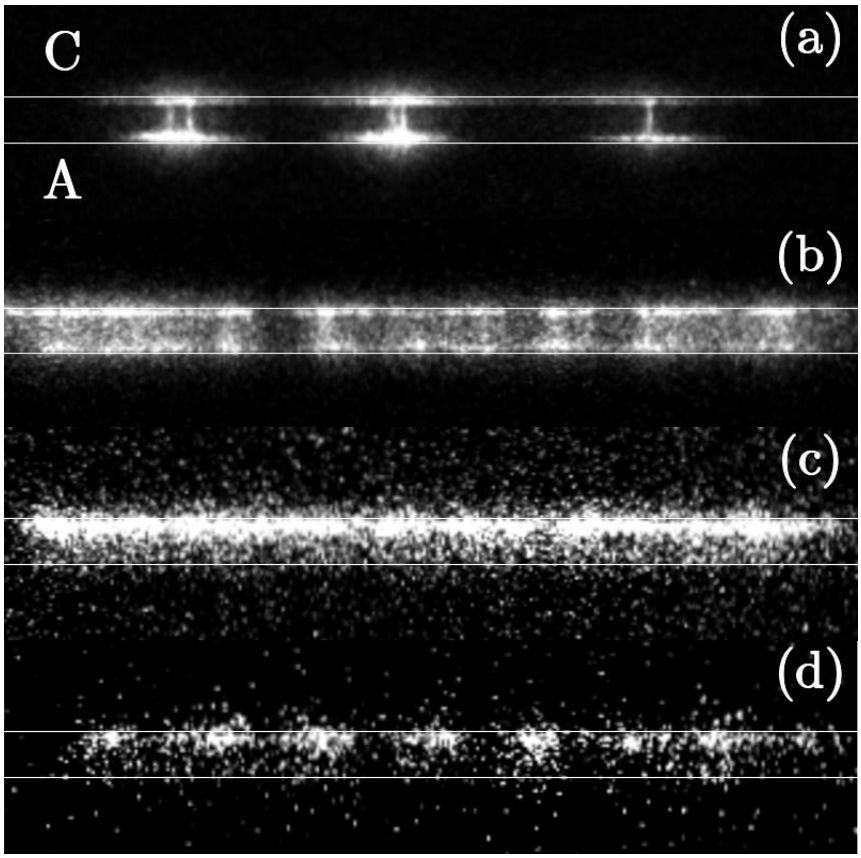


Fig. 3. ICCD images of discharges. (a) filamentary DBD in pure argon, (b) filamentary DBD in argon with 0.41% admixture of methane, (c), (d) APGD in argon with 0.41% admixture of acetylene. Exposition time: (a)-(c) 80 μs (one half period), (d) 5 μs. Horizontal lines indicate the dielectric surfaces, the upper electrode is the instantaneous cathode in all images.

burn at the same time in whole discharge gap. The images of discharges taken by fast ICCD camera are presented in figure 3. Again the change of the discharge after acetylene adding can be clearly seen. The images of DBD in argon and in argon with methane admixture show the filamentary structure of these discharges. The image of DBD in argon with acetylene admixture shows a luminous layer at instantaneous cathode, see figure 3c. This identifies this discharge with APGD. The images with shorter exposition time show that this discharge is not fully homogeneous, see figure 3d. However, this is not significant at CNTs deposition.

The CNTs were deposited at substrate temperatures from 650°C to 750°C. It was found that CNTs deposited at 650°C have lower density and lower quality than CNTs deposited at 750°C. Also the influence of discharge was studied, no CNTs growth was observed without discharge. The silicon substrates were prepared as follows. The SiO_2 layer with thickness of 300 nm was created by thermal oxidation, on this oxide layer a iron catalyst layer with thickness of 4.7 nm was vacuum evaporated. The CNTs were deposited directly on such prepared substrate without any pretreatment process. The deposited CNTs are shown on SEM images, see figure 4 and figure 5. It was determined from these images that the nanotube diameter was about 20 nm and nanotube length was about 5 μm. It can be seen from this value of CNTs thickness that deposited CTNs were multi-wall carbon nanotubes.

4. Acknowledgement

The present work was supported by the Czech Science Foundation under contracts 104/09/H080 and P205/10/1374 and by the projects "R&D center for low-cost plasma and nanotechnology surface modifications" (CZ.1.05/2.1.00/03.0086) and "CEITEC - Central European Institute of Technology" (CZ.1.05/1.1.00/02.0068) funding by European Regional Development Fund.

5. References

[1] Kogelschatz U 2003 *Plasma Chem. Plasma Process*. **23** 1.
[2] Kanazawa S, Kogoma M, Moriwaki T and Okazaki S 1988 *J. Phys. D: Appl Phys.* **21** 838.
[3] Trunec D, Brablec A and Buchta J 2001 *J. Phys. D: Appl. Phys.* **34** 1697.
[4] Gherardi N, Gouda G, Gat E, Ricard A and Massines F 2000 *Plasma Sources Sci. Technol.* **9** 340.
[5] Sawada Y, Ogawa S and Kogoma M 1995 *J. Phys. D: Appl Phys.* **28** 1661.
[6] Prat R, Koh Y J, Babukutty Y, Kogoma M, Okazaki S and Kodama M 2000 *Polymer* **41** 7355.
[7] Gherardi N, Martin S and Massines F 2000 *J. Phys. D: Appl Phys.* **33** L104.
[8] Foest R, Adler F, Sigeneger F and Schmidt M 2003 *Surf. Coating Technol.* **163-16**4 323.
[9] Trunec D, Zajickova L, Bursikova V, Studnicka F, Stahel P, Prysiazhnyi V, Perina V, Houdkova J, Navratil Z and Franta 2010 *J. Phys. D: Appl. Phys.* **43** 225403.
[10] Nozaki T, Kimura Y and Okazaki K 2002 *J. Phys. D: Appl. Phys.* **35** 2779.
[11] Nozaki T, Ohnishi K, Okazaki K and Kortshagen U 2007 *Carbon* **45** 364.

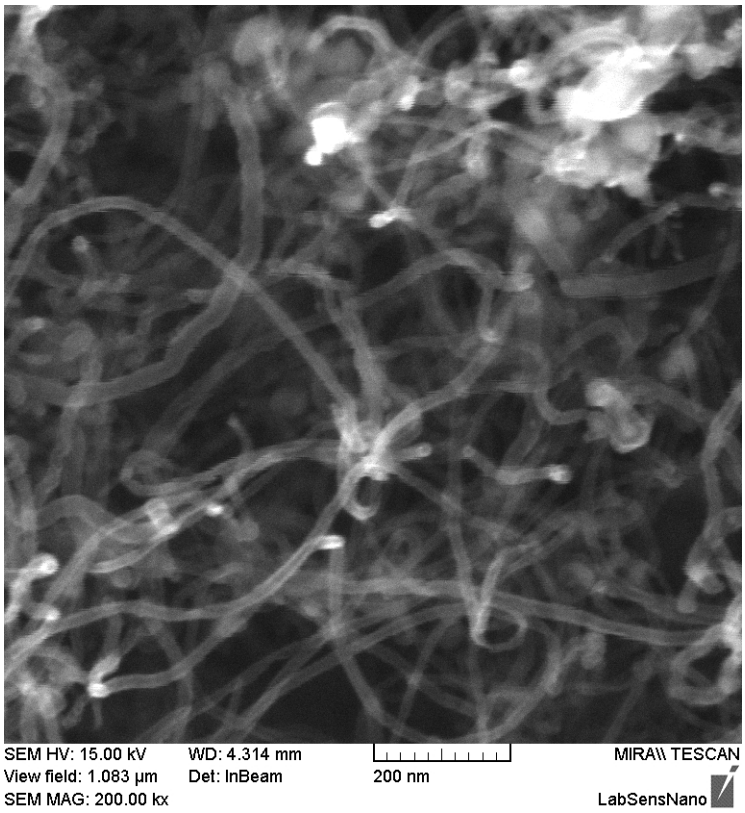


Fig.4. SEM image of deposited CNTs. The substrate temperature at deposition was 750°C.

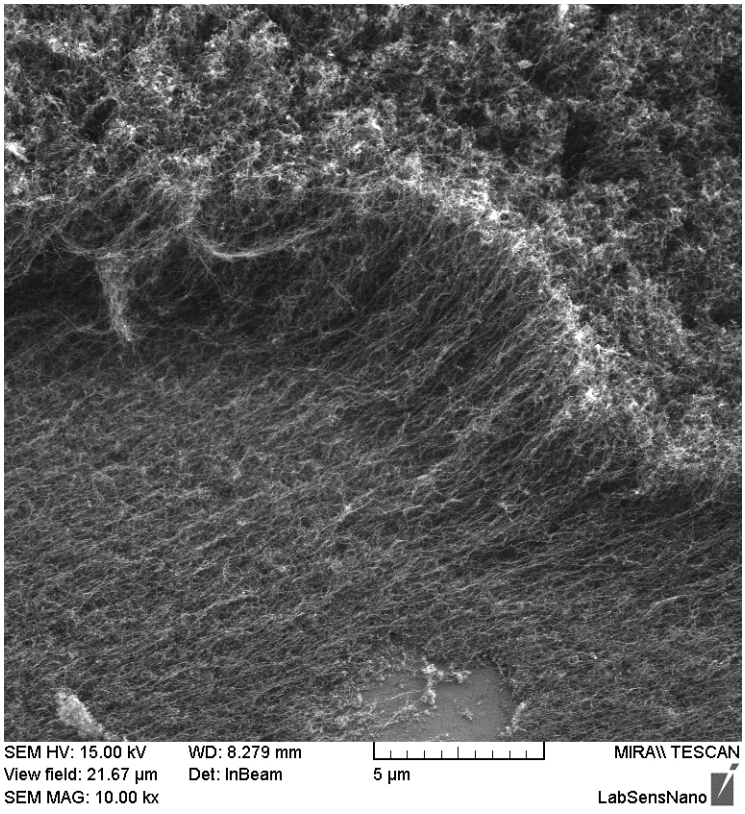


Fig 5. SEM image of deposited CNTs. Side view from the scratch in the CNTs layer.

DECOMPOSITION OF CHLORINATED ORGANIC COMPOUNDS USING NON-EQUILIBRIUM PLASMA REACTOR

Bogdan Ulejczyk, Krzysztof Krawczyk, Magdalena Hajduk, Marta Musiał, Bartłomiej Wnęk, Michał Młotek, Krzysztof Schmidt-Szałowski

Faculty of Chemisty, Warsaw University of Technology, Noakowskiego 3, 00-664 Warszawa, POLAND

E-mail: bulejczyk@ch.pw.edu.pl

In this paper the results of decomposition of chloroform, tetrachloromethane and trichloroethylene in argon – oxygen mixtures in a new type of non-equilibrium plasma reactor are described. The newly designed reactor was made of a quartz-glass tube of inner diameter of 16.4 mm and a porous stainless steel tube of outer diameter of 10 mm. The porous stainless steel tube was a high voltage electrode. Gas permeating through a porous wall of the high voltage electrode was passing through the active zone of plasma, located around of the high voltage electrode.

The reactor was powered by a pulsed supply system. Chlorine was main reaction products of VOCs decompossition. The conversion of chlorinated organic compounds in the new reactor reached 98%.

1. Introduction

Volatile organic compounds (VOCs) cause the greenhouse effect. They often possess toxic properties. Moreover some of them cause decomposition of ozone. Sources of emission of VOCs are very diverse and concern almost each field of technology, such as use of fertilizers in agriculture, transportation, manufacturing processes, generation of electricity. Significant part of emission of VOCs comes from small and dispersed sources, where VOCs are used in degreasing and painting processes. Reduction of emission of VOCs from these sources is a great challenge, because concentration of VOCs is small. Moreover composition and concentration of VOCs change in time of technological process. For example in the degreasing process the main components of contaminations are from solvent. In the painting process the main air contaminations are from paint. It causes that the method should be able to work at various conditions.

For the utilization of pollutants in the place of their emissions one can use biological decomposition [1], catalytic decomposition [2], plasma decomposition [3-5] or plasma-catalytic processes [6]. Huge potential of application in the reduction of emissions VOCs can be seen in plasma decomposition. Plasma which is used for the decomposition pollutants, can be generated in electron beam [7] or various electric discharges: corona [8], barrier [9], gliding [4], microwave [3], spark [5].

In this paper, we presents results of the decomposition of CCl_4, $CHCl_3$ and C_2HCl_3 using a semi-corona discharge. The decomposition process was run in a new construction of the reactor to improve the efficiency of the chemical reactions initiated by the discharge. In this reactor, a high-voltage electrode was made from a porous tube of stainlees steel. Gas stream was passed through channels in the porous tube into the active zone of discharge, located around of the high-voltage electrode. This construction enables a good contact of the gas stream with plasma.

2. Experimental

Decomposition of $CHCl_3$, C_2HCl_3 and CCl_4 in the argon-oxygen mixture was carried out in the reactor, which are shown in Fig. 1. The reactor consisted of a quartz tube, high-voltage and ground electrodes. The high-voltage electrode was made of a stainless steel porous tube with an outer diameter of 10 mm. The electrode had small flow resistance (Fig. 2), which was due the high (19%) effective porosity.

Gas was introduced by the porous electrode into the active zone of discharge. It is the main advantage of the reactor. The grounded electrode was made by applying a silver paste into the quartz tube. An outer diameter of the quartz tube was 19 mm and the wall thickness was 1.2 mm.

Total gas flow was keept at 10 Nl/h. Concentration of oxygen in gas was 25% vol. Concentration of $CHCl_3$, C_2HCl_3 and CCl_4 in gas was keept at 0.4% vol.

Purity of oxygen and argon was 99.999%. Purity of C_2HCl_3 and CCl_4 was 99%. Purity of $CHCl_3$ was 98.5%

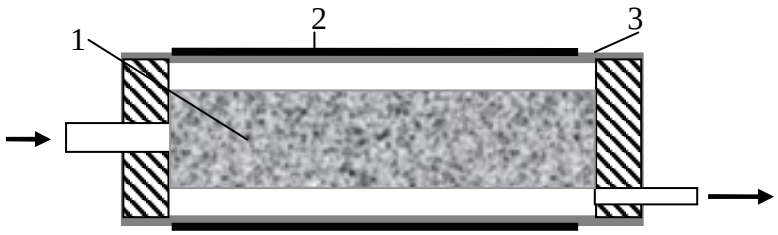


Fig. 1. Schema of reactor. 1 – high-voltage electrode, 2 – grounded electrode, 3 – dielectric barrier.

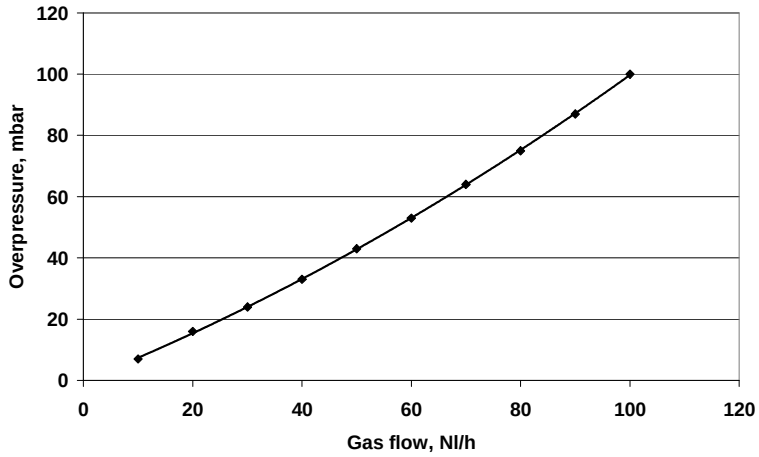


Fig. 2. Influence of gas flow on the gas pressure

The reactor was powered by a pulsed supply system. The frequency, the current and voltage traces of a given pulse were recorded by using oscilloscope Tektronix TDS 3052 with a voltage probe Tektronix P6015A and a current probe Tektronix TCP202. The discharge power was calculated according to the formula:

$$P = f \int I(t)U(t)d(t) \tag{1}$$

P – discharge power, W
f – frequency, Hz
I – current, A
U – voltage, V
t – time of the pulse start and end, s

Products of the plasma decomposition of VOCs were analyzed using gas chromatography and titrate analysis. Hewlett-Packard HP 6890 with an FID detector and packed column with 5% Fluorocol on 60/80 Carbopack B was used to determine the concentrations of $CHCl_3$, C_2HCl_3 and CCl_4. Cl_2 and HCl were periodically passed by two bubblers with KI solution. In this solution Cl_2 reacts with KI to I_2 and KCl. HCl was absorbed in this solution. The solution was titrated with a 0.05 M $Na_2S_2O_3$ solution to determine the amount of I_2. 0.1 M NaOH was used to determine the amount of HCl. Basing on these measuring data a flow rate of products of the VOCs decomposition was calculated.
The VOCs conversion and the specific energy was calculated according to formulas:

$$X = \frac{W_0[CCl_4] - W[CCl_4]}{W_0[CCl_4]} \qquad X = \frac{W_0[CHCl_3] - W[CHCl_3]}{W_0[CHCl_3]} \qquad X = \frac{W_0[C_2HCl_3] - W[C_2HCl_3]}{W_0[C_2HCl_3]} \tag{2}$$

X – overall VOCs conversion
$W_0[CCl_4]$, $W_0[CHCl_3]$, $W_0[C_2HCl_3]$ – VOCs flow rate at the inlet, mol/h
$W[CCl_4]$, $W[CHCl_3]$, $W[C_2HCl_3]$ – VOCs flow rate at the outlet, mol/h

$$X_{HCl} = \frac{W[HCl]}{3 \cdot W_0[CHCl_3]} \qquad X_{HCl} = \frac{W[HCl]}{3 \cdot W_0[C_2HCl_3]} \tag{3}$$

X_{HCl} – $CHCl_3$ or C_2HCl_3 conversion to HCl
W[HCl] – HCl flow rate at the outlet, mol/h

$$X_{CCl4} = \frac{\cdot W[COCl_2]}{2 \cdot W_0[CCl_4]} \tag{4}$$

X_{CCl4} – CCl_4 conversion to $COCl_2$
$W[Cl_2]$ – CCl_4 flow rate at the outlet, mol/h

$$X_{Cl2} = \frac{W[Cl_2]}{2 \cdot W_0[CCl_4]} \qquad X_{Cl2} = \frac{2 \cdot W[Cl_2]}{3 \cdot W_0[CHCl_3]} \qquad X_{Cl2} = \frac{2 \cdot W[Cl_2]}{3 \cdot W_0[C_2HCl_3]} \tag{5}$$

X_{Cl2} – CCl_4, $CHCl_3$ or C_2HCl_3 conversion to Cl_2
$W[Cl_2]$ – Cl_2 flow rate at the outlet, mol/h

$$SE = \frac{P \cdot 3.6}{W_0} \tag{6}$$

SE – specific energy, kJ/mol of gas
W_0 – total gas flow rate at the inlet, mol/h

3. Results and discussion

Fig. 3 shows the results for $CHCl_3$, C_2HCl_3 and CCl_4 decomposition. In this figure one can see that the overall C_2HCl_3 and $CHCl_3$ conversions were much higher than overall CCl_4 conversion. Overall $CHCl_3$ and C_2HCl_3 conversion was high (0.95-0.98) in the investigated range of the specific energy changes. CCl_4 was more difficult to decompose than C_2HCl_3 and $CHCl_3$. Overall CCl_4 conversion increased from 0.6 to 0.78 with specific energy increasng from 16 to 38 kJ/mol.

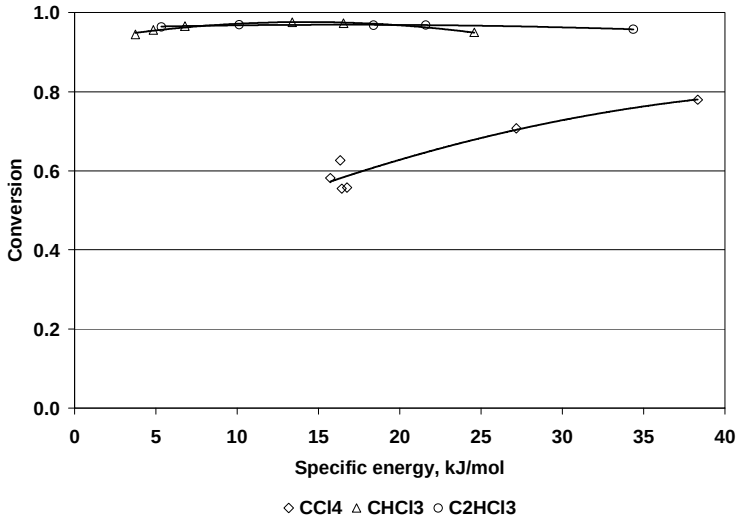


Fig. 3. The dependence between type of VOCs and overall VOCs conversion

Fig. 4-6 shows the results for VOCs decomposition for various specific energies. The main product of VOCs decomposition was Cl_2. The product of $CHCl_3$ and C_2HCl_3 decomposition was also HCl. $COCl_2$ was formed during the CCl_4 decomposition process. All these products are easy to remove from gas steam by absorption.
Fig. 4-6 shows that the conversion of VOCs to Cl_2 increase with increasing specific energy. The conversion of VOCs to HCl or $COCl_2$ decreased with increasing specific energy. These results demonstrate that the composition of the products can be regulated by controlling the specific energy.

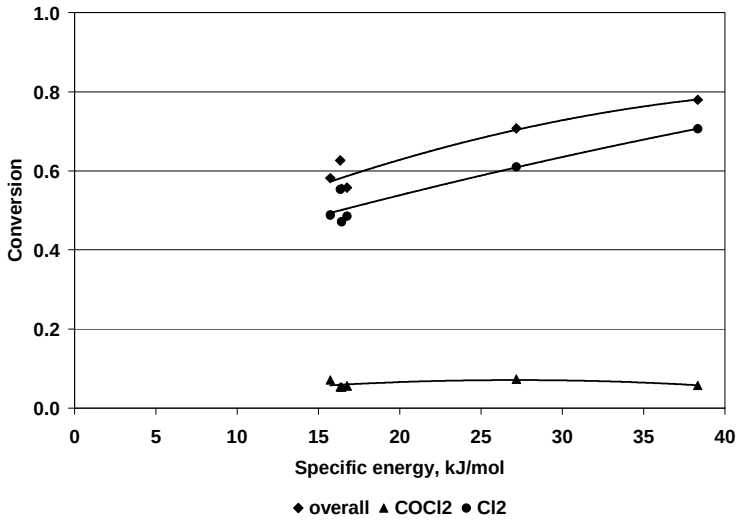


Fig. 4. The dependence between the CCl_4 conversion and specific energy

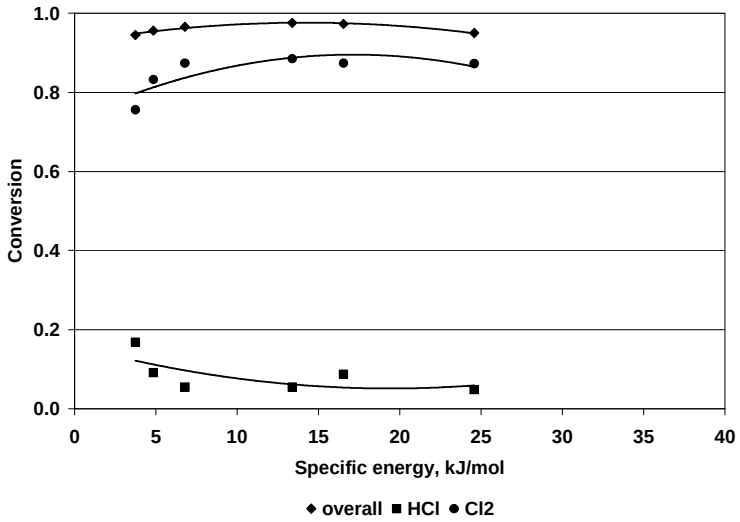


Fig. 5. The dependence between the $CHCl_3$ conversion and specific energy

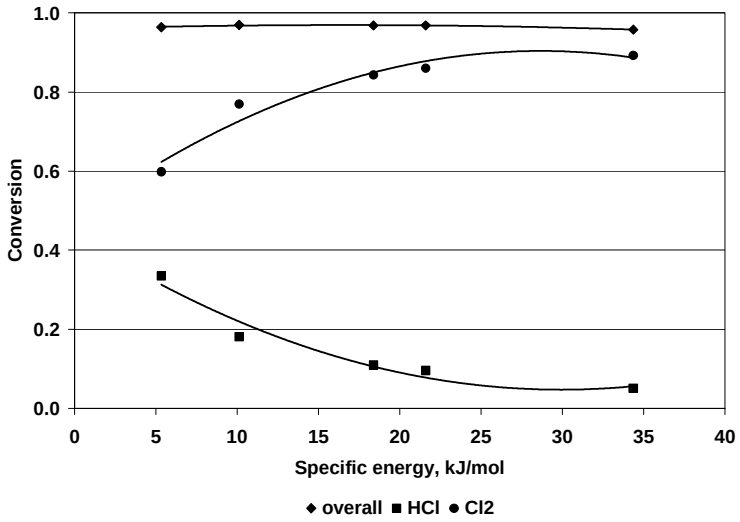


Fig. 6. The dependence between the C_2HCl_3 conversion and specific energy

4. Conclusions

Non-equilibrium plasma reactor with gas passing through the porous electrode into the active zone of discharge can be effectively used in the decompositon of VOCs.
The overall $CHCl_3$ and C_2HCl_3 conversion was 95-98%.
CCl_4 was more difficult to decompose than $CHCl_3$ and C_2HCl_3.
Overall CCl_4 conversion reached 78%.
Main products of VOCs decomposition was Cl_2.

5. Acknowledgment

This work was financially supported by Warsaw Uniwersity of Technology.

6. References

[1] Chmiel K., Jarzębski A.B., Palica M., 2005 *Przemysł Chemiczny* **84** 442.
[2] Szynkowska M.I., Wojciechowska E., Węglińska A., Paryjczak T., 2009 *Przemysł Chemiczny* **88** 712.
[3] Jasiński M., Szczucki P., Dors M., Mizeraczyk J., Lubański M., Zakrzewski Z., 2000 *Czechoslovak Journal of Physics* **50/S3** 285.
[4] Krawczyk K., Ulejczyk B., 2004 *Plasma Chemistry and Plasma Processing* **24** 155.
[5] Krawczyk K., Jodzis S., Lamenta A., Kostka K., Ulejczyk B., Schmidt-Szałowski K., 2011 *IEEE Transactions on Plasma Scence* **39** 3203.
[6] Krawczyk K., Ulejczyk B., Song H.K., Lamenta A., Paluch B., Schmidt-Szałowski K., 2009 *Plasma Chemistry and Plasma Processing* **29** 27.
[7] Sun Y., Chmielewski A.G., Bułka S., Zimek Z., 2006 *Plasma Chemistry and Plasma Processing* **26** 347.
[8] Kirkpatrick M.J., Finney W.C., Locke B.R., 2003 *Plasmas and Polymers* **8** 165.
[9] Han S.B., Oda T., 2005 *IEEE Transactions on Industry Applications* **41** 1343.

COMPARATIVE STUDY OF DECOMPOSITION OF TETRACHLOROMETHANE USING DIELECTRIC BARRIER DISCHARGE POWERED BY DIFFERENT POWER SUPPLIES

Bogdan Ulejczyk[1], Krzysztof Krawczyk[1], Alicja Kosik[1], Michał Młotek[1], Krzysztof Schmidt-Szałowski[1], Łukasz Nogal[2], Bolesław Kuca[2]

[1]*Faculty of Chemisty, Warsaw University of Technology, Noakowskiego 3, 00-664 Warszawa, POLAND*

[2] *Faculty of Electrical Engineering, Warsaw University of Technology, Pl. Politechniki 1, 00-661 Warszawa, POLAND*

E-mail: bulejczyk@ch.pw.edu.pl

The conversion of CCl_4 in air was investigated at normal pressure in a new type of dielectric barrier discharge reactor. In this reactor, the gas stream was introduced into the reactor through internal channels of the high-voltage electrode to active zone of DBD. This design allows the introduction of the gas in the entire volume of the reactor. The reactor was powered by three different power supplies. Maximum reached conversion of tetrachloromethane depended on the power supply. 55, 72 and 89% were the maximum achieved conversions of tetrachloromethane for tested power supplies.

1. Introduction

Volatile organic compounds (VOCs) cause the greenhouse effect. They often possess toxic properties. Moreover some of them cause the decomposition of ozone. Hence, there is a need to reduce their emission. Sources of emission of VOCs are very diverse and concern almost each field of technology. A significant part of of VOCs was emitted to the air as solvents and products of many processes [1].

The issue of cleaning gases from VOCs was the subject of numerous studies that were carried out in many research centers. For the utilization of pollutants in the place of their emissions one can use biological decomposition [2], catalytic decomposition [3], plasma decomposition [4-6] or plasma-catalytic processes [7].

Huge potential of application in the reduction of VOCs emissions can be seen in plasma decomposition. Plasma, which is used for pollutants decomposition, can be generated in electron beam [8] or various electric discharges: surface [9], corona [10], barrier [11], gliding [5], microwave [4], spark [6].

In this paper, we present results of the decomposition of CCl_4 using the dielectric barrier discharge (DBD). Plasma, which is generated in the barrier discharge, is a non-equilibrium plasma. This plasma is characterised by a moderate temperature of the gas and the presence of the high-energetic electrons (1-10 eV). In such conditions, chemical reactions are initiated by the inelastic collisions of gas molecules with high-energetic electrons. Therefore, very stable compounds are activated and oxidized in the presence of oxygen.

2. Experimental

Decomposition of CCl_4 in the air (synthetic air to the FID) was carried out in the reactor, which is shown in Fig. 1. The reactor has a special design of the high-voltage electrode. This electrode has internal channels. Gas is introduced into the whole reactor by one group of channels. The gas passes through the discharge zone. Then the gas is carried from the reactor by the next channels. This design aims to improve the energy efficiency supply of DBD.

The reactor was powered by three power suply systems: AC, pulsed of low frequency (<1 kHz) and pulsed current of 15 kHz frequency. The frequency, the current and voltage traces of a given pulse were recorded by using oscilloscope Tektronix TDS 3052 with a voltage probe Tektronix P6015A and a current probe Tektronix TCP202. The courses of the discharge current and voltage, for each power supply system, are shown in Fig. 2-4. The discharge power and specific energy were calculated according to the formulas:

$$P = f\int I(t)U(t)d(t) \tag{1}$$

P – discharge power, W
f – frequency, Hz
I – current, A
U – voltage, V
t – time of the pulse start and end, s

$$SE = \frac{P \cdot 3.6}{W} \tag{2}$$

SE – specific energy, kJ/mol of gas
W – total gas (air nad VOCs) flow rate at the inlet, mol/h

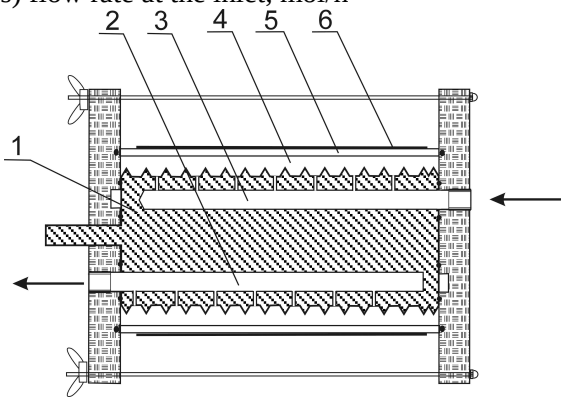


Fig. 1. Schema of reactor. 1 – high-voltage electrode, 2, 3 – internal channels, 4 – discharge zone, 5 – dielectric barrier, 5 – grounded electrode.

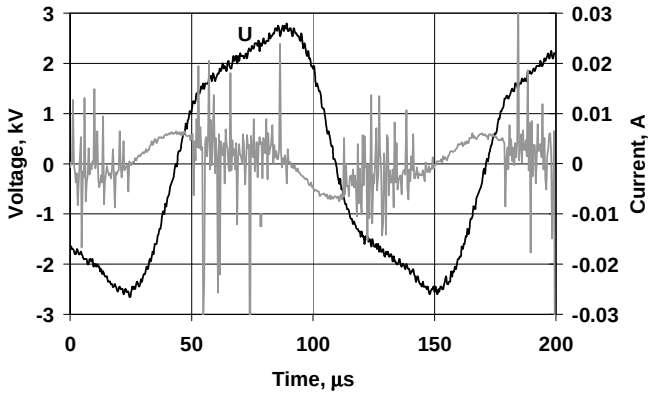


Fig. 2. Traces of pulses voltage and current for AC power supply system.

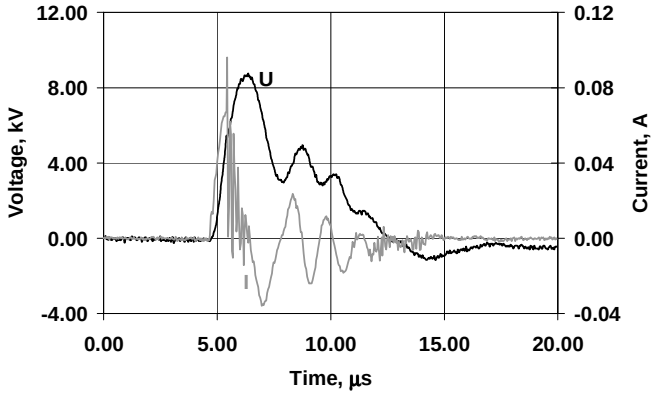


Fig. 3. Traces of pulses voltage and current for pulsed of low frequency (<1 kHz) power supply system.

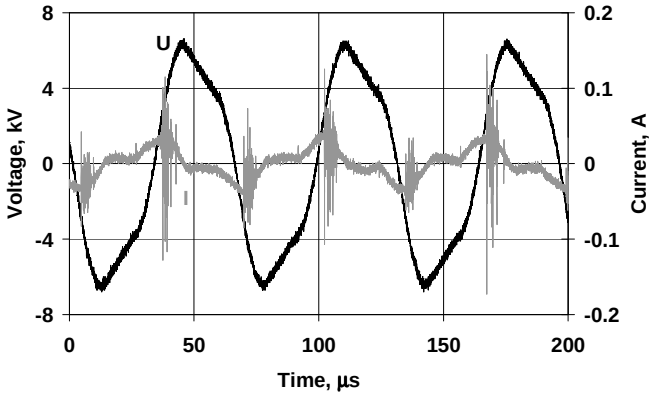


Fig. 4. Traces of pulses voltage and current for pulsed current of 15 kHz frequency power supply system.

CCl_4 concentration was analyzed using Hewlett-Packard HP 6890 with an FID detector and packed column with 5% Fluorocol on 60/80 Carbopack B. Products of CCl_4 decomposition were analized using titrate analysis. Gas was periodically passed by two bubblers with KI solution. In this solution Cl_2 reacts with KI to I_2 and KCl. $COCl_2$ reacts with H_2O to HCl and CO_2. The solution was titrated with a 0.05 M $Na_2S_2O_3$ solution to determine the amount of I_2 and 0.1 M NaOH was used to determine the amount of HCl. Basing on these measuring data a flow rate of products of the CCl_4 decomposition was calculated.
The CCl_4 conversions were calculated according to formulas:

$$X = \frac{W_0[CCl_4] - W[CCl_4]}{W_0[CCl_4]} \bullet 100 \quad (3)$$

X – overall CCl_4 conversion, %
$W_0[CCl_4]$ - CCl_4 flow rate at the inlet, mol/h
$W[CCl_4]$ - CCl_4 flow rate at the outlet, mol/h

$$X_{C0Cl2} = \frac{\cdot W[COCl_2]}{2 \cdot W_0[CCl_4]} \bullet 100 \quad (4)$$

X_{CCl4} – CCl_4 conversion to $COCl_2$, %
$W[COCl_2]$ – $COCl_2$ flow rate at the outlet, mol/h

$$X_{Cl2} = \frac{W[Cl_2]}{2 \cdot W_0[CCl_4]} \bullet 100 \quad (5)$$

X_{Cl2} – CCl_4 conversion to Cl_2, %
$W[Cl_2]$ – Cl_2 flow rate at the outlet, mol/h

Total gas flow was keept at 10 Nl/h.
Concentration of CCl_4 in gas was keept at 0.1% vol.

3. Results

Results of decomposition CCl_4 for various power supply systems and various specific energy are shown in Fig. 5-7. The specific energy influenced on CCl_4 dconversion for each power suply systems. It is seen in Fig. 3-5 that the overall CCl_4 conversion increases with the increasing sepecific energy for all power supply systems. Power supply systems work in different power ranges. This is a construction feature of these systems. Therefore, at the same gas flow rate, the specific energy ranges were different. The pulsed power supply system of low frequency (<1 kHz) was working at the lowest specific energy. For this reason, the lowest overall CCl_4 conversions were obtained. The power supply system with pulsed current of 15 kHz frequency was working at the higest specific energy. However, the obtained conversions were not the higest. The highest overall CCl_4 conversion was obtained for the AC power

supply system, which was intermediate range of the specific energy. For this system the overall CCl_4 conversion in air reached 98% for specific energy above 20 kJ/mol.
The main product of CCl_4 decomposition was Cl_2 for all power supply systems. A smaller amount of $COCl_2$ was formed for two power supply systems (Fig. 3,4). It is worth noting that the ratio of Cl_2 to $COCl_2$ ranged from 15 to 40 and from 7 to 15 respectively for AC and pulsed of low frequency (<1 kHz) power supply systems.
The use of pulsed current of 15 kHz frequency power supply system caused that $COCl_2$ was not produced and chlorine occured only as Cl_2. These results show that the composition of the products of CCl_4 conversioncan be controlled by applying the appropriate power supply system.

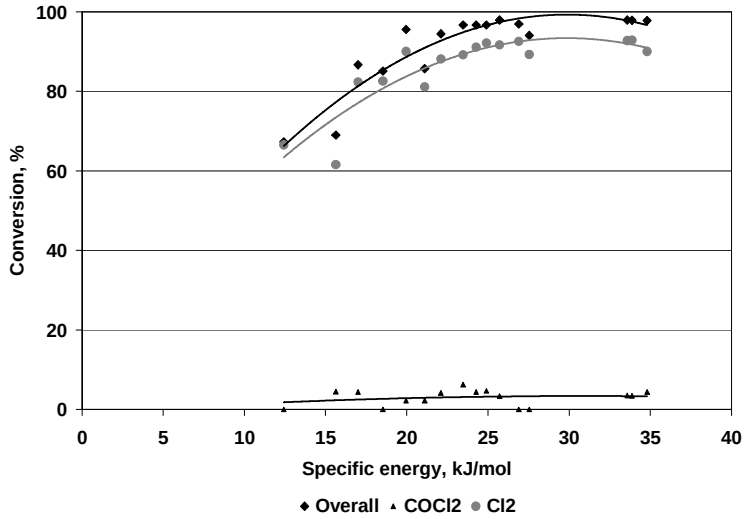


Fig. 5. The dependence between the CCl_4 conversion and specific energy for AC power supply system.

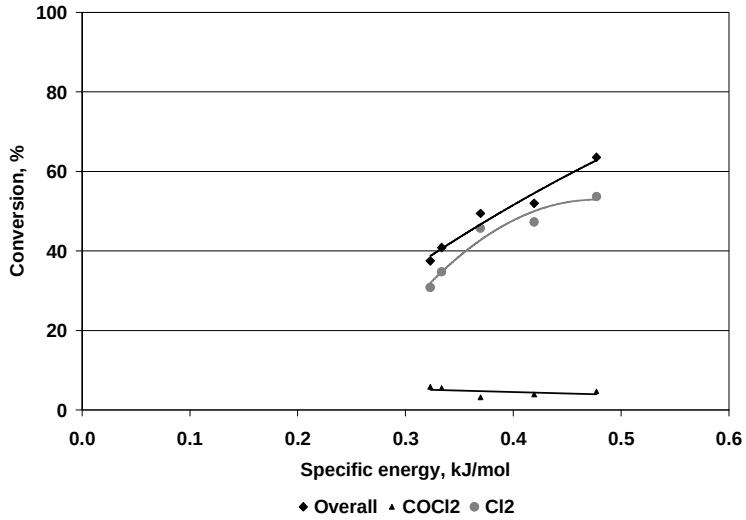


Fig. 6. The dependence between the CCl_4 conversion and specific energy for pulsed of low frequency (<1 kHz) power supply system.

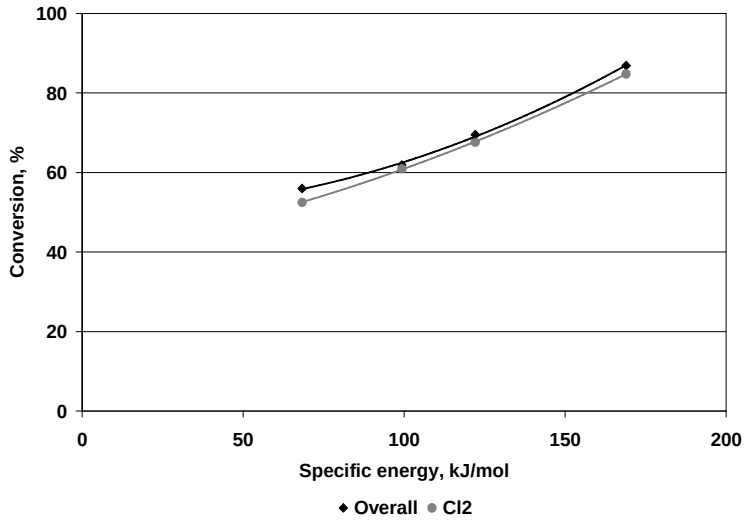


Fig. 7. The dependence between the CCl_4 conversion and specific energy for pulsed current of 15 kHz frequency power supply system.

4. Conclusions

The reactor with the special high-voltage electrode can be effectively used for decompositon of CCl_4 in air.
Effects of CCl_4 decomposition depends on the type of power supply system.
The best overall CCl_4 conversion have been obtained for the AC power supply system (98%).
Main product of CCl_4 decomposition was Cl_2.
$COCl_2$ was not produced in the reactor powered by pulsed current of 15 kHz frequency power supply system.

5. Acknowledgment

This work was financially supported by Warsaw Uniwersity of Technology.

6. References

[1] Central Statistical Office, *Environment 2011*, Warsaw
[2] Chmiel K., Jarzębski A.B., Palica M., 2005 *Przemysł Chemiczny* **84** 442.
[3] Szynkowska M.I., Wojciechowska E., Węglińska A., Paryjczak T., 2009 *Przemysł Chemiczny* **88** 712.
[4] Jasiński M., Szczucki P., Dors M., Mizeraczyk J., Lubański M., Zakrzewski Z., 2000 *Czechoslovak Journal of Physics* **50/S3** 285.
[5] Krawczyk K., Ulejczyk B., 2004 *Plasma Chemistry and Plasma Processing* **24** 155.
[6] Krawczyk K., Jodzis S., Lamenta A., Kostka K., Ulejczyk B., Schmidt-Szałowski K., 2011 *IEEE Transactions on Plasma Scence* **39** 3203.
[7] Krawczyk K., Ulejczyk B., Song H.K., Lamenta A., Paluch B., Schmidt-Szałowski K., 2009 *Plasma Chemistry and Plasma Processing* **29** 27.
[8] Sun Y., Chmielewski A.G., Bułka S., Zimek Z., 2006 *Plasma Chemistry and Plasma Processing* **26** 347.
[9] Harada N., Matsuyama T., Yamamoto H., 2007 *Journal of Electrostatics* **64** 43.
[10] Kirkpatrick M.J., Finney W.C., Locke B.R., 2003 *Plasmas and Polymers* **8** 165.
[11] Han S.B., Oda T., 2005 *IEEE Transactions on Industry Applications* **41** 1343.

BREAKDOWN OF ORDER IN A SELF-ORGANISED BARRIER DISCHARGE

Robert Wild[1], Lars Stollenwerk[1]

[1]*Institute of Physics, University Greifswald*
E-mail: wild@physik.uni-greifswald.de

The diffuse mode of a dielectric barrier discharge shows under certain conditions (p = 200 hPa, f = 10...200 kHz, d < 1 mm) deviations in the lateral homogeneity of the light emission density. The formation of self-organised structures may then be favoured. In this contribution, the transition from a hexagonally patterned discharge to a random distribution of filaments during a voltage reduction is observed and investigated. The patterns are examined with the triple correlation function. Following this, a measure of order is introduced that corresponds to the quality of the pattern. It is shown that this quantity bifurcates supercritically during the transition of the two structures. It is furthermore shown that the bifurcation voltage of the angular order does not coincide with the bifurcation voltage of the radial order. The latter generally occurs at a lower voltage.

1. Experimental setup and methods

Dielectric barrier discharges are plasma sources whose electrodes confine a discharge gap that hosts at least one dielectric barrier. These discharge systems permit applications such as ozone generation, plasma display panels, and surface modification [1-3]. Recent investigations even deal with the application in the medical sector [4-5].

Laterally extended systems are systems, in which the electrode distance d is generally much smaller than the lateral extension. They have been found to produce diffuse discharges, whose lateral homogeneity deviates yielding self-organised patterns. Since the mid-1990s, many different structures, such as hexagonal, concentric or rectangular patterns have been found.

The subject of this contribution is the transition from a regular hexagonal pattern into a random arrangement of strongly localised discharge areas, the so-called filaments. The transition is induced by a constant reduction of the applied voltage.

A schematic of the discharge cell is drawn in Fig. 1. It consists of two glass plates with a thickness of 0.7mm each at a distance of 0.5mm from each other. They are both covered with an ITO (indium tin oxide) layer on the outside to permit an observation in current direction. These layers act as electrodes.

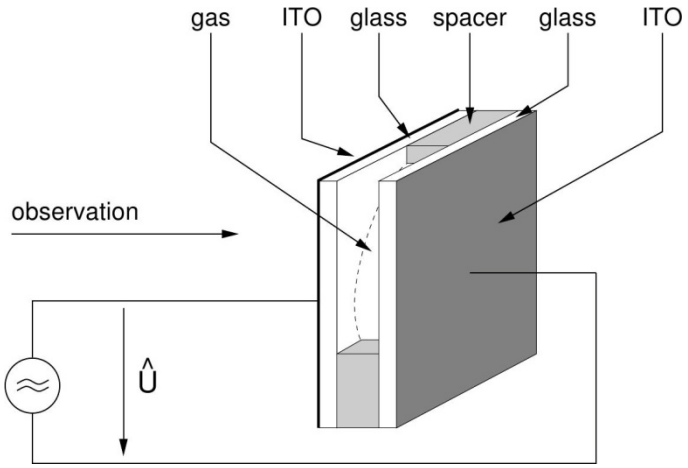


Fig. 1.: Schematic of the discharge cell. The glass plates with a thickness of 0.7mm are at a distance of 0.5 mm from each other. Both have been covered with an ITO layer, that acts as electrodes and allows the lateral observation in current flow direction.

The glass plates have been roughened to a roughness some orders of magnitude smaller than the diameter of one filament. That way, erosional effects the filament could have on the dielectrics may be compensated. The discharge cell is mounted into a closed chamber, which is evacuated and refilled with helium at a pressure of p=200hPa after each measurement. The discharge is electrically supplied by a function generator whose sinusoidal signal is amplified to an amplitude of several hundred volts. The frequency is set to 80 kHz. The applied voltage is measured via voltage divider, the current is measured via voltage drop over a 10Ω resistor. In order to distinguish the discharge current from the displacement current, a capacitive Wheatstone bridge is used.
The lateral light emission of the discharge is monitored by an ICCD camera with a resolution of 512x480 px, 200 µs exposure time, and a frame rate of 250 fps.
Upon acquisition, the images of the discharge are post-processed using a recursive algorithm that extracts the position of the filaments. Criterion for a filament to be detected is a minimum area and brightness. The position of a filament is defined as weighed center of its luminescence density.

For further analysis, the Triple Correlation Function (TCF) is applied to the filament positions. Unlike the two-dimensional fourier transformation, which is commonly used to analyse spatial patterns, the TCF ignores the geometry of the substructures and considers only the filament positions. This technique is already utilised in the field of dusty plasmas [6-7], but has to the authors knowledge never been used to patterned discharges. Its purpose is to analyse the filament positions and to estimate a probability distribution of finding a second filament at a certain angle and distance from a first filament.
Considered is any filament triple (i, j, k). The interfilamentary distances r = |ji| and r = |jk| as well as the enclosed angle φ = angle(i, j, k) are determined. As we want to investigate a hexagonal lattice, we know that there is a typical nearest neighbour distance d_0 of filaments. Hence, the value of r is limited to r_{max}, which is chosen to be slightly larger than the typical neighbour distance d_0. Triples with r larger than r_{max} are discarded, the other ones are sorted into bins with the dimensions Δr and Δφ. The counts for these bins give the abundance of occurrence $n_y(r, \varphi)$. Finally, the normalised abundance y is computed as n_y normalised to the radius r .

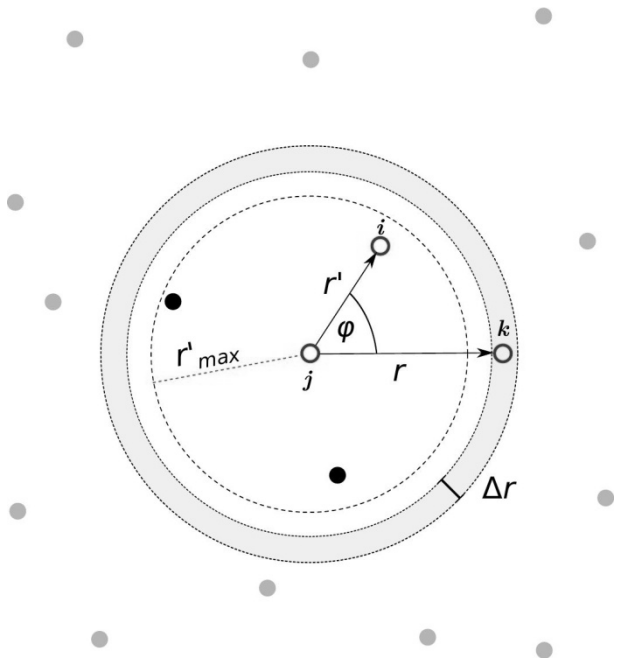


Fig. 2.: Graphical representation of the Triple Correlation Function (TCF). The distances r' and r and the angle φ of any filament triple (i,j,k) are determined. Filaments within a distance r'_{max} are considered for calculation of both r and r' relative to j, others are solely used for calculation of r relative to j.

2. Breakdown of order during voltage reduction

In order to produce a hexagonally patterned discharge, the applied voltage is set to 400 V. The lateral emission is observed as the voltage is reduced by steps of 1V each until the discharge disappears. While the lateral discharge pattern at the applied voltage down to about U = 363 V is clearly hexagonal, the arrangement of the filaments becomes random for values of U < 363 V, see Fig. 3. During the entire process, the number of filaments is constantly reduced. Nevertheless, rate of filament reduction is unaffected by the the apparent breakdown of order at approximately U=350V, see Fig. 4.
The transition is examined using the TCF. A preceding analysis of the breakdown via 2D Fourier transformation already revealed evidence of a bifurcation process, but produced due to the global nature of that method a rather large scattering of the corresponding values, which makes the determination of a bifurcation type impossible [8].

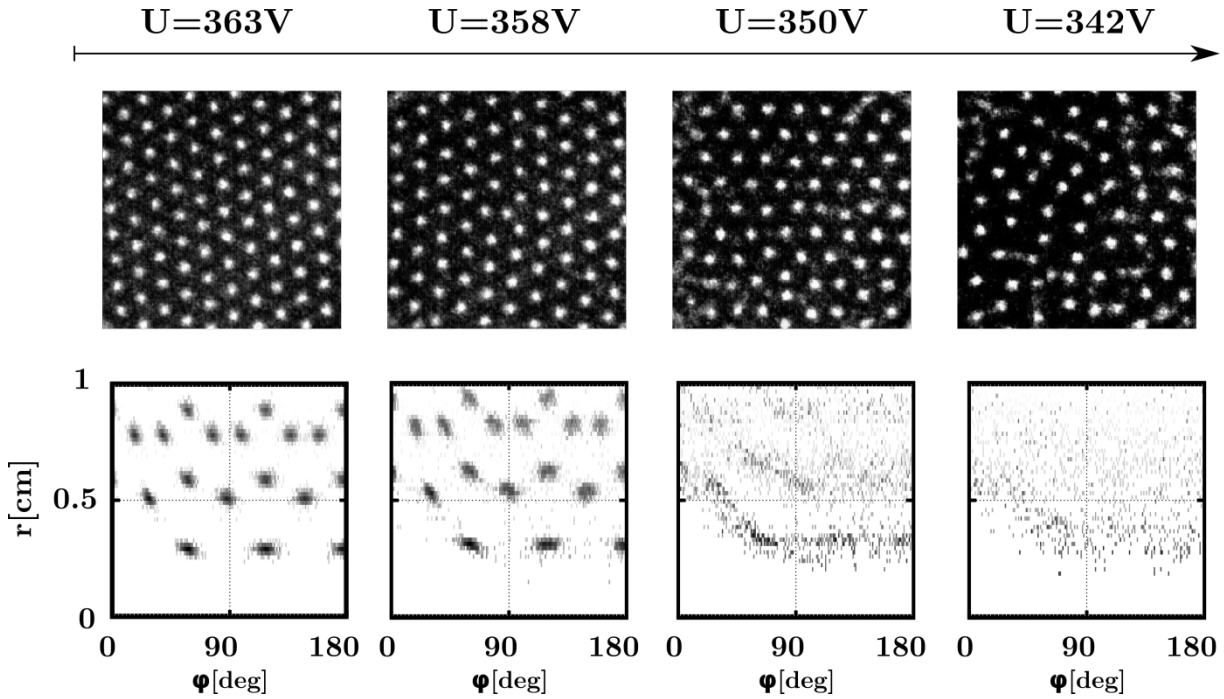


Fig.3.: Upper row: Light density distribution images at voltages close to the bifurcation point. Lower row: Triple correlation functions of the corresponding light density distribution. f = 80 kHz sinusoidal, Helium, without gas flow, exposure time 200 μs.

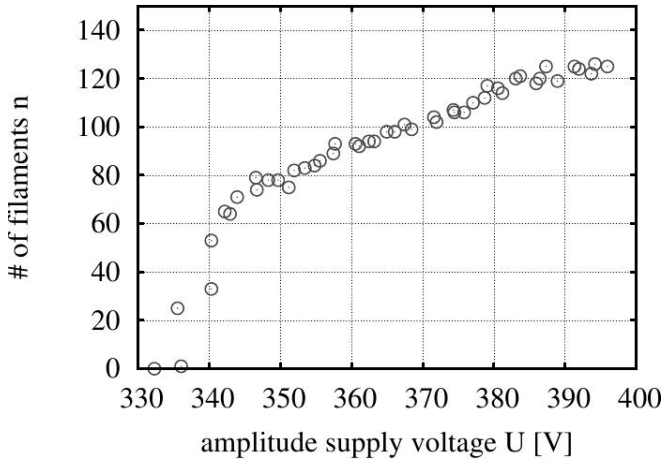


Fig.4. : Number of filaments as a function of the applied voltage.

The lower row of Fig 3. shows the corresponding TCF's for the luminescence density images in the upper row. For distances below the distance of nearest neighbours d_0 (e. g. d_0 = 3.15 mm in figure 3, TCF at U = 363 V), the abundance is close to zero. The same lower limit for the distance of neighbouring filaments is also responsible for the nearly vanishing abundance at small angles. Physically, the lowest filament distance is determined by the inhibition of ignition in the vicinity of a filament [9-10]. Hence, the minimal filament distance is independent from the hexagonal pattern, and so the low abundance for small distances and small angles stays stable after the pattern breakdown (Figure 3, TCF at U = 342 V). For an intact hexagonal pattern (Figure 3, TCF at U = 363 V), the abundance at the distance d_0 has three peaks, namely at 60°, 120°, and 180°. As the hexagonal pattern dissolves with decreasing supply voltage, the peaks get broader. At the end of this transition, the peaks have completely disappeared in azimuthal direction. In radial direction, only a small modulation stays visible.

As the peak at (r, φ) = (d_0, 60°) is a well defined feature of the hexagonal pattern, its height $y_{60} = y(d_0, 60°)$ is taken as the basis for a measure of order. To classify the angular order, y_{60} relative to the average abundance at the fixed distance d_0 is calculated. Similarly, for the radial order y_{60} relative to the average abundance at the fixed angle of 60° is chosen. Hence, two quantities being a measure for the hexagonal order are defined:

$$H_{ang} = \frac{y_{60}}{\langle y(d_0,\varphi)\rangle_\varphi} \quad (1)$$

$$H_{rad} = \frac{y_{60}}{\langle y(r,60°)\rangle_r} \quad (2)$$

Figure 5 shows the order analysis using H_{ang} and H_{rad} for the previously observed breakdown in figure 3. Basically, both plots display the same behaviour: for high voltages the measure of order remains nearly constant. For very low voltages (approximately 340 V in figure 5), the peak y_{60} vanishes in the noise. This is due to low order and additionally due to a decreased number of filaments (Figure 4). Hence, below a certain supply voltage H_{ang} and H_{rad} are not meaningful anymore.

The transition from a nearly constant H_{ang}, or H_{rad} to a decreasing order is rather abrupt, so obviously there is a bifurcation from an ordered to an unordered system via a supercritical bifurcation. For a reliable computation of the bifurcation point U_b, the curves are fitted with a set of linear functions. In all measurements, the bifurcation point $U_{b,rad}$ for the radial order is at lower voltages than the bifurcation point $U_{b,ang}$ for the angular order. However, the absolute bifurcation point may vary.

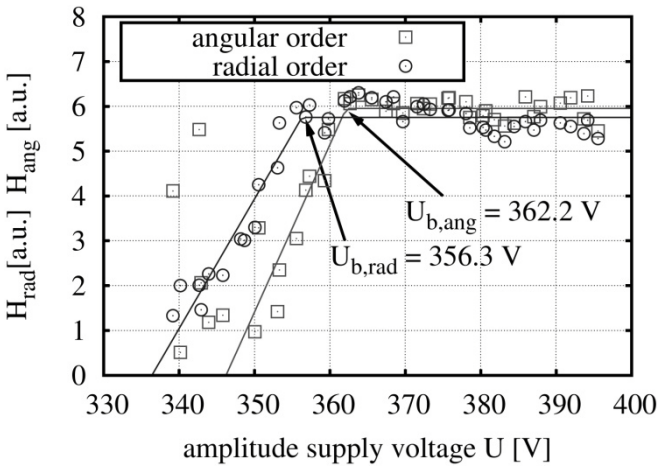


Fig.5.: Analysis of the transition from the hexagonal pattern to the stochastic arrangement of the filaments. Evaluated are the ratios of the 60°-peak at nearest neighbor distance to the mean background in angular and radial direction, $H_{ang} = y_{60} / \langle y(d_0, \varphi)\rangle_\varphi$ and $H_{rad} = y_{60} / \langle y(r, 60°)\rangle_r$, respectively.

While bifurcation was reproduced, the actual value for the bifurcation voltage varies between 350 V and 365 V. The analysis via TCF thereby reveals a distinct bifurcation in the radial and angular measure of order.
In order to discuss the transition from a physical point of view, one has to bear in mind that it occurs close to the ignition voltage of the discharge. Above the ignition voltage, the discharge is ignited everywhere, where the the applied voltage is sufficient. This would result in a discharge pattern with the highest packing density, hence a hexagonal pattern. Reducing the voltage below ignition voltage results in a pattern that consists only of the filaments that are maintained by residual surface charges, reignition of new filaments in unoccupied places can no longer occur. Thus, filaments may arrange randomly with an arbitrarily large inter-filament distance. This is consistent with the observed behaviour below the bifurcation voltage.

This work has been funded by the Deutsche Forschungsgemeinschaft, SFB-TRR 24, B14. We also acknowledge the supportive work of Peter Druckrey, Uwe Meißner and Thomas Schumann.
We would like to thank André Schella and André Melzer for the hint at the TCF and fruitful discussions.

3. References

[1] Kogelschatz U 2003 *Plasma Chem. Plasma Process.* **23** 1–46
[2] Wagner H-E, Brandenburg R, Kozlov K V, Sonnenfeld A, Michel P, Behnke J F 2003 *Vakuum* **71** 417–436
[3] Boeuf J-P 2003 *J. Phys. D: Appl. Phys.* **36** R53–R79
[4] Fridman G, Friedman G, Gutsol A, Shekhter A B, Vasilets V N, Fridman A 2008 *Plasma Process. Polym.* **5** 503–533
[5] Weltmann K-D, Kindel E, von Woedtke T, Hähnel M, Stieber M, Brandenburg R 2010 *Pure Appl. Chem.* **82** 1223–1237
[6] Ludwig P, Thomsen H, Balzer K, Filinov A, Bonitz M 2010 *Plasma Phys. Control. Fusion* **52** 124013
[7] Schella A, Miksch T, Melzer A, Schablinski J, Block D, Piel A, Thomsen H, Ludwig P, Bonitz M, 2011 *Phys. Rev. E* **84** 056402
[8] Wild R and Stollenwerk L 2012 *Eur. Phys. J. D,* accepted for publication
[9] Stollenwerk L and Purwins H-G 2005 *Contrib. Plas. Phys.* **70** 22–28
[10] Stollenwerk L 2009 *New J. Phys.* **11** 103034
[11] Brauer I, Bode M, Ammelt E, Purwins H-G 2000 *Phys. Rev. Lett.* **84** 4104–4107
[12] Stollenwerk L, Gurevich S V, Laven J G, Purwins H-G 2007 *Eur. Phys. J. D* **42** 273–278

VUV IRRADIATION OF BIOLOGICAL OBJECTS

Galina Zvereva

SPb State University of Civil Aviation , Russia, 196210, St-Petersburg, Pilotov str-38
S.I.Vavilov State Optical Institute , Russia, St-Petersburg, Birzhevaya line - 12

E-mail: zvereva@soi.spb.ru

Water is known to generate reactive oxygen species (ROS) - OH, H_2O_2 etc. when irradiating by vacuum ultraviolet (VUV) emission. In the work numerical simulation of ROS interaction with DNA in model cell were carried out. Results show, that VUV irradiation (λ=172 nm, I=100 mW/cm^2) of model cell consisting of cytosol and nucleus leads to 5 times decreasing of non injured nucleotides concentration during 8 10^{-3} s.

1. Introduction

Effect on the biological objects (molecules, cells, tissue) by means of reactive oxygen species (ROS) is one of quickly developing direction at the meeting point of medicine and physics. In most cases gas discharge is used for this purposes. Investigations are carried out in wide range of medical problems from wound treatment to oncology [1]. It was shown [2] that depending on intensity effect of ROS can lead to different results: from increasing of cells reproduction velocity to their apoptosis. It was found that in the base of these results lays ROS generation in the intercellular media.

One of the possible ways of ROS generation is decomposition of water molecules. Role of water decomposition products in DNA destruction was investigated in [3-7]. In [3,4] water solutions of thymine were irradiated by Hg lamps at the wavelengths λ=254 and 185 nm. Quantum yield for thymine destruction at 254 nm was found to be equal to $4\cdot10^{-4}$ independently of O_2 concentration. Quantum yield at 185 nm depended of O_2 concentration in solution and reached 0.25 at O_2 $2.5\cdot10^{-5}$ M. These results were explained by appearance of water decomposition high reactive products $^{\bullet}$OH, H$^{\bullet}$ and their interaction with thymine with generation of stable products of its destruction in the case of O_2 presence. Destruction was found to take place due to attachment $^{\bullet}$OH and O_2 with double bond 5,6 breaking . In works [5,6] thymine in aqueous solution was decomposed with quantum yields of 0.3 and 0.4 under N_2-saturated and aerated conditions by far UV light (185 nm), and quantum yields 2 10^{-4} and 3 10^{-4} by near UV light (254 nm). Mechanism of destruction was found to be the same as in [3,4].

Works [3-7] shows that under VUV irradiation of nuclear acids big role play reactive oxygen products of water photolysis. Under influence of VUV emission (λ<190 nm) water is effectively decomposed with $^{\bullet}$OH radical formation. The main reaction of decomposition is:

$$H_2O + h\nu \rightarrow {}^{\bullet}OH + H^{\bullet}$$

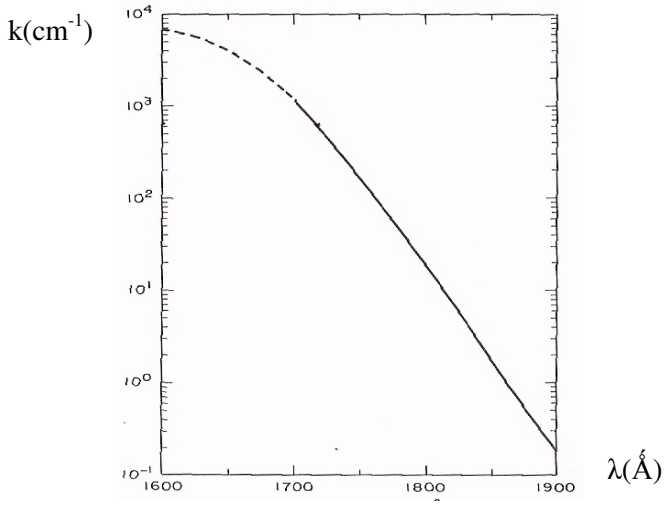


Fig.1.Absorption coefficient of distilled water [9].

Quantum yield of photolysis at wavelength λ=172 nm is equal to 0.42 in the case of liquid water [8]. Absorption coefficient of liquid water in wavelength region λ<172 nm has values 10^3-10^4 cm^{-1} [9] Figure 1. These high values provide 90% emission absorption in thin 10^{-3}-10^{-4} cm water layer .
As effective VUV light sources excimer lamps based on barrier discharges in high pressure rare gases [10,11] can be used. Radiation efficiency of excilamps can reaches 60%, they produce light with different wavelengths Ar (120 nm), Kr (147 nm), Xe (172 nm).
In this work calculations of DNA destruction in the model cell irradiated by VUV emission was carried out. As a source of ROS were considered products of VUV photolysis water molecules.

2. Calculation model and results

In the Fig.2 simplified scheme of a cell, which was used in calculations, is presented. Cell was proposed to consist of 2 layers: layer 1 – cytosol and layer 2- nucleus, containing DNA. It was proposed, that cytosol is consisted of water with pH=7 [12] and antioxidant gluthatione with concentration 5 mM.

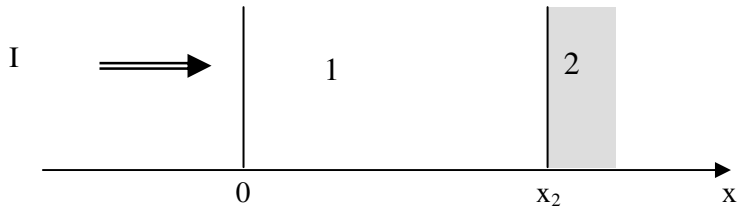


Fig. 2 Simplified scheme of cell. I – VUV emission , 1 - cytosol, 2 - nuclear.

Thickness of layer 1 was equal to 1μ [13]. Thicker layers were not considered because of fast VUV absorption across it. As the layer 2 was proposed to be uniform media consisted of nucleotides with density $\rho_n(x,0)=2\cdot10^{19}$ $см^{-3}$ ($x>x_2$) at initial time moment. As a nucleus has complicate structure, it wasn't considered completely, thickness of layer 2 was proposed to be $\Delta x_2 \sim 10^{-6}$ cm. This *in vivo* corresponds to surface DNA layers of nucleus.
VUV emission with intensity *I* was proposed to penetrate to cytosol (layer 1) and to decompose water with ROS production. ROS by means of diffuse penetrate to nuclear and interact with DNA. Concentrations of ROS in layer 1 were calculated by means of system of equations:

$$\frac{\partial N_i(x,t)}{\partial t} - \frac{\partial}{\partial x}\left(D_i \frac{\partial N_i(x,t)}{\partial x}\right) = S_i(x,t) \qquad i=1,..,\ L \qquad (1)$$

where $N_i(x,t)$- concentration of *i*-th product of water photolysis, $S_i(x,t) = \sum_l F_{il}^{+} - \sum_m F_{im}^{-}$ – sources of generation and decomposition of *i*-th product, D_i – diffusion coefficient of *i*-th product, *L*= 12 – number of unknown products
As it was shown in overview, stable products of DNA - ROS interaction appear in the case of O_2 presence. That is why two equations for determination in layer 2 concentration of non injured by ROS nucleotides $\rho_n(x,t)$ and concentration of stable injured nucleotides - $\rho_f(x,t)$, have been formed due to DNA-ROS interaction with O_2 presence, were solved together with system (1):

$$\begin{cases} \dfrac{\partial \rho_n(x,t)}{\partial t} = -\sum_i F_i(x,t) \\ \dfrac{\partial \rho_f(x,t)}{\partial t} = -\sum_j F_j(x,t) \end{cases} \qquad (2)$$

where $F_i(x,t)=\rho_n(x,t)\cdot N_i(x,t)\cdot k_i$ ($cm^{-3}s^{-1}$) – number of nucleotides in volume unite injured by ROS *i*-th component per time unit, $F_j(x,t)=(\rho_n(x,0) - \rho_n(x,t))\cdot k_j \cdot N_{O2}$ ($cm^{-3}s^{-1}$) – number of stable injured nucleotides in volume unit, having been formed due to DNA-ROS interaction with O_2 presence per

time unit. Initial and edge conditions for O_2 concentration were following: $N_{O2}(x,0)=N_{O2}(0,t)=1.7\cdot10^{17}$ cm^{-3} (it was proposed, that O_2 penetrates inside cell through its membrane). Values of ROS diffusion coefficients were taken from [14,15,16], values of ROS reaction velocities - from [17]. Reaction velocities of DNA with $^{\bullet}$OH, H$^{\bullet}$ and e_{aq}^- at neutral pH for one nucleotide were taken equal to $1.3\cdot10^{-12}$ cm^{3}s^{-1}, $1.2\cdot10^{-13}$ cm^{3}s^{-1} and $2.2\cdot10^{-13}$ cm^{3}s^{-1} correspondingly, reaction velocity of injured nucleotides with O_2 - $1.6\cdot10^{-13}$ cm^3 s^{-1} [18]. Reaction velocities of gluthatione with ROS were taken equal to $0.8\text{-}1.6\cdot10^{-9}$ cm^{3}s^{-1} [19,20].

Results of calculation for the cases of irradiation of model cell by Xe excilamps (λ=172 nm) with surface intensities 100 mW/cm^2 are presented in the Figure 3. During time interval $6\cdot10^{-3}$ s gluthatione concentration falls due to fast destruction in reactions with ROS and long time of generations [21]. After that concentrations of ROS ($^{\bullet}$OH Figure 3) increase leading to decreasing of non injured nucleotide concentration. Their concentration became 5 times lower by the time of $8\ 10^{-2}$ s from beginning of VUV irradiation.

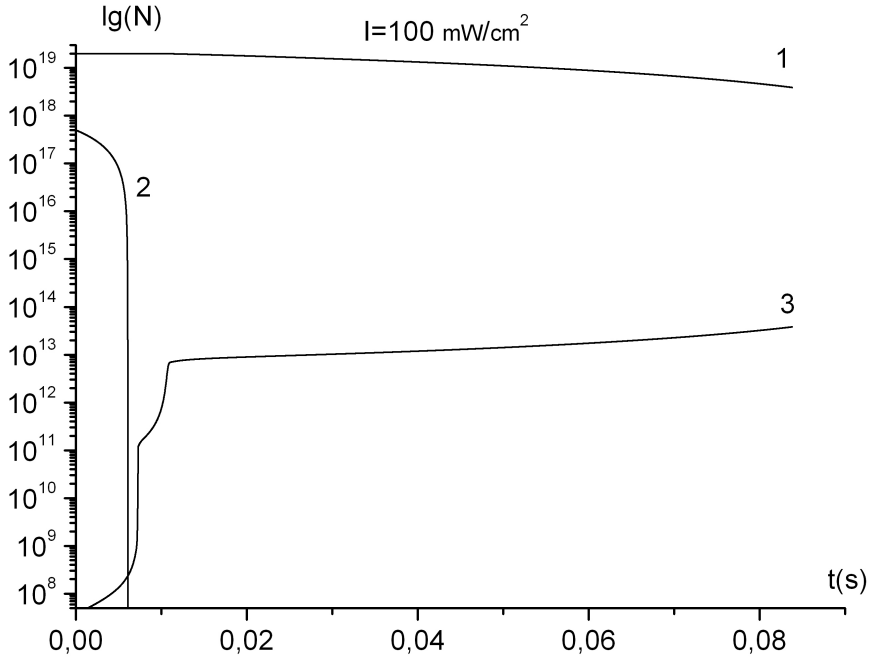


Fig.3 Time dependence of concentrations N(cm^{-3}): 1- non injured nucleotides, 2-gluthatione, 3-$^{\bullet}$OH radicals. I=100 mW/cm^2.

3.References

[1] Weltmann K.D., Kindel E., Woedtke T., Hähnel M., Stieber M., and Brandenburg R. 2010 *Pure Appl. Chem.* **82** 1223.

[2] Kalghatgi S., Kelly C.M., Cerchar E., Torabi B., Alekseev O., Fridman A., Friedman G., Azizkhan-Clifford J. 2011 *PLos One.* **6**(1) 1.

[3] Daniels M. and Grimison A. 1963 *Nature* **197** 484.

[4] Daniels M. and Grimison A. 1967 *Biochim. Biophys. Acta* **142** 292.

[5] Ohtani B., Nagasaki H., Nishimoto S., Sakano K. and Kagiya T. 1986 *Can. J. Chem.* **64** 2297.

[6] Ohtani B., Nagasaki H., Sakano K., Nishimoto S., and Kagiya T. 1987 *J.Photochem. Photob. A* **41** 141.

[7] Swarts S.G., Sevilla M.D., Becker D., Tokar C.J. and Wheeler K.T 1992 *Rad. Res.* **129** 333.

[8] Heit G., Neuner A., Saugy P.-Y., Braun A.M. 1998 *J. Chem. Phys. A.* **102** 5551.

[9].Weeks J.L, Meaburn G.M.A.C. and Gordon S. 1963 *Rad.Research* **19** 559.

[10] Volkova G.A., Kirillova N.N., Pavlovskaya E.N. and Podmoshenskii I.V. 1982 Bill. Tov. Zn. (rus.) **41** 179.
[11] Kogelschatz U. 2003 *Plasma Chem. and Plasma Process.* **23** (1) 1.
[12] Ito T., Ito A., Hieda K. and Kobayashi K. 1983 *Rad.Research.* **96** 532.
[13] Coohill T.P. and Sutherland J.C. 1989 *J.Opt.Soc.Am.B.* **6**(5) 1079.
[14] Bielski B. H. J., Cabelli D.E., Arudi R.L. 1985 *J.Phys.Chem. Ref. Data.* **14** N4 1041.
[15] Bugaenko V.L. and Byakov V.M. 1998 High energy chemistry **32** N6 407 (Rus).
[16] Radiation Research 1967 Ed. By G.Slimi 927 c.
[17] Zvereva G. 2010 *Optics and Spectr.* **108** N6 915.
[18] Bensasson, Land E.J. and Truacott T.G. 1983 Flash Photolysis and Pulse Radiolysis, Pergam Press
[19] Liphard M., Bothe E. and Schulte-Frohlinde D. 1990 *Int. J. Radiat. Biol.* **58** 589.
[20] Hoffman M.Z. and Hayon E. 1973 *J.Phys. Chem*. **77** 990.
[21] Deneke S.M. and Fanburg B.L. 1989 *Am. J. Physiol.* **257** L163.

POWER CONTROL OF GLIDING ARC DISCHARGE BY CHANGING THE TRANSFORMERS LEAKAGE REACTANCE

Grzegorz Komarzyniec

Lublin University of Technology,
Institute of Electrical Engineering and Electrotechnologies,
ul. Nadbystrzycka 38A, 20-618 Lublin, Poland
E-mail: g.komarzyniec@pollub

GlidArc plasma reactor power regulation by leakage reactance control is presented. The system allows adjusting the power of discharge while maintaining stable plasma generation conditions. Power regulation relies on discharge current value, which is sinusoidal in all range of regulation while the power supply voltage is constant.

1. Introduction

When a electric arc discharge of constant pressure is concerned, voltage between electrodes in a set distance of each other is not dependent on current changes. Limiting the current value, on which the arc discharge power is dependent, must therefore be done outside the arc discharge.

As far as alternating current is concerned it is important for the current to flow constantly, because a currentless breaks cause de-ionization of the space between electrodes which deteriorate plasma reactor's work stability and worsen the generated plasma quality. If the current limiting was due to additional resistance connected to the power circuit of the reactor there would be breaks in the current's flow and the reactor's efficiency would decrease. Using capacitor as a current limiter would require its huge capacity as well as causes dangerous oscillations and unstable reactor's work.

The only efficient way to limit the discharge power is limiting current with inductance. Installing inductors into current circuit complicates needlessly the power system and decreases its efficiency. The effective method of discharge power regulation in reactor is limiting current by variable leakage reactance of power transformers [1],[2],[3].

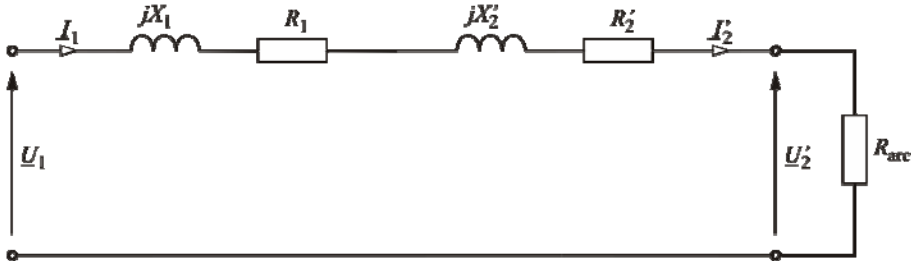


Fig. 1. Simplified equivalent scheme of loaded transformer.

When we assume, in order to simplify our speculations, that a transformer works in the short circuit conditions, with the arc discharge resistance equal to $R_{arc}= 0$, then for a equivalent scheme from Fig. 1 we can note:

$$\underline{Z}_z = \left(R_1 + R_2^{'}\right) + j\left(X_1 + X_2^{'}\right) = R_z + jX_z \tag{1.1}$$

and

$$I_1 = \frac{U_N}{Z_z} \tag{1.2}$$

$$I_2 = \vartheta \frac{U_N}{Z_z} \tag{1.3}$$

Resistances R_1 and R_2 are constant values, specified by resistance of copper used for primary and secondary windings of transformer. Reactances X_1 and X_2 can be influenced by changing of

transformer's windings geometries. Changing leakage reactance of transformer we can change impedance *Z*, and therefore we can influence the arc discharge current value.

2. Analyzed system

We used for experiment three-electrode GlidArc plasma reactor, with electrodes'dimensions presented in the Fig. 2. The appliance was powered from three one-phase transformers, connected into $Y_N y_N$ three phase system (Fig. 3). Discharge initiation was executed with two additional ignition electrodes, powered from separate ignition system. This allowed to control the discharge power in the reactor without worsen conditions for its ignition. [4],[5],[6].

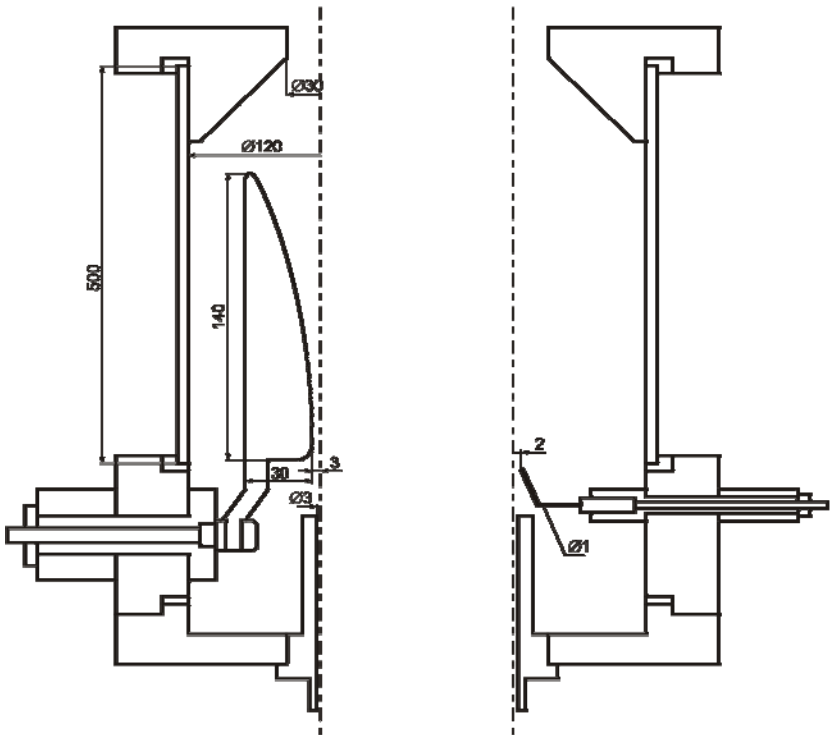


Fig. 2. Geometry of plasma reactor electrodes; a) basic dimensions of discharge chamber with working electrodes; b) ignition electrode

Table 1. Plasma reactor data

Number of ignition electrodes	2
Number of working electrodes	3
Process gases	argon, nitrogen, helium, air
The volumetric flow rate of gas through the nozzle	0.5÷8 m^3/h

If the primary and secondary transformer's windings are set in one limb and are wound concentrically, the leakage reactance is of the lowest value. When the windings are set separately in different limbs, the leakage reactance is of the highest value. Calculating reactance of that kind of transformer is difficult because you must take into account the geometry of the magnetic circuit, partition the flux yoke into separate components and consider a great deal of different factors.

In our case the primary and secondary windings are separated into different limbs. The primary winding is made of higher number of windings than the calculated number. It was tapped and distributed into both limbs (Fig. 4). Regulation of discharge power in the reactor works due to switching tapped primary winding with the constant number of windings. By changing connections pattern you can regulate short circuit impedance within certain limits, that is between 5.7 Ω and 13.4 Ω.

The highest discharge power is obtained at feeding transformer from tapped AA0+B0B4, and the lowest at feeding from tapped AA4. By changing tapped secondary windings the voltage in reactor's electrodes is regulated.

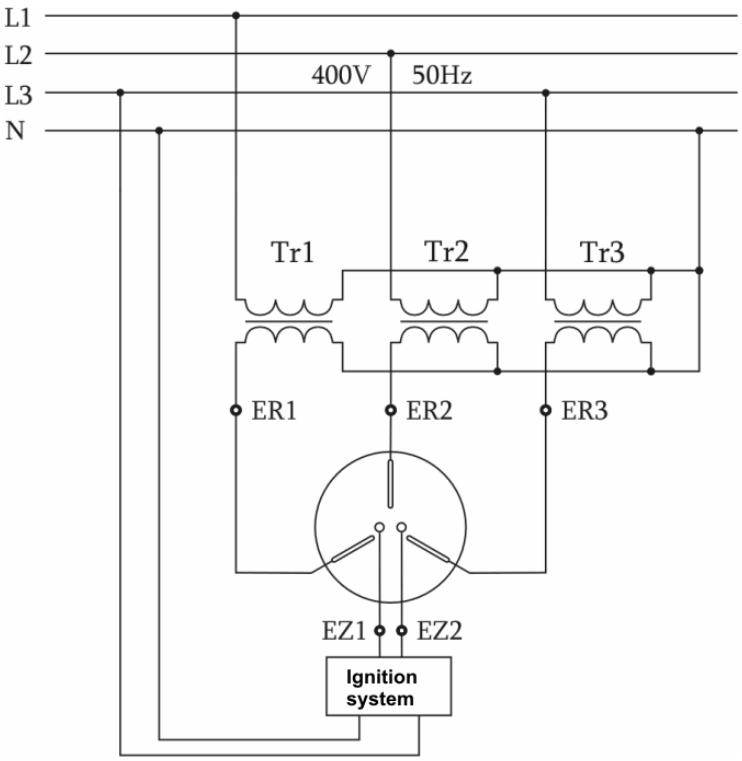


Fig. 3. Power system of GlidArc reactor

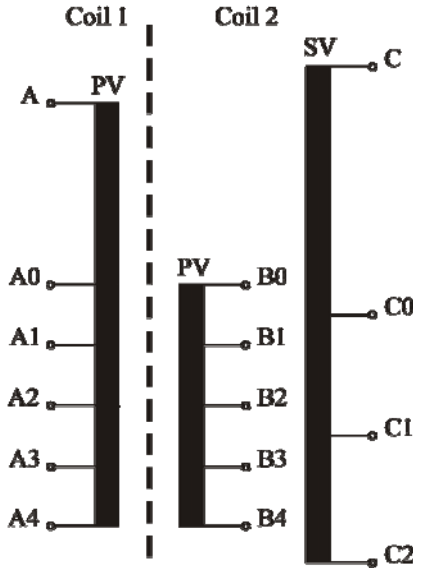


Fig. 4. Position of transformer's windings

Table 2. Power system parameters

	Power transformer	Ignitron system
Power	9.2 kVA	60 VA
Voltage	230 V	230 V
Current	40 A	0.25 A
Input frequency	50 Hz	50 Hz
The output voltage	1.4 kV	15 kV
The output current	6.5 A	40 mA
The output frequency	50 Hz	20 kHz

3. Transformers experiments

In tables 3 and 4 results of transformers experiments are given. Experiment of short circuit was done with feeding transformer with rated voltage and short circuiting the secondary winding by connecting its terminals with copper wire.

Table 3. Unloaded transformer parameters

Tap AA4 (the highest possible leakage reactance)					
Primary side			Secondary side		
U_1	I_1	P_1	U_2 tap CC0	U_2 tap CC1	U_2 tap CC2
230 V	0.5 A	20 W	600 V	1000 V	1400 V
Tap AA0+B0B4 (lowest possible leakage reactance)					
Primary side			Secondary side		
U_1	I_1	P_1	U_2 tap CC0	U_2 tap CC1	U_2 tap CC2
230 V	0.5 A	20 W	600 V	1000 V	1400 V

Table 4. Transformer's short circuit state

Tap AA4 (maximum leakage)				Tap AA0+B0B4 (minimum leakage)			
Tap CC0				Tap CC0			
U_1	I_1	P_1	I_2	U_1	I_1	P_1	I_2
230 V	17 A	600 W	6.2 A	120 V	15.5 A	320 W	6 A
Tap CC1				Tap CC1			
U_1	I_1	P_1	I_2	U_1	I_1	P_1	I_2
230 V	17 A	600 W	3.8 A	175 V	27 A	760 W	6 A
Tap CC2				Tap CC2			
U_1	I_1	P_1	I_2	U_1	I_1	P_1	I_2
230 V	17 A	600 W	2.7 A	230 V	40 A	1400 W	6 A

At the no-load state the transformer uses 115 VA and at the measuring short circuit state 9.2 kVA. The lowest transformer's impedance is chosen in the manner that the short circuit current at the rated voltage is limited to 40 A at the primary side and 6A at the secondary side. For the maximal impedance the values are 17 A and 2.7 A.

4. Discharge power regulation

Plasma reactor was powered with voltage of 1.4 kV from the tapped CC2 of the transformer's secondary side. Measurements were done for two plasma-creating gases: nitrogen and argon. By changing the leakage reactance of the transformers with changing tapped primary winding, and with the constant windings number, we can regulate discharge power in nitrogen from 2400 W to 8400 W (table 5). Power regulation is possible thanks to limiting the current value. Feeding voltage of reactor in all the scope of regulation is constant and the current's waveform is sinusoidal. This way we obtain constant conditions for ignition and developing of discharge in all range of power regulation.

Table 5. Power regulation by changing tapped (nitrogen)

Tap	P_1 (total)
AA1+ B0B3	8400 W
AA2+ B0B2	5800 W
AA3+ B0B1	3600 W
AA4	2400 W

It is also possible to regulate power by changing transformers' turns ratio (Table 6). In this case the discharge power regulation is done by simultaneous limiting the current value and reactor's supply

voltage value. For tapped secondary side CC2 the voltage changes from 1400 V at discharge power 7200 W to 1100 V at discharge power 4400 W.

Table 6. Power regulation by changing the number of windings (argon)

Tap	P_1 (total)
AA1+B0B3	7200 W
AA2+B0B3	6200 W
AA3+B0B3	5200 W
AA4+B0B3	4400 W

5. Summary

Discharge power regulation in the gliding arc reactor by changing leakage reactance of transformers allows stable conditions of reactor's work in all the scope of settings. The power regulation is done by changing discharge current value with its sine waveform. Change of transformers' reactance does not affect the arc voltage. When it is necessary to change supply voltage it can be done in two ways: 1) changing the number of windings of the primary side by switching tapped; 2) by switching tapped on the secondary side.

1. References

[1] Janowski T., Stryczewska H. D., Komarzyniec G., Janowski W., Transformatory o rdzeniach zwijanych w zasilaczach trójfazowych reaktorów plazmowych (A wound cores transformers in the three phase power supplies of plasma reactors), Przegląd Elektrotechniczny, nr 4/2010, 245-248.

[2] Komarzyniec G., Janowski, T., Stryczewska H. D., Diatczyk J., Multi-electrode gliding arc plasma reactors powered from special transformers, The 17th International Symposium on Plasma Chemistry, Toronto, Canada August 7-12, 2005.

[3] Komarzyniec G., Stryczewska H. D., Diatczyk J., Arc plasma reactor power system with 5-limb transformer, Journal of Advanced Oxidation Technologies, vol. 9, no 2, July 31, 2006, pp. 178-181.

[4] Komarzyniec G., Janowski W., Diatczyk J., Pawłat J., Stryczewska H. D., Analiza rozchodzenia się zaburzeń elektromagnetycznych w systemach generacji plazmy łukowej (Disturbances propagation in the arc plasma reactor systems), Konferencja Naukowo-Techniczna: Modelowanie i Sterowanie Procesów Elektrotermicznych, Kielce, 22-24 września 2010, 101-107.

[5] Komarzyniec G., Stryczewska H. D., Janowski T., Comparison of the Features of Arc Plasma Reactor Powered from Transformer and Inverter Type Supplied, 11th International Symposium on High Pressure, Low Temperatura Plasma Chemistry HAKONE, Oleron Island, France, 7-12 September 2008, 555-559.

[6] Komarzyniec G., Stryczewska H. D., Sikorski A., Ruszczyk A., Gliding arc plasma reactor supplied from AC/DC/AC inverter, 18th International Symposium on Plasma Chemistry, Kyoto, Japan, August 26-31, 2007.

RF-POWERED ATMOSPHERIC PRESSURE PLASMA JET FOR SURFACE TREATMENT

Joanna Pawłat, Radosław Samoń, Tomasz Giżewski, Jarosław Diatczyk, Włodzimierz Janowski, Henryka D. Stryczewska

Lublin University of Technology
ul. Nadbystrzycka 38a, 20-618 Lublin, Poland
E-mail: askmik@hotmail.com

Atmospheric pressure plasma jet (APPJ) was developed for decontamination purposes. Features of the device are ability to work with various feed-gases at the atmospheric pressure in several gas flow, frequency and current- voltage regimes. LabVIEW based TGAs virtual measurement sub-system for monitoring and measurement process through subsequent setting of electrical and gas-flow parameters (digital control of flow-meters), conditioning and amplification of electrical signals and collection of the data from peripheral measuring devices was applied.

1. Introduction

Plasma and Advanced Oxidation Processes (AOPs) are well known of excellent efficiency towards variety of chemical and biological contaminants [1-4].
Many research groups concentrate on the efforts of designing plasma sterilizing device working in the ambient conditions [5-17] using variety of methods such as barrier discharges, corona reactors or plasma jets. The main objective of this research was development of operator- and environmental- friendly low temperature atmospheric pressure plasma decontamination device, which should have operation cycle length at least the same as traditional set-ups, should be applicable toward broad range of materials and surfaces without damaging them irreversibly.

2. Experimental set-up

Experimental set-up, consisted of the following sub-systems:

- gas and liquid dosing sub-system,
- electrical discharge generating sub-system
- control and data acquisition sub-system
- chemical and biological analyzing sub-system

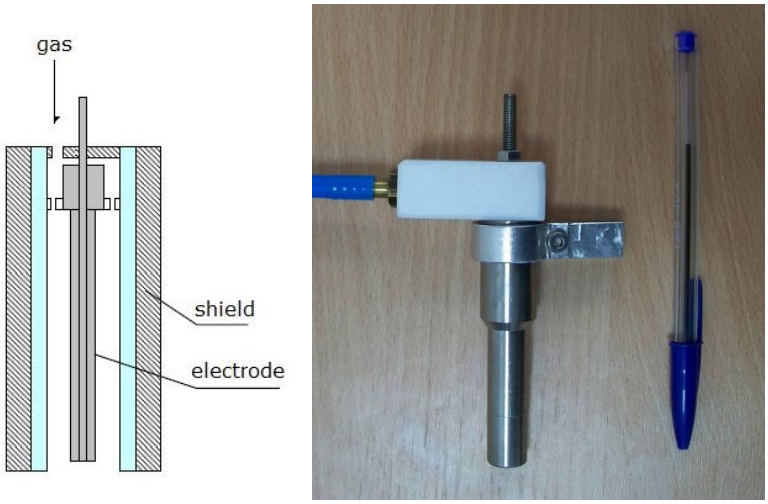


Fig.1. Schema and photo of atmospheric pressure plasma jet.

The main part of the device, which is presented in Fig. 1. was RF-powered changeable rod electrode of tungsten or acid-proof stainless steel. 3 types of electrode shapes: flat surface, screw-type

and turtle-type surface of diameters ranging from 4 to 6 mm were tested. The electrode was powered by a regulated RF supply (AG 1021 RF generator, T&C Power Conversion) via impedance matching network. It was possible to power plasma reactor with frequencies from 10 kHz to 20 MHz. The schema of electrical supply is depicted in Fig. 2.

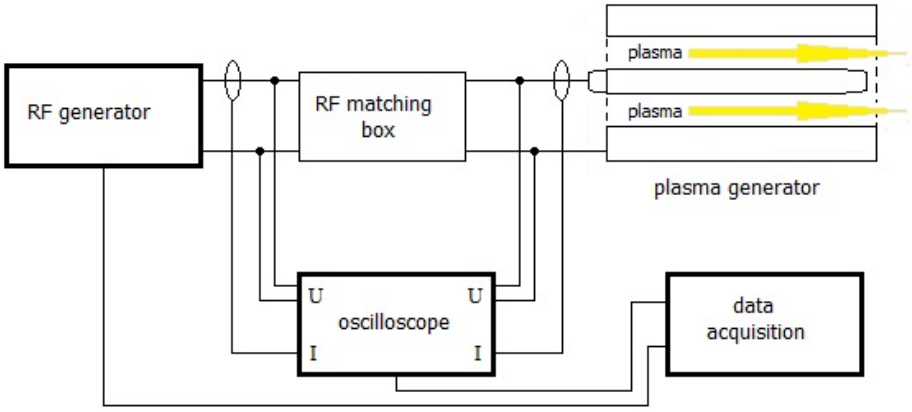


Fig.2. Electrical supply of APPJ.

LabVIEW based TGAs virtual measurement sub-system was developed for the purpose of this project. Main screen of the system, presented in Fig.3, enables whole monitoring and measurement process through subsequent setting of electrical and gas-flow parameters (digital control of flowmeters), conditioning and amplification of electrical signals. TGAs also automatically collects the data from Tektronix TDS2024B oscilloscope, voltage and current probes.
Elaborated application was divided into 4 modules: data acquisition, digital signal processing, reporting and flow-rate control. Main loop consists of decision events and event handler. Change of the settings on the front panel by user leads to direct communication and data streaming to generator, oscilloscope and flow meters. Application also uses functions defined in external module- report, which enables creating of reports in MS Office documents. Basic operations on discrete sequence representing measured signal are performed in the main loop. It is a data set of constant number of elements (2500 for each channel). Whole TGAs system represents integrated virtual environment communicating with devices using built-in communication tools for management of devices' work parameters and for data acquisition. Physically those tasks are realized via RS232 port or USB port.



Fig. 3. Developed TGAs subsystem for control of gas flow and electrical parameters.

3. Results and discussion

Current/voltage characteristics on the primary and secondary side are presented in Fig. 4. Discharge homogeneity changed in dependence on all tested parameters: feed gas, gas flow rate, power supply parameters. The most homogenous plasma was generated in gas mixtures containing argon and helium and at gas flow rates exceeding 7,5 l/min. This is in a good accordance with literature data. From the discharge homogeneity point of view, the most beneficial were flat and turtle shape tungsten electrodes.

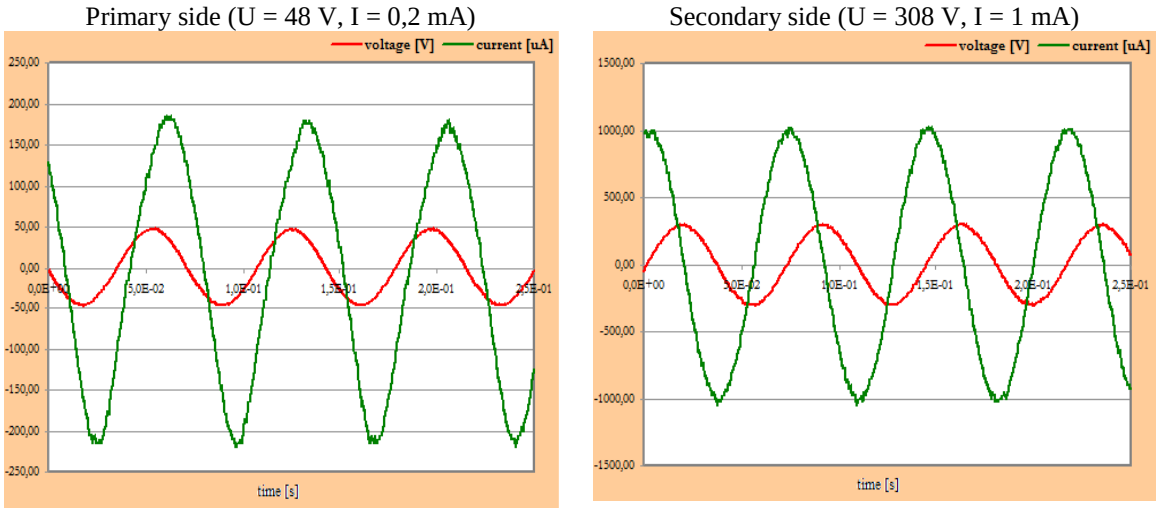


Fig. 4. Voltage/current characteristics

From the RF generator point of view, the most stable operation, which resulted in the lowest ratio of reflected power was achieved at frequency range 12-15 MHz (depending on the feedgas type). Examples of the discharge regimes in feed gas mixtures oxygen/argon and oxygen/helium (30/70%) with the current/voltage characteristics on secondary side are shown in Fig.5.

In dependence on the gas flow rate, discharge plasma sizing from 10 to 20 mm and 5-15 mm in diameter and length was produced. It is possible to achieve temperatures below 40^{o}C compromising applied power, frequency and gas flow-rate.

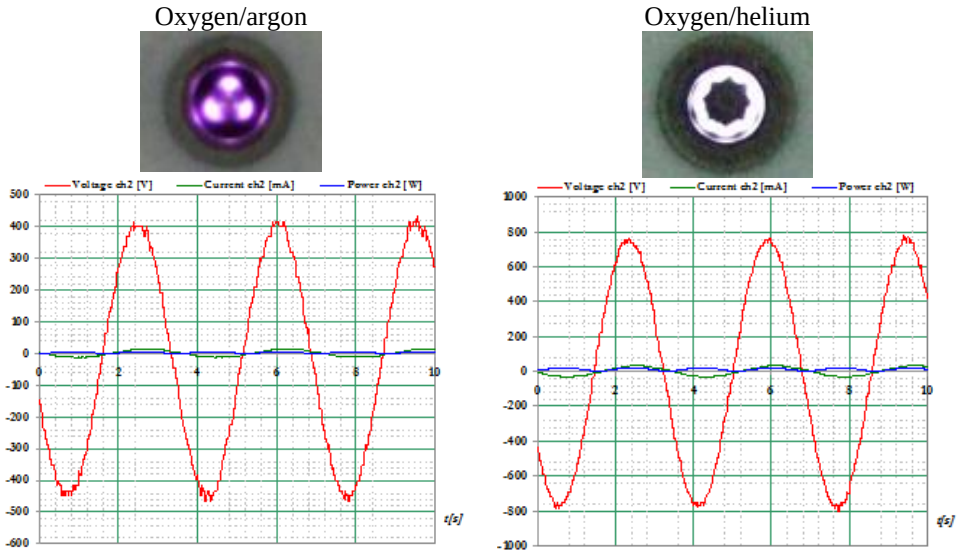


Fig. 5. Examples of discharge regimes obtained in APPJ.

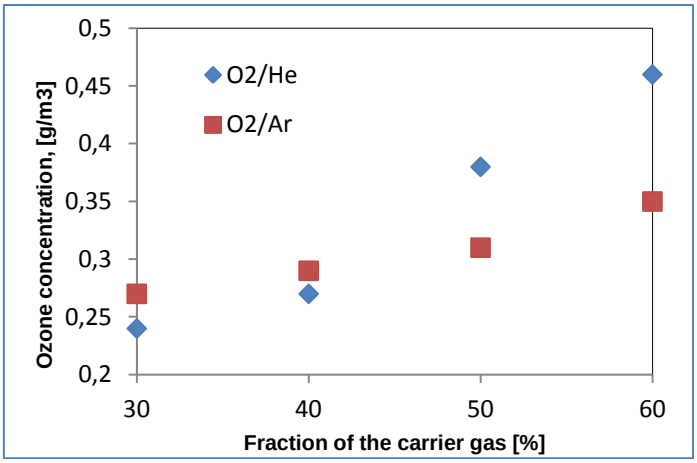


Fig. 6. Ozone concentration in dependence on the fraction of carrier gas: helium or argon. Process gas: oxygen, total flowrate: 10 l/min, P= 55 W, f=14,05 MHz.

Ozone concentration was measured in dependence on the gas type, gas flow rate, power and the type of electrode. Comparison of ozone concentration depending on the fraction of the argon and helium as a carrier gas added to oxygen, at 5 mm diameter, flat-surface electrode condition is presented in Fig. 6. Achieved ozone concentrations were low and ranged 0,82 g/m^3.

4. Conclusions

Compact device: atmospheric pressure plasma jet for decontamination purposes was developed. Achieved temperatures of the working gas in the outlet vicinity depended on the discharge conditions-mainly on the gas flow rate and it was possible lower temperature below 40 ^{o}C. Device may be applied for the treatment of the heat-sensitive surfaces in the future.

5. References

[1] Kamgang Youbi G., Naitali M., Herry J.-M., Hnatiuc E., Brisset J.-L. 2010 *12th International Conference on Optimization of Electrical and Electronic Equipment (OPTIM)*, Basov, 1336-1342.
[2] Pawłat J., Ihara S. 2007 *Plasma Process. Polym*., **4(7-8)** 753-759.
[3] Laroussi M., Leipold F. 2004 *Int. J. Mass Spectrum*, **233** 81–86.
[4] Eliasson B., Kogelschatz U. 1991 *IEEE Trans Plasma Sci.*, **19** 1063–1077.
[5] Moreau M., Orange N., Feuilloley M. 2008 *Biotechnology Advances*, **26** 610–617.
[6] Moisan M., Barbeau J., Pelletier J., Philip N., Saoudi B. 2001 *13th CIP*, 12–18.
[7] Ohkawa H., Akitsu T.,Tsuji M., Kimura H., Kogoma M., Fukushima K. 2006 *Surface and Coatings Tech.* **200(20-21)** 5829-5835.
[8] Kelly-Wintenberg K., Hodge A., Montie T., Deleanu L., Sherman D., Roth J. 1999 *Vac. Sci. Technol. A.*, **17(4)** 1539–*1544.*
[9] Vleugels, M., Shama,G., Deng, X., Greenacre, E., Brocklehurst, T., Kong, M. 2005 *IEEE Trans Plasma Sci.*, **33** 824–828.
[10] Weltmann K., Brandenburg R., Bussiahn R., Haehnel M., Polak M., von Woedtke T., Ehlbeck J. 2011 *NATO Advanced Research Workshop Plasma for bio-decontamination, medicine and food security*, Jasná, Slovakia, 13-14.
[11] Ehlbeck, J., Schnabel, U., Polak, M., Winter, J., von Woedtke, T., Brandenburg, R.,von dem Hagen, T,, Weltmann, K. 2011 *J. Phys. D: Appl. Phys*., **44** 013002.
[12] Dobrynin D., Fridman Gr., Friedman Gr., Fridman A. 2009 *New J. Phys*., **11** 1367-2630.
[13] Machala Z., Jedlovský I., Chládeková L., Pongrác B., Giertl D., Janda M., Šikurová L., Polčic P., 2009 *Eur. Phys. J.*, **D54** 195-204.
[14] Kamgang-Youbi G., Herry J., Meylheuc T., Brisset J. L., Bellon-Fontaine M., Doubla A., Naďtali M. 2008 *Let. Appl. Microbiology*, **48(1)** 13-8.

[15] Kolb J., Mohamed A., Price R., Swanson R., Bowman A., Chiavarini R., Stacey M., Schoenbach K. 2008 *Appl. Phys. Lett.*, **92** 241501.
[16] Pawłat J. 2011 *ELMECO-7– AoS-10*, Nałęczów. Poland, 123-124.
[17] Pawłat J., Giżewski T., Stryczewska H. D. 2011 *17th International Conference on Advanced Oxidation Technologies for Treatment of Water and Soil,* San Diego, California, USA, 54.

ANALYSIS OF OXIDATION NO AND NO_2 WITH THE APPLIED LOW TEMPERATURE PLASMA PRODUCTS

Justyna Jaroszyńska-Wolińska

Faculty of Civil Engineering and Architecture, Lublin University of Technology, Nadbystrzycka 40, 20-618 Lublin, Poland

E-mail: j.wolinska@gmail.com

Four different chemical models were applied to analyses energetic process of oxidation NO and NO_2 reacting with plasma products. The potential energy surface of systems comprising NO and NO_2 were characterized. The NO oxidation processes , well known at the molecular level, were modelled by *ab initio* quantum chemistry methods in attempt to detect the presence of any transitions states and calculate the relative reaction energy, E_r and the activation energy, E_a of each reaction. The MP2 level of theory was further applied to reactions (1) $NO + O_3$ and (2) $NO_2 + O_3$ with three different basis sets and finer potential energy scan resolution and the activation energies, E_a were determined.

1. Introduction

Of interest to industry are techniques to destroy NO_x at the post-combustion stage, commonly called end-of-pipe removal or abatement techniques. These include selective catalytic reduction (SCR), selective non-catalytic reduction (SNCR) and plasma chemistry. SCR and SNCR techniques require substantial investment in equipment and have limitations in efficiency. These problems motivate development of an energy and chemicals efficient, widely applicable, and of- pipe exhaust NO_x abatement technology. Industrial plasma systems appears to offer technically feasible and commercially interesting solutions based on the Gas State conversion of NO_x into industrially useful by-products, such as nitric acid.

The overall oxidation process by plasma generated ozone can be described by the following global reactions some or all of which reactions almost certainly incorporate intermediate stages in which intermediate species are generated:

$$NO + O_3 \rightarrow NO_2 + O_2 \quad (1)$$

$$NO_2 + O_3 \rightarrow NO_3 + O_2 \quad (2)$$

$$NO_2 + NO_3 \rightarrow N_2O_5 \quad (3)$$

$$2NO_2 + O_3 \rightarrow N_2O_5 + O_2 \quad (4)$$

$$N_2O_5 + H_2O \rightarrow 2HNO_3 \quad (5)$$

The detailed mechanisms of these reactions are complex and not well known but their understanding is key to making this method of NO_x conversion efficient and applicable in practice. One way to determine major factors which govern the process might be to perform exhaustive and expensive experimental studies but there would be no certainty that these would reveal the important processes. An attractive alternative seems to be molecular modelling based on quantum chemical methods. Quantum chemistry today delivers very powerful tools for studying varied chemical problems.

We have applied quantum chemistry methods to describe the energetic of elementary reactions comprising the oxidation process. The modern theoretical techniques, involving the density functional theory (DFT) and *ab initio* multiconfigurational approach (MCSCF), are well suited for this kind of calculations. In the following we present our theoretical investigations of the energetics of the molecules generated by intermediate reactions incorporated within the global reactions (1) – (4) and the energy change of each intermediate reaction defined as $\Delta E = E_{intermediates} - E_{reactants}$. From these we hope to determine the relative thermodynamic probability of competing reaction paths, e.g. (1) → (2) → (3) → (5) versus (1) → (4) → (5) might be in competition.

2. Computational details and discussion

To investigate such oxidation processes, however, each reaction must be characterized at the molecular level and this was attempted using a total of six quantum chemical techniques:

1. Techniques to determine relative energies of reactions:
   a. Density Functional Theory (DFT) based Becke-3-Lee Yang Parr (B3LYP)
   b. Complete Active Space Self-Consistent Field (CASSCF)
2. Techniques to investigate transition states as work towards estimation of activation energies:
   a. Hartree Fock (HF)
   b. Moller Plesset Perturbation (MP2)
   c. Density Functional Theory (DFT) based Becke-3-Lee Yang Parr (B3LYP)
   d. Coupled Cluster with Singles and Doubles (CCSD) substitutions

Techniques 1a and 1b above were applied in the attempted determination of the relative energies, defined as $\Delta E = E_{\text{products}} - E_{reactants,}$ for reactions (1) – (4) above. The equilibrium geometries and electronic energies of substrates and products, namely the oxygen molecule, the ozone molecule, the mono-nitrogen oxide molecules, NO and NO_2 and the product molecules NO_3 and N_2O_5, were calculated as well as their zero-point vibration energy (ZPE).

DFT calculations were carried out using the parallel version of the Parallel Quantum Solutions quantum chemistry software [1] while the CASSCF calculations were carried out using the DALTON quantum chemistry software [2].

The calculations were done at the DFT/B3LYP/6-311G(d,p) and the CASSCF (σ- and π-derived)/6-31G(d,p) levels of theory. It was demonstrated that the DFT/B3LYP technique is superior to the *ab initio* CASSCF approach. The DFT method provides an efficient way of estimating the static and dynamic correlation energies for the strongly multi-configurationally species such as those considered in this work. Good agreement between the DFT/B3LYP and the experimental geometries as well as harmonic frequencies, where available experimentally, was achieved. In contrast, the CASSCF approach either tended to give the wrong structure of the molecule, e.g. the NO_3 molecule, or could not be applied due to computational problems, as for the N_2O_5 molecule. Accordingly, the ZPE corrected relative energies for reactions (1) – (4) above were computed at the DFT level only. The negative values of $\Delta E^{(\text{ZPE})}$ showed that energy was released and all the reactions are exothermic.

However, $\Delta E = E_{\text{final products}} - E_{reactant,}$ alone is not sufficient to determine the relative probability of competing reactions paths. Only by determination of the complete energy scheme of each competing reaction path, including any critical intermediate or transmission reactions and the energy change for intermediate reactions, $\Delta E_i = E_{\text{intermediates}} - E_{reactants}$ can the relative thermodynamic probability of competing reactions be found. Four different quantum chemistry methods were, therefore, applied to try to determine the presence or absence of transitional or intermediate states. The methods partially characterized the potential energy surface computed as a function of the bond distance between the N-atom of the mono-nitrogen oxide (NO or NO_2) and the O-atom of ozone.

The 6-311g (d, p) 5d basis set level of theory was used in all four of the quantum chemical techniques.

2.1 Determination of relative reaction energies, E_r

From application of the DFT and MCSCF methods described in previous work [1] the relative energies, defined as $E_r = E_{\text{final products}} - E_{\text{reactants}}$, for the reactions (1) – (4) were determined by calculating the equilibrium geometries and electronic energies of substrates and final reaction products. These are the oxygen molecule, the ozone molecule and a few nitrogen oxide molecules NO_x, as well as their zero-point vibration energy (ZPE). The following table [1] shows the relative energies ($E_r = E_{\text{final products}} - E_{\text{reactants}}$) and the relative energies corrected for the zero point energy (ZPE) for reactions (1) – (4) calculated at the DFT/B3LYP/6-311G(d,p) and the CASSCF(σ- and π-derived)/6-31G(d,p) levels of theory.

Table 1. The relative energies, $E_r = E_{products} - E_{reactants}$, and relative energies corrected for the zero –point vibrational energy, $E_r^{(ZPE)}$, of the reactions (1)- (4) calculated at the this method.

Reaction	Metod	E_r [kcal/mol]	$E_r^{(ZPE)}$ [kcal/mol]
$NO + O_3 \rightarrow NO_2 + O_2$	DFT/B3LYP	-62.78	-62.31
	CASSCF	-31.36	-30.54
$NO_2 + O_3 \rightarrow NO_3 + O_2$	DFT/B3LYP	-37.56	-38.59
	CASSCF	-15.63	-14.69
$NO_2 + NO_3 \rightarrow N_2O_5$	DFT/B3LYP	-21.62	-16.90
	CASSCF	-	-
$2NO_2 + O_3 \rightarrow N_2O_5 + O_2$	DFT/B3LYP	-59.18	-55.49
	CASSCF	-	-

2.2 Determination of activation energies, E_a

Reactions (1) and (2) above have been computationally modelled assuming a direct reaction of ozone with NO_x proceeding via formation of transition states followed by breaking of the $O\text{-}O_2$ bond according to the following schemes:

$NO + O_3 \rightarrow \{ON\ldots O\ldots O_2\}^{\ddagger} \rightarrow NO_2 + O_2$ (6)

$NO_2 + O_3 \rightarrow \{O_2N\ldots O\ldots O_2\}^{\ddagger} \rightarrow NO_3 + O_2$ (7)

In the present study we applied four different quantum chemical models to characterize the potential energy surface of a system comprising nitrogen oxide reacting with ozone: HF, MP2, DFT/ B3LYP and CCSD [3].

Energy was computed as a function of the distance between the N-atom of the nitrogen oxide and the O-atom of ozone. All calculations were carried out using the Gaussian 03 [4] suite of programs for electronic structure calculations. All calculations were performed using the 6-311g (d, p) basis set.

To compute the potential energy scans, the distance between the N-atom of nitrogen oxides (NO and NO_2) and the O-atom of ozone was systematically varied between 1.25Å and 2.50Å in increments of 0.05Å. At each point, the geometries were optimized using HF, MP2 and B3LYP levels of theory. For calculations using the CCSD quantum chemical method, the structures optimized at MP2 levels of theory were used and only single point calculations were carried out. The optimized geometries were verified as global minima by carrying out the frequency calculations. The geometries with positive frequency values were considered to minima while the geometries with one negative frequency correspond to transition states. The grids were intensified between 1.40Å and 1.80Å to increments of 0.01Å to better locate any transition states.

Following results from these calculations, reactions (1) and (2) were again modeled using the MP2 level of theory but at higher energy scan resolution with varying finer increments down to as low as 0.0001Å and with three different basis sets, namely 6-311G(d,p) , cc-pVDZ and aug-cc-pVDZ.

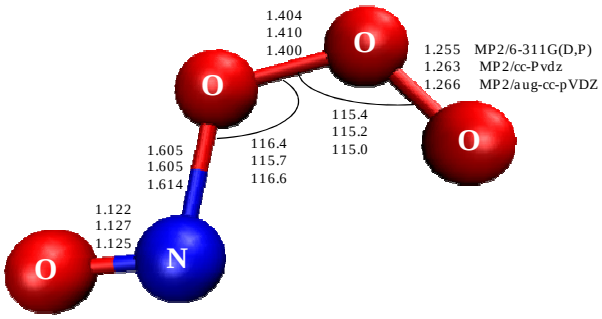
The plots of potential energy vs. N-O bond distance for the reactions of NO and NO_2 with O_3 indicated the presence of transition states in both reactions in the HF, MP2 and CCSD models but no clear indication could be seen in the B3LYP analysis. N-O bond distance for the O_3-NO reaction was indicated at about 1.6 Å by all three positive models while N-O bond distance for the O_3-NO_2 reaction was calculated at 1.6 Å by the MP2 and CCSD techniques and at 1.78 Å by the HF method.

A tentative conclusion could be drawn that the reactions of ozone with nitrogen oxides do not go directly from reactants to products but involve at least one intermediate state. Further analysis would require multi-reference wave functions, such as obtained from CASSCF calculations, and inclusion of dynamical correlations energy via second order multi-reference perturbation theory.

As stated above, in an attempt to better define the potential energy surfaces, the MP2 level of theory was further applied to reactions (1) and (2) with three different basis function sets and finer potential energy scan resolution. Figure 3 shows the potential energy surface for the three basis sets for reaction (1) (NO with O_3) and Figure 4 shows the same for reaction (2)

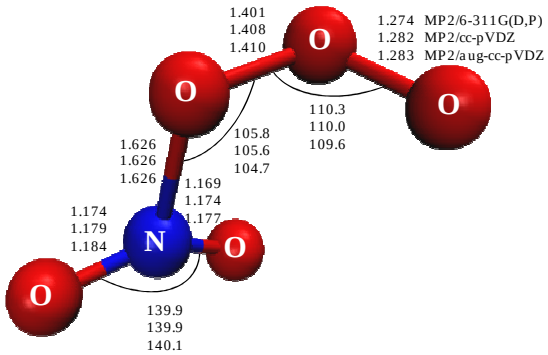
(NO_2 with O_3):

These finer energy scans show the presence of transition states. With respect to reaction (1) of NO with O_3, the MP2/6-311g(d,p) and MP2/cc-pVDZ basis sets show the transition state at an N-O distance of 1.605Å while in the MP2/aug-cc-pVDZ basis set the transition state is at 1.6146Å and, in this case, the transition state is an in-plane type complex Figure1. With respect to reaction (2) of NO_2 with O_3, all three basis sets showed a transition state at an N-O bond distance of 1.626Å in the form of a non-planar complex Figure 2.



Transition State for NO + O_3 reaction

Figure 1. The molecular and transition state geometrical (NO+ O_3) parameters obtained at the MP2/6 311G(d,p) , MP2/cc-pVDZ and MP2/aug-cc-pVDZ levels theory (bond lengths in Å, valence angles in degrees).



Transition State for NO_2 + O_3 reaction

Figure 2. The molecular and transition state geometrical (NO_2 +O_3) parameters obtained at the MP2/6-311G(d,p) , MP2/cc-pVDZ and MP2/aug-cc-pVDZ levels theory (bond lengths in Å, valence angles in degrees).

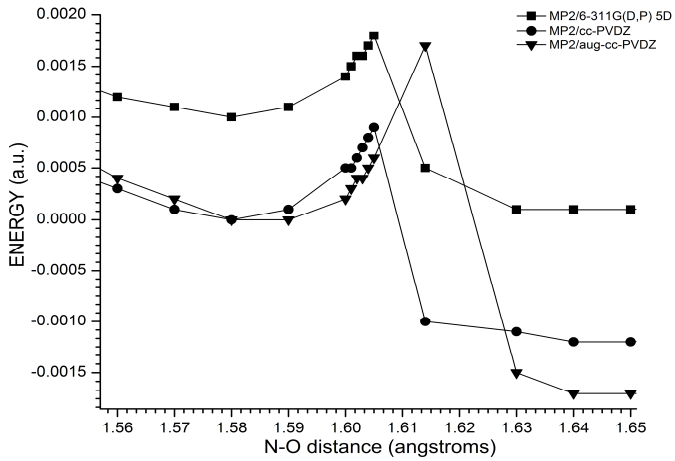


Figure 3. Potential energy vs. N-O distance for the reaction of O_3 with NO modeled using the MP2 level of theory with three basis sets, 6-311G(d,p), cc-pVDZ and aug-cc-pVDZ.

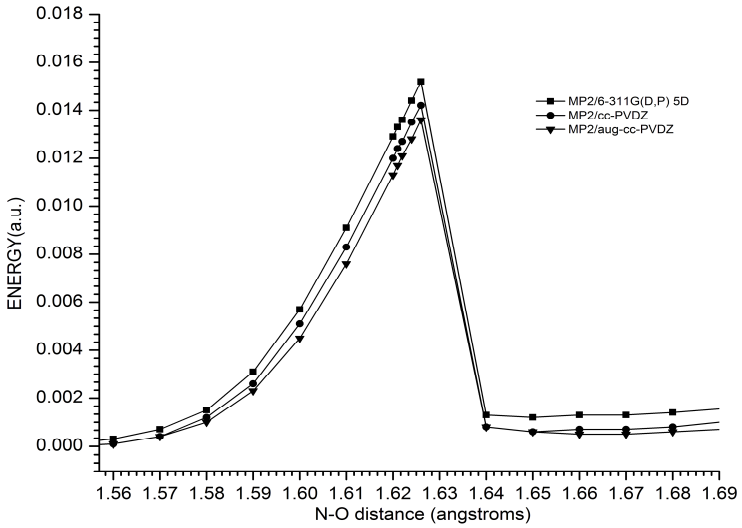


Figure 4. Potential energy vs. N-O distance for the reaction of O_3 with NO_2 modeled using the MP2 level of theory with three basis sets, 6-311G(d,p), cc-pVDZ and aug-cc-pVDZ.

3. Conclusions

The NO_x – O_3 reaction oxidation processes, well known at the molecular level, were modelled by ab initio quantum chemistry methods in an attempt to detect the presence of any transition states and to calculate the relative reaction energy, E_r, and the activation energy, E_a, of each reaction.
For reaction (1), E_a was calculated to be 1.1 kcal/mol for the 6-311G(d,p) basis set, 1.3 kcal/mol for the cc-pVDZ basis set and 2.2 kcal/mol for the aug-cc-pVDZ basis set. This compared reasonably well with the experimental Arrhenius activation energy of 1.2 kcal/mol.

For reaction (2), E_a was calculated to be 8.7 kcal/mol for the 6-311G(d,p) basis set, 8.5 kcal/mol for the cc-pVDZ basis set and 8.2 kcal/mol for the aug-cc-pVDZ basis set, a factor of 4 higher than the experimental Arrhenius activation energy of 2.2 kcal/mol.

4. References

[1] PQS *version 3.1, Parallel Quantum Solutions*, 2013 Green Acres Road, Fayetteville, Arkansas 72703.
[2] *Dalton, a molecular electronic structure program, Release 1.2*, (2001), written by T. Helgaker, H.J.Aa. Jensen, P. Joergensen, J. Olsen, K. Ruud, H. Aagren, A.A. Auer, K.L. Bak, V. Bakken, O. Christiansen, S. Coriani, P. Dahle, E.K. Dalskov, T. Enevoldsen, B. Fernandez, C. Haettig, K. Hald, A. Halkier, H. Heiberg, H. Hettema, D. Jonsson, S. Kirpekar, R. Kobayashi, H. Koch, K.V. Mikkelsen, P. Norman, M.J. Packer, T.B. Pedersen, T.A. Ruden, A. Sanchez, T. Saue, S.P.A. Sauer, B. Schimmelpfennig, K.O. Sylvester-Hvid, P.R. Taylor, and O. Vahtras.
[3] Gaussian 03, Revision V.05, M. J. Frisch et al., Gaussian, Inc., Wallingford, CT, USA , (2004)
[4] Jaroszyńska-Wolińska J. 2010 *Journal of Molecular Structure: THEOCHEM 952 (2010)74-83.*

INVESTIGATION OF A HOMOGENEOUS DISCHARGE GENERATED IN A BARRIER DISCHARGE DEVICE USING ALUMINA

Yoshio Yoshioka[1], Naoki Osawa[1]

[1]*Kanazawa Institute of Technology*
E-mail: yoshioka@neptune.kanazawa-it.ac.jp

Barrier discharges generated in a barrier discharge device using alumina (Kyocera A473) is homogeneous at 60 Hz, and they are generated even in pure oxygen, in which the conventional APTD cannot be generated. However, they become filamentary discharges at 18 kHz. Why such a difference appeared was investigated by various experiments. The experiments were carried out at frequencies less than 1kHz, 18kHz and superimposed 18 kHz on low frequencies. These experiments and calculation showed that at high frequency, a magnitude of displacement current and also the rate of rise the current at the inception of discharge are very large in comparison with those at power frequency. Therefore, release of electrons from the surface of alumina barrier cannot catch up the current to maintain the continuous discharge in the gap. The results suggested that the difference appears due to a difference of current and not to a difference of the frequency.

1. Introduction

Dielectric barrier discharge has a feature that many pulse micro discharges generate between barriers, and so it is called as filamentary discharge (FD). However, in 1988 a group of Sophia University found that a uniform discharge can be generated in He or in Ar at a frequency larger than 1kHz [1]. This homogeneous discharge was recognized as a glow discharge by many researchers, and thereafter it was called as atmospheric pressure glow discharge (APGD). On the other hand, so far it was found that another homogeneous discharge can be generated in pure nitrogen and in a range of power frequency [2]. This discharge is called as atmospheric pressure Townsend discharge (APTD). The difference between APGD and APGD is the current wave form and the gap voltage during discharge. Namely, in APGD, one big pulse current flows in a half cycle and the gap voltage during discharge decreases. In APTD, the current during discharge coincides with the current flowing through the capacitance of barriers and the gap voltage is constant during discharge. The APTD has a feature that during discharge, luminescence of the discharge is big in front of the barrier surface of the anode side.

However, a very small amount of oxygen is added in nitrogen, the APTD changes to FD [3].

In 2009, the authors found that APTD can be generated in air in a frequency range of 32 Hz to 1 kHz if we use alumina (Kyocera A473) plate as barrier [4]. This APTD had a typical features of APTD ever reported, and it is generated in various gases including pure oxygen. It was also found that this APTD is greatly influenced by material components included in alumina. Namely black faced alumina (Kyocera A440) with components of two other metal oxides cannot generate APTD [5]. Besides, it is strange that APTD cannot be generated at a high frequency like 18kHz [5] .If APTD can be generated at a high frequency, much discharge power can be obtained and possibility of the application of this APTD may increase. An objective of this research is to discuss why the APTD using alumina A473 cannot be generated at high frequency ranges.

TABLE 1 Material components of Alumina A473 (Kyocera)

Item	A473 (Kyocera)
tan δ	5×10^{-4}
ε	9.1
Color	White
Main component	Al_2O_3 92%

2. Experimental setup

Fig.1 shows a barrier discharge device (DBD) consists of two alumina (A473) plates with a size of 100mm by 100mm and thickness of 2mm. Tungsten thin electrode with a thickness of 0.01mm and with a size of 80mm by 80mm is implanted into the center of the plate. Gap length is adjusted as 2mm. The DBD is set in a box with width of 240mm, depth of 380mm and height of 270mm. A cross flow fan was set beside the DBD so as to send air to the barrier gap.

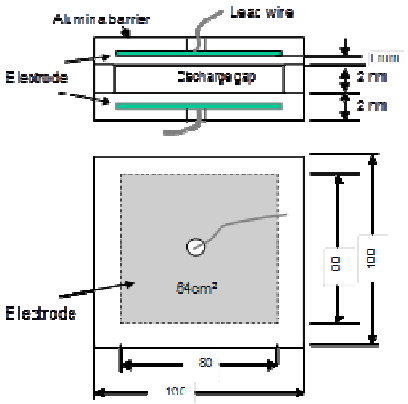


Fig. 1 Barrier discharge device

We used three kinds of high voltage sources. Fig.2 (a) shows a high voltage source generating 50 Hz to 1 kHz AC high voltage. Fig.2 (b) shows a combination circuit of two high voltage sources. Namely the high voltage source of Fig.1 (a) and an inverter neon transformer which generates voltage of 18 kHz are connected in series. The inverter neon transformer can be excited by AC voltage and also by DC voltage. The high voltage source of Fig.2 (b) can be used in two ways; a superimposed mode and a separate mode of single frequency of 18kHz.

Voltage applied to the DBD was measured by using a high voltage divider, and current was measured by using shunt resistor of 105 ohms. The integral of current was measured by using integral capacitor with 44.3nF capacitance.

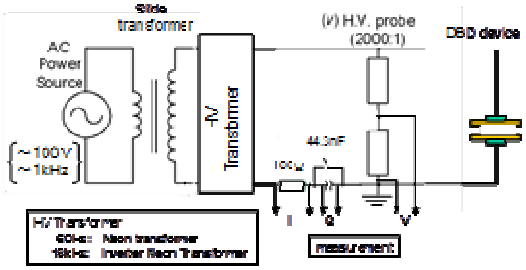


Fig. 2 (a) AC high voltage source

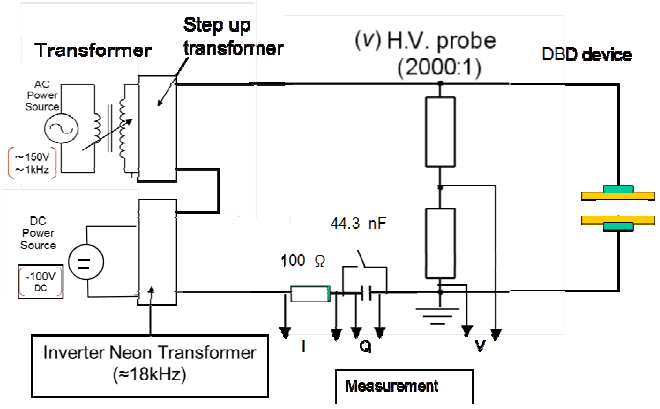


Fig.2 (b) 2 frequency superimposed high voltage circuit

3. Experimental results

3.1 Discharge tests at 60Hz

Using Fig.2 (a) power source, experiments were carried out. With increasing the applied voltage, discharge began at 9.2 kV. Fig.3 shows a typical APTD generated at 14.8kV. A record of current and applied voltage is shown in Fig.4. After discharge initiation, the current increased rapidly and attained to 1.4mA in this case. Discharge maintained until the applied voltage came to its peak. When the applied voltage was further increased, the discharge changed to FD.

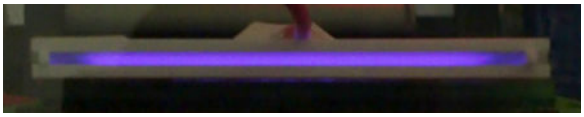


Fig. 3 APTD (60Hz)

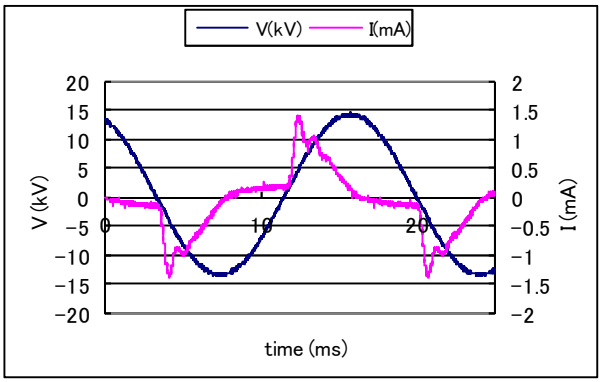


Fig. 4 Oscillogram of APTD (60Hz)

3.2 Discharge test at 18kHz

Using the inverter neon transformer excited by DC voltage, discharge experiments at 18kHz were carried out. Fig.5 shows discharge photograph. The discharge is apparently a filamentary mode. The record of voltage and current is shown in Fig. 6. At around 8kVp, discharge began and current with multi pulses flown, which is a feature of typical FD. The peak current before discharge started was around 20mA.



Fig. 5 Filamentary discharge (18KHz)

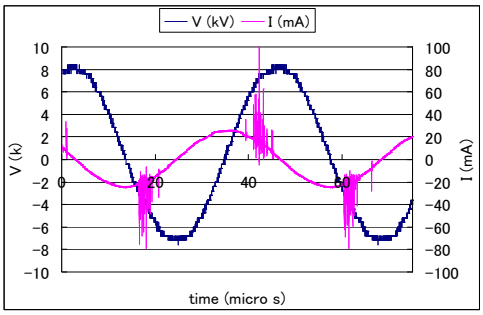


Fig. 6 Oscillogram, FD (18KHz)

3.3 Discharge at a frequency range of 200Hz to 950Hz

In order to investigate the discharge at a frequency between 100Hz and 950Hz, a series of experiments were carried out using the high voltage source of Fig.2 (a). Fig. 7, Fig.8 and Fig.9 show the oscillograms of the experiment of 200Hz, 500Hz and 950Hz respectively. Because of a small capacity of the transformer, the applied voltage wave forms were deformed from the sinusoidal wave. However the APTDs were observed at every frequency. The displacement current increases principally in proportion to the frequency. Therefore, if discharge started at the same applied voltage, the displacement current at the insect of discharge becomes large in proportion to the frequency. From these oscillograms, it is seen that the discharge current was about 4mA at 200Hz, about 9mA at 500Hz and about 16.4mA at 950Hz respectively.

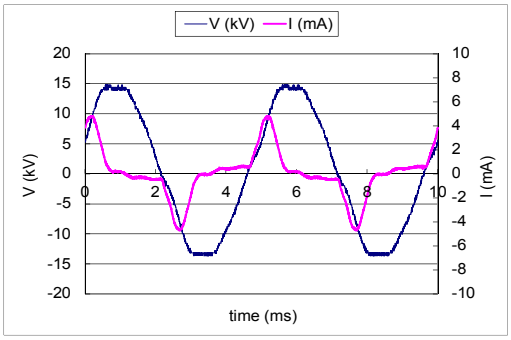


Fig. 7 Oscillogra of APTD (200Hz)

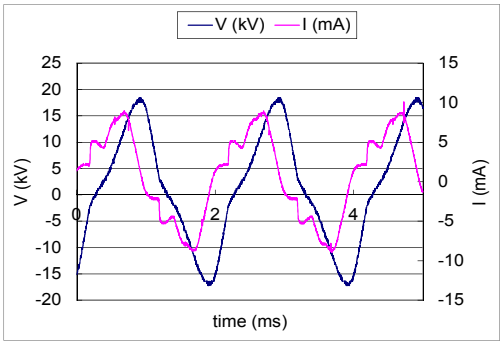


Fig. 8 Oscillogram of APTD (500Hz)

3.4 Discharge experiments at superimposed voltage

As already described, the displacement current when discharge started is very large at 18kHz in comparison with the current at lower frequency. In order to test at intermediate current, we used the two frequency superimposed circuit of Fig.2 (b). Using this circuit and by changing the ratio of superimposition of voltage from two voltage sources, we can change the peak values of discharge current.

Fig. 10 shows an oscillogram of a superimposed voltage test. Although the applied voltage has very small component of 18kHz, a considerable magnitude of the high frequency current is superimposed on 250Hz current. Fig.11 shows an enlargement of a similar oscillogram. The current has projecting parts in every cycle but no pulses are recognized. Therefore this discharge was an APTD. The peak current is around 10mA. Fig.12 shows a case that the discharge is going to change APTD to FD. Among the three cycles in the oscillgram, the middle cycle has three pulse currents and it is different from the current of the other two cycles. It is considered that the discharge in the middle cycle is going to transfer from APTD to FD. Fig.13 shows that a case that the discharge had completely changed to FD. High pulse currents are flowing in

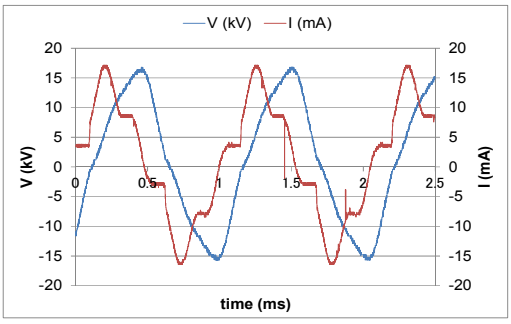


Fig. 9 Oscillogram of APTD (950Hz)

every cycle. In the experiment, the sound generated from the DBD became loud with high frequency components.

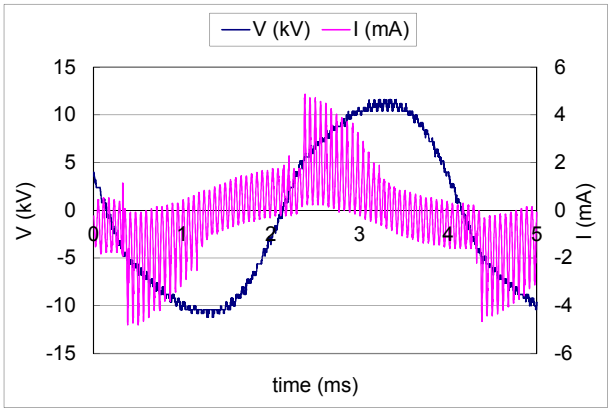


Fig. 10 Oscillogram at a superimposed voltage test(250Hz and 18kHz)

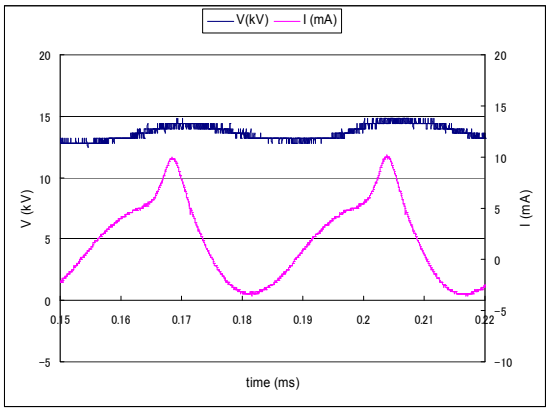


Fig. 11 Enlargement of time scale of Oscillogram of Superimposed voltage test

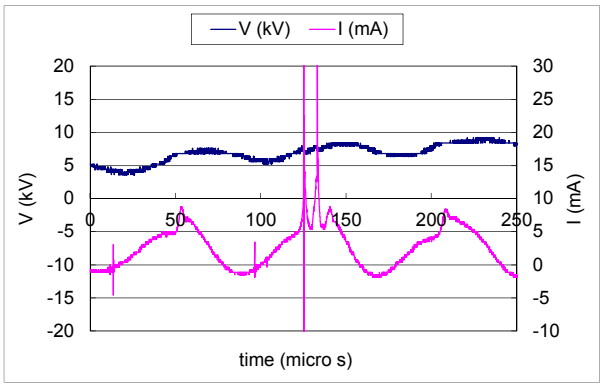


Fig. 12 Boundary between APTD and FD

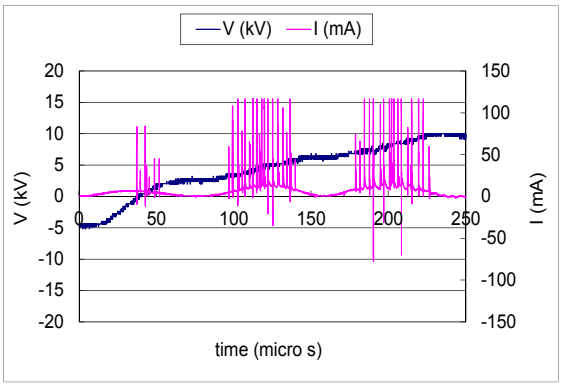


Fig. 13 Oscillgram after a transition to FD

4. Discussion

The objective of this investigation was to find a reason why the APTD cannot be generated at high frequency.We have been considering that the high displacement current at high frequency is a reason to become FD. However, as shown in Fig.9, the APTD was generated at least up to 16.4mA. However, as can be seen in Fig.12 and 13, the discharge changed from APTD to FD at around 10mA or less. Thus a magnitude of current seems to be not a dicisive factor of transition to FD. Instead, a sharp rise of discharge current at high frequency is considered to be a cause of a transition to FD. In order to confirm this idea, the rate of rise of the current was investigated in experiments. Fig.14 shows an oscillogram of 60Hz test. A displacement current without dischrage can be calculated from the voltage waveform, and it is added in the oscillogram.

As can be seen in the figure, we can check the instanteneous current when the discharge started (denoted as Is). After the initiation of discharge, the discharge current increase rapidly. We can also

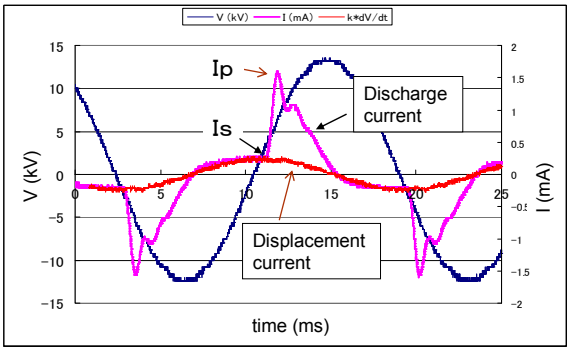


Fig. 14 Distinction between discharge current and displacement current

check the rate of rise of discharge current (dI/dt). The maximum current is denoted here as Ip. Now we can investigate the relation between the discharge mode and these parameters. Table 2 shows the result. APTD generated at the current less than 3.4mA and it was maintained up to 16.4mA. The maximum dI/dt value was 570A/s in the APTD mode. On the otherhand, when high frquency voltage was applied, the dI/dt values are more than 1150 A/s,. The discharge starting currents were less than 10.6mA, but they are larger than those of APTD mode. Since APTD generated in 16.4mA, the current less than 10.6mA is not big enough to prevent a generation of APTD. However, because of a high frequency voltage, after discharge started, the rate of rise of discharge current is large as shown in Table 2. In APTD, enough electrons have to be supplied to sustain the contineous current. If dI/dt becomes too high, the supply of electrons becomes difficult. Therefore, as a concluion, we think the large dI/dt is a reason that the discharges change from APTD to FD at high frequency.

Table 2 Relation between the discharge mode and parameters (Is,Ip and dI/dt)

	Experimental condition		dI/dt (A/s)	Is (mA)	Ip (mAp)	note
	Frq(Hz)	V (kVp)				
1	500	8.8	23	0.91	1.67	APTD
2	950	11.6	257	2.66	9.52	APTD
3	950	16.4	570	3.4	16.4	APTD
4	500+ 18000	Super-impose	1430	11	58.3	FD
5	500+ 18000	Super-impose	3050	6.8	58	FD
6	18000	5.4	1150	10	32.7	FD
7	18000	5.6	1380	10.6	75.4	FD

5.Conclusion

Barrier discharge device using alumina (Kyocera 473) generates atmospheric pressure Townsend discharge (APTD) in various gases. However, it can not be generated at high frequency like 18kHz. In order to find the reason, experiments were carried out in a frequency range of 60Hz to 950Hz, and at 18kHz and also using superimposed volage of 18kHz and lower frequency less than 950Hz.

As a result, the high rate of rise of discharge curent (dI/dt) at high frequency is considered to be a reason that discharge becomes filamentary discharge (FD). In a high frequency experiments of 18kHz, the dI/dt attained to more than 1150A/s, while in the tests at a frequency less than 950Hz, the dI/dt values are less than 570A/s. In a 950Hz experiment, APTD was maintained at a peak current of 16.4mA. Although the discharge started at less than 10mA at high frequency tests, the discharge became FD. Therefore, the magnitude of current seems to be not a decisive parameter of a transition to FD.

The authors acknowledge to Kyocera Company for supplying barrier material.

References

[1] Kanazawa S, Kogoma. M, Moriwaki.T and Okazaki.S, , 1988,J. Phys. D: Appl. Phys., Vol. 21, No. 5, pp.838-840

[2] Massines.F, Gherardi.N, Naudé.N and Ségur.P: 2009,Eur. Phys. J. Appl. Phys, Vol. 47, 22805

[3] Brandenburg.R， Maiorov.V A， Goluvski.Yu Bi、 Wagner.H E, Behnke.J and Behnke.J F, 2005,J of Phys. D: Applied Physics Vol.38, pp2187-2197

[4] Osawa.N, Yoshioka.Y, Mochizuki.Y, Kobayashi.Y, Yamada.Y, Hanaoka.R, Takata.S:, 2009,Proc of the 19th Int. Conf. Plasma Chemistry (ISPC-19), P1.3.02

[5] Osawa N and Yoshioka Y, 2012, IEEE Trans on Plasma Sci., Vol. 40, No. 1, 2-8.

[6] Yoshioka.Y, Osawa.N, 2010, Proceeding, HAKONE, pp94-98

MECHANISTIC STUDIES OF ADVANCED OXIDATION OF BINARY MIXTURES OF ORGANIC POLLUTANTS IN AIR NON-THERMAL PLASMA

Ester Marotta, Milko Schiorlin, Elisa Ceriani, Volodymyr Shapoval, Cristina Paradisi

Department of Chemical Sciences, University of Padova, via Marzolo 1, 35131 Padova, Italy
E-mail: cristina.paradisi@unipd.it

There is a growing interest in exploiting air non-thermal plasmas in novel advanced oxidation processes (AOPs) for the degradation of organic pollutants to be applied both to water and to air decontamination [1]. Specifically, air non-thermal plasma can be developed into a “green” means to activate drastic chemical reactivity: it works at room temperature and at ambient pressure, thus reducing energy costs, and it affords the degradation of any kind of organic pollutants, including those very resistant to oxidation. Therefore, the “green” goal of minimized wastes, i.e. the exhaustive oxidation of organic pollutants to CO_2, also appears to be within reach for this approach. Knowledge of the chemistry involved in these complex systems is obviously essential to master their performance and to optimize the process efficiency and selectivity to CO_2 production. Our research focuses on the chemical aspects of air non-thermal plasma induced oxidation of organic pollutants in air [2-4] and in water directly exposed to the plasma [5,6]. Prototype lab scale plasma reactors have been developed and are used with a wide array of diagnostic tools to study and characterize the process efficiency and selectivity and the plasma short-lived species. Efficiency and selectivity are determined by measuring the decay of pollutant concentration as a function of input energy and the oxidation products and intermediates (FT-IR, gas chromatography, liquid chromatography and ion chromatography). The plasma short lived reactive species are determined by means of optical emission spectroscopy, atmospheric pressure mass spectrometry [7] and specific chemical probes [2,8]. An account will be given of our most recent findings on the reciprocal influence of two different pollutants reacting within the same plasma activated by corona discharges. Such interactions can affect quite significantly the process efficiency. Depending on the specific compounds used, inhibition, entrainment or little or no kinetic effects are observed. Examples will be presented and discussed dealing with the oxidation of organic pollutants in air as well as in water. Specifically it will be shown how the analysis of these two-pollutant reacting systems can provide important insight into which species are involved in the initial step leading to the oxidation of the organic pollutants.

References

[1] Fridman A Plasma Chemistry Cambridge University Press, New York 2008.
[2] Marotta E, Callea A, Ren X, Rea M and Paradisi C 2008 *Plasma Process. Polym.* 5 146-154.
[3] Schiorlin M, Marotta E, Rea M and Paradisi C 2009 *Environ. Sci. Technol.* 43 9386-9392.
[4] Marotta M, Ceriani E, Shapoval V, Schiorlin M, Ceretta C, Rea M and Paradisi C 2011 *Eur. Phys. J. - Appl. Phys.* 55 13811.
[5] Marotta E, Schiorlin M, Rea M and Paradisi C 2010 *J. Phys. D - Appl. Phys.* 43 124011.
[6] Marotta E, Schiorlin M, Ren X, Rea M and Paradisi C 2011 *Plasma Process. Polym.* 8 867-875.
[7] Marotta E and Paradisi C 2010 *J. Am. Mass Spectrom. Soc.* 20 697-707.
[8] Schiorlin M, Marotta E, Kim H-H, Paradisi C and Ogata A 2011 *Plasma Process. Polym.* 8 859-866.

DIELECTRIC BARRIER TOWNSEND DISCHARGE IN AIR AT ATMOSPHERIC PRESSURE

Haiyun Luo [1], Junxia Ran [2], Xinxin Wang [3]

[1] *Department of Electrical Engineering, Tsinghua University, Beijing 100084, China*
E-mail: lhy@tsinghua.edu.cn

Nonthermal plasma produced by homogenous discharge in air at atmospheric pressure has advantages in the industrial application of the plasma surface modification. However, the discharge in atmospheric air usually behaves as filamentary discharge rather than homogenous discharge. It was found that homogeneous discharge can be produced in a 3mm gap of air at atmospheric pressure using two plane parallel electrodes each covered by one specific alumina plate with a thickness of about 2 mm. Based on the discharge photographs of short exposure time taken with an ICCD camera, the homogenous discharge was identified with Townsend discharge. The Townsend breakdown voltage for this 3mm air gap is about 8.3 kV, significantly lower than 11.2 kV, the streamer breakdown voltage of this gap. If the alumina plate is too thin, the discharge transits to filamentary discharge. If it is too thick, the discharge is too weak to observe. The uniqueness of the shallow traps on the surface of the specific alumina plate and the common effect of the current limitation by dielectric work together, leading to a Townsend discharge. The detail mechanisms for the formation of Townsend discharge are still under investigation.

1. Introduction

Dielectric barrier discharge (DBD) in air at atmospheric pressure normally occurs in a large number of short-lived and narrow current filaments that are randomly distributed in time and space over the dielectric surface [1]. Non-thermal plasma produced by homogeneous DBD in air is most attractive for the industrial applications. However, the realization of homogeneous DBD is usually much more difficult in air than in noble gases and other gases. Air is an electronegative gas consisting of oxygen, nitrogen and water vapour. The oxygen molecules in air efficiently quench nitrogen metastable species and tend to induce electron attachments in air discharges, so the DBD atmospheric-pressure air usually exhibits a filamentary mode. In recent years, the generation of homogeneous DBD in atmospheric air is one of the most remarkable research works in the plasma field. For obtaining a homogeneous DBD in atmospheric air, many methods and special barrier materials have been explored. [2–9]. Ráheľ J found within the frequency range 1~15 kHz, discharge gaps smaller than 1.5mm a diffuse discharge could be obtained in air at at atmospheric pressure[2-3]. Garamoon A A and El-zeer D M found a uniform discharge can be obtained with a frequency 50 Hz and a gap distance 1.1mm[4]. Up to now, there was no report of a homogeneous DBD in atmospheric-pressure air with a gap distance larger than 2mm in high frequency.

In this paper we firstly report a homogenous DBD in as larger as 3 mm air gap at atmospheric pressure. Experimental setup, the generation and diagnostics of the discharge were introduced, and the discussion focus on the effect of the ceramic.

2. Experimental Setup

The arrangement of the experimental was similar to our previous works[6], shown in Figure 1. Ceramic plates with various thicknesses between 0.5~3.25mm were chosen as the dielectric barriers. The air gap d is fixed at 3mm. A sinusoidal high voltage with a frequency that could be continuously changed from 1k~10 kHz was applied to the electrodes. An intensified-CCD- camera was used to take the discharge photographs with an exposure time down to 10 ns.

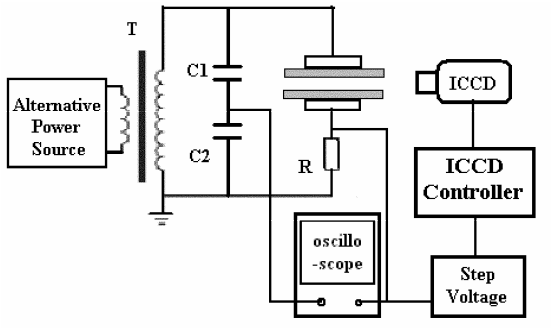


Figure 1. Schematic diagram for the experimental system

3. Results and Discussions

3.1 Generation of the homogeneous DBD in air

It showed that when the barrier thickness was smaller than 1.5mm, a mixed mode of diffuse and filamentary discharge was found and the current shown many short-pulse per half cycle of the applied voltage. For example, when the barrier thickness was 0.5mm, the filamentary discharge is very intensity and its current pulse is un-orderly. With the barrier thickness increasing, the filaments began to decreasing. When the barrier thickness was greater than 1.5mm, the filaments disappeared and a stable homogeneous discharge was produced. It was characterized by one current pulse per half cycle of the applied voltage.

3.2 The characteristic of the homogeneous DBD

In order to investigating the discharge characteristic of the homogeneous discharge, the time resolution photograph was measured by ICCD with a gap distance 3mm and ceramic plate thickness 2.285mm.

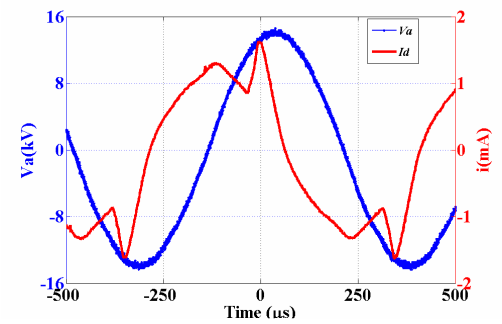


Figure 2. Applied voltage(*Va*) and total current(*I*)



Figure 3. Side-view photograph of the discharge

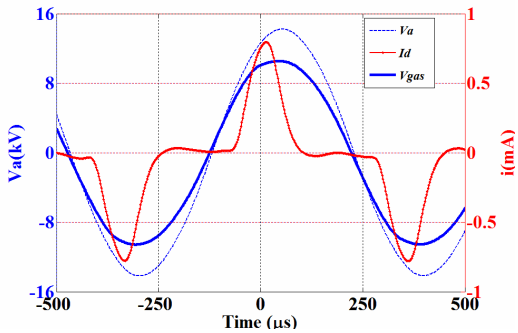


Figure 4. Calculated discharge current *Id* and gap votlage *Vgas*

In order to obtain bigger current the applied frequency f is 1.32kHz. the typtical waveform was shown in Figure 2. Side-view photographs with 10 ns exposure time taken at the time about the peak of the current pulse showed that there were no filaments in the discharge gap. A luminous layer close

to the instantaneous anode was observed, indicating the homogeneous DBD was a Townsend discharge, as shown in Figure 3.By subtracting the displacement current from the total current, the discharge current and gap voltage was calculated. It was shown in Figure 4. It appears one current peak per half cycle of the applied sinusoidal voltage, which was typical for homogeneous DBD. The current peak was 1 mA in amplitude and about 85μs in FWHM (full width at half magnitude). The breakdown voltage was determined to be only 8.3 kV, much lower than the static breakdown voltage of 11.2 kV for the same air gap of 3 mm in length.

The results prove a stable homogeneous discharge in air at atmospheric pressure was a Townsend discharge. It was suggested that the unique feature of the shallow traps on the surface of the specific ceramic plate and the common effect of the current limitation by dielectric barrier play important roles in the formation of the Townsend discharge. The details of the mechanism for the Townsend discharge were still under investigation.

3.3 The influence of ceramic plate

The Townsend discharge can only be produced under the condition that both electrodes were covered by a specific ceramic plate with a thickness of about 2 mm. If the ceramic plate was too thin, the discharge would transit to filamentary discharge. If the ceramic plate was too thick, the Townsend discharge would be too weak to observe. The formation of Townsend discharge in air was attributed to that the release of the shallowly trapped electrons on the surface of the dielectric covering the cathode provide the discharge with a limited amount of the seed electrons, which leaded to an extraordinary extinction of the Townsend discharge and made the glow discharge not to be reached. Our next step is to do some diagnostics of the ceramic surface.

4. Conclusions

Homogenous Townsend dielectric barrier discharge (DBD) in atmospheric-pressure air was generated in 3 mm air gap. Ceramic plates as the barrier material had great impact on generating homogenous Townsend DBD. Next work was to do on the ceramic and the mechanism for the Townsend discharge .

5. References

[1] Kogelschatz U, “Dielectric-barrier Discharges: Their History, Discharge Physics, and Industrial Applications”, Plasma Chemistry and Plasma Processing Vol. 23, No. 1, pp.1-46, 2003.

[2] Ráheľ J, Sherman D M, “The transition from a filamentary dielectric barrier discharge to a diffuse barrier discharge in air at atmospheric pressure” J. Phys. D: Appl. Phys., Vol.38, No.4, pp. 547-554, 2005.

[3] Rahel J, Sira M, Stahel P, Trunec D., “The Transition Between Different Discharge Regimes in Atmospheric Pressure Air Barrier Discharge”, Contrib. Plasma Phys. vol.47,No.1-2, pp. 34-39,2007.

[4] Garamoon A A, El-zeer D M, “Atmospheric pressure glow discharge plasma in air at frequency 50 Hz”, Plasma Sources Sci. Technol. Vol.18, pp.0450064 , 2009.

[5] Fang Z, Qiu Y, Zhang C and Kuffel E “Factors influencing the existence of the homogeneous dielectric barrier discharge in air at atmospheric pressure”, J. Phys. D: Appl. Phys. Vol.40,No.140,pp.1–7 , 2007.

[6] Wang X, Luo H, Liang Z, Mao T and Ma R, “Influence of wire mesh electrodes on dielectric barrier discharge” , Plasma Sources Sci. Technol. Vol.15 No.4, pp.845–8, 2006.

[7] Okazaki S, Kogoma M, Uehara M and Kimura Y, “Appearance of stable glow discharge in air, argon, oxygen and nitrogen at atmospheric pressure using a 50 Hz source”, J. Phys.D: Appl. Phys.Vol. 26,No.5, pp. 889–892,1993

[8] Tepper J and Lindmayer M Proc., “Investigations on two Different Kinds of Homogeneous Barrier Discharges at Atmospheric Pressure”, HAKONE 7th Int.Symp. High Pressure Low Temperature Plasma Chemistry (Greifswald, 10–13 September 2000) vol.1 pp. 38, 2000

[9] Kruger C H, Laux C O, Yu L, Packan D M and Pierrot L , “Nonequilibrium discharges in air and nitrogen plasmas at atmospheric pressure”, Pure Appl. Chem. Vol. 74, No. 3, pp. 337–347, 2002.

AUTHOR INDEX

A
Agarwal B. 6
Aitken F. 28
Aoqui S. 23, 205
Arkhipenko V. I. 248
Atrazhev V.M. 28

B
Baba S. 144
Becker K. 6
Bogaczyk M. 33, 129
Bonifaci N. 28
Bradu C. 195
Brandenburg R. 38, 134, 139, 175, 180

C
Chmielewski A. G. 258
Colasuonno M. 149
Costacurta S. 149
Czajkowska D. 79, 243

D
Danko M. 225
Ceriani E. 323
Diatczyk J. 308
Dors M. 43, 48, 79
Duten X. 116
Dziadczyk P. 243

E
Ebert U. 10
Ebihara K. 144
Edtbauer A. 6
Elias M. 279
Eloranta J. 28
Erme K. 58

F
Fabianowski W. 243
Fantin M. 149
Favaro M. 149
Feil S. 6
Furukawa J. 205

G
Gambirasi A. 149
Gericke K. H 63
Giżewski T. 308
Gosteyev S. G. 99
Gręda K. 160

H
Haeften K. von 28
Haidacher S. 6
Hajduk M. 284
Haljaste A. 58
Hanaoka R. 94
Hanel G. 6
Hänsch M. 180
Hartungen E. 6
Hashimoto Y. 144
Hassouni K. 116
Hensel K. 73
Hoder T. 38, 134
Höft H. 38
Hołub T. 155
Hrycak B. 79

I
Ihara S. 121
Ikegami R. 210
Ikegami T. 144
Itoh H. 220, 263
Iwasaki F. 210
Izdebski T. 43, 48

J
Jaksch S. 6
Jakubowski T. 155
Jamróz P. 160
Janda M. 185
Janowski W. 308
Jaroszyńska-Wolińska J. 313
Jasek O. 279
Jasiński M. 79
Jia Z. 116
Jodzis S. 53, 165
Jõgi I. 58, 238
Jordan A. 6
Jürschik S. 6

K
Kalisiak S. 155
Kanazawa S. 170
Kashiwagi Y. 263
Kawasaki H. 23, 205
Kawasaki T. 23, 205
Kettlitz M. 38
Kirillov A. A. 248
Klett C. 116
Kloc P. 279
Kocik M. 43, 170

Kolacinski Z. 1, 268
Kolb T. 63
Komarzyniec G. 303
Kosik A. 289
Koskulics J. 134
Kovačević V. V. 175, 180, 253
Kozlov K. V. 111
Krawczyk K. 68, 84, 243, 284, 289
Krstić I. B. 253
Kuca B. 289
Kuraica M. M. 175, 180, 253
Kwiatkowski M. P. 121

L

Laan M. 58, 238
Lacoste D. A. 185
Laux C. O. 185
Lukeš P. 73
Luo H. 324

M

Machala Z. 73, 185, 190
Magureanu M. 195
Majdak M. 89, 200
Mandache N. B. 195
Märk L. 6
Märk T. D. 6
Marotta E. 323
Masanori N. 121
Matejčík S. 220, 225
Mayhew C. A. 6
Mazankova V. 279
Meichsner J. 215
Mitin A. N. 111
Mitsugi F. 23, 144, 205, 210
Mizeraczek J. 43, 48, 79, 170
Młotek M. 68, 84, 284, 289
Musiał M. 284

N

Nakamiya T. 210
Nakamura N. 144
Nemschokmichal S. 215
Nguyen H. van 28
Nijdam S. 10
Nogal Ł. 289

O

Obradović B. M. 175, 180, 253
Oehmigen K. 139
Ohshima T. 23, 205
Okuyama Y. 220
Opalińska T. 89, 200
Országh J. 225
Osawa N. 94, 318

P

Paradisi C. 323
Parvulescu V. 195
Patelli A. 149
Pawelska E. 84
Pawłat J. 144, 308
Petersson F. 6
Piechna J. 89
Pipa A.V. 134
Piroi D. 195
Pohl P. 160
Ponizovsky A. Z. 99
Prantsidou M. 104
Pryciak K. 68

R

Ran J. 324
Raniszewski G. 228, 233, 268
Raud J. 238
Ribar A. 225
Rżanek-Boroch Z. 243

S

Sabo M. 220
Saburoh S. 121
Samoń R. 308
Sato T. 170
Schiorlin M. 323
Schmidt-Szałowski K. 68, 84, 284, 289
Schottkovsky R. 6
Scopece P. 149
Seehauser H. 6
Selerowicz W. 89
Shapoval V. 323
Šikurová L. 73
Simonchik L. V. 248
Šipoldová Z. 190
Sokolova M.V. 111
Sonoda Y. 210
Špetlíková E. 73
Sretenović G. B. 129, 175, 180, 253
Stancu G. D. 185
Stollenwerk L. 294
Stryczewska H. D. 144, 205, 308
Sulzer P. 6
Sun Y. 258
Sung T. L. 144
Suzuki S. 263
Szymanski L. 268, 274

T

Takashi A. 94
Tarabová B. 73

Tatarenko P. A. 111
Teii S. 144
Touchard S. 116
Trunec D. 279
Tsuda R. 210

U
Ulejczyk B. 68, 84, 284, 289

V
Vega-Gonzalez A. 116
Veldhuizen E.M. van 10
Vermeulen G. 28
Voigt J. H. 63

W
Wagner H. E. 33, 129
Wang X. 324
Weltmann K. D. 38, 139
Whitehead J. C. 104
Wild R. 294
Wnęk B. 89, 200, 284
Woedtke T. von 139, 180

Y
Yamabe C. 121
Yamashita Y. 144
Yasuoka K. 15
Yoshioka Y. 94, 318

Z
Zajickova L. 279
Zgirouski S. M. 248
Zvereva G. 299
Żyrnicki W. 160

ISBN 978-83-62596-99-7